

Bottom-up Solution Synthesis of Structurally Defined Graphene Nanoribbons

Dissertation

zur Erlangung des Grades

„Doktor der Naturwissenschaften“

im Fachbereich Chemie, Pharmazie, und Geowissenschaften der
Johannes Gutenberg-Universität Mainz und in Kooperation mit
dem Max-Planck-Institut für Polymerforschung Mainz

vorgelegt von

Akimitsu Narita

geboren in Yokohama / Japan

Mainz, 2014

Dekan: Prof. Dr.

1. Berichterstatter: Prof. Dr.

2. Berichterstatter: Prof. Dr.

Tag der mündlichen Prüfung:

Die vorliegende Arbeit wurde in der Zeit von April 2010 bis November 2013 im Max-Planck-Institut für Polymerforschung in Mainz unter der Betreuung von [REDACTED] durchgeführt.

Ich danke [REDACTED] für seine wissenschaftliche und persönliche Unterstützung sowie für seine ständige Diskussionsbereitschaft.

Table of Contents

Abbreviations.....	VIII
Chapter 1. Introduction.....	1
1.1. Graphene.....	2
1.2 Graphene Nanoribbons (GNRs)	6
1.2.1 “Top-down” fabrications of GNRs.....	6
1.2.2 “Bottom-up” syntheses of GNRs	10
1.3 Raman spectroscopy of graphene and related materials.....	25
1.4 THz spectroscopy	26
1.5 Field-effect transistor	28
1.6 Motivation and objectives.....	30
1.7 References	35
Chapter 2. Laterally Extended GNRs via <i>Yamamoto</i> Polymerization	47
2.1 Laterally extended GNRs with a mixture of cove and armchair edge structures.....	47
2.1.1 Synthetic strategy	47
2.1.2 Investigation of a monomeric model system.....	48
2.1.3 Fabrication of laterally extended GNRs.....	51
2.1.4 Preliminary attempt for processing laterally extended GNRs.....	62
2.1.5 Summary	64
2.2 $N = 18$ armchair GNRs	65
2.2.1 Synthetic strategy	65
2.2.2 Investigation of a monomeric model system.....	67
2.2.3 Fabrication of $N = 18$ armchair GNRs	70
2.2.4 Fabrication of FETs with the $N = 18$ armchair GNRs.....	80
2.2.5 Summary	83
2.3 References	84
Chapter 3. Liquid-Phase-Processable and Structurally Well-Defined GNRs with High Longitudinal Extension	89
3.1 Synthetic strategy	89
3.2 Investigation of model systems.....	93
3.2.1 Synthesis and characterization of dimer 3-5	94
3.2.2 Synthesis and characterization of trimer 3-7	97

3.3 Synthesis of longitudinally extended GNRs via <i>Diels–Alder</i> polymerization	100
3.3.1 Synthesis of <i>AB</i> -type monomer 3-1	100
3.3.2 <i>AB</i> -type <i>Diels–Alder</i> polymerization	101
3.3.3 MALDI-TOF MS analysis of precursor 3-2	103
3.3.4 SEC analysis of precursor 3-2	105
3.3.5 Photon correlation spectroscopy analysis of precursor 3-2	108
3.3.6 Limiting factors for the polymer growth	112
3.3.7 “Graphitization” and “planarization”	112
3.4 Characterizations of the GNRs	115
3.4.1 FTIR spectroscopy	115
3.4.2 Raman spectroscopy	116
3.4.3 NMR spectroscopy	119
3.4.4 UV–vis absorption spectroscopy and DFT calculation	121
3.4.5 Liquid-phase processing and STM visualization	122
3.5 Investigation of electronic properties by THz spectroscopy	129
3.5.1 THz spectroscopy on GNR 3-3 in dispersions	129
3.5.2 THz spectroscopy on a solid film of GNR 3-3	131
3.5.3 THz spectroscopy on dimer 3-5	133
3.6 GNRs with enhanced solution processability	134
3.6.1 Synthesis of GNRs with bulkier side chains	134
3.6.2 Spectroscopic characterizations of GNR 3-26	139
3.6.3 AFM visualization of GNR 3-26	141
3.7 Edge chlorination of structurally defined GNRs	146
3.7.1 Design for the edge chlorination of GNRs	146
3.7.2 Synthesis of GNR 3-32 with <i>tert</i> -butyl groups	147
3.7.3 Edge chlorination of GNR 3-32 with <i>tert</i> -butyl groups	153
3.8 Preliminary investigations on the transport properties of the GNRs	156
3.8.1 FET devices on GNR films	156
3.8.2 GNRs with acetylthio groups at the termini	159
3.9 Photovoltaic devices with GNRs in an active layer	163
3.10 Attempts on the surface-assisted fabrication of GNRs via <i>Diels–Alder</i> polymerization	165
3.11 Summary	167
3.12 References	168

Chapter 4. Laterally and Longitudinally Extended GNRs with Liquid-Phase Processability	175
4.1 Synthetic strategy	175
4.2 Synthesis of broad and long GNRs	178
4.2.1 Synthesis of laterally extended <i>AB</i> -type monomers.....	178
4.2.2 <i>Diels–Alder</i> polymerization	179
4.2.3 Isolation of small oligomers	188
4.2.4 “Graphitization” of the polyphenylene precursors.....	191
4.3 Characterization of broad and long GNRs	193
4.3.1 FTIR spectroscopy	193
4.3.2 Raman spectroscopy.....	194
4.3.3 UV–vis absorption and photoelectron spectroscopy and DFT calculation ..	195
4.3.4 AFM visualization.....	196
4.4 Investigation of photoconductivities by THz spectroscopy	200
4.5 Summary	202
4.6 References	203
Chapter 5. Conclusion and Outlook.....	205
5.1 Conclusion.....	205
5.2 Outlook.....	209
Chapter 6. Experimental Part.....	213
6.1 General	213
6.1.1 Materials.....	213
6.1.2 General methods.....	213
6.2 Analytical techniques	214
6.2.1 Mass spectrometry.....	214
6.2.2 NMR spectroscopy	214
6.2.3 Elemental analysis.....	215
6.2.4 UV–vis absorption spectroscopy.....	215
6.2.5 Photoluminescence spectroscopy	215
6.2.6 FTIR spectroscopy	216
6.2.7 Raman spectroscopy.....	216
6.2.8 Photoelectron spectroscopy	216
6.2.9 Size-exclusion chromatography analysis	216
6.2.10 Photon correlation spectroscopy	217

6.2.11 STM visualization.....	217
6.2.12 AFM visualization.....	218
6.2.13 THz spectroscopy.....	218
6.2.14 Determination of the concentration of GNR dispersions.....	219
6.2.15 DFT calculation.....	219
6.2.16 Fabrications and characterizations of FET devices.....	219
6.2.17 Fabrications and characterizations of photovoltaic devices.....	220
6.3 Synthetic procedures.....	221
6.3.1 Synthesis of laterally extended GNR 2-3	221
6.3.2 Synthesis of PAHs 2-19 and 2-20	222
6.3.3 Synthesis of $N = 18$ armchair GNR 2-13	225
6.3.4 Synthesis of dimer 3-5	225
6.3.5 Synthesis of trimer 3-7	229
6.3.6 Synthesis of GNR 3-3 with dodecyl chains.....	235
6.3.7 Synthesis of GNR 3-26 with 2-decyltetradecyl chains.....	239
6.3.8 Synthesis of chlorinated GNR 3-33	245
6.3.9 Synthesis of GNR 3-43 with acetylthio groups.....	250
6.3.10 Synthesis of AB-type monomer 3-47	253
6.3.11 Synthesis of laterally extended GNR 4-3a with dodecyl chains.....	255
6.3.12 Synthesis of laterally extended GNR 4-3b with 2-decyltetradecyl chains.....	262
6.4 References.....	268
List of Publications.....	271
Curriculum Vitae.....	273
Acknowledgements.....	275

Abbreviations

AFM	atomic force microscopy
ARPES	angle-resolved photoelectron spectroscopy
a.u.	arbitrary unit
CNT	carbon nanotube
COSY	correlation spectroscopy
CVD	chemical vapor deposition
d	doublet (NMR)
DFT	density functional theory
DLS	dynamic light scattering
DP	degree of polymerization
ESI	Electrospray ionization
DMF	<i>N,N</i> -dimethylformamide
FD MS	field-desorption mass spectrometry
FET	field-effect transistor
FTIR	Fourier transform infrared (spectroscopy)
FWHM	full width at half maximum
GNR	graphene nanoribbon
GO	graphene oxide
GONR	graphene oxide nanoribbon
HBC	hexa- <i>peri</i> -hexabenzocoronene
HOMO	highest occupied molecular orbital
HOPG	highly oriented pyrolytic graphite
L	length (average)
l_k	Kuhn segment length
l_p	persistence length
LUMO	lowest unoccupied molecular orbital
LSI	large-scale integrated circuit
m	multiplet (NMR)
M_n	number-average molecular weight
M_p	peak molecular weight
M_w	weight-average molecular weight
MALDI	matrix-assisted laser desorption/ionization

MAS	magic angle spinning
MeOH	methanol
MP	melting point
MS	mass spectrometry
MWCNT	multiwalled carbon nanotube
NIR	near infrared
NMP	<i>N</i> -methylpyrrolidone
NMR	nuclear magnetic resonance
NOESY	nuclear Overhauser enhancement spectroscopy
ODCB	<i>ortho</i> -dichlorobenzene
PAH	polycyclic aromatic hydrocarbon
PDI	polydispersity index
PPP	poly(<i>para</i> -phenylene)
PS	poly(styrene)
R_g	radius of gyration
R_h	hydrodynamic radius
rGO	reduced graphene oxide
rpm	rounds per minute
s	singlet (NMR)
SEC	size-exclusion chromatography
SEM	scanning electron microscopy
SiC	silicon carbide
SLS	static light scattering
SPM	scanning probe microscopy
STM	scanning tunneling microscopy
STS	scanning tunneling spectroscopy
t	triplet (NMR)
TBAF	tetra- <i>n</i> -butylammonium fluoride
TCB	1,2,4-trichlorobenzene
TCNQ	7,7,8,8-tetracyanoquinodimethane
TFA	trifluoroacetic acid
THF	tetrahydrofuran
THz	terahertz
TIPS	triisopropylsilyl
TLC	thin-layer chromatography

TMS	trimethylsilyl
TOF	time of flight
TPa	terapascal
TTF	tetrathiafulvalene
UHV	ultrahigh vacuum
UV–vis	ultraviolet–visible (absorption spectroscopy)

Chapter 1. Introduction

We have experienced dramatic advances in the semiconductor and large-scale integrated circuit (LSI) technologies over the recent decades. In 1971, the first commercialized processor “Intel 4004” included only 2300 transistors, operating at a clock frequency of 108 kHz.¹ After 37 years, in 2008, the processor “Core i7” commercialized by the same company contained ca. 730,000,000 transistors and reached the maximum operating frequency of 3.6 GHz. Such drastic advancement was possible thanks to the exponential improvement of silicon-based LSI technologies in accordance with Moore’s law, i.e. the number of transistors in a same area of substrates doubled approximately every two years. However, such ceaseless progress in the performance of LSIs, which has been predominantly achieved by the miniaturization of field-effect transistors (FETs), is approaching its limit. It is expected that further improvement of the performance will be achievable by scaling the linewidth down to ca. 10 nm through new lithographic processes as well as by adopting novel device structures such as three-dimensional integration.²⁻⁶ Nevertheless, ~5 nm will presumably be the ultimate limit of the linewidth due to the overwhelming off-leakage current by source-to-drain tunneling.⁷⁻⁹

In order to circumvent this limitation of the silicon-based technology and further improve the performance of LSIs, other semiconducting materials with higher charge-carrier mobilities are attracting an increasing attention as substitute channel materials, which can potentially improve the LSI performance without scaling down the linewidth. Currently, SiGe, Ge, and III–V materials such as InGaAs, GaAs, and GaN are considered as most promising next-generation semiconductor materials. For instance, GaAs shows an electron mobility of ~8,600 cm²/V·s, which is approximately six times higher than that of silicon, i.e. ~1,350 cm²/V·s. Meanwhile, unprecedented preparation of a thin layer graphene was reported in 2004 by *Geim* and *Novoselov*, demonstrating its high mobility of ~10,000 cm²/V·s.¹⁰ Following experiments further revealed an exceptionally high mobility of a single-layer graphene, reaching as high as ~200,000 cm²/V·s, when suspended above a Si/SiO₂ substrate.¹¹⁻¹³ This remarkably high mobility of graphene with other fascinating properties has rendered graphene and its nano-stripe analogues, graphene nanoribbons, one of the most promising materials for the development of future nanoelectronics.

1.1. Graphene

Graphene, i.e. two-dimensional allotrope of carbon and one layer of graphite, has been a target of theoretical studies for more than 60 years.¹⁴⁻¹⁸ However, the feasibility of free-standing graphene was doubted until the unexpected preparation of stable single- to few-layer graphene by *Geim* and *Novoselov* in 2004 (Figure 1-1).^{10,19,20} They have demonstrated the facile and reliable preparation method for high-quality graphene, simply by peeling off highly oriented pyrolytic graphite (HOPG) with a regular adhesive tape (mechanical exfoliation) (Figure 1-2a).^{10,21} This simplicity of the method allowed a great number of researchers throughout the world to follow up their experiments. It was subsequently revealed that the single-layer graphene shows a quantum Hall effect even at room temperature,^{22,23} and its electron transport conforms to relativistic Dirac's equation rather than to the non-relativistic Schrödinger equation.²⁴ Further, mobility of as high as 200,000 cm²/V·s was measured by suspending graphene ca. 150 nm above a Si/SiO₂ gate electrode.¹¹ Graphene transistors with an intrinsic cut-off frequency of as high as ca. 300 GHz has already been achieved with a channel length of 140 nm.²⁵ Graphene has also revealed other exceptional physical properties such as high thermal conductivity of 3,000–5,000 W/mK,^{26,27} remarkably high Young's modulus of ~1 TPa and intrinsic tensile strength of ~130 GPa,²⁸ as well as high transparency of 97.7% to incident light for wide wavelength range.^{29,30} In 2010, *Geim* and *Novoselov* were awarded the Nobel Prize in physics for their groundbreaking experiments regarding the two-dimensional material graphene, which further boosted the research activities in the graphene field.^{31,32}

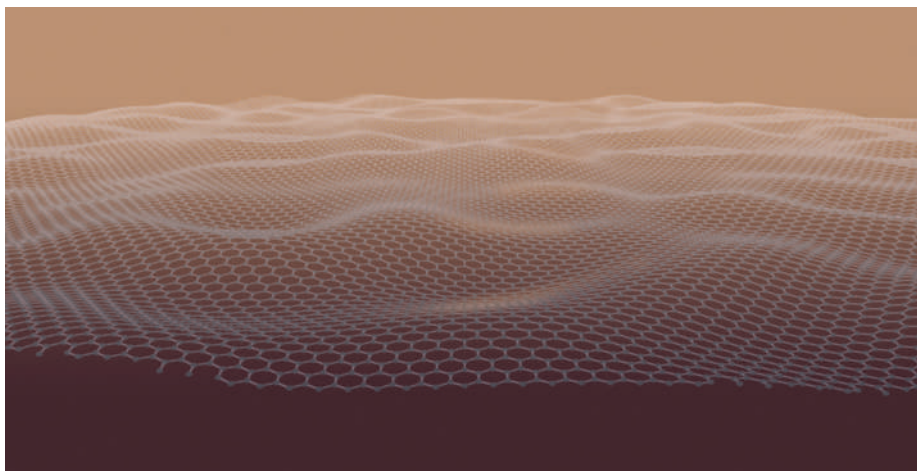


Figure 1-1. Schematic structure of graphene. Reprinted with permission from Ref. [31]; Copyright 2011, Nature publishing group.

Although the mechanical exfoliation provides facile and reliable access to high-quality graphene, this method is incapable of large-scale preparation, making it imperative to develop other scalable methodologies for practical applications. One alternative way is to exfoliate graphite in a liquid phase through ultrasonic cleavage, which provides a stable dispersion of single- to few-layer graphene (Figure 1-2b).^{33,34} Such dispersion of graphene allows liquid-phase processing to prepare graphene films by standard deposition methods such as drop-casting and spin-coating, as well as arbitrary patterning of graphene by means of inkjet printing.³⁵⁻³⁷

Another way is to oxidize graphite to prepare graphite oxide, which was first reported in 1859 by *Brodie* through repeated treatments with a mixture of fuming nitric acid and potassium chlorate.³⁸ Safer and more efficient oxidation method of graphite was established in 1958 by *Hummers* and *Offeman*, using a mixture of concentrated sulfuric acid, sodium nitrate, and potassium permanganate.³⁹ This so-called Hummers method is currently the most ubiquitously employed method for the preparation of graphite oxide. Graphite oxide can be readily and fully exfoliated into single-layer graphene oxide (GO) by sonication in water or in organic solvents such as *N,N*-dimethylformamide (DMF) and tetrahydrofuran (THF).^{40,41} GO can thus be deposited from a liquid phase on a variety of substrates and over large areas.⁴² However, GO does not preserve the fascinating electronic properties of graphene and is

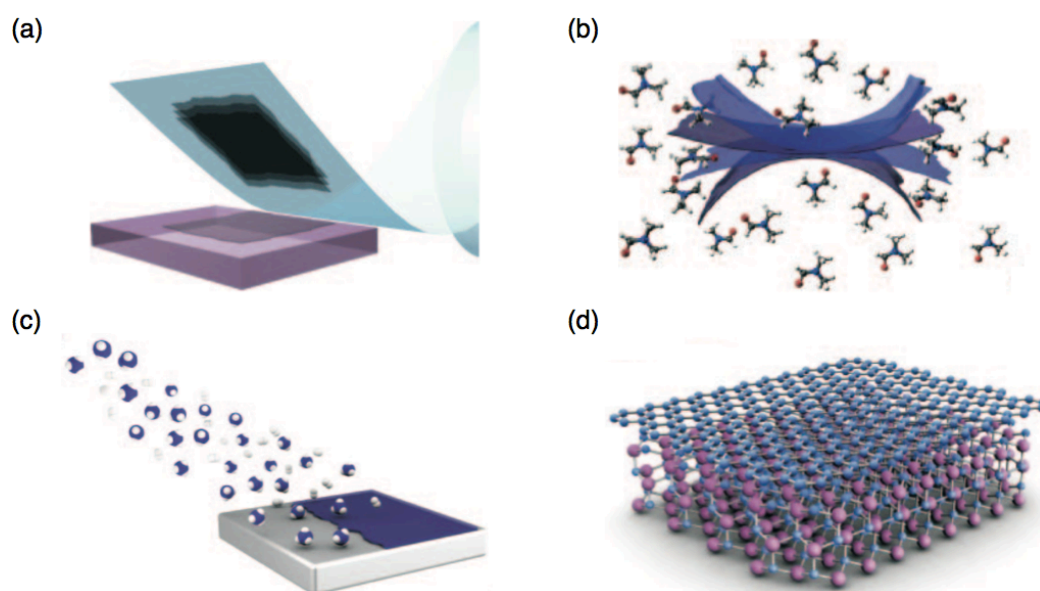


Figure 1-2. Schematic illustrations of the fabrication methods of graphene: (a) mechanical exfoliation; (b) exfoliation in organic solvents; (c) chemical vapor deposition; (d) epitaxial growth on SiC. Adapted with permission from Ref. [32]; Copyright 2012, Nature publishing group.

intrinsically insulating because of the strong disruption of the aromatic system by covalent addition of oxygen-containing groups such as hydroxy and epoxide.⁴³⁻⁴⁵ Therefore, GO needs to be reduced to reduced graphene oxide (rGO) by using hydrazine or through heat treatment after the deposition, but the electronic properties of the pristine graphene cannot be fully recovered.^{42,44,46}

It is also possible to grow graphene on transition-metal surfaces at high temperatures under low pressure or ultrahigh vacuum (UHV) through chemical vapor deposition (CVD), employing small molecules such as methane or acetylene as carbon source (Figure 1-2c).^{30,47-49} Successful growth of monolayer graphene has been reported on various transition-metals such as platinum,⁵⁰ iridium,⁵¹ ruthenium,^{52,53} and nickel.⁵⁴⁻⁵⁶ Remarkably, large-area fabrications of uniform polycrystalline graphene films have recently been achieved on copper foils,⁴⁷ and production of 30-inch graphene films as well as their application as transparent electrodes have been demonstrated.³⁰ Moreover, radio-frequency transistors with cut-off frequency of as high as 155 GHz were demonstrated for the gate length of 40 nm, using CVD graphene on wafers of diamond-like carbon.⁵⁷ However, the mobilities measured for CVD graphene are considerably lower than that of mechanically exfoliated graphene because of defects such as grain boundaries and presence of few layer regions.⁵⁸⁻⁶⁰ On the other hand, it has been reported that the elastic stiffness and strength of CVD graphene can be as high as those of pristine graphene.⁶¹ Given that the CVD method requires the use of metals as support, a transfer process from the metal surfaces to insulating substrates is a critical issue for the practical applications of CVD graphene.^{32,61,62}

Another commonly used method for the fabrication of graphene is epitaxial growth by thermally expelling Si atoms from a single crystalline surface of silicon carbide (SiC) (Figure 1-2d).⁶³⁻⁶⁷ Graphitic layers can be grown both on the silicon face and the carbon face of SiC,⁶⁸ but the electronic properties of the resulting single- or multi-layer graphene starkly depend on the face used for the growth.^{58,69} Multi-layer graphene grown on the carbon face has demonstrated a mobility of $\sim 5,000$ cm²/V·s at room temperature,⁶⁹ which is higher than that of $\sim 1,000$ cm²/V·s reported for graphene prepared on the silicon face.^{65,69} However, the number of layers can be more easily controlled on the silicon face,^{70,71} rendering graphene grown on this face more appropriate for applications.⁵⁸ FET devices with a cutoff frequency as high as 100 GHz were demonstrated for a gate length of 240 nm, using 2-inch graphene epitaxially grown on the silicon face of a SiC wafer, which indicated the high potential of epitaxial graphene for applications in electronic devices.⁷² Importantly, this epitaxial growth

method can circumvent the problem caused by the necessity of transferring graphene from metal surfaces to insulating substrates.⁷³ Fabrication of graphene using the epitaxy of transition metals such as ruthenium is also possible.⁷⁴ This method can achieve single-crystalline domains larger than on SiC, but requires subsequent transfer of the graphene layer to another substrate for further device integrations.⁷⁴

Despite all these fascinating results, the conduction in graphene cannot be switched off because of the zero bandgap, which renders it critical to open a bandgap for the future LSI applications.⁵⁸ Alternative device structures have been recently proposed to obtain high on-off ratios without opening the bandgap of graphene,^{75,76} but it is straightforward if sufficiently large bandgap can be achieved without significantly degrading the electronic properties of the pristine graphene. One way to open a bandgap is to vary the carrier concentration in bilayer graphene through chemical doping^{66,77} or by applying perpendicular electric field.^{78,79} The bandgap can be tuned up to 250 meV by varying the strength of the electric field,⁷⁸ and an on-off ratio of 100 and 2,000 has been reported at room temperature and 20 K, respectively.⁷⁹ However, the preparation of bilayer graphene with required AB stacking is not simple, limiting the practicability of such methods.⁸⁰ Application of uniaxial strain in a graphene layer has also been proposed for opening a bandgap,^{81,82} but a required global uniaxial strain of over 20% seems impractical.⁵⁸ Several other methods have also been investigated to open the bandgap such as fabrication of graphene sheets with a number of regularly patterned holes, i.e. “graphene nanomesh”,⁸³ and patterned adsorption of hydrogen on graphene surfaces.⁸⁴ However, currently the most promising method for opening larger and tunable bandgaps is structural confinement of graphene into nanometer-wide strips, which are defined as graphene nanoribbons (GNRs).^{80,85,86}

1.2 Graphene Nanoribbons (GNRs)

GNRs can be classified by their widths and edge structures, which define their band structures. Typically, two edge structures, namely armchair and zigzag, have predominantly been the targets of theoretical studies (Figure 1-3). The widths of the GNRs are defined by the number “N” as shown in Figure 1-3. It has been predicted that GNRs with zigzag-type edge structures possess half-metallic properties with zero bandgap, showing strongly localized charge density of the edge state at the zigzag sites.^{87,88} In contrast, when the edge structure is armchair or mixtures of armchair and zigzag, GNRs are predicted to show no or limited localized states, behaving as semiconductors with open bandgaps.^{87,89} Their bandgaps critically depend on their lateral width, and generally increase as the GNRs become narrower.^{87,89,90} A small difference in the width leads to a large variation of the bandgap,⁹⁰ which render it imperative to precisely control the structure of GNRs for obtaining the desired bandgap with high reproducibility and accuracy.

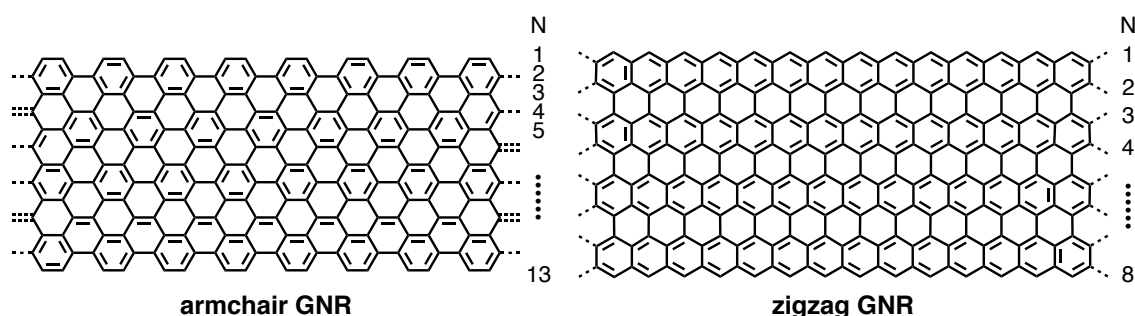


Figure 1-3. Chemical structures of $N = 13$ armchair and $N = 8$ zigzag GNRs.

1.2.1 “Top-down” fabrications of GNRs

Fabrication of GNRs has been predominantly performed through “top-down” approaches, which are in principle based on three strategies, i.e. 1. lithographical⁹¹⁻⁹³ or metal-nanoparticle catalyzed^{94,95} cutting of graphene (Figure 1-4a), 2. sonochemical extraction from expanded graphite (Figure 1-4b–d),^{96,97} and 3. unzipping^{98,99} or polymer-protected plasma etching^{100,101} of carbon nanotubes (CNTs) (Figure 1-5). The unzipping of CNTs can be carried out through oxidation-mediated,^{98,99} metal-nanoparticle catalyzed,^{102,103} electrochemical,¹⁰⁴ or sonochemical^{105,106} methods.

It is also reported that GNRs can be directly grown by using CVD method¹⁰⁷⁻¹⁰⁹ as well as epitaxially on a templated silicon carbide substrate.¹¹⁰ A variety of GNRs have thus been fabricated with lateral width ranging from over 500 nm down to sub 5 nm.^{85,111}

The first strategy, cutting of graphene on a surface, was first carried out in 2007 by employing electron-beam lithographical patterning of a mask followed by oxygen plasma etching to obtain GNRs with various widths, i.e. ca. 15–500 nm (Figure 1-4a).^{91,92} Investigation of the electronic properties of these GNRs revealed that the bandgap changes inversely with the lateral width,⁹¹ confirming the theoretical prediction.⁹⁰ However, no systematic dependence was observed between the bandgaps and the crystallographic direction of the GNRs, indicating defective and undefined edge structures.^{91,112} In 2009, GNRs with the lateral width of down to 6 nm were fabricated lithographically by using silicon nanowires as masks for the plasma etching.¹¹² The width could be well controlled by tuning the nanowire diameter and etching time. A room-temperature on-off ratio of ca. 160 was demonstrated on an 8-nm GNR-FET with

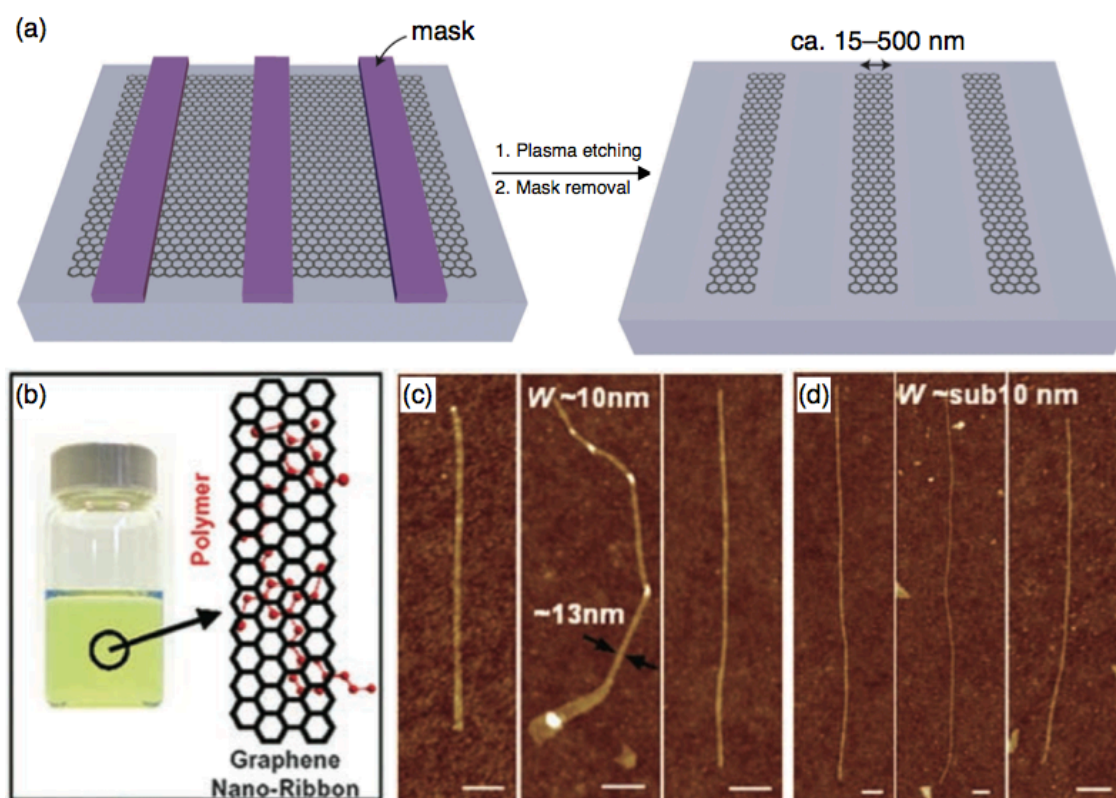


Figure 1-4. (a) A schematic illustration of the fabrication of GNRs through plasma etching of graphene with lithographically formed masks. Adapted with permission from Ref. [111]; Copyright 2010, Nature publishing group. (b) A picture of a stable suspension of GNRs in PmPV/CH₂Cl₂ and a schematic illustration of the interaction of two PmPVs with a GNR via π - π stacking. (c), (d) AFM images of GNRs with the widths of (c) ~10 nm and (d) sub 10 nm. Reprinted with permission from Ref. [96]; Copyright 2008, AAAS.

a suggested bandgap of ca. 170 meV. It was also found that the logarithm of the on-off ratio scales inversely with the lateral width of the GNRs. Furthermore, in 2010, gas-phase chemical etching of electron-beam lithographically patterned GNR arrays (ca. 20–30 nm) allowed narrowing of GNRs down to ca. 4 nm without damaging the basal plane. Thus prepared GNRs demonstrated a high room-temperature on-off ratio of up to ca. 10^4 with an estimated bandgap of ca. 0.4 eV.¹¹¹ Patterning of GNRs was also achieved by utilizing purposely formed wrinkles of graphene as self-masks for the plasma etching.¹¹³ A regularly wrinkled graphene was grown by the CVD method on a corrugated copper foil and subsequently transferred onto a Si/SiO₂ substrate while preserving the wrinkled structure. Arrays of sub-10-nm GNRs could be facilely prepared by this method, demonstrating the on-off ratio of ~ 30 with a suggested bandgap of ~ 0.1 eV.

The second strategy was first reported in 2008 by *Dai et al.*, where fabrication of high quality GNRs with the width down to sub 10 nm was achieved through solution-based sonochemical extraction from expandable graphite under the presence of poly(*m*-phenylene-co-2,5-dioctoxy-*p*-phenylenevinylene) (PmPV) (Figure 1-4b-d).⁹⁶ FET devices fabricated on the sub-10-nm GNRs showed remarkably high on-off ratios of up to 10^6 at room temperature with estimated hole mobility of ca. 50–200 cm²/V·s, indicating the high quality of the GNRs.⁹⁷ Importantly, all the sub 10 nm GNRs showed semiconducting properties in stark contrast to CNTs that possess semiconducting or metallic properties, depending on the chirality, even with the same diameter. However, this method suffered from low yields as well as uncontrollable and broad width distribution, i.e. from sub 10 nm to ~ 100 nm.¹⁰⁰ *Dai et al.* have also demonstrated covalent functionalization of such chemically derived GNRs with ammonia by means of high-power electrical joule heating, realizing unprecedented n-doped GNRs showing n-type properties¹¹⁴

The third strategy, fabrication of GNRs from CNTs, was first achieved in 2009 based on two different methods, i.e. oxidation-mediated unzipping⁹⁸ and plasma etching¹⁰⁰ of multiwalled CNTs (MWCNTs), which were reported by *Tour et al.* and *Dai et al.*, respectively (Figure 1-5). By treatment with a mixture of concentrated sulfuric acid and potassium permanganate, MWCNTs (diameter: 40–80 nm) were unzipped in the longitudinal direction through oxidation, leading to graphene oxide nanoribbons (GONRs) with lateral width of >100 nm and typical length of ~ 4 μm .⁹⁸ Although the GONRs were obtained in exceptionally high yields of $\sim 100\%$, oxidized defect sites at the edges as well as holes in the basal planes were unavoidable even after

the chemical or thermal reduction. This method was later optimized by choosing milder acids to allow the formation of GONRs with fewer holes in the basal plane, smaller width of 75–200 nm, and larger length of $>5\ \mu\text{m}$.⁹⁹ Nevertheless, the width achievable with this method was still too large to open the bandgap.

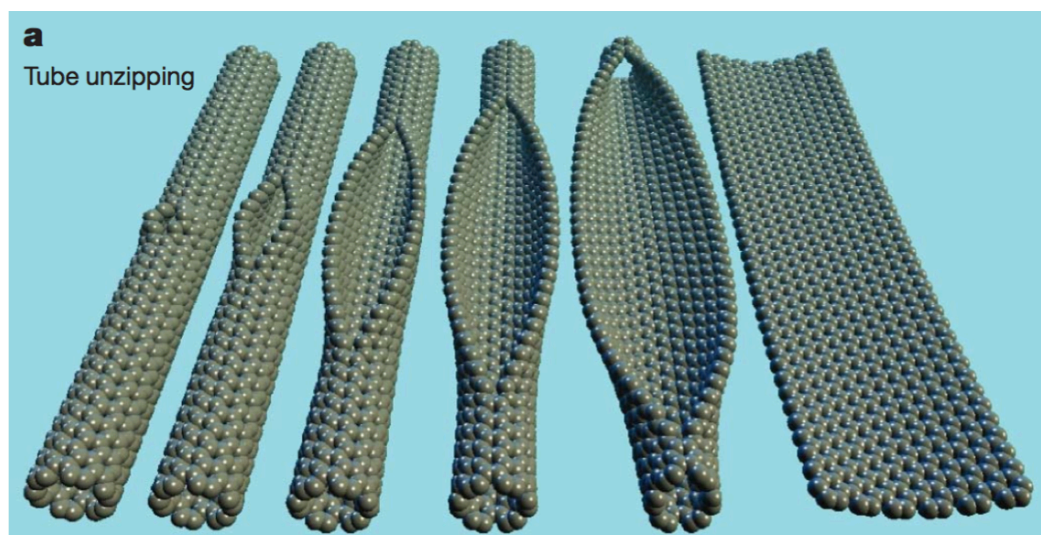


Figure 1-5. A schematic illustration of the fabrication of GNRs through unzipping of CNTs. Reprinted with permission from Ref. [98]; Copyright 2009, Nature publishing group.

Narrower and less defective GNRs were fabricated through Ar plasma etching of MWCNTs (diameter: $\sim 2\text{--}18\ \text{nm}$) partly embedded in a poly(methyl methacrylate) (PMMA) film.^{100,101} The resulting GNRs showed a narrower width distribution of sub 10 to 20 nm. Device investigations revealed the on-off ratio of up to 10^3 for thus prepared GNRs.¹⁰¹ In 2010, fabrication of high-quality, few-layer GNRs with the width of 10–30 nm was achieved by *Dai et al.* through sonochemical unzipping of mildly gas-phase oxidized MWCNTs.¹⁰⁵ High mobility of $1,500\ \text{cm}^2/\text{V}\cdot\text{s}$ was measured on GNRs with the lateral width of ca. 14 nm and estimated bandgap of 10–15 meV. This mobility is the highest value reported for GNRs with similar width,^{97,105} indicating relatively high quality of the GNRs produced by this method. Such GNRs could be further narrowed down to sub 5 nm by selective plasma etching at the edges, displaying the on-off ratio of ca. 10^3 .¹¹⁶

These “top-down” fabrications have revealed the high potential of GNRs, demonstrating the semiconducting properties with the on-off ratio of up to 10^6 for sub-10-nm GNRs.⁹⁶ However, these methods are starkly limited by low yields and lack of structural control. The yields of “high quality” GNRs are considerably poor (only up to ca. 2%),^{96,100,105} and even the “high quality” GNRs with “smooth edges” are mixtures

of GNRs with different widths and random edge structures, both of which critically affect their electronic properties.^{87,89,117} This means that all the GNRs in one sample have different bandgaps and various intrinsic mobilities, which strongly hinders practical applications in electronic devices of such “top-down” fabricated GNRs. The lack of structural control renders it apparently impossible to produce “high-quality” GNRs with the lateral width of sub 5 nm, which is, however, required to open sufficient bandgaps. For instance, a bandgap of 0.67 eV, i.e. that of Ge, can be obtained with the lateral width of 2–3 nm.⁸⁹

1.2.2 “Bottom-up” syntheses of GNRs

1.2.2.1 Fully conjugated ladder-type polymers

In contrast to the “top-down” approach, a “bottom-up” chemical synthetic approach enables a controlled fabrication of structurally well-defined, sub-5-nm GNRs with uniform lateral structures. The solution-mediated synthesis of GNRs can date back to 1970, when the first attempt for a synthesis of fully conjugated, ladder-type polymer **1-2a**, consisting of hexagonal and pentagonal aromatic rings, was reported by *Stille et al.* (Figure 1-6).¹¹⁸ Although such aromatic ladder-type polymers were not recognized as “GNRs” in those days, their aromatic, ribbon-like structures can indeed be seen as those of GNRs (Figure 1-6). The synthesis of ladder-type polymer **1-2a** was attempted by *AB*-type *Diels-Alder* polymerization of 2,5-diphenyl-3,4-(5,6-acenaphthylenylene)-cyclopentadienone (**1-1a**). Importantly, they designed and synthesized **1-1a** as an *AB*-type monomer that incorporates both the diene and the dienophile in one molecule for the *AB*-type polymerization. However, much of the polymerization product was insoluble due to the strong π - π stacking interaction, leaving the structural characterization inconclusive at that time.¹¹⁹

This solubility problem was solved later by *Schlüter et al.* in 1994 through a use of monomer **1-1b** with a flexible alkyl loop.¹¹⁹ Thanks to the increased solubility and improved synthetic procedure, the formation of ladder-type polymer **1-2b** was unambiguously validated by elemental analysis, solid-state ¹³C NMR, and transmission ultraviolet spectroscopy, as well as based on investigation of structurally related model compounds. *Schlüter et al.* also reported extended analogues of ladder-type polymer **1-2b** with naphthalene¹¹⁹ and anthracene¹²⁰ units instead of the benzene unit between

the two five-membered rings. In 1991, *Scherf* and *Müllen* reported a synthesis of ladder-type polymer **1-4** through intramolecular *Friedel–Crafts* alkylation of functionalized poly(*p*-phenylene) (PPP) **1-3**.^{121,122} Polymer **1-4** was soluble in organic solvents and showed number-average molecular weight (M_n) of up to 50,000 g/mol with polydispersity index (PDI) of ca. 2¹²³ as well as the longest-wavelength absorption maximum at 440–450 nm.¹²¹ In 1993, *Chmil* and *Scherf* successfully synthesized ladder-type polymer **1-6a**, which is also called “angular polyacene”, by carbonyl olefination of functionalized PPP **1-5** with B_2S_3 .^{124,125} McMurry coupling was also found to be a powerful method for the selective and complete conversion of **1-5** into **1-6a**.¹²³ Soluble polymer **1-6a** showed M_w of up to 25,000 g/mol¹²³ and the longest wavelength absorption maximum at 440 nm,¹²⁴ similar to polymer **1-4**. In 1994, *Swager et al.* synthesized ladder-type polymer **1-6b** with the same backbone structure as **1-6a** from functionalized PPP **1-7**.¹²⁶ They employed intramolecular electrophilic substitution via formation of vinyl cation under an acidic condition. The ladder-type polymers **1-2**, **1-4**, and **1-6** can be regarded as the narrowest, structurally defined GNRs.

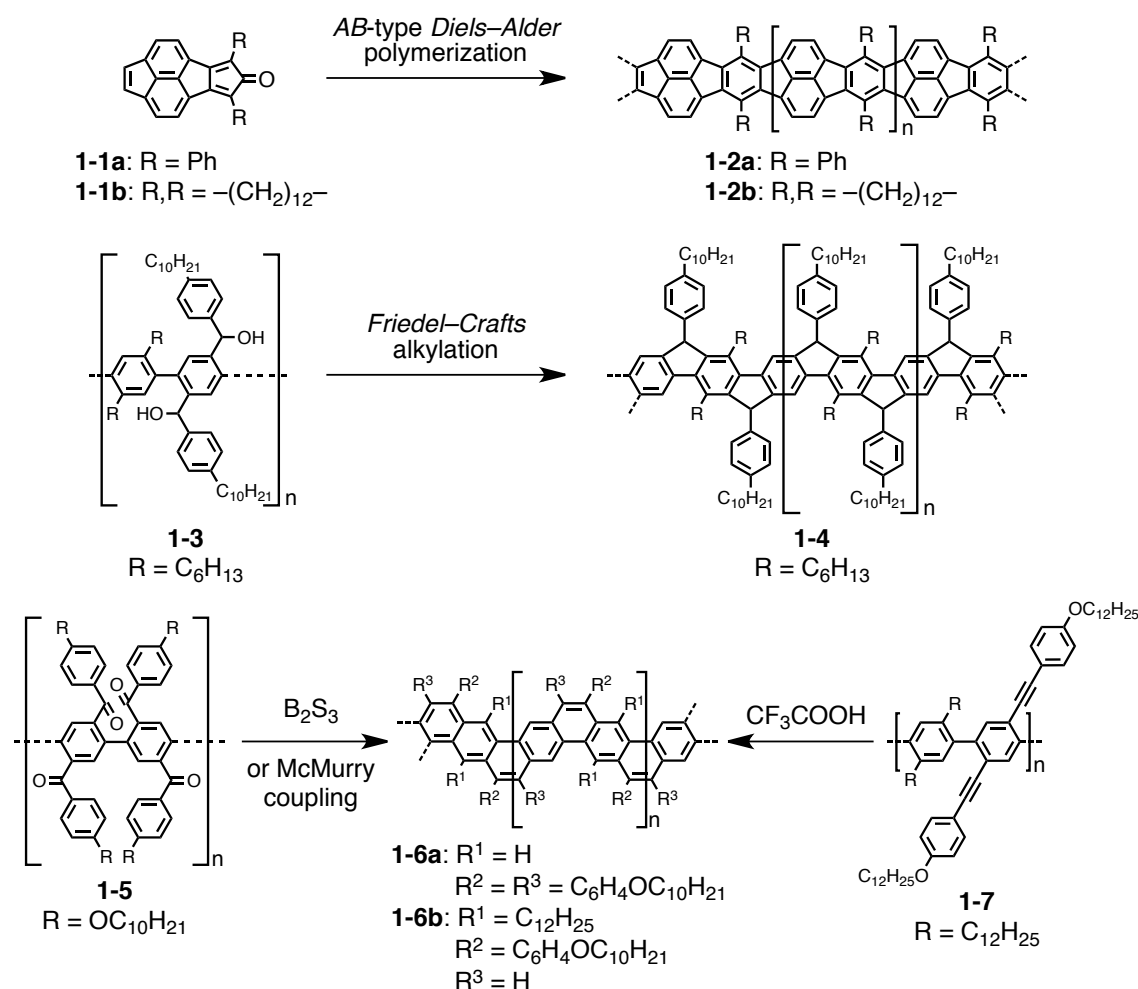


Figure 1-6. Fully conjugated ladder-type polymers that can be considered as narrowest GNRs.

1.2.2.2 Heteroaromatic ladder-type polymers

Heteroaromatic ladder-type polymers, which can be considered as selectively doped GNRs, have also been reported since 1970's, although most of the early works are devoid of conclusive characterizations.^{123,127} Representatively, in 1972, *Marvel et al.* reported a synthesis of N-containing graphitic polymer **1-10** by polycondensation of 1,4,5,8-tetraaminoanthraquinon (**1-8**) and 1,3,6,8-tetraketo-1,2,3,6,7,8-hexahydropyrene (**1-9**), but polymer **1-10** was totally insoluble and could not be sufficiently characterized.^{128,129} In 1993, *Tour and Lamba* reported heteroaromatic ladder-type polymer **1-12**, which is an aza-analogue of angular polyacenes **1-6**.^{130,131} Polymer **1-12** was synthesized from functionalized PPP **1-11**, where the acidic removal of *tert*-butyloxycarbonyl (BOC) protecting group was immediately followed by intramolecular cyclization between the amine and the ketone groups to form the imine bridges. Although polymer **1-12** was insoluble in common organic solvents, a mixture of dichloromethane and trifluoroacetic acid (TFA) allowed solubilization of polymer **1-12**, revealing the absorption maximum at around 400 nm.¹³¹ However, the use of TFA lead to the protonation of the nitrogens, hindering comprehensive characterizations of polymer **1-12**.¹²³

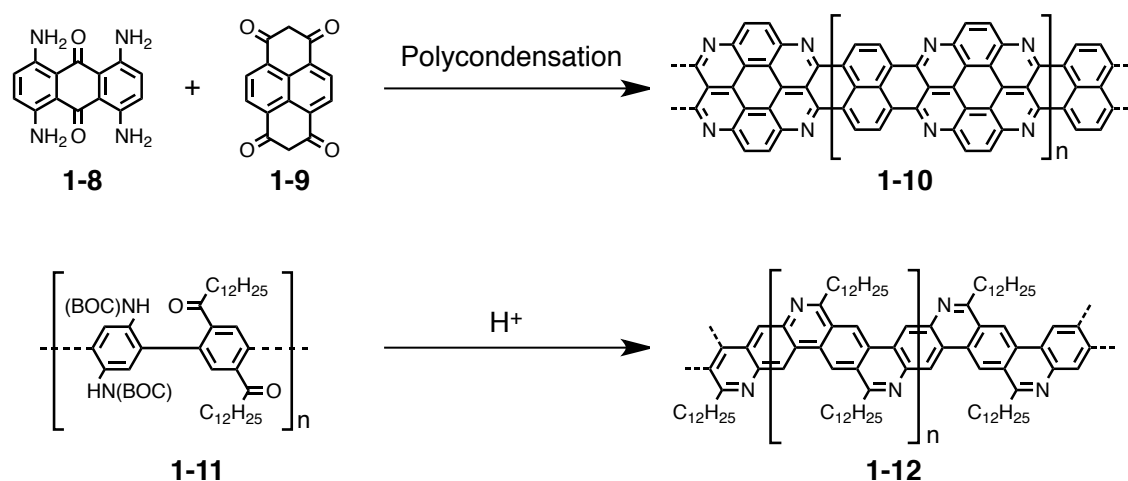


Figure 1-7. N-containing ladder-type polymers that can be regarded as selectively N-doped GNRs.

Syntheses of N-containing ladder-type polymers **1-13**¹³² and **1-14**¹³³ were reported by *Scherf et al.* in 2003 and by *Müllen et al.* in 2004, respectively (Figure 1-8). Both **1-13** and **1-14** have N-doped structures of ladder-type polymer **1-4** and were synthesized in a similar manner to the preparation of polymer **1-4**. Furthermore, *Müllen et al.* simultaneously presented a synthesis of N-containing ladder-type polymer **1-15** with two-carbon bridges in a similar manner to the preparation of ladder-type polymer **1-6a**.¹³³ Synthesis of S-containing ladder-type polymer **1-16** has also been achieved by *Scherf et al.* through a similar synthetic strategy to the one used for the synthesis of ladder-type polymer **1-4**.¹³⁴

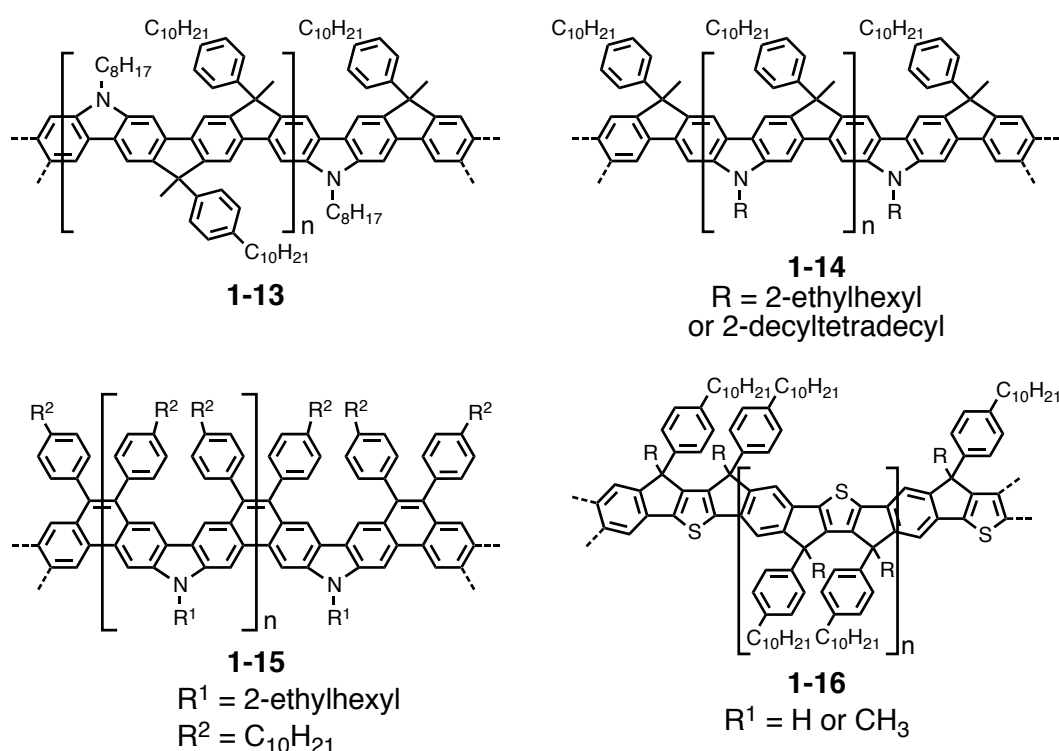


Figure 1-8. Heteroaromatic ladder-type polymers that can be regarded as selectively N- or S-doped GNRs.

Although the above-mentioned fully conjugated ladder-type polymers can be considered as the narrowest structurally defined GNRs, they are too narrow to exhibit the electronic properties expected for “GNRs”, i.e. high charge-carrier mobilities. It has been theoretically revealed that the mobilities of GNRs decline as they become narrower,¹³⁵ because the lateral confinement increases not only the bandgap, but also the effective carrier mass and scattering of the charge carriers at the ribbon boundaries, which both reduce the mobilities.¹³⁶ It is therefore imperative to synthesize laterally

extended GNRs while retaining the high structural precision. “Bottom-up” synthesis of wider and structurally defined GNRs has been achieved by *Müllen et al.* based on solution-mediated¹³⁷⁻¹³⁹ or surface-assisted¹⁴⁰ intramolecular cyclodehydrogenation of tailor-made polyphenylene precursors. Initially, the intramolecular cyclodehydrogenation reaction based on dendritic oligophenylene precursors has been developed for the synthesis of large polycyclic aromatic hydrocarbons (PAHs) or nanographenes.¹⁴¹⁻¹⁴³

1.2.2.3 Solution synthesis of nanographenes

In 1995, *Müllen et al.* reported a facile and highly efficient synthesis of hexa-*peri*-hexabenzocoronene (HBC, **1-18**) based on the oxidative intramolecular cyclodehydrogenation of hexaphenylbenzene.¹⁴⁴ The synthesis of HBC was first reported in 1958 by *Clar et al.*^{145,146} and *Halleux et al.*,¹⁴⁷ and later in 1986 by *Schmidt et al.*¹⁴⁸ However, all these procedures required harsh reaction conditions and could provide HBC only in small quantities. *Müllen et al.* achieved the first scalable and clean conversion of hexaphenylbenzene (**1-17**) into HBC at room temperature by employing copper(II) triflate as an oxidant and aluminum(III) chloride as a Lewis acid (Figure 1-9). Such reaction condition had been reported by *Kovacic et al.* for the intermolecular cyclodehydrogenation of benzene to prepare PPP,¹⁴⁹⁻¹⁵² but it was demonstrated to be more useful for the intramolecular cyclodehydrogenation of polyphenylenes.¹⁴¹

They later found that the use of aluminum(III) chloride could induce cleavage or migration of alkyl chains, depending on the structure of the polyphenylene precursor because of the strong acidity. Nevertheless, this problem was solved by the use of iron(III) chloride, which is a weaker Lewis acid.¹⁵³ Because iron(III) chloride can also function as an oxidant, the copper(II) salt became unnecessary, rendering the synthetic procedure even more simple. Since then, a variety of extended PAHs have been synthesized by employing this cyclodehydrogenation protocol, including C60 (**1-19**),¹⁵³ C72 (**1-20**),¹⁵⁴⁻¹⁵⁶ C78 (**1-21**),^{154,157} C96 (**1-22**),^{155,158} C132 with square (**1-23**)^{159,160} and triangular (**1-24**)¹⁵⁵ structures, C150 (**1-25**),¹⁵⁸ and C222 (**1-26**),¹⁶¹ where the numbers indicate the number of carbon atoms in the aromatic core (Figure 1-9). Further, *Müllen* and his colleagues extended this synthetic protocol to the fabrication of GNRs from tailor-made polyphenylene polymers as precursors.⁸⁰

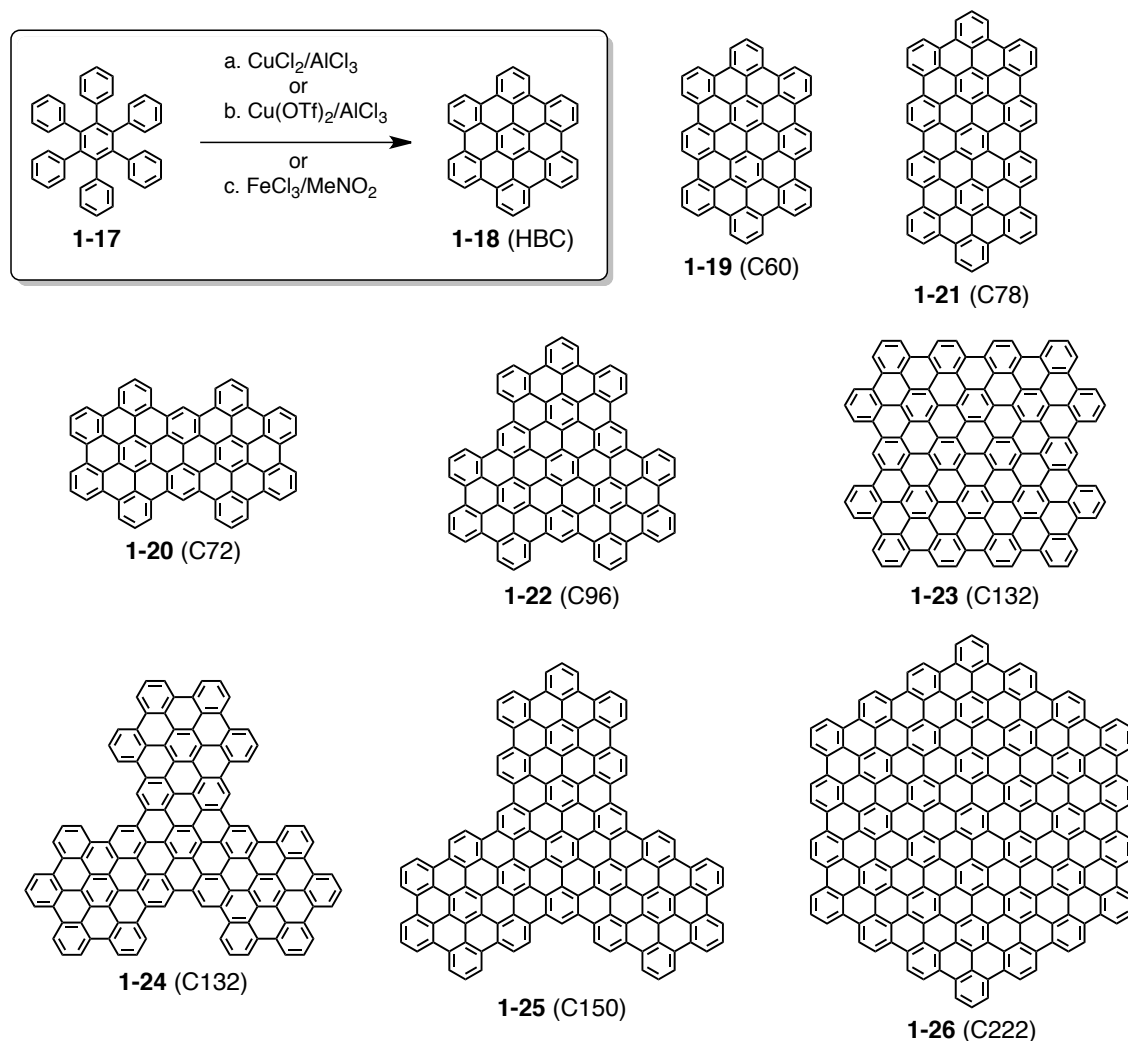


Figure 1-9. Synthesis of HBC (1-18) and structures of extended PAHs.

1.2.2.4 Solution synthesis of GNRs from polyphenylene precursors

In 2000, a synthesis of GNRs was attempted for the first time through the oxidative cyclodehydrogenation of polyphenylene polymer **1-29**, which was prepared by A_2B_2 -type *Diels-Alder* polymerization of 1,4-bis(2,4,5-triphenylcyclopentadienone-3-yl)benzene (**1-27**) as the bisdiene and 1,4-diethynylbenzene (**1-28**) as the bisdienophile (Figure 1-10).¹⁶² Based on the SEC analysis against PS standard, the weight-average molecular weight (M_w) of polymer **1-29** ranged from 12,000 to 120,000 g/mol, where higher M_w was obtained at higher concentrations of the monomers and longer reaction times. Raman and FTIR spectroscopic analyses of the cyclodehydrogenation product **1-30** and an investigation of a model compound corroborated successful cyclodehydrogenation, but further characterizations were

hindered by the insolubility of **1-30**. Polymer **1-29** contained a random mixture of three regioisomeric repeating units, because both **1-27** and **1-28** had unsymmetrically substituted diene and dienophile units, respectively, causing structural isomerization upon each *Diels-Alder* cycloaddition step. The graphitized polymer **1-30** included even more regioisomers because of the free rotation of **1-29** within the main polyphenylene chains during the cyclodehydrogenation. Moreover, the lateral structure of polymer **1-30** was irregular, containing huge “gaps” between each repeating unit.

At least the problem with the “gaps” was settled in 2003 by using 1,4-diethynyl-2,5-di(4'-*tert*-butylphenyl)benzene (**1-31**) instead of 1,4-diethynylbenzene (**1-28**) as the bisdienophile (Figure 1-10).¹³⁷ A_2B_2 -type *Diels-Alder* polymerization of **1-27** and **1-31** yielded polyphenylene polymer **1-32**, which lead to armchair-edge GNR **1-33** with the regular lateral width. However, the problem of structural isomerization during the polymerization step remained unresolved, and GNR **1-33** contained a mixture of non-straight, irregularly kinked structures.

In 2008, a synthesis of straight, armchair GNR was achieved for the first time by employing A_2B_2 -type *Suzuki* polymerization of 1,4-diiodo-2,3,5,6-tetraphenylbenzene (**1-34**) and bis-boronic ester (**1-35**) (Figure 1-10).¹³⁸ Despite the high steric hindrance, the *Suzuki* polymerization successfully provided polyphenylene polymer **1-36** with M_n of 14,000 g/mol and PDI of 1.2 against PS standard calibration. The high efficiency of the cyclodehydrogenation of polymer **1-36** into $N = 9$ armchair GNR **1-37** was demonstrated by matrix-assisted laser desorption/ionization time-of-flight (MALDI-TOF) mass spectrometry (MS) and UV–vis absorption spectroscopy. GNR **1-37** showed high dispersibility in organic solvents due to the bulky alkyl chains densely attached on the peripheral positions, and its straight and uniform structure could be visualized by scanning tunneling microscopy (STM) at the solid/liquid interface on HOPG. However, the GNRs observed by STM were only up to 12 nm, which was indeed in agreement with the molecular modeling based on the M_n estimated by the SEC analysis. The absorption edge of the UV–vis absorption spectrum was ~ 550 nm, corresponding to the optical bandgap of ca. 2.3 eV. This large bandgap also indicated that the longitudinal extension of GNR **1-37** was not sufficient to reach the bandgap expected for the corresponding infinite armchair GNR with the same lateral width, i.e. ~ 1 eV.⁹⁰

The main reason for the short length of GNR **1-37**, i.e. the low efficiency of the polymerization, was not only the high steric hindrance between **1-34** and **1-35**, but also the rigid PPP backbone of precursor **1-36**, which limited the solubility of the polymer intermediates, precluding them from further polymerization. Recently, a use of kinked polyphenylene structure, poly(*o*-phenylene-*p*-phenylene) **1-40** was proposed to circumvent this problem.¹³⁹ Polymer **1-40** was synthesized through a microwave-assisted A_2B_2 -type *Suzuki* polymerization of *o*-dibromobenzenes **1-38** and benzene-1,4-diboronic ester (**1-39**) (Figure 1-11). M_n and PDI against PS standard calibration of the obtained polymer **1-40b** with dodecyl chains were 9,900 g/mol and 1.4, respectively, corresponding to the average longitudinal length of ca. 25 nm for GNR **1-41b** after the “planarization”. While non-substituted GNR **1-41a** was insoluble, GNR **1-41b** with dodecyl chains demonstrated a good solubility of higher than 40 mg/mL in common organic solvents such as toluene, THF, and dichloromethane, allowing its spectroscopic characterizations in solutions. The length obtained for GNR **1-41** was larger than that of GNR **1-37** reached by the aforementioned approach, supporting the superiority of the kinked backbone structure over the PPP backbone during the *Suzuki* polymerization.

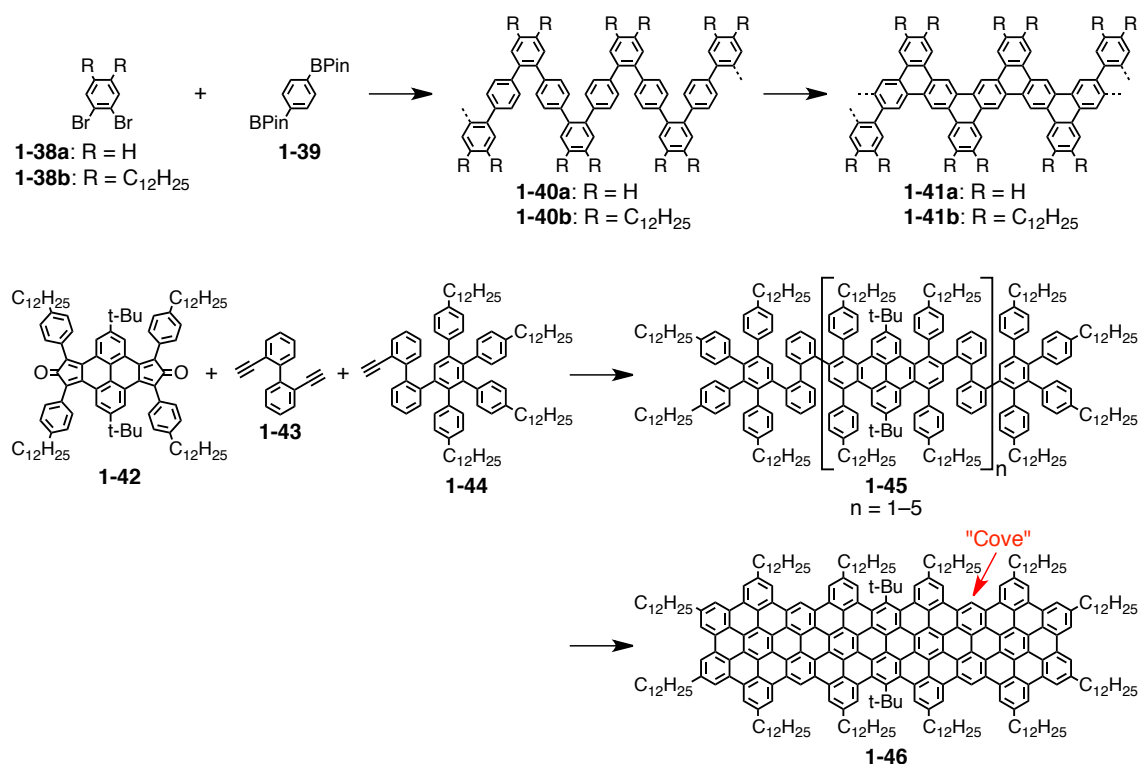


Figure 1-11. “Bottom-up” fabrication of GNR **1-41** from kinked polyphenylene **1-40** and synthesis of cove-edge ribbon-type PAH **1-46**.

In 2009, synthesis of GNRs with a different edge structure, i.e. cove-type edge, was attempted through repeated *Diels-Alder* cycloaddition reactions, involving pyrene-based diene **1-42**, 2,2'-diethynylbiphenyl (**1-43**), and 1,2,3,4-tetra-(4-dodecylphenyl)-5-(2'-ethynylbiphen-2-yl) (**1-44**) (Figure 1-11).¹⁶³ Oligophenylene precursors **1-45**, corresponding to ribbon-type PAHs, of up to C373 ($n = 5$) could be obtained through multi-step repetitive *Diels-Alder* cycloadditions, but the cyclodehydrogenation products of the larger oligomers were barely soluble in conventional organic solvents, hindering their comprehensive characterizations. Only the smallest oligomer C132 (**1-46**) could be unambiguously characterized after the “graphitization”, leaving the synthesis of longitudinally extended, cove-edge GNRs elusive.¹⁶³

Different types of GNRs could thus be synthesized through the bottom-up solution synthesis via the intramolecular oxidative cyclodehydrogenation of tailor-made polyphenylene precursors. Although the A_2B_2 -type *Diels-Alder* polymerization approach enabled preparation of high-molecular-weight precursors, the resulting GNR **1-33** was structurally undefined with the “kinks” and hardly dispersible in organic solvents, hindering the deposition onto substrates for structural characterizations and investigation of the electronic properties. Use of the A_2B_2 -type *Suzuki* polymerization allowed the synthesis of structurally defined GNRs **1-37** and **1-41** with high dispersibility, but the longitudinal extension of these GNRs was limited due to the low efficiency of the *Suzuki* polymerization, limiting their applicability. Furthermore, the lateral width of the GNRs thus far obtained was only up to ca. 1 nm, whereas larger widths are required for GNRs with lower bandgap and higher intrinsic mobilities.

1.2.2.5 Surface syntheses of a nanographene and GNRs

While the solution-mediated synthesis of the GNRs suffers from the above-mentioned problems with low processability or short longitudinal length, these problems can be circumvented if it is possible to grow GNRs directly on a surface with high efficiency. It has been proved that coupling reactions between aryl halides can be carried out on metal surfaces, yielding linear polymers as well as covalently bonded networks with atomic precision, which can be *in situ* visualized by high-resolution STM.¹⁶⁴⁻¹⁶⁷ This on-surface coupling reaction can be applied for the preparation of polymer precursors for the synthesis of GNRs on a surface. In 2010, *Müllen* and *Fasel*

et al. demonstrated the feasibility of on-surface intramolecular cyclodehydrogenation, synthesizing triangular PAH **1-48** on a metal surface from a cyclic polyphenylene, cyclohexa-*o-p-o-p-o-p*-phenylene (CHP, **1-47**) (Figure 1-12).¹⁶⁸ CHP **1-47** was first vacuum-sublimated onto a Cu(111) surface, and then annealed to ca. 230 °C to obtain the planarized product **1-48** (Figure 1-12a). The atomically precise structure of PAH **1-48** was unambiguously demonstrated by the *in-situ* STM visualization (Figure 1-12b). By annealing at lower temperatures, they could also visualize two reaction intermediates, which, in combination with *ab initio* simulations, provided a further insight into the mechanism of the on-surface cyclodehydrogenation reaction.

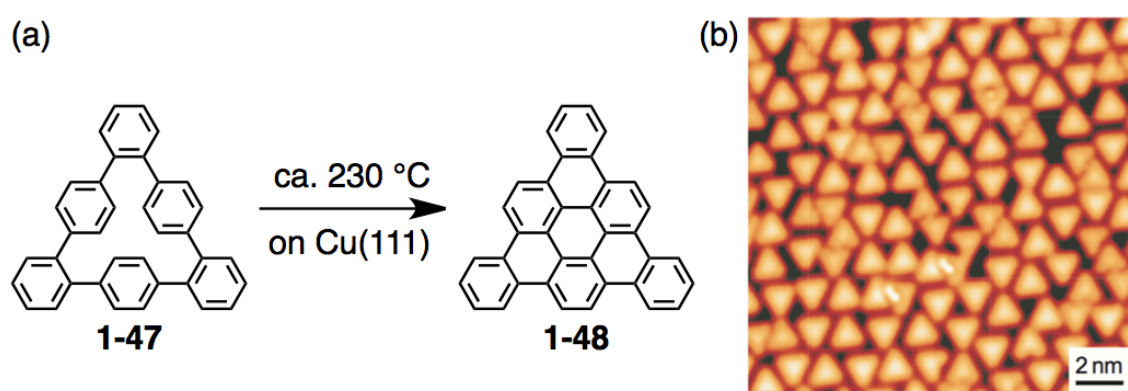


Figure 1-12. (a) Surface-assisted synthesis of triangular PAH **1-48** from CHP **1-47**. (b) An STM image of PAH **1-48** synthesized on a Cu(111) surface by annealing at ~470 K. Reprinted with permission from Ref. [168]; Copyright 2011, Nature publishing group.

By combining the on-surface coupling reaction of aryl halides with the surface-assisted cyclodehydrogenation, *Müllen* and *Fasel et al.* demonstrated the first surface-assisted synthesis of GNRs in 2010.¹⁴⁰ This synthetic protocol in principle involved three steps, i.e. 1) vacuum sublimation of dihalogenated monomers onto a metal surface, 2) radical polymerization of the surface-stabilized biradical intermediates, which were formed upon slight heating, and 3) surface-assisted cyclodehydrogenation upon thermal activation (Figure 1-13). By employing 10,10'-dibromo-9,9'-bianthryl (**1-49**) as a dihalogenated monomer, armchair $N = 7$ GNR **1-51** could be efficiently synthesized with atomic precision, which was evidently demonstrated by the *in-situ* STM visualization (Figure 1-13a and b).^{140,169}

The bandgap of GNR **1-51** was elucidated to be ca. 2.3 eV, along with an effective mass of 0.21 m_0 at the top of the valence band and an energy-dependent charge carrier velocity up to 8.2×10^5 m/s in the linear part of the valence band, based on

angle-resolved photoelectron spectroscopy (ARPES) and scanning tunneling spectroscopy (STS) analyses.¹⁷⁰ Furthermore, the cyclodehydrogenation step could be well controlled to allow the fabrication of $N = 7$ GNRs containing partially reacted $N = 5^+$ polyanthrylene segments, which could be regarded as intraribbon heterojunction.¹⁷¹ Covalent colligations of GNRs in parallel was also observed, leading to the formation of $N = 14$ and 21 armchair GNRs.^{172,173} More recently, the conductivity of a single nanoribbon was measured by *Grill et al.* for $N = 7$ GNR **1-51** by using an STM pulling technique.¹⁷⁴ *Liljeroth* and *Swart et al.* demonstrated atomically resolved atomic force microscopy (AFM) images of GNR **1-51** and successfully created a single GNR-Au bond by removing one hydrogen atom with a local high voltage pulse.¹⁷⁵

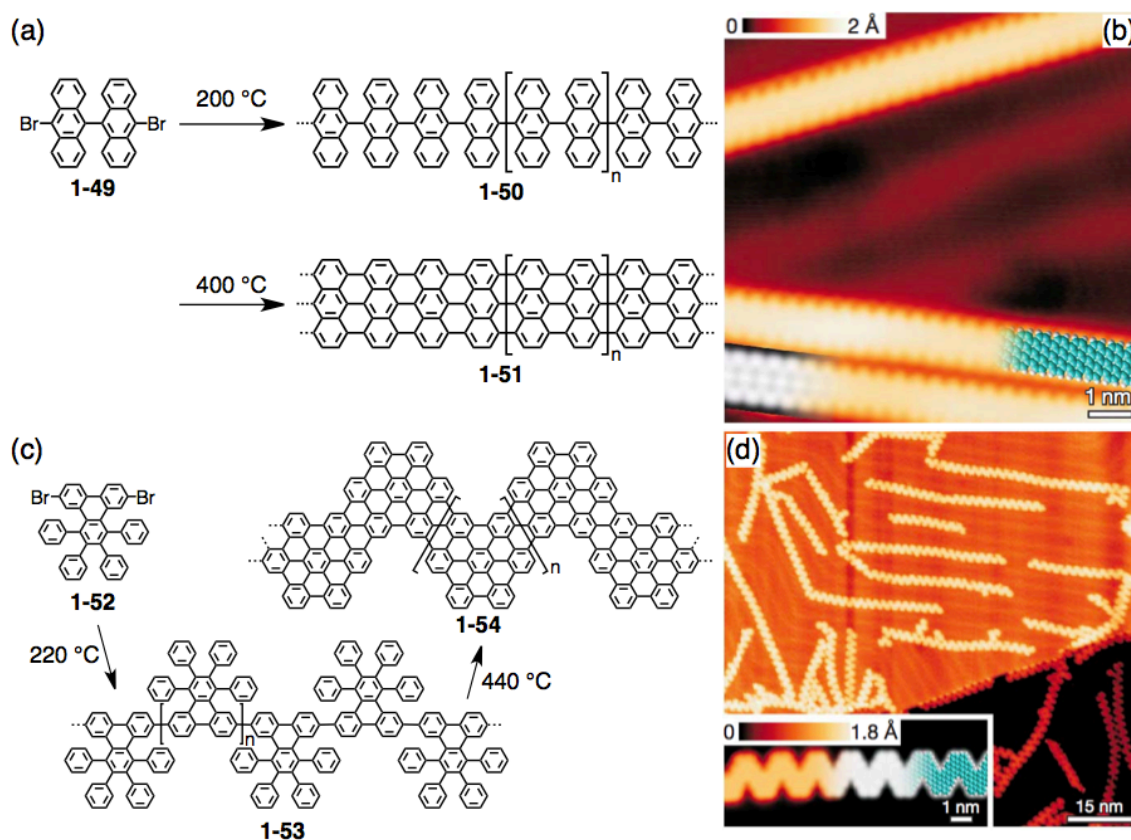


Figure 1-13. (a), (c) Surface-assisted syntheses of GNRs (a) **1-51** and (c) **1-54**. (b), (d) STM images of GNRs (b) **1-51** and (d) **1-54** on Au(111) surfaces with partly overlaid molecular model (blue) and DFT-based STM simulation (gray scale). Reprinted with permission from Ref. [140]; Copyright 2010, Nature publishing group.

Furthermore, this surface-assisted method could be applied to other monomers to provide GNRs with different architectures. By employing 6,11-dibromo-1,2,3,4-tetraphenyltriphenylene (**1-52**) as a monomer, chevron-type GNR

1-54 could be synthesized with atomic precision (Figure 1-13).^{140,172} Later *Hecht* and *Tegeeder et al.* reported that it is possible to synthesize selectively N-doped, chevron-type GNR **1-57** by using an N-doped monomer, 6,11-dibromo-1,4-diphenyl-2,3-di(4-pyridyl)triphenylene (**1-55**) (Figure 1-14).¹⁷⁶ Although no microscopic image was provided, it was revealed that N-doping caused lowering of the energy levels while basically unaffected the bandgap energy. $N = 13$ armchair GNR **1-60** was also synthesized through this method by using extended dibromobianthryl **1-58**.¹⁷⁷ The bandgap of $N = 13$ GNR **1-60** was elucidated to be ca. 1.4 eV by STS measurements, which is about 1 eV lower than the value reported for $N = 7$ GNR **1-51**.^{170,172,174}

Although a variety of GNRs with different width and edge structures have been synthesized with atomic precision, GNRs prepared by this surface-assisted method need to be transferred from the metal surfaces onto dielectric substrates for further studies on their electronic properties as well as integration into electronic devices. Optimization of such transfer process is now ongoing, but efficient, non-destructive, and clean transfer is still elusive.

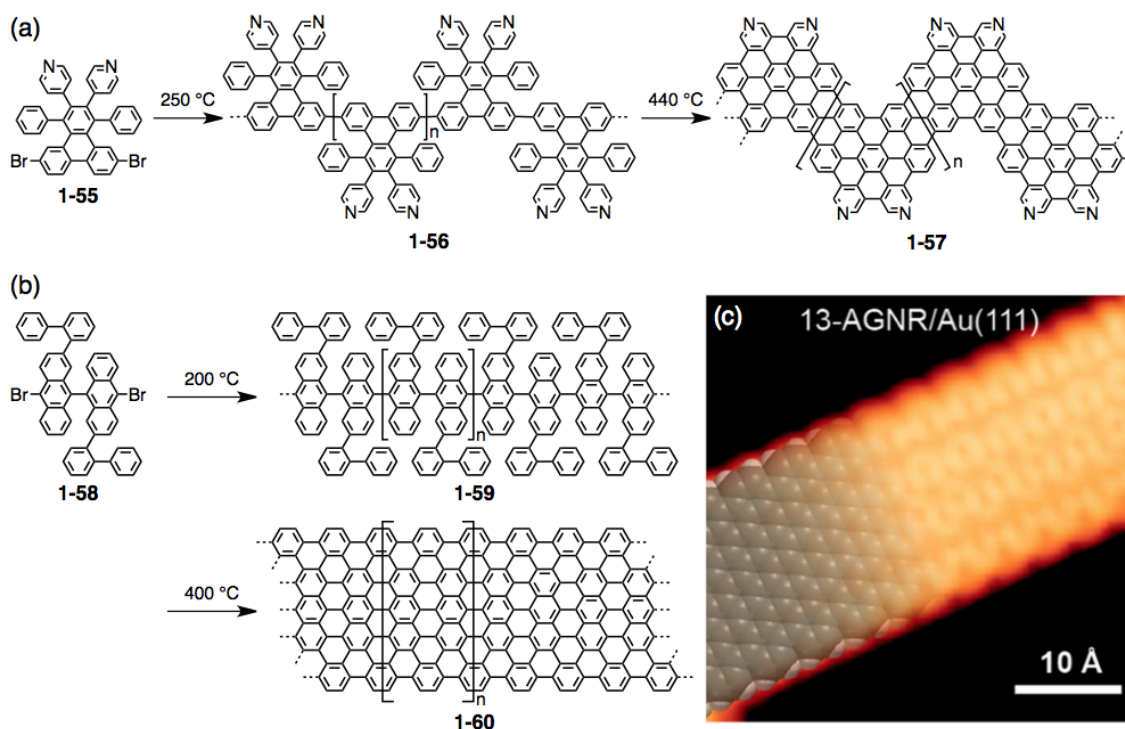


Figure 1-14. (a), (b) Surface-assisted synthesis of (a) N-doped, chevron-type GNR **1-57** and (b) $N = 13$ armchair GNR **1-60**. (c) An STM image of GNR **1-60** on a Au(111) surface with partly overlaid molecular model. Reprinted with permission from Ref. [177]; Copyright 2013, American Chemical Society.

1.2.2.6 Syntheses of GNRs confined in CNTs

Fabrication of GNRs has also been reported through polymerization and fusion of aromatic molecules confined inside single-walled CNTs (SWCNTs) by means of heat or electron beam.¹⁷⁸⁻¹⁸⁰ In 2011, *Talyzin and Anoshkin et al.* demonstrated that small PAHs, perylene and coronene (**1-61**), confined in a SWCNT can be converted into a GNR encapsulated in the SWCNT (GNR@SWCNT) by heat treatment at ca. 400–500 °C (Figure 1-15a and c).¹⁸⁰ The PAHs were closely aligned one-dimensionally inside the SWCNT, enabling the polymerization and fusion. Coronene (**1-61**) and perylene lead to GNRs with different shapes, indicating the possibility of structural control by employing different PAH molecules as monomers. In the same year, *Khlobystov et al.* reported a fabrication of GNRs with sulfur-terminated edges in SWCNTs by using S-containing fullerene derivative **1-62** (Figure 1-15b) or a mixture of pristine fullerene and tetrathiafulvalene (TTF).¹⁷⁸ In contrast to pristine fullerenes that

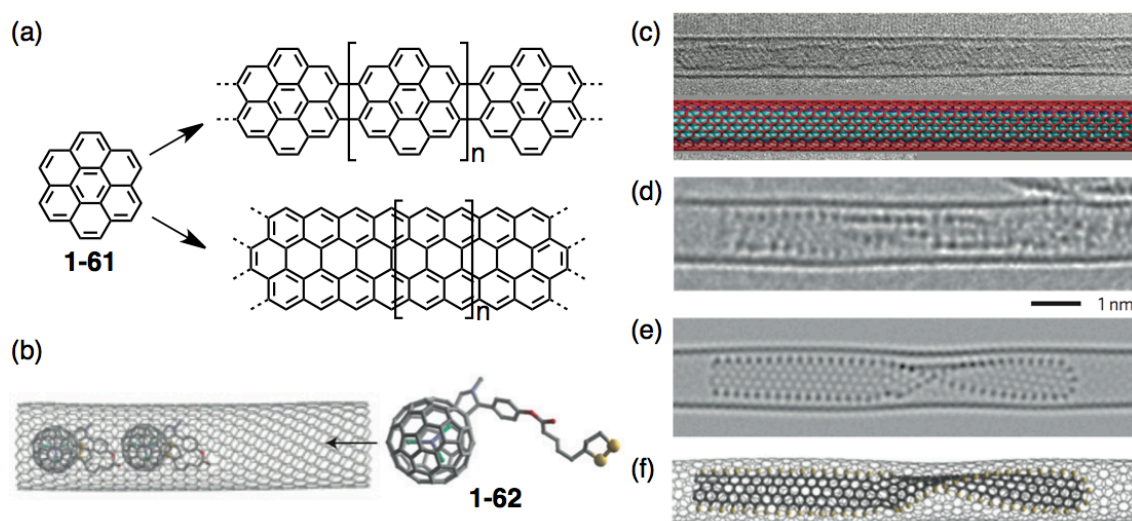


Figure 1-15. (a) Proposed structures of GNRs formed from coronene (**1-61**) confined in SWCNTs. (b) A schematic illustration of the confinement of fullerene derivative **1-62** in a SWCNT; gray: carbon, red: oxygen, purple: nitrogen, yellow: sulfur. (c) A TEM image of a GNR@SWCNT prepared from coronene (**1-61**) (top) and its model (bottom); light blue: GNR, red: SWCNT. Reprinted with permission from Ref. [180]; Copyright 2011, American Chemical Society. (d) An aberration-corrected high resolution TEM image, (e) a simulated TEM image, and (f) a molecular model of a GNR with sulfur-terminated edges confined in a SWCNT; gray: carbon, yellow: sulfur. (b), (d), (e), (f) Adapted/reprinted with permission from Ref. [178]; Copyright 2011, Nature publishing group.

transform into narrower guest-SWCNTs inside host-SWCNTs,¹⁸¹ fullerene derivative **1-62** as well as the mixture of fullerene and TTF could be converted to GNRs by e-beam irradiation, where the S atoms terminated the reactive edges of as-formed GNRs (Figure 1-15d-f). They further found that such GNRs could also be generated from TTF alone confined in SWCNTs.^{178,179} Nevertheless, the selective removal of the CNTs without affecting the confined GNRs is highly challenging, hindering further studies and applications of such GNRs.

1.3 Raman spectroscopy of graphene and related materials

Raman spectroscopy has long been one of the most facile and powerful methods for the characterization of carbon based materials. All graphitic materials show a G peak at $\sim 1582 \text{ cm}^{-1}$ and a G' peak at $\sim 2,700 \text{ cm}^{-1}$ with the excitation at 514 nm (Figure 1-16a).¹⁸² Graphene also displays a D peak at $\sim 1,350 \text{ cm}^{-1}$ at an edge or when its structure is defective. Therefore, the ratio of intensities of the G and D peaks are normally used to evaluate their quality, i.e. defect density. A D' peak observed at $\sim 1,620 \text{ cm}^{-1}$ is also induced by the disorder in the structure. In contrast, nanographenes and GNRs show the D peak regardless of the disorder due to the confinement of π -electrons in finite-size domains.^{140,183,184} The feature of the G' peak of graphene varies depending on the number of layers, rendering it possible to facilely distinguish mono-, bi-, tri-, and multilayer graphene from the Raman spectra (Figure 1-16b).¹⁸⁵

In addition to these peaks common for all graphitic materials, CNTs show typical resonant peaks from radial-breathing mode (RBM) in the low-frequency region.¹⁸⁶ The RBM is sensitive to the diameter of CNTs and can be used to characterize their (n, m) chirality. It has been revealed that GNRs also display resonant, low frequency peaks related to the RBM, which is called radial-breathing-like mode (RBLM).^{140,187} The frequency of the RBLM (ν_{RBLM}) critically depends on the lateral width of a GNR (w), and can be estimated by the equation: $\nu_{\text{RBLM}} = 3,222 (\text{\AA}/\text{cm})/w$.¹⁸⁸ Thus, the RBLM enables facile and swift estimation of the width of GNRs as well as the evaluation of the uniformity of GNRs in a sample by means of Raman spectroscopy.

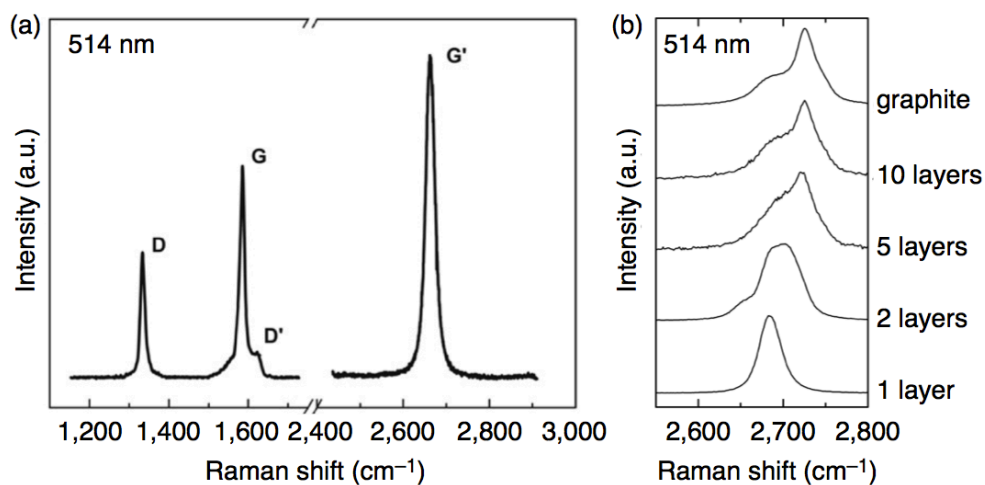


Figure 1-16. (a) Raman spectrum of a graphene edge at 514 nm. (b) Variation of the G' peak of graphene at 514 nm, depending of the number of layers. Reprinted with permission from (a) Ref. [182]; Copyright 2009, Elsevier, (b) Ref. [185]; Copyright 2007, Elsevier.

1.4 THz spectroscopy

In contrast to device fabrication, which is often highly challenging and requires considerable time and efforts, contact-free terahertz (THz) spectroscopy offers a facile and quick analysis of the intrinsic conductivity of semiconductor materials.^{189,190} In this method, charges in the materials are optically mobilized by the above-bandgap excitation with a short femtosecond pulse of light (pump pulse), followed by determination of the photoconductivity using a single-cycle THz pulse, which is applied after a certain delay (τ) (Figure 1-17a).¹⁹¹ The THz pulse essentially consists of a very fast succession of positive and negative fields (Figure 1-17b),¹⁹² which accelerate the mobilized charges. The transmitted THz pulse is altered through the interaction between the THz field and the mobilized charges, and directly related to the complex conductivity of electrons and holes in the materials.¹⁹⁰ The complex conductivity has real and imaginary parts, which give the photoconductivity and polarizability, respectively. The magnitude of the photoconductivity corresponds to the real part of the conductivity response, whereas the polarizability can be determined from the slope of the imaginary conductivity.¹⁹³

The THz spectroscopy method has been utilized for studying the nature and dynamics of photoexcited species in a variety of semiconductors, including inorganic and organic materials, quantum dots, as well as graphitic nanostructures.¹⁹⁰ The

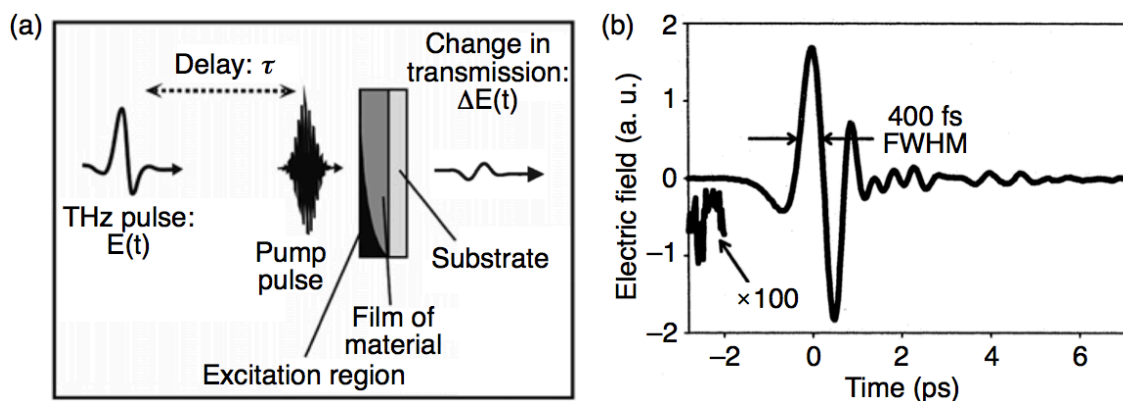


Figure 1-17. (a) A schematic illustration of the THz spectroscopy experiment. Adapted with permission from Ref. [191]; Copyright 2006, Elsevier. (b) A plot of a typical THz pulse with the duration of ca. 400 fs (full width at half maximum, FWHM) and a signal-to-noise ratio of around 1000:1. Reprinted with permission from Ref. [192]; Copyright 2000, American Physical Society.

investigation of graphene and graphite by this method was primarily performed either on films exfoliated from HOPG¹⁹⁴ or epitaxially grown on SiC.¹⁹⁵⁻¹⁹⁷ It has been found that intraband transitions are predominantly observed in the low-frequency range (<3 THz), whereas interband transitions become significant in the conductivity at higher THz frequencies, especially when the THz phonon energies amount to or exceed the double of the Fermi energy.^{190,193} Very recently, monolayer graphene grown by the CVD method was investigated to reveal efficient carrier-carrier scattering in the conduction band, leading to the generation of secondary hot electrons.¹⁹⁸ CNTs have been also studied by the THz spectroscopy, and it has been revealed that the primary photoexcitation products are excitons in CNTs.^{199,200} However, there has hitherto been no report on the THz spectroscopic investigations of GNRs.

1.5 Field-effect transistor

The first transistor, point-contact transistor, was realized in 1947 by *Bardeen*, *Shockley*, and *Brattain*, and then in 1962, the first field-effect transistor (FET) was developed by *Hofstein* and *Heiman*. A typical FET device consists of a semiconductor layer, a dielectric layer, a gate electrode, and source–drain (S–D) electrodes as shown in Figure 1-18.²⁰¹ The current flow between the S–D electrodes (drain current) can be controlled by a voltage applied to the gate electrode (gate voltage). Inorganic materials, especially silicon, have been predominantly employed for the semiconductor layer, but alternative materials such as organic semiconductors²⁰¹⁻²⁰³ as well as graphene and related materials^{58,204} are recently attracting more and more attention.

Figure 1-18 depicts representative device structures of FETs, where organic materials are used for the semiconductor layers. The gate electrode can be located either at the bottom or on the top of the devices, i.e. bottom-gate (Figure 1-18a and b) and top-gate (Figure 1-18c) geometry, respectively. Depending on the sequences of the S–D electrodes and the semiconductor layer, the bottom-gate FET devices can have two different configurations, namely top and bottom contact (Figure 1-18a and b,

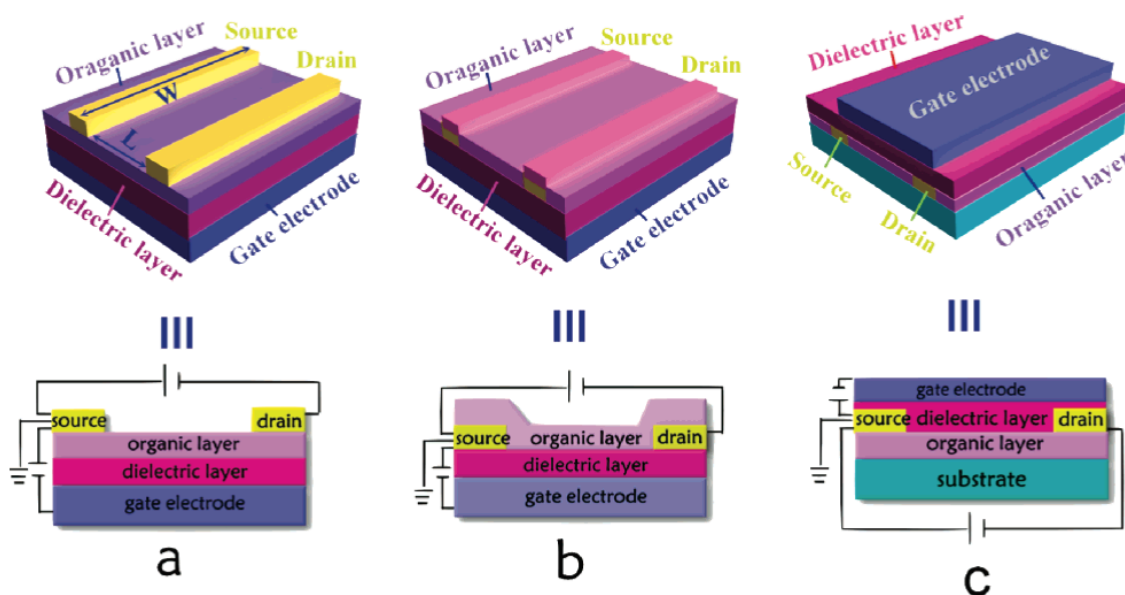


Figure 1-18. Schematic illustrations of FET devices with different geometries. (a), (b) Bottom-gate devices with (a) top- and (b) bottom-contact configurations. (c) A top-gate device. Organic materials are used in the semiconductor layers. Reprinted with permission from Ref. [201]; Copyright 2007, American Chemical Society.

respectively).²⁰¹ The bottom-contact devices can be facily fabricated by photolithographic patterning of the S–D electrodes on the dielectric layer followed by the deposition of the semiconductor material, although their performances are generally lower than those of the top-contact devices because of poorer contact. On the other hand, the top-down devices show better contact and thus higher performance, but their preparation via the deposition of the S–D electrodes through a shadow mask in the final step is less practical.

The field-effect transistor of graphene was first demonstrated by *Novoselov and Geim et al.* in 2004 with a bottom-gate device geometry,¹⁰ and later the first top-gate FET device of graphene was fabricated by *Lemme et al.* in 2007.²⁰⁵ Since then the FETs of graphene have been drastically improved, realizing cut-off frequency of as high as 427 GHz in 2012,²⁰⁶ although the problem with switching off due to the zero bandgap still remains valid. Top-down fabricated GNRs have simultaneously been integrated into FET devices as discussed in section 1.1 and subsection 1.2.1, respectively. However, realization of FET devices with bottom-up synthesized, structurally well-defined GNRs has remained a major challenge due to their relatively short length and/or poor processability, inhibiting their deposition on substrates and subsequent contacting.

1.6 Motivation and objectives

As described in the previous sections, top-down fabrications of the GNRs based on the cutting of graphene sheets,⁹¹⁻⁹⁵ the unzipping of CNTs,⁹⁸⁻¹⁰⁶ and the sonochemical extraction from an expanded graphite^{96,97} have demonstrated remarkable potential of these emerging materials with high charge-carrier mobilities and on-off ratios. Nevertheless, these top-down methods critically lack the structural control of the resulting GNRs, deteriorating their electric properties as well as inhibiting their fine-tuning. In contrast, fabrication of structurally well-defined GNRs has been realized by bottom-up synthetic approaches based on solution-mediated^{138,139} as well as surface-assisted¹⁴⁰ cyclodehydrogenation of tailor-made polyphenylene precursors. The surface-assisted method enabled the direct growth of atomically precise GNRs on metal surfaces, which could be unambiguously demonstrated by the in-situ STM visualizations. However, this surface-assisted method requires a complicated fabrication process, which can yield only a small amount of the GNRs bound to the metal surface.^{140,176,177} Further, the GNRs need to be subsequently transferred onto dielectric surfaces for fabrication of electronic devices on them, which is still highly challenging. In contrast, the solution-mediated approach has provided a way to the large-scale synthesis of GNRs. By rationally introducing solubilizing groups at the peripheral positions, the GNRs can be rendered liquid-phase processable, which makes this solution-mediated method more promising for the fabrication of practical GNRs.^{138,139} Nevertheless, the solution-synthesized GNRs have been limited by the small lateral width (up to ca. 1 nm), short longitudinal length (<100 nm), and/or poor processability.¹³⁷⁻¹³⁹

For the application of GNRs in electronic devices, a fine-tuning of the bandgap is prerequisite, which can be generally achieved by changing the lateral width of the GNRs.^{87,89-91} Furthermore, sufficient longitudinal extension (>100 nm) as well as high liquid-phase processability are required for the fabrication of GNR-based FET devices, especially on a single GNR. It has been indicated from the experimental results of top-down fabricated GNRs that a lateral width smaller than 5 nm is required in order to obtain a sufficiently high on-off ratio at room temperature.^{96,100,111} On the other hand, it has been theoretically^{135,136} as well as experimentally^{97,112} demonstrated that the charge-carrier mobility of GNRs drops as their lateral width decreases. It is therefore highly desirable to synthesize GNRs with various lateral widths up to 5 nm, while

keeping their high structural definition.

In order to fabricate structurally well-defined GNRs with larger widths based on the solution-mediated method, two different approaches are conceivable, which are exemplified in Figure 1-19 based on a feasible monomer **1-63**. One approach is to use a laterally extended monomer that leads to expanded polyphenylene precursors corresponding to wide GNRs. For instance, laterally extended monomer **1-66** can be assumed by introducing additional phenyl rings at the peripheries of monomer **1-63**. While monomer **1-63** leads to $N = 9$ armchair GNR **1-65** through polymerization and cyclodehydrogenation, laterally extended monomer **1-66** provides wider $N = 15$ armchair GNR **1-68** via expanded polyphenylene precursor **1-67** (Figure 1-19). The other approach toward laterally extended GNRs is to employ a monomer with V-shaped polymerizable backbone structure such as monomer **1-69**, which yields polyphenylene precursor **1-70** with twice the lateral width of the monomer, leading to $N = 18$ armchair GNR **1-71** with a width of ca. 2.1 nm. This method allows fabrications of wide GNRs from smaller monomers, the preparations of which are relatively simple and facile compared to laterally extended monomers such as **1-66**.

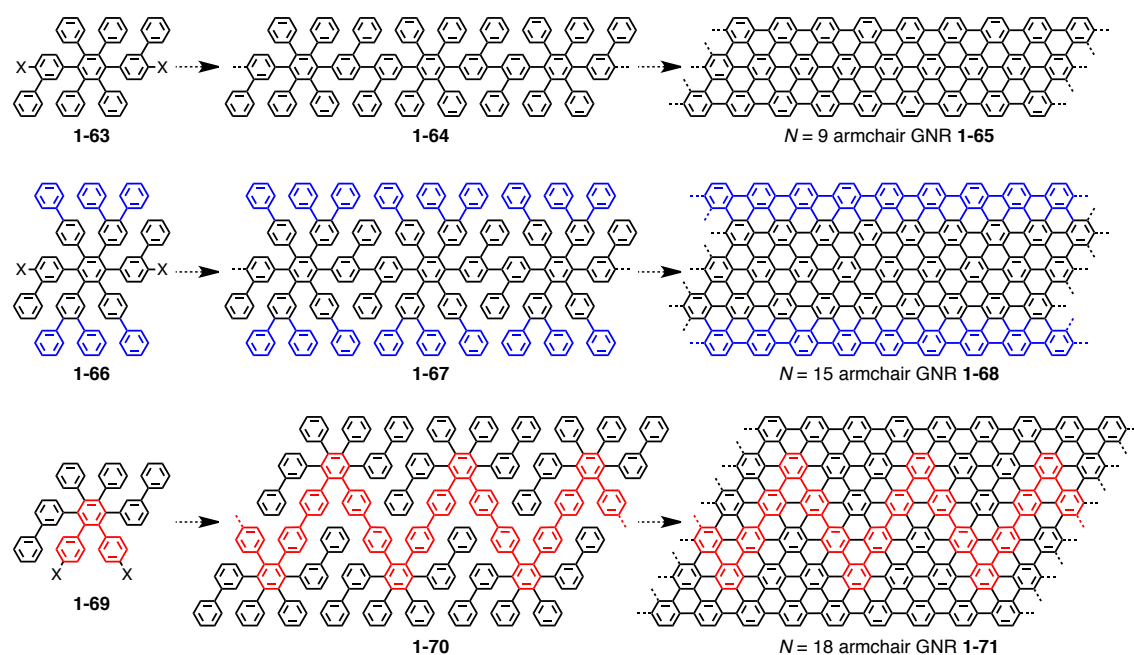


Figure 1-19. Assumed designs for the syntheses of laterally extended GNRs based on a feasible monomer **1-63** that would lead to $N = 9$ armchair GNR **1-65**. Laterally extended monomer **1-66** would give $N = 15$ armchair GNR **1-68**, and monomer **1-69** with V-shaped polymerizable backbone structure would provide $N = 18$ armchair GNR **1-71** with twice the width of the monomer. X represents a reactive functional group such as chloro and bromo group.

Regarding the polymerization method, A_2B_2 -type *Suzuki* polymerization has been employed in the previous syntheses of structurally defined and dispersible GNRs.^{138,139} However, this polymerization method involves two different monomers and is critically affected by the stoichiometry,^{207,208} which has hindered the preparation of high-molecular-weight precursors. In contrast, AA -type *Yamamoto* polymerization requires only one monomer structure and thus is free of this stoichiometry problem, which is expected to allow more efficient polymerization to reach higher molecular weights.^{209,210} Similarly, A_2B_2 -type *Diels–Alder* polymerization also requires two different monomers and is sensitive to the stoichiometry although it has proved to be a remarkably efficient polymerization method for the preparation of polyphenylene precursors with high molecular weights ($>100,000$ g/mol).^{137,162} Thereby, stoichiometry-free AB -type *Diels–Alder* polymerization is a highly promising method for achieving even higher molecular weight, which enables a synthesis of GNRs sufficiently elongated (e.g. >100 nm) for fabrication of single-ribbon FET devices.

The preparation of monomer **1-66** is rather complicated, especially when the rational introduction of bulky alkyl chains is considered for improving the dispersibility of the resulting GNRs. In contrast, laterally extended monomer **1-72** is obtainable through relatively simple synthetic steps, even with alkyl chains. Notably, monomer **1-72** yields GNR **1-74** with the lateral width of ca. 2.0 nm, which is larger than that of $N = 15$ armchair GNR **1-68** (Figure 1-20). For these reasons, a synthesis of an alkylated analogue of laterally extended GNR **1-74** via alkylated derivative of monomer **1-72** was set as the first objective for this dissertation, which will be discussed in the first half of chapter 2. AA -type *Yamamoto* polymerization was chosen as the polymerization method, instead of the conventional A_2B_2 -type *Suzuki* polymerization, in order to attain higher-molecular-weight polyphenylene precursors, which leads to longer GNRs.

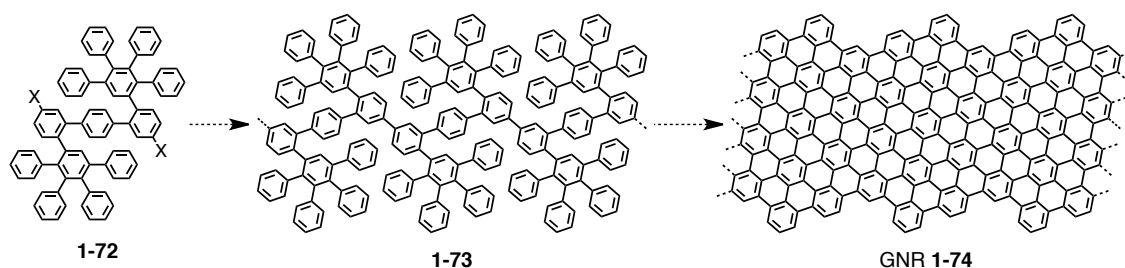


Figure 1-20. Synthetic design for GNR **1-74** from laterally extended monomer **1-72**. X represents a reactive functional group such as chloro and bromo group.

Syntheses of GNRs with higher lateral extensions are more challenging through the first approach, i.e. the use of laterally extended monomers, because of complicated synthetic steps required for the preparations of more extended monomers. In contrast, the second approach, i.e. the use of monomers bearing V-shaped polymerizable backbones structure, provides a facile access to broader GNRs from smaller and simpler monomers. As exemplified in Figure 1-19, small monomer **1-69** leads to $N = 18$ armchair GNR **1-71**, which is broader than $N = 15$ armchair GNR **1-68** derived from more complex monomer **1-66**. The second half of chapter 2 will be devoted to the synthesis of $N = 18$ armchair GNR with long alkyl chains from an alkylated derivative of monomer **1-69**.

Although the *AA*-type *Yamamoto* polymerization proves to be superior to the *A₂B₂*-type *Suzuki* polymerization for the synthesis of high-molecular-weight polyphenylene precursors, it turns out that it is not efficient enough to achieve the longitudinal length of >100 nm required for the fabrication of single-ribbon FET devices. In order to achieve such high longitudinal extension, a synthesis of GNRs via highly efficient *AB*-type *Diels-Alder* polymerization is desirable. To this aim, *AB*-type monomer **1-75** can be conceived, which leads to GNR **1-77** through the polymerization and cyclodehydrogenation (Figure 1-21). GNR **1-77** will be decorated with bulky alkyl chains to render them liquid-phase processable, which allows their spectroscopic and

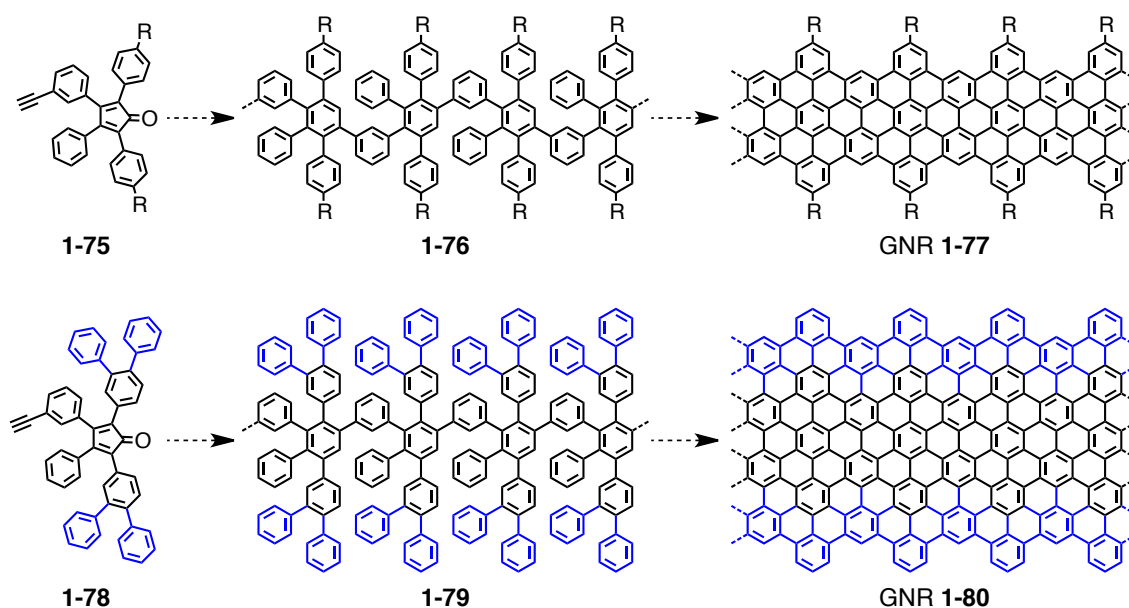


Figure 1-21. Synthetic designs for GNR **1-77** and laterally extended GNR **1-80** from *AB*-type *Diels-Alder* monomers **1-75** and **1-78**, respectively. R represents bulky alkyl groups such as dodecyl and *tert*-butyl.

microscopic characterizations as well as investigations of their electronic properties and integration into electronic devices (chapter 3).

In order to obtain wider GNRs with high longitudinal extension (>100 nm), *AB*-type *Diels-Alder* monomer **1-75** can be laterally extended to monomer **1-78**, which leads to GNR **1-80** with the width of ca. 2.0 nm, as will be discussed in chapter 4 (Figure 1-21). Laterally extended GNR **1-80** is expected to show lower bandgap and higher charge-carrier mobility than those of GNR **1-77** according to the theoretical predictions. Bulky alkyl chains will be installed at the peripheral positions of the broad GNRs in order to enable their liquid-phase processing for their structural and electronic characterizations. The effect of the lateral extension on the bandgap and charge-carrier mobilities will be discussed.

1.7 References

- (1) Patt, Y. *Proc. IEEE* **2001**, *89*, 1553.
- (2) Ohba, T.; Maeda, N.; Kitada, H.; Fujimoto, K.; Suzuki, K.; Nakamura, T.; Kawai, A.; Arai, K. *Microelectron. Eng.* **2010**, *87*, 485.
- (3) Kim, K. In *Electron Devices Meeting (IEDM), 2010 IEEE International* 2010, p 1.1.1.
- (4) Jourdain, A.; Stoukatch, S.; De Moor, P.; Ruythooren, W. In *International Interconnect Technology Conference, IEEE 2007* 2007, p 207.
- (5) Liu, F.; Yu, R. R.; Young, A. M.; Doyle, J. P.; Wang, X.; Shi, L.; Chen, K. N.; Li, X.; Dipaola, D. A.; Brown, D.; Ryan, C. T.; Hagan, J. A.; Wong, K. H.; Lu, M.; Gu, X.; Klymko, N. R.; Perfecto, E. D.; Merryman, A. G.; Kelly, K. A.; Purushothaman, S.; Koester, S. J.; Wisnieff, R.; Haensch, W. In *Electron Devices Meeting, 2008. IEDM 2008. IEEE International* 2008, p 1.
- (6) Miyakawa, N. In *Proceedings of the 2009 Asia and South Pacific Design Automation Conference*; IEEE Press: Yokohama, Japan, 2009, p 416.
- (7) Iwai, H. *Microelectron. Eng.* **2009**, *86*, 1520.
- (8) Jing, W.; Lundstrom, M. In *Electron Devices Meeting, 2002. IEDM '02. International* 2002, p 707.
- (9) Frank, D. J.; Dennard, R. H.; Nowak, E.; Solomon, P. M.; Yuan, T.; Hen-Sum Philip, W. *Proc. IEEE* **2001**, *89*, 259.
- (10) Novoselov, K. S.; Geim, A. K.; Morozov, S. V.; Jiang, D.; Zhang, Y.; Dubonos, S. V.; Grigorieva, I. V.; Firsov, A. A. *Science* **2004**, *306*, 666.
- (11) Bolotin, K. I.; Sikes, K. J.; Jiang, Z.; Klima, M.; Fudenberg, G.; Hone, J.; Kim, P.; Stormer, H. L. *Solid State Commun.* **2008**, *146*, 351.
- (12) Du, X.; Skachko, I.; Barker, A.; Andrei, E. Y. *Nature Nanotech.* **2008**, *3*, 491.
- (13) Bolotin, K. I.; Sikes, K. J.; Hone, J.; Stormer, H. L.; Kim, P. *Phys Rev Lett* **2008**, *101*, 096802.
- (14) Wallace, P. R. *Phys. Rev.* **1947**, *71*, 622.
- (15) McClure, J. W. *Phys. Rev.* **1956**, *104*, 666.
- (16) Slonczewski, J. C.; Weiss, P. R. *Phys. Rev.* **1958**, *109*, 272.
- (17) Semenoff, G. W. *Phys. Rev. Lett.* **1984**, *53*, 2449.
- (18) Haldane, F. D. M. *Phys. Rev. Lett.* **1988**, *61*, 2015.

- (19) Geim, A. K.; Novoselov, K. S. *Nature Mater.* **2007**, *6*, 183.
- (20) Service, R. F. *Science* **2009**, *324*, 875.
- (21) Novoselov, K. S.; Jiang, D.; Schedin, F.; Booth, T. J.; Khotkevich, V. V.; Morozov, S. V.; Geim, A. K. *Proc. Natl. Acad. Sci. USA* **2005**, *102*, 10451.
- (22) Zhang, Y.; Tan, Y. W.; Stormer, H. L.; Kim, P. *Nature* **2005**, *438*, 201.
- (23) Novoselov, K. S.; Jiang, Z.; Zhang, Y.; Morozov, S. V.; Stormer, H. L.; Zeitler, U.; Maan, J. C.; Boebinger, G. S.; Kim, P.; Geim, A. K. *Science* **2007**, *315*, 1379.
- (24) Novoselov, K. S.; Geim, A. K.; Morozov, S. V.; Jiang, D.; Katsnelson, M. I.; Grigorieva, I. V.; Dubonos, S. V.; Firsov, A. A. *Nature* **2005**, *438*, 197.
- (25) Liao, L.; Lin, Y.-C.; Bao, M.; Cheng, R.; Bai, J.; Liu, Y.; Qu, Y.; Wang, K. L.; Huang, Y.; Duan, X. *Nature* **2010**, *467*, 305.
- (26) Balandin, A. A.; Ghosh, S.; Bao, W.; Calizo, I.; Teweldebrhan, D.; Miao, F.; Lau, C. N. *Nano Lett.* **2008**, *8*, 902.
- (27) Ghosh, S.; Calizo, I.; Teweldebrhan, D.; Pokatilov, E. P.; Nika, D. L.; Balandin, A. A.; Bao, W.; Miao, F.; Lau, C. N. *Appl. Phys. Lett.* **2008**, *92*, 151911.
- (28) Lee, C.; Wei, X.; Kysar, J. W.; Hone, J. *Science* **2008**, *321*, 385.
- (29) Nair, R. R.; Blake, P.; Grigorenko, A. N.; Novoselov, K. S.; Booth, T. J.; Stauber, T.; Peres, N. M. R.; Geim, A. K. *Science* **2008**, *320*, 1308.
- (30) Bae, S.; Kim, H.; Lee, Y.; Xu, X.; Park, J.-S.; Zheng, Y.; Balakrishnan, J.; Lei, T.; Ri Kim, H.; Song, Y. I.; Kim, Y.-J.; Kim, K. S.; Ozyilmaz, B.; Ahn, J.-H.; Hong, B. H.; Iijima, S. *Nature Nanotech.* **2010**, *5*, 574.
- (31) *Nature Mater.* **2011**, *10*, 1.
- (32) Novoselov, K. S.; Falko, V. I.; Colombo, L.; Gellert, P. R.; Schwab, M. G.; Kim, K. *Nature* **2012**, *490*, 192.
- (33) Hernandez, Y.; Nicolosi, V.; Lotya, M.; Blighe, F. M.; Sun, Z.; De, S.; McGovern, I. T.; Holland, B.; Byrne, M.; Gun'Ko, Y. K.; Boland, J. J.; Niraj, P.; Duesberg, G.; Krishnamurthy, S.; Goodhue, R.; Hutchison, J.; Scardaci, V.; Ferrari, A. C.; Coleman, J. N. *Nature Nanotech.* **2008**, *3*, 563.
- (34) Coleman, J. N. *Adv. Funct. Mater.* **2009**, *19*, 3680.
- (35) Torrisi, F.; Hasan, T.; Wu, W.; Sun, Z.; Lombardo, A.; Kulmala, T. S.; Hsieh, G.-W.; Jung, S.; Bonaccorso, F.; Paul, P. J.; Chu, D.; Ferrari, A. C. *ACS Nano* **2012**, *6*, 2992.
- (36) Li, J.; Ye, F.; Vaziri, S.; Muhammed, M.; Lemme, M. C.; Östling, M. *Adv. Mater.* **2013**, *25*, 3985.

-
- (37) Secor, E. B.; Prabhmirashi, P. L.; Puntambekar, K.; Geier, M. L.; Hersam, M. *C. J. Phys. Chem. Lett.* **2013**, *4*, 1347.
- (38) Brodie, B. C. *Phil. Trans.* **1859**, *149*, 249.
- (39) Hummers, W. S.; Offeman, R. E. *J. Am. Chem. Soc.* **1958**, *80*, 1339.
- (40) Eda, G.; Chhowalla, M. *Adv. Mater.* **2010**, *22*, 2392.
- (41) Paredes, J. I.; Villar-Rodil, S.; Martínez-Alonso, A.; Tascón, J. M. D. *Langmuir* **2008**, *24*, 10560.
- (42) Eda, G.; Fanchini, G.; Chhowalla, M. *Nature Nanotech.* **2008**, *3*, 270.
- (43) Cai, W.; Piner, R. D.; Stadermann, F. J.; Park, S.; Shaibat, M. A.; Ishii, Y.; Yang, D.; Velamakanni, A.; An, S. J.; Stoller, M.; An, J.; Chen, D.; Ruoff, R. S. *Science* **2008**, *321*, 1815.
- (44) Mattevi, C.; Eda, G.; Agnoli, S.; Miller, S.; Mkhoyan, K. A.; Celik, O.; Mastrogiovanni, D.; Granozzi, G.; Garfunkel, E.; Chhowalla, M. *Adv. Funct. Mater.* **2009**, *19*, 2577.
- (45) He, H.; Klinowski, J.; Forster, M.; Lurf, A. *Chem. Phys. Lett.* **1998**, *287*, 53.
- (46) Stankovich, S.; Dikin, D. A.; Piner, R. D.; Kohlhaas, K. A.; Kleinhammes, A.; Jia, Y.; Wu, Y.; Nguyen, S. T.; Ruoff, R. S. *Carbon* **2007**, *45*, 1558.
- (47) Li, X.; Cai, W.; An, J.; Kim, S.; Nah, J.; Yang, D.; Piner, R.; Velamakanni, A.; Jung, I.; Tutuc, E.; Banerjee, S. K.; Colombo, L.; Ruoff, R. S. *Science* **2009**, *324*, 1312.
- (48) Karu, A. E.; Beer, M. *J. Appl. Phys.* **1966**, *37*, 2179.
- (49) Obraztsov, A. N.; Obraztsova, E. A.; Tyurnina, A. V.; Zolotukhin, A. A. *Carbon* **2007**, *45*, 2017.
- (50) Ueta, H.; Saida, M.; Nakai, C.; Yamada, Y.; Sasaki, M.; Yamamoto, S. *Surf. Sci.* **2004**, *560*, 183.
- (51) Coraux, J.; N'Diaye, A. T.; Busse, C.; Michely, T. *Nano Lett.* **2008**, *8*, 565.
- (52) Vázquez de Parga, A. L.; Calleja, F.; Borca, B.; Passeggi, M. C. G., Jr.; Hinarejos, J. J.; Guinea, F.; Miranda, R. *Phys. Rev. Lett.* **2008**, *100*, 056807.
- (53) Marchini, S.; Günther, S.; Wintterlin, J. *Phys. Rev. B* **2007**, *76*, 075429.
- (54) Gamo, Y.; Nagashima, A.; Wakabayashi, M.; Terai, M.; Oshima, C. *Surf. Sci.* **1997**, *374*, 61.
- (55) Reina, A.; Jia, X.; Ho, J.; Nezich, D.; Son, H.; Bulovic, V.; Dresselhaus, M. S.; Kong, J. *Nano Lett.* **2009**, *9*, 30.

- (56) Kim, K. S.; Zhao, Y.; Jang, H.; Lee, S. Y.; Kim, J. M.; Kim, K. S.; Ahn, J.-H.; Kim, P.; Choi, J.-Y.; Hong, B. H. *Nature* **2009**, *457*, 706.
- (57) Wu, Y.; Lin, Y.-m.; Bol, A. A.; Jenkins, K. A.; Xia, F.; Farmer, D. B.; Zhu, Y.; Avouris, P. *Nature* **2011**, *472*, 74.
- (58) Schwierz, F. *Nature Nanotech.* **2010**, *5*, 487.
- (59) Liang, Y. T.; Hersam, M. C. *Macromolecul. Chem. Phys.* **2012**, *213*, 1091.
- (60) Banhart, F.; Kotakoski, J.; Krasheninnikov, A. V. *ACS Nano* **2010**, *5*, 26.
- (61) Lee, G.-H.; Cooper, R. C.; An, S. J.; Lee, S.; van der Zande, A.; Petrone, N.; Hammerberg, A. G.; Lee, C.; Crawford, B.; Oliver, W.; Kysar, J. W.; Hone, J. *Science* **2013**, *340*, 1073.
- (62) Dean, C. R.; Young, A. F.; Meric, I.; Lee, C.; Wang, L.; Sorgenfrei, S.; Watanabe, K.; Taniguchi, T.; Kim, P.; Shepard, K. L.; Hone, J. *Nature Nanotech.* **2010**, *5*, 722.
- (63) Berger, C.; Song, Z.; Li, T.; Li, X.; Ogbazghi, A. Y.; Feng, R.; Dai, Z.; Marchenkov, A. N.; Conrad, E. H.; First, P. N.; de Heer, W. A. *J. Phys. Chem. B* **2004**, *108*, 19912.
- (64) Berger, C.; Song, Z.; Li, X.; Wu, X.; Brown, N.; Naud, C. c.; Mayou, D.; Li, T.; Hass, J.; Marchenkov, A. N.; Conrad, E. H.; First, P. N.; de Heer, W. A. *Science* **2006**, *312*, 1191.
- (65) Emtsev, K. V.; Bostwick, A.; Horn, K.; Jobst, J.; Kellogg, G. L.; Ley, L.; McChesney, J. L.; Ohta, T.; Reshanov, S. A.; Rohrl, J.; Rotenberg, E.; Schmid, A. K.; Waldmann, D.; Weber, H. B.; Seyller, T. *Nature Mater.* **2009**, *8*, 203.
- (66) Ohta, T.; Bostwick, A.; Seyller, T.; Horn, K.; Rotenberg, E. *Science* **2006**, *313*, 951.
- (67) de Heer, W. A.; Berger, C.; Wu, X.; First, P. N.; Conrad, E. H.; Li, X.; Li, T.; Sprinkle, M.; Hass, J.; Sadowski, M. L.; Potemski, M.; Martinez, G. *Solid State Commun.* **2007**, *143*, 92.
- (68) Forbeaux, I.; Themlin, J. M.; Debever, J. M. *Phys. Rev. B* **1998**, *58*, 16396.
- (69) Kedzierski, J.; Pei-Lan, H.; Healey, P.; Wyatt, P. W.; Keast, C. L.; Sprinkle, M.; Berger, C.; De Heer, W. A. *IEEE Trans. Electron. Dev.* **2008**, *55*, 2078.
- (70) Huang, H.; Chen, W.; Chen, S.; Wee, A. T. S. *ACS Nano* **2008**, *2*, 2513.
- (71) Zhou, S. Y.; Gweon, G. H.; Fedorov, A. V.; First, P. N.; de Heer, W. A.; Lee, D. H.; Guinea, F.; Castro Neto, A. H.; Lanzara, A. *Nature Mater.* **2007**, *6*, 770.
- (72) Lin, Y.-M.; Dimitrakopoulos, C.; Jenkins, K. A.; Farmer, D. B.; Chiu, H.-Y.; Grill, A.; Avouris, P. *Science* **2010**, *327*, 662.

-
- (73) Hertel, S.; Waldmann, D.; Jobst, J.; Albert, A.; Albrecht, M.; Reshanov, S.; Schöner, A.; Krieger, M.; Weber, H. B. *Nat. Commun.* **2012**, *3*, 957.
- (74) Sutter, P. W.; Flege, J.-I.; Sutter, E. A. *Nature Mater.* **2008**, *7*, 406.
- (75) Yang, H.; Heo, J.; Park, S.; Song, H. J.; Seo, D. H.; Byun, K. E.; Kim, P.; Yoo, I.; Chung, H. J.; Kim, K. *Science* **2012**, *336*, 1140.
- (76) Britnell, L.; Gorbachev, R. V.; Jalil, R.; Belle, B. D.; Schedin, F.; Mishchenko, A.; Georgiou, T.; Katsnelson, M. I.; Eaves, L.; Morozov, S. V.; Peres, N. M. R.; Leist, J.; Geim, A. K.; Novoselov, K. S.; Ponomarenko, L. A. *Science* **2012**, *335*, 947.
- (77) Castro, E. V.; Novoselov, K. S.; Morozov, S. V.; Peres, N. M. R.; dos Santos, J. M. B. L.; Nilsson, J.; Guinea, F.; Geim, A. K.; Neto, A. H. C. *Phys. Rev. Lett.* **2007**, *99*, 216802.
- (78) Zhang, Y.; Tang, T.-T.; Girit, C.; Hao, Z.; Martin, M. C.; Zettl, A.; Crommie, M. F.; Shen, Y. R.; Wang, F. *Nature* **2009**, *459*, 820.
- (79) Xia, F.; Farmer, D. B.; Lin, Y.-m.; Avouris, P. *Nano Lett.* **2010**, *10*, 715.
- (80) Chen, L.; Hernandez, Y.; Feng, X.; Müllen, K. *Angew Chem Int Ed Engl* **2012**, *51*, 7640.
- (81) Pereira, V. M.; Castro Neto, A. H.; Peres, N. M. R. *Phys. Rev. B* **2009**, *80*, 045401.
- (82) Ni, Z. H.; Yu, T.; Lu, Y. H.; Wang, Y. Y.; Feng, Y. P.; Shen, Z. X. *ACS Nano* **2008**, *2*, 2301.
- (83) Bai, J.; Zhong, X.; Jiang, S.; Huang, Y.; Duan, X. *Nature Nanotech.* **2010**, *5*, 190.
- (84) Balog, R.; Jørgensen, B.; Nilsson, L.; Andersen, M.; Rienks, E.; Bianchi, M.; Fanetti, M.; Lægsgaard, E.; Baraldi, A.; Lizzit, S.; Sljivancanin, Z.; Besenbacher, F.; Hammer, B.; Pedersen, T. G.; Hofmann, P.; Hornekær, L. *Nature Mater.* **2010**, *9*, 315.
- (85) Ma, L.; Wang, J.; Ding, F. *ChemPhysChem* **2013**, *14*, 47.
- (86) Bai, J.; Huang, Y. *Mater. Sci. Eng. R-Rep.* **2010**, *70*, 341.
- (87) Nakada, K.; Fujita, M.; Dresselhaus, G.; Dresselhaus, M. S. *Phys. Rev. B* **1996**, *54*, 17954.
- (88) Son, Y. W.; Cohen, M. L.; Louie, S. G. *Nature* **2006**, *444*, 347.
- (89) Barone, V.; Hod, O.; Scuseria, G. E. *Nano Lett.* **2006**, *6*, 2748.
- (90) Son, Y.-W.; Cohen, M. L.; Louie, S. G. *Phys. Rev. Lett.* **2006**, *97*, 216803.

- (91) Han, M.; Özyilmaz, B.; Zhang, Y.; Kim, P. *Phys. Rev. Lett.* **2007**, *98*, 206805.
- (92) Chen, Z.; Lin, Y.; Rooks, M.; Avouris, P. *Physica E* **2007**, *40*, 228.
- (93) Tapasztó, L.; Dobrik, G.; Lambin, P.; Biro, L. P. *Nature Nanotech.* **2008**, *3*, 397.
- (94) Datta, S. S.; Strachan, D. R.; Khamis, S. M.; Johnson, A. T. C. *Nano Lett.* **2008**, *8*, 1912.
- (95) Ci, L.; Xu, Z.; Wang, L.; Gao, W.; Ding, F.; Kelly, K.; Yakobson, B.; Ajayan, P. *Nano Res.* **2008**, *1*, 116.
- (96) Li, X.; Wang, X.; Zhang, L.; Lee, S.; Dai, H. *Science* **2008**, *319*, 1229.
- (97) Wang, X.; Ouyang, Y.; Li, X.; Wang, H.; Guo, J.; Dai, H. *Phys. Rev. Lett.* **2008**, *100*, 206803.
- (98) Kosynkin, D. V.; Higginbotham, A. L.; Sinitskii, A.; Lomeda, J. R.; Dimiev, A.; Price, B. K.; Tour, J. M. *Nature* **2009**, *458*, 872.
- (99) Higginbotham, A. L.; Kosynkin, D. V.; Sinitskii, A.; Sun, Z.; Tour, J. M. *ACS Nano* **2010**, *4*, 2059.
- (100) Jiao, L.; Zhang, L.; Wang, X.; Diankov, G.; Dai, H. *Nature* **2009**, *458*, 877.
- (101) Jiao, L.; Zhang, L.; Ding, L.; Liu, J.; Dai, H. *Nano Res.* **2010**, *3*, 387.
- (102) Elías, A. L.; Botello-Méndez, A. s. R.; Meneses-Rodríguez, D.; Jehová González, V.; Ramírez-González, D.; Ci, L.; Muñoz-Sandoval, E.; Ajayan, P. M.; Terrones, H.; Terrones, M. *Nano Lett.* **2009**, *10*, 366.
- (103) Parashar, U. K.; Bhandari, S.; Srivastava, R. K.; Jariwala, D.; Srivastava, A. *Nanoscale* **2011**, *3*, 3876.
- (104) Shinde, D. B.; Debgupta, J.; Kushwaha, A.; Aslam, M.; Pillai, V. K. *J. Am. Chem. Soc.* **2011**, *133*, 4168.
- (105) Jiao, L. Y.; Wang, X. R.; Diankov, G.; Wang, H. L.; Dai, H. J. *Nature Nanotech.* **2010**, *5*, 321.
- (106) Xie, L.; Wang, H.; Jin, C.; Wang, X.; Jiao, L.; Suenaga, K.; Dai, H. *J. Am. Chem. Soc.* **2011**, *133*, 10394.
- (107) Campos-Delgado, J.; Romo-Herrera, J. M.; Jia, X.; Cullen, D. A.; Muramatsu, H.; Kim, Y. A.; Hayashi, T.; Ren, Z.; Smith, D. J.; Okuno, Y.; Ohba, T.; Kanoh, H.; Kaneko, K.; Endo, M.; Terrones, H.; Dresselhaus, M. S.; Terrones, M. *Nano Lett.* **2008**, *8*, 2773.
- (108) Wei, D.; Liu, Y.; Zhang, H.; Huang, L.; Wu, B.; Chen, J.; Yu, G. *J. Am. Chem. Soc.* **2009**, *131*, 11147.

-
- (109) Song, W.; Kim, S. Y.; Kim, Y.; Kim, S. H.; Lee, S. I.; Song, I.; Jeon, C.; Park, C.-Y. *J. Phys. Chem. C* **2012**, *116*, 20023.
- (110) Sprinkle, M.; Ruan, M.; Hu, Y.; Hankinson, J.; Rubio-Roy, M.; Zhang, B.; Wu, X.; Berger, C.; de Heer, W. A. *Nature Nanotech.* **2010**, *5*, 727.
- (111) Wang, X.; Dai, H. *Nature Chem.* **2010**, *2*, 661.
- (112) Bai, J.; Duan, X.; Huang, Y. *Nano Lett.* **2009**, *9*, 2083.
- (113) Pan, Z.; Liu, N.; Fu, L.; Liu, Z. *J. Am. Chem. Soc.* **2011**, *133*, 17578.
- (114) Wang, X.; Li, X.; Zhang, L.; Yoon, Y.; Weber, P. K.; Wang, H.; Guo, J.; Dai, H. *Science* **2009**, *324*, 768.
- (115) Lin, Y.-M.; Avouris, P. *Nano Lett.* **2008**, *8*, 2119.
- (116) Xie, L.; Jiao, L.; Dai, H. *J. Am. Chem. Soc.* **2010**, *132*, 14751.
- (117) Wang, Z. F.; Li, Q.; Zheng, H.; Ren, H.; Su, H.; Shi, Q. W.; Chen, J. *Phys. Rev. B* **2007**, *75*, 113406.
- (118) Stille, J. K.; Noren, G. K.; Green, L. *J. Polym. Sci. A-1, Polym. Chem.* **1970**, *8*, 2245.
- (119) Schlüter, A. D.; Löffler, M.; Enkelmann, V. *Nature* **1994**, *368*, 831.
- (120) Löffler, M.; Schlüter, A.-D.; Gessler, K.; Saenger, W.; Toussaint, J.-M.; Brédas, J.-L. *Angew. Chem. Int. Ed. Engl.* **1994**, *33*, 2209.
- (121) Scherf, U.; Müllen, K. *Makromol. Chem., Rapid Commun.* **1991**, *12*, 489.
- (122) Scherf, U.; Müllen, K. *Macromolecules* **1992**, *25*, 3546.
- (123) Scherf, U. *J. Mater. Chem.* **1999**, *9*, 1853.
- (124) Chmil, K.; Scherf, U. *Makromol. Chem., Rapid Commun.* **1993**, *14*, 217.
- (125) Chmil, K.; Scherf, U. *Acta Polym.* **1997**, *48*, 208.
- (126) Goldfinger, M. B.; Swager, T. M. *J. Am. Chem. Soc.* **1994**, *116*, 7895.
- (127) Yu, L.; Chen, M.; Dalton, L. R. *Chem. Mater.* **1990**, *2*, 649.
- (128) Kellman, R.; Marvel, C. S. *J. Polym. Sci. Polym. Chem. Ed.* **1975**, *13*, 2125.
- (129) Hurley, S. A.; Dutt, P. K.; Marvel, C. S. *J. Polym. Sci. A-1 Polym. Chem.* **1972**, *10*, 1243.
- (130) Tour, J. M.; Lamba, J. J. S. *J. Am. Chem. Soc.* **1993**, *115*, 4935.
- (131) Lamba, J. J. S.; Tour, J. M. *J. Am. Chem. Soc.* **1994**, *116*, 11723.
- (132) Patil, S. A.; Scherf, U.; Kadashchuk, A. *Adv. Funct. Mater.* **2003**, *13*, 609.
- (133) Dierschke, F.; Grimsdale, A. C.; Müllen, K. *Macromol. Chem. Phys.* **2004**, *205*, 1147.
- (134) Forster, M.; Annan, K. O.; Scherf, U. *Macromolecules* **1999**, *32*, 3159.

- (135) Obradovic, B.; Kotlyar, R.; Heinz, F.; Matagne, P.; Rakshit, T.; Giles, M. D.; Stettler, M. A.; Nikonov, D. E. *Appl. Phys. Lett.* **2006**, *88*, 142102.
- (136) Wang, J.; Zhao, R.; Yang, M.; Liu, Z. *J. Chem. Phys.* **2013**, *138*, 084701.
- (137) Wu, J. S.; Gherghel, L.; Watson, M. D.; Li, J. X.; Wang, Z. H.; Simpson, C. D.; Kolb, U.; Müllen, K. *Macromolecules* **2003**, *36*, 7082.
- (138) Yang, X. Y.; Dou, X.; Rouhanipour, A.; Zhi, L. J.; Rader, H. J.; Müllen, K. *J. Am. Chem. Soc.* **2008**, *130*, 4216.
- (139) Dössel, L.; Gherghel, L.; Feng, X.; Müllen, K. *Angew. Chem. Int. Ed.* **2011**, *50*, 2540.
- (140) Cai, J.; Ruffieux, P.; Jaafar, R.; Bieri, M.; Braun, T.; Blankenburg, S.; Muoth, M.; Seitsonen, A. P.; Saleh, M.; Feng, X.; Müllen, K.; Fasel, R. *Nature* **2010**, *466*, 470.
- (141) Berresheim, A. J.; Müller, M.; Müllen, K. *Chem. Rev.* **1999**, *99*, 1747.
- (142) Watson, M. D.; Fechtenkötter, A.; Müllen, K. *Chem. Rev.* **2001**, *101*, 1267.
- (143) Wu, J.; Pisula, W.; Müllen, K. *Chem. Rev.* **2007**, *107*, 718.
- (144) Stabel, A.; Herwig, P.; Müllen, K.; Rabe, J. P. *Angew. Chem. Int. Ed. Engl.* **1995**, *34*, 1609.
- (145) Clar, E.; Ironside, C. T. *Proc. Chem. Soc.* **1958**, 150.
- (146) Clar, E.; Ironside, C. T.; Zander, M. *J. Chem. Soc.* **1959**, 142.
- (147) Halleux, A.; Martin, R. H.; King, G. S. D. *Helv. Chim. Acta* **1958**, *41*, 1177.
- (148) Hendel, W.; Khan, Z. H.; Schmidt, W. *Tetrahedron* **1986**, *42*, 1127.
- (149) Kovacic, P.; Jones, M. B. *Chem. Rev.* **1987**, *87*, 357.
- (150) Kovacic, P.; Kyriakis, A. *Tetrahedron Lett.* **1962**, *3*, 467.
- (151) Kovacic, P.; Kyriakis, A. *J. Am. Chem. Soc.* **1963**, *85*, 454.
- (152) Kovacic, P.; Oziomek, J. *J. Org. Chem.* **1964**, *29*, 100.
- (153) Iyer, V. S.; Yoshimura, K.; Enkelmann, V.; Epsch, R.; Rabe, J. P.; Müllen, K. *Angew. Chem. Int. Ed.* **1998**, *37*, 2696.
- (154) Müller, M.; Iyer, V. S.; Kübel, C.; Enkelmann, V.; Müllen, K. *Angew. Chem. Int. Ed. Engl.* **1997**, *36*, 1607.
- (155) Iyer, V. S.; Wehmeier, M.; Brand, J. D.; Keegstra, M. A.; Müllen, K. *Angew. Chem. Int. Ed. Engl.* **1997**, *36*, 1604.
- (156) Wasserfallen, D.; Kastler, M.; Pisula, W.; Hofer, W. A.; Fogel, Y.; Wang, Z.; Müllen, K. *J. Am. Chem. Soc.* **2006**, *128*, 1334.

-
- (157) Böhme, T.; Simpson, C. D.; Müllen, K.; Rabe, J. P. *Chem.—Eur. J.* **2007**, *13*, 7349.
- (158) Tomović, Ž.; Watson, M. D.; Müllen, K. *Angew. Chem. Int. Ed.* **2004**, *43*, 755.
- (159) Morgenroth, F.; Reuther, E.; Müllen, K. *Angew. Chem. Int. Ed. Engl.* **1997**, *36*, 631.
- (160) Palermo, V.; Morelli, S.; Simpson, C.; Müllen, K.; Samori, P. *J. Mater. Chem.* **2006**, *16*, 266.
- (161) Simpson, C. D.; Brand, J. D.; Berresheim, A. J.; Przybilla, L.; Räder, H. J.; Müllen, K. *Chem.—Eur. J.* **2002**, *8*, 1424.
- (162) Shifrina, Z. B.; Averina, M. S.; Rusanov, A. L.; Wagner, M.; Müllen, K. *Macromolecules* **2000**, *33*, 3525.
- (163) Fogel, Y.; Zhi, L.; Rouhanipour, A.; Andrienko, D.; Räder, H. J.; Müllen, K. *Macromolecules* **2009**, *42*, 6878.
- (164) Grill, L.; Dyer, M.; Lafferentz, L.; Persson, M.; Peters, M. V.; Hecht, S. *Nature Nanotech.* **2007**, *2*, 687.
- (165) Bieri, M.; Treier, M.; Cai, J.; Aït-Mansour, K.; Ruffieux, P.; Groning, O.; Groning, P.; Kastler, M.; Rieger, R.; Feng, X.; Müllen, K.; Fasel, R. *Chem. Commun.* **2009**, 6919.
- (166) Bieri, M.; Nguyen, M.-T.; Gröning, O.; Cai, J.; Treier, M.; Aït-Mansour, K.; Ruffieux, P.; Pignedoli, C. A.; Passerone, D.; Kastler, M.; Müllen, K.; Fasel, R. *J. Am. Chem. Soc.* **2010**, *132*, 16669.
- (167) Lafferentz, L.; Eberhardt, V.; Dri, C.; Africh, C.; Comelli, G.; Esch, F.; Hecht, S.; Grill, L. *Nature Chem.* **2012**, *4*, 215.
- (168) Treier, M.; Pignedoli, C. A.; Laino, T.; Rieger, R.; Müllen, K.; Passerone, D.; Fasel, R. *Nature Chem.* **2011**, *3*, 61.
- (169) Talirz, L.; Söde, H.; Cai, J.; Ruffieux, P.; Blankenburg, S.; Jafaar, R.; Berger, R.; Feng, X.; Müllen, K.; Passerone, D.; Fasel, R.; Pignedoli, C. A. *J. Am. Chem. Soc.* **2013**, *135*, 2060.
- (170) Ruffieux, P.; Cai, J.; Plumb, N. C.; Patthey, L.; Prezzi, D.; Ferretti, A.; Molinari, E.; Feng, X.; Müllen, K.; Pignedoli, C. A.; Fasel, R. *ACS Nano* **2012**, *6*, 6930.
- (171) Blankenburg, S.; Cai, J.; Ruffieux, P.; Jaafar, R.; Passerone, D.; Feng, X.; Müllen, K.; Fasel, R.; Pignedoli, C. A. *ACS Nano* **2012**, *6*, 2020.
- (172) Linden, S.; Zhong, D.; Timmer, A.; Aghdassi, N.; Franke, J. H.; Zhang, H.; Feng, X.; Müllen, K.; Fuchs, H.; Chi, L.; Zacharias, H. *Phys. Rev. Lett.* **2012**, *108*, 216801.

- (173) Huang, H.; Wei, D.; Sun, J.; Wong, S. L.; Feng, Y. P.; Neto, A. H. C.; Wee, A. T. S. *Sci. Rep.* **2012**, *2*.
- (174) Koch, M.; Ample, F.; Joachim, C.; Grill, L. *Nature Nanotech.* **2012**, *7*, 713-717.
- (175) van der Lit, J.; Boneschanscher, M. P.; Vanmaekelbergh, D.; Ijäs, M.; Uppstu, A.; Ervasti, M.; Harju, A.; Liljeroth, P.; Swart, I. *Nature Commun.* **2013**, *4*, 2023.
- (176) Bronner, C.; Stremlau, S.; Gille, M.; Brauße, F.; Haase, A.; Hecht, S.; Tegeder, P. *Angew. Chem. Int. Ed.* **2013**, *52*, 4422.
- (177) Chen, Y.-C.; de Oteyza, D. G.; Pedramrazi, Z.; Chen, C.; Fischer, F. R.; Crommie, M. F. *ACS Nano* **2013**, *7*, 6123.
- (178) Chuvilin, A.; Bichoutskaia, E.; Gimenez-Lopez, M. C.; Chamberlain, T. W.; Rance, G. A.; Kuganathan, N.; Biskupek, J.; Kaiser, U.; Khlobystov, A. N. *Nature Mater.* **2011**, *10*, 687.
- (179) Chamberlain, T. W.; Biskupek, J.; Rance, G. A.; Chuvilin, A.; Alexander, T. J.; Bichoutskaia, E.; Kaiser, U.; Khlobystov, A. N. *ACS Nano* **2012**, *6*, 3943.
- (180) Talyzin, A. V.; Anoshkin, I. V.; Krasheninnikov, A. V.; Nieminen, R. M.; Nasibulin, A. G.; Jiang, H.; Kauppinen, E. I. *Nano Lett.* **2011**, *11*, 4352.
- (181) Bandow, S.; Takizawa, M.; Hirahara, K.; Yudasaka, M.; Iijima, S. *Chem. Phys. Lett.* **2001**, *337*, 48.
- (182) Malard, L. M.; Pimenta, M. A.; Dresselhaus, G.; Dresselhaus, M. S. *Phys. Rep.* **2009**, *473*, 51.
- (183) Castiglioni, C.; Tommasini, M.; Zerbi, G. *Philos. Transact. A Math. Phys. Eng. Sci.* **2004**, *362*, 2425.
- (184) Negri, F.; Castiglioni, C.; Tommasini, M.; Zerbi, G. *J. Phys. Chem. A* **2002**, *106*, 3306.
- (185) Ferrari, A. *Solid State Commun.* **2007**, *143*, 47.
- (186) Saito, R.; Hofmann, M.; Dresselhaus, G.; Jorio, A.; Dresselhaus, M. S. *Adv. Phys.* **2011**, *60*, 413.
- (187) Zhou, J.; Dong, J. *Appl. Phys. Lett.* **2007**, *91*, 173108.
- (188) Gillen, R.; Mohr, M.; Maultzsch, J. *Phys. Rev. B* **2010**, *81*, 205426.
- (189) Beard, M. C.; Turner, G. M.; Schmittenmaer, C. A. *J. Phys. Chem. B* **2002**, *106*, 7146.
- (190) Ulbricht, R.; Hendry, E.; Shan, J.; Heinz, T.; Bonn, M. *Rev. Mod. Phys.* **2011**, *83*, 543.

-
- (191) Hendry, E.; Koeberg, M.; Schins, J. M.; Siebbeles, L. D. A.; Bonn, M. *Chemical Physics Letters* **2006**, *432*, 441.
- (192) Beard, M. C.; Turner, G. M.; Schmittenmaer, C. A. *Phys. Rev. B* **2000**, *62*, 15764.
- (193) Wang, F.; Shan, J.; Islam, M. A.; Herman, I. P.; Bonn, M.; Heinz, T. F. *Nature Mater.* **2006**, *5*, 861.
- (194) Kampfrath, T.; Perfetti, L.; Schapper, F.; Frischkorn, C.; Wolf, M. *Phys. Rev. Lett.* **2005**, *95*, 187403.
- (195) Choi, H.; Borondics, F.; Siegel, D. A.; Zhou, S. Y.; Martin, M. C.; Lanzara, A.; Kaindl, R. A. *Appl. Phys. Lett.* **2009**, *94*, 172102.
- (196) George, P. A.; Strait, J.; Dawlaty, J.; Shivaraman, S.; Chandrashekar, M.; Rana, F.; Spencer, M. G. *Nano Lett.* **2008**, *8*, 4248.
- (197) Strait, J. H.; Wang, H.; Shivaraman, S.; Shields, V.; Spencer, M.; Rana, F. *Nano Lett.* **2011**, *11*, 4902.
- (198) Tielrooij, K. J.; Song, J. C. W.; Jensen, S. A.; Centeno, A.; Pesquera, A.; Zurutuza Elorza, A.; Bonn, M.; Levitov, L. S.; Koppens, F. H. L. *Nature Phys.* **2013**, *9*, 248.
- (199) Beard, M. C.; Blackburn, J. L.; Heben, M. J. *Nano Lett.* **2008**, *8*, 4238-4242.
- (200) Xu, X.; Chuang, K.; Nicholas, R. J.; Johnston, M. B.; Herz, L. M. *J. Phys. Chem. C* **2009**, *113*, 18106.
- (201) Di, C.-a.; Yu, G.; Liu, Y.; Zhu, D. *J. Phys. Chem. B* **2007**, *111*, 14083.
- (202) Horowitz, G. *Adv. Mater.* **1998**, *10*, 365.
- (203) Muccini, M. *Nature Mater.* **2006**, *5*, 605.
- (204) Avouris, P.; Chen, J. *Mater. Today* **2006**, *9*, 46.
- (205) Lemme, M. C.; Echtermeyer, T. J.; Baus, M.; Kurz, H. *IEEE Electron Dev. Lett.* **2007**, *28*, 282.
- (206) Cheng, R.; Bai, J.; Liao, L.; Zhou, H.; Chen, Y.; Liu, L.; Lin, Y.-C.; Jiang, S.; Huang, Y.; Duan, X. *Proc. Natl. Acad. Sci. USA* **109**, 11588.
- (207) Carothers, W. H. *Trans. Faraday Soc.* **1936**, *32*, 39.
- (208) Odian, G. G. *Principles of Polymerization*; J. Wiley & Sons: Hoboken, NJ, 2004.
- (209) Lee, J.; Cho, H.-J.; Jung, B.-J.; Cho, N. S.; Shim, H.-K. *Macromolecules* **2004**, *37*, 8523.

- (210) Setayesh, S.; Grimsdale, A. C.; Weil, T.; Enkelmann, V.; Müllen, K.; Meghdadi, F.; List, E. J. W.; Leising, G. *J. Am. Chem. Soc.* **2001**, *123*, 946.

Chapter 2. Laterally Extended GNRs via *Yamamoto*

Polymerization

In this chapter, two bottom-up, solution-synthetic approaches are described for the fabrication of laterally extended GNRs. The first approach is based on a use of a laterally extended monomer, which undergoes linear polymerization to afford broad (1.54–1.98 nm) GNRs with a mixture of cove-type¹ and armchair edge structures. The second approach employs a monomer with a V-shaped polymerizable backbone structure, realizing $N = 18$ armchair GNRs with twice the width of the monomer, i.e. ~2.1 nm. *AA*-type *Yamamoto* polymerization is utilized for both monomers, achieving higher molecular weight compared to previously reported GNRs fabricated via A_2B_2 -type *Suzuki* polymerization.^{2,3} Successful syntheses of these GNRs are demonstrated by optical spectroscopies and mass spectrometry as well as through investigation of monomeric model systems. Application of $N = 18$ armchair GNRs in liquid-phase-processed FET devices is also discussed. The syntheses and characterizations reported in sections 2.1 and 2.2 were carried out in collaboration with [REDACTED] and [REDACTED], respectively, in our research group.

2.1 Laterally extended GNRs with a mixture of cove and armchair edge structures

2.1.1 Synthetic strategy

The simplest way to achieve the lateral extension of GNRs is to use a laterally extended monomer for the synthesis of a polyphenylene precursor. *p*-Terphenyl-based monomer **2-1** was thus designed to fabricate wider GNR **2-3** with the calculated lateral width of 1.54–1.98 nm, featuring a combination of cove-type¹ and armchair edge structures (Figure 2-1).⁴ Syntheses of polyphenylene precursors have thus far been carried out based on A_2B_2 -type *Suzuki*^{2,3} or *Diels-Alder*^{5,6} polymerization, which require two different monomers. *Suzuki* polymerization allowed fabrication of uniform GNRs **1-37** and **1-41** with high structural definition, but they were relatively short with low molecular weight (see subsection 1.2.2.4).^{2,3} A_2B_2 -type *Diels-Alder* polymerization, on

the other hand, could afford high molecular weight, but inevitably generated uncountable structural isomers depending on the molecular orientation upon each cycloaddition step, leading to structurally undefined GNR **1-33** with kinks at arbitrary positions (subsection 1.2.2.4).^{13,14} In contrast, monomer **2-1** with reactive halogen groups at both sides undergoes *AA*-type *Yamamoto* polymerization,⁷⁻¹⁰ which is unrestricted by the stoichiometry problem and thus more efficient than *A₂B₂*-type polymerization methods (Figure 2-1).^{11,12} Further, *Yamamoto* polymerization is known to be highly efficient even in sterically demanding systems,^{13,14} which enables the fabrication of high-molecular-weight polyphenylene precursor **2-2** from monomer **2-1**. The resulting precursor **2-2** has a defined structure without any isomer, and all the undesired conformations during the intramolecular oxidative cyclodehydrogenation are hampered by the steric hindrance between the phenyl rings, ensuring the exclusive formation of straight and uniform GNR **2-3**.

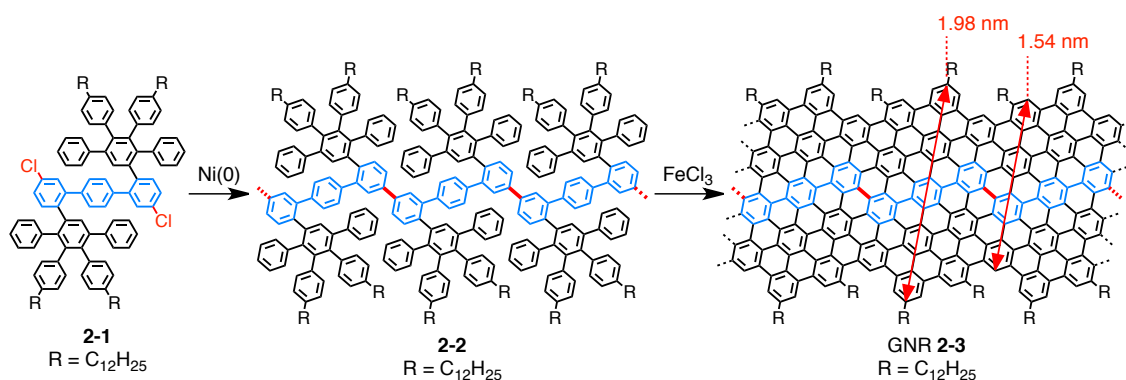


Figure 2-1. Synthetic route to laterally extended GNR **2-3** via *AA*-type *Yamamoto* polymerization of *p*-terphenyl-based monomer **2-1**. Geometric dimensions of GNR **2-3** were obtained by Merck Molecular Force Field 94 (MMFF94) calculations.⁴

2.1.2 Investigation of a monomeric model system

Prior to commencing the fabrication of GNR **2-3**, investigation of a monomeric model system was carried out by [REDACTED] in order to examine the suitability of precursor **2-2** for the synthesis of GNR **2-3** via oxidative cyclodehydrogenation, which is presented here for reference.⁴ *para*-Terphenyl-based oligophenylene precursor **2-7**, which corresponds to a repeating unit of polyphenylene **2-2**, was designed as a model compound and synthesized as shown in Figure 2-2. 2,2''-Diethynylterphenyl **2-5** was obtained by *Sonogashira* coupling of 2,2''-diiodoterphenyl **2-4**⁴ with trimethylsilyl

2.1 Laterally extended GNRs with a mixture of cove and armchair edge structures

acetylene followed by removal of the trimethylsilyl protecting groups. Subsequently, **2-5** was subjected to two-fold *Diels-Alder* cycloaddition with functionalized tetraphenylcyclopentadienone **2-6**¹⁵ under microwave irradiation to give model oligophenylene **2-7** in 81% yield.

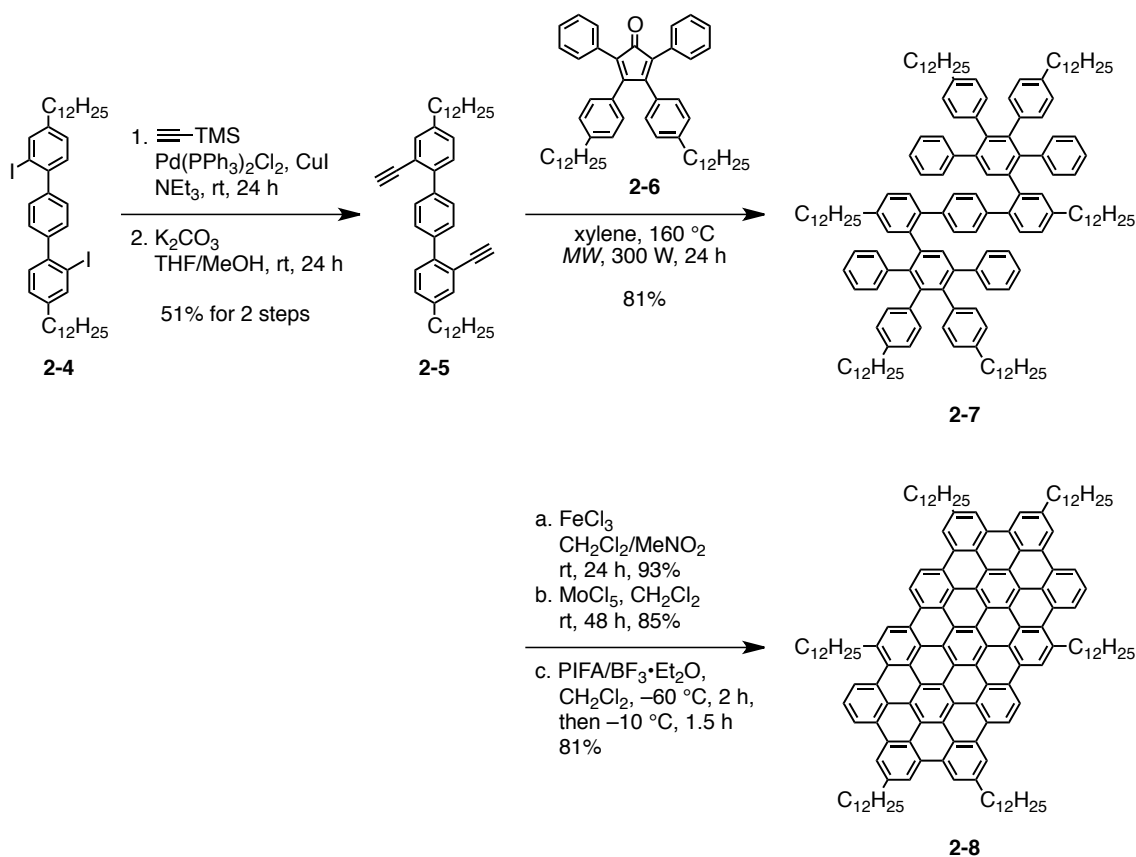


Figure 2-2. Synthetic route to model oligophenylene **2-7** and model PAH **2-8** (C₇₈).

The intramolecular oxidative cyclodehydrogenation of oligophenylene **2-7** leading to model PAH **2-8**, i.e. C₇₈,¹⁶⁻¹⁸ was then investigated by using three different procedures, namely with FeCl₃,¹⁹⁻²¹ MoCl₅,^{20,22,23} or PIFA/BF₃·Et₂O as Lewis acid and oxidant.^{15,20,23} Notably, oligophenylene **2-7** was successfully converted to PAH **2-8** in high yields by all the three protocols. The structural perfection of PAH **2-8** was demonstrated by a combination of MALDI-TOF MS, ¹H NMR spectroscopy, and STM visualization. MALDI-TOF MS analysis of PAH **2-8** showed no signal from chlorinated or other side products, but only one peak at $m/z = 1973$, corresponding to the mass of **2-8** (Figure 2-3a). Further, the isotopic distribution was in a perfect match with the simulation, attesting highly efficient formation of PAH **2-8** without detectable amount of partially fused species (Figure 2-3a, inset).²⁴ It is frequently a problem in the characterization of PAHs that their strong aggregation behavior hinders NMR analyses

in solutions.^{25,26} ^1H NMR analysis of PAH **2-8** however displayed a remarkably well-resolved spectrum at 170 °C by employing high-boiling-point solvent, 1,2-dichlorobenzene- d_4 (Figure 2-3b). The signals from aromatic protons were strongly down-shifted to the range of $\delta = 8.0\text{--}9.5$ ppm owing to the extended aromatic system. Nuclear *Overhauser* enhancement spectroscopy (NOESY) measurements and peak integrations allowed the assignment of aliphatic as well as aromatic signals as shown in Figure 2-3b, further corroborating the structural perfection of PAH **2-8**. It is to be noted that this is thus far the largest PAH molecule that provided a well-resolved ^1H NMR spectrum.

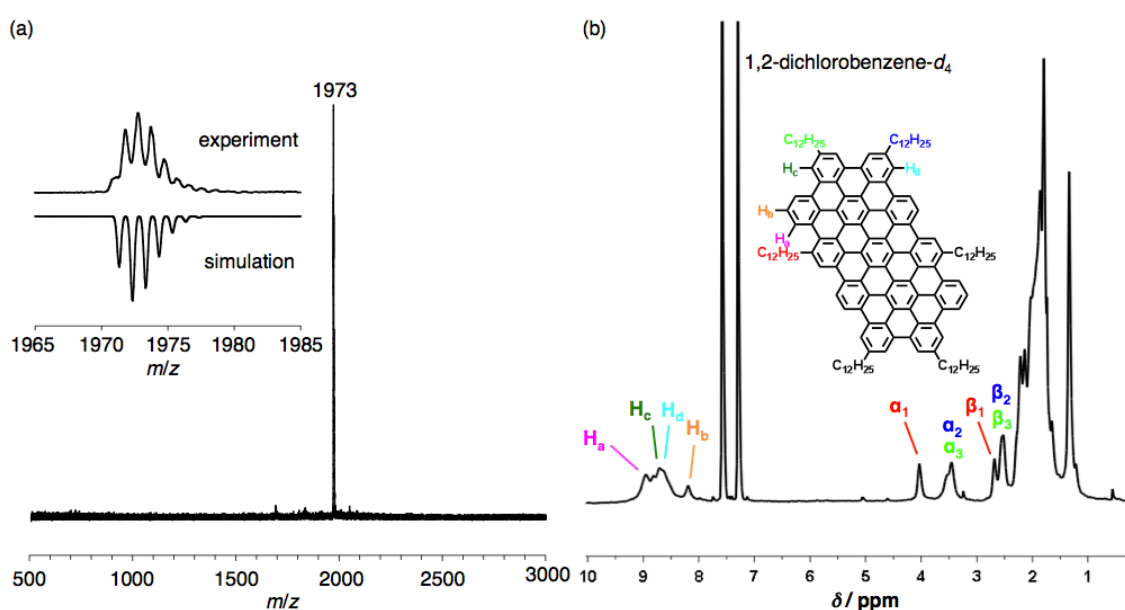


Figure 2-3. (a) MALDI-TOF MS spectrum of PAH **2-8**; inset shows the isotopic distribution in a perfect match with the simulation (reflectron mode, solid-state sample preparation, matrix: TCNQ). (b) ^1H NMR spectrum of PAH **2-8** in 1,2-dichlorobenzene- d_4 at 170 °C (500 MHz).⁴

In order to further verify the flawless synthesis of PAH **2-8**, STM characterization was performed by the group of [REDACTED] at Katholieke Universiteit Leuven, Belgium. Remarkably, STM images of PAH **2-8** obtained at the solid-liquid interface of Au(111)/1,2,4-trichlorobenzene (TCB) demonstrated unmistakably perfect structures of the C78 molecules with the dimensions (length = 2.3 ± 0.1 nm and width = 1.4 ± 0.1 nm) consistent with the molecular modeling (Figure 2-4). The six dodecyl chains of PAH **2-8** were also clearly visualized, where four of them were extended to the lateral direction and the other two to the longitudinal direction. On the aromatic core of PAH **2-8** three parallel stripes were observed, which

2.1 Laterally extended GNRs with a mixture of cove and armchair edge structures

could be correlated with the electron densities in the highest occupied molecular orbital.¹⁸ TCB molecules were entrapped in the remaining space between four C78 molecules as indicated by blue circles in Figure 2-4a. It is well known that the synthesis of PAHs is always accompanied by the possibility of rearrangement during the oxidative cyclodehydrogenation. Nevertheless, these characterization results undoubtedly proved the perfect synthesis of PAH **2-8** without any rearrangement, clearly demonstrating the advantage of this synthetic protocol over the previously reported ones for the synthesis of C78.¹⁶⁻¹⁸

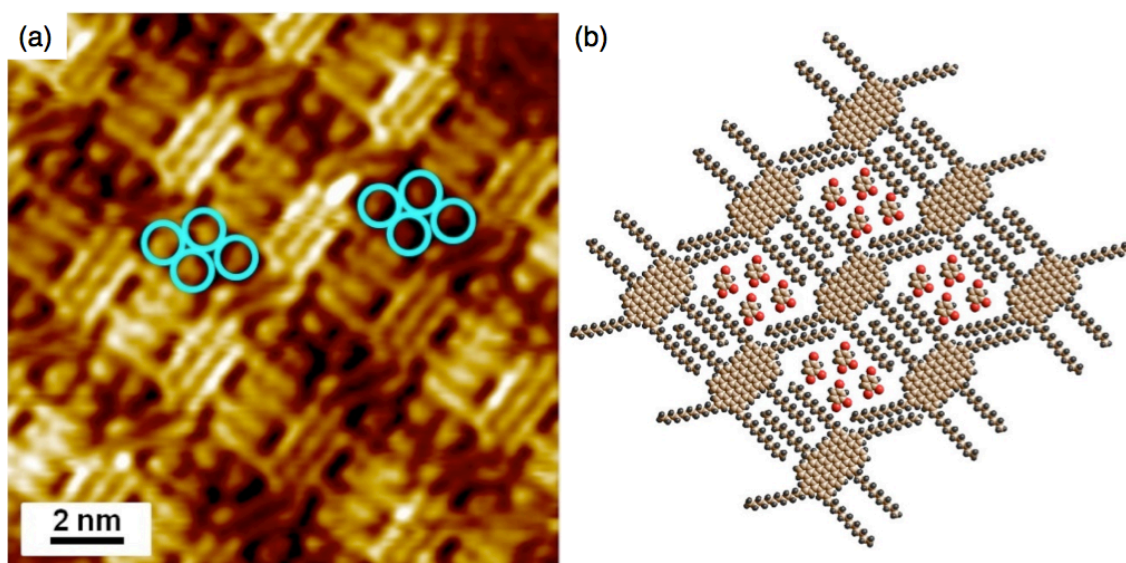


Figure 2-4. (a) An STM image of PAH **2-8** at the Au(111)/TCB interface; blue circles: entrapped TCB molecules; imaging conditions: $I_t = 0.1$ nA, $V_{\text{bias}} = 464$ mV. (b) Molecular model for the self-assembly of PAH **2-8** with trapped TCB molecules on Au (111).⁴

2.1.3 Fabrication of laterally extended GNRs

With the success of the cyclodehydrogenation of model precursor **2-7** into PAH **2-8**, the synthesis and characterization of laterally extended GNR **2-3** was carried out in cooperation with [REDACTED], who developed the synthetic route and conducted preliminary characterizations. Within the scope of this dissertation, fractionation of polyphenylene precursor **2-2** and subsequent cyclodehydrogenation into GNR **2-3** as well as their in-depth analyses based on size-exclusion chromatography (SEC), MALDI-TOF MS, and Raman, UV-vis absorption, photoluminescence, and photoelectron spectroscopies were accomplished.

Monomer **2-1** was synthesized in a similar manner to the synthesis of oligophenylene **2-7**, using 5,5''-dichloro-2,2''-diiodoterphenyl **2-9** instead of 4,4''-didodecyl-2,2''-diiodoterphenyl **2-4** (Figure 2-5). First, 5,5''-dichloro-2,2''-diethynylterphenyl **2-10** was prepared by *Sonogashira* coupling of **2-9**⁴ with trimethylsilyl acetylene and subsequent removal of the trimethylsilyl protecting group with potassium carbonate. Functionalized terphenyl **2-10** was then reacted with tetraphenylcyclopentadienone **2-6** through two-fold *Diels–Alder* cycloaddition under microwave irradiation to yield monomer **2-1** in 74% yield.

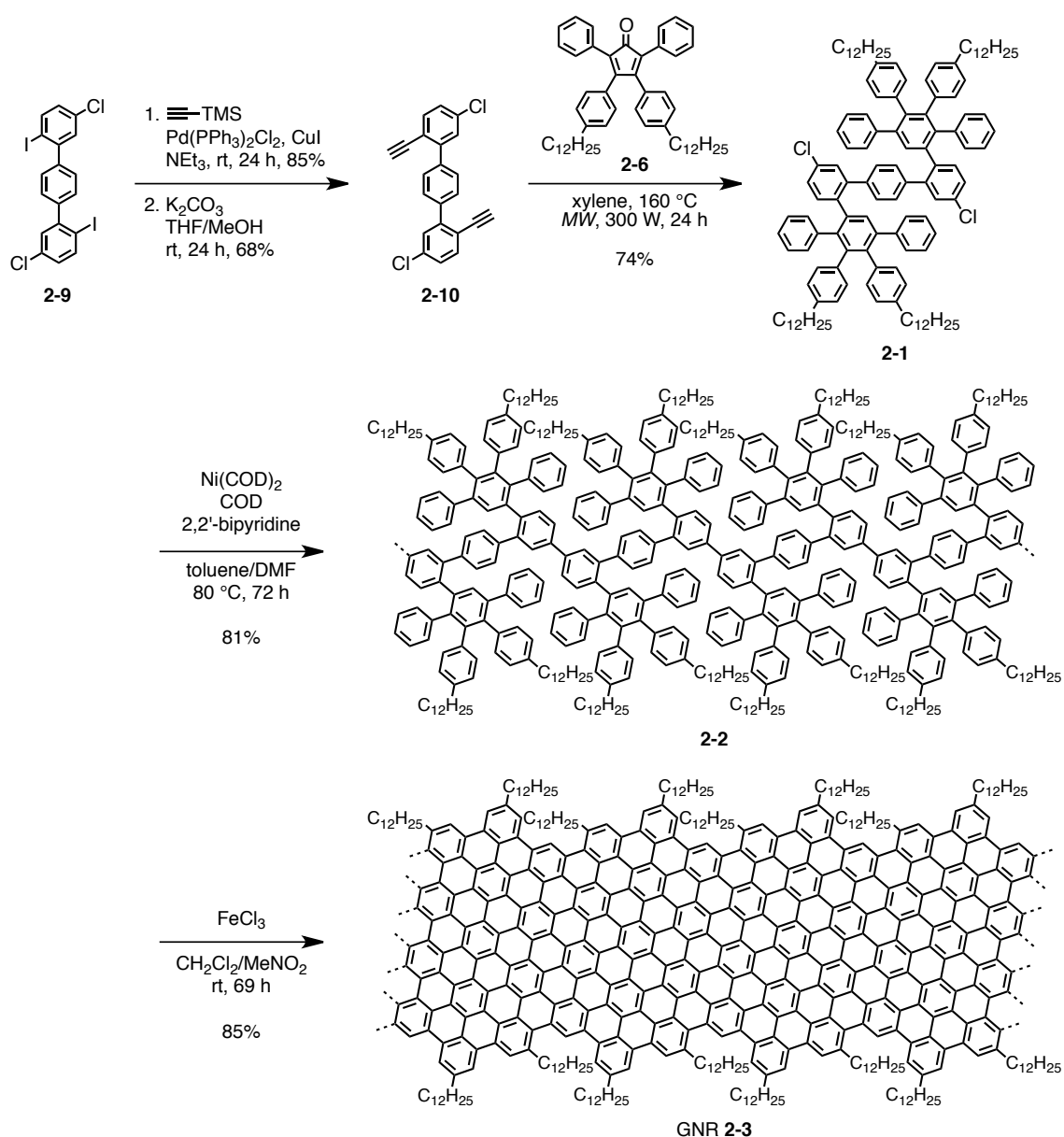


Figure 2-5. Synthetic route to GNR **2-3**.

2.1 Laterally extended GNRs with a mixture of cove and armchair edge structures

Yamamoto polymerization of monomer **2-1** was then carried out employing a standard protocol (Figure 2-5).^{7,8} Briefly, the nickel(0) catalyst was preactivated at 60 °C followed by adding a solution of monomer **2-1**. The reaction mixture was then stirred at 80 °C for three days, and then an excess amount of chlorobenzene was added for the end capping. MALDI-TOF MS analysis of the resulting polyphenylene precursor **2-2** in linear mode showed a regular pattern of signals up to $m/z = 35,000$ – $40,000$, which corresponded to the molecular weight of 21–24 repeating units (Figure 2-6a). The length of GNR **2-3** with this number of repeating units was ca. 30 nm based on a molecular modeling. This is however most likely not the highest value, considering the limitation of MALDI-TOF MS for the characterization of high-molecular-weight polymers with broad molecular weight distribution.^{3,27}

More accurate values of the molecular weights were obtained by reflectron-mode analysis of precursor **2-2** (Figure 2-6b). Signals from trimer, tetramer, pentamer, and hexamer of **2-2** were observed at $m/z = 4,990$, 6,653, 8,317, and 9,982, respectively, in good agreement with calculated molecular weights of the oligomers without chloro groups or additional phenyl rings (Figure 2-7). This result indicated that these oligomers were formed by dechlorination during the polymerization, and precluded from further polymer growth. Notably, no other side product was detected both by linear- and reflectron-mode measurements, corroborating the high purity of thus prepared polyphenylene precursor **2-2**.

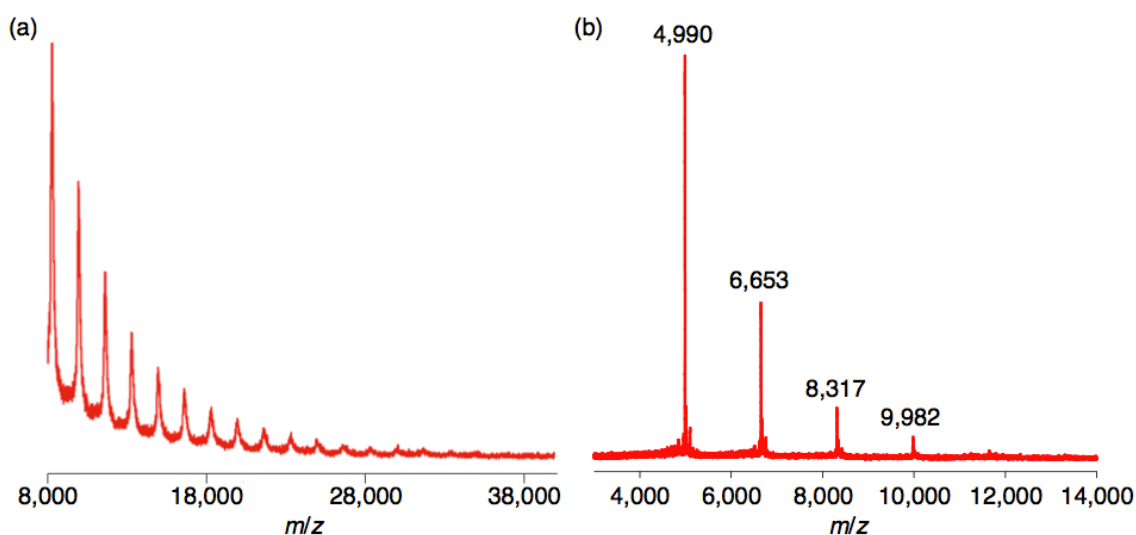


Figure 2-6. MALDI-TOF MS spectra of polyphenylene precursor **2-2** (a) in linear mode and (b) in reflectron mode (solid-state sample preparation, matrix: TCNQ).⁴

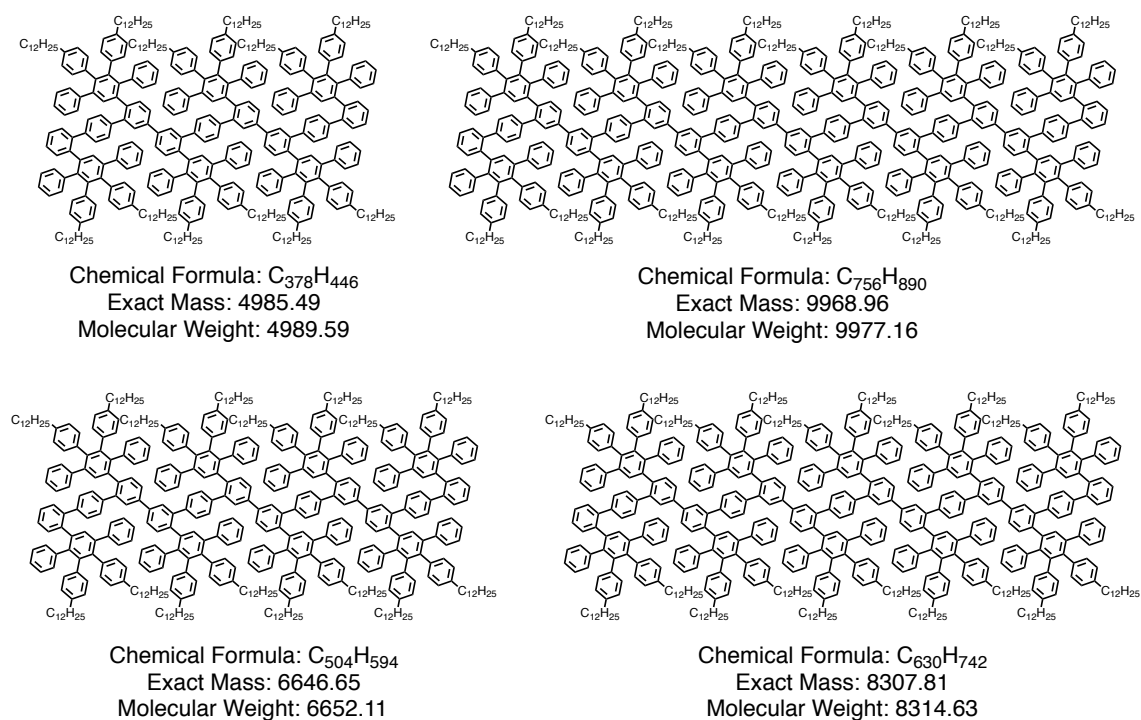


Figure 2-7. Structures and molecular weight of oligomers of polyphenylene precursor **2-2**.

For estimating the molecular weights of polymer samples, SEC analysis is a potent method, especially when MALDI-TOF MS analysis fails to provide appropriate characterization due to large molecular weights and/or broad molecular weight distribution. SEC analysis was thus performed for the as-prepared polyphenylene precursor **2-2**, which showed weight-average molecular weight (M_w) of 29,000 g/mol, number-average molecular weight (M_n) of 13,000 g/mol, and polydispersity index (PDI) of 2.2 against polystyrene (PS) standards. The molecular weight distribution of **2-2** based on PS standards showed two peaks at $\sim 5,900$ and $\sim 45,000$ g/mol (Figure 2-8a). The peak at $\sim 5,900$ g/mol corresponded to the short oligomers formed by the dechlorination, which were observed by the reflectron-mode MALDI-TOF MS analysis (Figure 2-6b). It had been found in our research group that existence of such short oligomers disturb the spectroscopic characterizations of GNRs after the subsequent cyclodehydrogenation, i.e. UV-vis absorption spectra become undefined due to the absorption of each oligomer with different bandgap, and Raman analysis is starkly hindered by the strong fluorescence from small oligomers.

In order to avoid this problem a part of polyphenylene precursor **2-2** was separated into two fractions, namely one with larger molecular weight (**2-2-I**) and the other with smaller molecular weight (**2-2-II**), by utilizing recycling preparative SEC.

2.1 Laterally extended GNRs with a mixture of cove and armchair edge structures

Fraction **2-2-I** showed M_w of 52,000 g/mol, M_n of 44,000 g/mol, and PDI of 1.2, whereas fraction **2-2-II** was featured by M_w of 7,200 g/mol, M_n of 6,700 g/mol, and PDI of 1.1 based on the SEC analysis with PS standards. The molecular weight distribution of both **2-2-I** and **2-2-II** demonstrated a single peak (Figure 2-8b), corresponding to each of the two peaks observed in the molecular weight distribution of the as-prepared **2-2** (Figure 2-8a). These values were approximate and relative estimations based on PS standard calibration, but the molecular weights of **2-2-I** were evidently higher than those of polyphenylene precursors **1-37** and **1-41** obtained by A_2B_2 -type *Suzuki* polymerization (subsection 1.2.2.4).^{2,3} This result highlights the remarkable advantage of the *AA*-type *Yamamoto* polymerization for the synthesis of large-molecular-weight polyphenylene polymers with narrow molecular weight distribution.

Although the SEC analysis of dendronized polyphenylene polymers has conventionally been performed with PS standards,^{2,3,5,6,28} it is also reasonable to apply poly(*para*-phenylene) (PPP) standards in parallel to obtain better insight into the actual molecular weights. Based on PPP standard calibration, the SEC analysis of precursor **2-2-I** gave M_w of 30,000 g/mol, M_n of 27,000 g/mol, and PDI of 1.1, and precursor **2-2-II** displayed M_w of 5,400 g/mol, M_n of 5,100 g/mol, and PDI of 1.1. Considering the structure of **2-2-I** and **2-2-II** with kinked polyphenylene backbones and long, flexible alkyl chains, it is likely that the actual molecular weights lie between the ones estimated by PPP and PS standard calibrations (see also subsection 3.3.5). For instance, the actual M_w of precursor **2-2-I** is most probably between 30,000 and 52,000 g/mol.

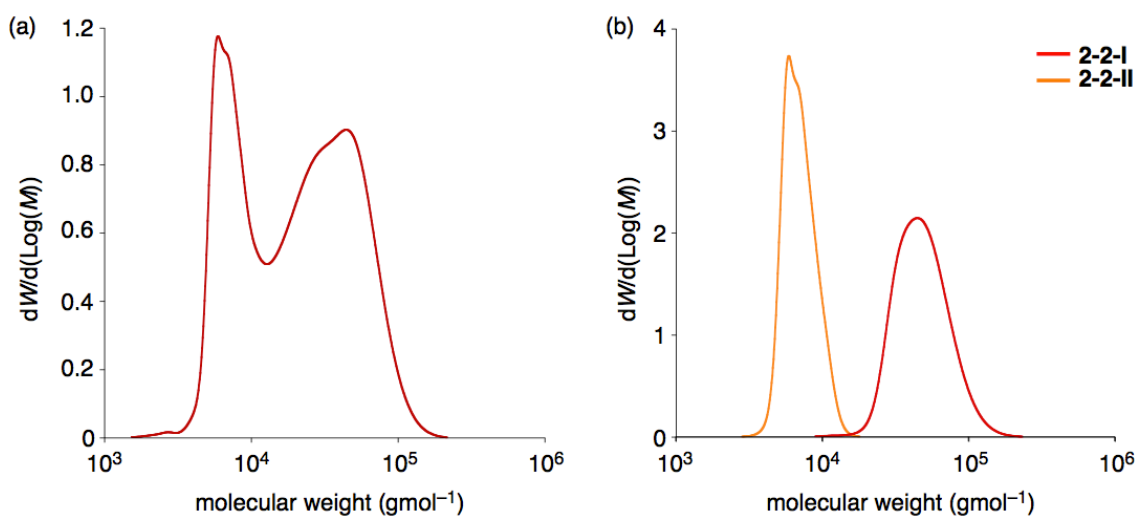


Figure 2-8. Molecular weight distribution of polyphenylene precursors (a) **2-2** (before fractionation), and (b) **2-2-I** and **2-2-II** (after fractionation) (SEC analysis, eluent: THF, UV detector, PS standard).⁴

Finally, polyphenylene precursors **2-2**, **2-2-I**, and **2-2-II** were “planarized” and “graphitized” into GNRs **2-3**, **2-3-I**, and **2-3-II**, respectively, by intramolecular oxidative cyclodehydrogenation using FeCl_3 as oxidant and Lewis acid under the same condition as the synthesis of model PAH **2-8** (Figure 2-5). The efficiency of the “graphitization” was subsequently examined by means of MALDI-TOF MS and FTIR, Raman, and UV-vis absorption spectroscopies. MALDI-TOF MS measurements of GNRs **2-3** and **2-3-I** did not show any signal both in the linear and reflectron modes presumably due to their strong aggregation as well as high molecular weight with broad distribution.^{3,27} However, linear-mode analysis of GNR **2-3-II** demonstrated a regular pattern of peaks similar to that of precursor **2-2**, but with a smaller interval of $m/z = \text{ca. } 1,620$ in good agreement with the molecular mass of one repeating unit of GNR **2-3**, i.e. $\text{C}_{126}\text{H}_{108} = 1,622$ (Figure 2-9). Although the observed peaks were broad due to the strong aggregation, this result supported the successful formation of the GNRs upon the cyclodehydrogenation. Attempts to obtain more accurate molecular weights by reflectron-mode measurements failed, again most probably because of the strong π - π stacking interaction between the GNRs.

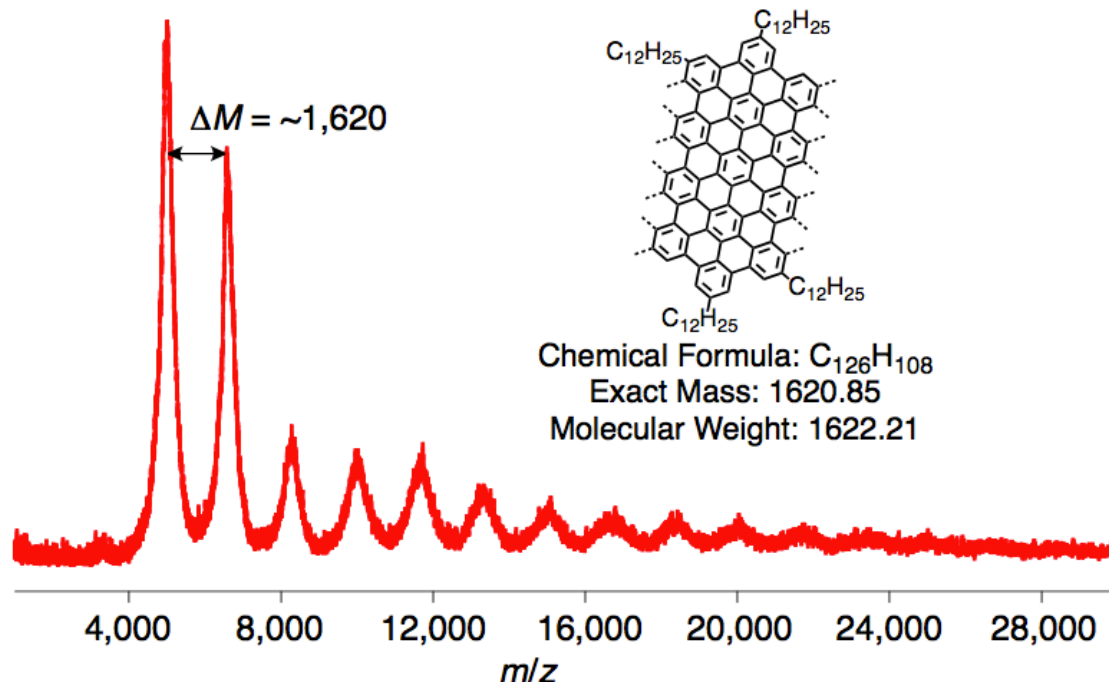


Figure 2-9. MALDI-TOF MS spectrum of GNR **2-3-II**; inset: structure, chemical formula, and molecular weight of one repeating unit of **2-3-II** (linear mode, solid-state sample preparation, matrix: TCNQ).

2.1 Laterally extended GNRs with a mixture of cove and armchair edge structures

Fourier transform infrared (FTIR) spectroscopy analysis of polyphenylene precursor **2-2** and GNR **2-3** was next performed and compared with the spectra obtained from oligophenylene precursor **2-7** and PAH **2-8** (Figure 2-10). Oligophenylene **2-7** and polyphenylene **2-2** showed similar changes upon the oxidative cyclodehydrogenation into PAH **2-8** and GNR **2-3**, respectively. The band at $4,050\text{ cm}^{-1}$ derived from the rotation of free phenyl rings disappeared, and the signal triad at $3,025$, $3,056$, and $3,083\text{ cm}^{-1}$ characteristic for aromatic C–H stretching vibrations was strongly attenuated.^{3,5,6,29} Further, disappearance of the out-of-plane (*opla*) C-H deformation bands at 698 and 755 cm^{-1} originating from monosubstituted benzene rings was also observed.^{5,6} All these changes were consistent between the polymer and the monomer, corroborating the high efficiency of the “graphitization” of polyphenylene precursor **2-2** based on the perfect synthesis of PAH **2-8** (subsection 2.1.2). Additionally, the bands appearing after the “graphitization” at 861 , 822 , 760 , and 718 cm^{-1} were most likely related to the *opla*

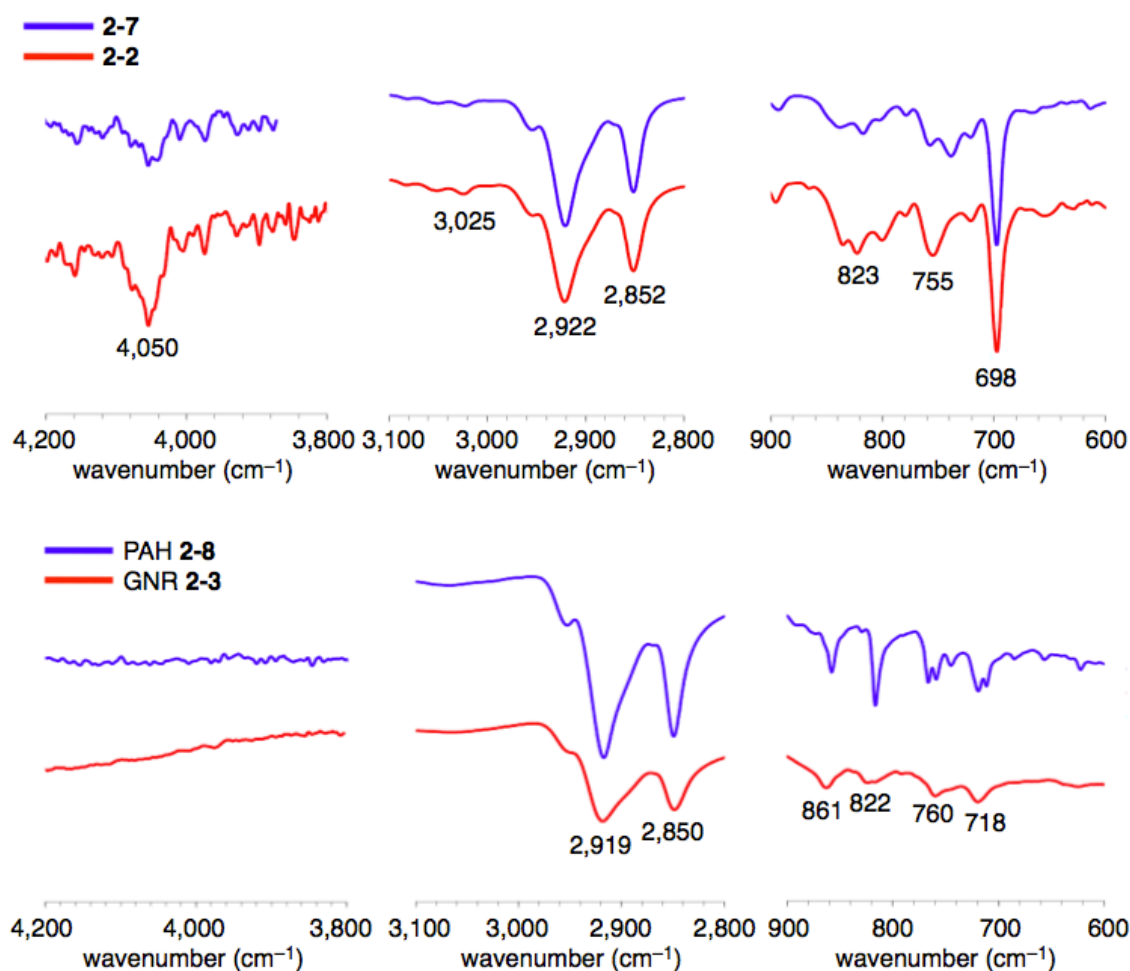


Figure 2-10. Representative FTIR spectral regions before (oligophenylene **2-7** and polyphenylene **2-2** in blue) and after (PAH **2-8** and GNR **2-3** in red) the “graphitization”.⁴

deformation of C–H bonds at the edges²⁹ as well as –CH₂– rocking mode from the dodecyl chains,³⁰ although unambiguous assignment requires theoretical investigations.³¹ Nevertheless, the IR spectrum of PAH **2-8** also displayed peaks at the same wavenumbers, verifying that these peaks were not related to unclosed bonds or defective structures.

Raman spectroscopic analysis of GNR **2-3-I** was carried out together with [REDACTED] in our research group. The measurements were performed on a powder sample at 488 nm with laser power of 1 mW. The obtained Raman spectrum showed first-order D and G bands at 1,316 and 1,595 cm⁻¹, respectively, which were consistent with the values observed for other bottom-up synthesized GNRs (Figure 2-11).^{3,32} The intense D peak shown in the spectrum did not derive from defects, but was activated by the confinement of π -electrons into a finite-size domain, and can be described by collective modes of the confined hexagonal rings,³³ as previously shown by Raman studies on polycyclic aromatic hydrocarbons (PAHs).^{34,35} In these systems, the modes associated with totally symmetric vibrations are strongly coupled with π -electrons, giving rise to a strong polarizability change for these vibrations. Further, well-resolved second-order signals were also observed at 2,632, 2,910, and 3,194 cm⁻¹, which could be assigned to 2D, D + G, and 2G bands, respectively.^{3,36-38}

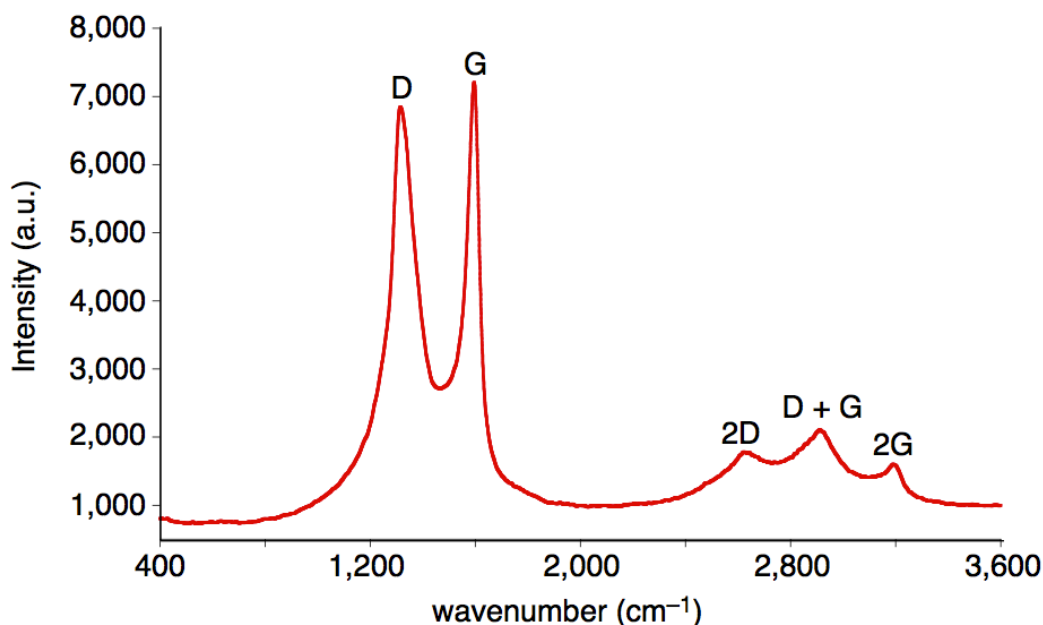


Figure 2-11. A Raman spectrum of GNR **2-3-I** measured at 488 nm (powder, laser power: 1 mW).⁴

2.1 Laterally extended GNRs with a mixture of cove and armchair edge structures

The GNR samples synthesized here were practically insoluble in standard organic solvents such as dichloromethane, chloroform, toluene, and tetrahydrofuran (THF). It has been recently elucidated that graphite can be exfoliated to graphene in liquid phase by using highly polar solvents such as *N*-methylpyrrolidone (NMP),^{39,40} which has been known to be able to debundle carbon nanotubes.⁴⁰⁻⁴² Likewise, exfoliation of GNRs **2-3-I** and **2-3-II** was attempted in NMP by applying mild sonication, together with [REDACTED]. Remarkably, orange and blue dispersions of GNRs **2-3-I** and **2-3-II**, respectively, could be obtained by this method, enabling UV-vis absorption analysis of the laterally extended GNRs (Figure 2-12).

The UV-vis absorption spectra of GNRs **2-3-I** and **2-3-II** were compared with that of PAH **2-8** recorded in THF as shown in Figure 2-12. PAH **2-8** displayed the most intense β -band at 431 nm with p - and α -band at 514 nm and 580 nm, respectively, in consistence with previously synthesized C78 molecules.¹⁸ The α -band was more intense compared to other PAHs because of the low symmetry of PAH **2-8**.^{18,43} Determination of the optical bandgap of PAH **2-8** from the onset of the p -band was difficult because of the broadened absorption bands,⁴³ but it could be estimated to be approximately 1.92 eV based on the absorption edge of 647 nm. Notably enough, the longer GNR **2-3-I** displayed absorption maxima at 690 and 960 nm with broad absorption extending well

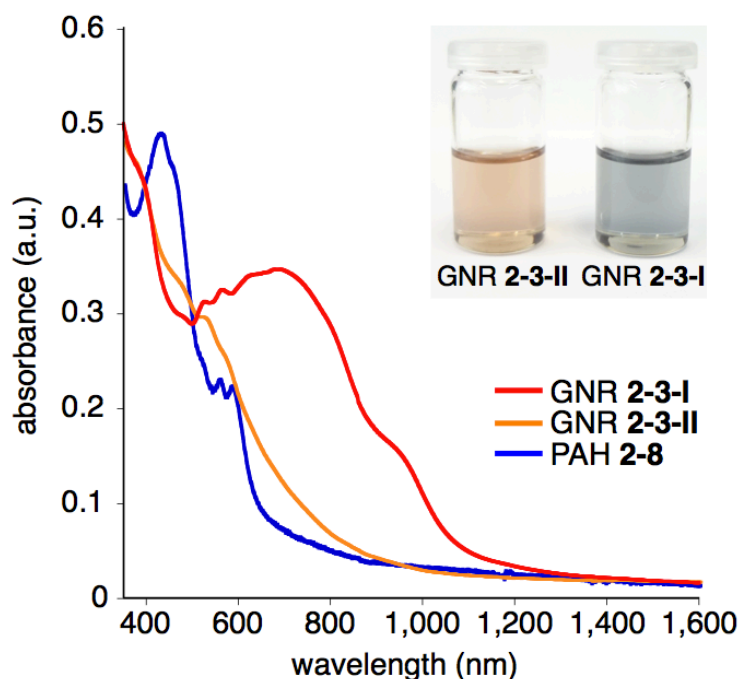


Figure 2-12. Normalized UV-vis absorption spectra of GNR **2-3-I** (red, in NMP), GNR **2-3-II** (orange, in NMP), and PAH **2-8** (blue, in THF); inset: a photograph of dispersions of GNRs **2-3-I** and **2-3-II** in NMP.⁴

into the near infrared (NIR) region. The small absorbance observed between 1,110 and 1,400 nm was most probably due to the scattering by the aggregates of the GNRs in the dispersion. The optical bandgap of GNR **2-3-I** could be determined based on the absorption edge of 1,109 nm to be as low as 1.12 eV, evidently demonstrating the considerable lowering of bandgap energy by the lateral extension. Addition of hydrazine did not cause any change in the spectrum, proving the absence of radical cation species.⁴

In order to obtain better insight into the bandgap of these laterally extended GNRs, theoretical studies were conducted by [REDACTED] and [REDACTED] at the University of Mons, Belgium. By means of density functional theory (DFT) calculations, it was elucidated that the bandgap of the GNRs decreases as the longitudinal extension, and reaches the lowest value of 1.08 eV when they are longer than ca. 20 nm with more than 15 repeating units.⁴⁴ This DFT-calculated bandgap of 1.08 eV is in excellent agreement with the optical bandgap of 1.12 eV, revealing that GNR **2-3-I** is sufficiently elongated to realize the lowest bandgap attainable with this lateral structure, i.e. the bandgap of the infinite GNRs. These results are also consistent with the M_w and M_n of precursor **2-2-I**, 30,000–52,000 and 27,000–44,000 g/mol, which correspond to 18–31 and 16–26 repeating units, respectively. This remarkable agreement between the theoretical and the experimental results offers further structural proof for GNR **2-3-I**.

In contrast, the UV–vis absorption spectrum of shorter GNR **2-3-II** showed a virtually featureless profile with the absorption edge of 812 nm, corresponding to the optical bandgap of 1.53 eV (Figure 2-12). According to the MALDI-TOF MS analysis (Figure 2-9), GNR **2-3-II** was a mixture of short oligomers, starting from the trimer, which have varying bandgaps depending on the length according to the DFT calculation.⁴⁴ Thus the featureless spectrum of GNR **2-3-II** could most likely be explained by the superposition of various absorption profiles from the different oligomers.

Further exploiting the dispersibility of the GNRs, photoluminescence (PL) spectroscopic analysis of GNR **2-3-I** was performed by [REDACTED] in the group of [REDACTED] at Trinity College Dublin, Ireland. The PL spectrum was recorded in *N*-cyclohexyl-2-pyrrolidone (CHP), in which the absorption spectrum was identical with that in NMP. Broad and defined fluorescence ranging from ca. 900 to 1,400 nm was observed with a maximum at 1,084 nm (1.14 eV) (Figure 2-13). This result was in good agreement with the optical and theoretical bandgaps, corroborating the high

2.1 Laterally extended GNRs with a mixture of cove and armchair edge structures

structural definition of GNR **2-3-I** and the uniformity of the GNRs in the sample. Interestingly, these UV–vis absorption and PL spectra of GNR **2-3-I** were comparable to those of carbon nanotubes with (6, 5) chirality reported in the literature.⁴⁵

In order to investigate the ionization potential of the GNR samples photoelectron spectroscopy measurements were carried out by [REDACTED] in the group of [REDACTED] at Institut de Science et d'Ingénierie Supramoléculaires (I.S.I.S.), Université de Strasbourg, France. The measurements were performed on powder samples under ambient conditions, and revealed the ionization potentials of GNRs **2-3-I** and **2-3-II** to be 5.01 and 5.19 eV, respectively, which is related to the valence band energies. It is difficult to determine the exact values of the ionization potential by such measurements in ambient conditions, but this result demonstrated the lowering of the ionization potential by the longitudinal extension consistent with the prediction by the DFT calculations.⁴⁴

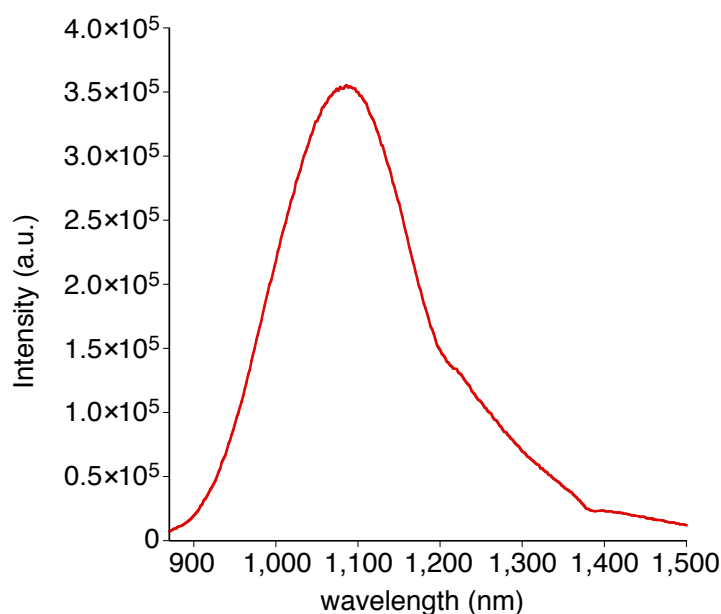


Figure 2-13. A photoluminescence spectrum of GNR **2-3-I** in cyclohexyl pyrrolidone.

2.1.4 Preliminary attempt for processing laterally extended GNRs

Although GNRs **2-3-I** and **2-3-II** could be successfully exfoliated in NMP to allow UV–vis absorption spectroscopic analysis, their dispersibility in NMP was insufficient for the deposition onto substrates, which was essential for further characterizations as well as applications of them in electronic devices. It has been reported that graphite can be spontaneously exfoliated into single-layer graphene at high concentrations in chlorosulphonic acid.⁴⁶ In order to obtain higher-concentration dispersions of the sparingly dispersible GNRs, this method was applied to GNR **2-3-I**.

Interestingly, GNR **2-3-I** gave a dark brown dispersion upon addition of chlorosulphonic acid without necessity of sonication. For the deposition, the dispersion of GNR **2-3-I** in chlorosulphonic acid was carefully dropped on SiO₂ substrate and then immediately quenched with deionized water. After washing with deionized water and 2-propanol, the substrate was dried under reduced pressure and measured by SEM (Figure 2-14). The SEM image showed fibrous structures of a film of GNR **2-3-I**, which resembled reported images of films of carbon nanotubes.^{47,48}

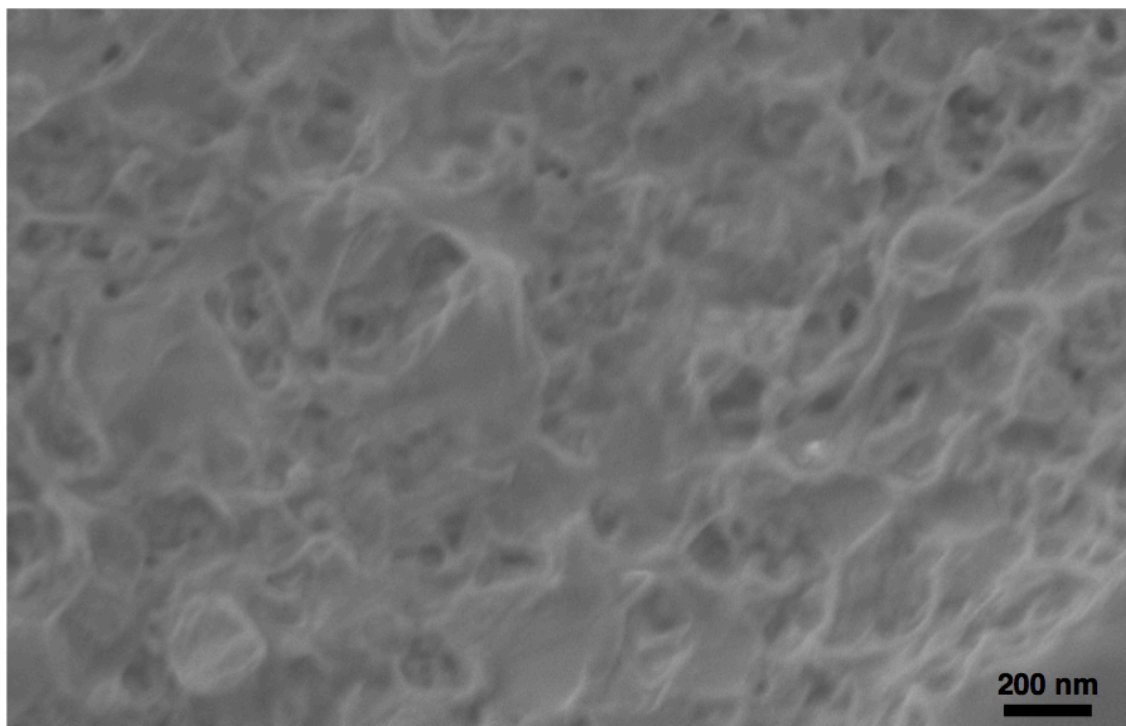


Figure 2-14. An SEM image of GNR **2-3-I** deposited on SiO₂ from a dispersion in chlorosulphonic acid, showing a fibrous structure similar to that of carbon nanotubes.

2.1 Laterally extended GNRs with a mixture of cove and armchair edge structures

Raman measurement on the same substrate showed signals consistent with the spectrum obtained from the measurements on a powder, which indicated successful deposition of GNR **2-3-I** (Figures 2-11 and 2-15). The intensity of the D peak did not increase in comparison to that of the G peak, indicating that the basal planes of the GNRs were not affected during the deposition process. However, the surface of the SiO₂ substrate was apparently damaged by the strong acidity of chlorosulphonic acid, rendering it difficult to apply this deposition method to the fabrication of GNR-based electronic devices. Nevertheless, this method provided a way to process GNRs from a liquid phase in spite of their highly limited dispersibility in organic solvents.

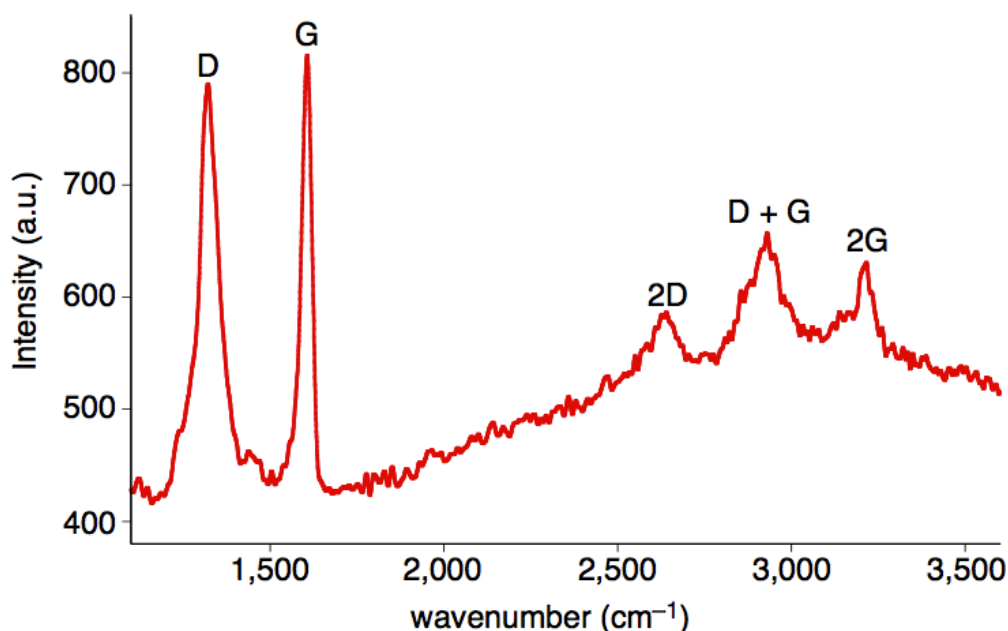


Figure 2-15. A Raman spectrum measured at 488 nm of GNR **2-3-I** deposited on SiO₂ from a dispersion in chlorosulphonic acid (laser power: 1 mW).

2.1.5 Summary

In summary, structurally well-defined and unprecedentedly broad (1.54–1.98 nm) GNR **2-3** with a mixture of cove-type and armchair edge structures was synthesized based on a bottom-up chemical approach, employing laterally extended monomer **2-1**. *AA*-type *Yamamoto* polymerization was utilized instead of previously used *A₂B₂*-type *Suzuki* polymerization, realizing a longitudinal extension of at least >20 nm while preserving the high structural definition. The oxidative cyclodehydrogenation of model precursor **2-7** into PAH **2-8** was independently studied, where its perfect “graphitization” was proved by means of MALDI-TOF MS, ¹H NMR, and STM analyses. Further, characterizations of GNR **2-3** by a combination of MALDI-TOF MS, FTIR, Raman, and UV–vis absorption spectroscopies clearly corroborated the high efficiency of the cyclodehydrogenation even for the polymers. The optical bandgap extracted from the UV–vis absorption spectrum was 1.12 eV, which was in excellent agreement with the DFT-calculated bandgap of 1.08 eV as well as the PL peak at 1.14 eV. This was the lowest value thus far achieved with structurally well-defined GNRs. Such laterally extended GNRs with broad absorption extending to the NIR region hold a great potential for the applications in photovoltaic cells.⁴⁴ For integrations into electronic devices, however, dispersibility of the GNRs needs to be improved to enable their deposition onto substrates without a use of strong acids such as chlorosulphonic acid. Moreover, the longitudinal length of ca. 30 nm estimated for GNR **2-3-I** from the *M_w* of precursor **2-2-I** is not sufficient to fabricate a FET device based on a single GNR, which typically requires longer (e.g. >100 nm) GNRs. This renders it necessary to develop another strategy for the synthesis of GNRs in order to achieve liquid-phase processable GNRs with higher longitudinal extensions.

2.2 $N = 18$ armchair GNRs

2.2.1 Synthetic strategy

Laterally extended GNR **2-3** was successfully synthesized by employing expanded monomer **2-1**, but this GNR features a combination of armchair and cove-type edge structures (Figure 2-1), leaving the fabrication of broad armchair GNRs elusive. Theoretical studies have predicted that armchair GNRs with comparable lateral widths to that of GNR **2-3**, i.e. ca. 2 nm, possess considerably lower bandgap energies of approximately 0.5 eV,⁴⁹ rendering the synthesis of such armchair GNRs of great importance. Further, although the use of laterally expanded monomers has proved to provide wider GNRs, synthesis of even wider GNRs based on this approach requires larger monomers, the preparation of which is more elaborate and time-consuming. In contrast, use of a monomer with a V-shaped polymerizable backbone structure allows relatively facile synthesis of laterally extended GNRs with twice the lateral width of the

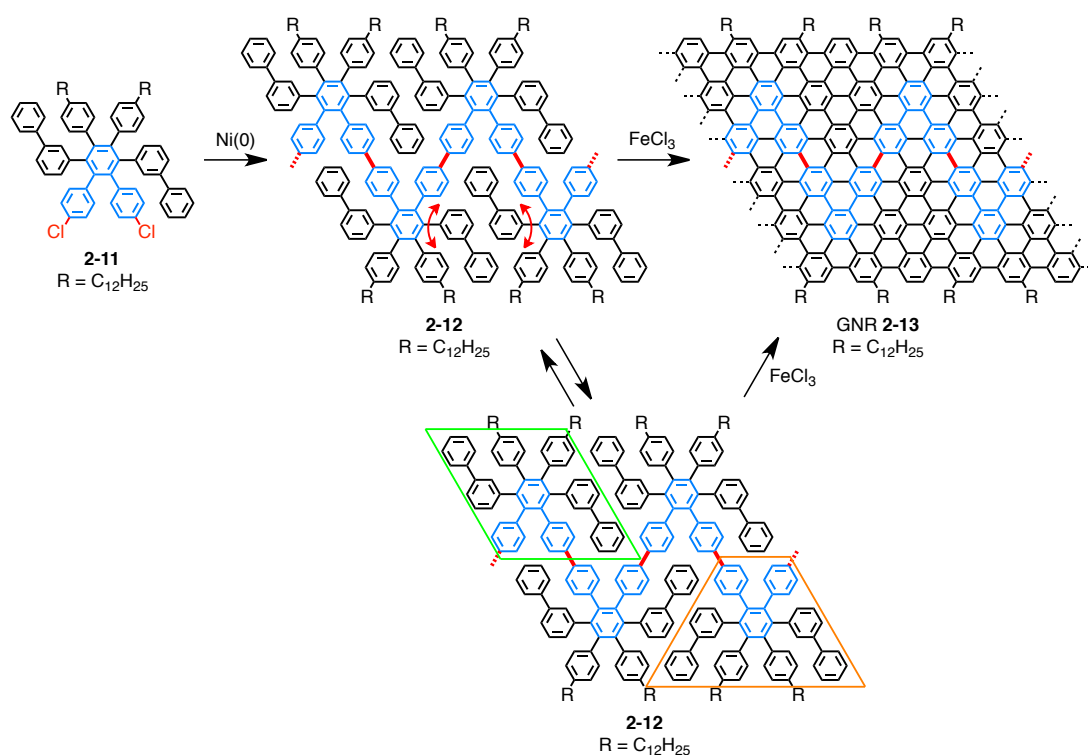


Figure 2-16. Synthetic route to $N = 18$ armchair GNR **2-13** via *AA*-type Yamamoto polymerization of *o*-terphenyl-based monomer **2-11** bearing a V-shaped polymerizable backbone. Each repeating unit of polyphenylene precursor **2-12** takes either rhombic (green) or trapezoidal (orange) conformation, both of which lead to the same GNR **2-13**.

monomer. Based on this notion, *o*-phenyl-based monomer **2-11** bearing two chloro groups was designed for a synthesis of GNR **2-13**, corresponding to an $N = 18$ armchair GNR (Figure 2-16). Monomer **2-11** undergoes *AA*-type *Yamamoto* polymerization, which was revealed to be superior to A_2B_2 -type *Suzuki* polymerization for the synthesis of large-molecular-weight polyphenylene polymers (see section 2.1). The resulting polyphenylene precursor **2-12** is twice as wide as monomer **2-11** and lead to $N = 18$ armchair GNR **2-13**, featuring the lateral width of ~ 2.1 nm. This synthetic approach provides a simpler route for the synthesis of laterally extended GNRs from smaller monomers without a need for the complicated preparations of laterally extended monomers. Importantly, GNR **2-13** with the lateral width of ~ 2.1 nm is the widest GNR thus far synthesized by the bottom-up chemical approach, surpassing GNR **2-3** with the lateral width of 1.54–1.98 nm.

Because of the free rotation of the biphenyl groups attached to the *o*-terphenyl core, each repeating units of polyphenylene precursor **2-12** takes either rhombic (green) or trapezoidal (orange) conformation during the cyclodehydrogenation reaction (Figure 2-16). In either case the neighboring repeating units take the same conformation to realize the synthesis of GNR **2-13** with high structural definition albeit with the structural isomerization at the termini of the GNRs (Figure 2-17).

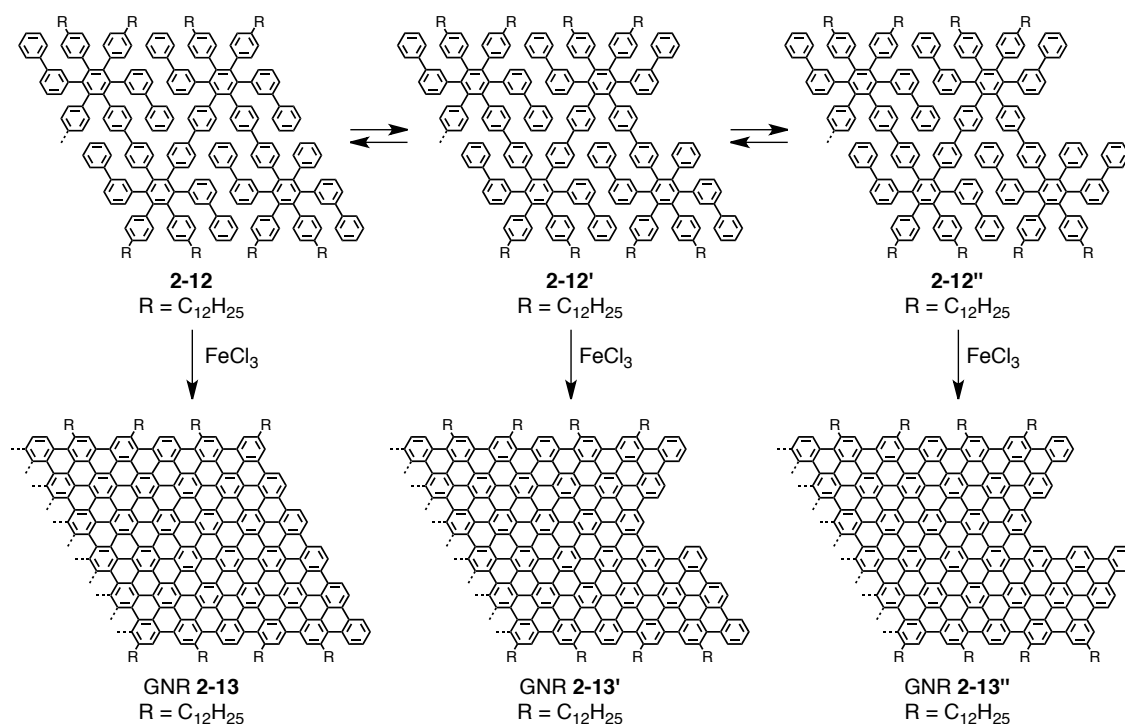


Figure 2-17. Structural isomerization at the termini of GNR **2-13**.

2.2.2 Investigation of a monomeric model system

In order to examine the feasibility of the cyclodehydrogenation of polyphenylene precursor **2-12** into GNR **2-13**, investigation of a monomeric model system was initially carried out. Thus, oligophenylene **2-18**, corresponding to the repeating unit of polyphenylene **2-12**, was designed and synthesized as shown in Figure 2-18. First, 1,3-di(biphenyl-3-yl)propan-2-one (**2-14**)⁵⁰ was subjected to *Knoevenagel* condensation with 4,4'-didodecylbenzil (**2-15**)⁵¹ to afford cyclopentadienone **2-16** in 66% yield. Subsequently, *Diels–Alder* reaction of cyclopentadienone **2-16** with bis(4-dodecylphenyl)acetylene (**2-17**)⁵¹ gave model oligophenylene **2-18** in 59% yield.

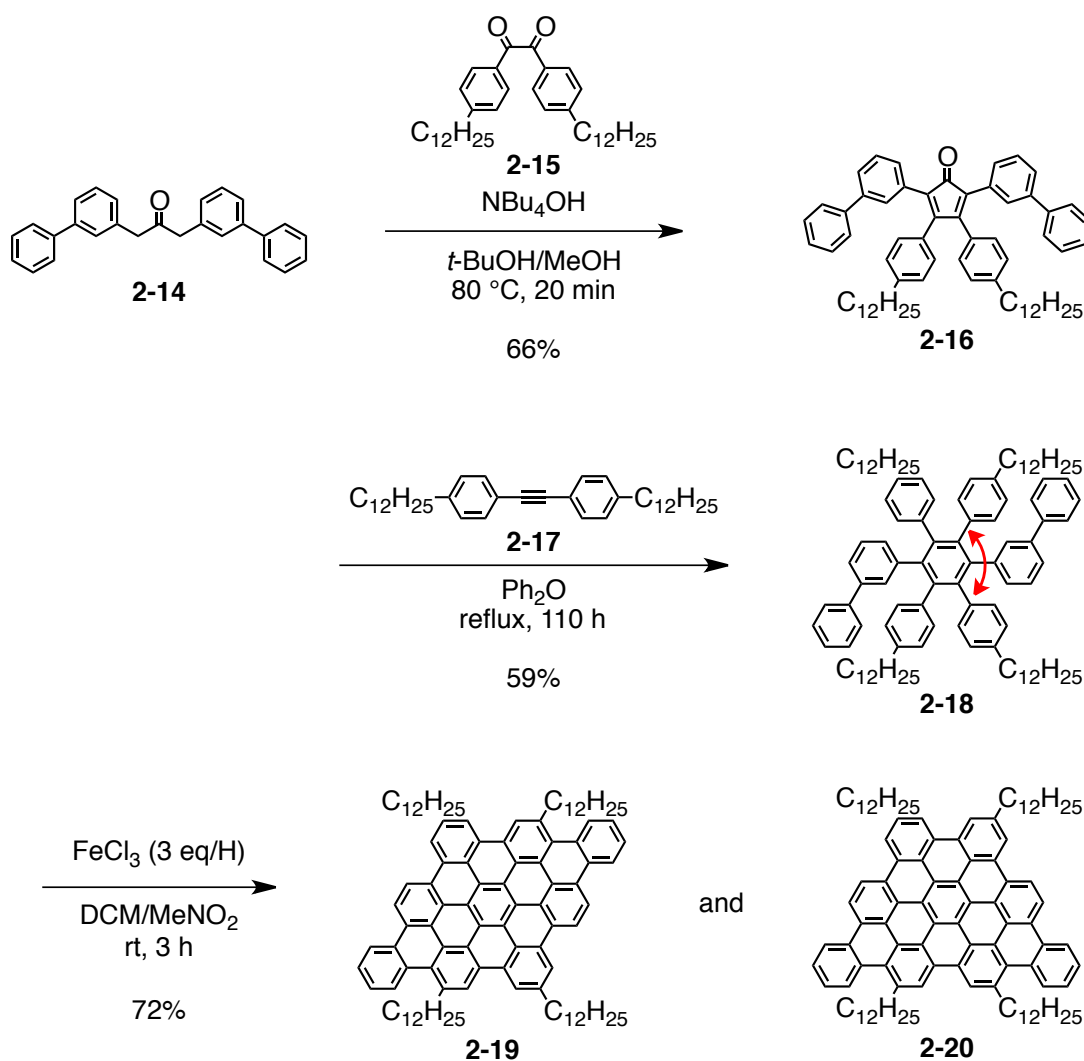


Figure 2-18. Synthetic route to model oligophenylene **2-18**, followed by the cyclodehydrogenation into a mixture of PAHs **2-19** and **2-20**.

The intramolecular oxidative cyclodehydrogenation of oligophenylene **2-18** was performed with three equivalents of iron(III) chloride for one hydrogen to be removed, leading to the successful formation of a mixture of PAHs **2-19** and **2-20**, which was validated by a combination of MALDI-TOF MS and ^1H NMR spectroscopy.

MALDI-TOF MS analysis of the obtained product showed a signal at $m/z = 1,344$, corresponding to the molecular weight of PAHs **2-19** and **2-20** (Figure 2-19). The isotopic distribution was in a perfect agreement with the simulated result, attesting the efficient formation of PAHs **2-19** and **2-20** without any partially fused species (Figure 2-19, inset). A signal from a mono-chlorinated product was also detected, but it is known that such signal could be highly overestimated.^{24,52} Although PAHs **2-19** and **2-20** cannot be distinguished by mass spectrometry due to the identical molecular formula, this result indicated highly efficient “graphitization” of model oligophenylene **2-18**.

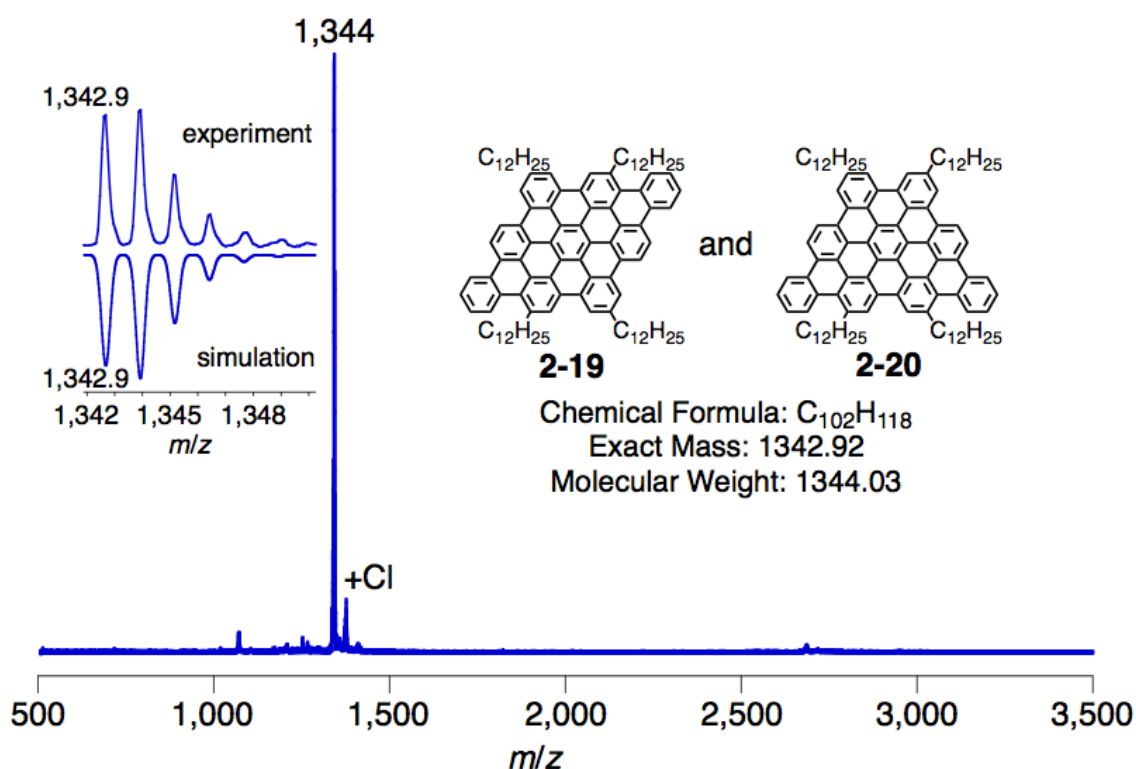


Figure 2-19. A MALDI-TOF MS spectrum of a mixture of PAHs **2-19** and **2-20**; inset shows the isotopic distribution in a perfect agreement with the simulation.⁵⁰

^1H NMR analysis of the product was carried out at elevated temperature of $120\text{ }^\circ\text{C}$ by using high-boiling-point solvent, 1,1,2,2-tetrachlorobenzene- d_2 , which allowed the observation of well-resolved signals at aliphatic as well as aromatic regions (Figure 2-20). Four independent signals were observed for $\alpha\text{-CH}_2$ protons at $\delta = 3.82$, 3.68, 3.22, and 3.08 ppm, evidently showing the existence of both PAHs **2-19** and **2-20** in the sample. The values of integration was basically the same for all the four signals, which indicated the 1:1 ratio between PAHs **2-19** and **2-20** statistically formed upon the cyclodehydrogenation. The signals from aromatic protons were down-shifted and appeared in the range of $\delta = 7.7\text{--}9.1$ ppm due to the large aromatic plane, similar to the ^1H NMR spectrum of PAH **2-8** (Figure 2-3b). The down-shifting was not as significant as that of PAH **2-8** apparently because of the smaller aromatic cores of PAHs **2-19** and **2-20**. ^{13}C NMR could not be recorded even at the elevated temperature due to the strong aggregation of the PAH molecules. Unambiguous assignment of the ^1H NMR signals was attempted by employing $^1\text{H}\text{-}^1\text{H}$ -COSY and NOESY measurements, but hindered by the complication of the spectrum by the presence of the two structural isomers. Nevertheless, the values of integration were consistent with those expected for a 1:1 mixture of PAHs **2-19** and **2-20**. These results clearly demonstrated the highly efficient cyclodehydrogenation of model oligophenylene **2-18** into rhombic and trapezoidal PAHs **2-19** and **2-20**, respectively, in 1:1 ratio.

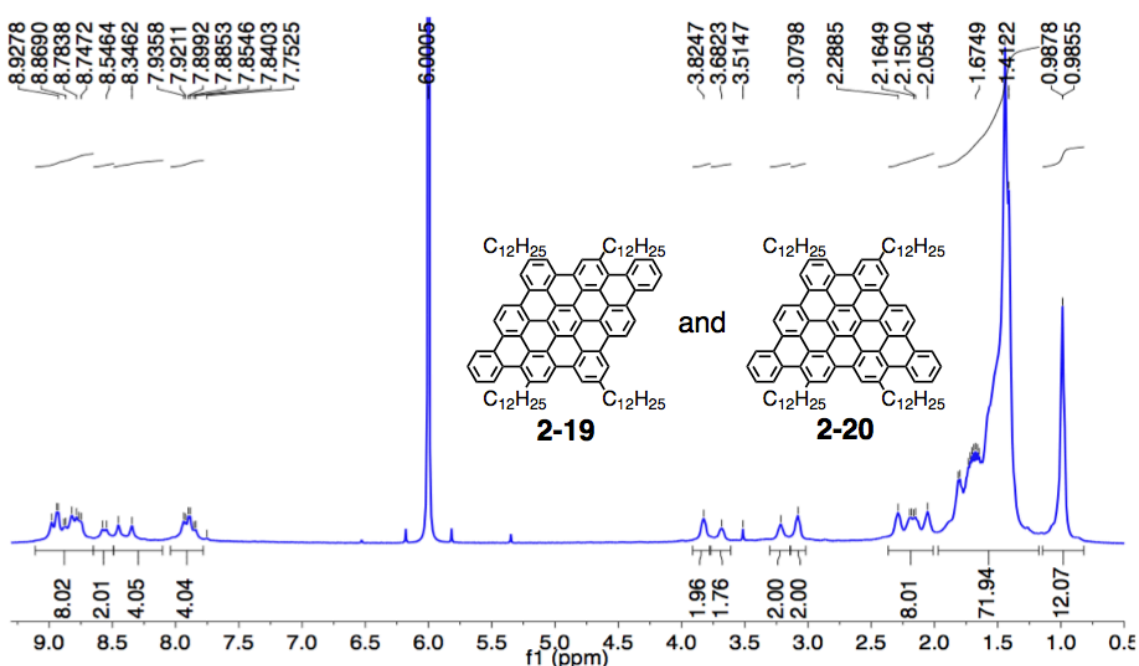


Figure 2-20. A ^1H NMR spectrum of a mixture of PAHs **2-19** and **2-20** in 1,1,2,2-tetrachloroethane- d_2 at $120\text{ }^\circ\text{C}$ (500 MHz).⁵⁰

2.2.3 Fabrication of $N = 18$ armchair GNRs

After validating the high efficiency of the “graphitization” of model oligophenylene **2-18**, the fabrication of $N = 18$ armchair GNR **2-13** was carried out in collaboration with [REDACTED], who developed the synthetic route and conducted preliminary characterizations. The cyclodehydrogenation of precursor **2-12-II** into GNR **2-13** as well as their in-depth analyses by MALDI-TOF MS, and FTIR, UV-vis absorption, NMR, and photoelectron spectroscopies were performed within the scope of this dissertation. To begin with, *o*-terphenyl-based, dihalogenated monomer **2-11** was synthesized as displayed in Figure 2-21. Cyclopentadienone **2-22**

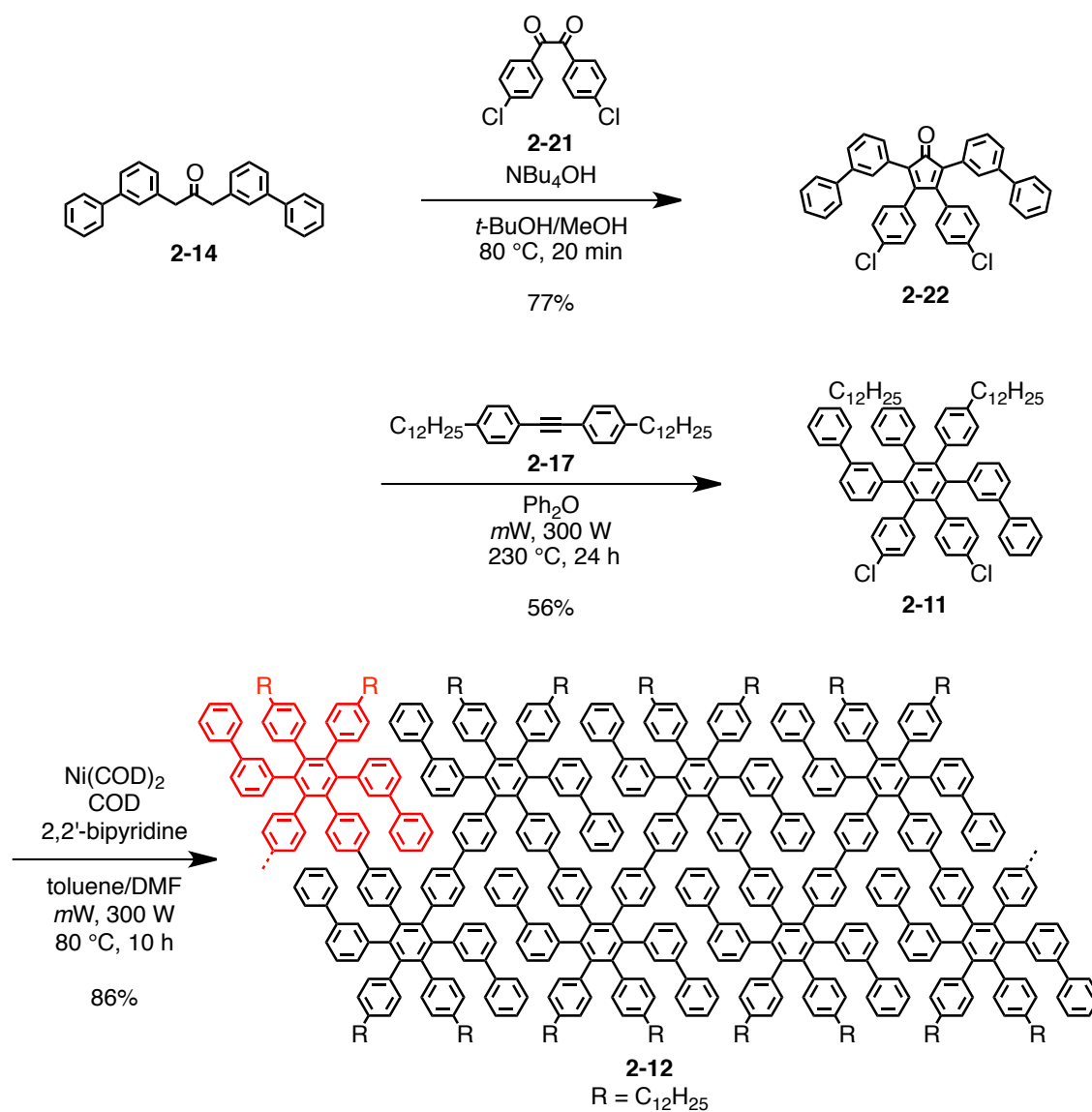


Figure 2-21. Synthetic route to polyphenylene precursor **2-12**.

was prepared via *Knoevenagel* condensation of di(3-biphenyl)acetone (**2-14**) and 4,4'-dichlorobenzil (**2-21**)⁵³ in 77% yield followed by *Diels-Alder* cycloaddition with bis(4-dodecylphenyl)acetylene (**2-17**) to afford monomer **2-11** in 56% yield.

Next, *Yamamoto* polymerization of monomer **2-11** was carried out based on the standard protocol,^{7,8} stirring at 80 °C for 10 days followed by end-capping with chlorobenzene (Figure 2-21). MALDI-TOF MS analysis of the resulting polyphenylene precursor **2-12** in linear mode displayed a regular mass pattern extending over $m/z = \sim 20,000$, which corresponded to the molecular weight of ~ 20 repeating units (Figure 2-22a). GNR **2-13** with such number of repeating units typically has a length of ~ 10 nm, but this was most probably not the highest value, considering the limitation of the MALDI-TOF MS analysis for the characterizations of high-molecular-weight samples with broad molecular weight distribution.^{3,27}

Subsequently, reflectron-mode MALDI-TOF MS analysis was conducted to obtain more accurate molecular weight of the resulting precursor **2-12** (Figure 2-22b). Signals from dimer, trimer, tetramer, pentamer, hexamer, heptamer, and octamer could be observed at $m/z = 2,044$, 3,065, 4,087, 5,109, 6,131, 7,153, and 8,175, respectively, corresponding to the molecular weights of oligomers of precursor **2-12** after the loss of two chloro groups (Figure 2-23). Notably, well-resolved isotopic distribution could be observed for the trimer, which was in perfect agreement with the simulation (Figure

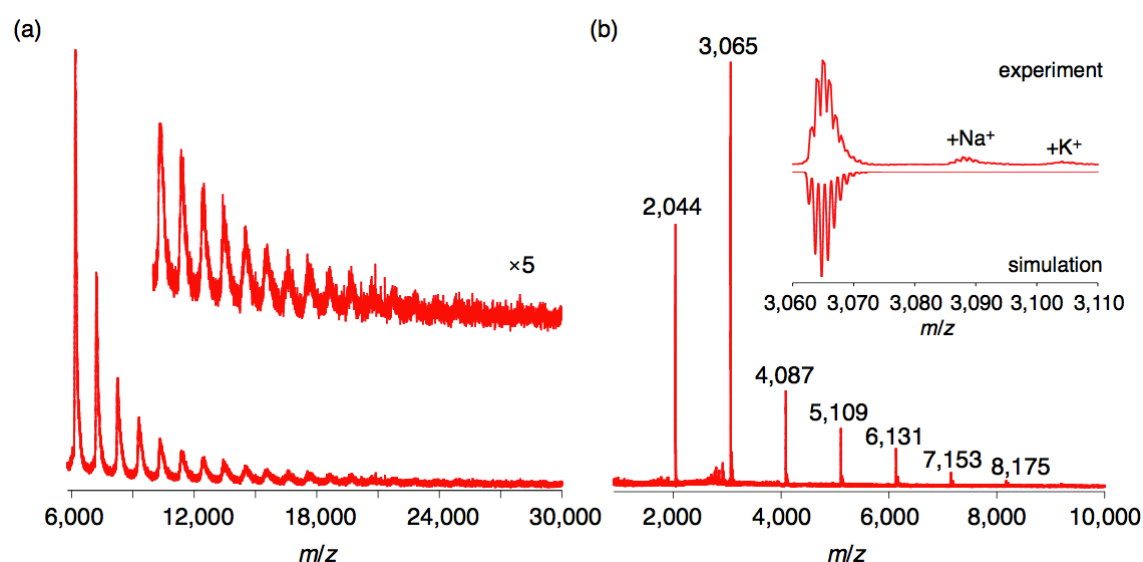


Figure 2-22. MALDI-TOF MS spectrum of precursor **2-12** (a) in linear mode; inset: magnified spectrum, and (b) in reflectron mode; inset: magnified spectrum showing the isotopic distribution of the trimer in a good agreement with the simulation (solid-state sample preparation, matrix: TCNQ).⁵⁰

2-22b, inset), further proving the formation of the oligomers displayed in Figure 2-23. No oligomer with remaining chloro group was detected, indicating that all of these oligomers were precluded from further polymerization due to dechlorination. In both linear- and reflectron-mode analyses, no signal was observed other than those expected for the oligomers of precursor **2-12**, corroborating the high purity of the obtained precursor **2-12**.

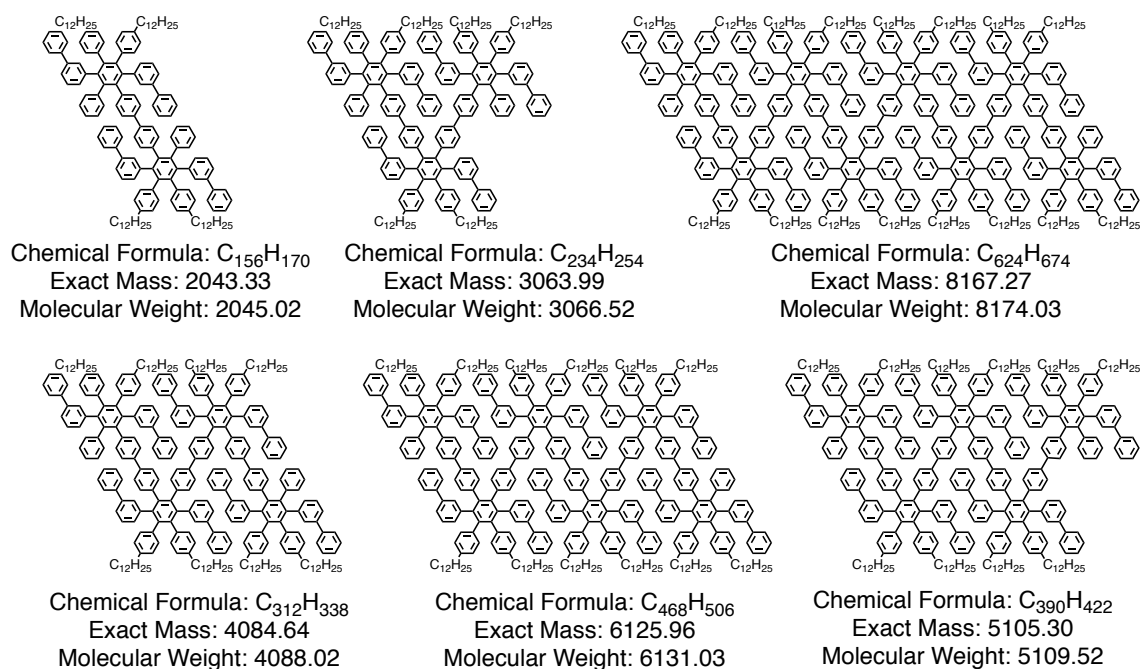


Figure 2-23. Structures and molecular weight of oligomers of polyphenylene precursor **2-12**.

SEC analysis was carried out based on PPP and PS standards in order to evaluate the average molecular weight of polyphenylene precursor **2-12**. M_w , M_n , and PDI of precursor **2-12** were thus estimated to be 4,700–6,300 g/mol, 3,300–3,900 g/mol, and 1.4–1.6, respectively, where the smaller values corresponded to the ones with PPP standard. As discussed in subsection 2.1.3 regarding polyphenylene precursor **2-2**, it is likely that the actual molecular weights of polyphenylene **2-12** with a nonrigid, kinked backbone structure and long alkyl chains can also be well approximated by these values obtained against PPP and PS standards (see also section 3.3). These values obtained for precursor **2-12** were considerably lower than those attained with precursor **2-2**, which was presumably due to the high steric hindrance in the *Yamamoto* polymerization of monomer **2-11**. Thus, smaller oligomers were precluded from further polymerization by the dechlorination as indicated by the results from reflectron-mode MALDI-TOF MS analysis (Figure 2-22b). The molecular weight distribution of precursor **2-12** displayed

a single peak at $\sim 3,400$ – $4,500$ g/mol with a shoulder at around $7,000$ – $10,000$ g/mol, corresponding to the small oligomers and relatively short polymers, respectively (Figure 2-24a).

In order to obtain a polymer fraction free of the smaller oligomers, polyphenylene precursor **2-12** was subsequently fractionated into six fractions together with Dr. Lukas F. Dössel, using recycling preparative SEC. The six fractions were named **2-12-I**, **2-12-II**, **2-12-III**, **2-12-IV**, **2-12-V**, and **2-12-VI**, in the order of the sample collection during the SEC fractionation, which showed smaller PDI values with different average molecular weights based on the SEC analysis as summarized in Table 2-1. While fractions **2-12-IV**–**VI** showed a small M_w of $<6,000$ g/mol, fractions **2-12-I**–**III** displayed a relatively high M_w , corresponding to the shoulder observed at $\sim 7,000$ – $10,000$ g/mol in the molecular weight distribution of as-prepared **2-12** (Figure 2-24a). Since the amount of fraction **2-12-I** was limited, fraction **2-12-II** with a higher M_w of

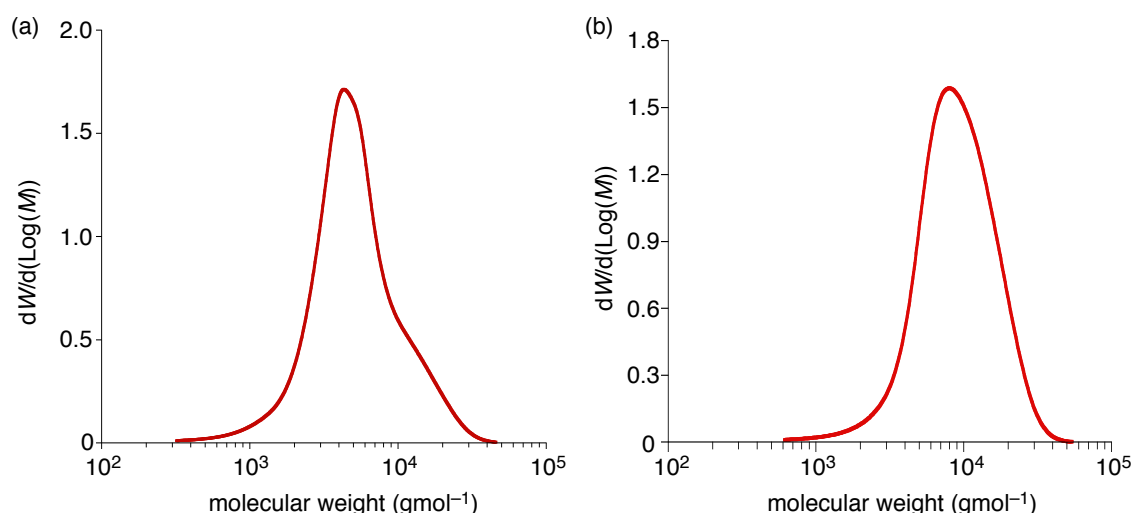


Figure 2-24. Molecular weight distribution of polyphenylene precursor (a) **2-12** (before fractionation) and (b) **2-12-II** (after fractionation) (SEC analysis, eluent: THF, PS standard).

Table 2-1. M_w , M_n , and PDI values of precursor **2-12** before and after the fractionation.

	2-12	2-12-I	2-12-II	2-12-III	2-12-IV	2-12-V	2-12-VI
M_w (kg/mol)	4.7–6.3	8.8–12	7.3–10	5.8–8.1	4.0–5.2	2.7–3.3	1.4–1.6
M_n (kg/mol)	3.3–3.9	6.9–9.3	5.5–7.2	4.3–5.3	3.0–3.5	2.3–2.7	1.0–1.1
PDI	1.4–1.6	1.3	1.3–1.4	1.3–1.5	1.3–1.5	1.2	1.4–1.5

M_w and M_n were estimated by the SEC analysis based on PPP and PS standards and given with ranges, corresponding to $M_{w,PPP}$ – $M_{w,PS}$ and $M_{n,PPP}$ – $M_{n,PS}$, respectively (eluent: THF, UV detector). PDI values were calculated by M_w/M_n . All the SEC results have a margin of error of $\pm 10\%$.

7,300–10,000 g/mol was selected for the synthesis of GNR **2-13**. The molecular weight distribution of **2-12-II** showed a single peak without any shoulder (Figure 2-14b), allowing the synthesis of GNR **2-13** with narrow length distribution.

The intramolecular oxidative cyclodehydrogenation of polyphenylene precursor **2-12-II** was performed with the established method, using iron(III) chloride as oxidant in a mixture of dichloromethane and nitromethane (Figure 2-25).^{2,3,6} The efficiency of the cyclodehydrogenation was subsequently studied by a combination of MALDI-TOF MS, FTIR, Raman, and solid-state NMR spectroscopic analyses. Linear-mode MALDI-TOF MS analysis of GNR **2-13** revealed a regular mass pattern similar to that of polyphenylene precursor **2-12-II** (Figure 2-26). Although the peaks were strongly broadened, the intervals between the peaks were roughly $m/z = \sim 1,000$, which was consistent with the molecular weight of one repeating unit of GNR **2-13**, i.e. $C_{78}H_{54} = 991$ (Figure 2-26, inset). Mass larger than $m/z = 15,000$ was not detected presumably because of the strong aggregation of larger GNRs.^{4,27} Reflectron-mode analysis was also attempted in order to obtain more accurate m/z values, but did not give any reasonable result, again due to the strong π - π stacking interaction of GNR **2-13**.

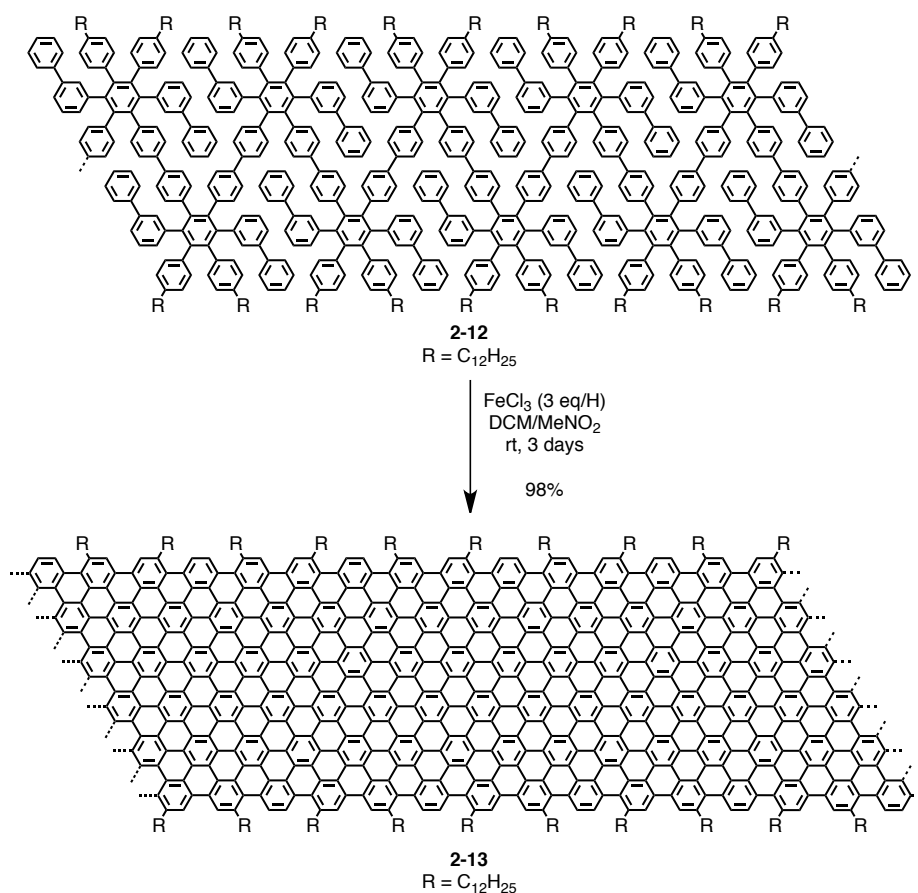


Figure 2-25. Cyclodehydrogenation of polyphenylene precursor **2-12** into GNR **2-13**.

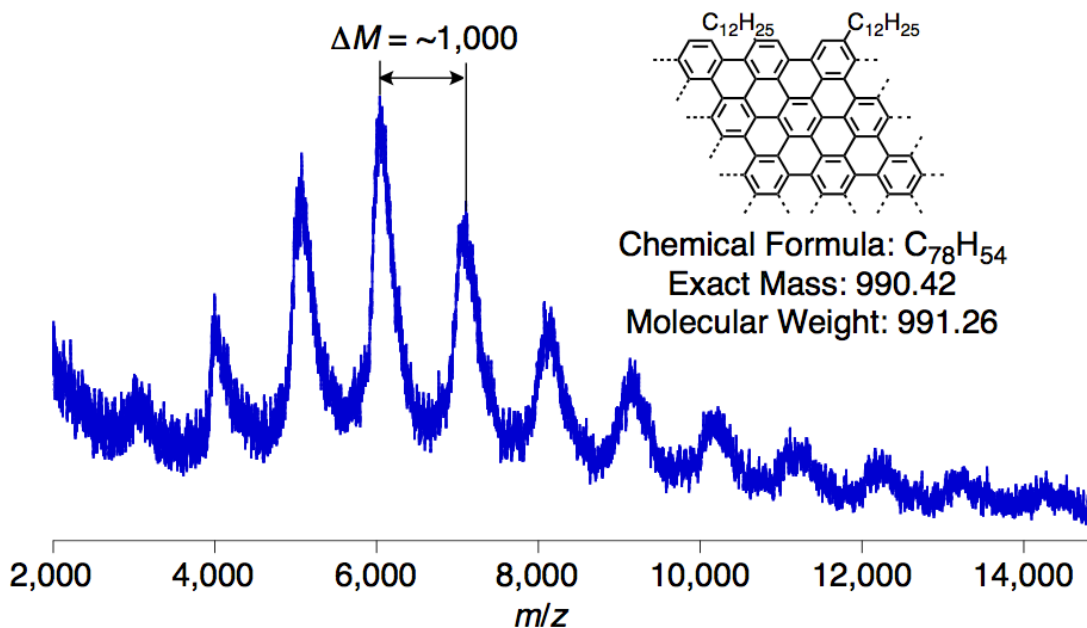


Figure 2-26. MALDI-TOF MS spectrum of GNR **2-13**; inset: structure, chemical formula, and molecular weight of one repeating unit of **2-13** (linear mode, solid-state sample preparation, matrix: TCNQ).⁵⁰

FTIR spectroscopic analysis of polyphenylene precursor **2-12** and GNR **2-13**, namely before and after the cyclodehydrogenation, provided strong evidences for the high efficiency of the cyclodehydrogenation (Figure 2-27). The band at $4,052\text{ cm}^{-1}$, originating from the free rotating phenyl rings, completely vanished and the signal triad at $3,029$, $3,054$, and $3,084\text{ cm}^{-1}$ from aromatic C–H stretching vibrations were strongly attenuated.^{3,4,6,29} Moreover, the disappearance of out-of-plane (*opla*) C–H deformation

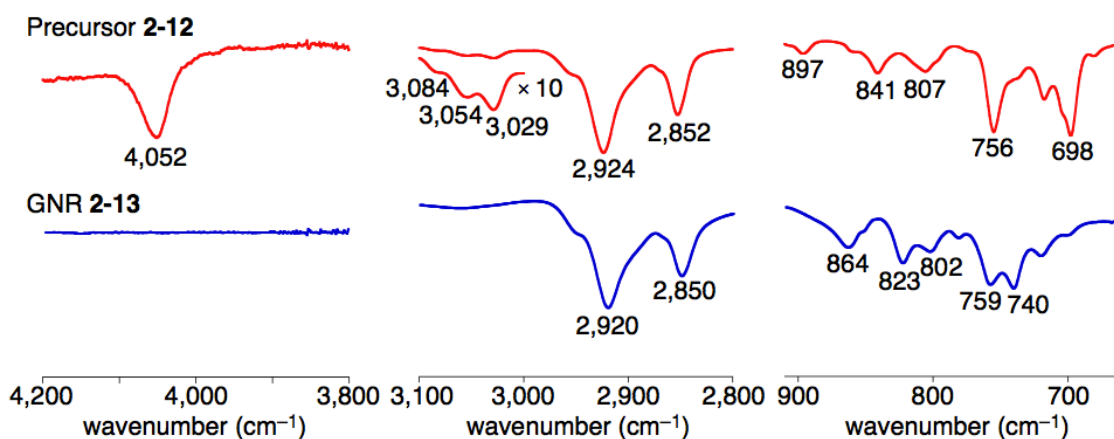


Figure 2-27. Representative FTIR spectral regions of polyphenylene precursor **2-12** (red) and GNR **2-13** (blue).

bands at 698, 841, and 897 cm^{-1} verified the absence of mono- and disubstituted benzene rings after the cyclodehydrogenation, corroborating the efficient formation of GNR **2-13**.^{4-6,29} The bands observed in the fingerprint region of GNR **2-13** such as at 864, 823, and 740 cm^{-1} were most probably derived from the C–H bonds at the edges²⁹ or from $-\text{CH}_2-$ of the dodecyl chains,³⁰ but rational assignment requires theoretical studies,³¹ similar to the IR spectrum of GNR **2-3** (see subsection 2.1.3).

Raman spectrum of GNR **2-13** was measured by [REDACTED] in our research group directly on a powder sample with the excitation at 488 nm (Figure 2-28). Raman spectrum of GNR **2-13** thus obtained displayed the typical D and G peaks at 1,325 and 1,578 cm^{-1} , respectively, which were in agreement with the values reported for previous bottom-up synthesized GNRs.^{3,4,32} The D peaks of such GNRs are not derived from the defects as known for graphene, but activated by the confinement of π -electrons into a finite-size domains³³ as was mentioned for the Raman spectrum of GNR **2-3** (see subsection 2.1.3). The second-order peaks observed at 2,725, 2,922, and 3,200 cm^{-1} could most probably be assigned to 2D, D + G, and 2G bands, respectively.^{4,36-38}

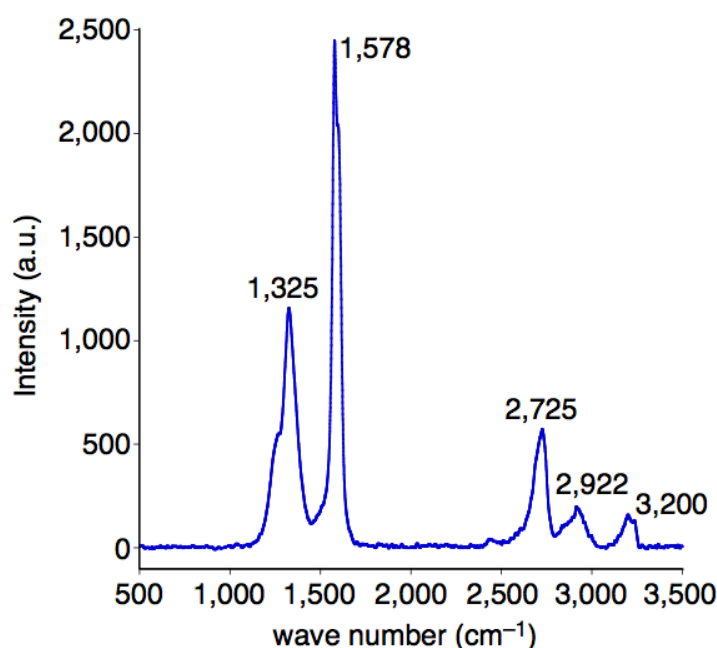


Figure 2-28. Raman spectrum of GNR **2-13** measured at 488 nm (powder, laser power: ~ 1 mW).

Liquid- and solid-state ^1H NMR spectroscopy analyses of polyphenylene precursor **2-12** and GNR **2-13** were performed in order to further evaluate the cyclodehydrogenation step in collaboration with [REDACTED] at Max Planck Institute for Polymer Research Mainz, Germany. Although GNR **2-13** could not be analyzed by the liquid-state NMR because of the strong aggregation, the solid-state NMR provided considerable structural information based on positions and linewidths of ^1H chemical shifts.⁵⁴⁻⁵⁷ Figure 2-29a and b display ^1H NMR spectra of precursor **2-12** in a dichloromethane- d_2 solution and in a solid state, respectively. Although the signals are broadened and unresolved in the solid-state NMR spectrum (Figure 2-29b), the linewidth of the aromatic signal at ~ 7.0 ppm is similar to that in the liquid-state spectrum (Figure 2-29a), denoting that precursor **2-12** possesses a relatively flexible structure. In contrast, ^1H magic-angle spinning (MAS) NMR spectrum of GNR **2-13** shows significantly broadened ^1H resonances, and the aromatic signals are shifted to higher frequency compared to the spectrum of precursor **2-12** (Figure 2-29c). These observations indicate that these aromatic protons are attached to an extended π -conjugated system and that GNR **2-13** behaves like a rigid solid, corroborating the successful formation of GNRs.

2D ^1H - ^1H double quantum-single quantum (DQ-SQ) NMR correlation experiments of precursor **2-12** and GNR **2-13** are displayed in Figure 2-29d and e, respectively. These experiments can map out the spatial proximity between different ^1H signals.^{58,59} The 2D ^1H - ^1H DQ-SQ spectrum of precursor **2-12** shows clear and narrow ^1H - ^1H correlation signals between the aromatic protons as well as between the aromatic protons and the aliphatic protons, consistent with the semiflexible/semirigid structure (Figure 2-29d). In contrast, the 2D ^1H - ^1H DQ-SQ spectrum of GNR **2-13** displays a broad and stretched ridge of ^1H - ^1H correlation signals, where the aromatic protons at ~ 6 – 9 ppm show correlation with the aliphatic protons, but those at ~ 9 – 12 ppm have correlation only with other aromatic protons (Figure 2-29e). Based on these observations, the aromatic signals at ~ 6 – 9 ppm can be assigned to the protons at the edge of GNR **2-13**, which are in spatial vicinity to the alkyl chains, and the signals at ~ 9 – 12 ppm to the protons at the termini of GNR **2-13** (red and blue dots, respectively, in Figure 2-29f). The observation of the protons at the termini is consistent with the length of GNR **2-13** expected from the MALDI-TOF MS and SEC analyses of precursor **2-12-II**. For instance, when the length of GNR **2-13** is ca. 10 nm, the ratio of the edge protons to the terminus protons is about 2 to 1. While the edge protons showed a relatively small shift of ca. 1–2 ppm to the high frequency compared to those of

precursor **2-12**, the terminus protons underwent a larger shift of ca. 2–5 ppm. This difference might be due to the fact that GNR **2-13** is heterogeneously packed, where the edge- and terminus-proton signals are shifted differently by the aromatic ring currents with varying magnitudes.^{60,61}

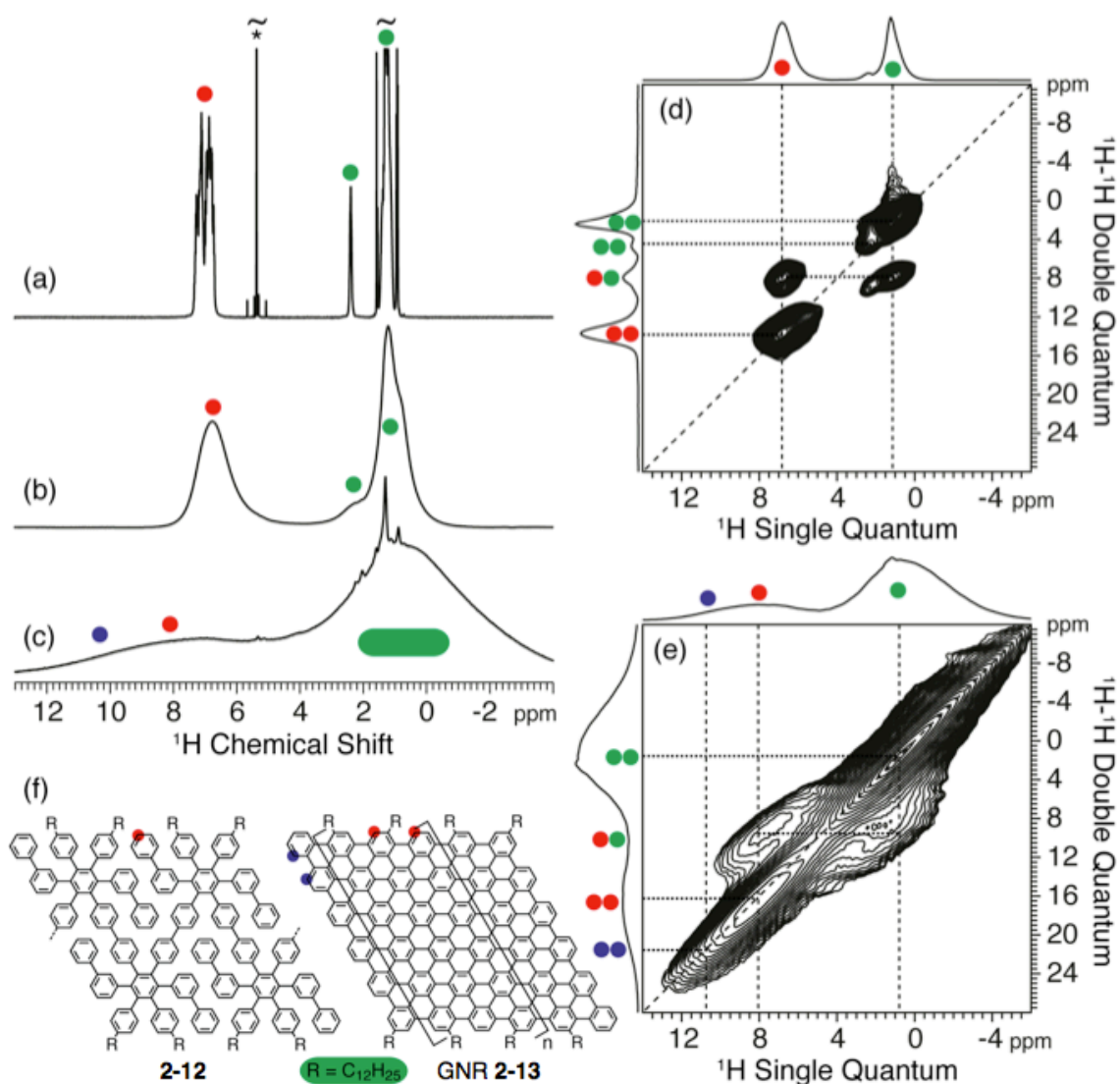


Figure 2-29. (a), (b) Liquid- and solid-state ^1H NMR spectra of precursor **2-12** (a) in CD_2Cl_2 and (b) as solid sample, respectively. The asterisk in (a) indicates the residual proton signal of CD_2Cl_2 . (c) Solid-state ^1H NMR spectrum of GNR **2-13**. The sharp signals in represent residual solvent present in the sample. (d), (e) The 2D ^1H - ^1H DQ-SQ correlation spectra of (d) precursor **2-12** and (e) GNR **2-13**, which were recorded using two rotor periods of DQ recoupling. The ^1H signals are assigned using the color code given in (f); all the aromatic signals of **2-12** are represented by the red color. The liquid-state spectrum in (a) was recorded at 7.05 T (300.13 MHz for ^1H), while the solid-state NMR experiments in (b-e) were obtained at 16.45 T (700.21 MHz for ^1H) using a MAS frequency of 59524 Hz.⁵⁰

GNR **2-13** was readily dispersible in common organic solvents such as THF, chlorobenzene, and *ortho*-dichlorobenzene (ODCB) with an assistance of mild sonication, which provided brown dispersions. The higher dispersibility of GNR **2-13** compared to that of GNR **2-3-I**, which gave no dispersion in such solvents, could be explained by the relatively short length of GNR **2-13** as evidenced by the relatively small averaged molecular weights of precursor **2-12-II** based on the SEC analysis. Indeed, the color and dispersibility of GNR **2-13** was closer to that of GNR **2-3-II**, which was prepared from precursor **2-2-II** with small M_w of 5,400–7,200 g/mol (subsection 2.1.3).

UV–vis absorption spectroscopic analysis of a dispersion of GNR **2-13** in NMP revealed an absorption maximum at 410 nm with the absorption edge at ~800–900 nm, corresponding to the optical bandgap of ~1.4–1.6 eV (Figure 2-30). The UV–vis spectrum of GNR **2-13** also showed two small peaks at 560 and 680 nm and a shoulder at ~820 nm, which were presumably absorption maxima of longer GNRs in the sample. The absorption maximum was at 410 nm, but this might be because the shortest GNRs in the sample were preferentially extracted into the dispersion, while longer GNRs remained in large aggregates, being removed before the measurement. Nevertheless, the optical bandgap of ~1.4–1.6 eV is much larger than the bandgap theoretically estimated for the infinite $N = 18$ armchair GNR, i.e. ~0.5 eV,⁴⁹ indicating that GNR **2-13** was not sufficiently extended to attain the energy level of the infinite GNR, in consistent with the results from MALDI-TOF MS, SEC, and solid-state NMR.

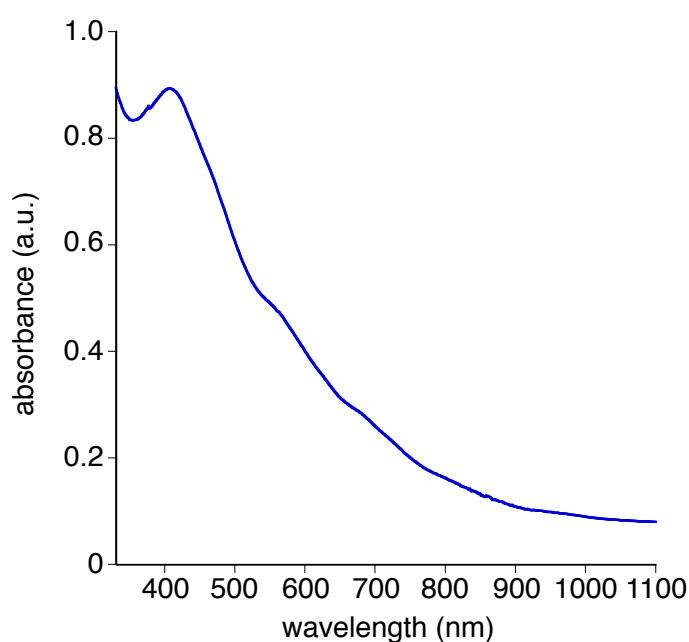


Figure 2-30. UV–vis absorption spectrum of GNR **2-13** in NMP.

In order to evaluate the ionization potential of GNR **2-13** an ambient photoelectron spectroscopy measurement was performed on a drop-cast film by ██████████ in the group of ██████████. Interestingly, the ionization potential of GNR **2-13** was estimated to be 5.010 ± 0.063 eV, which was comparable to that of laterally extended GNR **2-3-I**. Although the above-mentioned results from spectroscopic characterizations could not unambiguously prove the structural perfection of GNR **2-13**, this result in combination with all the characterization results corroborated the successful conversion of precursor **2-12** into GNR **2-13**. The relatively short length of GNR **2-13** indicated the limitation of this synthetic approach for the fabrication of longitudinally well-extended $N=18$ GNRs, but the high dispersibility of GNR **2-13** enabled their liquid-phase processing for integration into electronic devices.

2.2.4 Fabrication of FETs with the $N = 18$ armchair GNRs

The relatively short length of GNR **2-13** did not allow the investigation of the electronic transport properties on individual GNRs, but the high dispersibility enabled the preparation of GNR films by simple drop casting, opening a way towards the applications of GNR **2-13** in electronic devices. Fabrication of FET devices was thus attempted using GNR **2-13** as the active layers by ██████████ in the group of ██████████. In the preliminary experiments, working FET devices could be successfully prepared by drop-casting dispersions, or suspensions, of GNR **2-13** in a 1:1 mixture of 1,2-dichlorobenzene and chloroform. Figures 2-31a and b show output and transfer characteristics of thus prepared GNR-based devices, which were featured by typical *p*-type behavior. Remarkably, the devices demonstrated hole field-effect mobility of $0.028 \text{ cm}^2/\text{V}\cdot\text{s}$ as the maximum value with on-off ratio of as high as $\sim 10^6$. The average value of the hole mobility was $0.012 \text{ cm}^2/\text{V}\cdot\text{s}$ from 13 transistors. The threshold voltage was low and typically $0 > V_T > -15$ V. The value of on-off ratio was far better than those obtained with GNRs fabricated by lithography and etching,⁶² and comparable with the highest values hitherto achieved with GNRs.⁶³⁻⁶⁵ The mobility was much smaller than the value expected for such GNRs,⁶⁶ because the FET devices were made on disordered films of GNR **2-13**, where the charge carriers needed to be transported between the GNRs. In order to prepare FET devices on single GNRs, another bottom-up synthetic method needs to be developed to obtain liquid-phase processable GNRs with high longitudinal extension.

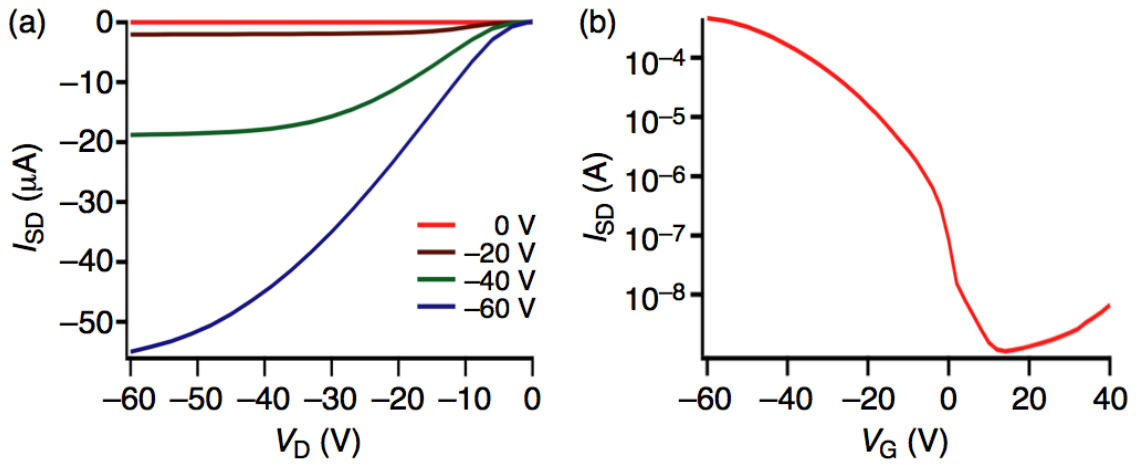


Figure 2-31. (a) Output and (b) transfer characteristics of bottom-gate bottom-contact device prepared with GNR **2-13**.

Further, photoresponse of the GNR-based devices was tested in order to examine the applicability of GNR **2-13** for phototransistors, which are an important building block for the fabrication of photosensors.⁶⁷⁻⁶⁹ Figure 2-32a shows the difference in the transfer characteristics of the GNR-based device in dark and under white light illumination ($5 \text{ mW}\cdot\text{cm}^{-2}$). The drain current notably increased upon the white light illumination, accompanied by a pronounced shift in the threshold voltage, which remarkably demonstrated the photoresponse of GNR **2-13**. This phenomenon can be explained by photogeneration of excitons, which dissociate into charge carriers and subsequently move to the electrodes under the electric field, supplying extra current to the devices.⁶⁷ There are two important parameters for the characterization of the phototransistors, namely photosensitivity (P) and responsibility (R).⁶⁹ P measures the increase in the current upon the light illumination, i.e. photocurrent (I_{ph}), in comparison to that in dark and defined as

$$P = \frac{I_{ph}}{I_{dark}} = \frac{I_{light} - I_{dark}}{I_{dark}} \quad (2-1)$$

where I_{light} and I_{dark} are the drain current under light illumination and in dark, respectively. On the other hand, R evaluates the efficiency of the conversion of light into the photocurrent and defined as

$$R = \frac{I_{light} - I_{dark}}{E \cdot A} \quad (2-2)$$

where E is the irradiance of the incident light and A is the effective device area. The device with GNR **2-13** showed high P of up to 10^6 with good R of up to 40 A/W, which indicated the high potential of such bottom-up synthesized GNRs for the applications as phototransistor materials (Figure 2-32b). R observed in this preliminary experiment was relatively low, but could most probably be enhanced by optimizing the deposition method to improve the organization of GNRs in the films.⁶⁸

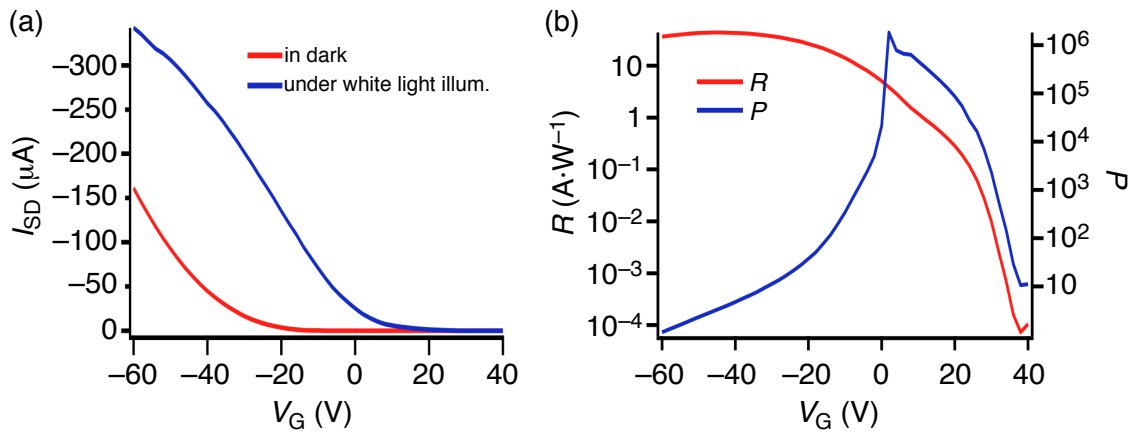


Figure 2-32. (a) Comparison of the transfer characteristics of the device prepared with GNR **2-13** in dark and under white light illumination ($5 \text{ mW}\cdot\text{cm}^{-2}$). (b) Variation of the responsivity R (red) and photosensitivity P (blue) with V_G .

2.2.5 Summary

In summary, $N = 18$ armchair GNR **2-13** with the lateral width of ca. 2.1 nm was synthesized by the bottom-up, solution-mediated method based on the oxidative cyclodehydrogenation of laterally extended polyphenylene precursor **2-12**. The *AA*-type *Yamamoto* polymerization of monomer **2-11** with the V-shaped polymerizable backbone structure allowed the preparation of precursor **2-12** with twice the width of the monomer. The successful “graphitization” of precursor **2-12** into GNR **2-13** was validated by a combination of MALDI-TOF MS and FTIR, Raman, solid-state ^1H NMR, and ultraviolet photoelectron spectroscopies. However, the SEC analysis of precursor **2-12** as well as solid-state NMR and UV–vis absorption spectra of GNR **2-13** indicated the relatively short length of the obtained GNR **2-13** compared to GNR **2-3-I**, denoting the low efficiency of this method for the synthesis of laterally and longitudinally extended GNRs, most probably because of the high steric hindrance in the polymerization of monomer **2-11**. Nevertheless, GNR **2-13** displayed high dispersibility in common organic solvents owing to the relatively short length, allowing their facile liquid-phase processing as well as integration into FET devices on them, revealing the remarkably high on-off ratio of $\sim 10^6$ as well as high photosensitivity of up to 10^6 , suggesting their potential for the application as phototransistor materials. However, the observed mobility was much lower than the value expected for such GNRs, because of the inter-ribbon transport. Longer and processable GNRs need to be synthesized for the investigation of the intra-ribbon mobilities of the GNRs.

2.3 References

- (1) Wu, J.; Pisula, W.; Müllen, K. *Chem. Rev.* **2007**, *107*, 718.
- (2) Yang, X. Y.; Dou, X.; Rouhanipour, A.; Zhi, L. J.; Rader, H. J.; Müllen, K. *J. Am. Chem. Soc.* **2008**, *130*, 4216.
- (3) Dössel, L.; Gherghel, L.; Feng, X.; Müllen, K. *Angew. Chem. Int. Ed.* **2011**, *50*, 2540.
- (4) Schwab, M. G.; Narita, A.; Hernandez, Y.; Balandina, T.; Mali, K. S.; De Feyter, S.; Feng, X.; Müllen, K. *J. Am. Chem. Soc.* **2012**, *134*, 18169.
- (5) Shifrina, Z. B.; Averina, M. S.; Rusanov, A. L.; Wagner, M.; Müllen, K. *Macromolecules* **2000**, *33*, 3525.
- (6) Wu, J. S.; Gherghel, L.; Watson, M. D.; Li, J. X.; Wang, Z. H.; Simpson, C. D.; Kolb, U.; Müllen, K. *Macromolecules* **2003**, *36*, 7082.
- (7) Yamamoto, T. *Progr. Polym. Sci.* **1992**, *17*, 1153.
- (8) Yamamoto, T. *Bull. Chem. Soc. Jpn.* **1999**, *72*, 621.
- (9) Yamamoto, T.; Morita, A.; Miyazaki, Y.; Maruyama, T.; Wakayama, H.; Zhou, Z. H.; Nakamura, Y.; Kanbara, T.; Sasaki, S.; Kubota, K. *Macromolecules* **1992**, *25*, 1214.
- (10) Yamamoto, T. *Macromol. Rapid Commun.* **2002**, *23*, 583.
- (11) Carothers, W. H. *Trans. Faraday Soc.* **1936**, *32*, 39.
- (12) Odian, G. G. *Principles of Polymerization*; J. Wiley & Sons: Hoboken, NJ, 2004.
- (13) Lee, J.; Cho, H.-J.; Jung, B.-J.; Cho, N. S.; Shim, H.-K. *Macromolecules* **2004**, *37*, 8523.
- (14) Setayesh, S.; Grimsdale, A. C.; Weil, T.; Enkelmann, V.; Müllen, K.; Meghdadi, F.; List, E. J. W.; Leising, G. *J. Am. Chem. Soc.* **2001**, *123*, 946.
- (15) Takada, T.; Arisawa, M.; Gyoten, M.; Hamada, R.; Tohma, H.; Kita, Y. *J. Org. Chem.* **1998**, *63*, 7698.
- (16) Iyer, V. S.; Wehmeier, M.; Brand, J. D.; Keegstra, M. A.; Müllen, K. *Angew. Chem. Int. Ed. Engl.* **1997**, *36*, 1604.
- (17) Morgenroth, F.; Kübel, C.; Müller, M.; Wiesler, U. M.; Berresheim, A. J.; Wagner, M.; Müllen, K. *Carbon* **1998**, *36*, 833.
- (18) Böhme, T.; Simpson, C. D.; Müllen, K.; Rabe, J. P. *Chem.–Eur. J.* **2007**, *13*, 7349.

-
- (19) Scholl, R.; Seer, C. *Liebigs Ann. Chem.* **1912**, 394, 111.
- (20) Rempala, P.; Kroulík, J.; King, B. T. *J. Am. Chem. Soc.* **2004**, 126, 15002.
- (21) Sarhan, A. A.; Bolm, C. *Chem. Soc. Rev.* **2009**, 38, 2730.
- (22) Waldvogel, S. R.; Trosien, S. *Chem. Commun.* **2012**, 48, 9109.
- (23) King, B. T.; Kroulík, J.; Robertson, C. R.; Rempala, P.; Hilton, C. L.; Korinek, J. D.; Gortari, L. M. *J. Org. Chem.* **2007**, 72, 2279.
- (24) Simpson, C. D.; Brand, J. D.; Berresheim, A. J.; Przybilla, L.; Räder, H. J.; Müllen, K. *Chem.—Eur. J.* **2002**, 8, 1424.
- (25) Kastler, M.; Pisula, W.; Wasserfallen, D.; Pakula, T.; Müllen, K. *J. Am. Chem. Soc.* **2005**, 127, 4286.
- (26) Wasserfallen, D.; Kastler, M.; Pisula, W.; Hofer, W. A.; Fogel, Y.; Wang, Z.; Müllen, K. *J. Am. Chem. Soc.* **2006**, 128, 1334.
- (27) Martin, K.; Spickermann, J.; Räder, H. J.; Müllen, K. *Rapid Commun. Mass Spectrom.* **1996**, 10, 1471.
- (28) Kumar, U.; Neenan, T. X. *Macromolecules* **1995**, 28, 124.
- (29) Centrone, A.; Brambilla, L.; Renouard, T.; Gherghel, L.; Mathis, C.; Müllen, K.; Zerbi, G. *Carbon* **2005**, 43, 1593.
- (30) Carminati, M.; Brambilla, L.; Zerbi, G.; Müllen, K.; Wu, J. *J Chem Phys* **2005**, 123, 144706.
- (31) Pathak, A.; Rastogi, S. *Spectrochimica Acta Part A* **2007**, 67, 898.
- (32) Cai, J.; Ruffieux, P.; Jaafar, R.; Bieri, M.; Braun, T.; Blankenburg, S.; Muoth, M.; Seitsonen, A. P.; Saleh, M.; Feng, X.; Müllen, K.; Fasel, R. *Nature* **2010**, 466, 470.
- (33) Castiglioni, C.; Tommasini, M.; Zerbi, G. *Philos. Transact. A Math. Phys. Eng. Sci.* **2004**, 362, 2425.
- (34) Negri, F.; Castiglioni, C.; Tommasini, M.; Zerbi, G. *J. Phys. Chem. A* **2002**, 106, 3306.
- (35) Castiglioni, C.; Mapelli, C.; Negri, F.; Zerbi, G. *J Chem Phys* **2001**, 114, 963.
- (36) Malard, L. M.; Pimenta, M. A.; Dresselhaus, G.; Dresselhaus, M. S. *Phys. Rep.* **2009**, 473, 51.
- (37) Bischoff, D.; Güttinger, J.; Dröscher, S.; Ihn, T.; Ensslin, K.; Stampfer, C. *J. Appl. Phys.* **2011**, 109, 073710.
- (38) Jiao, L.; Zhang, L.; Wang, X.; Diankov, G.; Dai, H. *Nature* **2009**, 458, 877.

- (39) Hernandez, Y.; Nicolosi, V.; Lotya, M.; Blighe, F. M.; Sun, Z.; De, S.; McGovern, I. T.; Holland, B.; Byrne, M.; Gun'Ko, Y. K.; Boland, J. J.; Niraj, P.; Duesberg, G.; Krishnamurthy, S.; Goodhue, R.; Hutchison, J.; Scardaci, V.; Ferrari, A. C.; Coleman, J. N. *Nature Nanotech.* **2008**, *3*, 563.
- (40) Coleman, J. N. *Adv. Funct. Mater.* **2009**, *19*, 3680.
- (41) Bergin, S. D.; Nicolosi, V.; Streich, P. V.; Giordani, S.; Sun, Z.; Windle, A. H.; Ryan, P.; Niraj, N. P. P.; Wang, Z.-T. T.; Carpenter, L.; Blau, W. J.; Boland, J. J.; Hamilton, J. P.; Coleman, J. N. *Adv. Mater.* **2008**, *20*, 1876.
- (42) Giordani, S.; Bergin, S. D.; Nicolosi, V.; Lebedkin, S.; Kappes, M. M.; Blau, W. J.; Coleman, J. N. *J. Phys. Chem. B* **2006**, *110*, 15708.
- (43) Rieger, R.; Müllen, K. *J. Phys. Org. Chem.* **2010**, *23*, 315.
- (44) Osella, S.; Narita, A.; Schwab, M. G.; Hernandez, Y.; Feng, X.; Müllen, K.; Beljonne, D. *ACS Nano* **2012**, *6*, 5539.
- (45) Weisman, R. B.; Bachilo, S. M. *Nano Lett.* **2003**, *3*, 1235.
- (46) Behabtu, N.; Lomeda, J. R.; Green, M. J.; Higginbotham, A. L.; Sinitskii, A.; Kosynkin, D. V.; Tsentalovich, D.; Parra-Vasquez, A. N. G.; Schmidt, J.; Kesselman, E.; Cohen, Y.; Talmon, Y.; Tour, J. M.; Pasquali, M. *Nature Nanotech.* **2010**, *5*, 406.
- (47) Al-Khedher, M. A.; Pezeshki, C.; McHale, J. L.; Knorr, F. J. *Nanotechnology* **2007**, *18*, 355703.
- (48) Imbaby, M.; Gottschalk, K. *J. Micromech. Microeng.* **2013**, *23*, 055012.
- (49) Son, Y.-W.; Cohen, M. L.; Louie, S. G. *Phys. Rev. Lett.* **2006**, *97*, 216803.
- (50) El Gemayel, M.; Narita, A.; Dössel, L.; Sundaram, R.; Kiersnowski, A.; Pisula, W.; Hansen, M. R.; Ferrari, A.; Orgiu, E.; Feng, X.; Müllen, K.; Samori, P. *Nanoscale*, **2014**, Accepted Manuscript, DOI: 10.1039/C4NR00256C.
- (51) Ito, S.; Wehmeier, M.; Brand, J. D.; Kübel, C.; Epsch, R.; Rabe, J. P.; Müllen, K. *Chem.—Eur. J.* **2000**, *6*, 4327.
- (52) Yoshimura, K.; Przybilla, L.; Ito, S.; Brand, J. D.; Wehmeier, M.; Räder, H. J.; Müllen, K. *Macromol. Chem. Phys.* **2001**, *202*, 215.
- (53) Neckers, D. C.; Hauck, G. *J. Org. Chem.* **1983**, *48*, 4691.
- (54) Bohle, A.; Brunklaus, G.; Hansen, M. R.; Schleuss, T. W.; Kilbinger, A. F. M.; Seltmann, J.; Spiess, H. W. *Macromolecules* **2010**, *43*, 4978.
- (55) Tasios, N.; Grigoriadis, C.; Hansen, M. R.; Wonneberger, H.; Li, C.; Spiess, H. W.; Müllen, K.; Floudas, G. *J. Am. Chem. Soc.* **2010**, *132*, 7478.

-
- (56) Brown, S. P. *Solid State Nucl. Magn. Reson.* **2012**, *41*, 1.
- (57) Shu, J.; Dudenko, D.; Esmaeili, M.; Park, J. H.; Puniredd, S. R.; Chang, J. Y.; Breiby, D. W.; Pisula, W.; Hansen, M. R. *J. Am. Chem. Soc.* **2013**, *135*, 11075.
- (58) Feike, M.; Demco, D. E.; Graf, R.; Gottwald, J.; Hafner, S.; Spiess, H. W. *J. Magn. Reson. Ser. A* **1996**, *122*, 214.
- (59) Saalwächter, K.; Lange, F.; Matyjaszewski, K.; Huang, C.-F.; Graf, R. *J. Magn. Reson.* **2011**, *212*, 204.
- (60) Chen, Z.; Wannere, C. S.; Corminboeuf, C.; Puchta, R.; Schleyer, P. v. R. *Chem. Rev.* **2005**, *105*, 3842.
- (61) Sebastiani, D.; Kudin, K. N. *ACS Nano* **2008**, *2*, 661.
- (62) Wang, X.; Dai, H. *Nature Chem.* **2010**, *2*, 661.
- (63) Wang, X.; Ouyang, Y.; Li, X.; Wang, H.; Guo, J.; Dai, H. *Phys. Rev. Lett.* **2008**, *100*, 206803.
- (64) Ma, L.; Wang, J.; Ding, F. *ChemPhysChem* **2013**, *14*, 47.
- (65) Bai, J.; Huang, Y. *Mater. Sci. Eng. R-Rep.* **2010**, *70*, 341.
- (66) Obradovic, B.; Kotlyar, R.; Heinz, F.; Matagne, P.; Rakshit, T.; Giles, M. D.; Stettler, M. A.; Nikonov, D. E. *Appl. Phys. Lett.* **2006**, *88*, 142102.
- (67) Pal, T.; Arif, M.; Khondaker, S. I. *Nanotechnology* **2010**, *21*, 325201.
- (68) Gemayel, M. E.; Treier, M.; Musumeci, C.; Li, C.; Müllen, K.; Samori, P. *J. Am. Chem. Soc.* **2012**, *134*, 2429.
- (69) Guo, Y.; Yu, G.; Liu, Y. *Adv. Mater.* **2010**, *22*, 4427.

Chapter 3. Liquid-Phase-Processable and Structurally Well-Defined GNRs with High Longitudinal Extension

As described in chapter 2, laterally extended GNRs could be successfully fabricated based on the bottom-up synthesis via *AA*-type *Yamamoto* polymerization. However, the obtained GNRs were relatively short (<50 nm), which did not allow the fabrication of single-ribbon FET devices with the modern e-beam lithography. Therefore, development of another method for the fabrication of longitudinally well-extended GNRs with lengths of >100 nm is required. In this chapter, synthesis of long (>600 nm) and liquid-phase processable GNRs based on *AB*-type *Diels–Alder* polymerization is described. Bulky alkyl chains densely installed at the peripheral positions of the GNRs rendered them dispersible in organic solvents, enabling their liquid-phase processing as well as investigation of their intrinsic mobilities by employing non-contact, time-resolved THz spectroscopy. Unprecedented edge chlorination of the GNRs for tuning of the energy levels as well as attempts for the fabrication of GNR-based electronic devices are also discussed.

3.1 Synthetic strategy

In light of the extremely high efficiency for the fabrication of large-molecular-weight polyphenylene polymers, *Diels–Alder* polymerization¹⁻⁴ can be considered as one of the most promising polymerization methods for the bottom-up solution synthesis of longitudinally well-extended GNRs (>100 nm). *A₂B₂*-type *Diels–Alder* polymerization, involving two different monomer precursors, i.e. a bisdiene and a bisdienophile, was previously employed for the fabrication of GNRs, where 1,4-bis(2,4,5-triphenylcyclopentadienone-3-yl)benzene (**1-27**) and diethynylterphenyl (**1-31**) were used as the bisdiene and the bisdienophile, respectively (Figure 1-10, subsection 1.2.2.4).⁵ The *Diels–Alder* polymerization of **1-27** and **1-31**, however, yielded numerous regioisomers because of the two possible molecular orientations at each cycloaddition step, resulting in randomly kinked and structurally undefined GNRs.

In order to accomplish the exclusive formation of straight and structurally well-defined GNRs, it is prerequisite that all the structural isomers of the polyphenylene precursor, which are unavoidably generated upon the repetitive *Diels–Alder* cycloaddition of unsymmetrical monomers, transform into one single GNR structure. It is also preferable for the maximization of the polymerization efficiency to utilize *AB*-type *Diels–Alder* polymerization^{6,7} instead of the *A₂B₂*-type polymerization. The *AB*-type *Diels–Alder* polymerization involves only one monomer bearing both diene and dienophile functionalities in one molecule, in contrast to the *A₂B₂*-type *Diels–Alder* polymerization that requires two different monomers and thus starkly affected by the stoichiometry problem.^{8,9} Taking the above-mentioned requirements into consideration, *AB*-type monomer **3-1** was conceived for the synthesis of GNR **3-3** as shown in Figure 3-1.¹⁰ Monomer **3-1** consists of a cyclopentadienone core as the conjugated diene and an ethynyl group as the dienophile, enabling the *AB*-type *Diels–Alder* polymerization to yield polyphenylene precursor **3-2**.

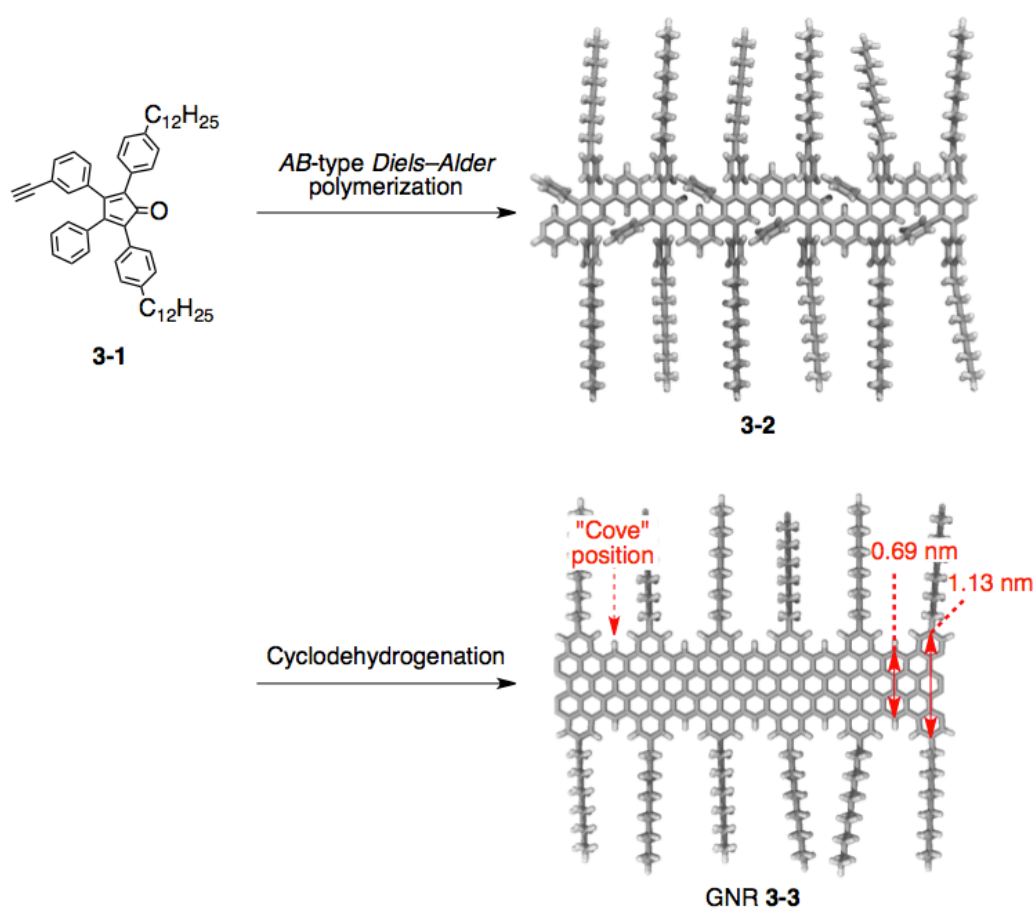


Figure 3-1. Schematic synthetic route to GNR **3-3** from monomer **3-1** via *AB*-type *Diels–Alder* polymerization. The structure of GNR **3-3** was optimized by Merck Molecular Force Field 94 (MMFF94) calculations; grey, carbon; white, hydrogen.¹⁰

A number of structural isomers such as **3-2'** and **3-2''** are formed upon the *Diels–Alder* polymerization of *AB*-type monomer **3-1** as shown in Figure 3-2, because there are two possible molecular orientations for the unsymmetrical monomer in each cycloaddition step (Figure 3-3). However, all of the different structural isomers are converted into one identical GNR with the straight structure upon the oxidative cyclodehydrogenation (Figure 3-2). The “graphitization” of precursor **3-2** at undesired conformations could also generate kinked and undefined GNRs as depicted in Figure 3-2, but such non-straight conformations are considerably disfavored owing to the steric hindrance between the benzene rings and the bulky alkyl chains installed on the

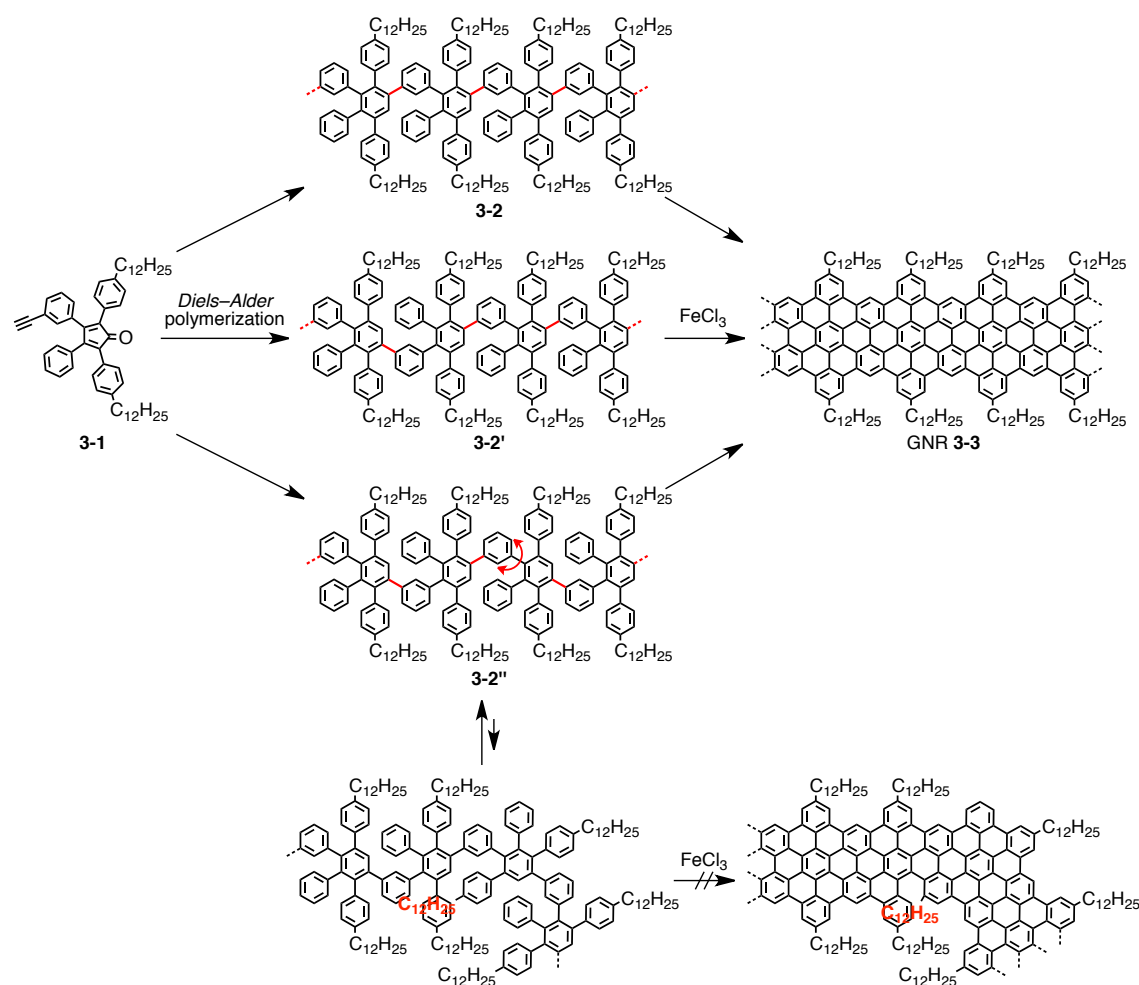


Figure 3-2. Schematic illustration of the structural isomerization of polyphenylene precursor **3-2** upon the *Diels–Alder* polymerization. All the structural isomers give identical GNR **3-3** with the straight structure after the cyclodehydrogenation. “Undesired” conformations of precursor **3-2** could also lead to the formation of kinked GNRs, but the cyclodehydrogenation takes place only in the “right” conformation because of the steric hindrance between the dodecyl chains and the benzene rings.

peripheral positions, which ensures the selective formation of straight GNR **3-3**. This is in stark contrast to the previous report based on the A_2B_2 -type *Diels–Alder* polymerization, which only provided a mixture of kinked and undefined GNRs (Figure 1-10, subsection 1.2.2.4).⁵

GNR **3-3** features the unique cove-type edge structure^{11,12} with the width of 0.69–1.13 nm as shown in Figure 3-1. The remarkable efficiency of the *AB*-type *Diels–Alder* polymerization allows significantly high longitudinal extension of GNR **3-3** over 600 nm. Furthermore, the bulky alkyl chains densely installed on the periphery, which are indispensable for the selective fabrication of straight GNRs, simultaneously enhance the dispersibility of GNR **3-3**. This enables extended physical characterizations in dispersions as well as liquid-phase processing of GNR **3-3** for integration into electronic devices.

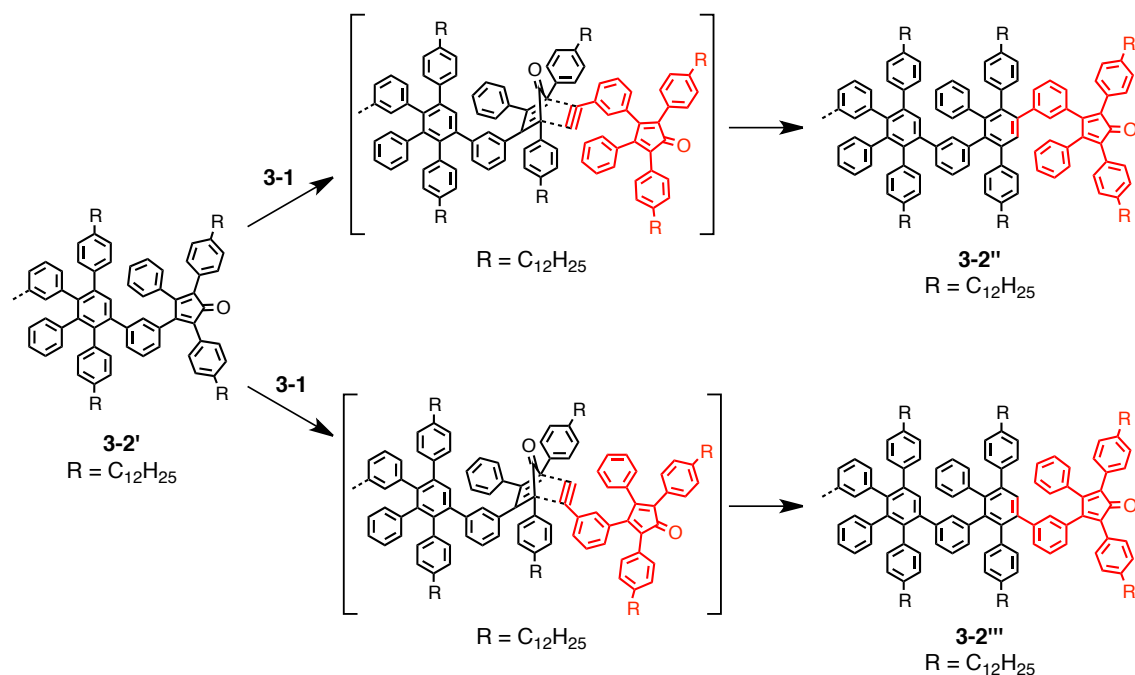


Figure 3-3. Schematic illustration of the two possible molecular orientations upon each *Diels–Alder* cycloaddition step during the polymerization of unsymmetrical monomer **3-1**, leading to different structural isomers of polyphenylene precursor **3-2**.

3.2 Investigation of model systems

In order to examine the suitability of polyphenylene precursor **3-2** for the fabrication of GNR **3-3** via intramolecular oxidative cyclodehydrogenation, oligophenylenes **3-4** and **3-6** were designed and synthesized as model compounds, which corresponded to short cutouts of precursor **3-2** (Figure 3-4). The efficiency of the oxidative cyclodehydrogenation of oligophenylenes **3-4** and **3-6** into PAHs, i.e. dimer **3-5** and trimer **3-7**, respectively, was investigated by means of MALDI-TOF MS and ^1H NMR spectroscopy.

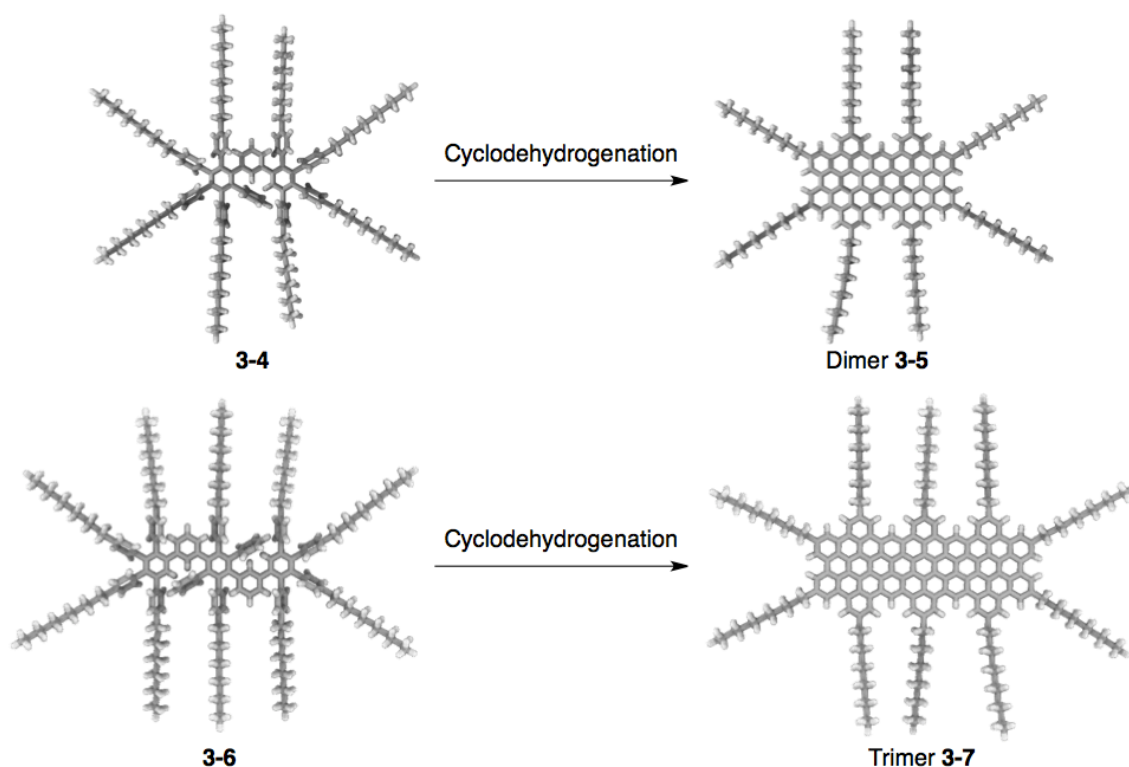


Figure 3-4. Schematic illustration of the cyclodehydrogenation of oligophenylenes **3-4** and **3-6** into dimer **3-5** and trimer **3-7**, respectively. Structures of **3-5** and **3-7** were optimized by Merck Molecular Force Field 94 (MMFF94) calculations; grey, carbon; white, hydrogen.¹⁰

3.2.1 Synthesis and characterization of dimer 3-5

The synthesis of oligophenylene **3-4** and the subsequent cyclodehydrogenation to dimer **3-5**¹³ was carried out as shown in Figure 3-5. First, 3-bromodiphenylacetylene (**3-10**)¹⁴ was prepared by *Sonogashira* coupling of 1-bromo-3-iodobenzene (**3-8**) and ethynylbenzene (**3-9**) in 98% yield, followed by another *Sonogashira* coupling with trimethylsilylacetylene to give 3-trimethylsilylethynylidiphenylacetylene (**3-11**) in 92% yield. Subsequently, deprotection of **3-11** with potassium carbonate provided 3-ethynylidiphenylacetylene (**3-12**)¹⁵ in 71% yield, and then oligophenylene **3-4** was obtained by two-fold *Diels-Alder* cycloaddition of **3-12** with tetraphenylcyclopentadienone **3-13**¹² in 46% yield. The cyclodehydrogenation of oligophenylene **3-4** was performed using 14 equivalents of iron(III) chloride for one bond to be formed, and the completion of the reaction was confirmed by MALDI-TOF MS analysis after stirring at room temperature for 4 h, providing dimer **3-5** in 96% yield (Figure 3-6).

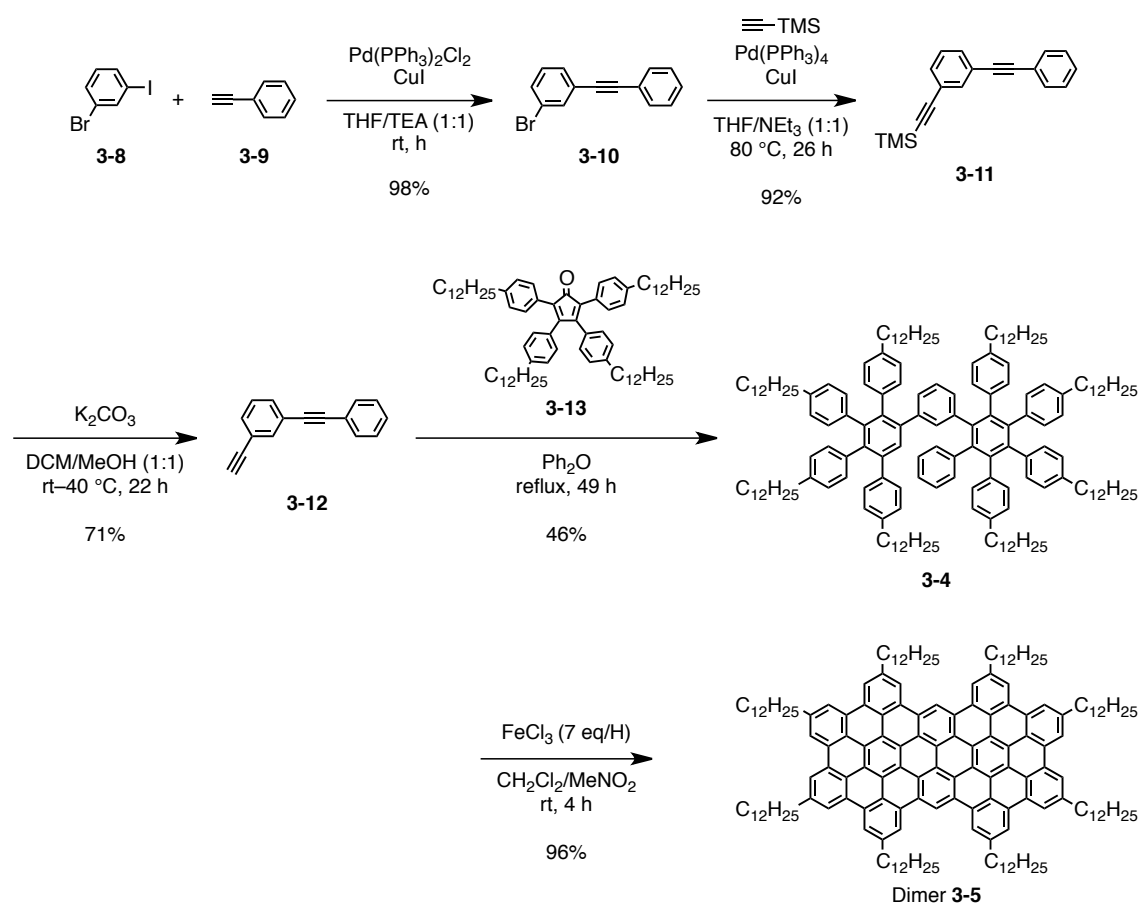


Figure 3-5. Synthesis of dimer **3-5**.

High-resolution MALDI-TOF MS analysis of dimer **3-5** displayed the exact molecular weight of $m/z = 2235.7047$, which was consistent with the simulated value of $m/z = 2235.7059$, attesting the formation of dimer **3-5** (Figure 3-6, inset). Moreover, the isotopic distribution of **3-5** was in perfect agreement with the simulated pattern. It is known that a presence of incompletely fused byproducts with several more hydrogens starkly disturbs the isotopic pattern, thus the agreement between the experimental and simulated patterns clearly demonstrated highly efficient “graphitization” of oligophenylene **3-4** into dimer **3-5**.¹⁶ Small shoulders could be seen for each peak in the isotopic distribution, but these could be ascribed to hydrogen elimination under the measurement conditions, depending on the laser power.¹⁷ In a reflectron-mode MALDI-TOF MS spectrum of dimer **3-5**, a small peak was observed at $m/z = 2,068$, corresponding to the loss of one dodecyl chain (Figure 3-6). Such fragmentation, depending on the laser attenuation, was previously reported for the same PAH substituted with different alkyl chains.¹⁸ There was no other peak in the spectrum, which supported the high purity of dimer **3-5**.¹⁶

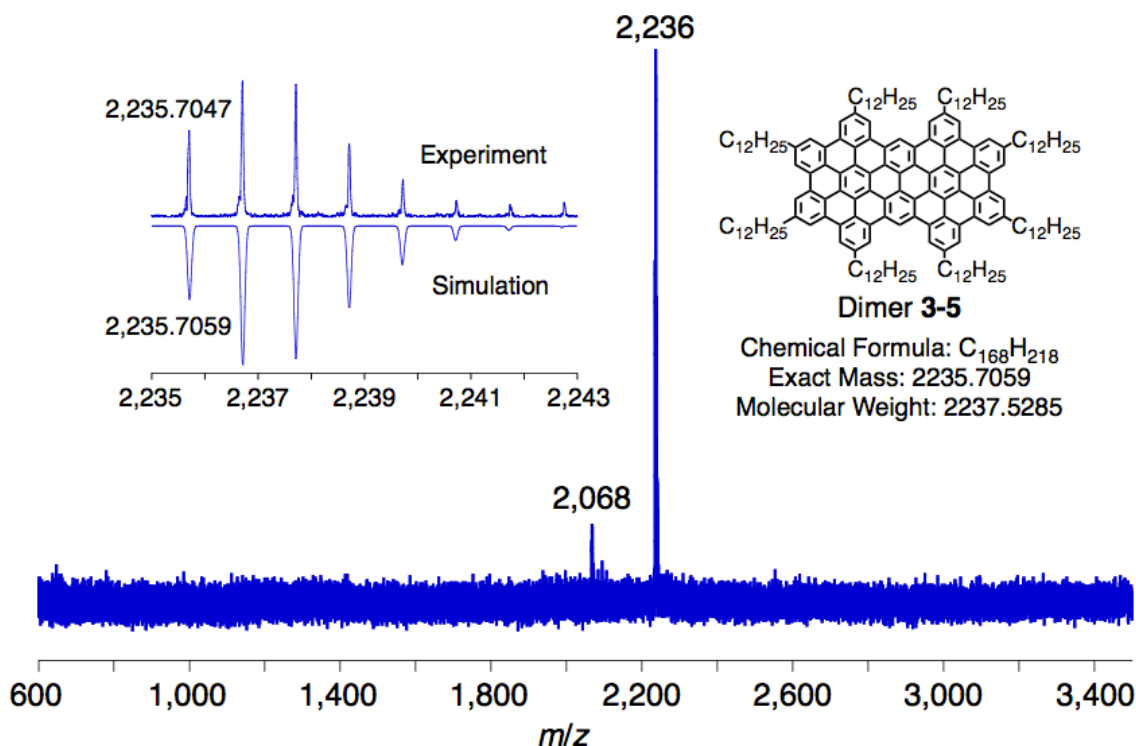


Figure 3-6. Reflectron-mode MALDI-TOF MS analysis of dimer **3-5** (solid-state sample preparation, matrix: TCNQ); inset: isotopic distribution obtained by high-resolution MALDI-TOF MS measurement of **3-5** in perfect agreement with the simulation (matrix: 3-hydroxypicolinic acid).¹⁰

^1H NMR analysis of dimer **3-5** was first attempted in tetrahydrofuran- d_8 at 60 °C as well as in a mixture of dichloromethane- d_2 and carbon disulfide (1:1 volume ratio) at 25 °C, but hardly any peak could be observed in the aromatic region due to the strong aggregation of the PAH molecules, which is a common problem for large PAHs.^{18,19} Next, ^1H NMR measurements were performed at elevated temperatures using high-boiling-point solvents, namely at 130 °C in 1,1,2,2-tetrachloroethane- d_2 and at 160 °C in 1,2-dichlorobenzene- d_4 , which enabled the observation of weak peaks in the aromatic region although considerable broadening could not be circumvented (Figure 3-7). The measurements were also carried out at lower concentrations, but the resolution of the signals was not improved. The aromatic signals of dimer **3-5** appeared in the range of $\delta = 7.5\text{--}10.0$ ppm, displaying a strong down-shift due to the extended aromatic plane (Figure 3-7, inset), which was similar to the ^1H NMR spectra of PAH **2-8** (Figure 2-3) and a mixture of PAHs **2-19** and **2-20** (Figure 2-10). Although the peaks were not resolved, the ratio between the integrations of the aromatic and the aliphatic protons was roughly 18 to 200, which was in agreement with the structure of dimer **3-5**. This result supported the results from the MALDI-TOF MS analysis, which corroborated the successful synthesis of dimer **3-5** from oligophenylene **3-4**.

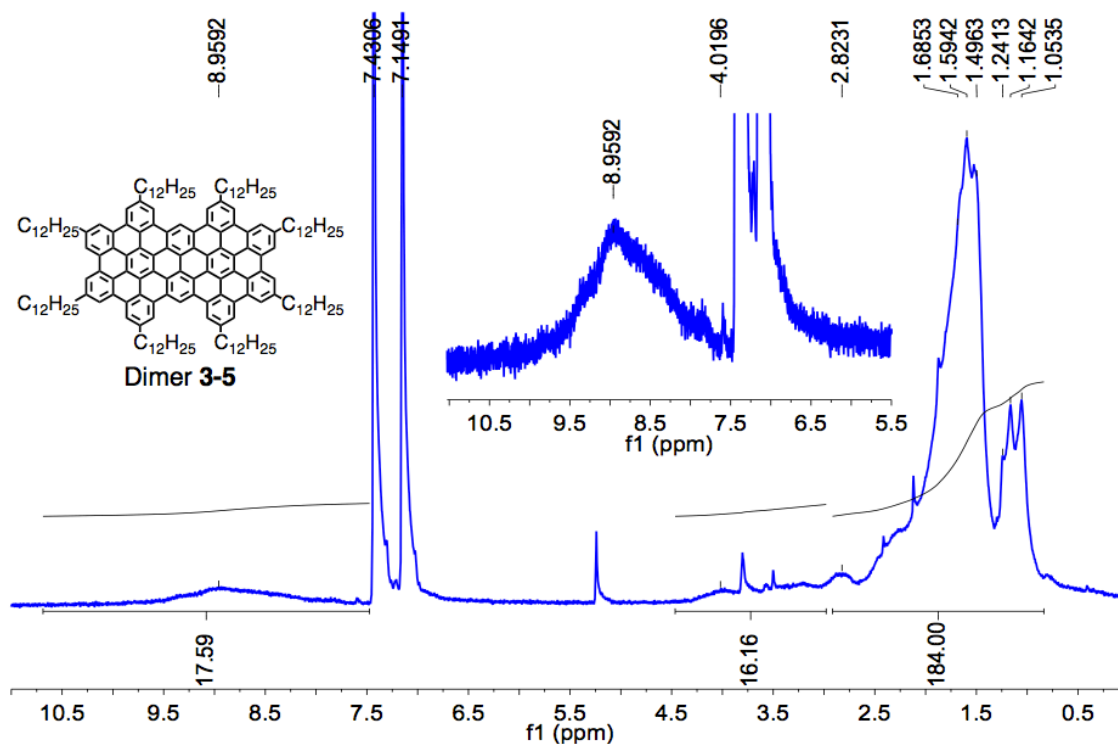


Figure 3-7. ^1H NMR spectrum of dimer **3-5** in 1,2-dichlorobenzene- d_4 at 160 °C (500 MHz); inset: a magnified spectrum of the aromatic region.¹⁰

3.2.2 Synthesis and characterization of trimer 3-7

With the results on the cyclodehydrogenation of oligophenylene **3-4** into dimer **3-5**, oligophenylene trimer **3-6** was synthesized as shown in Figure 3-8 in order to further examine the suitability of precursor **3-2** for the fabrication of GNR **3-3**. First, bis(4-dodecylphenyl)acetone **3-16**²⁰ was synthesized from bis(4-bromophenyl)acetone **3-15**²¹ through *Negishi* coupling with dodecylzinc bromide, which was generated in situ from 1-bromododecane (**3-14**). 3-Bromobenzil (**3-17**) was prepared from

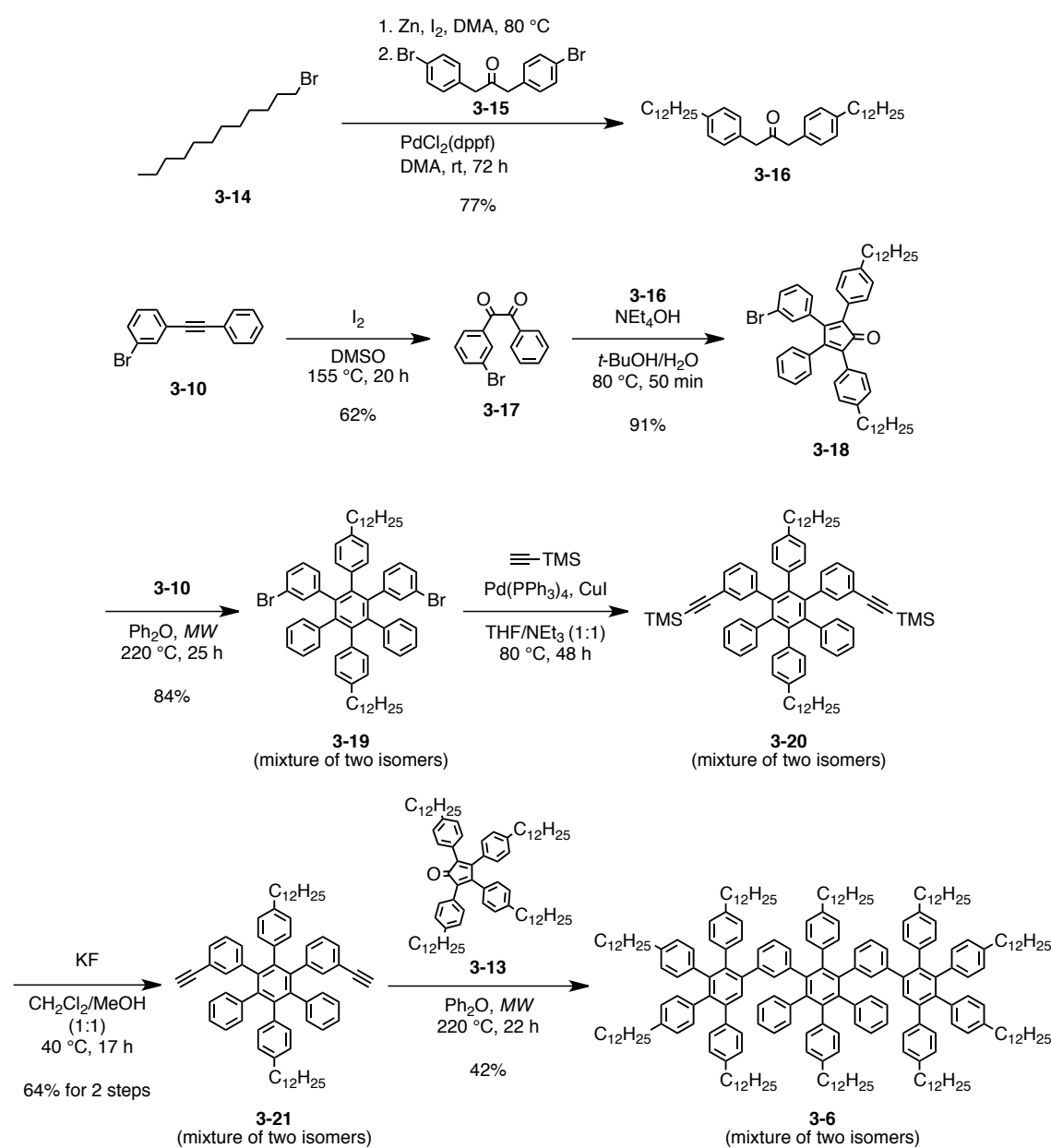


Figure 3-8. Synthesis of oligophenylene precursor **3-6**.

3-bromodiphenylacetylene (**3-10**) by oxidation with iodine in DMSO in 44% yield, followed by *Knoevenagel* condensation with bis(4-dodecylphenyl)acetone **3-16** to afford tetraphenylcyclopentadienone **3-18** in 91% yield. *Diels-Alder* reaction of **3-18** with 3-bromodiphenylacetylene (**3-10**) provided oligophenylene **3-19** in 84%, which was obtained as a mixture of two structural isomers inseparable by standard isolation methods. Nevertheless, both isomers eventually provide identical trimer **3-7**, therefore oligophenylene **3-19** as well as all the following oligophenylenes were employed for the next reactions without further purification.

Next, oligophenylene **3-19** was subjected to *Sonogashira* coupling with trimethylsilylacetylene followed by the removal of the trimethylsilyl protecting group with potassium fluoride to afford oligophenylene **3-21** in 64% for two steps. Oligophenylene **3-21** was further reacted with tetraphenylcyclopentadienone **3-13**¹² through *Diels-Alder* reaction to provide oligophenylene precursor **3-6** in 42% yield. The intramolecular oxidative cyclodehydrogenation of oligophenylene **3-6** was performed under the same condition as the synthesis of dimer **3-5**, namely using 14 equivalents of iron(III) chloride for one bond to be formed, to obtain trimer **3-7** in 99% yield (Figure 3-9).

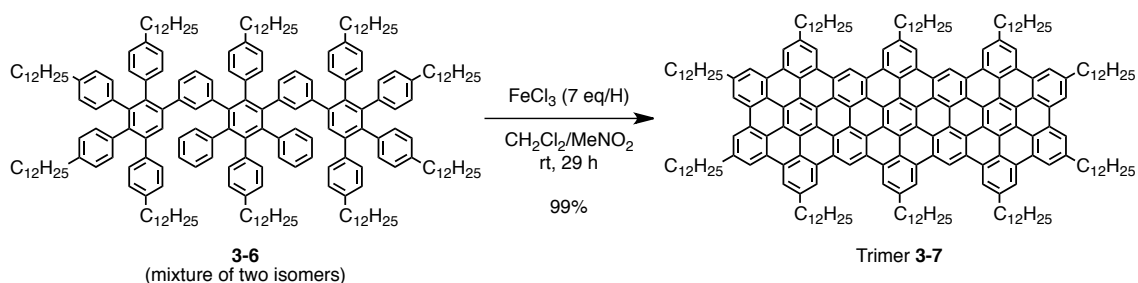


Figure 3-9. Synthesis of trimer **3-7**.

Reflectron-mode MALDI-TOF MS analysis of trimer **3-7** displayed the isotopic distribution in perfect agreement with the simulation, attesting the successful “graphitization” of oligophenylene **3-6** into trimer **3-7** without any remaining partially fused intermediates (Figure 3-10, inset).¹⁶ Fragmentation of trimer **3-7** was more significant than that of dimer **3-5** under the MALDI-TOF MS analysis, resulting in the observation of more than one peak at smaller m/z , e.g. at 2,774 and 2,605 for loss of one and two dodecyl chains, respectively (Figure 3-10). The intensities of these peaks changed depending on the laser power during the measurement, verifying that these peaks were derived from the fragmentations of trimer **3-7**.^{18,22}

^1H NMR analysis of trimer **3-7** displayed hardly any signal from the aromatic protons even at 170 °C in 1,2-dichlorobenzene- d_4 , which was not surprising, considering the extended aromatic core and thus stronger π - π interaction of trimer **3-7** compared to that of dimer **3-5**.^{18,19} Nevertheless, the MALDI-TOF MS spectrum with the isotopic distribution perfectly matching the simulated pattern corroborated the efficient formation of trimer **3-7** from oligophenylene **3-6**.¹⁶ These results on the successful syntheses of dimer **3-5** and trimer **3-7** from oligophenylenes **3-4** and **3-6**, respectively, thus indicated the suitability of polyphenylene precursor **3-2** for the fabrication of GNR **3-3** by the oxidative cyclodehydrogenation.

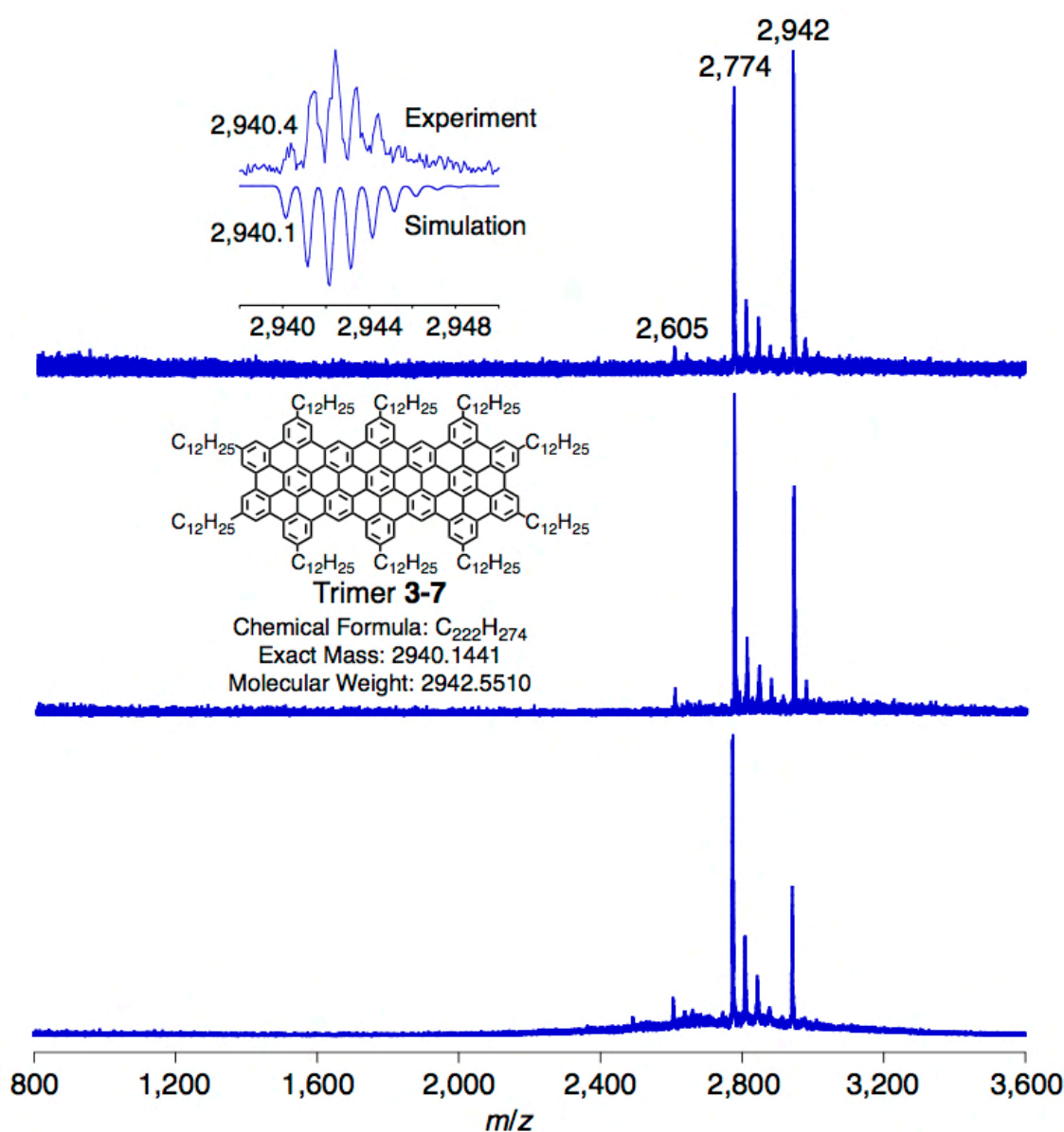


Figure 3-10. Reflectron-mode MALDI-TOF MS spectra of trimer **3-7** recorded at different laser power, showing the fragmentation of dodecyl chains (solid-state sample preparation, matrix: TCNQ); inset: isotopic distribution of **3-7** in perfect agreement with the simulation.¹⁰

3.3 Synthesis of longitudinally extended GNRs via *Diels–Alder* polymerization

3.3.1 Synthesis of *AB*-type monomer **3-1**

For the fabrication of GNR **3-3**, *AB*-type *Diels–Alder* monomer **3-1** was synthesized as shown in Figure 3-11, starting from functionalized tetraphenylcyclopentadienone **3-18** prepared for the synthesis of trimer **3-7** (Figure 3-8). Tetraphenylcyclopentadienone **3-18** was thus subjected to *Sonogashira* coupling with trimethylsilylacetylene to give TMS-protected monomer **3-22** in 69% yield. Subsequently, removal of the trimethylsilyl protecting group with potassium fluoride yielded monomer **3-1** in 84%. It is to be noted that the use of potassium carbonate for the deprotection lead to a lower yield presumably due to the instability of **3-1** under strongly basic conditions. The formation of monomer **3-1** was confirmed by ^1H and ^{13}C NMR spectroscopy as well as a high-resolution electrospray ionization (ESI) MS analysis, which revealed the exact mass of $m/z = 745.5334$ in perfect agreement with the calculated mass of $m/z = 745.5348$ for $\text{C}_{55}\text{H}_{69}\text{O}$, namely $[\text{M}+\text{H}]^+$.

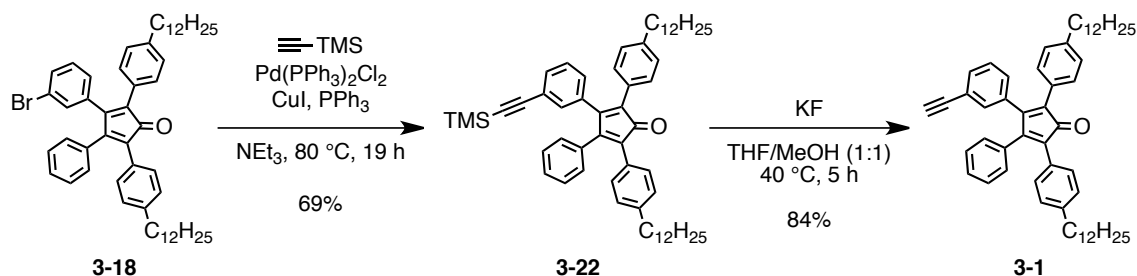
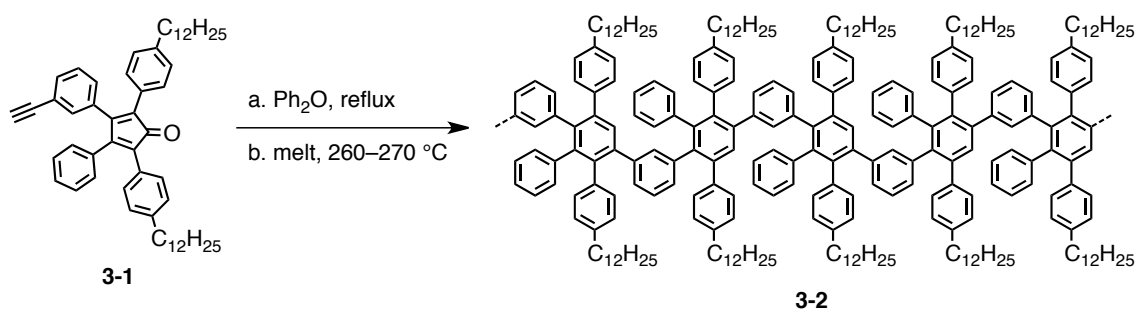


Figure 3-11. Synthesis of *AB*-type *Diels–Alder* monomer **3-1**.

3.3.2 *AB-type Diels–Alder* polymerization

With monomer **3-1** in hand the *AB-type Diels–Alder* polymerization of **3-1** was investigated for the controllable synthesis of polyphenylene precursor **3-2** (Table 3-1). First, the polymerization was attempted by refluxing a solution of monomer **3-1** (20 mg) in diphenyl ether (2.0 mL), namely at the concentration of 36.6 mM, without addition of any other reagent or catalyst (Table 3-1, entry 1). The purple color of **3-1**, which is typical for the tetraphenylcyclopentadienone structure, gradually faded away during the polymerization, and totally disappeared eventually after 25 h. This color change indicated the completion of the reaction, yielding a pale yellow solution of polyphenylene precursor **3-2**. SEC analysis of the obtained precursor **3-2-I** based on

Table 3-1. Polymerization conditions for monomer **3-1** and resulting molecular weights and PDI values of precursor **3-2** based on the SEC analysis.¹⁰



Entry	Solvent	C (mM)	Time (h)	M_w (kg/mol)	M_n (kg/mol)	PDI
1	Ph ₂ O	36.6	25	14–24	6.1–7.9	2.3–3.0
2	Ph ₂ O	228	28	73–150	19–27	3.8–5.6
2'	—	—	—	100–220	65–120	1.5–1.8
3	Ph ₂ O	1,410	20	220–530	29–41	7.6–13
3'	—	—	—	270–640	160–340	1.7–1.9
4	melt	—	1.5	150–350	29–41	5.2–8.5
4'	—	—	—	150–380	69–120	2.2–3.1
5	melt	—	5.0	250–620	32–45	7.8–14

M_w and M_n were estimated by the SEC analysis of as-prepared polymers based on PPP and PS standards and given with ranges, corresponding to $M_{w,PPP}-M_{w,PS}$ and $M_{n,PPP}-M_{n,PS}$, respectively (eluent: THF, UV detector). PDI values were calculated by M_w/M_n . Entries 2', 3', and 4' represent M_w , M_n , and PDI obtained after the fractionation of precursors **3-2** in entries 2, 3, and 4, respectively. All the SEC results have a margin of error of $\pm 10\%$.

PPP and PS standards revealed M_w of 14,000–24,000 g/mol and M_n of 6,100–7,900 g/mol with PDI of 2.3–3.0 (Table 3-1, entry 1). Precursor **3-2** has kinked polyphenylene backbone structures, which are most probably more rigid than PS, but less rigid compared to PPP. Considering these backbone structures with a number of long flexible alkyl chains at the peripheral positions, the actual molecular weight of **3-2** was expected to be within the range estimated by the SEC analysis based on PPP and PS standards, i.e. M_w : $M_{w,PPP} - M_{w,PS}$. The validity of this estimation was indeed proven through photon correlation spectroscopy analyses, which will be discussed in detail in subsection 3.3.5.

Next, aiming at the preparation of polyphenylene precursor **3-2** with higher molecular weight, the *Diels–Alder* polymerization was carried out with higher concentration (228 mM) of monomer **3-1** (100 mg) in diphenyl ether (0.600 mL) (Table 3-1, entry 2). The polymerization was completed after 28 h, and the resulting polyphenylene precursor **3-2-II** showed M_w of 73,000–150,000 g/mol, M_n of 19,000–27,000 g/mol, and PDI of 3.8–5.6, where M_w was almost one order of magnitude higher than that from the first condition. Notably, further increasing the concentration of monomer **3-1** to 1.41 M lead to polyphenylene precursor **3-2-III** with remarkably high M_w of 220,000–530,000 g/mol, M_n of 29,000–41,000 g/mol, and PDI of 7.6–13 (Table 3-1, entry 3), exceeding the highest M_w of linear polyphenylene polymers ever achieved by A_2B_2 -type *Suzuki*,^{23,24} AA -type *Yamamoto*,²⁵ and A_2B_2 -type *Diels–Alder* polymerizations.^{4,5,26}

Furthermore, monomer **3-1** underwent the polymerization also in a melt, simply by heating the purple powder of **3-1** at 260–270 °C. The powder first melted and then lost its purple color, resulting in a pale yellow solid of polyphenylene precursor **3-2-IV** with M_w of 150,000–350,000 g/mol, M_n of 29,000–41,000 g/mol, and PDI of 5.2–8.5 after heating for 1.5 h (Table 3-1, entry 4). When the reaction time was increased to 5 h, the resulting polyphenylene precursor **3-2-V** possessed M_w of 250,000–620,000 g/mol, M_n of 32,000–45,000 g/mol, and PDI of 7.8–14 (Table 3-1, entry 5). These results evidently demonstrated the extraordinary high efficiency of the AB -type *Diels–Alder* polymerization for the fabrication of large-molecular-weight polyphenylene precursors, enabling the fabrication of GNRs with unprecedentedly high longitudinal extension. Further, the molecular weight of polyphenylene precursor **3-2** was apparently dependent on the concentration of monomer **3-1** and reaction time as is reported for previous *Diels–Alder* polymerizations,^{3,4} which rendered it possible to control the length of the resulting GNR **3-3**.

3.3.3 MALDI-TOF MS analysis of precursor 3-2

MALDI-TOF MS analysis in linear mode of the obtained polyphenylene polymer **3-2-I** showed regular peaks from $m/z = \sim 2,000$ up to $\sim 13,000$ with an interval of $m/z = \sim 715$, corresponding to the mass of one repeating unit, i.e. 717 (Figure 3-12). Polymers with molecular weight higher than 13,000 g/mol were not detected owing to the limitation of MALDI-TOF MS for the analysis of high-molecular-weight polymers with a broad molecular weight distribution.^{24,27}

Reflectron-mode MALDI-TOF MS analysis of as-prepared polyphenylene **3-2** generally showed peaks of trimer, tetramer, pentamer, hexamer, heptamer, and octamer at $m/z = 2,250, 2,869, 3,586, 4,303, 5,020,$ and $5,737$, respectively (Figure 3-13). These masses corresponded to oligomer structures without carbon monoxide, indicating that the ethynyl group and tetraphenylcyclopentadienone moiety at each end had undergone head-to-tail intramolecular *Diels–Alder* cycloaddition to form cyclic oligomers (Representative case of the pentamer is depicted in Figure 3-14).²⁸ No peak was observed other than those expected for the oligomers of **3-2-I** both in the linear- and reflectron-mode spectra, corroborating the high purity of polyphenylene **3-2-I**.

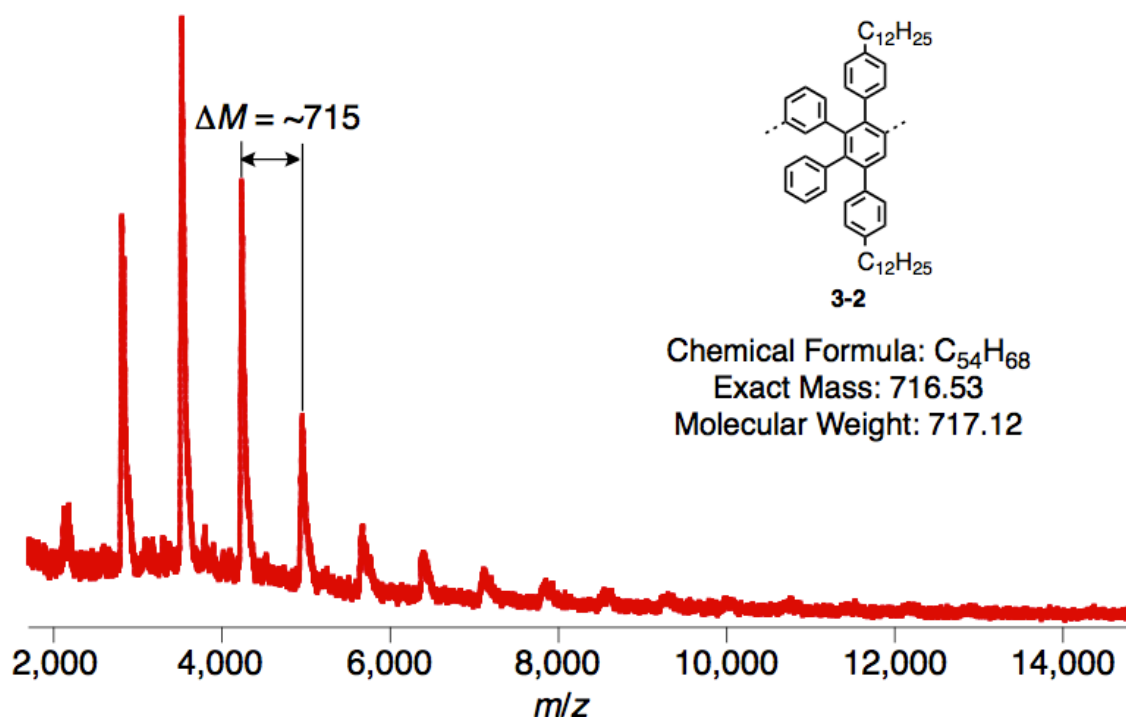


Figure 3-12. Linear-mode MALDI-TOF MS analysis of polyphenylene polymer **3-2-I** (Table 4-1, entry 1; solid-state sample preparation, matrix: TCNQ).¹⁰

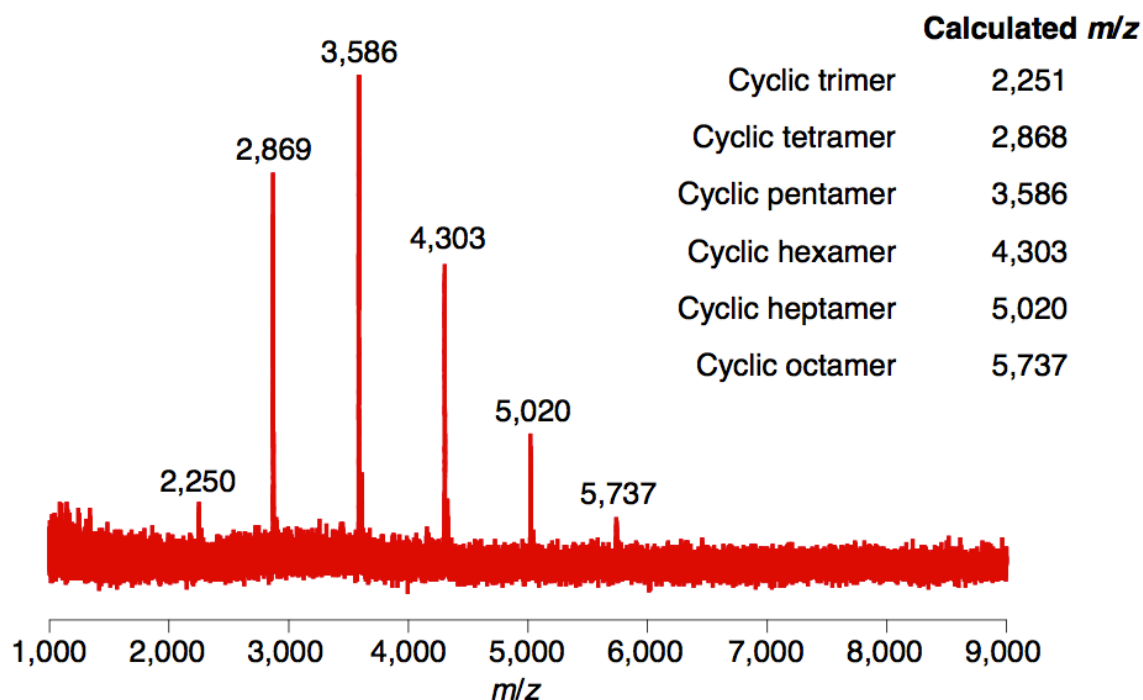


Figure 3-13. Reflectron-mode MALDI-TOF MS analysis of as-prepared polyphenylene precursor **3-2** (solid-state sample preparation, matrix: TCNQ), inset: calculated m/z of cyclic oligomers.¹⁰

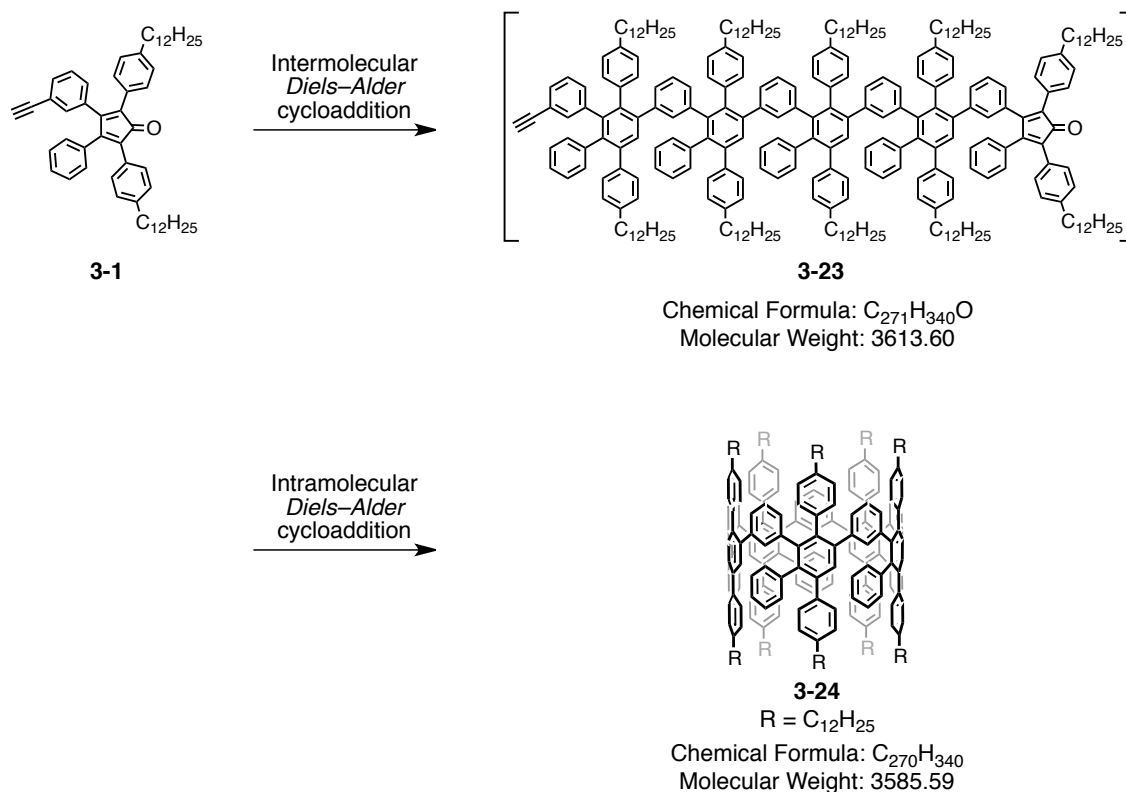


Figure 3-14. Proposed formation of cyclic pentamer **3-24** via intramolecular *Diels-Alder* cycloaddition of linear pentamer **3-23**.¹⁰

3.3.4 SEC analysis of precursor **3-2**

SEC profiles of polyphenylene precursors **3-2-I–V** all displayed a peak at retention time of ~ 27.5 min, corresponding to the peak molecular weight (M_p) of 2,800–3,900 g/mol (Figure 3-15). Based on the results from the MALDI-TOF MS analysis, this peak was assignable to the cyclic oligomers, which were formed through the head-to-tail intramolecular cycloaddition and thus precluded from further polymer growth (Figures 3-13 and 3-14).²⁸ Indeed, this peak displayed higher intensity when the polymerization was conducted with lower concentration of monomer **3-1** as expected for the formation of cyclic oligomers in kinetically controlled step-growth polymerizations.²⁸

Isolation of the oligomers by preparative recycling SEC was difficult due to the relatively small difference in the hydrodynamic volume. Moreover, each oligomer contained regioisomers (Figure 3-16), which were formed due to two possible molecular orientations upon each *Diels–Alder* cycloaddition step (see Figure 3-3), prohibiting unambiguous characterizations by NMR spectroscopy. However, such small oligomers could be removed by fractionation with recycling preparative SEC or by repeated reprecipitation from THF in MeOH with optimized conditions (Table 3-1 and Figure 3-15). Representatively, precursor **3-2-II** was fractionated with recycling preparative SEC to give precursor **3-2-II'** with M_w of 100,000–220,000 g/mol, M_n of 65,000–120,000 g/mol, and PDI of 1.5–1.8, which was free of the small oligomers (Table 3-1, entries 2 and 2', Figure 3-15b and c). On the other hand, fractionation of precursor **3-2-III** (Table 3-1, entry 3 and Figure 3-15d) was carried out by the repeated reprecipitation with an optimized condition: methanol (MeOH) was gradually added to a solution of **3-2-III** in THF until the precipitation of **3-2-III** started (THF:MeOH = 2:1 in volume ratio). The precipitates were subsequently collected by centrifugation (13,400 rpm, 1 min) and washed with a mixture of THF and MeOH (2:1 in volume ratio). This cycle was repeated for five times to provide precursor **3-2-III'** with M_w of 270,000–640,000 g/mol, M_n of 160,000–340,000 g/mol, and PDI of 1.7–1.9 (Table 3-1, entry 3' and Figure 3-15e). These results indicated that the relatively high PDI values of as-prepared polyphenylene precursor **3-2** were due to the presence of the small oligomers, which could be facily removed to provide precursor **3-2** with narrow molecular weight distribution, often with PDI < 2.0.

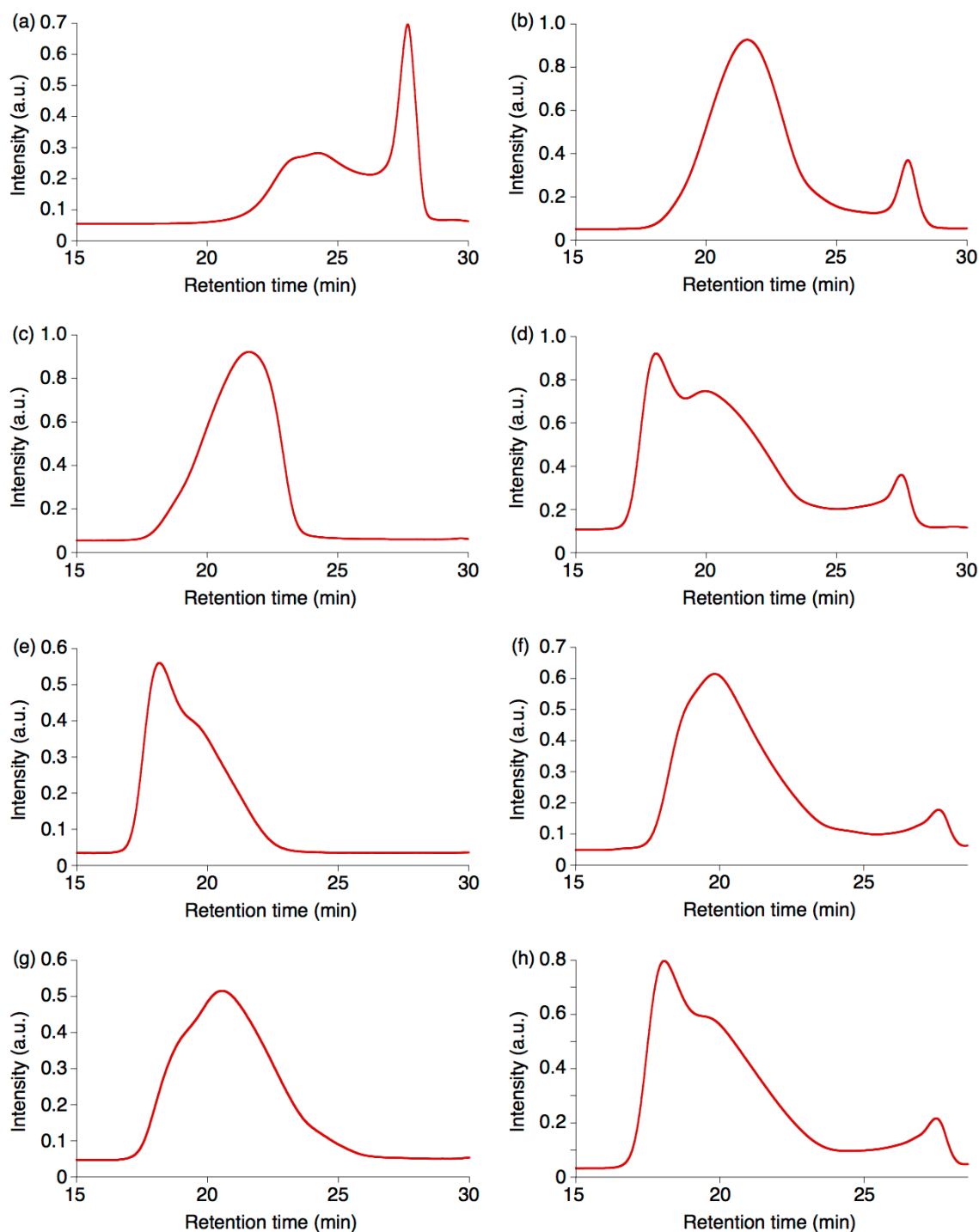


Figure 3-15. Normalized SEC profiles of polyphenylene precursor **3-2** prepared under different conditions as listed in Table 3-1; (a) entry 1, (b) entry 2, (c) entry 2' (after fractionation with recycling preparative SEC), (d) entry 3, (d) entry 3' (after fractionation by reprecipitation), (f) entry 4, (g) entry 4' (after fractionation with recycling preparative SEC), and (h) entry 5 (eluent: THF, 1.0 mL/min, UV detector).¹⁰

3.3 Synthesis of longitudinally extended GNRs via *Diels–Alder* polymerization

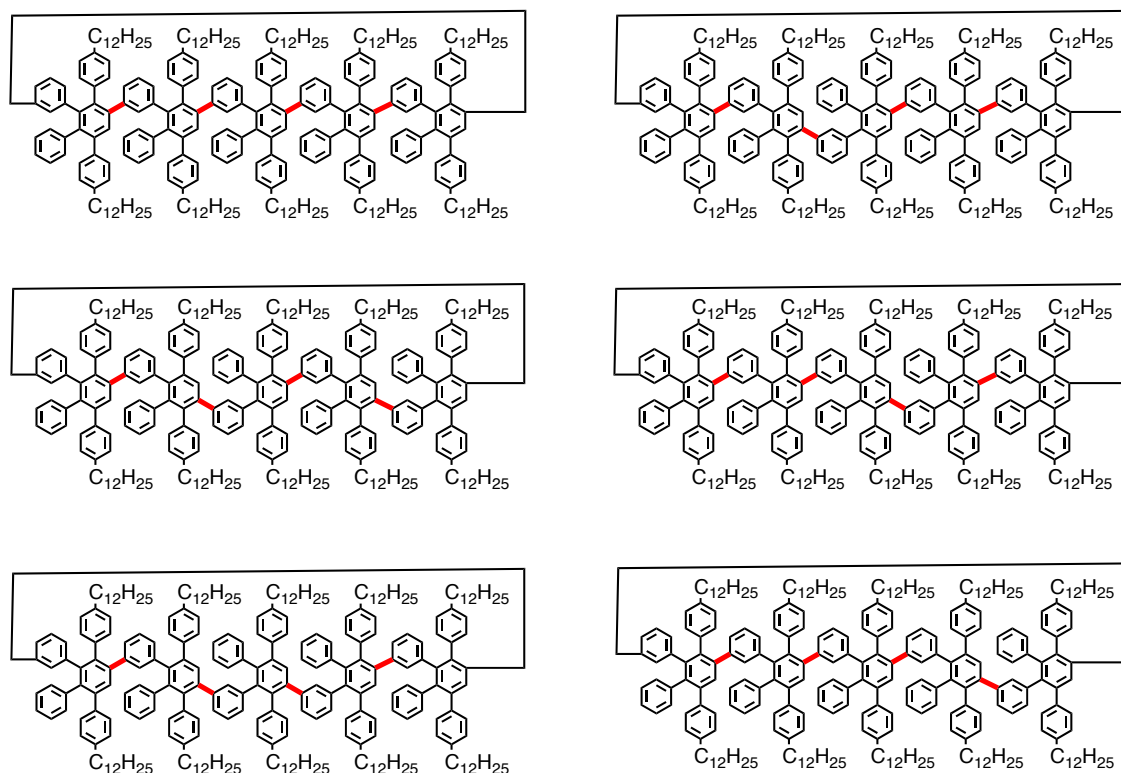


Figure 3-16. Schematic illustration for six examples of regioisomers of the cyclic pentamer of precursor **3-2**, which are formed due to two possible molecular orientations upon each *Diels–Alder* cycloaddition step.

The main peak in the SEC profiles of polyphenylene precursor **3-2** at ~18–23 min was separated into two peaks when the polymerization was carried out in a melt or in a highly concentrated solution of monomer **3-1** for sufficiently long time, i.e. precursors **3-2-III** and **3-2-V**, which suggested the presence of two polymer species with different hydrodynamic volumes in these samples (Figure 3-15d and h). The first peak was observed at ~18 min and the second at ~20 min, corresponding to M_p of 390,000–1,000,000 and 140,000–360,000 g/mol, respectively.

Figure 3-15f and h show SEC profiles of precursors **3-2-IV** and **3-2-V**, which were prepared in a melt with different reaction times of 1.5 and 5 h, respectively. Comparison of these two profiles revealed that the peak at ~20 min did not shift after the longer reaction time, and instead a new peak appeared at ~18 min. This might suggest that a part of precursor **3-2** formed cyclic polymers through intramolecular cycloaddition, and were precluded from further polymerization, corresponding to the peak at ~20 min.^{28,29}

Nevertheless, no cyclic structure was observed during SPM investigations of

precursor **3-2** in the group of [REDACTED]. Complete separation of these two peaks by using preparative recycling SEC was hindered by the high molecular weight, but it was possible to remove a large part of the peak at ~20 min by repeated reprecipitation from THF in MeOH (2:1 volume ratio) (Figure 3-15d and e). This result in combination of the fact that the shape of the SEC profiles did not change depending on the concentration of **3-2** in the measurements suggested that the peak at ~18 min was not from aggregates of precursor **3-2**.

3.3.5 Photon correlation spectroscopy analysis of precursor **3-2**

In order to unambiguously determine the absolute M_w of polyphenylene precursor **3-2**, photon correlation spectroscopy analysis³⁰ was carried out by [REDACTED] and [REDACTED] at Max Planck Institute for Polymer Research Mainz, Germany. The laser light scattering experiment was first performed on precursor **3-2-IV'** in THF at a concentration of $c = 1.5$ mg/mL, which was well below the overlap concentration c^* (~11 mg/mL).³¹ Dynamic light scattering analysis of precursor **3-2-IV'** indicated the presence of a single population (Figure 3-17), showing one process with a diffusive relaxation rate, i.e. proportional to the square of the scattering wave vector q^2 (Figure 3-17, inset). The static light scattering experiments revealed the absolute M_w and the radius of gyration (R_g) of precursor **3-2-IV'** to be $470,000 \pm 30,000$ g/mol and 37 ± 2 nm, respectively, from the equation:

$$cK/R_{vv}(q) = 1/M_w + (1/3)q^2R_g^2 \quad (3-1)$$

which is plotted in the inset of Figure 3-18. The optical constant K could be estimated from the equation:

$$K = [2\pi n(dn/dc)]^2 / (N_A \lambda^4) \quad (3-2)$$

where n is the refractive index of the solution, N_A is the Avogadro number, λ is the laser wavelength ($\lambda = 632$ nm), and the refractive index contrast $(dn/dc) = 0.173$ ml/g was measured for precursor **3-2-IV'** in THF. On the other hand, the absolute scattering Rayleigh ratio could be obtained from the equation:

$$R_{\text{VV}}(q) = R_{\text{T}}[(I(q)-I(q)_{\text{solv}})/I(q)_{\text{T}}](n_{\text{solv}}/n_{\text{T}})^2 \quad (3-3)$$

where $I(q)$, $I(q)_{\text{solv}}$, and $I(q)_{\text{T}}$ are the intensities of the solution, the solvent, and the standard toluene, respectively, n_{solv} and n_{T} are the refractive indexes of the solvent and the standard toluene, respectively, and absolute Rayleigh ratio is $R_{\text{T}} = (1.35 \times 10^{-5} \text{ cm}^{-1})$ at 632 nm. The absolute M_{w} thus determined for precursor **3-2-IV'** was well approximated by $M_{\text{w,PS}}$ of 380,000 g/mol obtained by the SEC analysis against the PS standard (Table 3-1, entry 4').

The hydrodynamic radius (R_{h}) of precursor **3-2-IV'** was determined as 29 ± 0.5 nm from the equation:

$$D(q) = \Gamma(q)/q^2 = D_0(1+CR_{\text{g}}^2 q^2) \quad (3-4)$$

where $\Gamma(q)$ is the relaxation time and the translational diffusion D_0 can be related to R_{h} based on the Stokes-Einstein equation $D_0 = k_{\text{B}}T/(6\pi\eta R_{\text{h}})$ with k_{B} , T , and η being the Boltzmann constant, the absolute temperature, and the solvent viscosity, respectively (Figure 3-17, inset). The ratio $R_{\text{g}}/R_{\text{h}}$ of ca. 1.3 as well as the slope C of ca. 0.17 suggested that precursor **3-2-IV'** took a shape of swollen coils in THF.³²

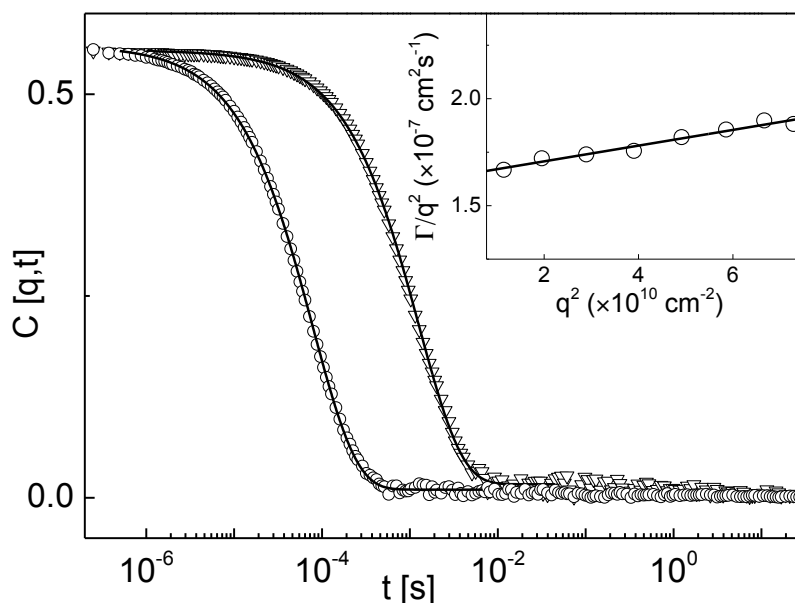


Figure 3-17. Relaxation function $C(q,t)$ for the translational diffusion of a dilute solution of precursor **3-IV'** in THF at two scattering wave vectors ($q = 0.00723 \text{ nm}^{-1}$ and $q = 0.02699 \text{ nm}^{-1}$) at 20 °C; inset: translational relaxation rate plotted according to eq. 3-4 based on the experimental $C(q,t) = \exp[-\Gamma(q)t]^\beta$. The size of the symbols captures the experimental error.¹⁰

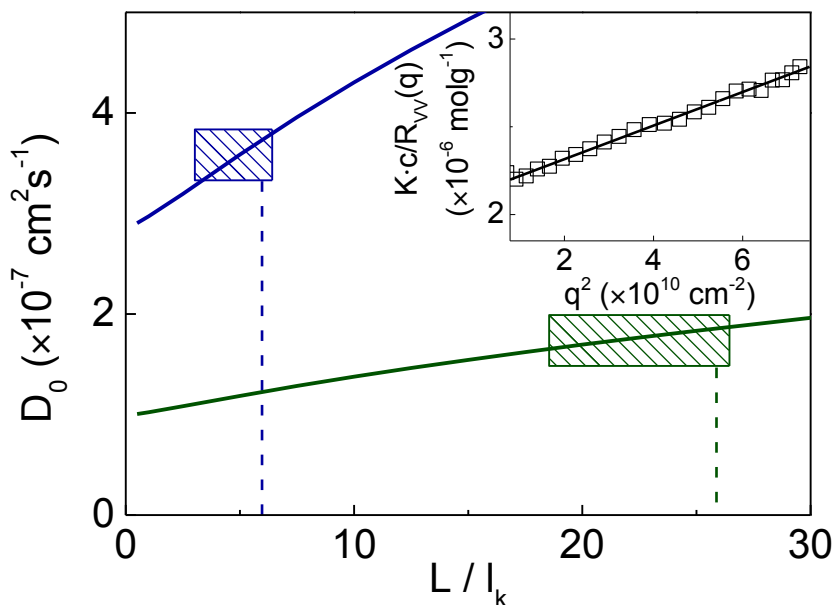


Figure 3-18. Translation diffusion D_0 of precursor **3-2** as a function of the flexibility ratio L/l_k theoretically obtained for two different chain lengths L (green line: 480 nm and blue line: 110 nm).³³ The vertical dashed lines correspond to the values of L/l_k obtained from eq. 3-5 and the hatch boxes represent the experimental D_0 ; blue: **3-2-II'**, green: **3-2-IV'**; inset: Normalized static light scattering of precursor **3-2-IV'** at different wave vectors represented by eq. 3-1. The size of the symbols captures the experimental error.¹⁰

The average chain length of precursor **3-2** could be obtained by $L = (M_w/M_{\text{mon}})l_{\text{mon}}$, where M_{mon} (= 717 g/mol) and l_{mon} (= 0.73 nm) are the molar mass and the length of the repeating unit, respectively. Based on the worm-like model,³³ the relationship between L and R_g can be represented by the equation:

$$R_g^2 = Ll_k/6 \{1 - (3/2)x + (3/2)x^2 - (3/4)x^3 [1 - \exp(-2x)]\} \quad (3-5)$$

where l_k is Kuhn segment length related to persistence length l_p , i.e. $l_k = 2l_p$. This equation was satisfied with $x \equiv l_k/L$ and the experimental values of R_g and L using $l_k \sim 18$ nm. This result was confirmed by comparing the experimental and theoretical values of the translational diffusion D_0 of precursor **3-2-IV'** with $L = 480$ nm. The theoretical calculation of D_0 with $L = 480$ nm is displayed in Figure 3-18 as a green line with variable chain flexibility L/l_k .³³ The experimental value of D_0 was well represented by $19 < L/l_k < 27$, i.e. the green hatch box in Figure 3-18, which was consistent with $L/l_k \sim 26$ obtained from eq. 3-5, i.e. the green vertical dashed line. The persistence length of $l_p \sim 9$

nm was considerably larger than the value expected for typical flexible chain polymers, i.e. $l_p \sim 1\text{--}2$ nm,³⁴ but smaller than that estimated for PPP, i.e. $l_p \sim 20$ nm,³⁵ which indicated the semirigid conformation of precursor **3-2-IV'**. Moreover, this value of precursor **3-2-IV'** was slightly larger than those reported for poly[9,9-bis(2-ethylhexyl)fluorene] and poly[tetra(2-ethylhexyl)indenofluorene], i.e. $l_p \sim 7$ nm³⁶ and $l_p \sim 8$ nm,³⁷ respectively.

For comparison precursor **3-2-II'** with smaller M_w of 100,000–220,000 g/mol based on the SEC analysis was also studied by the phonon correlation spectroscopy (Table 3-1, entry 2'). The laser light scattering experiments on precursor **3-2-II'** in THF at $c = 0.7$ g/L revealed $R_h = 14 \pm 0.3$ nm and the absolute $M_w = 108,000 \pm 8,000$ g/mol, corresponding to $L = 110$ nm. $R_{vv}(q)$ of precursor **3-2-II'** showed weaker variation against q compared to precursor **3-2-IV'** because of the smaller size, and therefore experimentally obtained R_g value, i.e. ~ 21 nm was subject to a large error. Considering the identical chemical structure of precursors **3-2-II'** and **3-2-IV'**, it is reasonable to assume that precursor **3-2-II'** has the same Kuhn length as that of precursor **3-2-IV'**, i.e. $l_k \sim 18$ nm. Indeed, the experimental D_0 of precursor **3-2-II'** (blue hatch box in Figure 3-18) could be well represented by the theoretical value obtained by applying $l_k \sim 18$ nm, namely $L/l_k \sim 6$ (blue vertical dashed line). Moreover, R_g of precursor **3-2-II'** could be estimated from eq. 3-5 to be ca. 16 nm, using $L/l_k \sim 6$, conforming to the weak q -dependence of the scattering $R_{vv}(q)$.

The absolute M_w of precursor **3-2-II'** was almost identical to $M_{w,PPP}$ based on PPP standards in stark contrast to that of precursor **3-2-IV'** which was closer to $M_{w,PS}$. This difference could be explained by the surprisingly large l_k of ca. 18 nm. While precursor **3-2-II'** with shorter length of $L = 110$ nm takes a semirigid conformation similar to PPP, precursor **3-2-IV'** with $L = 480$ nm assumes a semiflexible conformation closer to PS. Notably, these results thus corroborated the validity of the SEC analysis based on the combination of PS and PPP standards for estimating the M_w of precursor **3-2**.

3.3.6 Limiting factors for the polymer growth

The *AB*-type *Diels-Alder* polymerization of monomer **3-1** afforded polyphenylene precursor **3-2** with extremely high M_w of 270,000–640,000 g/mol, but it is important to consider limiting factors that restrict the polymer growth in order to realize even higher molecular weights. One possible limiting factor is the intramolecular cycloaddition of polymers, which is likely to occur at the later stage of the polymerization. Because of the “self-dilution”, the concentration of the reaction mixture eventually becomes low enough to favor the intramolecular reaction, irrespective of the initial concentration of monomer **3-1**.²⁸ However, the formation of cyclic polymers could not be confirmed during the SPM analyses of polyphenylene precursor **3-2**.

Another possible limiting factor is the purity of monomer **3-1**. Considering that the molecular weight of one repeating unit of precursor **3-2** is 717 g/mol, formation of one polymer with molecular weight of 620,000 g/mol requires ~865 molecules of monomer **3-1**. Thus, it is very likely that a slight amount (~0.1% in the above case) of defective monomer contained as impurity limits the ultimate molecular weight. It is also possible that monomer **3-1** and/or as-grown oligomers and polymers are deteriorated under the reaction condition, namely at the high temperature of 260–270 °C, taking into account the intrinsic instability of cyclopentadienone structure. This also explains the dependence of the resulting molecular weight on the concentration of **3-1**: higher concentration enhances the polymerization rate and thus shorten the reaction time, while the longer reaction time allows the deterioration of more monomers and oligomers, which stops the polymer growth at lower molecular weights.

3.3.7 “Graphitization” and “planarization”

Finally, polyphenylene precursor **3-2** was “graphitized” and “planarized” into GNR **3-3** by intramolecular oxidative cyclodehydrogenation using iron(III) chloride as the Lewis acid and oxidant (Figure 3-19). It is known that the cyclodehydrogenation of large PAH systems can take longer than 1 day, so precursor **3-2** was subjected to the cyclodehydrogenation for 3 days with 7 equivalents of iron(III) chloride for one hydrogen to be removed, following the cyclodehydrogenation condition employed for the fabrication of laterally extended GNRs **2-3** and **2-13** (subsections 2.1.3 and 2.2.3).²⁵

3.3 Synthesis of longitudinally extended GNRs via *Diels–Alder* polymerization

Representatively, polyphenylene precursors **3-2-II'** and **3-2-III'** were converted into GNRs **3-3-II** and **3-3-III**, respectively (Figure 3-19). The high efficiency of the cyclodehydrogenation as well as well-defined structures of GNR **3-3** were evidently demonstrated by a combination of FTIR, Raman, NMR, and UV–vis absorption spectroscopic analyses and SPM visualizations.

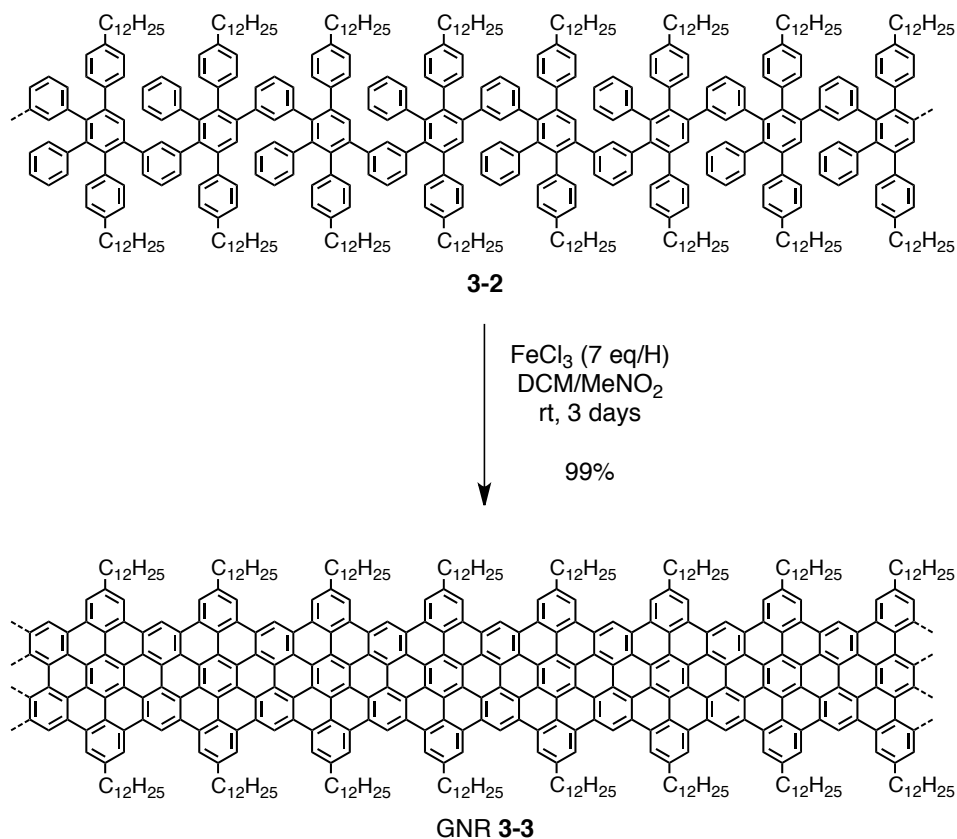


Figure 3-19. Cyclodehydrogenation of polyphenylene precursor **3-2** into GNR **3-3**.

GNR **3-3-II** had the average length of 110 ± 8 nm according to the results from the photon correlation spectroscopy analysis of precursor **3-2-II'** (subsection 3.3.5). The average length of GNR **3-3-III** could be estimated to be ca. 270–650 nm based on the M_w of precursor **3-2-III'** from the SEC analysis (Table 3-1, entry 3'). The photon correlation spectroscopy analysis revealed that the absolute M_w of precursor **3-2** could be well approximated by the $M_{w,PS}$ based on PS standards when M_w became larger. Specifically, the absolute M_w of precursor **3-2-IV'** was determined to be $470,000 \pm 30,000$ g/mol by the photo correlation spectroscopy, which was larger than $M_{w,PS}$ of 380,000 g/mol. Therefore, the absolute average length of GNR **3-3-III** was most probably larger than 650 nm. GNRs **3-3-II** and **3-3-III** were identical within the realm of FTIR, Raman, UV–vis absorption, and THz spectroscopic analyses (see

section 3.5), indicating the sufficiency of their longitudinal extension to reach the plateau in their properties such as electronic band structure and photoconductivity.

Because of the bulky dodecyl groups densely installed on the peripheral positions as well as relatively small width with the cove-type edge structure, GNR **3-3** displayed good dispersibility in common organic solvents such as THF, chlorobenzene, ODCB, and 1,2,4-trichlorobenzene (TCB). This notably contrasts with carbon nanotubes, graphene, and previously reported GNRs (>30 nm), which necessitate special highly polar and high-boiling-point solvents such as *N*-methylpyrrolidone (NMP) for debundling/exfoliation.^{25,38-41} Transparent, purple dispersions of GNR **3-3** (see the inset of Figure 3-24) could be readily obtained by mild sonication in such solvents followed by removal of larger aggregates and undispersed particles through centrifugation or filtration with syringe filters (pore size: 5 μm). Such macroscopic aggregates remained undispersed even with an increased volume of the solvent and elongated sonication time, which suggested that only relatively shorter, and thus more dispersible GNRs could be extracted out during the sonication, or some GNR aggregates had more tightly packed structure that could not be disentangled by this method. This result implied that the GNRs might have been “fractionated” during this process, where shorter GNRs have preferentially extracted into the dispersions.

For the determination of the concentration, a certain amount of the dispersion in THF was filtered through a membrane filter (pore size: 200 nm) to collect all the GNRs in the dispersion on the filter. After complete removal of the solvent under reduced pressure, the membrane filter with GNRs was carefully weighed using a microbalance and compared with the weight without the GNRs. Thus the concentration of a stable dispersion of GNR **3-3** was determined to be typically ~ 0.01 mg/mL. Such dispersions were highly stable showing no visible precipitation at least for three months although dispersions with higher concentrations tended to show precipitation after certain times, depending on the concentration, i.e. highly concentrated dispersions underwent precipitation just after stopping the sonication while dispersions with relatively high concentrations displayed gradual sedimentation over several days to several weeks. This good dispersibility of GNR **3-3** allowed unprecedented characterizations in dispersions, including THz photoconductivity analysis, as well as liquid-phase processing of the GNRs for microscopic visualizations and integration into electronic devices.

3.4 Characterizations of the GNRs

3.4.1 FTIR spectroscopy

Fourier transform infrared (FTIR) spectroscopy is a versatile and powerful method for the structural characterization of carbonaceous materials.^{4,5,25,42} In order to evaluate the efficiency of the cyclodehydrogenation step, polyphenylene precursors **3-2** and GNR **3-3** were analyzed by FTIR spectroscopy and compared with the FTIR spectra of oligophenylenes **3-4** and **3-6**, dimer **3-5**, and trimer **3-7** (Figure 3-20). Polyphenylene **3-2** showed out-of-plane (*opla*) C-H deformation bands at 698, 795, 838, and 896 cm^{-1} , which are typical for mono-, and di-substituted benzene rings. These four *opla* bands all disappeared in the spectrum of GNR **3-3**, corroborating the high efficiency of the cyclodehydrogenation.^{4,5,25,42} Further, the signal triad from aromatic C-H stretching vibrations at 3,025, 3,057, and 3,085 cm^{-1} starkly attenuated, and the *opla* band typical for aromatic C-H at the cove position (see Figure 3-1) appeared at 863 cm^{-1} .^{4,5,25,42} All these observations were in line with the changes displayed upon the cyclodehydrogenation of oligophenylenes **3-4** and **3-6** into dimer **3-5** and trimer **3-7**, respectively. Additionally, the band appearing at 751 cm^{-1} was presumably *opla* bands derived from the other aromatic C-H bonds of GNR **3-5**,⁴² and the band at 720 cm^{-1} could be assigned to $-\text{CH}_2-$ rocking mode from the dodecyl chains (see also subsection 3.7.2).⁴³ FTIR could not be a sufficient proof for the structural perfection; nevertheless these results clearly supported the successful conversion of polyphenylene precursor **3-2** into GNR **3-3**.

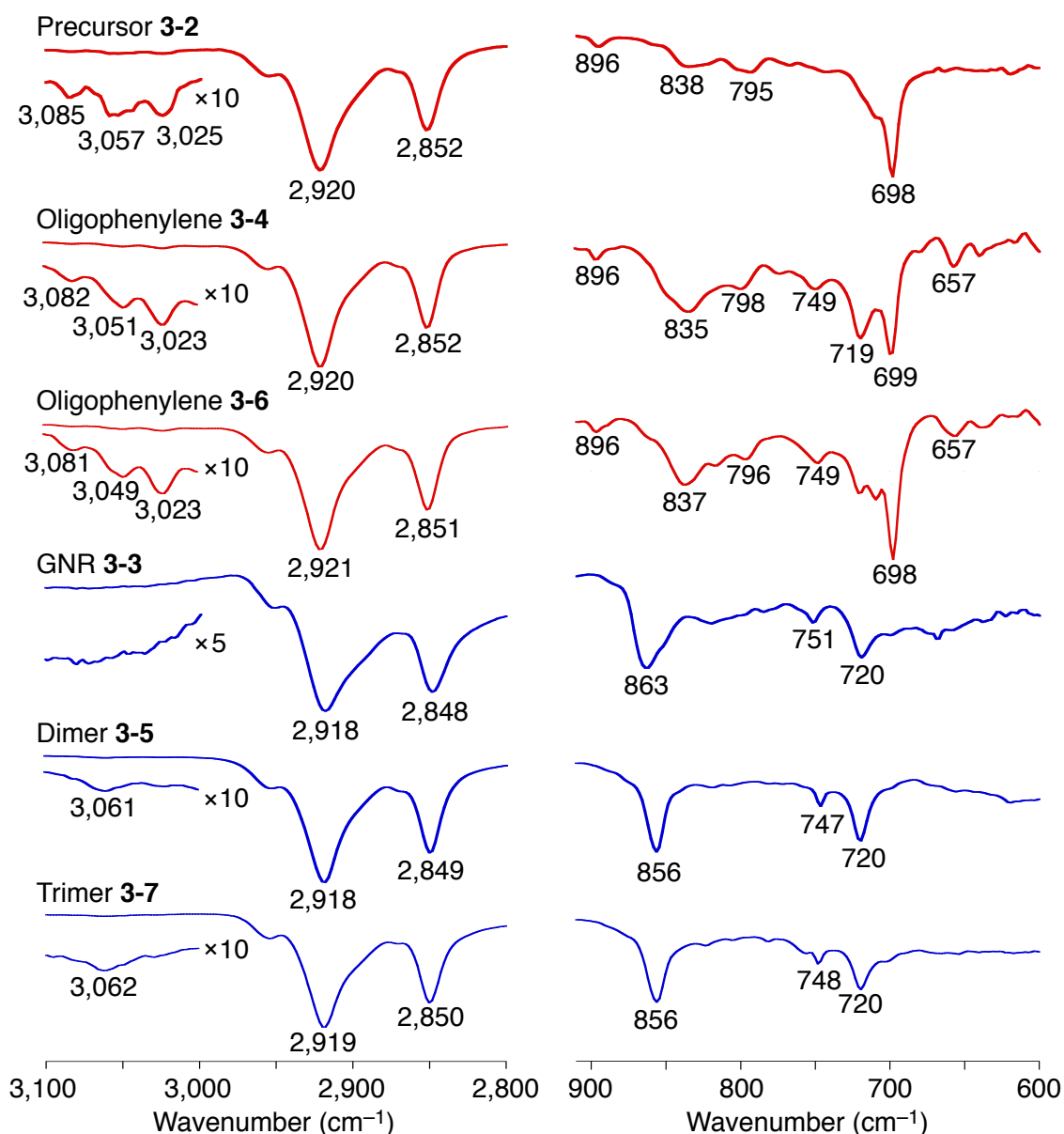


Figure 3-20. Magnified FTIR spectral regions of precursors **3-2**, **3-4**, and **3-6** (red lines) and GNR **3-3**, dimer **3-5**, and trimer **3-7** (blue lines).

3.4.2 Raman spectroscopy

Raman spectroscopy is another potent method for the investigation of carbonaceous materials, and universally employed for the characterization of graphite,^{44,45} graphene,⁴⁵⁻⁵⁰ CNTs,^{47,49,51} as well as GNRs.^{25,46,47,52} Raman spectroscopic investigation of GNR **3-3** was carried out in order to obtain further insight into the quality, structural definition and uniformity, of GNR **3-3** by [REDACTED] and

██████████ in the groups of ██████████ at Freie Universität Berlin, Germany, and University of Manchester, UK, respectively. Raman spectrum of GNR **3-3** was thus measured directly on a powder sample with the excitation wavelength of 532 nm (Figure 3-21).

The Raman spectrum of GNR **3-3** displayed similar features to those of GNRs previously synthesized by the bottom-up synthesis.^{25,53} The G peak was slightly up-shifted ($\sim 1,605 \text{ cm}^{-1}$) compared to that of graphene, and showed a relatively large Full Width at Half Maximum (FWHM) of $\sim 25 \text{ cm}^{-1}$ in agreement with the expectation from quantum confinement which relaxes the Raman selection rule. The intense D peak observed here was not activated by the defects, but by the confinement of π -electrons into the narrow ribbon structures^{54,55,56} as discussed for GNR **2-3-I** in subsection 2.1.3. The Raman spectrum of GNR **3-3** also showed second-order 2D, D + D', and 2D' peaks in agreement with the previous bottom-up synthesized GNRs.²⁵ Additionally, no peak was observed at 994 cm^{-1} , supporting the absence of monosubstituted benzene rings.⁴

Remarkably, a distinct peak from a width-specific low-frequency mode, namely the radial-breathing-like mode (RBLM),⁵⁷⁻⁶⁰ was also displayed in the spectrum at $\sim 235 \text{ cm}^{-1}$, indicating high homogeneity of the GNRs with the uniform width (Figure 3-21, inset).⁵³ The RBLM is related to a breathing-like expansion and compression of the

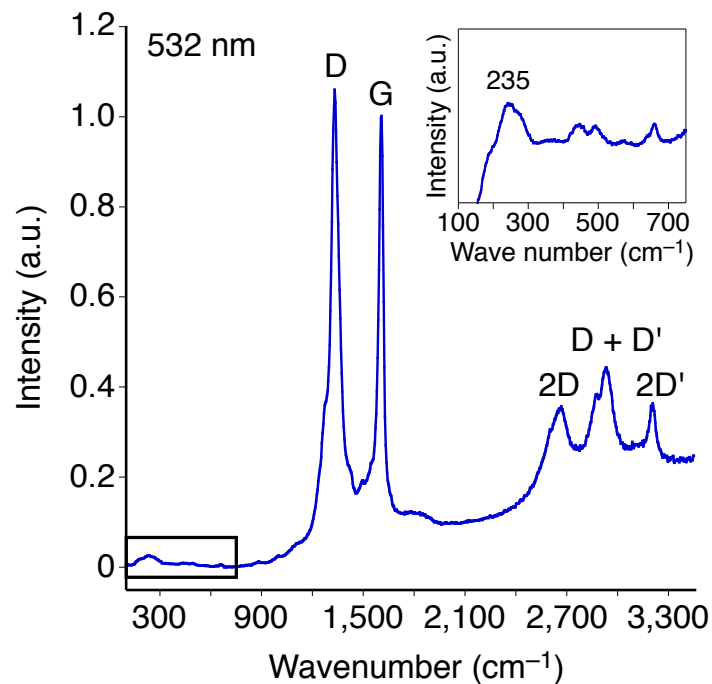


Figure 3-21. Raman spectrum of GNR **3-3** measured at 532 nm (2.33 eV) on a powder sample with laser power below 0.1 mW. The inset displays a zoomed-in spectrum of the squared area, showing the radial-breathing-like mode at 235 cm^{-1} .¹⁰

nanoribbons,⁵⁹ which is similar to the radial breathing mode (RBM) of CNTs.^{47,49,51} The RBLMs correlate with the in-plane longitudinal acoustic (LA) phonons in the limit of the infinite graphene sheet and shift towards lower wave-numbers as the width of the ribbons increase.⁶¹ The RBLM peak was visible with excitation at 532 nm, but not at 633 nm, indicating its resonant nature consistent with the RBM of CNTs.⁴⁹ The broadening of the peak was most likely due to the interactions between aggregated GNRs in the powder.

Unlike G, D, and other second-order peaks that were also observed in Raman spectra of dimer **3-5** and trimer **3-7**, the RBLM peak was visible only in the spectrum of GNR **3-3** (Figure 3-22), denoting that this peak is related to the longitudinally extended structure of the GNRs. According to the calculation by *R. Gillen* and co-workers, the wavenumber of the RBLM peak (ν_{RBLM}) is almost independent of the edge structure and can be approximately estimated by $\nu_{\text{RBLM}} = 3,222/w$ (cm^{-1}), where w (\AA) is the width of a GNR.⁶¹ The RBLM of GNR **3-3** with the width of $w = 11.3$ \AA was thus estimated based on this equation to be 285 cm^{-1} , which was in good agreement with the experimental result. These results verified the high homogeneity of GNR **3-3** with uniform lateral width of ~ 1 nm.

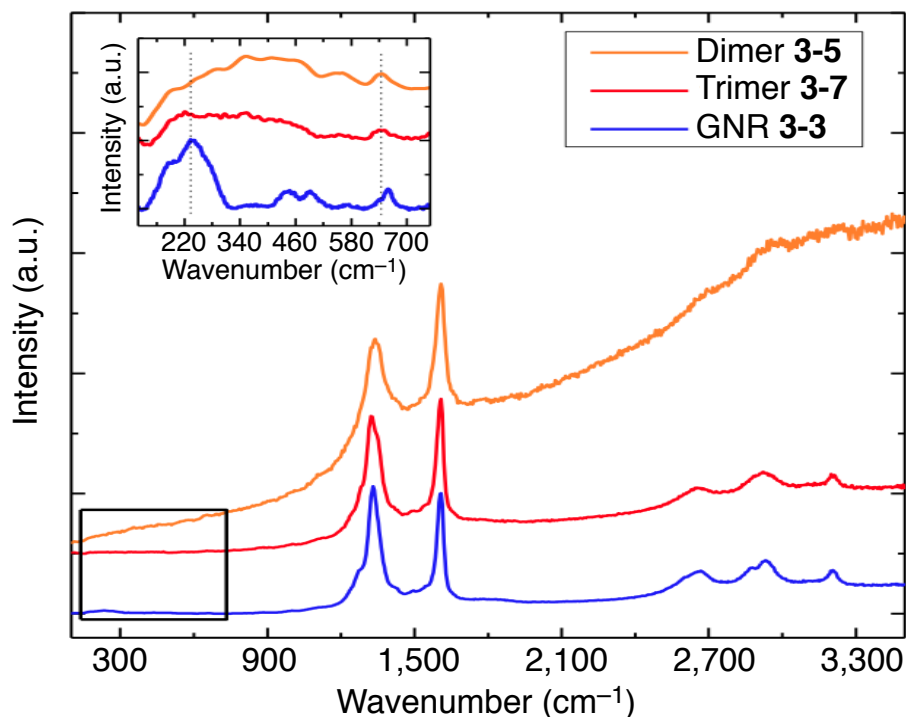


Figure 3-22. Comparison of the Raman spectra of GNR **3-3**, dimer **3-5**, and trimer **3-7** measured at 514.5 nm on powder samples with the laser power of 0.1 mW.¹⁰

3.4.3 NMR spectroscopy

Although liquid-state NMR spectroscopic analysis of GNR **3-3** was hindered by its strong aggregation behavior, solid-state NMR analysis of precursor **3-2** and GNR **3-3** provided further structural information on these polymers (see also subsection 2.2.3). The solid-state NMR experiments were performed by [REDACTED] at Max Planck Institute for Polymer Research Mainz, Germany. Figure 3-23 displays the results acquired from the liquid- and solid-state NMR investigations of precursor **3-2** and GNR **3-3**. The liquid- and solid-state NMR spectra of precursor **3-2** showed huge difference in the resolution, but the overall ^1H line width was almost unchanged (Figure 3-23a and b), which indicated relatively flexible structure of precursor **3-2** in agreement with the results from the photon correlation spectroscopy analysis (subsection 3.3.5). The solid-state ^1H MAS NMR analysis of precursor **3-2** and GNR **3-3** revealed significant broadening as well as a shift of both aliphatic and aromatic ^1H signals upon the cyclodehydrogenation as indicated by the arrows in between Figure 3-23b and c. These observations corroborated that both aliphatic and aromatic protons of GNR **3-3** belonged to an extended π -conjugated system,⁶² and that GNR **3-3** had a rigid structure as expected for the formation of GNRs.

Further, 2D ^1H - ^1H double quantum-single quantum (DQ-SQ) NMR correlation experiments were performed to elucidate the spatial proximity between the different ^1H signals (Figure 3-23d and e).⁶³ The 2D ^1H - ^1H DQ-SQ spectrum of precursor **3-2** revealed narrow ^1H - ^1H correlation signals between the aromatic protons of the polyphenylene backbone as well as between the aromatic protons and the aliphatic protons of the dodecyl chains, corroborating the relatively high flexibility of precursor **3-2** (Figure 3-23d). On the other hand, the 2D ^1H - ^1H DQ-SQ spectrum of GNR **3-3** showed a broad and stretched ridge of ^1H - ^1H correlation signals for the aromatic protons between 6 and 13 ppm (Figure 3-23e). The correlation signal between the aromatic and aliphatic protons was also observed, but it spread only from 6 to 10 ppm. Based on this difference the high-frequency part of the ridge could be assigned to the inner most proton (blue circle) at the “cove” position, whereas the low-frequency part to the outer proton (red circle), which was located in the close vicinity of the dodecyl chains. Additionally, the broadness of the ^1H signals could be explained by complex shielding and deshielding of the protons, depending on their positions in the heterogeneously packed solid of GNR **3-3**, which shifted the ^1H signals in opposite

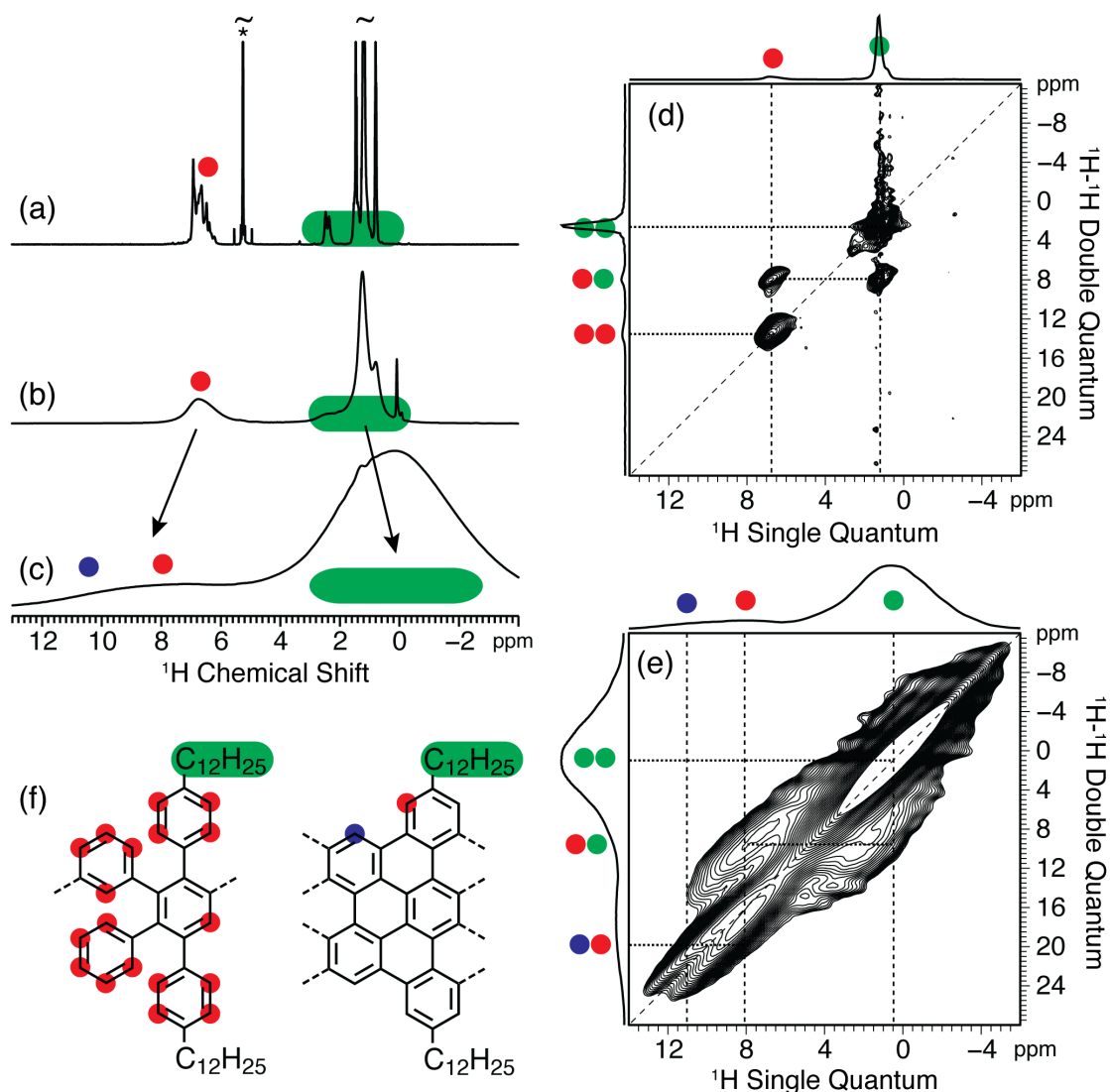
directions.^{64,65}

Figure 3-23. (a), (b) Liquid- and solid-state ^1H NMR spectra of precursor **3-2** (a) in CD_2Cl_2 and (b) as solid sample, respectively. The asterisk in (a) indicates the residual proton signal of CD_2Cl_2 . (c) Solid-state ^1H NMR spectrum of GNR **3-3**. (d), (e) The 2D ^1H - ^1H DQ-SQ correlation spectra of (d) precursor **3-2** and (e) GNR **3-3**, which were recorded using eight and two rotor periods of DQ recoupling, respectively. The ^1H signals are assigned using the scheme given in (f). The liquid-state spectrum in (a) was acquired at 7.05 T (300.13 MHz for ^1H), while the solid-state NMR experiments in (b-e) were recorded at 16.45 T (700.21 MHz for ^1H) using a MAS frequency of 59,524 Hz.¹⁰

3.4.4 UV-vis absorption spectroscopy and DFT calculation

Profiting from the high dispersibility, UV-vis absorption spectroscopic analysis of GNR **3-3** was performed in a dispersion, and the obtained spectrum was compared with those of dimer **3-5** and trimer **3-7** (Figure 3-24). The UV-vis absorption spectrum of dimer **3-5** in THF showed the most intense β -band at 420 nm and relatively small p-band at 490 nm in consistence with previously reported dimer with different alkyl chains,¹⁸ which further provided a structural proof for dimer **3-5**. The optical bandgap was calculated from the onset of the p-band, i.e. 553 nm, to be 2.24 eV. The spectrum of trimer **3-7** in THF showed similar spectral features to those of dimer **3-5** with red-shifted absorption maximum at 467 nm and optical bandgaps of 2.09 eV. Interestingly, the absorption spectrum of GNR **3-3** measured in a NMP dispersion showed the similar features with further red-shifted absorption maximum at 550 nm and the absorption edge of 659 nm, corresponding to the optical bandgaps of 1.88 eV. The absorbance observed over 700 nm was most probably due to scattering by the aggregates of the GNRs in the dispersion. These results demonstrated decreases of the optical bandgap along with the longitudinal extension. GNRs **3-3-II** and **3-3-III** showed

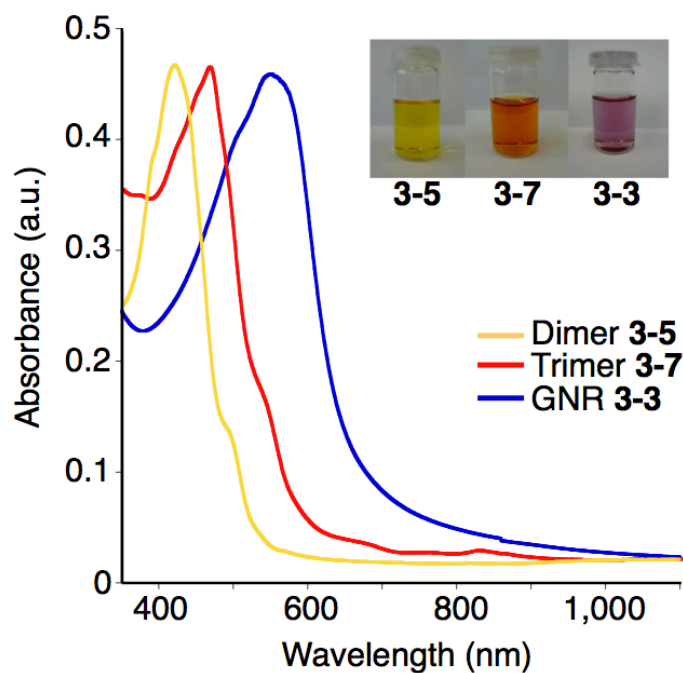


Figure 3-24. Normalized UV-vis absorption spectra of dimer **3-5** in THF (yellow), trimer **3-7** in THF (red), and GNR **3-3** in NMP (blue); inset: photographs of dispersions of dimer **3-5**, trimer **3-7**, and GNR **3-3**.¹⁰

basically the identical absorption spectra, which indicated that the optical bandgap of GNR **3-3** reached a plateau at 1.88 eV with the longitudinal extension of ca. 110 nm, i.e. the calculated length of GNR **3-3-II**.

In order to obtain a better insight into the optoelectronic properties of GNR **3-3**, the electronic energy levels of GNR **3-3** were studied based on density functional theory (DFT)/Heyd-Scuseria-Ernzerhof (HSE) in collaboration with [REDACTED] and [REDACTED] from the University of Mons, Belgium. The calculation results indicated that the bandgap of GNR **3-3** decreases as the longitudinal extension and reaches the plateau of 2.04 eV with ~15 repeating units in agreement with the experimental results.⁶⁶ The consistency of the experimental optical bandgap of 1.88 eV with this theoretical bandgap of 2.04 eV provided further evidence for the successful formation of GNR **3-3**. Additionally, the valence and conduction band energies of GNR **3-3** were theoretically estimated to be -4.63 and -2.59 eV, respectively.⁶⁶

3.4.5 Liquid-phase processing and STM visualization

All the long (>50 nm) GNRs thus far synthesized via the bottom-up solution synthesis were precluded from liquid-phase processing as well as precise structural characterizations by means of microscopic visualization, owing to the strong aggregation behavior and low dispersibility.^{5,25} Thus, it was impossible to visually demonstrate the formation of GNRs or to obtain their actual dimensions, let alone to form well-organized films of the GNRs. Remarkably, GNR **3-3** with the enhanced dispersibility enabled unprecedented liquid-phase processing of the GNRs to form highly organized self-assembled films, which could be visualized by the STM to reveal their actual dimensions.

The STM visualization of GNR **3-3** was carried out by the group of [REDACTED] at Katholieke Universiteit Leuven, Belgium. Films of GNR **3-3** could be easily prepared by conventional spin-coating and drop-casting methods, although GNRs in such films were not well ordered. For the preparation of highly ordered films of GNRs, a small amount of the GNR powder was put inside a semi-closed capillary, which was placed orthogonally over a HOPG surface preheated at ~130 °C. Small drops of TCB were then repeatedly applied to gradually extract out the GNRs, which were radially deposited on the HOPG surface in the vicinity of the GNR powder during the evaporation of the solvent. Apparently, much of the GNRs remained in the powder and

only a part of the GNRs could be leached out during the deposition. This process probably caused “fractionation” of the GNRs, which lead to a preferential deposition of shorter and more soluble GNRs on the surface while longer and less soluble GNRs stayed in the powder or aggregates.

STM visualization was subsequently performed on the dry film, namely at the solid-air interface, which demonstrated self-assembled and highly ordered domains of uniform and mostly straight GNRs (Figure 3-25a). Such self-assembled domains with noodle-like structure were similar to those of conventional conjugated polymers such as polythiophenes and polyanilines.⁶⁷⁻⁶⁹ The height of these domains was 0.3~0.4 nm, indicating the monolayer nature of this GNR film. The average interval of the GNRs in the domains was 1.8 ± 0.2 nm, where the simulated lateral width of GNR **3-3** was ~3.80 nm including the alkyl chains (Figure 3-25b). This result indicated partial stacking of the neighboring GNRs owing to the strong self-interaction (Figure 3-25c). GNRs with the longitudinal lengths of up to ca. 60 nm were observed for GNR **3-3-II**, the average length of which was determined to be ca. 110 nm based on the photon correlation spectroscopy analysis of the precursor (subsection 3.3.5). The observation of only the

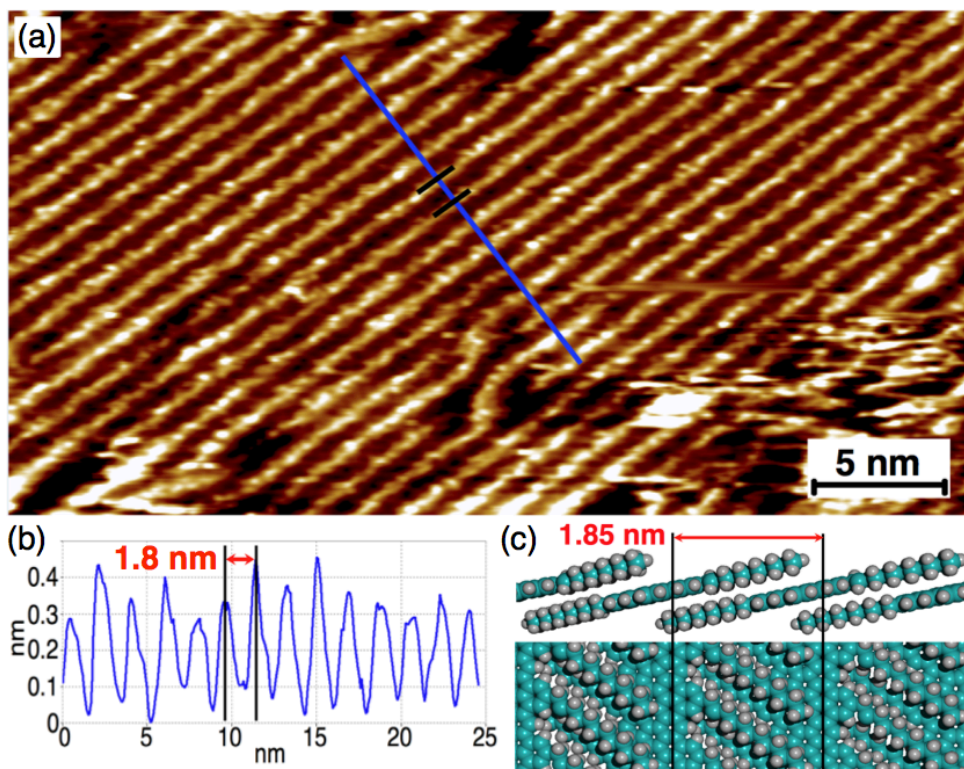


Figure 3-25. (a) An STM image of GNR **3-3** on HOPG (dry film). (b) Line profile along the blue line in panel (a), showing the periodicity of the self-assembled structure of GNR **3-3**. (c) Molecular model of partially stacked GNR **3-3**; blue, carbon; grey, hydrogen.¹⁰

relatively short GNRs was most likely because they were more soluble than the longer GNRs, and thus could be preferentially extracted out during the formation of the films (see also subsection 3.6.3). The longer GNRs were probably left inside the powders or as three-dimensional (3D) aggregates, which were observed during the STM analysis along with the self-assembled layers. In fact, the formation of self-assembled films was not observed for GNR **3-3-III** with larger estimated average length of ca. 270–600 nm, which indicated that this deposition method, i.e. gradual leaching with hot TCB, could not extract out such longer GNRs due to their lower solubility. This result corroborated the notion that the GNRs were “fractionated” during the deposition process, which resulted in the observation of only shorter GNRs, i.e. up to ca. 60 nm, by STM.

On the other hand, when a dispersion of longer GNR **3-3-III** in THF, which was prepared beforehand with assistance of sonication, was drop-cast on HOPG surfaces, multilayered films of self-assembled GNRs could be observed by Atomic force microscopy (AFM) (Figure 3-26). This experiment was carried out in collaboration with [REDACTED] in the group of [REDACTED] at Johannes Gutenberg-Universität Mainz, Germany, and [REDACTED] in the group of [REDACTED]. Phase images (Figure 3-26b and d) demonstrated the fibrous structures of the GNRs more clearly than height images (Figure 3-26a and c). The films consisted of small domains of the self-assembled GNRs with different orientations, which lay on top of the other. The lengths of the GNRs in such domains were seemingly over 100 nm, but a reliable analysis was hindered by the low resolution of the image, which could not be improved due to the high density of the GNRs. Nevertheless, this result revealed that the drop-casting of a dispersion is a superior deposition method for the longer GNRs compared to the leaching method, which failed to deposit the GNRs longer than 60 nm.

In order to obtain microscopic images of the GNRs with higher resolution, the STM measurements were next performed at the Au(111)/TCB interface for shorter and thus better dispersible GNRs with the estimated longitudinal length of ca. 20–33 nm, based on M_w of the precursor obtained by the SEC analysis. Remarkably, isolated GNRs could be clearly visualized owing to the stronger interactions between the GNRs and the Au(111) surfaces in contrast to the HOPG surfaces, where only self-assembled structures could be observed (Figure 3-27a). The lengths of the isolated GNRs could be measured on the STM images and were ca. 14–27 nm, which was in good agreement with the values estimated from the M_w of the precursor (Figure 3-27b). Moreover, the STM image partially demonstrated the edge structure of the isolated GNR, showing parts of the alkyl chains (Figure 3-27c). The periodicity observed between the alkyl

chains was ~ 0.8 nm in good agreement with the length of one repeating unit, i.e., ~ 0.7 nm, which further corroborated the well-defined structure of GNR **3-3** (Figure 3-27d).

In contrast to the STM image of a dry film of GNR **3-3** on HOPG, which displayed self-assembled structures of mostly straight GNRs (Figure 3-25a), the isolated GNRs observed at the Au(111)/TCB interface generally showed non-straight, kinked or folded structures (Figure 3-27). It has been theoretically as well as experimentally reported that GNRs are not mechanically robust and can easily be bent, folded, and twisted in contrast to MWCNTs.^{52,70-76} Indeed, the AFM image of folded GNRs reported in the literature resembled the STM image of the isolated GNRs shown in

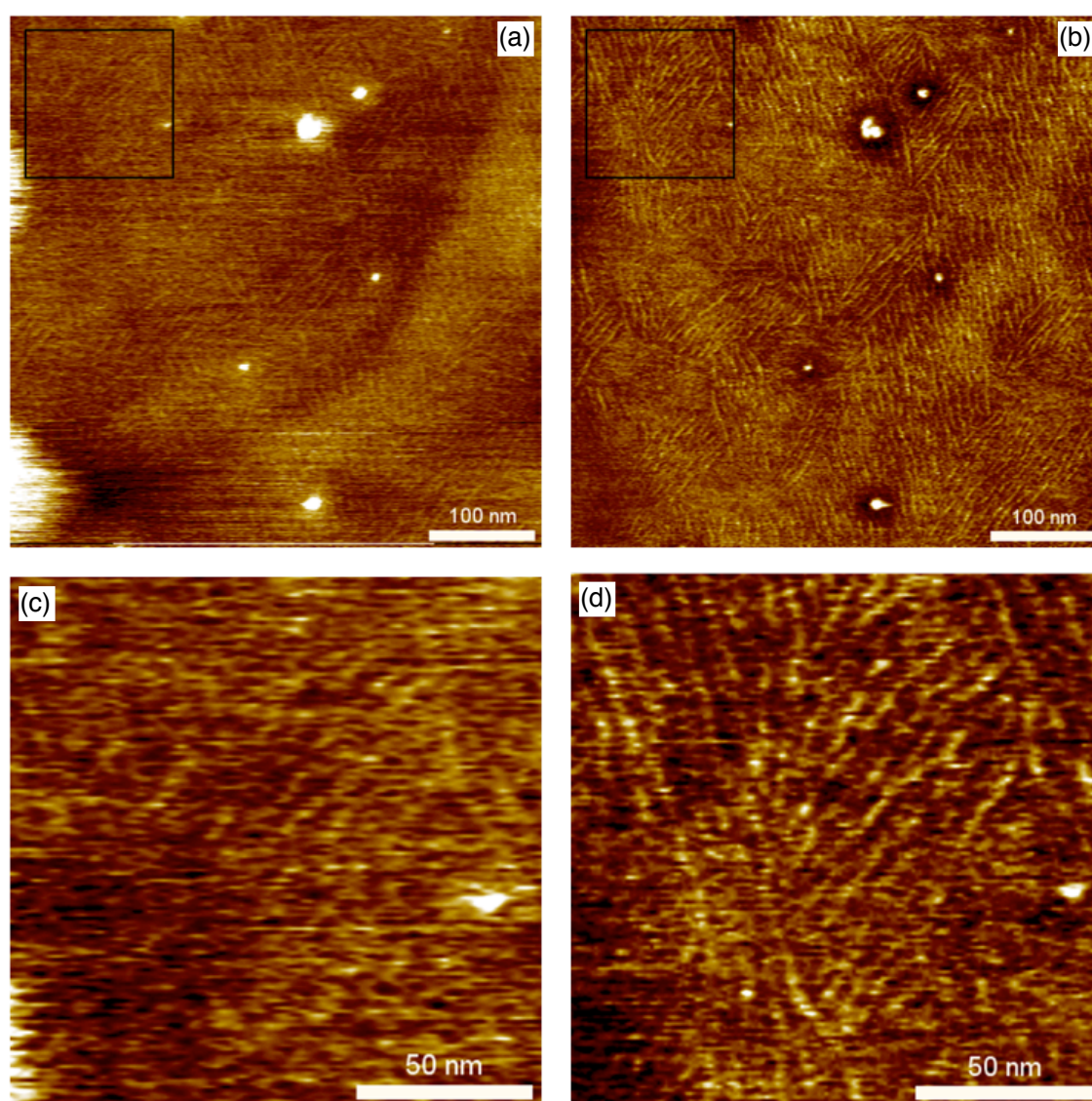


Figure 3-26. AFM (a) height and (b) phase images of GNR **3-3-III** drop-cast on a HOPG surface from a dispersion in THF, showing multilayered films of the GNRs. (c) and (d) display magnified images of the squared areas in (a) and (c), respectively.

Figure 3-27.^{52,70} Based on these results reported for top-down made GNRs with the width of $\sim 10\text{--}25$ nm as well as narrow (ca. 1 nm) GNRs bottom-up fabricated inside CNTs, it is reasonable that GNR **3-3** is also mechanically flexible and undergoes folding and bending at arbitrary positions. Considering the extremely large number of bonds to be closed in one step of the cyclodehydrogenation, it might also be possible that there are unclosed bonds within the GNR structures, which could facilitate the folding and bending.

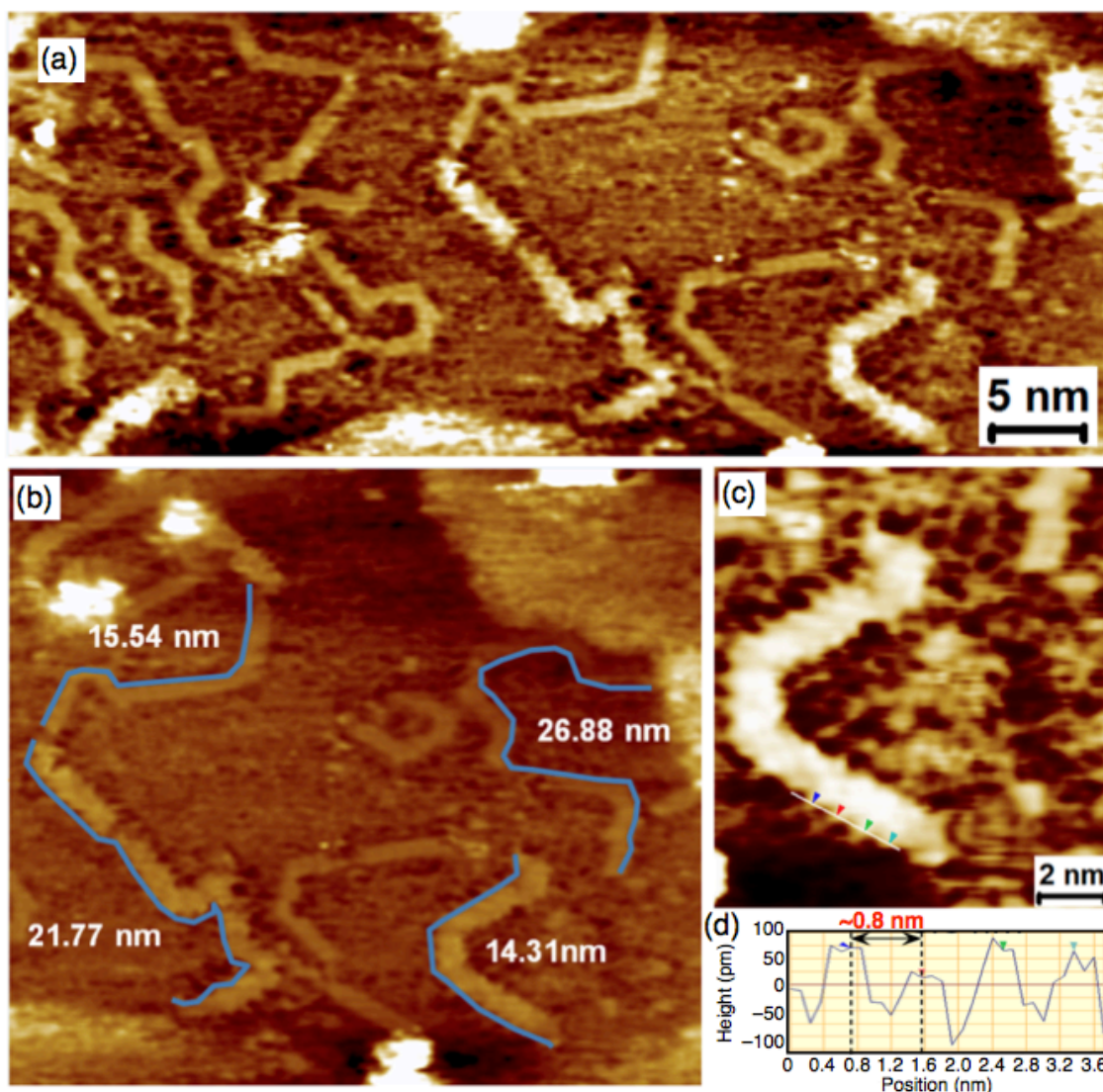


Figure 3-27. (a) An STM image of shorter GNR **3-3** at the Au(111)/TCB interface, displaying isolated GNRs. (b) The lengths of the GNRs could be measured on the image. (c) A magnified STM image of an isolated GNR, showing the edge structure. (d) Line profile along the white line in panel (c), which reveals the periodicity at the edge of the GNR.¹⁰

These kinked structures could also be due to “graphitization” at undesired conformations or rearrangements of the phenyl rings,⁷⁷ but this would contradict the fact that much less “kinks” were observed in the STM image of dry films of GNR **3-3** on HOPG (Figure 3-25a). In other words, if all the “kinks” of the GNRs observed in Figures 3-25a and 3-27a were structural defects due to the cyclodehydrogenation at “wrong” conformations, the clear difference in the number of “kinks” in these two images would be unreasonable, because the frequency of the structural defects is most probably statistically the same for the two GNR samples in spite of the different lengths. Figure 3-25a shows an image of a dry film of the GNRs, where all the GNRs extracted out from the powder were deposited on the surface. The absence of “highly kinked” GNRs in Figure 3-25a thus suggests that at least some of the “kinks” observed in Figure 3-27 were derived from the folding and bending of the GNRs. The observation of mostly the straight GNRs on the dry film can be explained by the fact that each GNR in the self-assembled monolayers is supported by neighboring GNRs, forming a domain (Figure 3-25a). In contrast, the isolated GNRs observed at the solid-liquid interface are not supported like in a domain and can take any shape as shown in Figure 3-27. The structural perfection of GNR **3-3** could not be unambiguously proved by the available characterization methods and the possibility of the cyclodehydrogenation at undesired conformations could not be completely excluded. Nevertheless, the kinks observed in the STM images were most likely because of the folding and bending of the mechanically flexible GNRs.

For comparison, STM measurements of dimer **3-5** and trimer **3-7** were also carried out at the Au(111)/TCB interface. The STM image of dimer **3-5** showed blob-like features, corresponding to the aromatic cores of the molecules, although high-resolution images of well-organized self-assembled molecules could not be obtained (Figure 3-28a). Three stripes were visible on some of the blobs, which were presumably related to the electron densities in the highest occupied molecular orbitals of dimer **3-5**.^{25,66,78} Trimer **3-7** typically showed formation of aggregated species, but blob-like features could also be observed, corresponding to the aromatic cores, similar to those of dimer **3-5** (Figure 3-28b). The stark difference between the image of the GNRs and those of dimer **3-5** and trimer **3-7** unambiguously attested that the ribbon-like structures observed for GNR **3-3** (Figure 3-27) were not derived from end-to-end packing of a number of shorter oligomers, but from longitudinally extended structures of the GNRs.

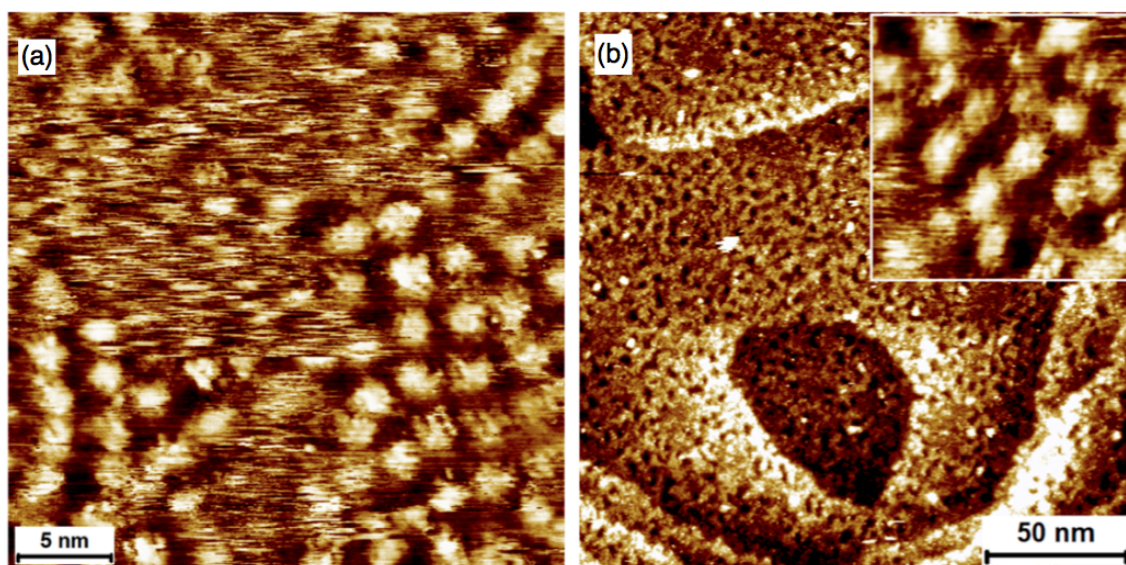


Figure 3-28. STM images of (a) dimer **3-5** and (b) trimer **3-7** at the Au(111)/TCB interface. The inset in panel (b) shows the magnified region (15 nm \times 15 nm) of the Au(111) surface.¹⁰

Thus, these results revealed the high liquid-phase processability of GNR **3-3**, which enabled the formation of their highly organized self-assembled monolayers on HOPG surfaces. The measurements at the Au(111)/TCB interface provided microscopic images of isolated GNRs, which further supported the highly defined structure of GNR **3-3**. However, it was simultaneously indicated that the solubilizing effect of the dodecyl groups was insufficient for the fabrication of well-ordered self-assembled films with GNRs longer than 60 nm. The partial stacking of the neighboring GNRs could also not be avoided due to the strong π - π interaction between the GNRs. In order to further enhance the solubility, GNRs with longer and branched alkyl chains were synthesized, which will be discussed in section 3.6.

3.5 Investigation of electronic properties by THz spectroscopy

3.5.1 THz spectroscopy on GNR 3-3 in dispersions

Taking advantage of the high dispersibility of GNR **3-3**, the intrinsic conductivity of the GNRs was studied in a liquid-phase by utilizing time-resolved THz spectroscopy (section 1.5)⁷⁹ in collaboration with [REDACTED] and [REDACTED] at Max Planck Institute for Polymer Research Mainz, Germany. Among the solvents that can disperse GNR **3-3**, THF and NMP absorbed the THz pulse and thus could not be used for the THz spectroscopy measurements. However, TCB was transparent to the THz pulse, and thus the THz experiments were carried out in TCB dispersions.

Time-dependent photoconductivity of GNR **3-3-III** showed a fast ingrowth after the excitation and subsequently a swift decay in both the real and the imaginary parts (Figure 3-29a). Frequency-resolved complex photoconductivity $\sigma(\omega; \tau)$ was probed $\tau=300$ fs after the optical mobilization of the charge carriers and showed significant positive real and negative imaginary conductivity, both of which increased with

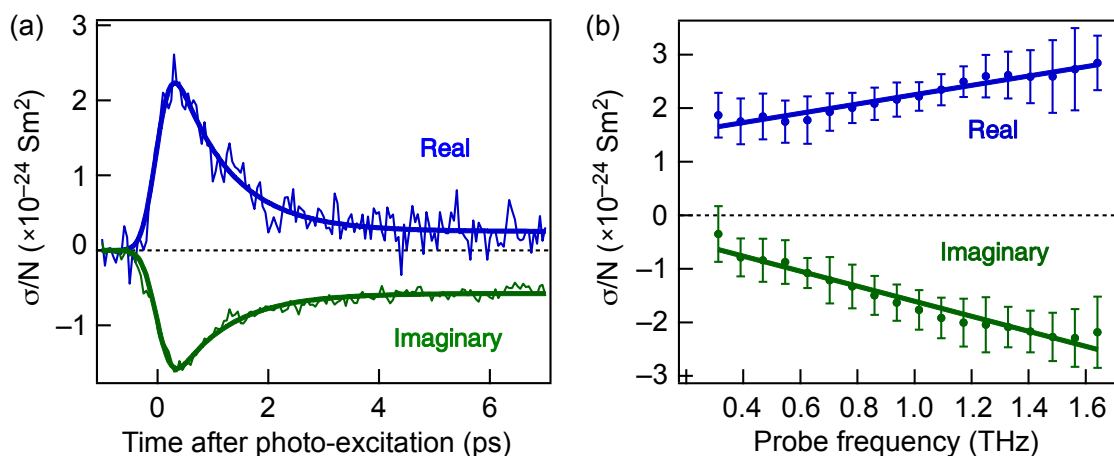


Figure 3-29. (a) Real and imaginary components of the photoconductivity of GNR **3-3-III** as function of time after the excitation. Thick lines represent simulations revealing free charge carrier lifetimes of ~ 1 ps. (b) Photoinduced complex conductivity of GNR **3-3-III** normalized to initial surface excitation density N measured 300 fs after excitation by a 400 nm pulse, fluence 4.3×10^{18} photons/m², for GNRs dispersed in TCB. Solid lines through the data points are guides to the eye. Error bars are based on the standard deviation obtained from 15 consecutive measurements of the THz waveform.¹⁰

frequency in absolute values (Figure 3-29b). With this THz spectroscopy investigation, the charges were probed on picosecond timescales, where they could be estimated to move on the order of 10 nm, thus providing the intrinsic conductivities of electrons and holes within the GNRs. Indeed, GNR **3-3** with shorter estimated average length of ca. 20–33 nm showed similar results, indicating that the THz spectroscopy analyses were not affected by the length of the GNRs.

Next, the THz-resolved photoconductivities of GNR **3-3-III** was compared to those reported for organic semiconducting polymers such as polythiophene (P3HT)^{80,81} and poly-phenylenevinylene (PPV)^{82,83} derivatives. The complex conductivity spectra $\sigma(\omega; \tau)$ of GNR **3-3**, especially the profiles of the real part (Figure 3-29b) resembled those of such semiconducting polymers, which has been concluded to show dispersive transport of free, unbound carriers with impeded long-range transport.⁸⁰⁻⁸³ These free carriers rapidly form excitons with typical lifetime on the order of 1 ps for the PPV derivatives,^{82,83} because the electrons and the holes are not well separated in such low-dielectric systems.

Excitons do not show any real conductivity because of the neutral charge, but contribute to the polarizability, which is measured as a negative imaginary conductivity in the THz response. The imaginary conductivities of the polymers are known to persist for long delay times, which was also observed for GNR **3-3-III** (Figure 3-29a).⁸² The initial increase in the relative magnitude of the imaginary conductivity could be explained by the formation of excitons (Figure 3-29a). The exciton polarizability α of GNR **3-3-III** could be determined from the slope of the imaginary conductivity response to be $1.5 \times 10^3 \text{ \AA}^3$, assuming the quantum efficiency for exciton formation of near 100% within 10 ps.^{83,84} This value of the exciton polarizability was comparable to those previously reported for the semiconducting polymers,⁸³ denoting that exciton dissociation is required also for such bottom-up synthesized GNRs in order to drive photocurrents, e.g. for the application in photovoltaic devices. Polymer solar cells are typically fabricated with bulk heterojunction structures for this purpose.

On the other hand, there were two notable differences between the photoconductivity response of GNR **3-3-III** and those of the conventional semiconducting polymers. First, the real conductivity of GNR **3-3-III** showed relatively weak dependence on the probe frequency (Figure 3-29b). Higher conductivities are generally observed at higher frequencies, where the conductivities are measured within shorter lengths and thus affected by fewer defects and/or irregularities. The conventional polymers typically display higher frequency dependence owing to torsions

and structural defects along the polymer backbones. The weak frequency dependence observed for GNR **3-3-III** was therefore indicative for a low defect density as well as a relatively rigid structure that allowed less torsions.

Moreover, GNR **3-3-III** showed the real conductivity with the amplitude, scaled to the excitation density, almost an order of magnitude larger than those reported for the conventional polymers.⁸³ Based on the observed photoconductivity, the intrinsic mobility of GNR **3-3-III** could be estimated to be within the range from 150 to 15,000 $\text{cm}^2/\text{V}\cdot\text{s}$, assuming the quantum efficiency for free carrier generation on the order of 10^{-3} and 10^{-5} , which have been reported for polymer films and polymers in solutions, respectively.⁸³ Although better estimation of the quantum efficiency for free carrier generation of GNR **3-3-III** was difficult, these mobility values were indeed in accordance with the theoretical predictions for narrow GNRs.^{85,86} Regardless of the precise value of the mobility, these results clearly demonstrated superior conductivity and mobility of GNR **3-3** over the conventional semiconducting polymers.

3.5.2 THz spectroscopy on a solid film of GNR **3-3**

In order to evaluate the effect of aggregation on the THz-resolved photoconductivities of the GNRs, the THz spectroscopy analysis was next performed on a solid film of GNR **3-3-III** deposited on a fused silica substrate through drop-casting of the dispersion in TCB (Figure 3-30). It could be considered that the degree of aggregation was higher for the GNRs on such solid films than those in the dispersions. The frequency resolved complex photoconductivity of the film of GNR **3-3-III** was very similar to that of the dispersion in the real part, but the imaginary part was completely different, showing much smaller imaginary conductivity (Figure 3-30). These results could be clearly understood by applying the Drude-Smith model, which assumes free motion of the charge carriers through the longitudinal direction of the GNRs as well as carrier backscattering at the edges.^{87,88} The difference in the imaginary part of the response could be explained, considering the geometrical effect. On the film, the GNRs were deposited on a two dimensional plane and thus, on average, less GNRs were oriented perpendicular to the polarization of the THz field compared to those in the dispersion, where the GNRs were oriented equally to all directions. As a result, less carrier backscattering at the ribbon edges occurred on the film, which lead to the smaller negative imaginary conductivity.

These results indicated that only the intramolecular charge transport within individual GNRs was probed by the THz spectroscopy while the intermolecular transport was negligible, which would lead to a different type of the conductivity response. This conclusion was also in line with the previous report on aligned conjugated polymers that their mobilities parallel to their polymer backbones, i.e. intramolecular mobilities, were an order of magnitude higher than those perpendicular to their backbones, i.e. intermolecular mobilities.⁸⁹ Therefore, the photoconductivity measured in the dispersion as well as on the film of GNR **3-3-III** was in principle not affected by the aggregation of the GNRs, and represented the intrinsic properties of the individual GNRs.

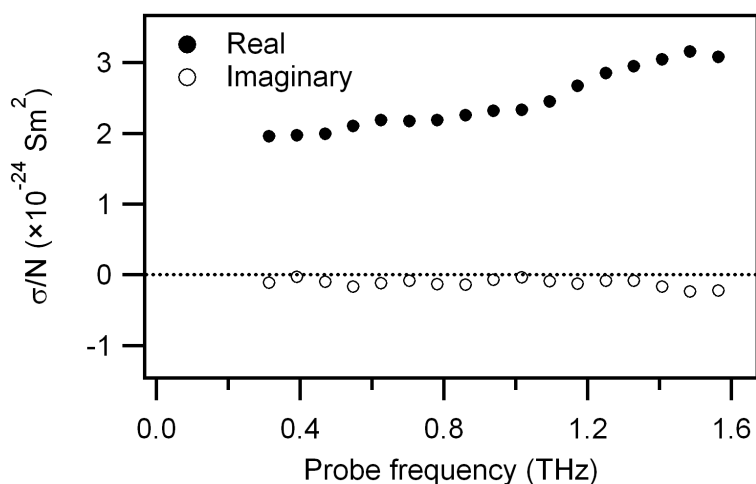


Figure 3-30. Frequency resolved complex photoconductivity of a film of GNR **3-3-III** drop-cast from a dispersion in TCB on a fused silica substrate. The sample was excited by 400 nm pulses with a sheet excitation density of 2.1×10^{18} photons/m². The conductivity is scaled to the density N of absorbed photons.¹⁰

3.5.3 THz spectroscopy on dimer 3-5

For comparison, the THz spectroscopy measurement was further performed on a TCB dispersion of dimer **3-5**, which could be considered as a fully confined system (Figure 3-31). Dimer **3-5** displayed almost no real conductivity in consistent with the confinement of the charge carriers in all directions within the small dimer molecules, where no long-range carrier transport was possible. Only a negative imaginary conductivity was observed, which increased in magnitude with the probe frequency, as expected for completely confined carriers.⁸⁴ The absence of the real conductivity clearly evidenced that the charge transport between graphene nanostructures was negligible in dispersions, further corroborating the notion that only the intramolecular conductivities were probed in the THz spectroscopy analysis of GNR **3-3**, regardless of the presence of aggregates in the dispersion.

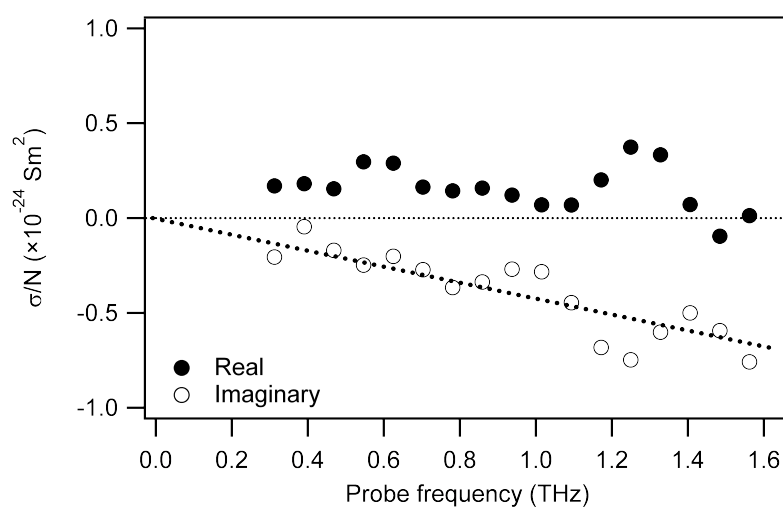


Figure 3-31. Complex photoconductivity of dimer **3-5** dispersed in TCB excited by 400 nm pulses at 3.3×10^{18} photons/m². The conductivity is scaled to the density N of absorbed photons. The dashed line shows the response expected for confined, excitonic charge carriers.¹⁰

3.6 GNRs with enhanced solution processability

3.6.1 Synthesis of GNRs with bulkier side chains

GNR **3-3** with dodecyl groups at peripheral positions showed remarkable dispersibility in normal organic solvents for this type of materials and allowed unprecedented liquid-phase processing of the GNRs to form self-assembled monolayers as well as photoconductivity studies by THz spectroscopy in dispersions. However, the GNRs were partially stacked with the neighboring GNRs in the self-assembled layers, which were consisted only of relatively short GNRs of up to 60 nm. Indeed, formation of self-assembled monolayers could not be observed with longer GNR **3-3-III** with the estimated average length of ca. 270–650 nm. These results rendered it highly desirable to further enhance the dispersibility of the GNRs. It has been revealed by studies on HBCs that longer and branched 2-decyltetradecyl chains can more effectively suppress their aggregations and thus drastically enhance their solubility compared with the

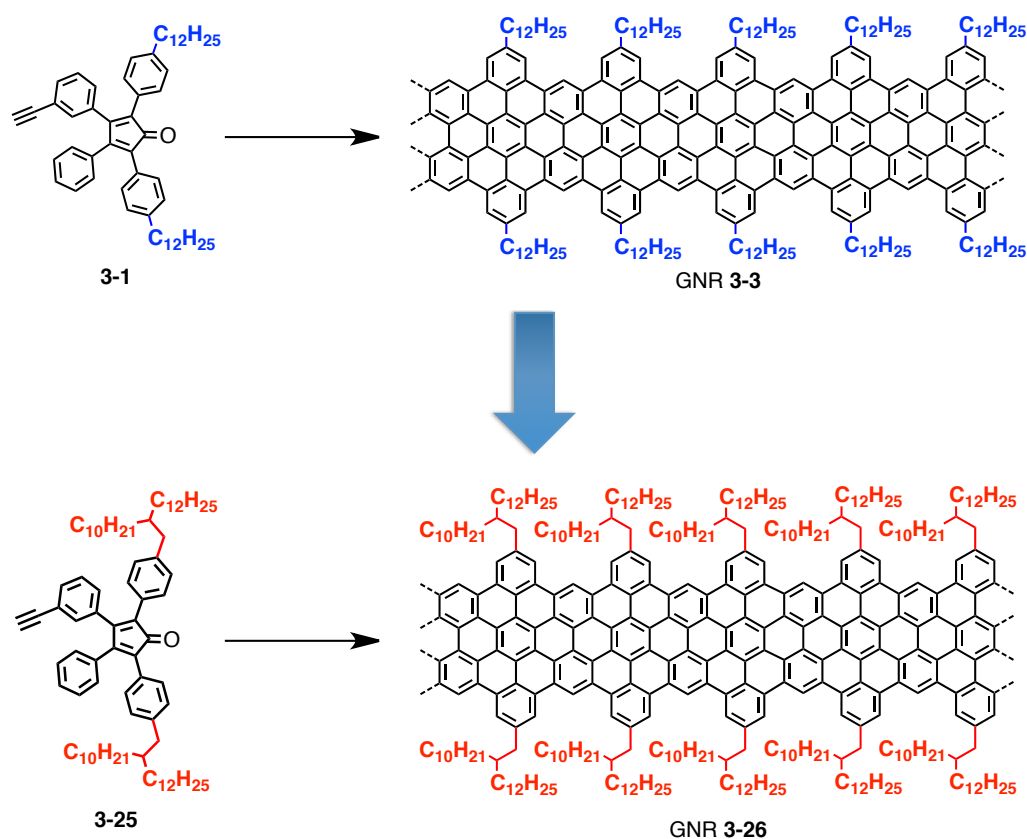


Figure 3-32. Introduction of sterically bulkier 2-decyltetradecyl chains (red) in place of the dodecyl chains (blue) for improving the dispersibility of the GNRs.

dodecyl chains.¹⁹ Therefore, in order to enhance the dispersibility of the GNRs, fabrication of GNR **3-26** with the sterically bulkier 2-decyltetradecyl chains was envisaged (Figure 3-32). GNR **3-26** could be synthesized in the same manner as GNR **3-3** by employing *AB*-type monomer **3-25** with 2-decyltetradecyl chains.

AB-type monomer precursor **3-25** was synthesized as shown in Figure 3-33. First, bis[4-(2-decyltetradecyl)phenyl]acetone **3-28** was synthesized by *Negishi* coupling of bis(4-bromophenyl)acetone **3-15**²¹ with the 2-decyltetradecylzinc reagent, which was generated in situ from 2-decyltetradecyl bromide (**3-27**).¹⁹ Subsequently, *Knoevenagel* condensation of **3-28** and 3-bromobenzil (**3-17**) gave functionalized

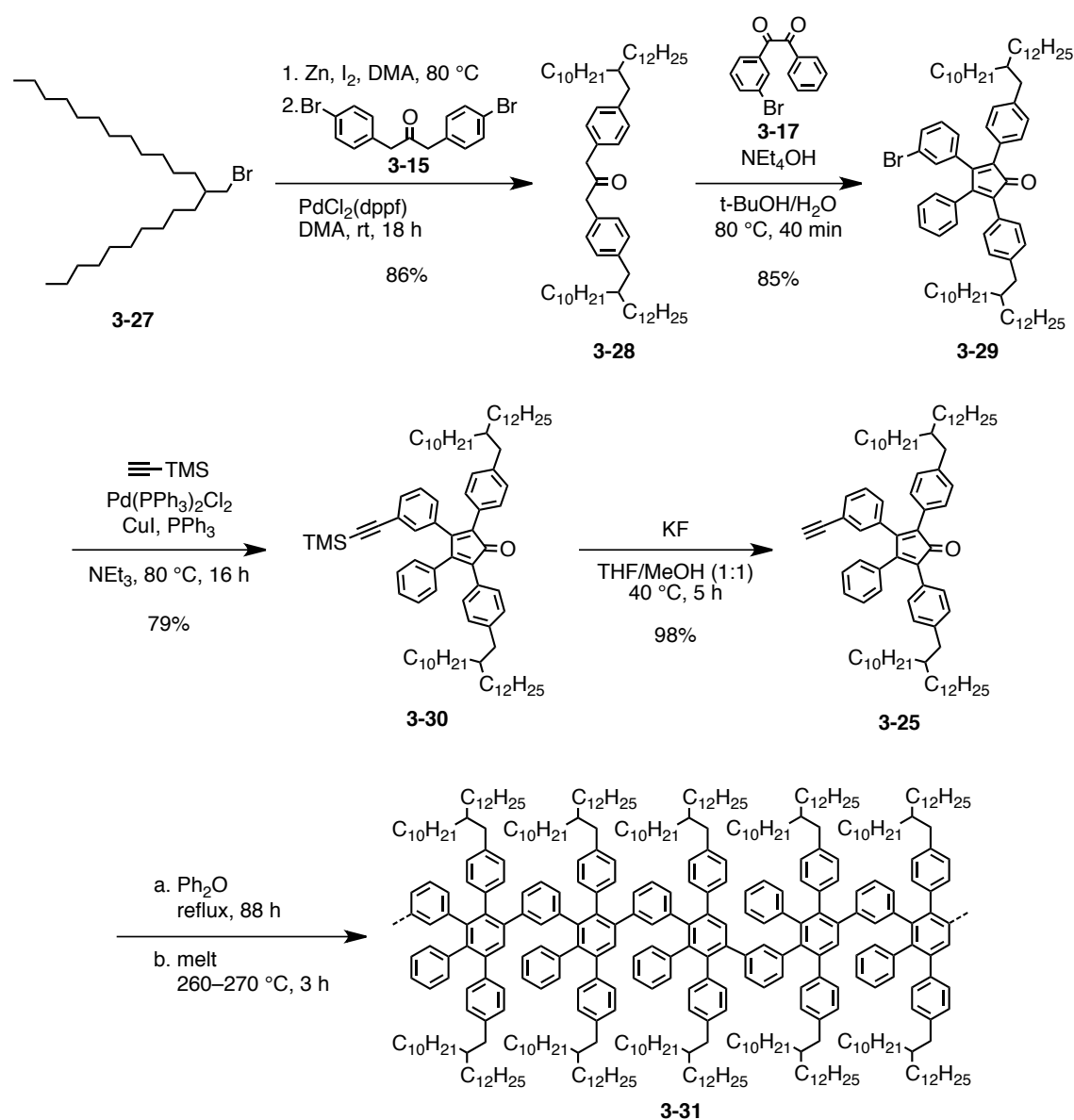


Figure 3-33. Synthesis of *AB*-type monomer **3-25** with 2-decyltetradecyl chains followed by *Diels-Alder* polymerization to polyphenylene precursor **3-31**.

tetraphenylcyclopentadienone **3-29** in 85% yield. Next, tetraphenylcyclopentadienone **3-29** was subjected to *Sonogashira* coupling with trimethylsilylacetylene to afford TMS-protected monomer **3-30** in 79% yield, followed by removal of the trimethylsilyl protecting group with potassium fluoride to obtain *AB*-type monomer **3-25** in 98% yield.

AB-type *Diels-Alder* polymerization of monomer **3-25** was carried out in a similar manner to that of monomer **3-1**. When monomer **3-25** was refluxed in diphenyl ether at the concentration of 151 mM for 88 h, polyphenylene precursor **3-31-I** with M_w of 31,000–54,000 g/mol, M_n of 17,000–21,000 g/mol, and PDI of 1.8–2.6 was obtained according to SEC analysis against PPP and PS standards. The SEC profile of precursor **3-31-I** showed a peak at ~27 min, corresponding to smaller oligomers with M_p of 4,100–5,900 g/mol (Figure 3-34a). These small oligomers were most likely cyclic oligomers that were precluded from further polymerization, as was suggested for the case of polyphenylene precursor **3-2** (see subsections 3.3.3 and 3.3.4). This peak could be completely removed by fractionation using recycling preparative SEC, providing precursor **3-31-I'** with M_w of 36,000–65,000 g/mol, M_n of 27,000–45,000 g/mol, and small PDI value of 1.3–1.4 based on the SEC analysis (Figure 3-34b).

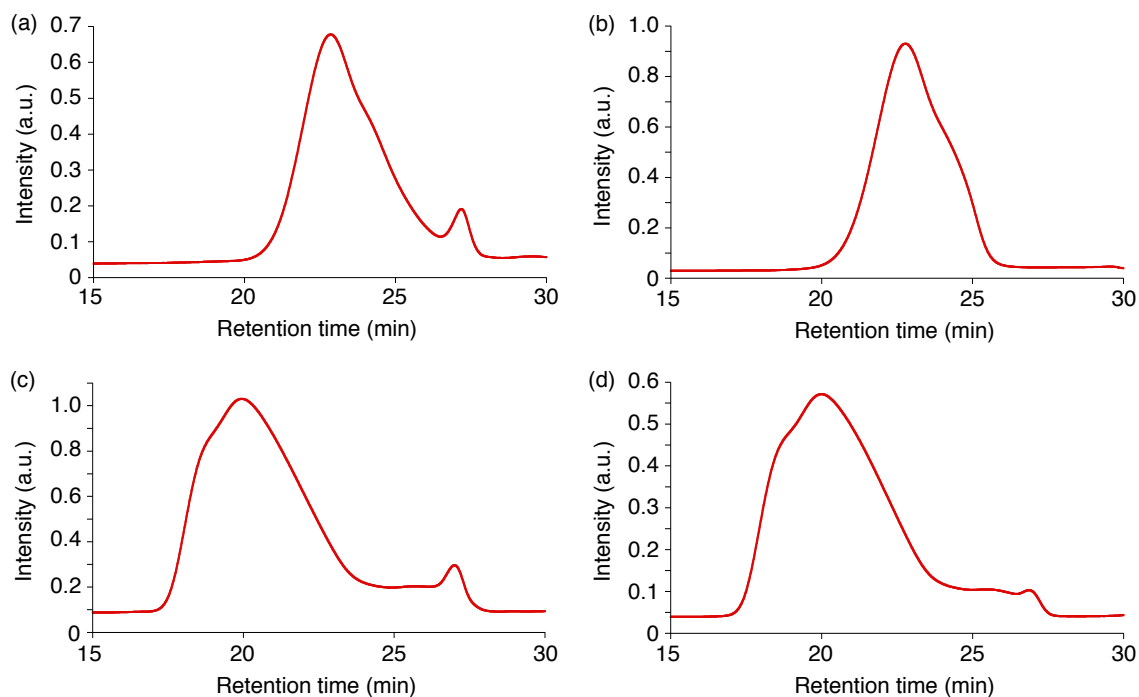


Figure 3-34. Normalized SEC profiles of polyphenylene precursor **3-31**; (a), (b) prepared in Ph_2O at 151 mM (a) before and (b) after fractionation by recycling preparative SEC; (c), (d) prepared in a melt (c) before and (d) after fractionation by using a preparative SEC column (eluent: THF, 1.0 mL/min, UV detector).¹⁰

When the polymerization of monomer **3-25** was carried out in a melt at 260–270 °C for 3 h, polyphenylene precursor **3-31-II** with M_w of 150,000–350,000 g/mol, M_n of 38,000–58,000 g/mol, and PDI of 3.9–6.0 was obtained based on the SEC analysis. Similar to the case of monomer **3-1** with the dodecyl chains, the polymerization of monomer **3-25** in a melt afforded precursor **3-31-II** with very high molecular weights, which was comparable to those obtained with precursor **3-2** in a melt (Table 3-1, entry 4). The SEC profile of **3-31-II** also displayed a peak at ~27 min, indicating the presence of small oligomers (Figure 3-34c). Precursor **3-31-II** did not pass through a syringe filter with 200-nm pores, and could not be fractionated by our recycling preparative SEC system. Precursor **3-31-II** was thus manually separated by using a preparative SEC column to give precursor **3-31-II'** with M_w of 160,000–370,000 g/mol, M_n of 47,000–75,000 g/mol, and PDI of 3.4–4.9. Much of the smaller oligomer, corresponding to the peak at ~27 min, could be removed by this method although not completely (Figure 3-34d). The reprecipitation method was not as effective for the fractionation of precursor **3-31** as it was for precursor **3-2**, presumably because of the higher solubility of precursor **3-31** with the bulkier alkyl chains.

Next, MALDI-TOF MS analysis of polyphenylene precursor **3-31** was carried out, using a fraction with M_w of 8,400–12,000 g/mol, M_n of 7,700–11,000 g/mol, and PDI of 1.1, which was obtained during the fractionation of **3-31-I** with recycling preparative SEC. The narrow molecular weight distribution of this sample allowed the MALDI-TOF MS analysis with better resolution. In the linear-mode analysis, a regular pattern of peaks were observed, reaching $m/z = \sim 25,000$ (Figure 3-35). The interval between the peaks was ~1,052, in agreement with the molecular weight of one repeating unit of **3-31**, i.e. 1,054. The small peaks visible between the main peaks were derived from the fragmentation of the alkyl chains.^{18,22} In the reflectron-mode analysis, five peaks were clearly observed at $m/z = 5,294, 6,348, 7,402, 8,455, 9,510$, which corresponded pentamer, hexamer, heptamer, octamer, and nonamer, respectively, with a sodium ion (Figure 3-36). All these peaks were consistent with the molecular weights of the oligomers without the carbonyl group, indicating the formation of cyclic oligomers through the intramolecular *Diels–Alder* cycloaddition, which was also observed for precursor **3-2** (Figure 3-14).²⁸

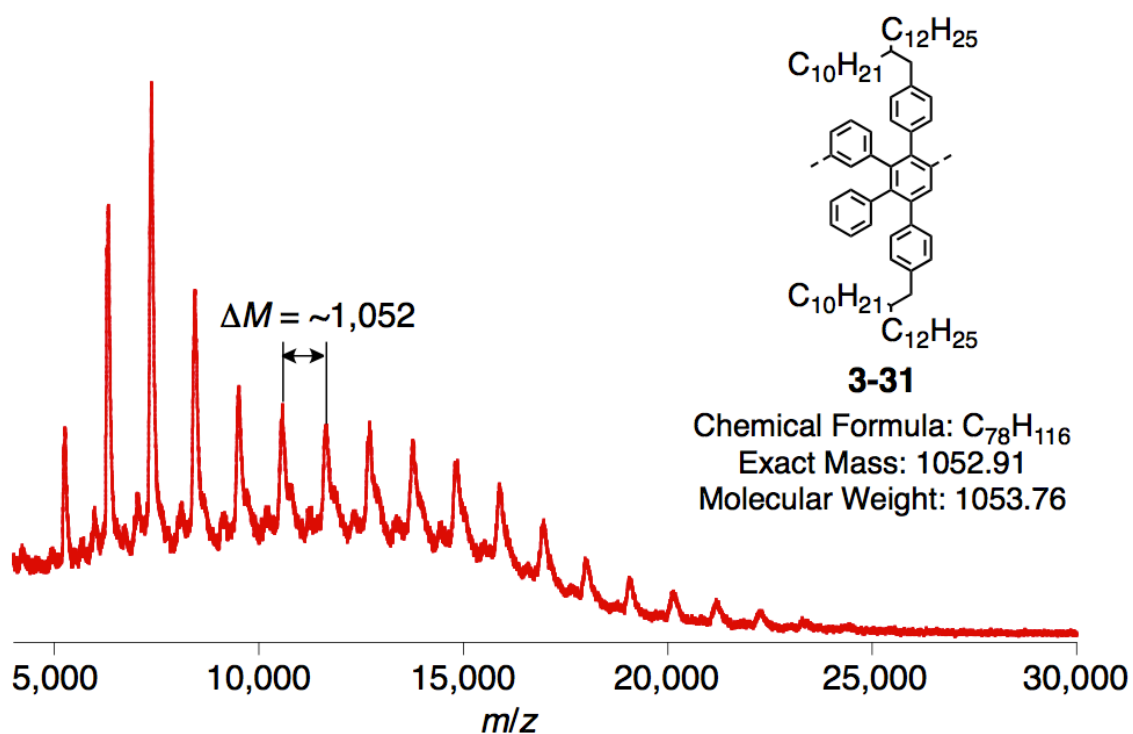


Figure 3-35. Linear-mode MALDI-TOF MS analysis of polyphenylene polymer **3-31** (solid-state sample preparation, matrix: TCNQ).¹⁰

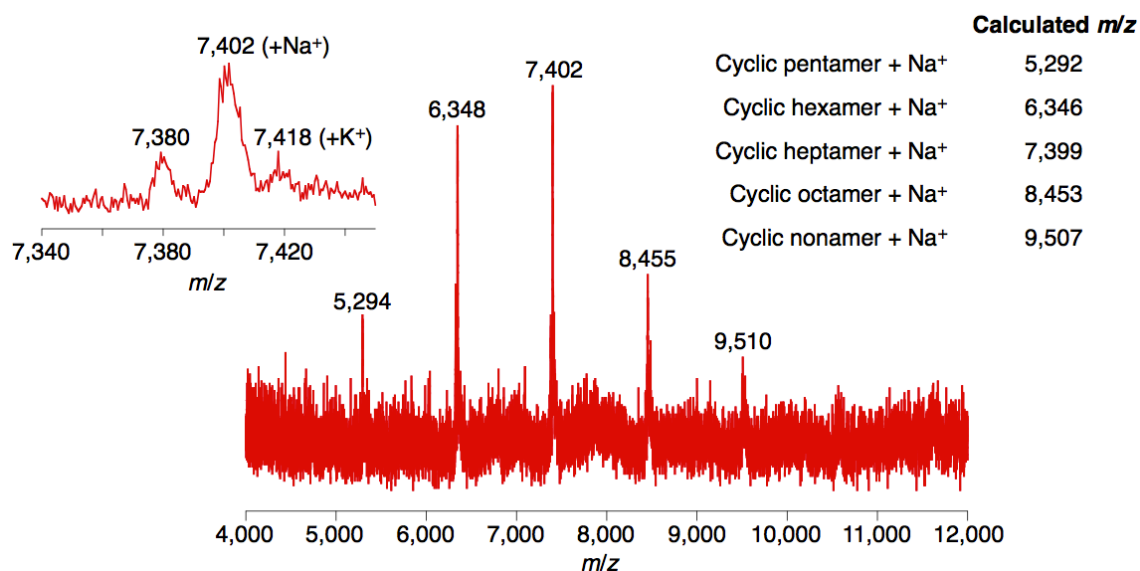


Figure 3-36. Reflectron-mode MALDI-TOF MS analysis of polyphenylene polymer **3-31** (solid-state sample preparation, matrix: TCNQ), inset: zoomed spectrum and calculated m/z of cyclic oligomers with a sodium ion.¹⁰

Finally, precursors **3-31-I'** and **3-31-II'** were subjected to the intramolecular oxidative cyclodehydrogenation in the same condition as the fabrication of GNR **3-3**, using seven equivalents of iron(III) chloride for one hydrogen to be removed, and yielded GNRs **3-26-I** and **3-26-II**, respectively, as dark purple powders (Figure 3-37). The highly defined structure of GNRs **3-26-I** and **3-26-II** was corroborated spectroscopically and microscopically as discussed in the next subsection. The average lengths of GNRs **3-26-I** and **3-26-II** could be estimated from M_w of the precursors to be ca. 25–45 and ca. 110–260 nm, respectively. Remarkably, the dispersibility of the GNRs was starkly enhanced by the substitution with 2-decyltetradecyl chains, and the concentration of stable dispersions of GNR **3-26** could reach as high as 0.2 mg/mL in THF, which was over one order of magnitude higher than that of GNR **3-3** with the dodecyl chains. Furthermore, GNR **3-26** was readily dispersible in other conventional organic solvents such as chloroform and dichloromethane, where GNR **3-3** showed no dispersibility.

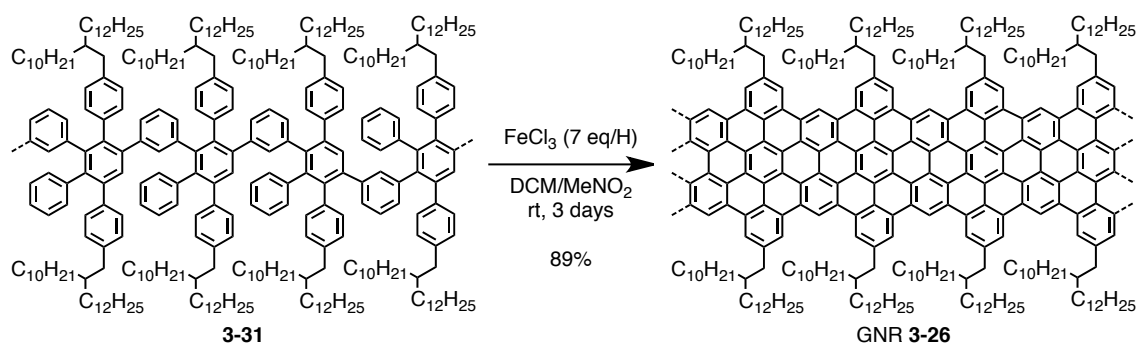


Figure 3-37. Cyclodehydrogenation of polyphenylene precursor **3-31** into GNR **3-26**.

3.6.2 Spectroscopic characterizations of GNR **3-26**

Polyphenylene **3-31** and GNR **3-26** were firstly analyzed by FTIR spectroscopy in order to evaluate the efficiency of the “graphitization” (Figure 3-38). Polyphenylene **3-31** as well as GNR **3-26** showed mostly identical spectra as those of precursor **3-2** and GNR **3-3**, respectively (see Figure 3-20). Briefly, the spectrum of precursor **3-31** displayed *opla* C-H deformation bands at 698, 793, 840, and 897 cm^{-1} , derived from mono-, and di-substituted benzene rings, which all disappeared after the cyclodehydrogenation to GNR **3-26**. The signal triad from aromatic C-H stretching vibrations at 3,022, 3,054, and 3,086 cm^{-1} were starkly suppressed, and a band appeared

at 868 cm^{-1} in the spectrum of GNR **3-26**, which could be assigned to the *opla* band from the aromatic C-H at the cove position.⁴² All these observations were in line with the spectra of GNR **3-3** as well as dimer **3-5** and trimer **3-7**, and there was no evident difference (Figure 3-20), supporting the efficient synthesis of GNR **3-26**.

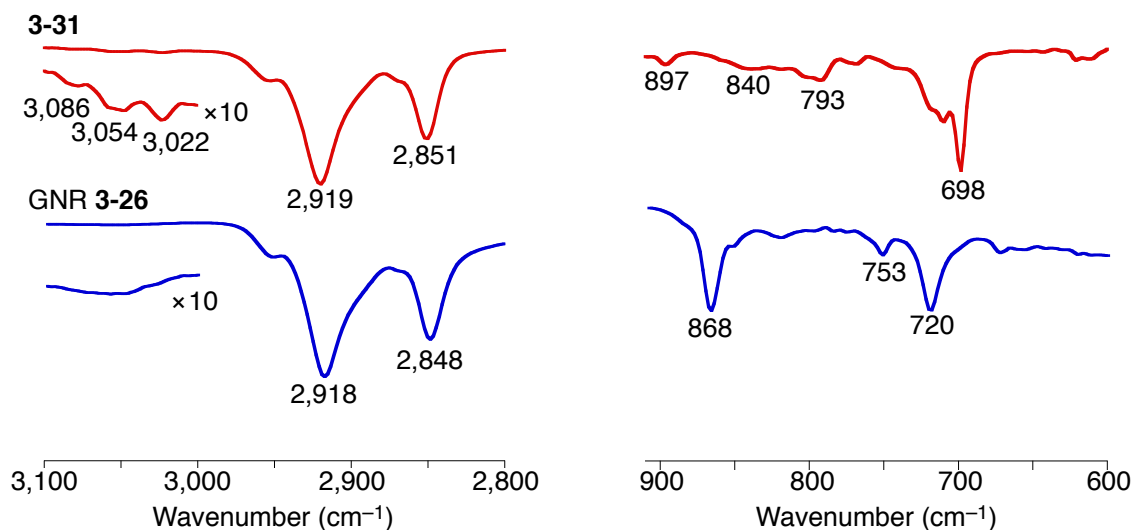


Figure 3-38. Representative FTIR spectral regions of polyphenylene precursor **3-31** (red line) and GNR **3-26** (blue line).¹⁰

Next, Raman spectroscopic analysis of GNR **3-26** was carried out by [REDACTED] and [REDACTED], and compared with that of GNR **3-3**. As shown in Figure 3-39, GNR **3-26** displayed basically the same spectrum as that of GNR **3-3** with all D, G, 2D, D + D', and 2D' peaks at the same wavenumbers. Further, the resonant peak from low-frequency RBLM was also observed for GNR **3-26** at the same position as that of GNR **3-3**, i.e. at $\sim 235\text{ cm}^{-1}$ (Figure 3-39, inset, see also subsection 3.4.2). There was no noticeable difference between the spectra of GNRs **3-3** and **3-26** except for those within the range of measurement error, which was in agreement with the fact that GNR **3-26** has the same core structure as that of GNR **3-3** and the alkyl chains do not affect their Raman spectra. This result corroborated the high uniformity of the GNRs in the obtained sample of GNR **3-26**, which was comparable to the case of GNR **3-3**. Additionally, the UV-vis absorption spectrum of GNR **3-26** was also very similar to that of GNR **3-3**.¹⁰ These results from spectroscopic characterizations supported the highly defined structure of GNR **3-26** comparable to that of GNR **3-3**.

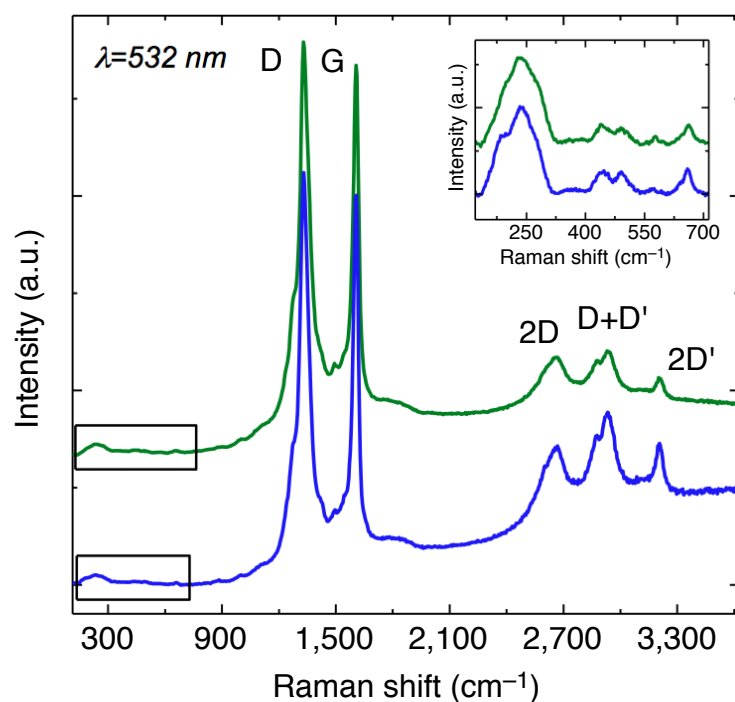


Figure 3-39. Comparison of Raman spectra of GNR 3-26 (green) and GNR 3-3 (blue) measured at 532 nm on powder samples with laser power below 0.1 mW.¹⁰

3.6.3 AFM visualization of GNR 3-26

AFM visualization was next performed on films of GNR 3-26-II drop-cast on HOPG surfaces from a dispersion in TCB, by the group of [REDACTED] at Katholieke Universiteit Leuven, Belgium. Remarkably, highly ordered self-assembled monolayers of straight and uniform GNRs was demonstrated with longitudinal length of over 200 nm (Figure 3-40a). The “kinked” structures observed in the STM images of GNR 3-3 (Figures 3-25 and 27) were not found in the AFM image of GNR 3-26-II. It is known that the persistence length of poly(phenylene vinylene) derivatives increases as the size of their side chains becomes larger.⁹⁰ On this basis, it is reasonable that GNR 3-26-II with the bulkier 2-decyltetradecyl chains has a stiffer structure than that of GNR 3-3 with the dodecyl chains, which might be the reason for the absence of the “kinks” in the AFM image of GNR 3-26-II. On the other hand, if the “kinks” observed for GNR 3-3 were related to structural defects formed through the cyclodehydrogenation at undesired conformations, the absence of the “kinks” for GNR 3-26-II could be explained by the fact that the bulkier 2-decyltetradecyl chains could more efficiently hamper the

“undesired” conformations, exclusively leading to the “straight” GNRs (see also Figure 3-2).

The periodicity observed in this self-assembled structure of GNR **3-26-II** was 4.1 ± 0.1 nm (Figure 3-40b), which was in good agreement with to the calculated width of GNR **3-26** including the alkyl chains, i.e. 4.15 nm (Figure 3-40c). This result indicated that the bulky 2-decyltetradecyl chains, densely attached to the peripheral positions of GNR **3-26**, did not allow interdigitation of the alkyl chain, and thus lead to the formation of the self-assembled layers, where the GNRs were simply aligned next by next parallel to each other without overlapping. This is in stark contrast to the self-assembled structures of GNR **3-3** with less bulky dodecyl chains, where the GNRs were partially stacked due to the strong π - π interaction (Figure 3-25). The observed length of over 200 nm was also consistent with the average length of ca. 110–260 nm estimated for GNR **3-26-II**, and further demonstrated the enhanced dispersibility of

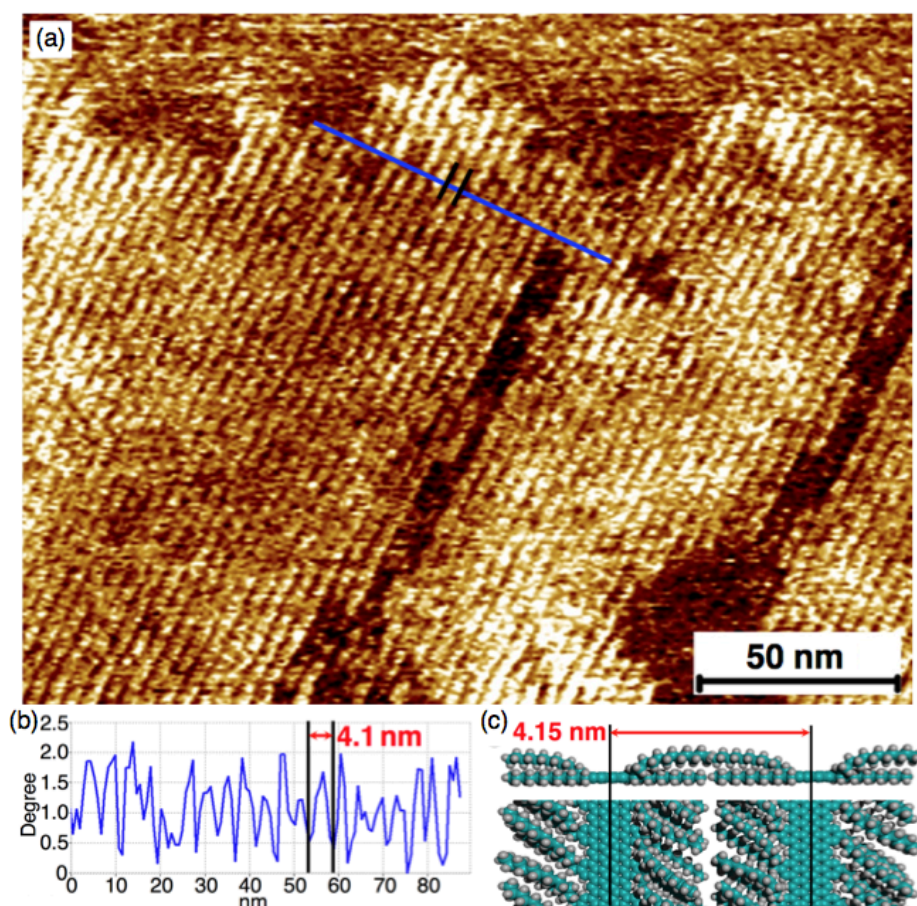


Figure 3-40. (a) An AFM phase image of GNR **3-26** on HOPG (dry film), demonstrating straight nanoribbons of over 200 nm in length. (b) Profile (along the blue line in the panel (a)) of the AFM phase image of GNR **3-26**. (c) Molecular model of GNR **3-26**; blue, carbon; grey, hydrogen.¹⁰

GNR 3-26 compared to that of GNR 3-3, which allowed the visualization of the GNRs with the length of only up to 60 nm, regardless of the average length estimated for the sample. Additionally, GNRs with various lengths could be visualized by AFM in agreement with the relatively broad molecular weight distribution expected for GNR 3-26-II (Figure 3-41). Figure 3-41a–c displays height and phase AFM images of GNR 3-26-II showing domains extended to several hundred nanometers, suggesting the presence of GNRs longer than 400 nm and/or end-to-end packing of more than one GNRs. On the other hand, shorter GNRs were also observed, during the AFM visualization of GNR 3-26-II, as separate patches on HOPG as shown in Figure 3-41d–g.

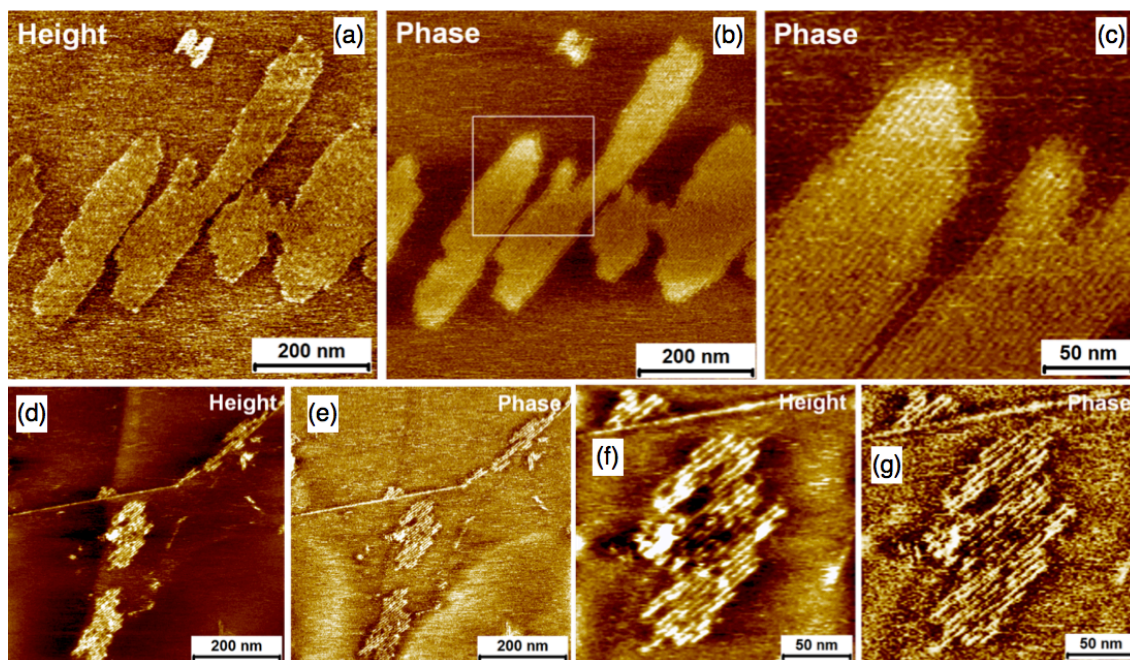


Figure 3-41. AFM images of GNR 3-26-II adsorbed on the HOPG surface: (a) a height and (b) a phase image showing domains that extend several hundred nanometers, (c) a magnified image of the squared region in panel (b), and (d), (f) height and (e), (g) phase images showing shorter GNRs segregated into separate patches on the surface of HOPG.¹⁰

In order to obtain further insight into the structure of GNR **3-26-II**, STM analysis was performed at the Au(111)/TCB interface by the group of Prof. Steven de Feyter at Katholieke Universiteit Leuven, Belgium (Figure 3-42). Interestingly, the obtained STM image displayed isolated GNRs with “kinked” structures, which closely resembled the result from GNR **3-3** (Figure 3-27), whereas the same sample of GNR **3-26-II** showed no “kink” in the dry films on the HOPG surfaces (Figure 3-40). Considering the fact that no “kink” was observed on the dry films, where all the GNRs extracted out from the powders into the dispersions were deposited, it is reasonable that the dispersions of GNR **3-26-II** did not contain structurally “kinked” GNRs, i.e. non-straight GNRs derived from the cyclodehydrogenation at undesired conformations. On this basis, the “kinked” structures observed in the STM image of GNR **3-26-II** at the Au(111)/TCB interface were most likely due to the folding and/or bending of structurally “straight”, but mechanically flexible GNRs (see also the discussion in subsection 3.4.5).

The lengths of the GNRs tracked in the STM image of GNR **3-26-II** were in the range of ~30–65 nm (Figure 3-42), which was shorter than the estimated average length of ca. 110–260 nm as well as many of the GNRs observed in the AFM image (>200 nm). This result was presumably because longer and less soluble GNRs stayed inside the aggregates in the dispersion, while shorter and more soluble GNRs were preferentially adsorbed at the solid-liquid interface. These shorter GNRs observed in the STM image corresponded to the shorter GNRs displayed in the AFM images inside the small patches isolated from the large domains (Figure 41d–g).

These results from AFM and STM investigations in combination with the spectroscopic characterizations demonstrated the efficient synthesis of structurally well-defined GNR **3-26** although the unambiguous elucidation of the structural perfection could not be achieved through the available methods. The dispersibility and liquid-phase processability were clearly improved compared to those of GNR **3-3** owing to the bulkier alkyl chains densely installed on the peripheral positions, which enabled the visualization of the GNRs longer than 200 nm. Despite the presence of aggregates in the dispersions, such high liquid-phase processability is expected to enable the fabrication of single-ribbon devices for further investigations on the electronic transport properties.

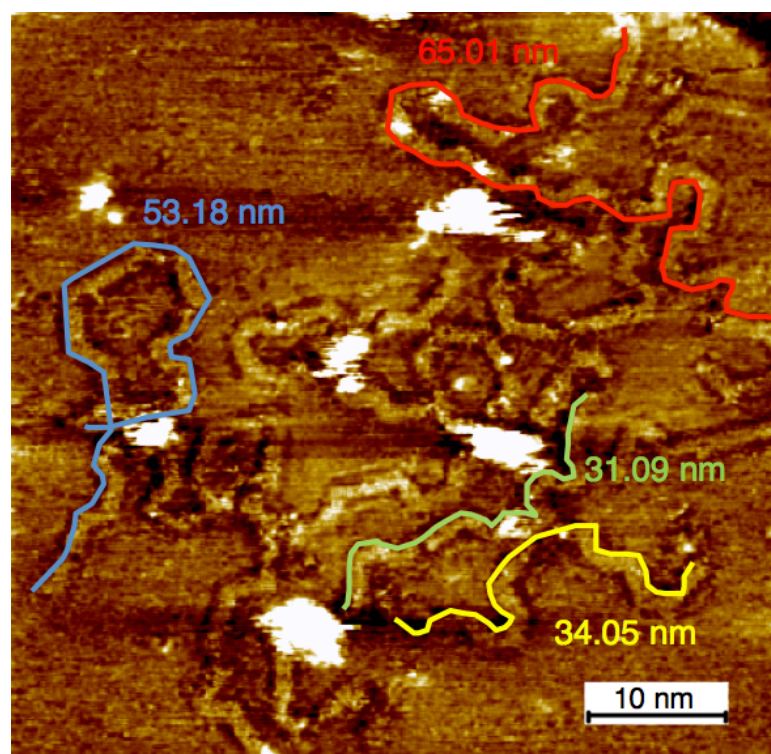


Figure 3-42. An STM image of GNR 3-26-II at the Au(111)/TCB interface, displaying isolated GNRs with “kinks”.

3.7 Edge chlorination of structurally defined GNRs

3.7.1 Design for the edge chlorination of GNRs

Recently, atomically precise edge chlorination of various PAHs was achieved by [REDACTED] in our research group, providing edge-chlorinated nanographenes with number of carbon atoms ranging from 42 to 222.⁹¹ The energy levels of the nanographenes were modified by the chloro groups installed on the edges to attain n-type nanographenes with lower bandgaps. Further, the planarity of the nanographene molecules was distorted by the steric hindrance between the chloro groups densely attached on the peripheral positions, which drastically enhanced the solubility of the nanographenes. The increased solubility enabled their characterizations in solutions, solution processing, and even the X-ray single crystal analysis of unprecedentedly large PAH molecules.

This edge-chlorination method is also beneficial for the bottom-up synthesized GNRs, which allows the modification of their energy levels to achieve GNRs with n-type properties and lower bandgaps. The dispersibility of the GNRs might also be enhanced by the distortion of the planarity, leading to GNRs with higher liquid-phase processability. In order to enable the efficient edge chlorination, preparation of non-substituted GNRs would be desirable, because the linear and branched alkyl chains of GNRs **3-3** and **3-26**, respectively, cannot be replaced with the chloro groups and presumably chlorinated at random positions. However, as discussed in section 3.1, the synthesis of longitudinally extended and straight GNRs through the *AB*-type *Diels–Alder* polymerization of monomer **3-1** or its derivatives can only be possible with bulky substituents at the peripheral positions, which hamper the cyclodehydrogenation at “undesired” conformations (Figure 3-2). Thus, a non-substituted derivative of monomer **3-1** will most probably yield structurally undefined GNRs with “kinks” at arbitrary positions.

On the other hand, [REDACTED] has revealed that *tert*-butyl groups can be readily substituted with the chloro groups under the chlorination condition, through a model reaction on hexa-*tert*-butyl-HBC.⁹¹ Based on this result, GNR **3-32**, bearing *tert*-butyl groups instead of long alkyl chains, was designed for the synthesis of chlorinated GNR **3-33** (Figure 3-43). The *tert*-butyl groups are most likely able to sterically hinder the undesired conformations during the “graphitization”, similar to the

dodecyl and 2-decyltetradecyl groups, to ensure the exclusive formation of straight GNRs. Further, the *tert*-butyl groups improve the solubility of the polyphenylene precursor to facilitate the removal of smaller oligomers as well as enable efficient cyclodehydrogenation into GNR **3-32**. It has been unambiguously revealed from the studies on the nanographenes that the cove position cannot be chlorinated, most probably because of the steric hindrance from the chloro groups installed on the neighboring positions.⁹¹ Therefore, chlorination of GNR **3-32** yields chlorinated GNR **3-33** most likely with the structure shown in Figure 3-43.

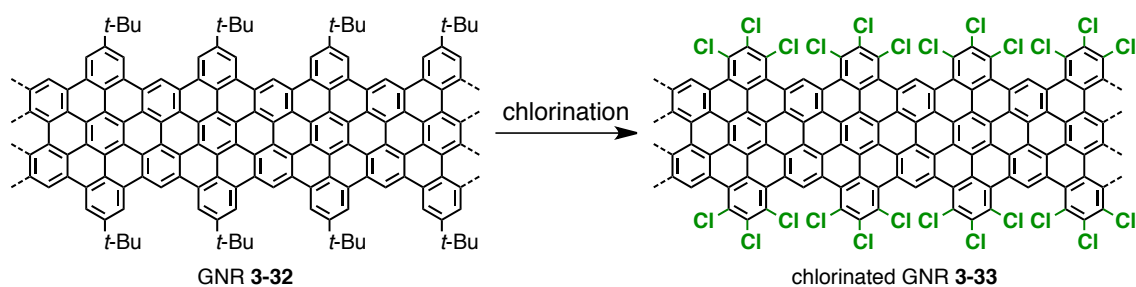


Figure 3-43. Edge chlorination of GNR **3-32** with *tert*-butyl groups.

3.7.2 Synthesis of GNR **3-32** with *tert*-butyl groups

For the fabrication of GNR **3-32**, *AB*-type monomer **3-38** with *tert*-butyl groups was initially synthesized as shown in Figure 3-44. Bis[4-(*tert*-butyl)phenyl]acetone **3-35** was prepared by the self-condensation of 4-*tert*-butylphenylacetic acid (**3-34**) with *N,N*-dicyclohexylcarbodiimide (DCC) and *N,N*-dimethyl-4-aminopyridine (DMAP).⁹² Benzil **3-36** was obtained by *Sonogashira* coupling of 3-bromobenzil (**3-17**) with triisopropylsilylacetylene in 99%, and then subjected to *Knoevenagel* condensation with **3-35** to give functionalized tetraphenylcyclopentadienone **3-37** in 53% yield. Subsequent removal of the triisopropylsilyl-protecting group from **3-37** by treatment with tetra-*n*-butylammonium fluoride (TBAF) provided *AB*-type monomer **3-38** in 97% yield.

AB-type *Diels–Alder* polymerization of monomer **3-38** was then carried out by refluxing in diphenyl ether at the concentration of 456 mM for 29 h, yielding polyphenylene precursor **3-39** with M_w of 83,000–170,000 g/mol, M_n of 16,000–21,000 g/mol, and PDI of 5.2–8.1 based on the SEC analysis against PPP and PS standards (Table 3-2). The SEC profile of precursor **3-39** displayed a peak at ~28 and ~21 min,

corresponding to M_p of ca. 2,000–2,300 and ca. 92,000–180,000 g/mol, respectively (Figure 3-45a), which indicated the presence of small oligomers as was observed for polyphenylene precursors **3-2** and **3-31** (see subsections 3.3.4 and 3.6.1). These small oligomers could be completely removed by repeated reprecipitation from a mixture of THF and MeOH with an optimized ratio, similar to the fractionation of precursor **3-2-III**: MeOH was gradually added to a solution of **3-39** in THF until the precipitation started (THF:MeOH = 2:1 in volume ratio), followed by the collection of the precipitates by centrifugation (13,400 rpm, 1 min). The precipitates were washed with a mixture of THF and MeOH (2:1 in volume ratio) to give precursor **3-39-I** with M_w of 120,000–260,000 g/mol, M_n of 87,000–160,000 g/mol, and PDI of 1.4–1.6, which did

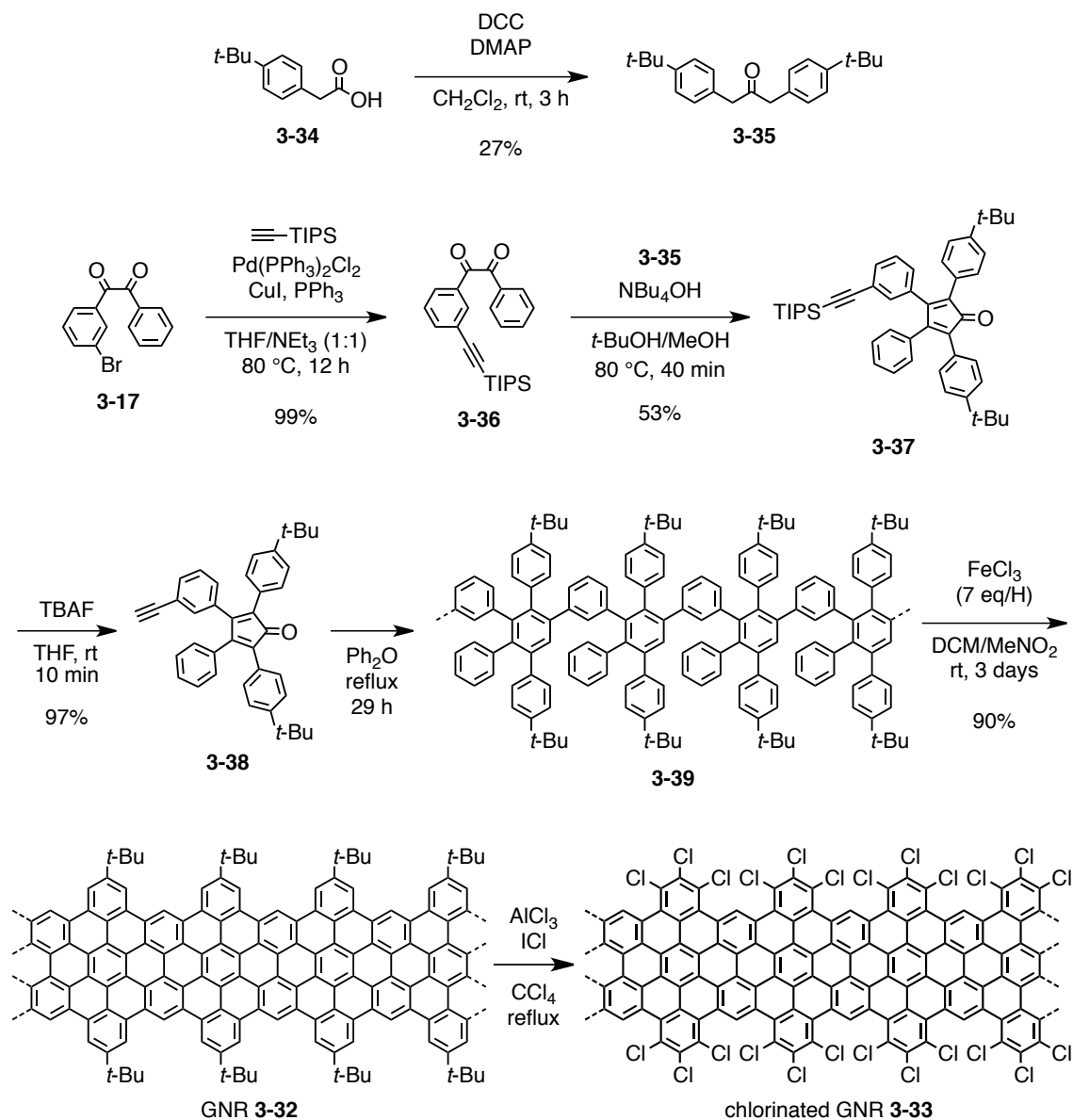


Figure 3-44. Synthesis of GNR **3-32** with *tert*-butyl groups and then chlorinated GNR **3-33**.

not show the peak at ~28 min in the SEC profile (Figure 3-45b). Next, the same reprecipitation protocol was applied to the polymers recovered from the supernatant solutions with THF:MeOH = 10:7 in volume ratio to provide precursor **3-39-II** with M_w of 120,000–250,000 g/mol, M_n of 81,000–160,000 g/mol, and PDI of 1.5–1.6. Considering the almost identical molecular weight values, precursors **3-39-I** and **3-39-II** were combined prior to the cyclodehydrogenation to give precursor **3-39-I+II** with M_w of 120,000–260,000 g/mol, M_n of 87,000–170,000 g/mol, and PDI of 1.4–1.5 (Figure 3-45b).

Table 3-2. M_w , M_n , and PDI values of precursor **3-39** before and after the fractionation.

	3-39	3-39-I	3-39-II	3-39-I+II	3-39-III	3-39-IV
M_w (kg/mol)	83–170	120–260	120–250	120–260	55–100	32–58
M_n (kg/mol)	16–21	87–160	81–160	87–170	44–77	16–24
PDI	5.2–8.1	1.4–1.6	1.5–1.6	1.4–1.5	1.3–1.4	2.0–2.4

M_w and M_n were estimated by the SEC analysis based on PPP and PS standards and given with ranges, corresponding to $M_{w,PPP}-M_{w,PS}$ and $M_{n,PPP}-M_{n,PS}$, respectively (eluent: THF, UV detector). PDI values were calculated by M_w/M_n . All the SEC results have a margin of error of $\pm 10\%$.

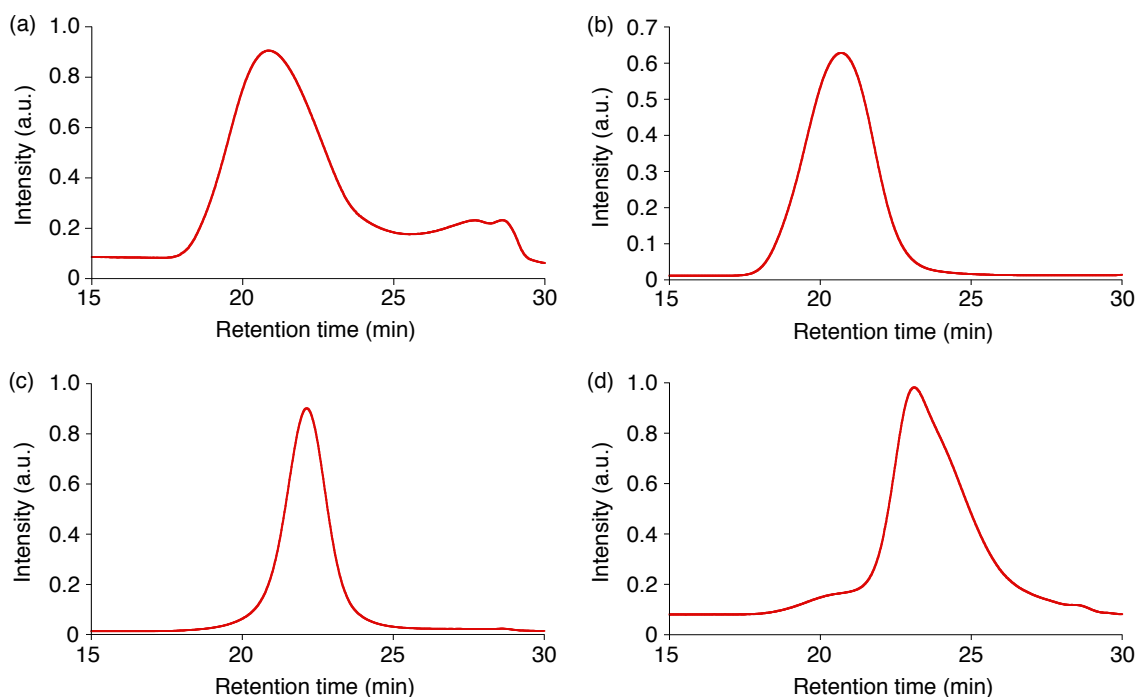


Figure 3-45. Normalized SEC profiles of (a) precursor **3-39** before the fractionation, (b) precursor **3-39-I+II**, (c) precursor **3-39-III**, and (d) precursor **3-39-IV** (eluent: THF, 1.0 mL/min, UV detector).

Notably, precursor **3-39** with various molecular weights could be obtained by further applying this reprecipitation protocol to the recovered polymers with different ratio of the solvents (Table 3-2): THF:MeOH = 5:4 in volume ratio yielded precursor **3-39-III** with M_w of 55,000–100,000 g/mol, M_n of 44,000–77,000 g/mol, and PDI of 1.3–1.4 (Figure 3-45c), and then reprecipitation of the recovered polymers with THF:MeOH = 5:6 in volume ratio afforded precursor **3-39-IV** with M_w of 32,000–58,000 g/mol, M_n of 16,000–24,000 g/mol, and PDI of 2.0–2.4 (Figure 3-45d). This result indicated that the solubility of precursor **3-39** decreases as the molecular weight increases. Importantly, these fractions with different molecular weights can be used for the fabrication of GNR **3-32** with different lengths.

Next, MALDI-TOF MS analysis was carried out on the oligomers of precursor **3-39**, corresponding to the peak at ~28 min in the SEC profile (Figure 3-45a), which were recovered from the supernatant solutions during the fractionation process. Linear-mode analysis of the oligomers showed a regular mass pattern, similar to those of precursors **3-2** and **3-31**, with the peaks extending up to $m/z = \sim 18,000$. The interval between the peaks was $m/z = \sim 494$ in agreement with the molecular mass of the repeating unit of precursor **3-39**, i.e. $C_{38}H_{36}$: 493 (Figure 3-46). Reflectron-mode measurement on the oligomers of precursor **3-39** displayed signals at $m/z = 1,972, 2,463, 2,956, 3,449, 3,942, 4,434, 4,927, 5,420, 5,912, 6,404, 6,989, 7,391, 7,882, 8,378, 8,869$, which all corresponded to the molecular masses of oligomer structures, i.e. from tetramer to octadecamer, without the cyclopentadienone moieties at the termini (Figure 3-47). This result suggested that these oligomers had undergone the head-to-tail *Diels–Alder* cycloaddition to form cyclic oligomers (see Figure 3-14). Notably, the well-dissolved isotopic distribution could be observed for the peak of the hexamer, which was in perfect agreement of the simulated pattern for the cyclic hexamer (Figure 3-47, inset). Formation of the cyclic oligomers was consistent with the results from precursors **3-2** and **3-31** and indicated that these oligomers were precluded from further polymerization by the intramolecular cycloaddition (see also subsection 3.3.3).

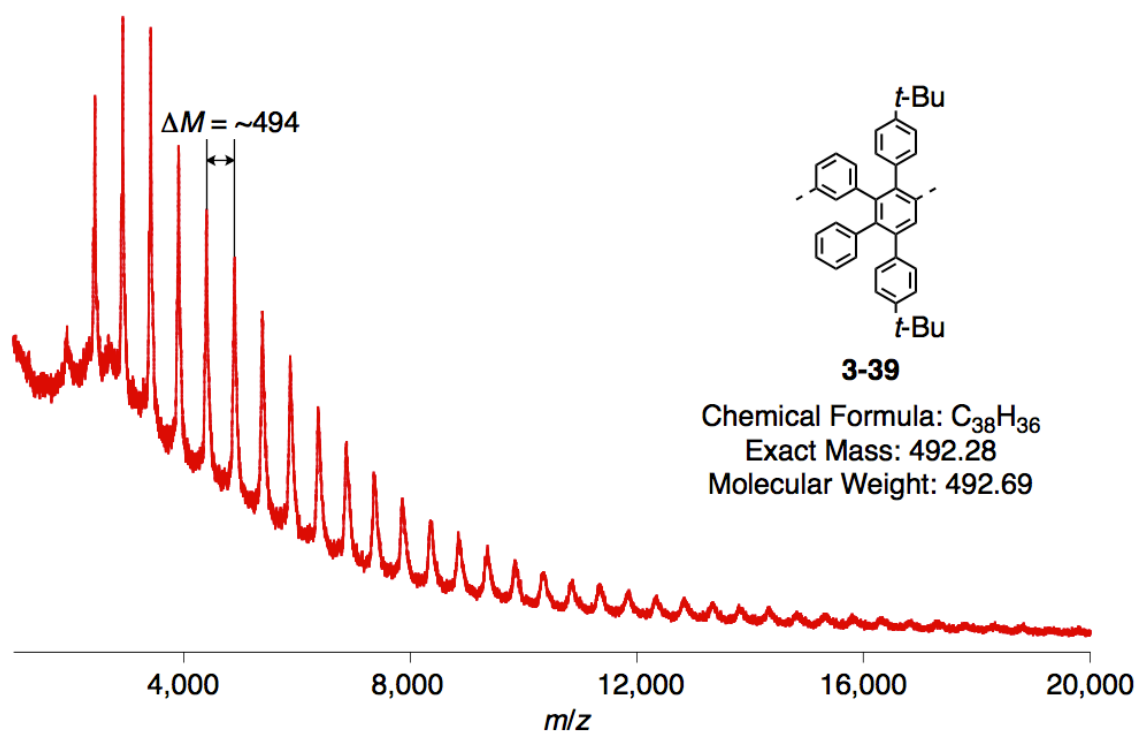


Figure 3-46. Linear-mode MALDI-TOF MS analysis of the oligomers of precursor **3-39** recovered from the supernatant solutions (solid-state sample preparation, matrix: TCNQ).

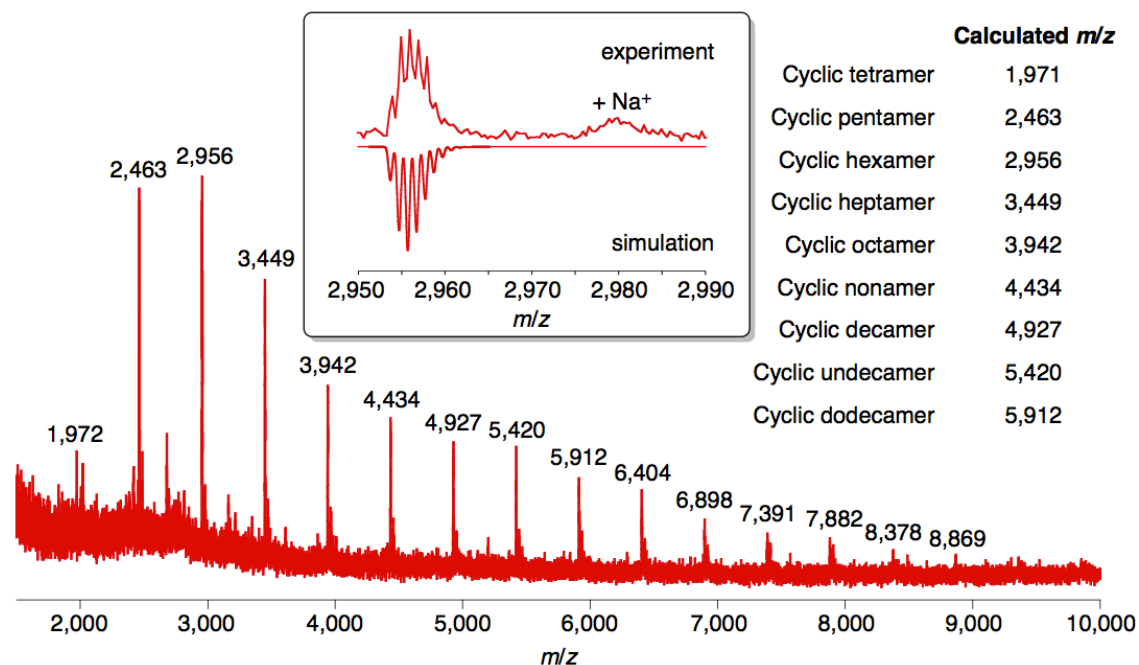


Figure 3-47. Reflectron-mode MALDI-TOF MS analysis of the oligomers of precursor **3-39** recovered from the supernatant solutions (solid-state sample preparation, matrix: TCNQ), inset: isotopic distribution of the hexamer in agreement with the simulation, and calculated m/z of cyclic oligomers.

Precursor **3-39-I+II** was “graphitized” into GNR **3-32** by the intramolecular oxidative cyclodehydrogenation in the same condition as the syntheses of GNRs **3-3** and **3-26**, employing seven equivalents of iron(III) chloride for one hydrogen to be removed (Figure 3-44). FTIR spectroscopic analysis of precursor **3-39** and GNR **3-32** showed the disappearance of the *opla* C-H deformation bands at 698, 749, 794, 834, and 895 cm^{-1} upon the cyclodehydrogenation, which were derived from mono-, and di-substituted benzene rings (Figure 3-48). Further, the signal triad from aromatic C-H stretching vibrations observed for precursor **3-39** at 3,081, 3,053, and 3,026 cm^{-1} was not detected in the spectrum of GNR **3-32**. A new band appeared at 866 cm^{-1} , corresponding to the *opla* band from the aromatic C-H at the cove position, which might also be overlapped with vibration bands from the *tert*-butyl groups.⁹¹ All these changes were in line with those observed for GNRs **3-3** and **3-26**, and corroborated the successful formation of GNR **3-32** (see subsections 3.3.4 and 3.6.2). Additionally, no band was observed at 720 cm^{-1} in the spectrum of GNR **3-32**, which confirmed the assignment of this band, observed in the spectra of GNRs **3-3** and **3-26**, to the long alkyl chains. Raman and UV-vis absorption spectra of GNR **3-32** were basically identical to those of GNRs **3-3** and **3-26**, which further supported the highly efficient synthesis of GNR **3-32**. The average length of GNR **3-32** could be estimated from M_w of precursor **3-39-I+II** to be ca. 180–390 nm.

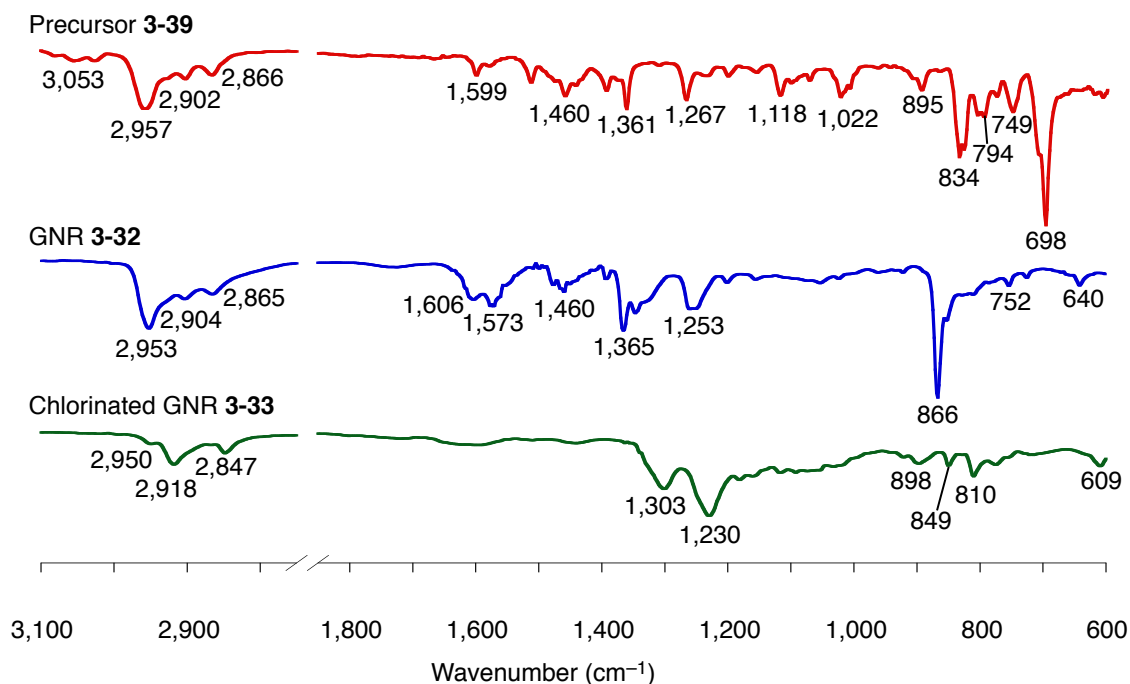


Figure 3-48. Normalized FTIR spectra of polyphenylene precursor **3-39** (red line), GNR **3-32** (blue line), and chlorinated GNR **3-33** (green line).

3.7.3 Edge chlorination of GNR 3-32 with *tert*-butyl groups

Next, the edge chlorination of GNR 3-32 was carried out by [REDACTED] by treatment with aluminum(III) chloride and iodine(I) chloride in refluxing carbon tetrachloride (Figure 3-44). In order to examine the efficiency of the chlorination, FTIR and X-ray photoelectron spectroscopy (XPS) analyses were subsequently performed. Comparison of the FTIR spectra of GNR 3-32 and chlorinated GNR 3-33 demonstrated stark attenuation of the stretching vibration and deformation bands derived from the *tert*-butyl groups at 2,953, 1,460, and 1,365 cm^{-1} (Figure 3-48). On the other hand, new bands appeared in the spectrum of chlorinated GNR 3-33 at 1,303, 1,230, 810, and 609 cm^{-1} , which were typical for the stretching modes of aromatic C–C and C–Cl bonds in chlorinated aromatic hydrocarbons.⁹³ These results were consistent with the FTIR spectra of chlorinated nanographenes, and corroborated the highly efficient substitution of the *tert*-butyl with the chloro groups upon the chlorination of GNR 3-32.⁹¹

XPS analysis of chlorinated GNR 3-33 provided more accurate data about the efficiency of the chlorination.⁹¹ Figure 3-49a and b display high-resolution XPS scans for C 1s and Cl 2p peaks, respectively. The bonding energies of these peaks were revealed to be the same as those of the chlorinated nanographenes, which proved that the chlorines were covalently attached to the aromatic cores of the GNRs.⁹¹ The atomic ratio of carbon to chlorine could be calculated from the peak areas in the spectra to be ca. 4.5 to 1, where the expected ratio for chlorinated GNR 3-33, i.e. $(\text{C}_{30}\text{Cl}_6\text{H}_2)_n$, was 5.0 to 1. This result suggested that the efficiency of the chlorination was approximately 90% for chlorinated GNR 3-33.

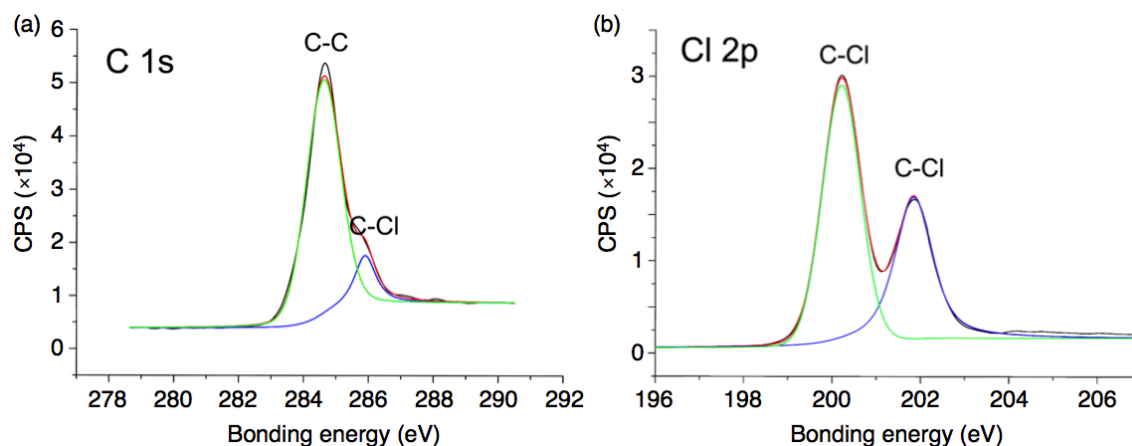


Figure 3-49. XPS spectra of chlorinated GNR 3-33; (a) C 1s XPS; signals at 284.6 and 285.9 eV; (b) Cl 2p XPS; signals at 200.2 eV (2p_{3/2}) and 201.8 eV (2p_{1/2}).⁹¹

Chlorinated GNR **3-33** showed good dispersibility in organic solvents such as NMP and TCB despite the absence of bulky alkyl chains, indicating the distortion of the planarity as was revealed for the chlorinated nanographenes. The concentration could reach ca. 0.05 mg/mL,⁹¹ which was comparable to that of GNR **3-3** with the dodecyl chains, demonstrating the effectiveness of the edge chlorination for enhancing the dispersibility of the GNRs. Nevertheless, this dispersibility was not as high as that of GNR **3-26** with the bulkier 2-decyltetradecyl chains, showing the limitation of this approach for the solubilization of the GNRs.

UV-vis absorption spectrum of chlorinated GNR **3-33** showed an absorption maximum at 590 nm, which was approximately 40 nm red-shifted compared to that of GNR **3-32** (Figure 3-50). The optical bandgap extracted from the spectrum was ca. 1.7 eV, demonstrating the lowering of the bandgap of about 0.2 eV by the edge chlorination. This red-shift of the absorption band upon the chlorination was very similar to those observed for the nanographenes, i.e. 40–50 nm.⁹¹ The decrease in the bandgap upon the chlorination could be explained based on the asymmetric stabilization of the HOMO and LUMO levels, i.e. The stabilization of the HOMO level was smaller, because the inductive effect of the electronegative chloro group was partially compensated by a mesomeric electron-donating effect.^{91,94,95}

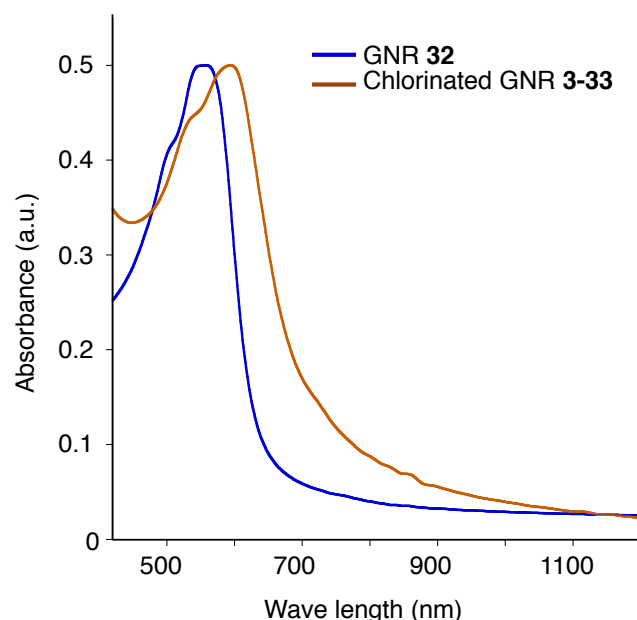


Figure 3-50. Normalized UV-Vis absorption spectra of GNR **32** (blue) and chlorinated GNR **3-33** (red) in TCB.⁹¹

These results demonstrated that GNR **3-32** could be efficiently (ca. 90%) chlorinated to GNR **3-33** with the *tert*-butyl groups also replaced by the chloro groups. The distortion of the planarity by the steric congestion bestowed good dispersibility on the chlorinated GNRs. The bandgap energy of the GNRs could be lowered by the chlorination, which provided an effective method for the tuning of the electronic properties of GNRs. Furthermore, a number of ligands have been developed in the recent years for efficient activation of aryl–Cl bonds in transition-metal-catalyzed coupling reactions such as *Suzuki*⁹⁶⁻⁹⁸ and *Sonogashira*⁹⁹⁻¹⁰² coupling. These methods as well as conventional nucleophilic substitution reactions can potentially be applied to chlorinated GNR **3-33**, where the chloro groups will serve as scaffolds for the introduction of a variety of other functional groups onto the edges of the GNRs. This will allow fabrication of GNRs with a broad range of functionalities for various purposes, including fine-tuning of their electronic properties, enhancement of their processability, as well as formation of GNR-based nanocomposites.

3.8 Preliminary investigations on the transport properties of the GNRs

3.8.1 FET devices on GNR films

In order to examine the applicability of thus synthesized liquid-phase processable GNRs, preliminary experiments on the fabrication of FET devices were performed by ██████████ in our research group. Highly doped silicon and a 230-nm thick SiO₂ film were employed as the gate electrode and the dielectric, respectively. Bottom-contact FET devices with channel lengths of 2.5–20 μm and a width of 10 mm were prepared by drop-casting dispersions, or suspensions, of GNR **3-3** in THF (2 mg/mL) onto Si/SiO₂ substrates with prepatterned contacts. Si/SiO₂ substrates were modified with self-assembled monolayers of hexamethyldisilazane (HMDS) by vapor deposition prior to the deposition of the GNRs, resulting in the contact angles of 93.2 ± 1.3°.

The FET devices thus prepared with GNR **3-3-III** showed low field-effect mobility of 6.1 × 10⁻⁴ cm²/V·s as an average from ~5 devices (Figure 3-51). FET devices with GNR **3-3-II** displayed slightly better average hole mobility of 8.7 × 10⁻⁴ cm²/V·s with maximum value of 0.001 cm²/V·s, but these values were more than one order of magnitude lower than that obtained with broader, but much shorter GNR **2-13**, i.e. 0.012 cm²/V·s (see subsection 2.2.4). The use of better-processable GNR **3-26** did not improve the roughness of the films and showed mobilities no better than those of GNR **3-3-III**. The mobility of GNR **3-26** was possibly lowered due to the bulkier and thus more insulating alkyl chains, which could interrupt the transport between the neighboring GNRs. The lower mobilities of GNRs **3-3** and **3-26** were most probably due to their lower dispersibility compared to that of shorter GNR **2-13**, which lead to worse organization of the GNRs in the films. Indeed, aggregation of the GNRs upon the solvent evaporation as well as rough morphology of the resulting films were obvious by the eye, rendering it necessary to develop another processing method to enable the preparation of homogeneous as well-organized films of the GNR.

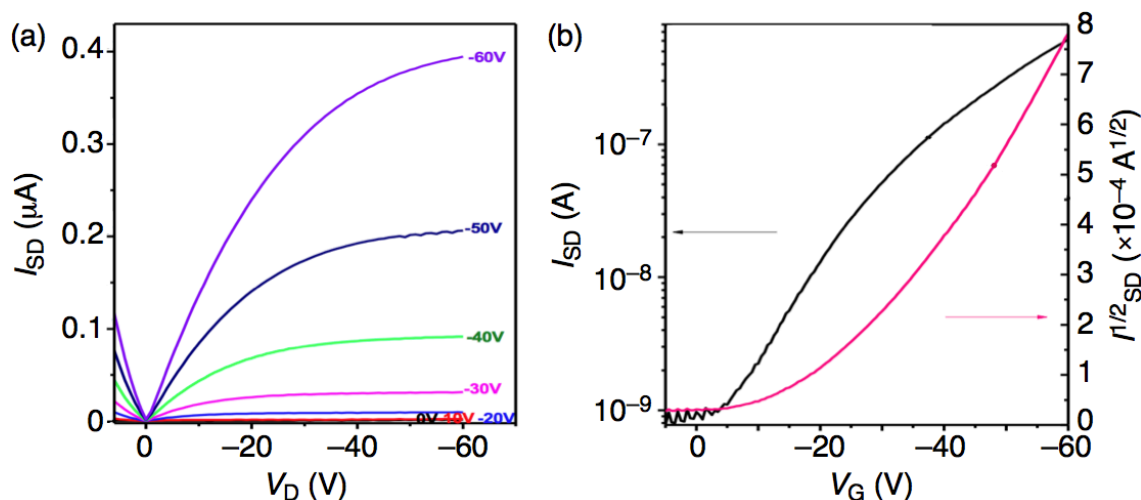


Figure 3-51. (a) Output characteristics at various gate biases V_G (0, -10, -20, -30, -40, -50, and -60 V) and (b) transfer curve at a source drain bias of $V_D = -60$ V of a bottom-gate bottom-contact device prepared with GNR 3-3-III.

In order to obtain homogeneous films of GNR 3-3, preparation of GNR films on PTFE membranes and subsequent transfer onto Si/SiO₂ substrates were attempted with [REDACTED] in our research group. First, a film of GNR 3-3 was prepared on a PTFE membrane (pore size: 200 nm) by filtering a transparent dispersion of GNR 3-3 in THF with concentration lower than 0.01 mg/mL (Figure 3-52). Next, the GNR film on the PTFE membrane was mechanically pressed onto a Si/SiO₂ substrate by using a vise, which lead to a successful transfer of the GNR film onto the substrate. Notably, the film thickness could be controlled by changing the amount and/or concentration of the dispersions filtered through the PTFE membrane.

Top-contact OFET devices were fabricated on thus transferred GNR films with thicknesses of e.g. ca. 100 and 760 nm, which were determined by a surface profiler (Figure 3-52). However, the mobilities obtained with these FET devices were all lower than 0.001 cm²/V·s, indicating that the quality of the films prepared by this method was similar to that of the drop-cast films. Indeed, observation by a surface profiler revealed the surface of the transferred GNR films to be very rough even with holes, which indicated the incomplete transfer of the GNR films from PTFE membranes to Si/SiO₂ substrates. These results denoted the necessity of rendering GNRs better processable in order to prepare well-organized films appropriate for the fabrication of FET device.

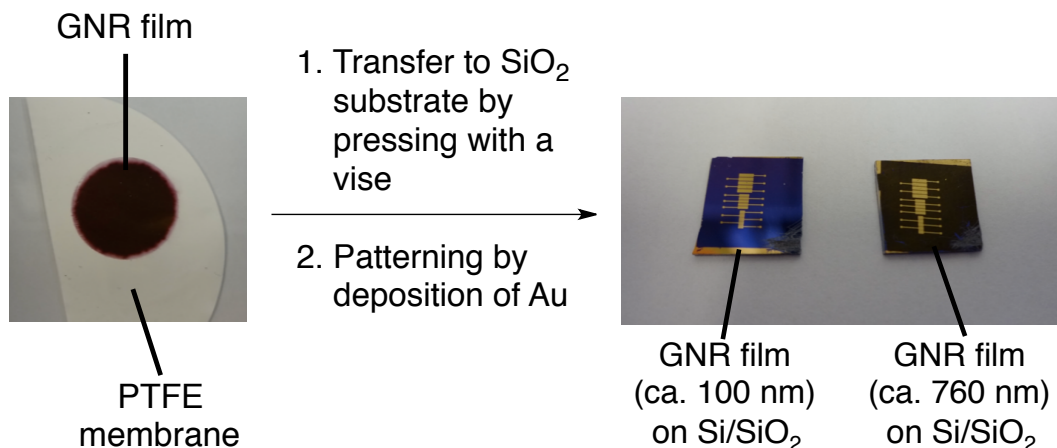


Figure 3-52. Preparation of a GNR film on a PTFE membrane and subsequent transfer onto a Si/SiO₂ substrate followed by fabrication of top-contact FET devices.

The mobilities observed for GNR **3-3** were far lower than the intrinsic mobility estimated by the THz spectroscopy studies (section 3.5), but at the same time reasonable, considering the fact that the channel lengths of 2.5–20 μm were too large to be bridged by continuous GNRs, and most likely the mobilities through a number of neighboring GNRs were measured. In contrast, only the intramolecular mobility was probed by the THz spectroscopy measurements and the effect from the intermolecular transport was negligible. This result indicated the necessity to build devices on single GNRs in order to appropriately evaluate the electronic properties of these bottom-up fabricated GNRs. GNR **3-3** with longitudinal extension of over 200 nm at least satisfies the length required for the fabrication of single-ribbon devices with the modern e-beam lithography technique. Investigation of the intramolecular transport properties of the GNRs has been attempted in collaboration with Prof. Mathias Kläui at Johannes Gutenberg-Universität Mainz. However, the deposition of extended GNRs on dielectric substrates turned out to be challenging because of the bad affinity between the GNRs and such substrates as well as high self-aggregation tendency of the GNRs.

3.8.2 GNRs with acetylthio groups at the termini

As discussed in the previous subsection, it turned out that the preparation of well-organized films with GNRs **3-3** or **3-26** on Si/SiO₂ substrates was still challenging and required optimization of the substrate surface to improve the interaction with the GNRs, e.g. by chemical functionalization with self-assembled monolayers, as well as further enhancement of the processability of the GNRs. Nevertheless, the low mobility observed from the FET devices on the rough films did not compromise the high intrinsic mobilities displayed by the THz spectroscopy experiments in dispersions, considering the absence of intramolecular transports in such bulk devices with micrometer-scale channel lengths. In order to investigate the intramolecular transport behavior of the GNRs, acetylthio groups were introduced at the termini of the GNRs as linkers, which could enhance the affinity of the GNR terminals to gold electrodes (Figure 3-53).¹⁰³ Thus, such GNRs with the thiol linkers can facilitate the bridging of the electrodes with continuous GNRs as well as potentially enable the fabrication of single-GNR transistors by employing the break junction method.¹⁰³⁻¹⁰⁵

The synthesis of GNR **3-43** terminated with the acetylthio groups was carried out through *Sonogashira* coupling of bromo-terminated GNR **3-41** as shown in Figure 3-53. For the endcapping with the bromo groups, the *AB*-type *Diels–Alder* polymerization of monomer **3-1** was stopped before the completion, i.e. after 7 h while the solution showed the purple color typical for the tetraphenylcyclopentadienone moiety. Subsequently, the ethynyl groups at the termini of the crude polymers were end-capped with cyclopentadienone **3-18** by refluxing for 4 h, and then an excess amount of 3-bromodiphenylacetylene (**3-10**) was added to the reaction mixture to end-cap the other side of the polymers. The reaction mixture was reflux for 35 h to complete the reaction, until when the purple color of the solution disappeared. Polyphenylene precursor **3-40** bearing bromo groups at termini was thus obtained with M_w of 20,000–34,000 g/mol, M_n of 9,800–13,000 g/mol, and PDI of 2.0–2.6 based on the SEC analysis against PPP and PS standards. The SEC profile of precursor **3-40** was similar to that of precursor **3-2-II** (Figure 3-15b), displaying a small peak at ~28 min in addition to the main peak at ~23 min, which indicated the presence of small oligomers.

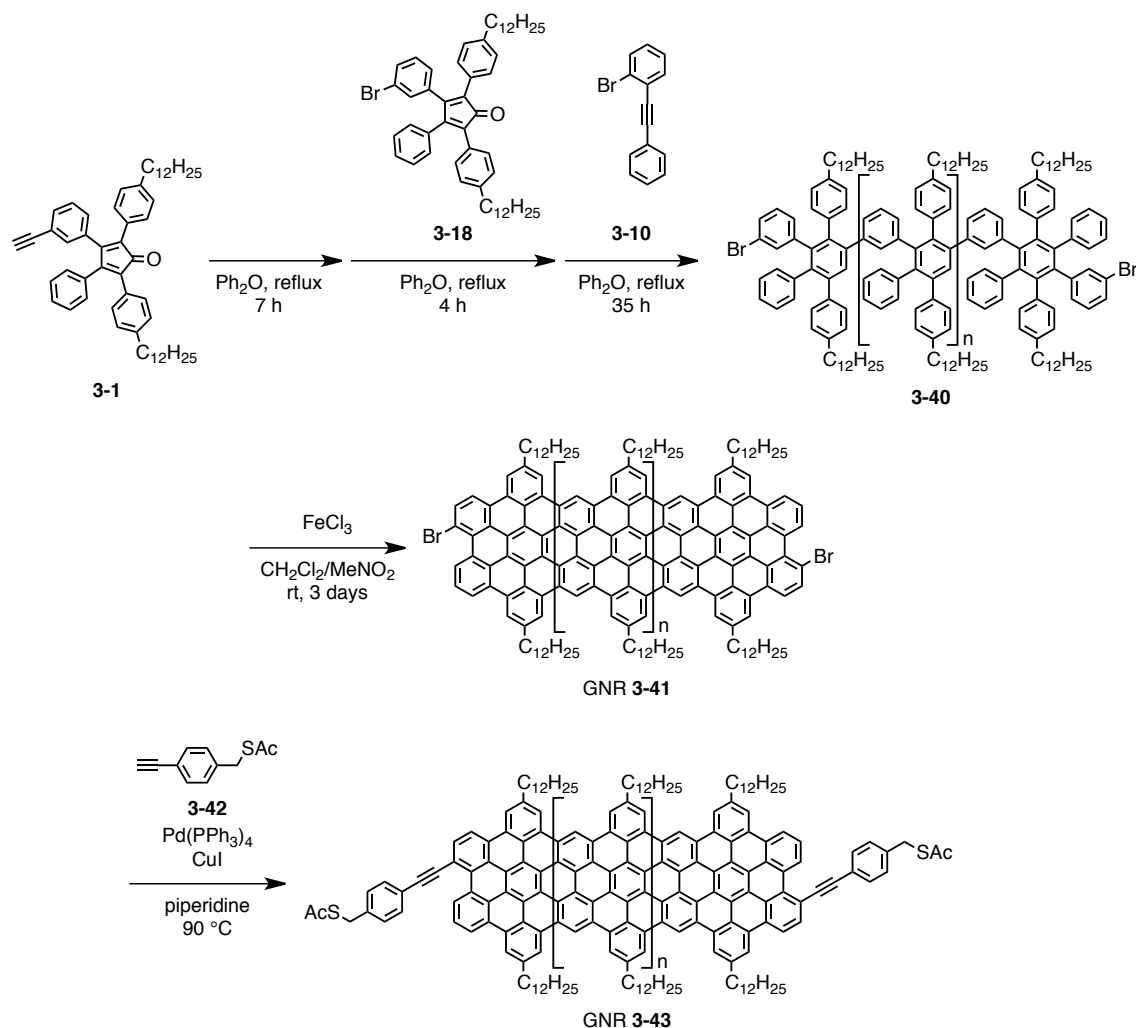


Figure 3-53. Synthetic route to GNR **3-43** bearing acetylthio groups.

Next, crude precursor **3-40** was isolated by reprecipitation and simultaneously fractionated into two fractions: precursor **3-40-I** with M_w of 63,000–130,000 g/mol, M_n of 40,000–70,000 g/mol, and PDI of 1.6–1.9, based on the SEC analysis, was first obtained by repeated reprecipitation and washing cycles with THF and MeOH in 2:1 volume ratio (see also subsection 3.7.2). Next, all the supernatant solutions and washings were combined and subjected to the reprecipitation protocol, using THF and MeOH in 1:1 volume ratio, to give precursor **3-40-II** with M_w of 20,000–32,000 g/mol, M_n of 12,000–18,000 g/mol, and PDI of 1.7–1.8. Both precursors **3-40-I** and **3-40-II** were basically free of the small oligomers according to the SEC chromatograms.

On the basis of the molecular weight, two bromo groups with the molecular mass of 159.8 g/mol account for only 0.5–0.8% of smaller precursor **3-40-II** with M_w of 20,000–32,000 g/mol. Considering this extremely small proportion of the two bromo

atoms in the polymer structure, it is the most likely that a reliable characterization of the end-capped structures of precursors **3-40-I** and **3-40-II** is only possible with mass spectrometric methods. Indeed, the FTIR spectrum of precursor **3-40-II** was identical with that of non-end-capped precursor **3-2** without any noticeable difference. However, linear- and reflectron-mode MALDI-TOF MS analyses of precursor **3-40-II** both showed spectra very similar to those of precursor **3-2** (see Figures 3-12 and 3-13) without any evidence for the end-capping. In the reflectron-mode spectrum, only the masses corresponding to the cyclic oligomers were observed, suggesting that all of the smaller oligomers had undergone the intramolecular cycloaddition before the reaction was stopped for the end-capping. The linear-mode spectrum displayed the mass peaks up to $m/z = \sim 16,000$, but the broadening of the peaks did not allow their assignment to exact chemical structures. Termination of precursor **3-40** with the bromo groups could not be confirmed, but the synthesis was continued, considering that even a small percentage of GNRs with the two linkers could probably yield statistically reasonable results. Especially, the break junction experiments can only measure the GNRs with the two linkers, and thus won't be affected by the presence of those with only one or no acetylthio group.

Both precursors **3-40-I** and **3-40-II** were thus “graphitized” into GNRs **3-41-I** and **3-41-II**, respectively, by the intramolecular oxidative cyclodehydrogenation with the same condition as the synthesis of GNR **3-3**. The average lengths of GNRs **3-41-I** and **3-41-II** bearing bromo groups at the termini could be estimated from M_w of the precursors to be ca. 64–130 and ca. 20–33 nm, respectively. The FTIR and UV–vis absorption spectra of GNR **3-41-II** were basically identical with those of GNR **3-3**, which confirmed the formation of the GNRs. However, there was no difference in the spectra that could prove the end-capping with the bromo groups.

GNRs **3-41-I** and **3-41-II** were subsequently subjected to *Sonogashira* coupling with 4-ethynylbenzyl thioacetate (**3-42**)¹⁰⁶ to afford GNRs **3-43-I** and **3-43-II**, respectively, bearing acetylthio groups at the terminals (Figure 3-53). The investigation of intramolecular transport properties of GNR **3-43-I** and **3-43-II** has been attempted through the break junction technique by ██████████ in the group of ██████████ ██████████ at Arizona State University, the United States, in a similar manner to the previous studies on HBC with the same functionalities.¹⁰³ The preliminary results thus obtained on GNRs **3-43-I** and **3-43-II** were to some extent comparable to those reported for the HBC derivative,¹⁰³ but could not reasonably be correlated with the structure of the GNRs, most probably because the measurements on single GNRs were interfered

with the strong and random aggregations of GNR **3-43**. The measured transport characteristics might also have been complicated due to the presence of GNRs with different lengths, showing different transport properties. Nevertheless, this preliminary result indicated that appreciable amount of the GNRs in the samples of GNRs **3-41-I** and **3-41-II** were indeed connected with the acetylthio groups. Furthermore, such GNRs with the thiol linkers at the termini are also expected to facilitate contacting of single GNRs with gold electrodes for the fabrication of single-GNR devices.

3.9 Photovoltaic devices with GNRs in an active layer

It has been theoretically predicted that bottom-up synthesized GNRs with broad absorption in the visible light region could become promising materials for photovoltaic cells.⁶⁶ In order to examine the applicability of such GNRs to photovoltaics, fabrication of solar cells using GNR **3-26** was performed together with [REDACTED] in the group of [REDACTED] at University College London, as a secondment within Marie Curie Initial Training Network “SUPERIOR”. Thus, bulk-heterojunction solar cells were prepared employing GNR **3-26-I** as the donor and [6,6]-phenyl-C₆₁-butyric acid methyl ester (PCBM) as the acceptor materials. The concentrations of GNR **3-26-I** in dispersions were too low to prepare thick enough layers by spin-coating. Therefore, the active layers were deposited on ITO substrates pretreated with PEDOT by repeatedly drop-casting dispersions of a mixture of GNR **3-26-I** and PCBM in chlorobenzene, followed by vapor deposition of Ca/Al electrodes (Figure 3-54).

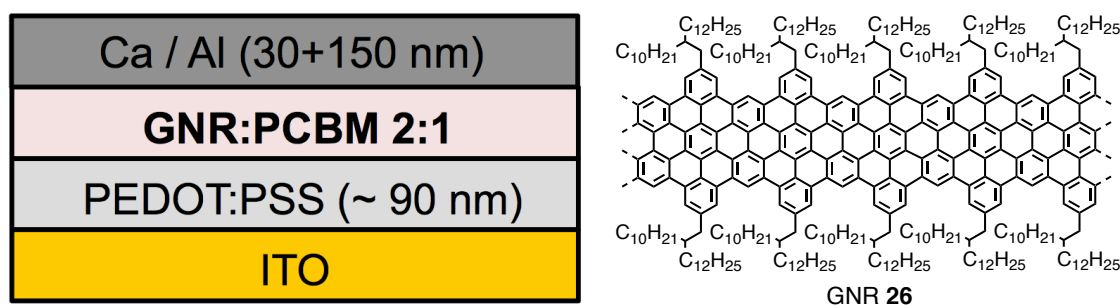


Figure 3-54. A schematic structure of the photovoltaic devices with a mixture of GNR **26** and PCBM as active layers.

GNR **3-26-I** and PCBM were mixed with various ratios and most of the devices thus prepared indeed functioned as solar cells. Among them, the photovoltaic devices fabricated with 2:1 weight ratio of GNR **3-26-I** and PCBM demonstrated the best performance with power conversion efficiency (PCE) of 0.19%, short-circuit current (J_{SC}) of 2.48 mA/cm², open-circuit voltage (V_{OC}) of 0.25 V, and fill-factor (FF) of 0.32, displaying the current–voltage characteristics shown as a green line in Figure 3-55. Devices fabricated with different number of drop-casts, i.e. different thickness, showed a different curve as plotted as a red line in Figure 3-55, featuring PCE of 0.17%, J_{SC} of 1.64 mA/cm², V_{OC} of 0.32 V, and FF of 0.33. Devices prepared with dispersions with other ratio of GNR **3-26-I** and PCBM (e.g. 1:1, 1:2, 1:4) all lead to lower PCE values of

<~0.1%. These preliminary results were obtained without optimization of the thickness of each layer within two weeks of the secondment, and displayed high potential of such GNRs for the application to photovoltaics. Further optimization of the structure of the devices, improvement of the processability of the GNRs, and/or use of laterally extended GNRs with broader absorption might be able to realize high-performance solar cells based on the bottom-up synthesized GNRs.

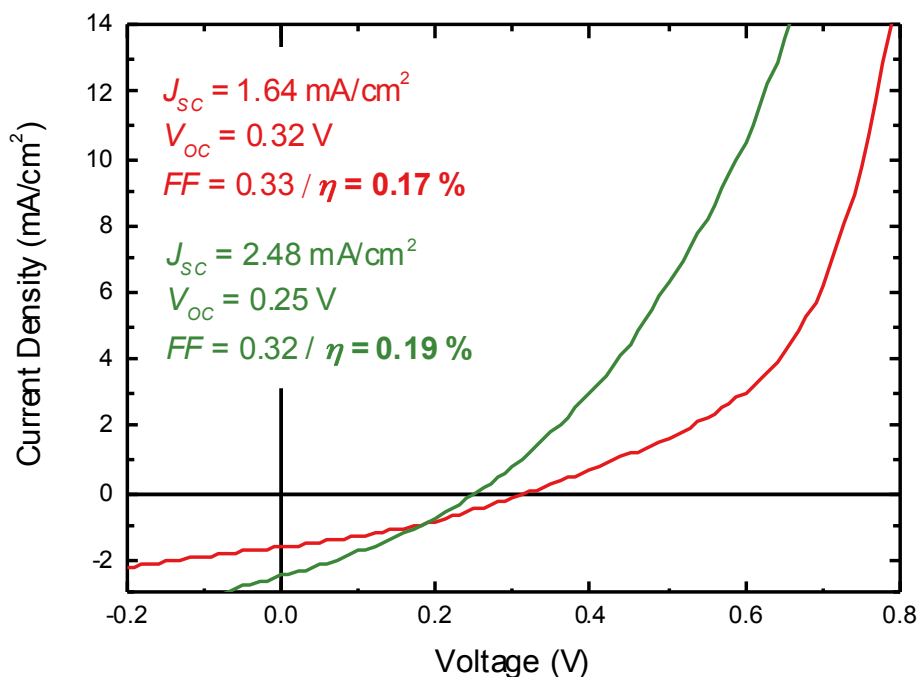


Figure 3-55. Current–voltage characteristics of two photovoltaic devices with a mixture of GNR **26** and PCBM (2:1 weight ratio) as active layers and different thickness (different number of drop-casts).

3.10 Attempts on the surface-assisted fabrication of GNRs via *Diels-Alder* polymerization

Considering the exceptionally high longitudinal extension of GNRs achieved via the *AB*-type *Diels-Alder* polymerization, this approach might also be effective for the surface-assisted synthesis of the GNRs. Currently it is still challenging to fabricate long (>100 nm) GNRs by the surface-synthesis approach,¹⁰⁷ and the development of the methodology to overcome this problem is highly desired. In order to test the feasibility of the *AB*-type *Diels-Alder* polymerization on a metal surface under ultra-high vacuum (UHV) conditions, *AB*-type monomer **3-47** was designed. Monomer **3-47** bore no alkyl group to sufficiently lower the sublimation temperature, which could prevent the polymerization during or before the sublimation (Figure 3-56).

Monomer **3-47** was prepared in the same manner as the synthesis of monomer **3-1**. *Knoevenagel* condensation of diphenylacetone **3-44** and benzil **3-17** gave tetraphenylcyclopentadienone **3-45** in 86% yield, which was further subjected to *Sonogashira* coupling with trimethylsilylacetylene to obtain trimethylsilyl-protected monomer **3-46** in 68% yield. Subsequent removal of the trimethylsilyl-protecting group with potassium fluoride afforded *AB*-type monomer **3-47** in 89% yield. *Diels-Alder* polymerization of monomer **3-47** on a metal surface under UHV conditions was then investigated by ██████████ in the group of ██████████, EMPA, Dübendorf, Switzerland (Figure 3-57).

AB-type monomer **3-47** was sublimed at 145 °C onto an Au(111) surface preheated at 60 °C, and subsequently annealed at 150–200 °C under in situ visualization with high-resolution STM (Figure 3-57a and b). The molecules of **3-47** displayed the surface reconstruction consistent with other monomers that formed GNRs, resulting in

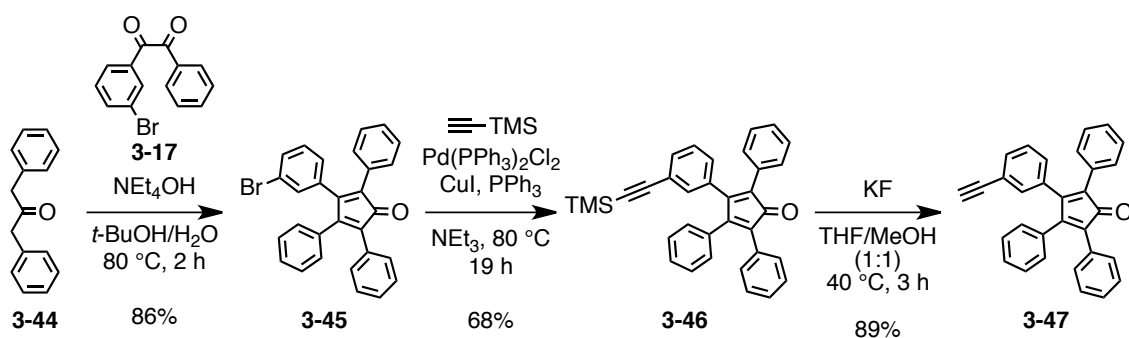


Figure 3-56. Synthetic route to *AB*-type monomer **3-47** without alkyl substituents.

molecular arrays with the approximate diameter of ca. 2 nm.⁵³ The distance between the centers of the molecules was roughly 2 nm and the arrays showed tilted structures, suggesting that the *Diels–Alder* polymerization did not occur at these temperatures. When monomer **3-47** was sublimed onto an Au(111) surface preheated at 150 °C and subsequently annealed at ca. 300 °C, the arrays showed non-tilted structures with the distance between the centers of the molecules seemingly smaller than ca. 1.5 nm, which suggested the possibility that the monomers underwent the *Diels–Alder* polymerization (Figure 3-57c). However, further annealing at 400 °C did not yield longer or planarized structures, indicating that the *AB*-type *Diels–Alder* monomer was not suitable for the surface-assisted fabrication of long and structurally defined GNRs (Figure 3-57d).

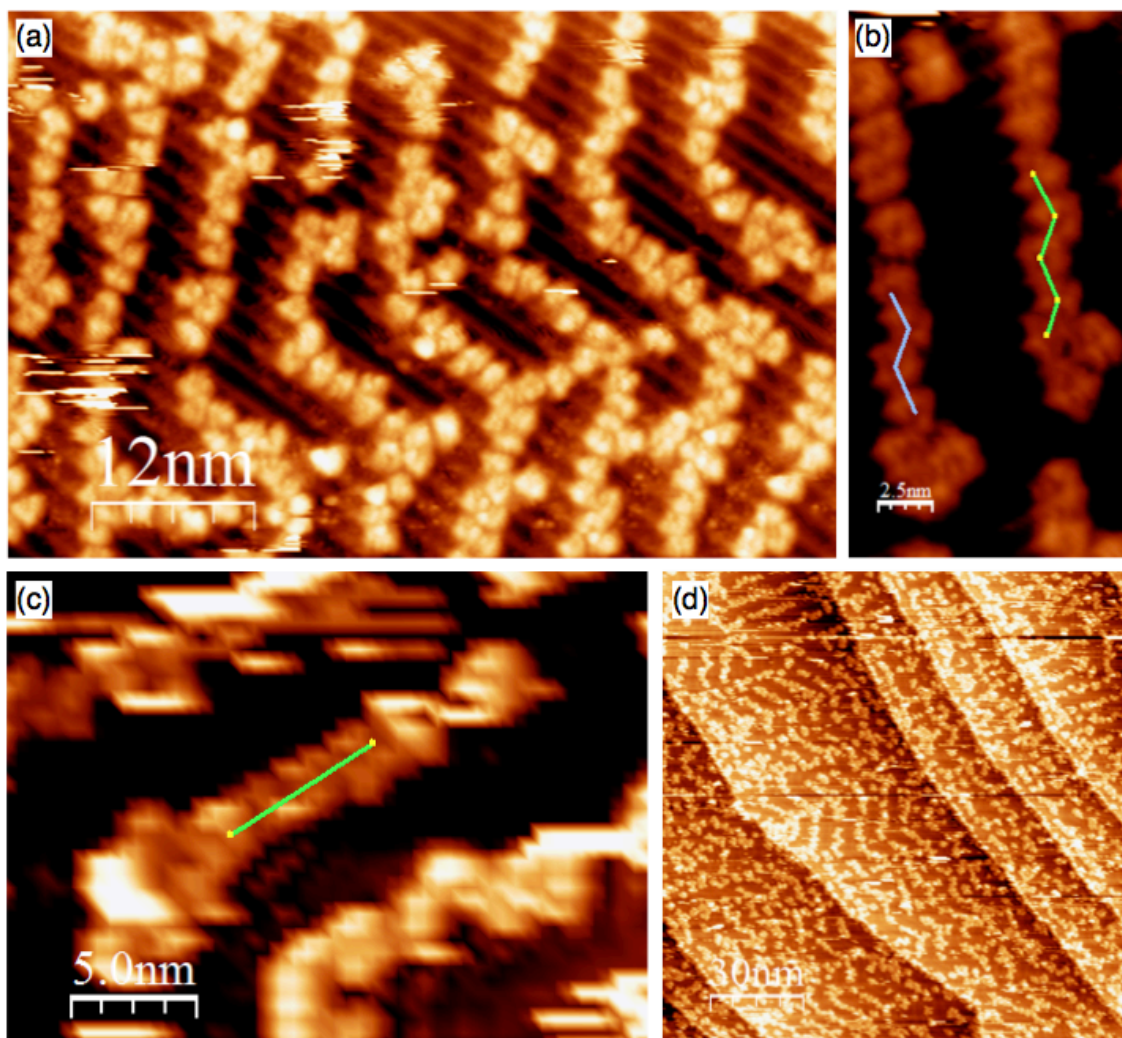


Figure 3-57. High-resolution STM images of *AB*-type monomer **3-47**; (a), (b) sublimed on a Au(111) surface preheated at 60 °C and subsequently annealed at 150 °C; (c) sublimed on a Au(111) surface preheated at 150 °C and subsequently annealed at 200 °C and then at 300 °C; (d) further annealed at 400 °C.

3.11 Summary

Narrow (ca. 1 nm) and structurally well-defined GNRs could be synthesized in solution with unprecedentedly high aspect ratio, through highly efficient *AB*-type *Diels–Alder* polymerization of tetraphenylcyclopentadienone-based monomers. The longitudinal length of the GNRs could exceed 600 nm based on the SEC and photon correlation spectroscopy analyses of the polyphenylene precursors. Successful formation of the long and uniform GNRs was unambiguously attested by FTIR, Raman, solid-state NMR, and UV–vis absorption spectroscopies as well as STM and AFM visualizations, which at the same time demonstrated high liquid-phase processability of the GNRs. Intrinsic mobility of the GNRs was revealed by the THz spectroscopy to be superior to those of conventional semiconducting polymers with the values approximately in agreement with the theoretical predictions. Fabrication of single-GNR devices is currently pursued in collaborations for the investigation of the intra-ribbon transport properties. Furthermore, the edges of the GNRs could be selectively chlorinated, enhancing the dispersibility by the distortion of the planarity as well as altering their energy levels to yield lower-bandgap GNRs. This method paved a way toward the bandgap engineering of the GNRs without modification of the widths and edge structures, which broadened the applicability of such bottom-up synthesized GNRs. Nevertheless, it has been theoretically as well as experimentally revealed that the mobility of the GNRs decreases as their width become smaller. Therefore, it is of great importance to synthesize laterally extended GNRs with a well-defined structure while keeping the high longitudinal extension over 100 nm.

3.12 References

- (1) Stille, J. K. In *Fortschritte Der Hochpolymeren-Forschung*; Springer Berlin Heidelberg: 1961; Vol. 3/1, p 48.
- (2) Stille, J. K.; Harris, F. W.; Rakutis, R. O.; Mukamal, H. *J. Polym. Sci. Part B* **1966**, *4*, 791.
- (3) Kumar, U.; Neenan, T. X. *Macromolecules* **1995**, *28*, 124.
- (4) Shifrina, Z. B.; Averina, M. S.; Rusanov, A. L.; Wagner, M.; Müllen, K. *Macromolecules* **2000**, *33*, 3525.
- (5) Wu, J. S.; Gherghel, L.; Watson, M. D.; Li, J. X.; Wang, Z. H.; Simpson, C. D.; Kolb, U.; Müllen, K. *Macromolecules* **2003**, *36*, 7082.
- (6) Stille, J. K.; Noren, G. K.; Green, L. *J. Polym. Sci. A-1, Polym. Chem.* **1970**, *8*, 2245.
- (7) Schlüter, A. D.; Löffler, M.; Enkelmann, V. *Nature* **1994**, *368*, 831.
- (8) Carothers, W. H. *Trans. Faraday Soc.* **1936**, *32*, 39.
- (9) Odian, G. G. *Principles of Polymerization*; J. Wiley & Sons: Hoboken, NJ, 2004.
- (10) Narita, A.; Feng, X.; Hernandez, Y.; Jensen, S. A.; Bonn, M.; Yang, H.; Verzhbitskiy, I. A.; Casiraghi, C.; Hansen, M. R.; Koch, A. H. R.; Fytas, G.; Ivasenko, O.; Li, B.; Mali, K. S.; Balandina, T.; Mahesh, S.; De Feyter, S.; Müllen, K. *Nature Chem.* **2014**, *6*, 126.
- (11) Wu, J.; Pisula, W.; Müllen, K. *Chem. Rev.* **2007**, *107*, 718.
- (12) Fogel, Y.; Zhi, L.; Rouhanipour, A.; Andrienko, D.; Räder, H. J.; Müllen, K. *Macromolecules* **2009**, *42*, 6878.
- (13) Müller, M.; Kübel, C.; Morgenroth, F.; Iyer, V. S.; Müllen, K. *Carbon* **1998**, *36*, 827.
- (14) Yan, X.; Cui, X.; Li, B.; Li, L.-s. *Nano Lett.* **2010**, *10*, 1869.
- (15) Li, J.; Huang, P. *Beilstein J. Org. Chem.* **2011**, *7*, 426.
- (16) Simpson, C. D.; Brand, J. D.; Berresheim, A. J.; Przybilla, L.; Räder, H. J.; Müllen, K. *Chem.—Eur. J.* **2002**, *8*, 1424.
- (17) Yoshimura, K.; Przybilla, L.; Ito, S.; Brand, J. D.; Wehmeir, M.; Räder, H. J.; Müllen, K. *Macromol. Chem. Phys.* **2001**, *202*, 215.
- (18) Wasserfallen, D.; Kastler, M.; Pisula, W.; Hofer, W. A.; Fogel, Y.; Wang, Z.; Müllen, K. *J. Am. Chem. Soc.* **2006**, *128*, 1334.

-
- (19) Kastler, M.; Pisula, W.; Wasserfallen, D.; Pakula, T.; Müllen, K. *J. Am. Chem. Soc.* **2005**, *127*, 4286.
- (20) Wehmeier, M.; Wagner, M.; Müllen, K. *Chem.—Eur. J.* **2001**, *7*, 2197.
- (21) Sauriat-Dorizon, H.; Maris, T.; Wuest, J. D.; Enright, G. D. *J. Org. Chem.* **2003**, *68*, 240.
- (22) Räder, H. J.; Spickermann, J.; Kreyenschmidt, M.; Müllen, K. *Macromol. Chem. Phys.* **1996**, *197*, 3285.
- (23) Yang, X. Y.; Dou, X.; Rouhanipour, A.; Zhi, L. J.; Rader, H. J.; Müllen, K. *J. Am. Chem. Soc.* **2008**, *130*, 4216.
- (24) Dössel, L.; Gherghel, L.; Feng, X.; Müllen, K. *Angew. Chem. Int. Ed.* **2011**, *50*, 2540.
- (25) Schwab, M. G.; Narita, A.; Hernandez, Y.; Balandina, T.; Mali, K. S.; De Feyter, S.; Feng, X.; Müllen, K. *J. Am. Chem. Soc.* **2012**, *134*, 18169.
- (26) Fujimoto, C. H.; Hickner, M. A.; Cornelius, C. J.; Loy, D. A. *Macromolecules* **2005**, *38*, 5010.
- (27) Martin, K.; Spickermann, J.; Räder, H. J.; Müllen, K. *Rapid Commun. Mass Spectrom.* **1996**, *10*, 1471.
- (28) Kricheldorf, H. R.; Schwarz, G. *Macromol. Rapid Commun.* **2003**, *24*, 359.
- (29) Glassner, M.; Blinco, J. P.; Barner-Kowollik, C. *Macromol. Rapid Commun.* **2011**, *32*, 724.
- (30) Kroeger, A.; Deimede, V.; Belack, J.; Lieberwirth, I.; Fytas, G.; Wegner, G. *Macromolecules* **2007**, *40*, 105.
- (31) Ying, Q.; Chu, B. *Macromolecules* **1987**, *20*, 362.
- (32) Burchard, W. In *Branched Polymers II*; Roovers, J., Ed.; Springer Berlin Heidelberg: 1999; Vol. 143, p 113.
- (33) Yamakawa, H.; Fujii, M. *Macromolecules* **1973**, *6*, 407.
- (34) Vanhee, S.; Rulkens, R.; Lehmann, U.; Rosenauer, C.; Schulze, M.; Köhler, W.; Wegner, G. *Macromolecules* **1996**, *29*, 5136.
- (35) Brodowski, G.; Horvath, A.; Ballauff, M.; Rehahn, M. *Macromolecules* **1996**, *29*, 6962.
- (36) Fytas, G.; Nothofer, H. G.; Scherf, U.; Vlassopoulos, D.; Meier, G. *Macromolecules* **2002**, *35*, 481.
- (37) Somma, E.; Loppinet, B.; Fytas, G.; Setayesh, S.; Jacob, J.; Grimsdale, A. C.; Müllen, K. *Colloid Polym. Sci.* **2004**, *282*, 867.

- (38) Hernandez, Y.; Nicolosi, V.; Lotya, M.; Blighe, F. M.; Sun, Z.; De, S.; McGovern, I. T.; Holland, B.; Byrne, M.; Gun'Ko, Y. K.; Boland, J. J.; Niraj, P.; Duesberg, G.; Krishnamurthy, S.; Goodhue, R.; Hutchison, J.; Scardaci, V.; Ferrari, A. C.; Coleman, J. N. *Nature Nanotech.* **2008**, *3*, 563.
- (39) Bergin, S. D.; Nicolosi, V.; Streich, P. V.; Giordani, S.; Sun, Z.; Windle, A. H.; Ryan, P.; Niraj, N. P. P.; Wang, Z.-T. T.; Carpenter, L.; Blau, W. J.; Boland, J. J.; Hamilton, J. P.; Coleman, J. N. *Adv. Mater.* **2008**, *20*, 1876.
- (40) Coleman, J. N. *Adv. Funct. Mater.* **2009**, *19*, 3680.
- (41) Giordani, S.; Bergin, S. D.; Nicolosi, V.; Lebedkin, S.; Kappes, M. M.; Blau, W. J.; Coleman, J. N. *J. Phys. Chem. B* **2006**, *110*, 15708.
- (42) Centrone, A.; Brambilla, L.; Renouard, T.; Gherghel, L.; Mathis, C.; Müllen, K.; Zerbi, G. *Carbon* **2005**, *43*, 1593.
- (43) Carminati, M.; Brambilla, L.; Zerbi, G.; Müllen, K.; Wu, J. *J. Chem. Phys.* **2005**, *123*, 144706.
- (44) Reich, S.; Thomsen, C. *Philos. Transact. A Math. Phys. Eng. Sci.* **2004**, *362*, 2271.
- (45) Ferrari, A. C. *Solid State Commun.* **2007**, *143*, 47.
- (46) Malard, L. M.; Pimenta, M. A.; Dresselhaus, G.; Dresselhaus, M. S. *Phys. Rep.* **2009**, *473*, 51.
- (47) Saito, R.; Hofmann, M.; Dresselhaus, G.; Jorio, A.; Dresselhaus, M. S. *Adv. Phys.* **2011**, *60*, 413.
- (48) Ferrari, A. C.; Basko, D. M. *Nature Nanotech.* **2013**, *8*, 235.
- (49) Dresselhaus, M. S.; Jorio, A.; Hofmann, M.; Dresselhaus, G.; Saito, R. *Nano Lett.* **2010**, *10*, 751.
- (50) Ferrari, A. C.; Meyer, J. C.; Scardaci, V.; Casiraghi, C.; Lazzeri, M.; Mauri, F.; Piscanec, S.; Jiang, D.; Novoselov, K. S.; Roth, S.; Geim, A. K. *Phys. Rev. Lett.* **2006**, *97*, 187401.
- (51) Dresselhaus, M. S.; Dresselhaus, G.; Saito, R.; Jorio, A. *Phys. Rep.* **2005**, *409*, 47.
- (52) Jiao, L.; Zhang, L.; Wang, X.; Diankov, G.; Dai, H. *Nature* **2009**, *458*, 877.
- (53) Cai, J.; Ruffieux, P.; Jaafar, R.; Bieri, M.; Braun, T.; Blankenburg, S.; Muoth, M.; Seitsonen, A. P.; Saleh, M.; Feng, X.; Müllen, K.; Fasel, R. *Nature* **2010**, *466*, 470.
- (54) Castiglioni, C.; Tommasini, M.; Zerbi, G. *Philos. Transact. A Math. Phys. Eng. Sci.* **2004**, *362*, 2425.

-
- (55) Negri, F.; Castiglioni, C.; Tommasini, M.; Zerbi, G. *J. Phys. Chem. A* **2002**, *106*, 3306.
- (56) Castiglioni, C.; Mapelli, C.; Negri, F.; Zerbi, G. *J. Chem. Phys.* **2001**, *114*, 963.
- (57) Yu, F.; Zhou, H.; Zhang, Z.; Tang, D.; Chen, M.; Yang, H.; Wang, G.; Yang, H.; Gu, C.; Sun, L. *Appl. Phys. Lett.* **2012**, *100*, 101904.
- (58) Sanders, G. D.; Nugraha, A. R. T.; Saito, R.; Stanton, C. J. *Phys. Rev. B* **2012**, *85*, 205401.
- (59) Vandescuren, M.; Hermet, P.; Meunier, V.; Henrard, L.; Lambin, P. *Phys. Rev. B* **2008**, *78*, 195401.
- (60) Zhou, J.; Dong, J. *Appl. Phys. Lett.* **2007**, *91*, 173108.
- (61) Gillen, R.; Mohr, M.; Maultzsch, J. *Phys. Rev. B* **2010**, *81*, 205426.
- (62) Elmahdy, M. M.; Dou, X.; Mondeshki, M.; Floudas, G.; Butt, H.-J.; Spiess, H. W.; Müllen, K. *J. Am. Chem. Soc.* **2008**, *130*, 5311.
- (63) Brown, S. P.; Spiess, H. W. *Chem. Rev.* **2001**, *101*, 4125.
- (64) Sebastiani, D.; Kudin, K. N. *ACS Nano* **2008**, *2*, 661.
- (65) Chen, Z.; Wannere, C. S.; Corminboeuf, C.; Puchta, R.; Schleyer, P. v. R. *Chem. Rev.* **2005**, *105*, 3842.
- (66) Osella, S.; Narita, A.; Schwab, M. G.; Hernandez, Y.; Feng, X.; Müllen, K.; Beljonne, D. *ACS Nano* **2012**, *6*, 5539.
- (67) Sakaguchi, H.; Matsumura, H.; Gong, H. *Nature Mater.* **2004**, *3*, 551.
- (68) Lee, Y.; Chang, C.; Yau, S.; Fan, L.; Yang, Y.; Yang, L. O.; Itaya, K. *J. Am. Chem. Soc.* **2009**, *131*, 6468.
- (69) Yang, L. Y. O.; Chang, C.; Liu, S.; Wu, C.; Yau, S. L. *J. Am. Chem. Soc.* **2007**, *129*, 8076.
- (70) Li, X.; Wang, X.; Zhang, L.; Lee, S.; Dai, H. *Science* **2008**, *319*, 1229.
- (71) Jiao, L. Y.; Wang, X. R.; Diankov, G.; Wang, H. L.; Dai, H. J. *Nature Nanotech.* **2010**, *5*, 321.
- (72) Shenoy, V. B.; Reddy, C. D.; Ramasubramaniam, A.; Zhang, Y. W. *Phys. Rev. Lett.* **2008**, *101*, 245501.
- (73) Bets, K.; Yakobson, B. *Nano Res.* **2009**, *2*, 161.
- (74) Chuvilin, A.; Bichoutskaia, E.; Gimenez-Lopez, M. C.; Chamberlain, T. W.; Rance, G. A.; Kuganathan, N.; Biskupek, J.; Kaiser, U.; Khlobystov, A. N. *Nature Mater.* **2011**, *10*, 687.

- (75) Talyzin, A. V.; Anoshkin, I. V.; Krasheninnikov, A. V.; Nieminen, R. M.; Nasibulin, A. G.; Jiang, H.; Kauppinen, E. I. *Nano Lett.* **2011**, *11*, 4352.
- (76) Chamberlain, T. W.; Biskupek, J.; Rance, G. A.; Chuvilin, A.; Alexander, T. J.; Bichoutskaia, E.; Kaiser, U.; Khlobystov, A. N. *ACS Nano* **2012**, *6*, 3943.
- (77) Dötz, F.; Brand, J. D.; Ito, S.; Gherghel, L.; Müllen, K. *J. Am. Chem. Soc.* **2000**, *122*, 7707.
- (78) Böhme, T.; Simpson, C. D.; Müllen, K.; Rabe, J. P. *Chem.–Eur. J.* **2007**, *13*, 7349.
- (79) Ulbricht, R.; Hendry, E.; Shan, J.; Heinz, T.; Bonn, M. *Rev. Mod. Phys.* **2011**, *83*, 543.
- (80) Ai, X.; Beard, M. C.; Knutsen, K. P.; Shaheen, S. E.; Rumbles, G.; Ellingson, R. *J. J. Phys. Chem. B* **2006**, *110*, 25462.
- (81) Cunningham, P. D.; Hayden, L. M. *J. Phys. Chem. C* **2008**, *112*, 7928.
- (82) Hendry, E.; Schins, J. M.; Candeias, L. P.; Siebbeles, L. D. A.; Bonn, M. *Phys. Rev. Lett.* **2004**, *92*, 196601.
- (83) Hendry, E.; Koeberg, M.; Schins, J. M.; Nienhuys, H. K.; Sundström, V.; Siebbeles, L. D. A.; Bonn, M. *Phys. Rev. B* **2005**, *71*, 125201.
- (84) Wang, F.; Shan, J.; Islam, M. A.; Herman, I. P.; Bonn, M.; Heinz, T. F. *Nature Mater.* **2006**, *5*, 861.
- (85) Obradovic, B.; Kotlyar, R.; Heinz, F.; Matagne, P.; Rakshit, T.; Giles, M. D.; Stettler, M. A.; Nikonov, D. E. *Appl. Phys. Lett.* **2006**, *88*, 142102.
- (86) Wang, J.; Zhao, R.; Yang, M.; Liu, Z. *J. Chem. Phys.* **2013**, *138*, 084701.
- (87) Smith, N. V. *Phys. Rev. B* **2001**, *64*, 155106.
- (88) Jensen, S. A.; Ulbricht, R.; Narita, A.; Feng, X.; Müllen, K.; Hertel, T.; Turchinovich, D.; Bonn, M. *Nano Lett.* **2013**, *13*, 5925.
- (89) Zheng, Z.; Yim, K.-H.; Saifullah, M. S. M.; Welland, M. E.; Friend, R. H.; Kim, J.-S.; Huck, W. T. S. *Nano Lett.* **2007**, *7*, 987.
- (90) Gettinger, C. L.; Heeger, A. J.; Drake, J. M.; Pine, D. J. *J. Chem. Phys.* **1994**, *101*, 1673.
- (91) Tan, Y.-Z.; Tang, B.; Parvez, K.; Narita, A.; Osella, S.; Beljonne, D.; Feng, X.; Müllen, K. *Nature Commun.* **2013**, *4*, 2646.
- (92) Bhandari, S.; Ray, S. *Synth. Commun.* **1998**, *28*, 765.
- (93) Ballester, M.; Castaner, J.; Riera, J. *Afinidad* **1978**, *35*, 97.

-
- (94) Klessinger, M.; Michl, J. *Excited States and Photochemistry of Organic Molecules*; VCH: New York, 1995.
- (95) Seo, J.; Kim, S.; Park, S.; Park, S. Y. *Bull. Korean Chem. Soc.* **2005**, *26*, 1706.
- (96) Fu, G. C. *Acc. Chem. Res.* **2008**, *41*, 1555.
- (97) Würtz, S.; Glorius, F. *Acc. Chem. Res.* **2008**, *41*, 1523.
- (98) Martin, R.; Buchwald, S. L. *Acc. Chem. Res.* **2008**, *41*, 1461.
- (99) Gelman, D.; Buchwald, S. L. *Angew. Chem. Int. Ed.* **2003**, *42*, 5993.
- (100) Köllhofer, A.; Pullmann, T.; Plenio, H. *Angew. Chem. Int. Ed.* **2003**, *42*, 1056.
- (101) Anderson, K. W.; Buchwald, S. L. *Angew. Chem. Int. Ed.* **2005**, *44*, 6173.
- (102) Huang, H.; Liu, H.; Jiang, H.; Chen, K. *J. Org. Chem.* **2008**, *73*, 6037.
- (103) Diez-Perez, I.; Li, Z.; Hihath, J.; Li, J.; Zhang, C.; Yang, X.; Zang, L.; Dai, Y.; Feng, X.; Müllen, K.; Tao, N. *Nature Commun.* **2010**, *1*, 31.
- (104) Song, H.; Kim, Y.; Jang, Y. H.; Jeong, H.; Reed, M. A.; Lee, T. *Nature* **2009**, *462*, 1039.
- (105) Diez-Perez, I.; Hihath, J.; Hines, T.; Wang, Z.-S.; Zhou, G.; Müllen, K.; Tao, N. *Nature Nanotech.* **2011**, *6*, 226.
- (106) Li, Q.; Rukavishnikov, A. V.; Petukhov, P. A.; Zaikova, T. O.; Jin, C.; Keana, J. F. W. *J. Org. Chem.* **2003**, *68*, 4862.
- (107) Linden, S.; Zhong, D.; Timmer, A.; Aghdassi, N.; Franke, J. H.; Zhang, H.; Feng, X.; Müllen, K.; Fuchs, H.; Chi, L.; Zacharias, H. *Phys. Rev. Lett.* **2012**, *108*, 216801.

Chapter 4. Laterally and Longitudinally Extended GNRs with Liquid-Phase Processability

The *AB*-type *Diels–Alder* polymerization has proved to be a highly promising method for the synthesis of polyphenylene precursors with extremely high molecular weight, which provide GNRs with well-defined structure and long length (>200 nm) as discussed in chapter 3. For the future applications of the GNRs in electronic devices, it is essential to tailor their band structure, including the bandgap, which can be achieved by altering the lateral width of the GNRs as demonstrated in chapter 2. However, the GNRs reported in chapter 2 are short, i.e. the average lengths smaller than 50 nm, which hamper the fabrication of FET devices on single GNRs. It is therefore highly important to establish a method for the fabrication of sufficiently long (e.g. >100 nm) GNRs with varying extended widths. In this chapter, bottom-up synthesis of laterally (ca. 2 nm) as well as longitudinally (>100 nm) extended GNRs with the cove-type edge structure is described based on the *AB*-type *Diels–Alder* polymerization approach. The UV–vis absorption spectroscopic analysis reveals a lowered bandgap of ~1.24 eV for the laterally extended GNRs compared to that of the narrower GNR described in chapter 3, i.e. 1.88 eV, in good agreement with the theoretical prediction. Remarkably, the long and broad GNRs displays residual dispersibility in organic solvents, enabling their liquid-phase processing to form self-assembled monolayers on HOPG surfaces as well as investigation of their photoconductivity in a dispersion by means of non-contact, ultrafast THz spectroscopy.

4.1 Synthetic strategy

Based on the successful fabrication of long (>200 nm) and structurally well-defined GNR **3-3** through the *Diels–Alder* polymerization of *AB*-type monomer **3-1** (chapter 3), the synthesis of laterally extended GNR **4-3** was designed as shown in Figure 4-1. *AB*-type monomer **4-1** has a structure with four additional benzene rings at the periphery of monomer **3-1**, and undergoes the *Diels–Alder* polymerization in the same manner as monomer **3-1** to yield laterally extended polyphenylene precursor **4-2**. The intramolecular oxidative cyclodehydrogenation of precursor **4-2** leads to GNR **4-3**

with the same cove-type edge structure as that of GNR **3-3** and larger width of 1.54–1.98 nm (Figure 4-1). This lateral width is the same as that of GNR **2-3** described in chapter 2, but GNR **4-3** is featured by the pure cove-type edge structure in contrast to GNR **2-3** with a mixture of armchair and cove-type edge structures. Precursor **4-2** is obtained as a mixture of numerous structural isomers owing to the two possible molecular orientations upon each *Diels–Alder* cycloaddition step, but all of these isomers lead to the same straight GNR structure (Figure 4-2) in analogy to the synthesis of GNR **3-3** (see section 3.1). In contrast to precursor **3-2** the “undesired” conformations, which lead to “kinked” GNRs upon the “graphitization”, are strongly hampered by the steric hindrance between the benzene rings (Figure 4-2), which renders the use of bulky alkyl chains unnecessary for ensuring the formation of the straight GNRs. Nevertheless, the bulky dodecyl or 2-decyltetradecyl groups were introduced at the peripheral positions to enhance the dispersibility of the resulting GNRs in organic solvents.

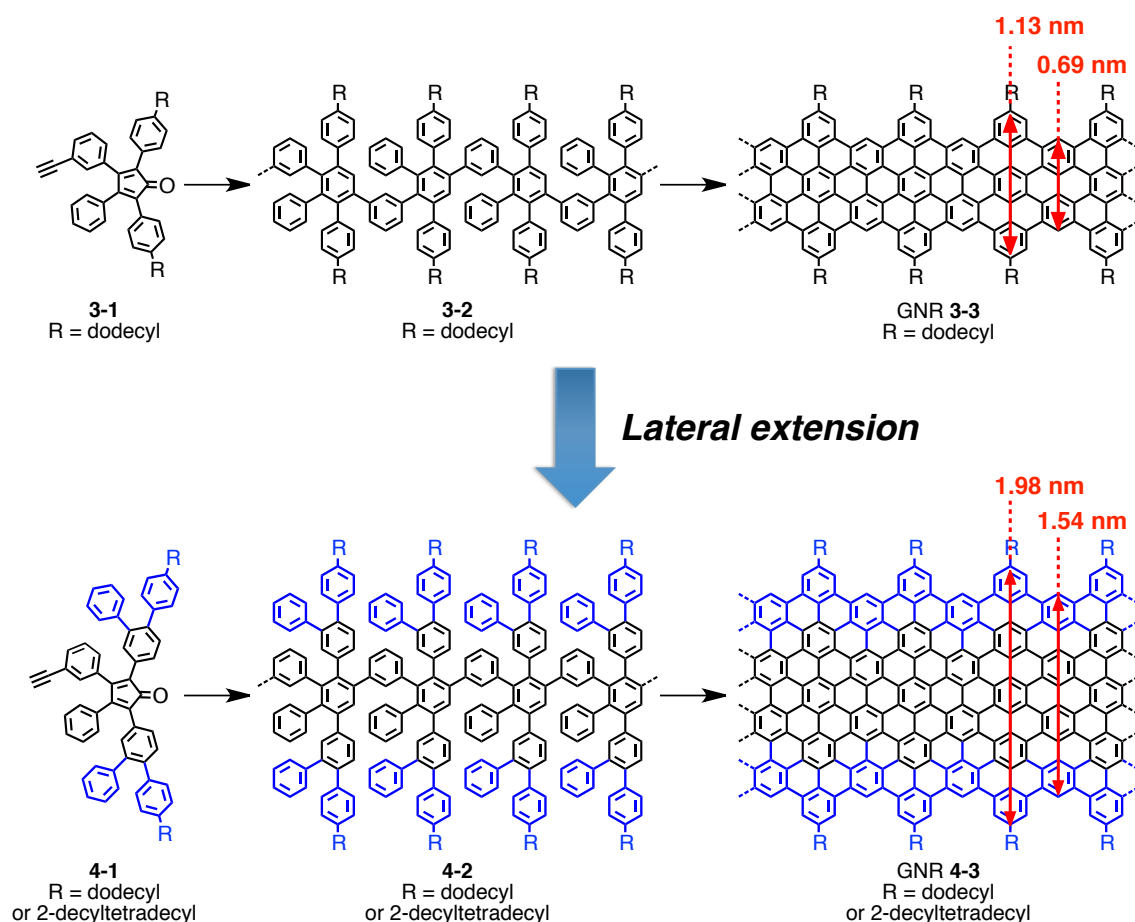


Figure 4-1. Lateral extension of the synthesis of GNRs based on *AB*-type *Diels–Alder* polymerization. Geometric dimensions of GNRs **3-3** and **4-3** were derived from Merck Molecular Force Field 94 (MMFF94) calculations.

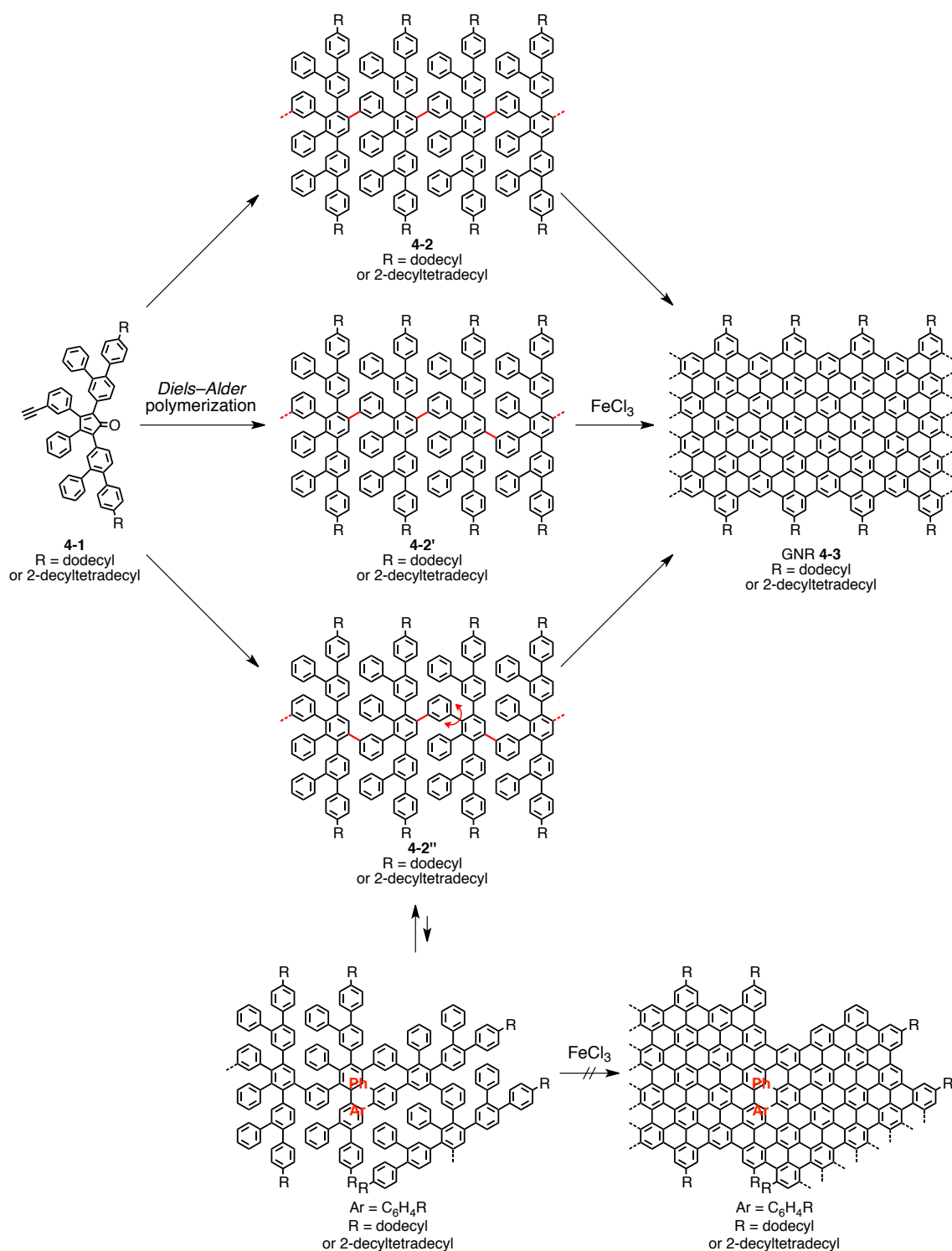


Figure 4-2. Schematic illustration of the structural isomerization of polyphenylene precursor 4-2 upon the *Diels-Alder* polymerization. All the structural isomers yield identical GNR 4-3 with the straight structure after the cyclodehydrogenation. “Undesired” conformations of precursor 4-2, which would lead to “kinked” GNRs, are strongly hampered by the steric hindrance between the benzene rings to ensure the exclusive formation of the straight GNR 4-3.

4.2 Synthesis of broad and long GNRs

4.2.1 Synthesis of laterally extended AB-type monomers

For the fabrication of GNR **4-3** laterally extended AB-type monomers **4-1a** and **4-1b** with dodecyl and 2-decyltetradecyl chains, respectively, were synthesized as shown in Figure 4-3. First, 1-(2-decyltetradecyl)-4-(trimethylsilyl)benzene (**4-5**) was prepared by *Negishi* coupling of 1-bromo-4-(trimethylsilyl)benzene (**4-4**) with 2-decyltetradecylzinc bromide, which was generated in situ from 2-decyltetradecylbromide (**3-27**).¹ Subsequently, **4-5** was treated with boron tribromide and then quenched with water^{2,3} to yield 4-(2-decyltetradecyl)phenylboronic acid (**4-6**) in 79% yield for two steps. 2-Bromo-5-methylbiphenyl (**4-8**) was synthesized by selective *Suzuki* coupling of 4-bromo-3-iodotoluene (**4-7**) with phenylboronic acid at 60 °C. The relatively low yield of 55% was due to the formation of a terphenyl byproduct through the coupling with the bromo group. Lowering the reaction temperature to 50 °C did not improve the yield. The relatively preferred formation of the terphenyl byproduct could be due to activation of the bromo group of **4-8** through the electron-donating effect of the methyl group as well as deactivation of the iodo group of **4-7** by the electron-withdrawing effect of the bromo group.

Next, bromination of **4-8** was attempted using 1.1 equivalent of *N*-bromosuccinimide (NBS) with a catalytic amount of benzoyl peroxide, but ¹H NMR analysis showed the formation of both mono- and dibrominated products with the presence of unreacted starting material **4-8**, which indicated that selective monobromination of **4-8** was impossible. Therefore, synthesis of bromomethylbiphenyl **4-9** was conducted by treatment of **4-8** with an excess amount of NBS to give a mixture of mono- and dibrominated products, followed by selective debromination using diethyl phosphite and *N,N*-diisopropylethylamine⁴ to afford **4-9** in 67%⁴ yield for two steps. Phase-transfer carbonylation of **4-9** with iron pentacarbonyl yielded bis(bromobiphenyl)acetone **4-10**, which was further reacted with boronic acid **4-11**^{5,6} via *Suzuki* coupling to afford bis(*o*-terphenyl)acetone **4-12a** bearing the dodecyl groups. Bis(*o*-terphenyl)acetone **4-12b** with the longer and branched 2-decyltetradecyl groups was also synthesized through *Suzuki* coupling of bis(bromobiphenyl)acetone **4-10** and boronic acid **4-6**. Finally, *Knoevenagel* condensation of **4-12a** and **4-12b** with benzil **3-36** followed by the removal of the triisopropylsilyl protecting group with TBAF

provided laterally extended monomers **4-1a** and **4-1b**, respectively. The formation of monomers **4-1a** and **4-1b** were verified by a combination of NMR and high-resolution ESI MS analyses, where exact masses of **4-1a** and **4-1b** were measured to be $m/z = 1071.6425$ and 1386.0356 in perfect agreement with the calculated masses of $m/z = 1071.6420$ for $C_{79}H_{84}ONa$, i.e. $[M+Na]^+$, and $m/z = 1386.0356$ for $C_{103}H_{133}O$, i.e. $[M+H]^+$, respectively.

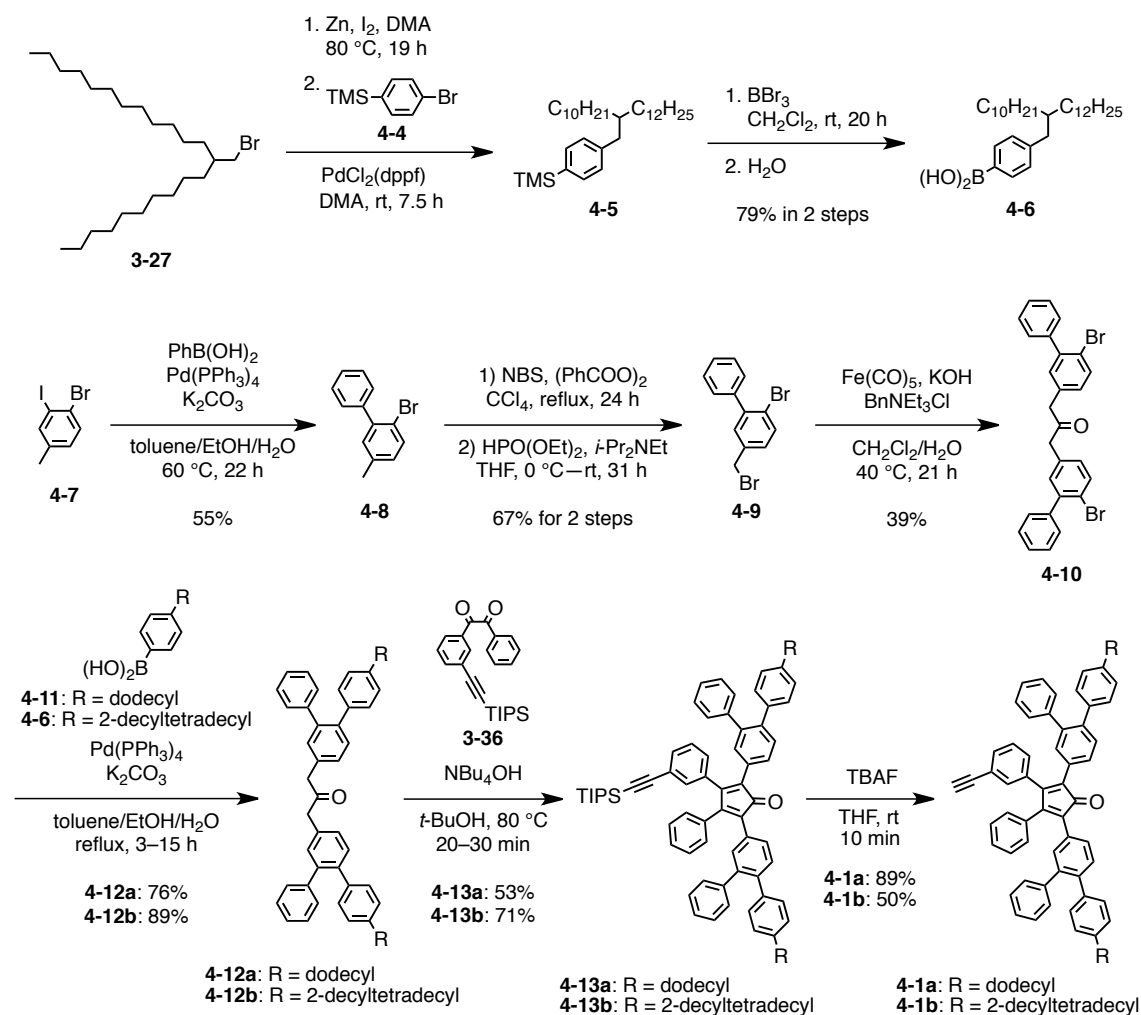


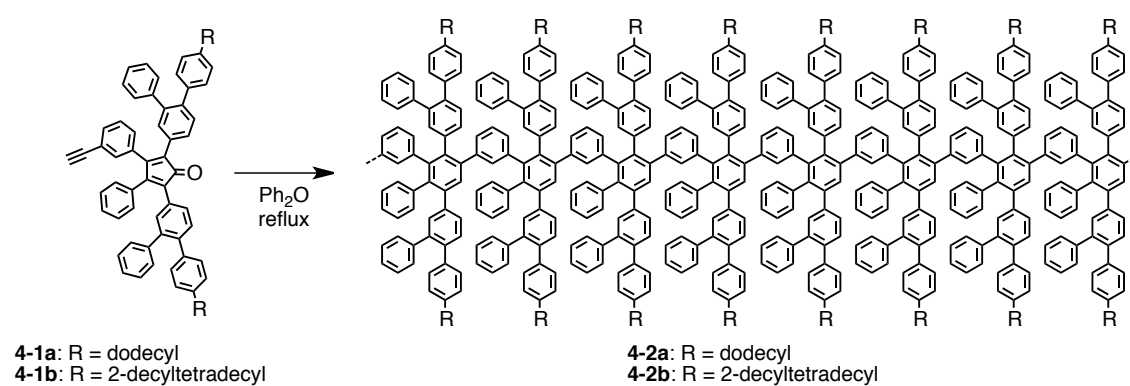
Figure 4-3. Synthetic route to laterally extended AB-type monomers **4-1a** and **4-1b**.

4.2.2 Diels–Alder polymerization

AB-type Diels–Alder polymerization of the laterally extended AB-type monomers was first carried out with monomer **4-1a** with the dodecyl chains in a similar manner to the polymerization of monomer **3-1** discussed in subsection 3.3.2. Thus, a solution of monomer **4-1a** in diphenyl ether with a concentration of 221 mM was refluxed for 20 h,

when the purple color characteristic for the tetraphenylcyclopentadienone structure had completely disappeared. SEC analysis of the resulting polyphenylene precursor **4-2a-I** showed M_w of 36,000–66,000 g/mol, M_n of 16,000–24,000 g/mol, and PDI of 2.3–2.5 based on PPP and PS standards (Table 4-1, entry 1). Considering the structural similarity between precursors **4-2** and **3-2**, the absolute molecular weights of precursor **4-2** can presumably be approximated by these estimated values according to PPP and PS standard calibrations (see subsection 3.3.5).

Table 4-1. Polymerization conditions for monomers **4-1a** and **4-1b**, and the resulting M_w , M_n , and PDI values of precursors **4-2a** and **4-2b** before and after the fractionation.



Entry	Mono.	Prod.	Solv.	C (M)	T (h)	M_w (kg/mol)	M_n (kg/mol)	PDI
1	4-1a	4-2a-I	Ph ₂ O	0.22	20	36–66	16–24	2.3–2.5
1'	—	4-2a-I'	—	—	—	42–78	31–53	1.4–1.5
2	4-1a	4-2a-II	melt	—	2.5	130–300	16–22	8.1–14
3	4-1a	4-2a-III	melt	—	5.0	150–350	17–22	8.8–16
3'	—	4-2a-III'	—	—	—	230–550	81–150	2.8–3.8
4	4-1b	4-2b-I	Ph ₂ O	0.10	14	25–58	31–53	2.5–3.9
4'	—	4-2b-I'	—	—	—	43–79	33–57	1.3–1.4
5	4-1b	4-2b-II	Ph ₂ O	1.0	14	190–460	34–51	5.6–9.0
5'	—	4-2b-II'	—	—	—	260–630	130–240	2.0–2.6
5''	—	4-2b-II''	—	—	—	160–360	76–140	2.1–2.6

M_w and M_n were estimated by the SEC analysis based on PPP and PS standards and given with ranges, corresponding to $M_{w,PPP}$ – $M_{w,PS}$ and $M_{n,PPP}$ – $M_{n,PS}$, respectively (eluent: THF, UV detector). PDI values were calculated by M_w/M_n . Entries 1', 3', 4', 5', and 5'' represent M_w , M_n , and PDI obtained after the fractionation of precursors **4-2a** and **4-2b** in entries 1, 3, 4, and 5, respectively. All the SEC results have a margin of error of $\pm 10\%$. Mono., monomer; prod., product; solv., solvent; C , concentration; T , time.

It was also possible to perform the polymerization of monomer **4-1a** in a melt, namely by heating **4-1a** at 260–270 °C without any other reagent or solvent, similar to the case of monomer **3-1** (see subsection 3.3.2). After the polymerization in a melt for 2.5 h, precursor **4-2a-II** with M_w of 130,000–300,000 g/mol, M_n of 16,000–22,000 g/mol, and PDI of 8.1–14 was obtained based on the SEC analysis (Table 4-1, entry 2). Notably, M_w of precursor **4-2a-II** obtained in a melt was around five times higher than that of **4-2a-I** prepared in a solution (Table 4, entries 2 and 1, respectively). When the polymerization time was extended to 5 h, precursor **4-2a-III** with M_w of 150,000–350,000 g/mol, M_n of 17,000–22,000 g/mol, and PDI of 8.8–16 was obtained, the molecular weights of which were comparable to those of precursor **4-2a-II** (Table 4-1, entry 3). These results suggested that the polymerization of monomer **4-1** in a melt was much faster than that in a solution, yielding precursor **4-2a** with considerably higher molecular weights. As discussed for the polymerization of monomer **3-1** in subsection 3.3.6, the higher molecular weights attained in a melt might be due to the instability at high temperatures, i.e. 260–270 °C, of the cyclopentadienone moiety of monomer **4-1a** and/or as-grown oligomers and polymers. Based on this assumption, more monomers, oligomers, and polymers can be deteriorated during longer reaction times, and thus the faster polymerizations in a melt, i.e. at higher “concentrations”, can lead to higher molecular weights than in solutions or at lower concentrations, where the polymerization is slower and necessitates longer time.

The SEC profiles of precursor **4-2a** all showed a peak at ~27 min in addition to the main peaks at ~19–23 min, regardless of the polymerization condition, which indicated the presence of small oligomers that could not undergo further polymerizations (Figure 4-4). Such oligomers could be possibly assigned to the cyclic structures formed through the head-to-tail *Diels–Alder* cycloaddition⁷ based on the MALDI-TOF MS analysis (see the next page), which was similar to the results obtained for the narrower counterpart, precursor **3-2** (see section 3.3). These small oligomers could be removed by fractionation of **4-2a** with recycling preparative SEC. For instance, fractionation of precursor **4-2a-I** provided precursor **4-2a-I'** with M_w of 42,000–78,000 g/mol, M_n of 31,000–53,000 g/mol, and PDI of 1.4–1.5, which did not contain the smaller oligomers according to the SEC analysis (Table 4-1 entry 1' and Figure 4-4b). Precursor **4-2a-III** could also be fractionated with recycling preparative SEC to yield precursor **4-2a-III'** with very high M_w of 230,000–550,000 g/mol, M_n of 81,000–150,000 g/mol, and PDI of 2.8–3.8, which were also free of the smaller oligomers (Table 4-1 entry 3' and Figure 4-4e). Moreover, the small oligomers could be further

separated by recycling preparative SEC to allow the isolation of each oligomer, which will be discussed in subsection 4.2.3.

Apart from the peak of the small oligomers observed at ~ 27 min, precursors **4-2a-II** and **4-2a-III** showed two peaks approximately at ~ 19 and ~ 21 min (Figure 4-4c and d), similar to the SEC profiles of precursors **3-2-III** and **3-2-V** (Figure 3-14d and h, respectively), which implied the presence of two polymer species with different hydrodynamic volumes in these samples of precursor **4-2a**. The SEC profiles did not change depending on the concentration of precursors **4-2a**, which indicated that the observation of the two peaks was not due to the aggregation of the polymers. Precursors **4-2a-II** and **4-2a-III** were both prepared through the polymerization in a melt, but with different reaction times of 2.5 and 5.0 h, respectively (Table 4-1, entries 2 and 3,

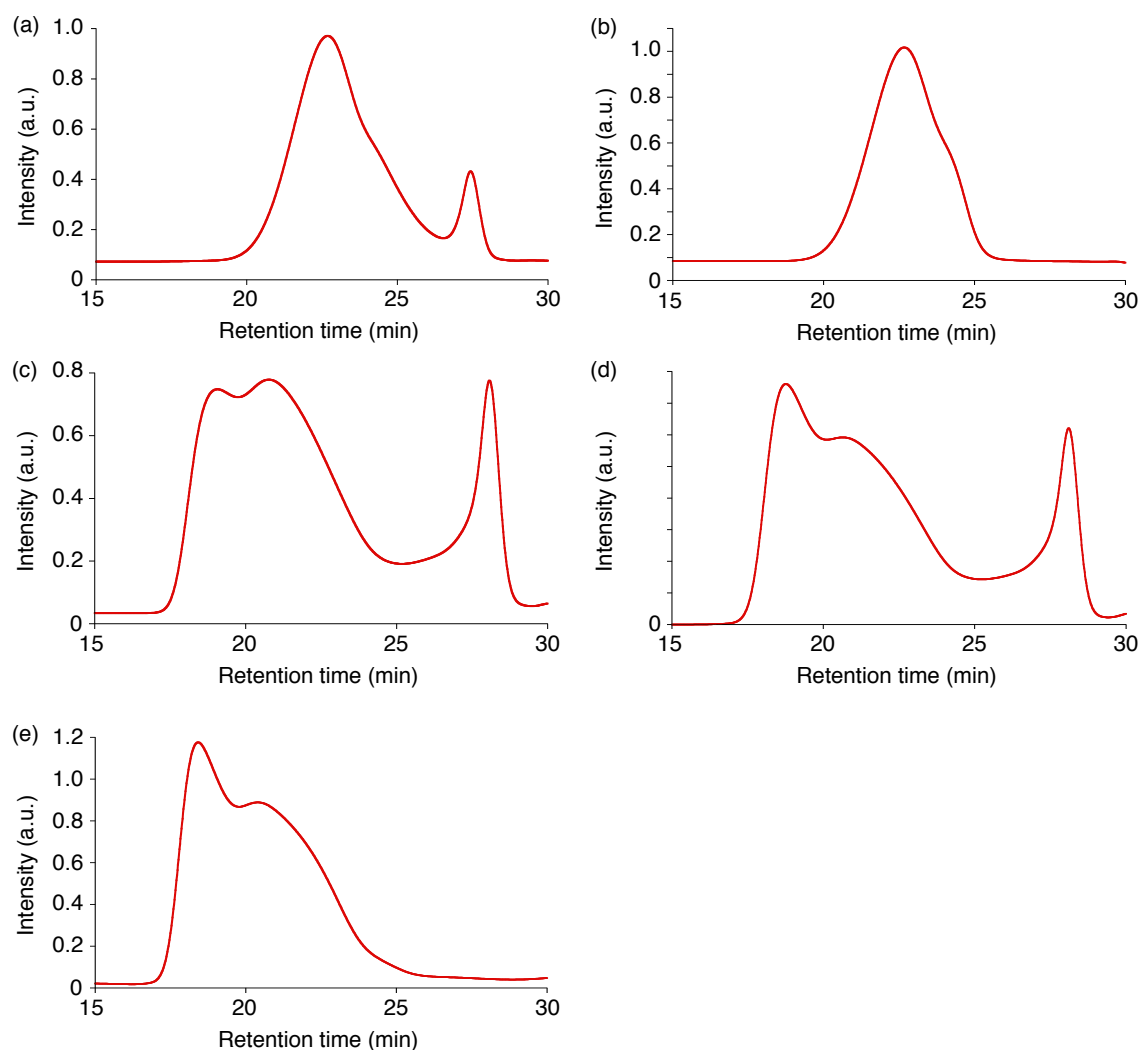


Figure 4-4. Normalized SEC profiles of polyphenylene precursors **4-2a**; (a) precursor **4-2a-I**, (b) precursor **4-2a-I'**, (c) precursor **4-2a-II**, (d) precursor **4-2a-III**, and (e) precursor **4-2a-III'** (eluent: THF, 1.0 mL/min, UV detector).

respectively). While precursors **4-2a-II** and **4-2a-III** displayed the second peak at the same retention time of 20.8 min, corresponding to M_p of 100,000–210,000 g/mol, the retention time of the first peak of precursor **4-2a-II**, i.e. 19.0 min; M_p : 300,000–720,000 g/mol, was slightly longer than that of precursor **4-2a-III**, i.e. 18.8 min; M_p : 340,000–840,000 g/mol. Furthermore, the intensity of the first peak was higher than that of the second peak in the SEC profile of precursor **4-2a-III**, whereas the second peak was larger than the first peak in the profile of precursor **4-2a-II**. These observations suggested that the second peak at 20.8 min might correspond to cyclic polymers, which were formed through the head-to-tail *Diels–Alder* cycloaddition and precluded from further polymer growth, while the first peak at ~19 min was derived from linear polymers that underwent further polymerization (see also subsections 3.3.4 and 3.3.6). This notion, however, requires further microscopic investigations, i.e. by STM and/or AFM for the verification.

MALDI-TOF MS analysis of precursors **4-2a-I–III** was performed in order to elucidate the structures of the small oligomers shown by the SEC analysis. MALDI-TOF MS spectra of the precursors in general displayed only weak signals due to the high average molecular weights, but a low-molecular-weight fraction of **4-2a-I** obtained during the SEC fractionation allowed reliable analysis of the oligomers of **4-2a**. Linear-mode analysis of the fraction of **4-2a-I** demonstrated a regular pattern of mass peaks extending up to $m/z = \text{ca. } 24,000$ (Figure 4-5). The broadening of the peaks in the

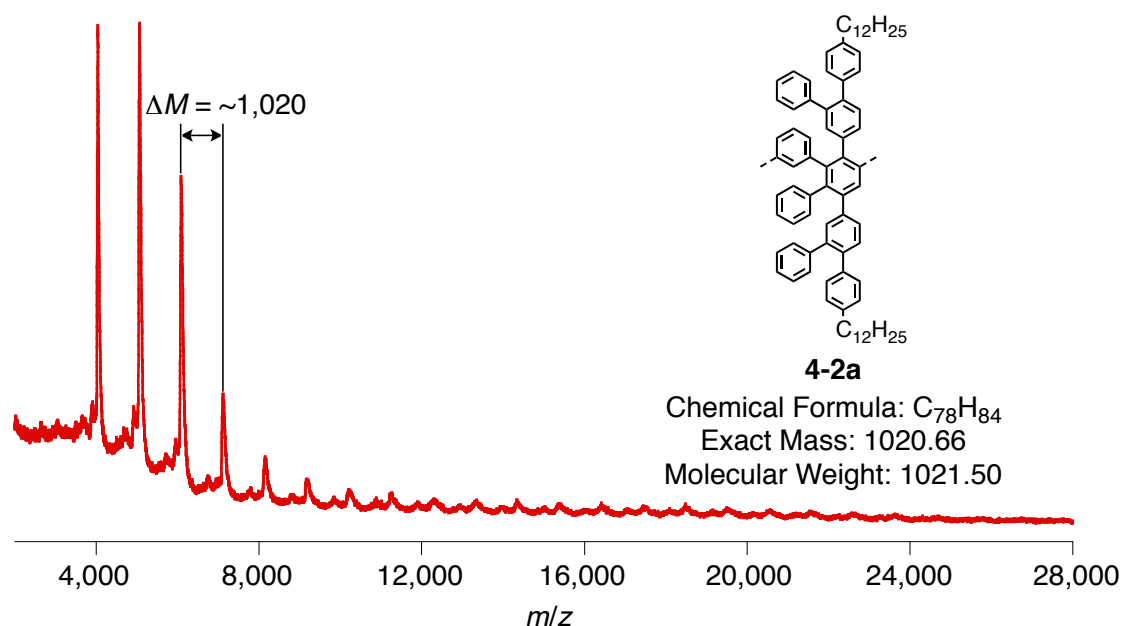


Figure 4-5. Linear-mode MALDI-TOF MS analysis of a fraction of precursor **4-2a** obtained during the SEC fractionation (solid-state sample preparation, matrix: TCNQ).

linear-mode measurement did not allow the determination of the exact mass values. Nevertheless, the interval of the signals was approximately $m/z = 1,020$ which was consistent with the molecular mass of the repeating unit of precursor **4-2a**, i.e. $C_{78}H_{84}$: 1,022. The small peaks and shoulders observed in the spectrum corresponded to the fragmentation of the dodecyl chains during the measurement.

Reflectron-mode MALDI-TOF MS analysis of the same fraction of precursor **4-2a-I** showed peaks of tetramer, pentamer, hexamer, heptamer, and octamer at $m/z = 4,083$, $5,104$, $6,125$, $7,147$, and $8,167$, which all corresponded to oligomer structures with a benzene ring instead of the cyclopentadienone moiety and the ethynyl group at the terminals (Figure 4-6). This result suggested the possible formation of laterally extended cyclic oligomers through the head-to-tail *Diels–Alder* cycloaddition of linear oligomers (Representative case of the pentamer is depicted in Figure 4-7), which were thus precluded from further polymer growth and observed as the sharp peak at ~ 27 min in the SEC profiles (Figure 4-4). Notably, several oligomers could be isolated with recycling preparative SEC. Such cyclic oligomers are highly interesting as oligophenylene precursors corresponding to short segments of CNTs, which will be discussed in subsection 4.2.3.

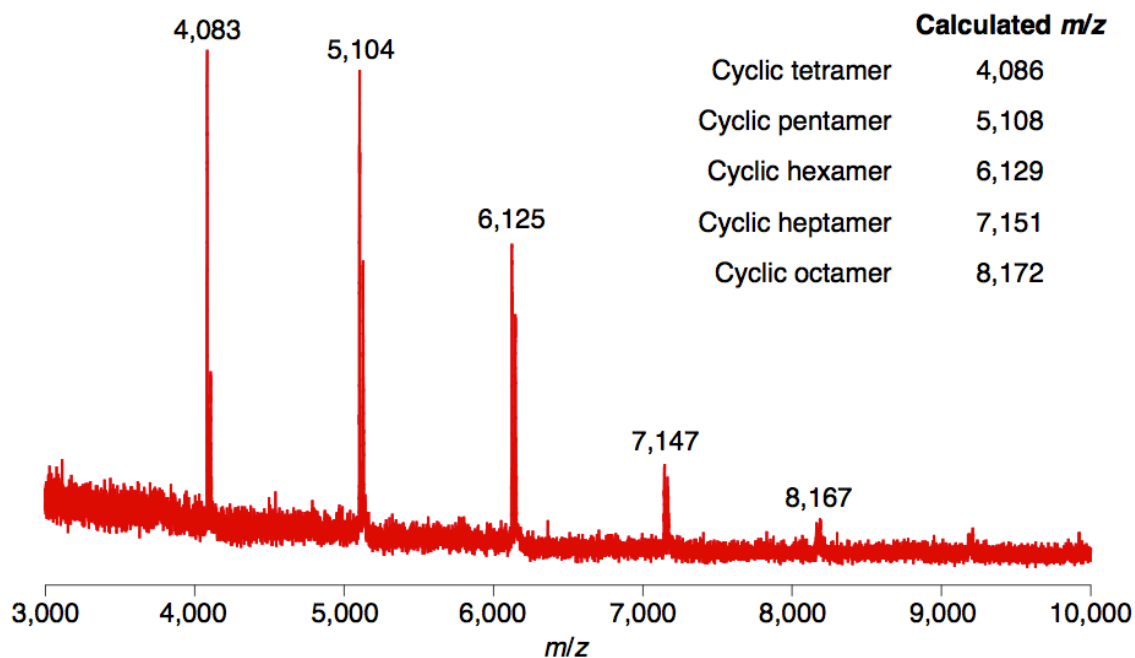


Figure 4-6. Reflectron-mode MALDI-TOF MS analysis of a fraction of precursor **4-2a** obtained during the SEC fractionation (solid-state sample preparation, matrix: TCNQ), inset: calculated m/z of cyclic oligomers. The shoulders of the peaks correspond to $[M + Na]^+$.

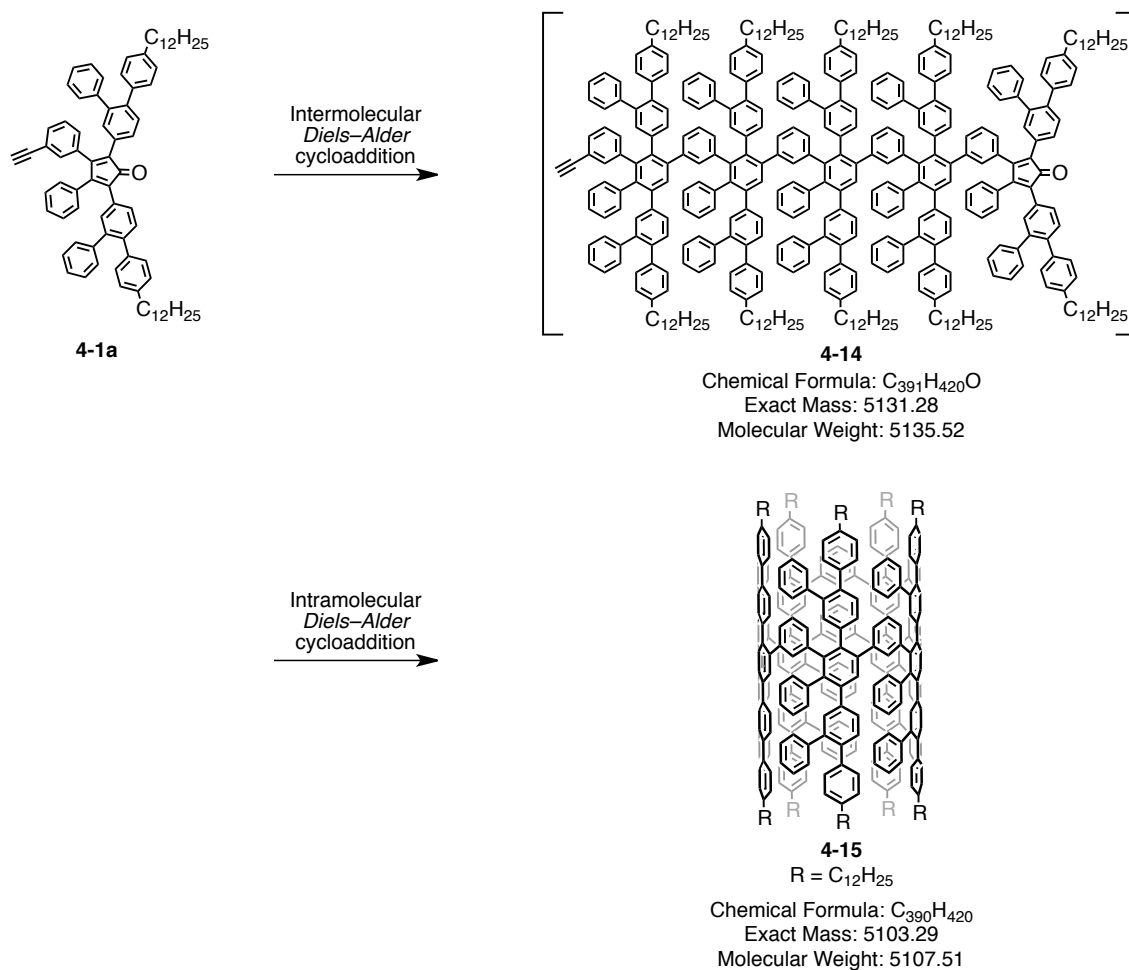


Figure 4-7. Proposed formation of cyclic pentamer **4-15** via intramolecular *Diels-Alder* cycloaddition of linear pentamer **4-14**.

Next, the *AB*-type *Diels-Alder* polymerization of monomer **4-1b** with the 2-decyltetradecyl chains was carried out by refluxing in diphenyl ether at two different concentrations, namely at 100 mM and 1.0 M. At 100 mM the resulting polyphenylene precursor **4-2b-I** showed M_w of 25,000–58,000 g/mol, M_n of 10,000–15,000 g/mol, and PDI of 2.5–3.9 (Table 4-1, entry 4), which were slightly smaller than those of precursor **4-2a-I** prepared in a solution with the concentration of 221 mM (Table 4-1, entry 1). Whereas the degree of polymerization (DP) of precursor **4-2b-I** could be calculated to be 18–43 based on the M_w , DP of precursor **4-2a-I** was 35–65, which was in line with the notion that higher DP was obtained at higher concentration. On the other hand, the polymerization at the concentration of 1.0 M yielded precursor **4-2b-II** with significantly higher M_w of 190,000–460,000 g/mol, M_n of 34,000–51,000 g/mol, and PDI of 5.6–9.0 (Table 4-1, entry 5). The DP of precursor **4-2b-II** was 140–340, which

was comparable with that of precursor **4-2a-III**, i.e. 150–340, indicating that the polymerization in a solution at the concentration of 1.0 M is as efficient as the polymerization in a melt.

The SEC profiles of precursors **4-2b-I** and **4-2b-II** both showed a peak at ~27 min, corresponding to small oligomers, similar to all the other precursors prepared through the *Diels–Alder* polymerization in the scope of this thesis (Figure 4-8a and b). Similar to the other cases, such small oligomers could be removed by fractionating with recycling preparative SEC. Fractionation of precursor **4-2b-I** thus gave precursor **4-2b-I'** with M_w of 43,000–79,000 g/mol, M_n of 33,000–57,000 g/mol, and PDI of 1.3–1.4 (Table 4-1, entries 4'). Precursor **4-2b-II** was fractionated into two fractions, removing the small oligomers, to provide precursor **4-2b-II'** with M_w of 260,000–630,000 g/mol, M_n of 130,000–240,000 g/mol, and PDI of 2.0–2.6 as well as precursor **4-2b-II''** with M_w of 160,000–360,000 g/mol, M_n of 76,000–140,000 g/mol, and PDI of 2.1–2.6 (Table 4-1, entries 5' and 5'', respectively). Both precursors **4-2b-II'** and **4-2b-II''** were free of the small oligomers as displayed by the SEC profiles (Figure 4-8c and d, respectively).

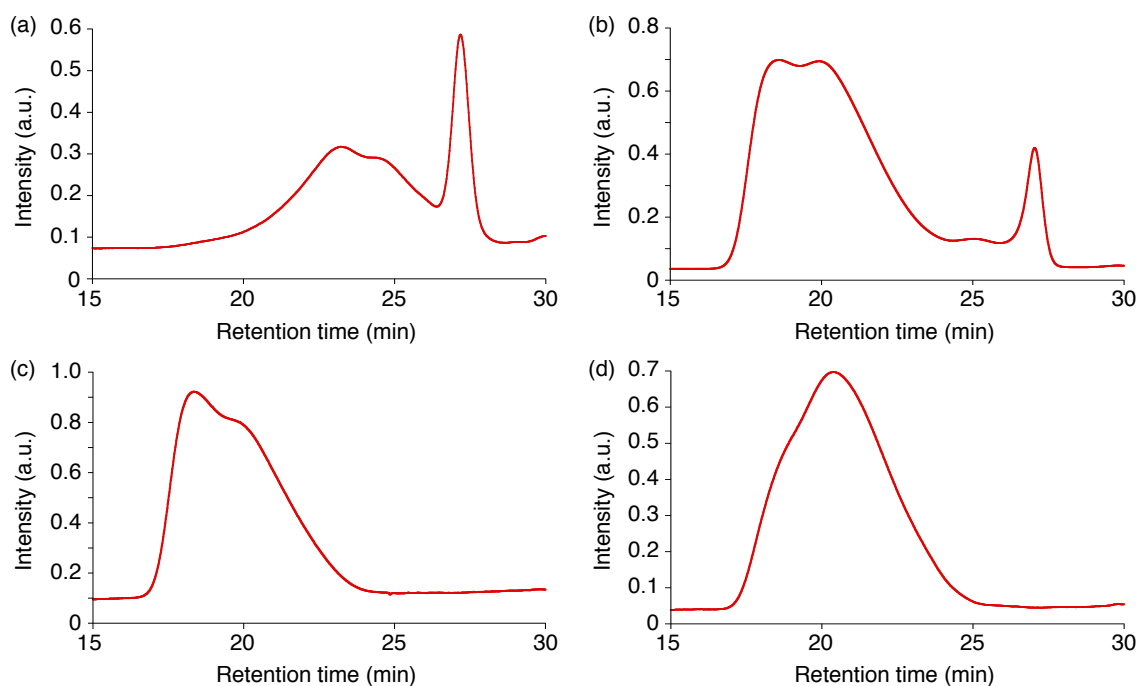


Figure 4-8. Normalized SEC profiles of polyphenylene precursors; (a) precursor **4-2b-I**, (b) precursor **4-2b-II**, (c) precursor **4-2b-II'**, and (d) precursor **4-2b-II''** (eluent: THF, 1.0 mL/min, UV detector). Precursors **4-2b-II'** and precursor **4-2b-II''** were obtained after the fractionation of precursor **4-2b-II** by recycling preparative SEC.

MALDI-TOF MS analysis was performed on a smaller-molecular-weight fraction of precursor **4-2b-II**, which was obtained during the fractionation with recycling preparative SEC. Smaller molecular weight with narrower distribution of this fraction allowed acquisition of MALDI-TOF MS spectra with higher resolution. Linear-mode analysis of this fraction displayed a regular pattern of mass signals extending to over $m/z = 50,000$ (Figure 4-9). The interval between the signals was $m/z =$ ca. 1,370 and slightly higher than the molecular mass of the repeating unit of precursor **4-2b**, namely $C_{102}H_{132}$: 1,358. However, this is most likely the measurement error in the linear-mode analysis, because an analysis of the same sample in the reflectron mode, which is less sensitive but more precise, showed an interval of $m/z = \sim 1,358$ in perfect agreement with the molecular mass of the repeating unit (Figure 4-9).

The reflectron-mode MALDI-TOF MS analysis of the fraction of precursor **4-2b-II** showed signals at $m/z = 5,452, 6,808, 8,165, 9,523, 10,879, 12,233, 13,592,$ and $14,954$, which all corresponded to cyclic oligomer structures with sodium ions (Figure 4-10). The slight deviations between the experimental and calculated values were most probably measurement errors. As representatively displayed in the inset of Figure 4-10, the pentamer showed a smaller peak at $m/z = 6,785$, which was 23 smaller than its main peak at $m/z = 6,808$, which unambiguously validated its assignment to the $[M + Na]^+$ species. This result was similar to those of all the other polyphenylene precursors

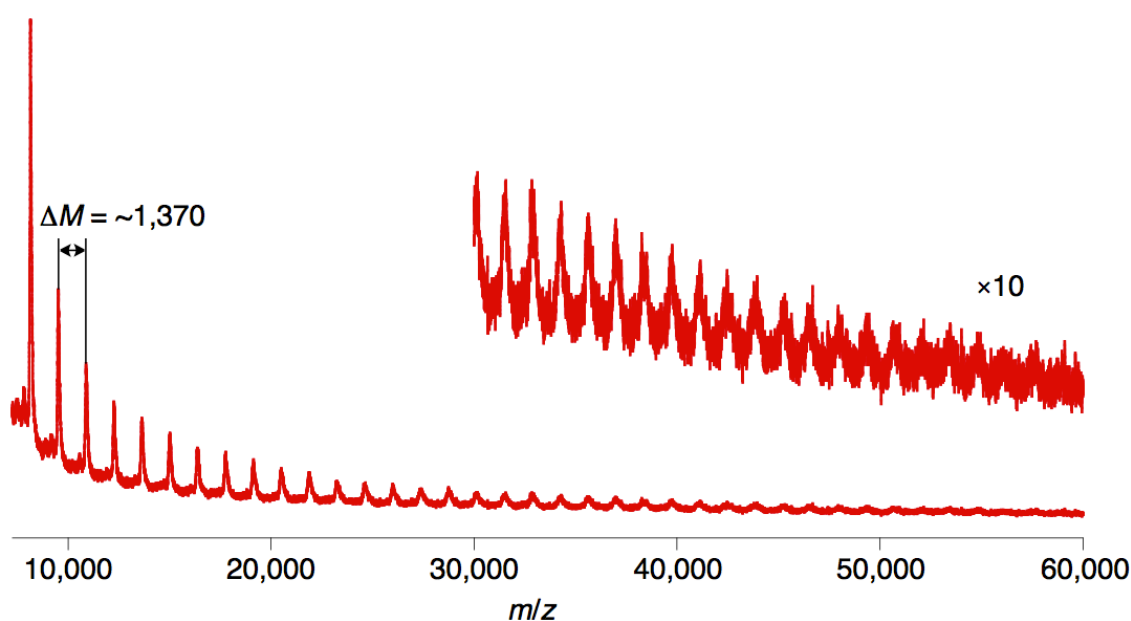


Figure 4-9. Linear-mode MALDI-TOF MS analysis of a fraction of precursor **4-2b-I** obtained during the SEC fractionation; inset: a magnified spectrum (solid-state sample preparation, matrix: TCNQ).

reported in chapters 3 and 4, and implied the formation of cyclic oligomers also for precursor **4-2b**, which were precluded from the polymerization and corresponded to the peak at ~27 min in the SEC profiles (Figure 4-8a and b).

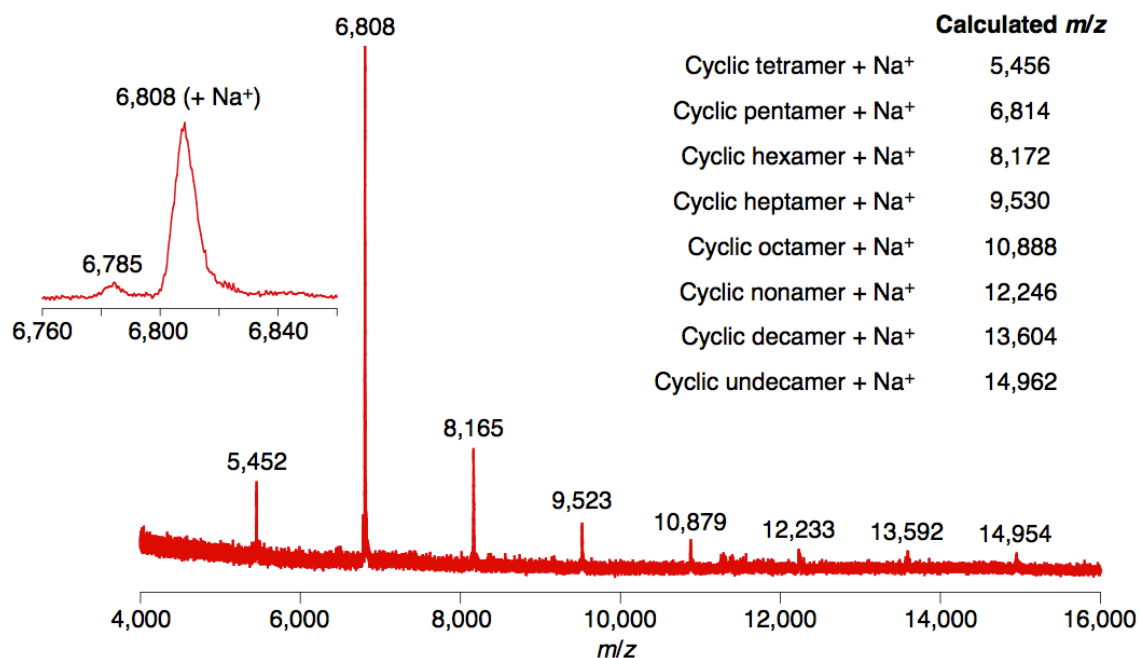


Figure 4-10. Reflectron-mode MALDI-TOF MS analysis of a fraction of precursor **4-2b-I** obtained during the SEC fractionation (solid-state sample preparation, matrix: TCNQ), inset: a zoomed spectrum showing the peaks from the pentamer and calculated m/z of cyclic oligomers.

4.2.3 Isolation of small oligomers

Notably, the small oligomers of polyphenylene precursor **4-2a-I** could be further separated by using recycling preparative SEC, which allowed the isolation of pentamer **4-15** (2.6% isolated yield) as demonstrated by the MALDI-TOF MS analysis (Figure 4-11). Although the isotopic distribution could not be resolved due to the relatively high molecular weight, the single peak observed at $m/z = 5,107.2$ was in good agreement with the calculated molecular mass of cyclic pentamer **4-15**, i.e. 5,107.5, supporting the formation of the cyclic structure. This result was in stark contrast to that of precursor **3-2** that did not allow the isolation of the oligomers by the same method. The isolation of oligomers of precursor **4-2a** was most likely thanks to the larger difference in the hydrodynamic volume between the different oligomer.

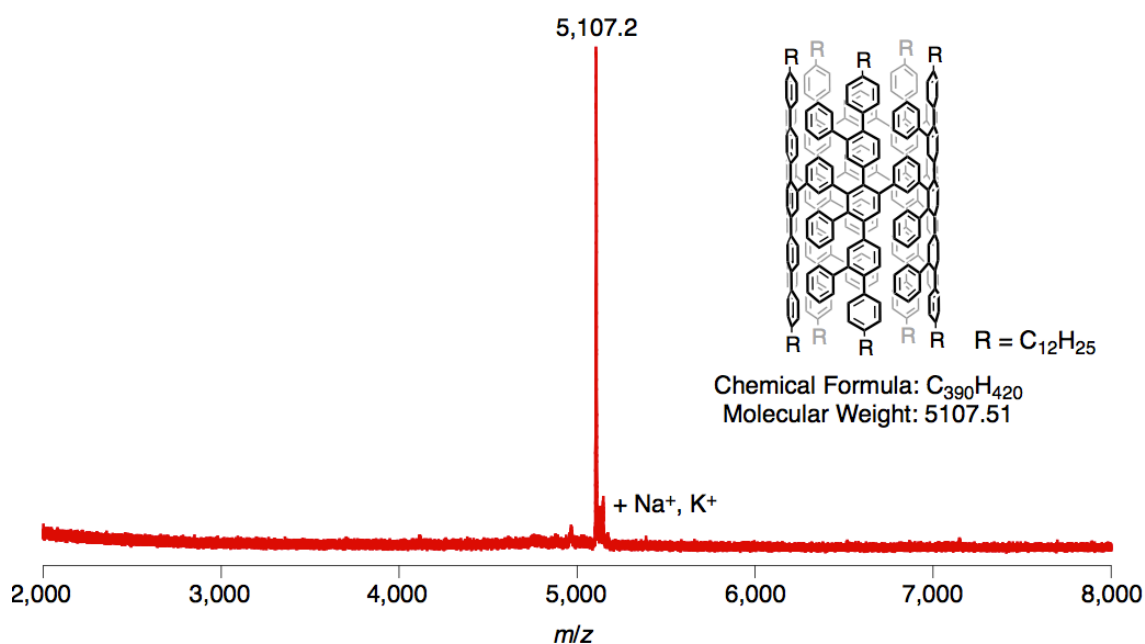


Figure 4-11. Reflectron-mode MALDI-TOF MS analysis of pentamer **4-15** isolated by recycling preparative SEC, inset: structure and molecular mass of the possibly formed cyclic pentamer.

¹H NMR analysis of pentamer **4-15** was performed for further structural characterization, but only showed broadened signals in the aromatic region. The broadening of the signals was most probably due to the presence of 16 regioisomers (Figure 4-12), which were formed during the five-fold *Diels–Alder* cycloaddition, where each step proceeded via two different molecular orientations (see also Figure 3-3). SPM visualization of pentamer **4-15** was also attempted in the group of [REDACTED], but unfortunately the molecular structure of **4-15** could not be imaged, rendering the unambiguous characterizations of pentamer **4-15** elusive. Additionally, other oligomers of precursor **4-2a** such as hexamer and heptamer could also be isolated by using recycling preparative SEC, but their characterizations suffered the same problems as those of the pentamer **4-15**.

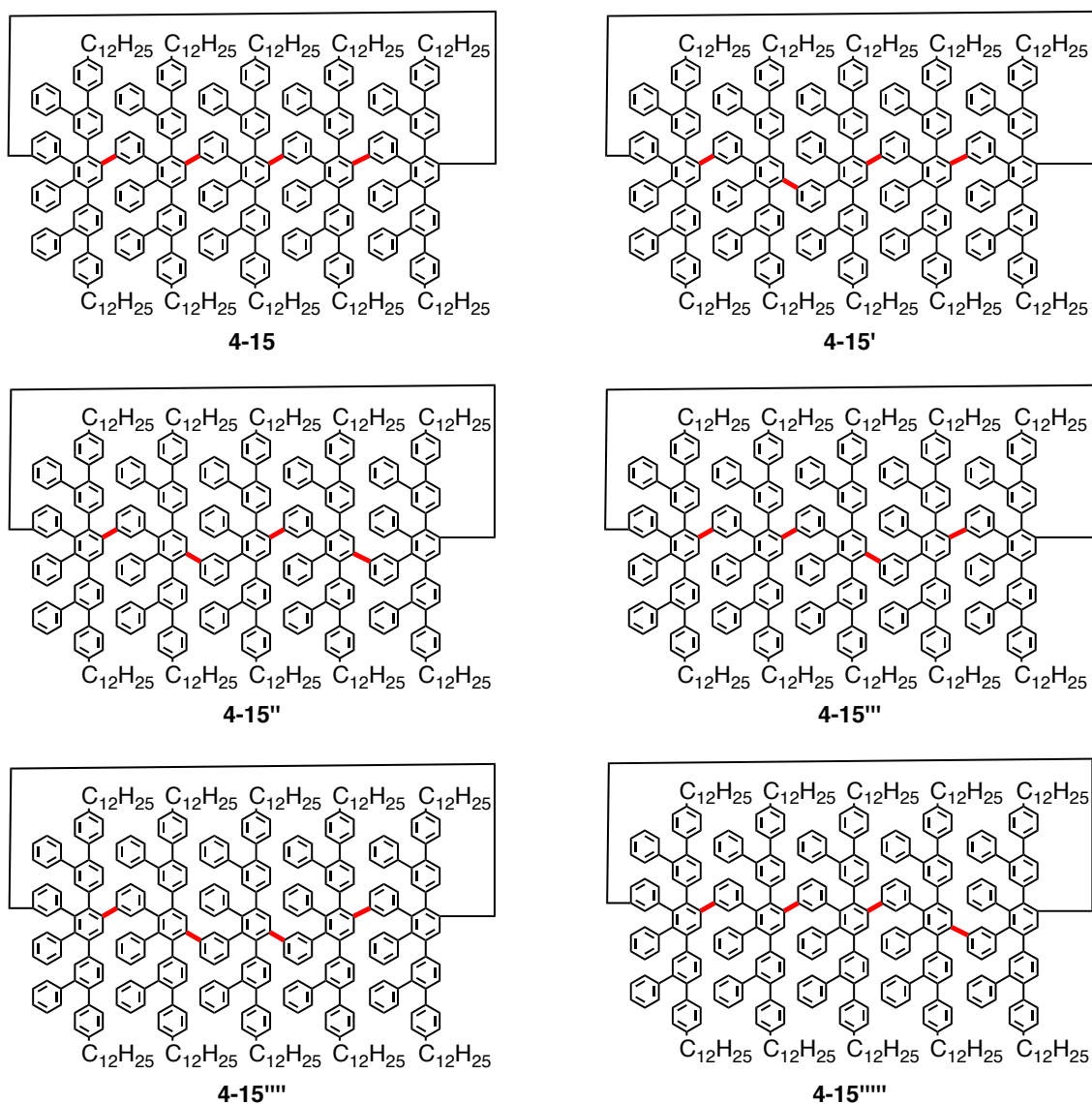


Figure 4-12. Schematic illustration for six examples of regioisomers of cyclic pentamer **4-15**, which are formed due to two possible molecular orientations upon each *Diels–Alder* cycloaddition step.

Nevertheless, the cyclic oligomers can be regarded as precursors that lead to short segments of CNTs by “graphitization”. Selective bottom-up synthesis of such short CNTs has intensively been pursued, but still remains highly challenging.⁸⁻¹⁴ Here, pentamer **4-15** was subjected the “graphitization”, which would possibly give short CNT **4-16** if pentamer **4-15** really had the cyclic structure (Figure 4-13). The cyclodehydrogenation of pentamer **4-15** was performed with iron(III) chloride as the oxidant and the Lewis acid in the same condition as the synthesis of the GNRs discussed in chapter 3. MALDI-TOF MS analysis of the resulting product however

displayed significantly broadened signals, ranging from $m/z = \text{ca. } 2,000$ to $\text{ca. } 6,000$, which suggested the formation of a mixture of partially-fused and chlorinated products, and/or difficulty of characterizing such product by MALDI-TOF MS due to complex fragmentation.

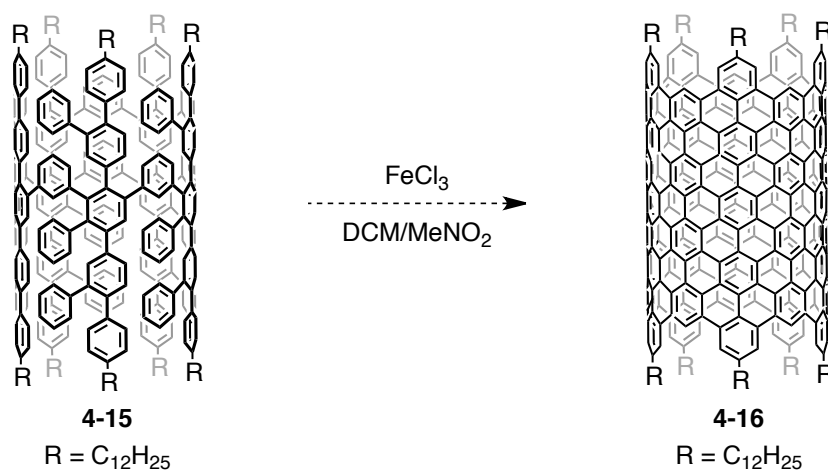


Figure 4-13. Attempted synthesis of short CNT **4-16** through intramolecular oxidative cyclodehydrogenation of pentamer **4-15** that presumably has the cyclic structure.

4.2.4 “Graphitization” of the polyphenylene precursors

Finally, polyphenylene precursor **4-2** was “planarized” and “graphitized” into laterally extended GNR **4-3** though intramolecular oxidative cyclodehydrogenation in the same manner as the synthesis of GNR **3-3**, using seven equivalent of iron(III) chloride for one hydrogen to be removed (Figure 4-14). Representatively, precursors **4-2a-I'** and **4-2b-II'** were converted to GNRs **4-3a** and **4-3b**, respectively. The average longitudinal lengths of GNRs **4-3a** and **4-3b** could be estimated from the M_w values of the precursors to be $\text{ca. } 30\text{--}56$ and $\text{ca. } 140\text{--}340$ nm, respectively. The dispersibility of laterally-extended GNRs **4-3a** and **4-3b** were limited compared to those of the narrower counterparts, i.e. GNRs **3-3** and **3-26**, but it was still possible to disperse them in organic solvents such as THF, chlorobenzene, and 1,2-dichlorobenzene with an assistance of sonication to give pale blue dispersions similar to that of GNR **2-3** (see the inset of Figure 4-17). Some of the GNRs remained as visible particles in the resulting dispersion, which indicated that only a part of them could be dispersed during this process. This result suggested that the GNR sample might have been “fractionated”, where only shorter and more soluble GNRs could be brought into the dispersion while

longer and less soluble GNRs remained inside the particles. It might also be the case that some GNR aggregates had tighter packing structures, which could not be broken by the sonication. Nevertheless, such visible particles could be removed by centrifugation or through filtration with a membrane filter (pore size: 5 μm). Although limited, this dispersibility of GNR **4-3** allowed their characterizations as well as processing from a liquid phase.

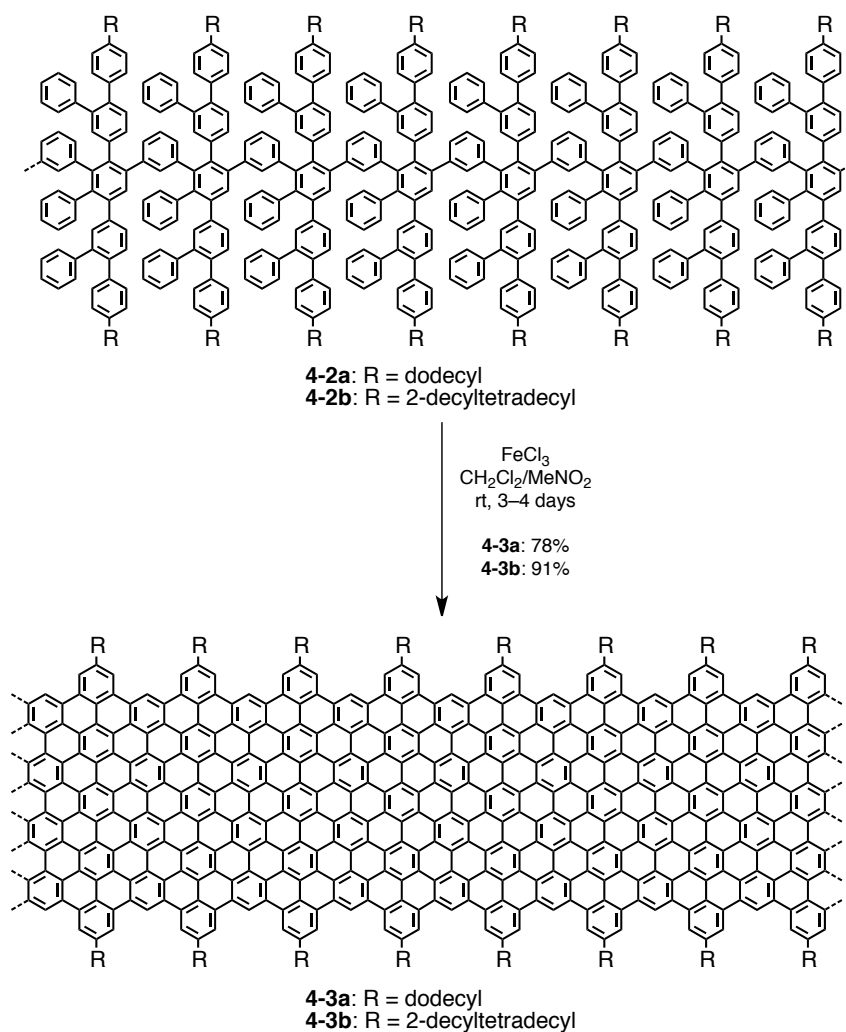


Figure 4-14. Synthesis of GNRs **4-3a** and **4-3b** through intramolecular oxidative cyclodehydrogenation of precursors **4-2a** and **4-2b**, respectively.

4.3 Characterization of broad and long GNRs

4.3.1 FTIR spectroscopy

Characterization of GNR **4-3** was first carried out by Fourier transform infrared (FTIR) spectroscopic analysis (Figure 4-15). Comparison of the FTIR spectra of precursor **4-2a-I'** and GNR **4-3a** displayed the disappearance upon the cyclodehydrogenation of out-of-plane (*opla*) C–H deformation bands at 698, 773, and 893 cm^{-1} , which are characteristic for mono- and di-substituted benzene rings.^{15,16} The signal triad derived from aromatic C–H stretching vibrations at 3025, 3058, and 3082 cm^{-1} was also starkly diminished, indicating a significant decrease in the number of aromatic C–H bonds in the structure, consistent with the “graphitization”.¹⁵⁻¹⁷ The peak appearing at 863 cm^{-1} was most likely an *opla* band from the C–H bond at the cove position,¹⁸ and the peak at 718 cm^{-1} could be assigned to –CH₂– rocking mode of the dodecyl chains, as discussed in subsections 3.4.1 and 3.7.2. These observations were in line with those of other GNRs discussed in chapters 2 and 3, supporting the successful cyclodehydrogenation of precursor **4-2a-I'** into GNR **4-3a**.

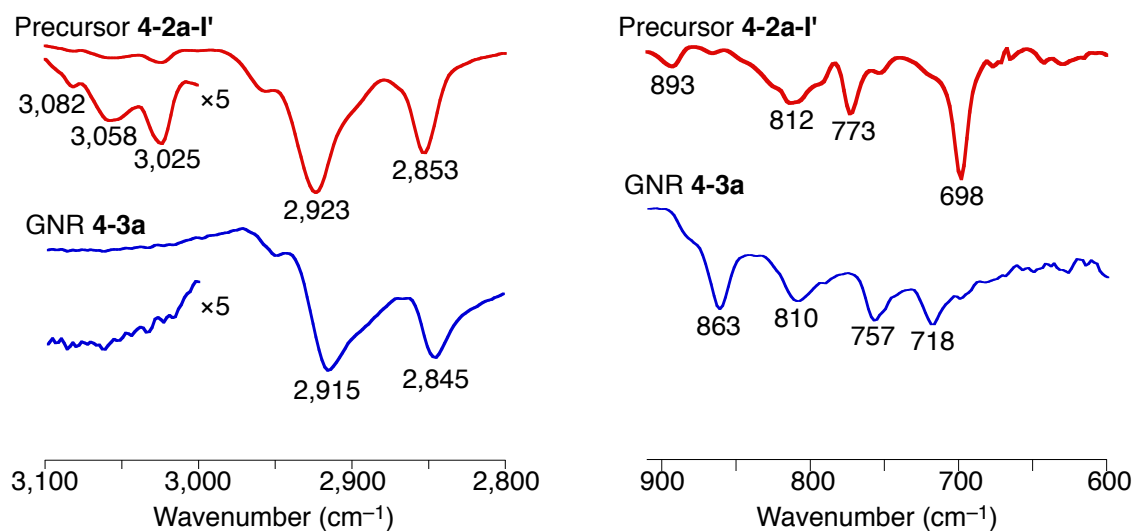


Figure 4-15. Representative FTIR spectral regions of polyphenylene precursor **4-2a-I'** (red line) and GNR **4-3a** (blue line).

4.3.2 Raman spectroscopy

Next, Raman spectroscopic analysis of GNR **4-3** was performed by [REDACTED] in the group of [REDACTED] at Freie Universität Berlin, Germany, in order to gain better insight into the structure and quality of the obtained GNRs. As displayed in Figure 4-16, GNR **4-3a** showed the first-order D and G peaks as well as the second-order 2D, D + D', and 2D' peaks, which was consistent with the Raman spectra of other bottom-up synthesized GNRs (see for example Figures 3-19 and 3-46).^{16,19,20} The intense D peak observed in these spectra did not imply the defects in the basal plane of GNR, but was activated by the structural confinement of the π -electrons as discussed in subsection 2.1.3.²¹⁻²³

Moreover, GNR **4-3a** displayed a distinct peak from the width-dependent radial-breathing-like mode (RBLM) at ~ 170 cm^{-1} (Figure 4-16, inset), which indicated the high uniformity of the obtained GNR sample (see also subsection 3.4.2).^{19,20} Based on the equation $\nu_{\text{RBLM}} = 3,222/w$ (cm^{-1}) reported by *R. Gillen et al.*,²⁴ the wavenumber of the RBLM peak (ν_{RBLM}) of GNR **4-3** with the width of $w = \sim 19.8$ Å could be estimated to be $\nu_{\text{RBLM}} = \sim 163$ cm^{-1} , which was in good agreement with the experimental

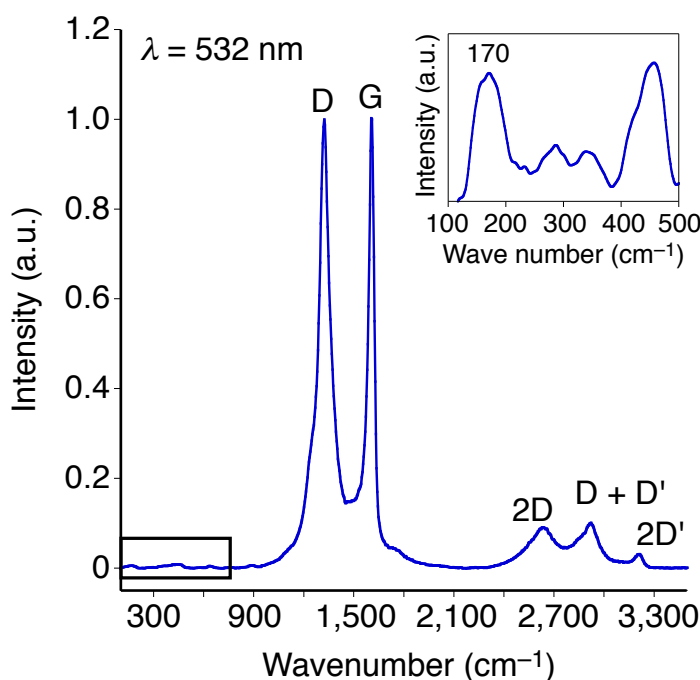


Figure 4-16. Raman spectrum of GNR **4-3a** measured at 532 nm (2.33 eV) on a powder sample with laser power below 0.1 mW. The inset displays a magnified area of the spectra (oblong, bottom left), showing the radial-breathing-like mode at ~ 170 cm^{-1} .

observation. GNR **4-3b** showed basically the identical Raman spectrum to that of GNR **4-3a** as expected for the GNRs with the same core structure. These results corroborated the successful formation of laterally extended GNRs **4-3a** and **4-3b** with highly uniform lateral width of the aromatic core of ~ 2 nm.

4.3.3 UV-vis absorption and photoelectron spectroscopy and DFT calculation

Exploiting the dispersibility of GNR **4-3a**, UV-vis absorption spectroscopic analysis was carried out on a dispersion in THF. The UV-vis spectrum of GNR **4-3a** displayed a broad absorption extending into the near-infrared region with an absorption maximum at 660 nm (Figure 4-17), which featured a red shift of 110 nm compared to that of the narrower counterpart, GNR **3-3** (Figure 3-22). Addition of hydrazine did not alter the absorption profile, indicating the absence of radical-cation species. The absorption observed over 1,000 nm was most probably caused by the scattering by the aggregates of the GNRs in the dispersion. The optical bandgap of GNR **4-3a** could be extracted from the absorption edge at ~ 996 nm to be ~ 1.24 eV, which was considerably smaller than that of narrower GNR **3-3**, i.e. 1.88 eV (subsection 3.4.4), demonstrating the lowering of the bandgap upon the lateral extension.

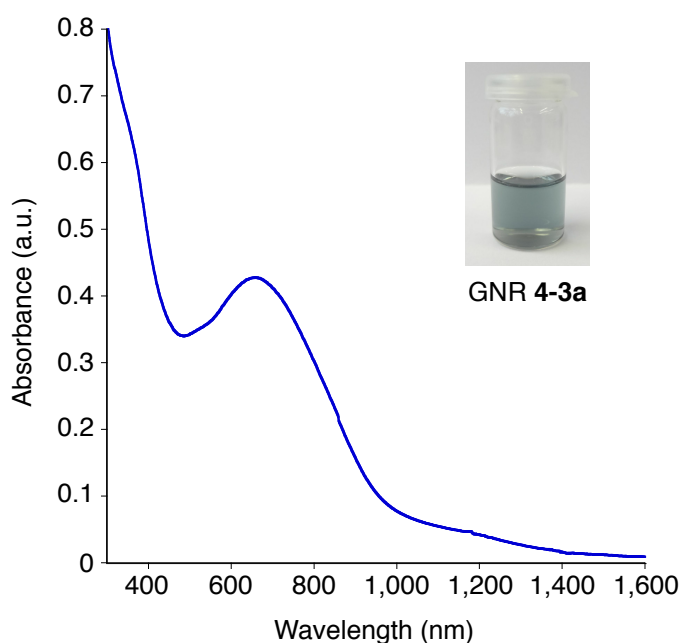


Figure 4-17. UV-vis absorption spectrum of GNR **4-3a** in THF, inset: a photograph of a dispersion of GNR **4-3a** in THF.

In order to obtain further insight into the energy levels of GNR **4-3**, photoelectron spectroscopy measurements of GNR **4-3a** were carried out under ambient conditions by [REDACTED] in the group of Prof. Paolo Samorì at Institut de Science et d'Ingénierie Supramoléculaires (I.S.I.S.), Université de Strasbourg, France. The ionization potential of GNR **4-3a** was thus estimated to be ca. 5.09 eV as a powder sample and ca. 5.02 eV as a film deposited from a dispersion/suspension in ODCB. It is difficult to accurately determine the valence band energy of GNR **4-3a** by such measurements under ambient conditions. Nevertheless, these results indicated that the valence band energy of GNR **4-3a** was comparable to those of laterally extended GNRs **2-3** and **2-13** described in chapter 2 (subsections 2.1.3 and 2.2.3, respectively).

For the theoretical elucidation of the bandgap and the energy levels of GNR **4-3**, density functional theory (DFT)/Heyd-Scuseria-Ernzerhof (HSE) calculations were carried out on an infinite structure of GNR **4-3**, employing a periodic boundary condition, by [REDACTED] in the group of [REDACTED] at the University of Mons, Belgium.²⁵ The bandgap of GNR **4-3** was thus theoretically estimated to be 1.18 eV, which was indeed in good agreement with the optical bandgap extracted from the UV–vis absorption spectrum. This consistency between the theoretical and experimental results provided further evidence for the successful synthesis of GNR **4-3**. The valence and conduction band energies of GNR **4-3** were also calculated by the DFT method to be –4.32 and –3.14 eV, respectively.

4.3.4 AFM visualization

In order to examine the liquid-phase processability of the GNRs and microscopically reveal their structures, film formation and AFM visualization of GNR **4-3a** were carried out by [REDACTED] and [REDACTED] in the group of [REDACTED] at Katholieke Universiteit Leuven, Belgium. In order to effectively disperse the GNRs for the deposition, GNR **4-3a** was sonicated in TCB for 2 h and subsequently heated at 120–130 °C for 15 min. As mentioned in subsection 4.2.4, some of the GNRs remained as visible particles in the dispersion, which suggested possible “fractionation” of the sample. The hot dispersion of GNR **4-3a** was drop-cast onto hot HOPG surfaces preheated at 120 °C, followed by heating for another 15 min and washing with pure TCB or THF.

Remarkably, this deposition procedure allowed formation of self-assembled

layers of laterally extended GNR **4-3a**, which could be evidently demonstrated by AFM analysis (Figure 4-18). The thickness of the films was ~ 0.3 nm, which indicated the monolayer nature of these GNR self-assemblies (Figure 4-19d and e). Highly covered areas extending over 500 nm as well as isolated domains of straight and uniform GNRs could be observed, demonstrating the remarkable liquid-phase processability of GNR **4-3a**, despite the strong aggregation of the GNRs in dispersions. The noodle-like features observed in these films of GNR **4-3a** were similar to those of GNRs **3-3** and **3-26** (see subsections 3.4.5 and 3.6.3, respectively). Length of each stripe in isolated domains exceeded 200 nm, which suggested end-to-end packing of the GNRs,

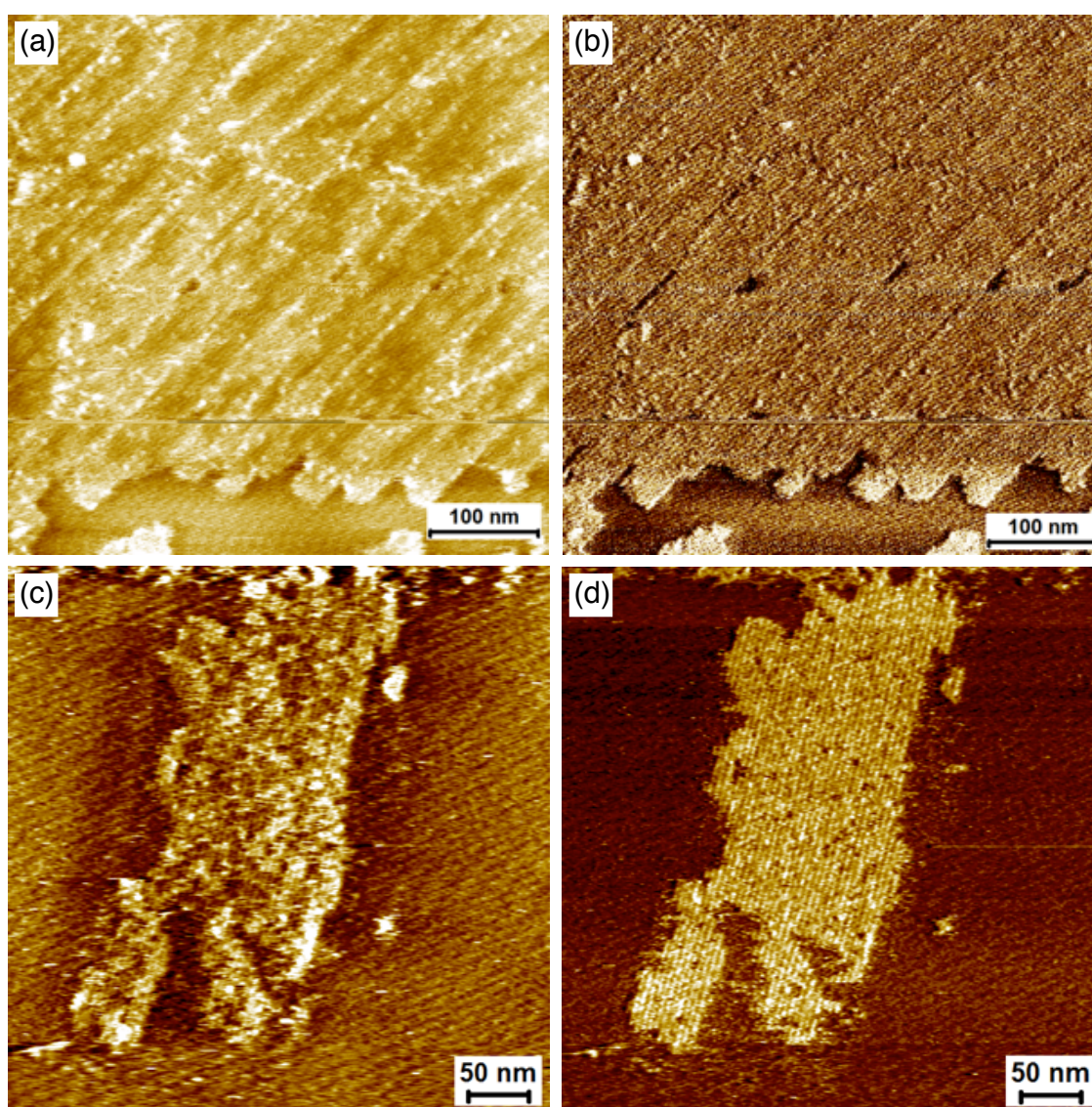


Figure 4-18. AFM images of self-assembled monolayers of GNR **4-3a** on HOPG (dry film); (a) height and (b) phase images of a highly covered area; (c) height and (d) phase images of an isolated domain of self-assembled GNRs.

considering the average length of $\sim 30\text{--}56$ nm estimated for GNR **4-3a** (Figure 4-18c and d). On the other hand, small patches of shorter GNRs with the length of ca. $20\text{--}30$ nm could also be observed, which was in agreement of the estimated average length (Figure 4-19a)

Analysis of the periodicity of the films, i.e. lateral width of the GNRs, was carried out with the phase images (Figure 4-18b and d), which were smoother than the height images (Figure 4-18a and c). The periodicity of the striped features was 5.0 ± 0.2 nm (Figure 4-19a and b) in good agreement with the expected lateral dimension of GNR **4-3a** including the alkyl chains, i.e. ca. 4.8 nm (Figure 4-19c), which further attested the successful synthesis of structurally defined GNR **4-3a** with high uniformity. This result

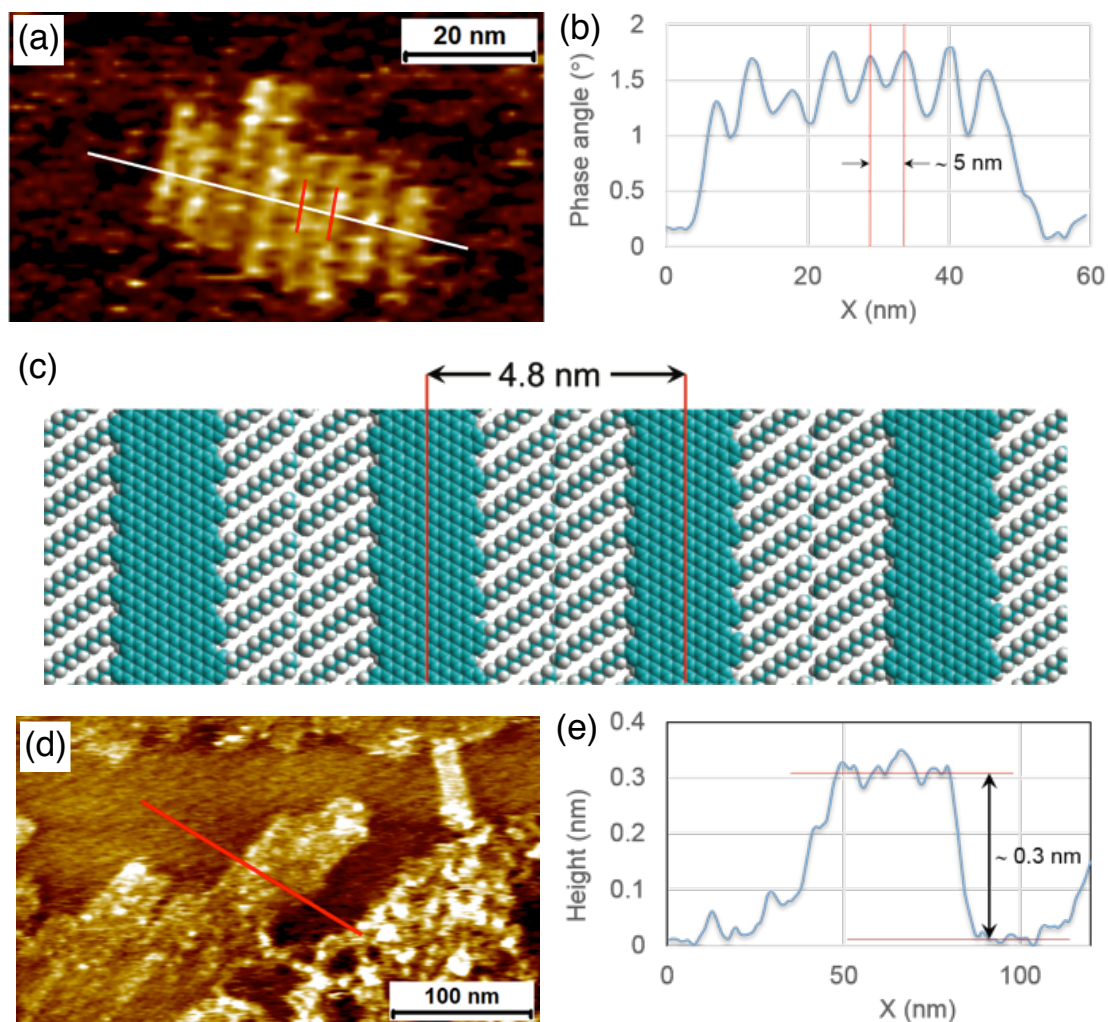


Figure 4-19. (a) AFM phase image of a small domain of GNR **4-3a** and (b) line profile along the white line in the phase image shown in panel a. (c) Molecular model of GNR **4-3a** depicting the packing of the GNRs in the self-assembled monolayer. (d) AFM height image and (e) line profile along the red line in the height image shown in panel d.

also indicated the adsorption of the GNRs next to each other without stacking of the aromatic cores or interdigitation of the alkyl chains, which was contrary to the partial stacking of the GNRs observed for GNR **3-3** with the same dodecyl chains (Figure 3-23). This difference was presumably due the enhanced interaction of the extended aromatic cores of GNR **4-3a** with the HOPG surfaces. Additionally, the lack of alkyl chain interdigitation could be explained by the small distance, i.e. ~ 0.7 nm, between the dodecyl chains on GNR **4-3a**, which could not accommodate another alkyl chain from a neighboring GNR. Efficient interdigitation of the alkyl chains normally require a distance of 1.0 nm or larger in order to allow optimal van der Waals interactions. A periodic feature was visible also in the background, especially on the bare HOPG surface, but this was due to a periodic noise that affected the system.

Deposition from a liquid phase of GNR **4-3b** with larger average length of 140–340 nm and 2-decyltetradecyl chains was also carried out, but formation of self-assembled layers could not be observed. Although the longer and branched alkyl chains enabled the visualization of GNRs longer than 200 nm in the case of narrow (~ 1 nm) GNR **3-26** (Figure 3-38), the absence of self-assemblies of GNR **4-3b** suggested that the enhanced solubilizing effect of the branched chains could not compensate the stronger aggregation and lower dispersibility of the broader (~ 2 nm) and longer (140–340 nm) GNRs. Nevertheless, GNR **4-3a** with the extended lateral width and such liquid-phase processability is expected to be a very important target for the fabrication of single-ribbon FET devices to investigate its transport properties as well as examine the potential of such GNRs for the future applications in nanoelectronics.

4.4 Investigation of photoconductivities by THz spectroscopy

The intrinsic charge-carrier transport properties of GNRs **4-3a** and **4-3b** were investigated in dispersions through the non-contact, time-resolved THz spectroscopy²⁶ by ██████████ in the group of ██████████ at Max Planck Institute for Polymer Research Mainz, Germany. The experiments were performed in the same manner as those on narrower GNR **3-3** (see subsection 3.5.1), and GNRs **4-3a** and **4-3b** showed similar THz-resolved photoconductivities with the features resembling those of GNR **3-3** as well as conventional semiconducting polymers.²⁷⁻³⁰ Representatively, the time-dependent and frequency-resolved photoconductivities of GNR **4-3b** are displayed in Figure 4-20a and b, respectively. The time-dependent photoconductivity revealed a quick rise upon excitation followed by a fast decay both in the real and imaginary parts (Figure 4-20a).

The imaginary conductivity, which persisted longer than the real conductivity, could be related to the formation of excitons, contributing to the polarizability, as was observed for GNR **3-3** as well as the semiconducting polymers. The magnitude of the real conductivity just after excitation was found to be comparable to that of GNR **3-3**, and superior to those of the organic semiconductors, demonstrating high intrinsic conductivities and mobilities of GNR **4-3**. The charge-carrier mobilities of GNR **4-3** were not apparently higher than that of GNR **3-3**, although higher mobilities have been theoretically predicted for broader GNRs with lower bandgaps.^{31,32} Nevertheless, considering the significantly lower optical bandgap experimentally elucidated for GNR **4-3** (subsection 4.3.3), the observed photoconductivities of GNR **4-3** was presumably not derived from structural defects, but underestimated possibly due to structural distortions such as folds and bends and/or significantly lower dispersibility of the broader GNRs. For comparison the THz spectroscopy measurements were also performed on a drop-cast film of GNR **4-3a** on a fused silica substrate, but the observed photoconductivities were comparable to those in the dispersion. It might be the case that GNR **4-3** with the extended aromatic plane undergoes stronger aggregation, which causes higher degree of structural distortion compared to GNR **3-3**, hindering the free movement of photogenerated charge carriers. However, further investigations are required for unambiguously elucidating the reason for the underestimated mobilities. For instance, THz spectroscopic analysis on self-assembled layers of GNR **4-3** like those shown in Figure 4-18 is desirable to exclude the effect of the aggregation although

formation of such ordered films on any substrate transparent to THz is still highly challenging.

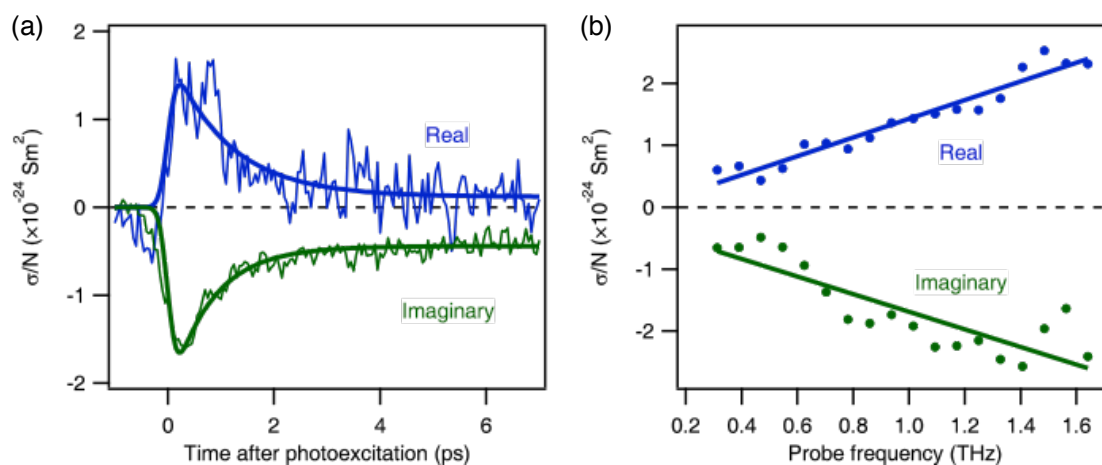


Figure 4-20. (a) Real and imaginary components of the photoconductivity of GNR **4-3b** as function of time after the excitation. Thick lines represent simulations revealing free charge carrier lifetimes of ~ 1 ps. (b) Frequency-resolved, photoinduced complex conductivity of GNR **4-3b** normalized to initial surface excitation density N measured 300 fs after excitation by a 800 nm pulse, fluence 2.4×10^{18} photons/m², for GNRs dispersed in TCB. Solid lines through the data points are guides to the eye.

4.5 Summary

Laterally extended GNRs could be successfully synthesized based on the *AB*-type *Diels–Alder* polymerization approach, realizing highly elongated GNRs with the length of at least over 100 nm according to the SEC analysis of the corresponding polyphenylene precursors. The formation of the desired GNRs with the lateral width of ca. 2 nm was corroborated by a combination of FTIR, Raman, and UV–vis absorption spectroscopies as well as the AFM analysis, which simultaneously demonstrated the low and defined optical bandgap of ~ 1.24 eV in good agreement with the DFT-calculated bandgap of 1.18 eV. The broad GNRs exhibited dispersibility in organic solvents thanks to the long alkyl chains at the peripheral positions, which enabled their liquid-phase processing to form highly ordered self-assembled monolayers on graphite surfaces in spite of the presence of aggregate in the dispersions. Further, THz spectroscopy analysis revealed the high intrinsic conductivity of the broad GNRs, which was comparable with that of their narrower counterparts. Although this result did not conform to the theoretical predictions that expect higher mobility for broader GNRs, the probed photoconductivity was most probably underestimated, possibly due to higher degree of structural distortion by stronger aggregation of the broader GNRs. These laterally and longitudinally extended GNRs with liquid-phase processability are very interesting targets for the single-ribbons FET studies and future applications to nanoelectronics.

4.6 References

- (1) Kastler, M.; Pisula, W.; Wasserfallen, D.; Pakula, T.; Müllen, K. *J. Am. Chem. Soc.* **2005**, *127*, 4286.
- (2) Tilford, R. W.; Gemmill, W. R.; zur Loye, H.-C.; Lavigne, J. J. *Chem. Mater.* **2006**, *18*, 5296.
- (3) Makino, T.; Yamasaki, R.; Azumaya, I.; Masu, H.; Saito, S. *Organometallics* **2010**, *29*, 6291.
- (4) Liu, P.; Chen, Y.; Deng, J.; Tu, Y. *Synthesis* **2001**, *14*, 2078.
- (5) Porada, J. H.; Neudörfl, J.; Blunk, D. *Cryst. Growth Des.* **2011**, *11*, 3648.
- (6) Horiba, K.; Hirose, H.; Imai, A.; Sato, K.; Agata, T. U.S. Pat. Appl. Publ., 20100243995, 30 Sep, 2010.
- (7) Kricheldorf, H. R.; Schwarz, G. *Macromol. Rapid Commun.* **2003**, *24*, 359.
- (8) Nishiuchi, T.; Feng, X. L.; Enkelmann, V.; Wagner, M.; Müllen, K. *Chem.—Eur. J.* **2012**, *18*, 16621.
- (9) Matsuno, T.; Kamata, S.; Hitosugi, S.; Isobe, H. *Chem. Sci.* **2013**, *4*, 3179.
- (10) Hitosugi, S.; Yamasaki, T.; Isobe, H. *J. Am. Chem. Soc.* **2012**, *134*, 12442.
- (11) Xia, J.; Golder, M. R.; Foster, M. E.; Wong, B. M.; Jasti, R. *J. Am. Chem. Soc.* **2012**, *134*, 19709.
- (12) Bunz, U. H. F.; Menning, S.; Martín, N. *Angew. Chem. Int. Ed.* **2012**, *51*, 7094.
- (13) Iwamoto, T.; Watanabe, Y.; Sakamoto, Y.; Suzuki, T.; Yamago, S. *J. Am. Chem. Soc.* **2011**, *133*, 8354.
- (14) Omachi, H.; Matsuura, S.; Segawa, Y.; Itami, K. *Angew. Chem. Int. Ed.* **2010**, *49*, 10202.
- (15) Wu, J. S.; Gherghel, L.; Watson, M. D.; Li, J. X.; Wang, Z. H.; Simpson, C. D.; Kolb, U.; Müllen, K. *Macromolecules* **2003**, *36*, 7082.
- (16) Schwab, M. G.; Narita, A.; Hernandez, Y.; Balandina, T.; Mali, K. S.; De Feyter, S.; Feng, X.; Müllen, K. *J. Am. Chem. Soc.* **2012**, *134*, 18169.
- (17) Shifrina, Z. B.; Averina, M. S.; Rusanov, A. L.; Wagner, M.; Müllen, K. *Macromolecules* **2000**, *33*, 3525.
- (18) Centrone, A.; Brambilla, L.; Renouard, T.; Gherghel, L.; Mathis, C.; Müllen, K.; Zerbi, G. *Carbon* **2005**, *43*, 1593.

- (19) Cai, J.; Ruffieux, P.; Jaafar, R.; Bieri, M.; Braun, T.; Blankenburg, S.; Muoth, M.; Seitsonen, A. P.; Saleh, M.; Feng, X.; Müllen, K.; Fasel, R. *Nature* **2010**, *466*, 470.
- (20) Narita, A.; Feng, X.; Hernandez, Y.; Jensen, S. A.; Bonn, M.; Yang, H.; Verzhbitskiy, I. A.; Casiraghi, C.; Hansen, M. R.; Koch, A. H. R.; Fytas, G.; Ivasenko, O.; Li, B.; Mali, K. S.; Balandina, T.; Mahesh, S.; De Feyter, S.; Müllen, K. *Nature Chem.* **2014**, *6*, 126–132.
- (21) Castiglioni, C.; Tommasini, M.; Zerbi, G. *Philos. Transact. A Math. Phys. Eng. Sci.* **2004**, *362*, 2425.
- (22) Negri, F.; Castiglioni, C.; Tommasini, M.; Zerbi, G. *J. Phys. Chem. A* **2002**, *106*, 3306.
- (23) Castiglioni, C.; Mapelli, C.; Negri, F.; Zerbi, G. *J. Chem. Phys.* **2001**, *114*, 963.
- (24) Gillen, R.; Mohr, M.; Maultzsch, J. *Phys. Rev. B* **2010**, *81*, 205426.
- (25) Osella, S.; Narita, A.; Schwab, M. G.; Hernandez, Y.; Feng, X.; Müllen, K.; Beljonne, D. *ACS Nano* **2012**, *6*, 5539.
- (26) Ulbricht, R.; Hendry, E.; Shan, J.; Heinz, T.; Bonn, M. *Rev. Mod. Phys.* **2011**, *83*, 543.
- (27) Ai, X.; Beard, M. C.; Knutsen, K. P.; Shaheen, S. E.; Rumbles, G.; Ellingson, R. *J. J. Phys. Chem. B* **2006**, *110*, 25462.
- (28) Cunningham, P. D.; Hayden, L. M. *J. Phys. Chem. C* **2008**, *112*, 7928.
- (29) Hendry, E.; Schins, J. M.; Candeias, L. P.; Siebbeles, L. D. A.; Bonn, M. *Phys. Rev. Lett.* **2004**, *92*, 196601.
- (30) Hendry, E.; Koeberg, M.; Schins, J. M.; Nienhuys, H. K.; Sundström, V.; Siebbeles, L. D. A.; Bonn, M. *Phys. Rev. B* **2005**, *71*, 125201.
- (31) Obradovic, B.; Kotlyar, R.; Heinz, F.; Matagne, P.; Rakshit, T.; Giles, M. D.; Stettler, M. A.; Nikonov, D. E. *Appl. Phys. Lett.* **2006**, *88*, 142102.
- (32) Wang, J.; Zhao, R.; Yang, M.; Liu, Z.; Liu, Z. *J. Chem. Phys.* **2013**, *138*, 084701.

Chapter 5. Conclusion and Outlook

5.1 Conclusion

In this PhD work, the bottom-up solution synthesis of structurally defined GNRs with three types of edge structures, i.e. armchair, cove-type, and a mixture of these two, lateral widths of from ca. 1 to 2 nm, and various longitudinal lengths has been achieved. The synthesis is based on the intramolecular oxidative cyclodehydrogenation of polyphenylene precursors, which are “built-up” from small molecules. Initially, lateral extension of the GNR structures has been carried out through two synthetic strategies. One is through a use of laterally expanded monomer **2-1**, which leads to broader GNR **2-3** with the same lateral width as the monomer (Figure 5-1). The other strategy is to employ monomer **2-11** with a V-shaped polymerizable backbone structure, which yields GNR **2-13** with twice the lateral width of the monomer (Figure 5-2).

AA-type *Yamamoto* polymerization was applied for the preparation of polyphenylene precursors, which was proved to be superior to the conventional *A₂B₂*-type *Suzuki* polymerization for attaining high-molecular-weight precursors. *Yamamoto* polymerization of laterally expanded monomer **2-1** enabled the synthesis of broad (1.54–1.98 nm) GNR **2-3**, which featured a mixture of armchair and cove-type edge structures (Figure 5-1) as well as higher longitudinal extension (18–31 nm) than what was previously reached with the *A₂B₂*-type *Suzuki* polymerization. GNR **2-3** demonstrated a low optical bandgap of 1.12 eV, which was in good agreement with the electronic bandgap of 1.08 eV theoretically calculated for an infinite GNR with the same lateral structure, based on the density functional theory. Such GNRs with broad absorption in the visible to near infrared region may be applicable in photovoltaic

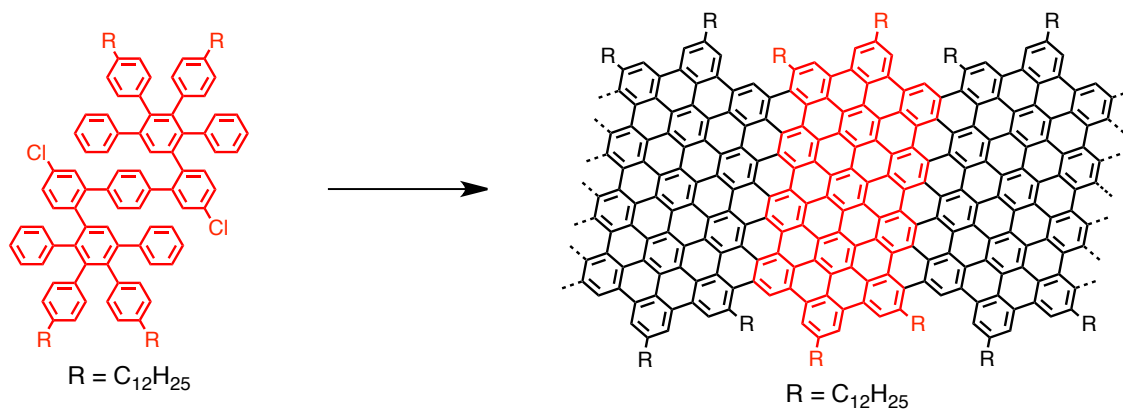


Figure 5-1. Synthesis of laterally extended GNR **2-3** from expanded monomer **2-1**.

systems, although their processability needs to be enhanced for such purposes, e.g. through introduction of longer and branched alkyl chains or charged functional groups.

Whereas the synthesis of broader GNRs through the first strategy, i.e. a use of laterally extended and larger monomers, generally requires more sophisticated and time-consuming synthetic steps, the second strategy allowed the synthesis of $N = 18$ armchair GNR **2-13** with the lateral width of ~ 2.1 nm from simpler and relatively smaller monomer **2-11** (Figure 5-2). However, the polymerization of monomer **2-11** was starkly inhibited most probably due to the high steric hindrance during the polymerization, resulting in laterally extended (~ 2.1 nm) but short GNR **2-13** with the estimated average length of around 5 nm.

On the other hand, broad GNR **2-13** obtained through the second strategy showed considerably higher dispersibility in organic solvents due to the short length, which permitted their liquid-phase processing for the fabrication of thin film FET devices. These devices displayed a mobility of $0.028 \text{ cm}^2/\text{V}\cdot\text{s}$ as the maximum value and an excellent on-off ratio of 10^6 , which suggested potential applicability of such GNRs, e.g. for flexible thin film FET devices. Further, such GNRs showed a remarkable photoresponse with the high photosensitivity of up to 10^6 and good responsibility of up to 40 A/W, which indicated their possible application in phototransistor devices. Nevertheless, investigation of transport properties within single GNRs, i.e. intraribbon transport, is more important for understanding the intrinsic properties and exploring the potential of such bottom-up synthesized GNRs, while the measurement on the thin films can only provide the information about the interribbon transport, namely through a number of neighboring GNRs. Investigations on the single-ribbon transport properties necessitates sufficiently elongated GNRs with the longitudinal length of over 100 nm.

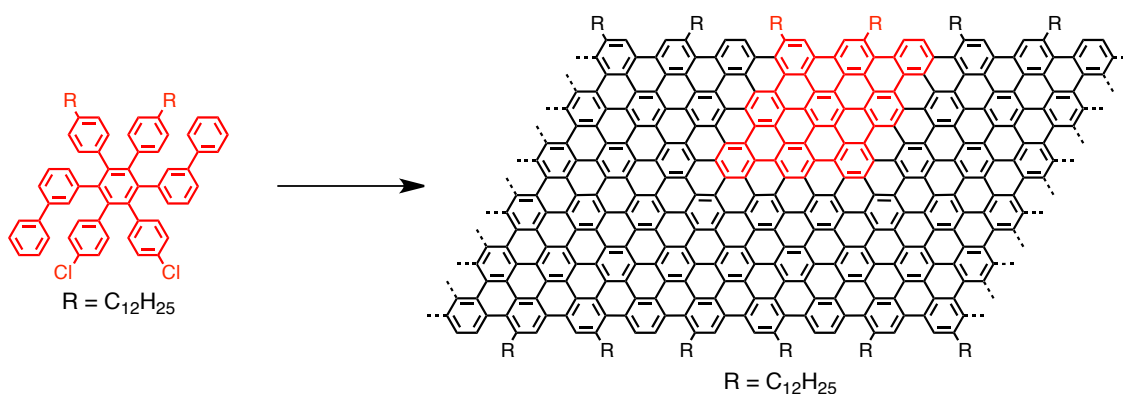


Figure 5-2. Synthesis of laterally extended, $N = 18$ armchair GNR **2-13** from monomer **2-11** with a V-shaped backbone structure.

In order to realize longitudinal extension of the GNRs over 100 nm, a synthesis of GNRs has been designed through the *Diels–Alder* polymerization, which was known to be exceptionally efficient for the preparation of high-molecular-weight polyphenylene polymers (Figure 5-3). Especially, *AB*-type *Diels–Alder* polymerization of a single monomer structure was expected to be superior to *A₂B₂*-type *Diels–Alder* polymerization, which involves two different monomers and so critically affected by the stoichiometry. A cyclopentadienone-based *AB*-type monomer **3-1** bearing an ethynyl group has thus been synthesized and subjected to the *Diels–Alder* polymerization, which has provided polyphenylene precursors with a variety of molecular weights, corresponding to different longitudinal lengths of the resulting GNR **3-3** with a cove-type edge structure (Figure 5-3). The maximum value of the absolute weight-average molecular weight has exceeded 600,000 g/mol according to the photon correlation spectroscopy and gel permeation chromatography analysis, which has allowed the synthesis of GNR **3-3** with the average length of over 600 nm.

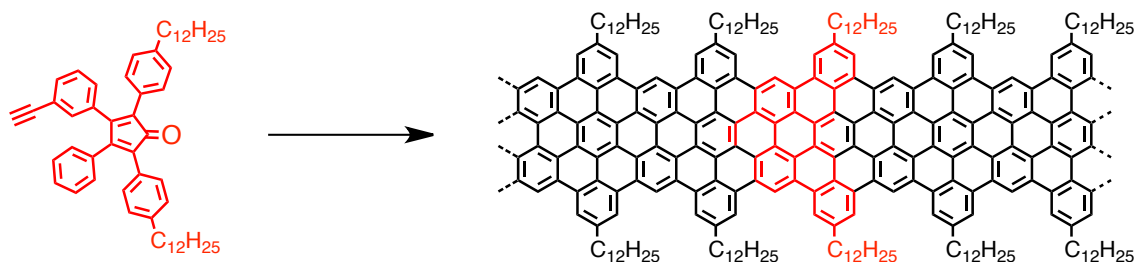


Figure 5-3. Synthesis of narrow (ca. 1 nm) GNR **3-3** with high longitudinal extension through *AB*-type *Diels–Alder* polymerization of tetraphenylcyclopentadienone-based monomer **3-1**.

Notably, such narrow (ca. 1 nm) and long (>600 nm) GNR **3-3** decorated with long and bulky alkyl chains have shown good dispersibility in normal organic solvents such as THF and chlorobenzene, which enabled their liquid-phase processing onto any substrates. Their high liquid-phase processability has been demonstrated by scanning probe microscopic (SPM) visualizations, which demonstrated the formation of exquisitely ordered self-assembled monolayers on graphite surfaces. The performance of thin-film FET devices fabricated with GNR **3-3** was lower than that of broad and short GNR **2-13** presumably owing to strong aggregation of the long GNRs. Nevertheless, such long and liquid-phase-processable GNRs may offer the possibility for an unprecedented fabrication of the single-ribbon FET devices. The good dispersibility has also enabled the investigation of the intrinsic transport properties of GNR **3-3** in a liquid phase by means of non-contact, ultrafast THz spectroscopy analysis,

which revealed that the photoconductivity of bottom-up synthesized GNR **3-3** is significantly higher than those of conventional conjugated polymers. Moreover, the edge of cove-type GNR **3-32** bearing *tert*-butyl groups could be selectively and efficiently chlorinated, which simultaneously replaced the *tert*-butyl groups with the chloro groups. The edge chlorinated GNR **3-33** showed good dispersibility due to the distortion of the planarity by the densely installed chloro groups. The energy levels could be lowered by the electron-withdrawing chloro groups, which lead to the unprecedented n-type GNRs with a lower bandgap.

Based on the *AB*-type *Diels–Alder* polymerization and by laterally expanding the cyclopentadienone-based monomer, laterally (~ 2 nm) and longitudinally (>100 nm) extended GNR **4-3** have been synthesized, while keeping the high structural definition (Figure 5-4). The long and bulky alkyl chains have bestowed, though limited, dispersibility on broad and long GNR **4-3**, which has enabled liquid-phase processing of such GNRs. On graphite surfaces GNR **4-3** formed highly ordered self-assembled monolayers upon drop-casting of its dispersion in 1,2,4-trichlorobenzene, which could be demonstrated by the SPM analysis. Furthermore, the photoconductivity measurements by the THz spectroscopy revealed the high intrinsic conductivity of GNR **4-3** that was comparable to that of narrower GNR **3-3**. Although fabrication of thin film FET devices with GNR **4-3** is highly challenging because of the enhanced aggregation behavior, such long, broad, and liquid-phase-processable GNRs are an important object of research for the fabrication of single-ribbon transistors.

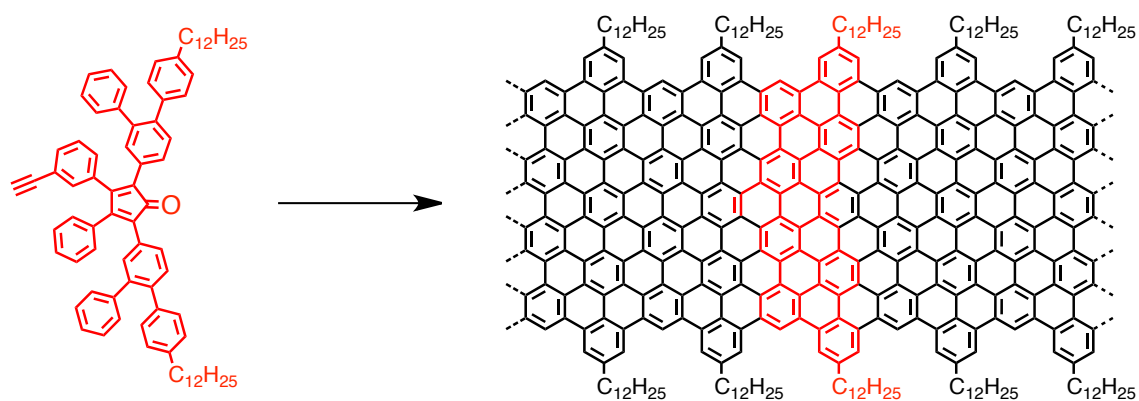


Figure 5-4. Synthesis of laterally extended (ca. 2 nm) GNR **4-3** with high longitudinal extension through *AB*-type *Diels–Alder* polymerization of expanded monomer **4-1**.

5.2 Outlook

Based on the synthetic strategies developed within the scope of this thesis, a variety of other GNRs can potentially be fabricated with different widths and various edge structures, including armchair, cove, cave, partially zigzag, and mixtures of more than one of these. Synthesis of GNRs with full zigzag edge peripheries by the solution-mediated method is highly challenging, considering their intrinsic instability, but it might be possible through the surface-assisted method under the UHV conditions. Because of the critical dependence of the band structures of the GNRs on their width and edge structures, all these GNRs are expected to show different electronic properties such as mobilities and bandgaps, which broadens the potential applicability of the bottom-up synthesized GNRs.

Especially, the *AB*-type *Diels–Alder* polymerization approach holds a great promise for the fabrication of long (>100 nm) GNRs with varying lateral widths. For instance, by further laterally expanding *AB*-type monomer **4-1** to monomer **5-1** with two extra phenyl rings at each periphery, a synthesis of long and broader, cove-edge GNR **5-1** with the lateral width of ~3 nm will be possible (Figure 5-5). Based on this approach, syntheses of even broader GNRs (>3 nm) might also be realized, although the increasing size of the aromatic plane drastically reduces their dispersibility as well as potentially lowers the efficiency of the cyclodehydrogenation step. A use of better solubilizing groups at the periphery and/or development of an effective exfoliation

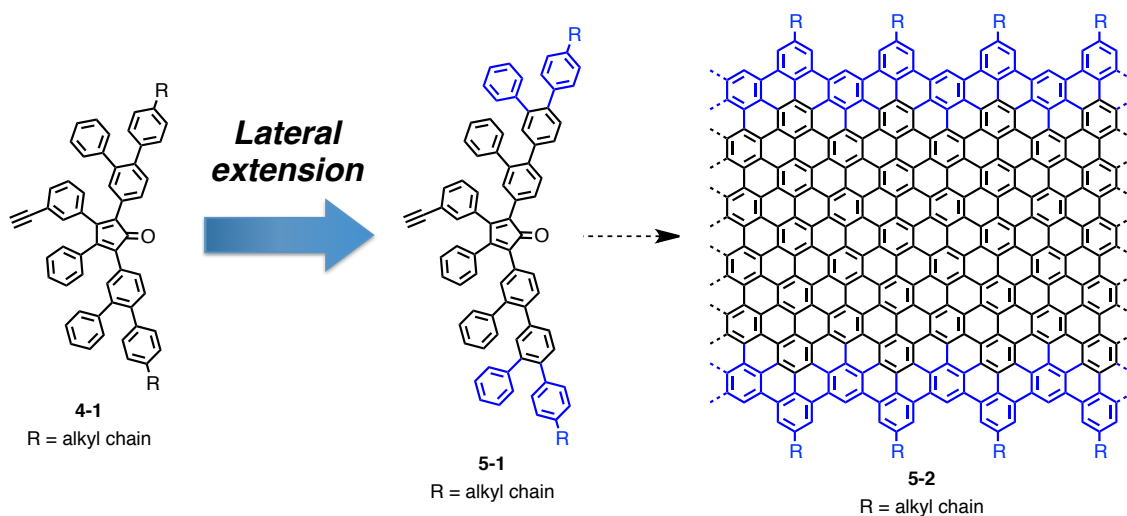


Figure 5-5. Possible lateral extension of monomer **4-1** for the synthesis of broad GNR **5-2** with the lateral width of ~3 nm through the *AB*-type *Diels–Alder* polymerization.

method might be prerequisite for the processing of such broader GNRs. The cyclodehydrogenation step also needs careful optimization for the structural perfection.

Because of the high molecular weight with broad distribution and the strong aggregation, the structural perfection of the solution synthesized GNRs cannot be effectively evaluated by the state of the art characterization methods except for high-resolution SPM, which is highly challenging especially for broader GNRs with limited processability. On the other hand, syntheses and characterizations of shorter model compounds can provide a better insight into the efficiency of the “graphitization” of the polyphenylene precursors into the GNRs. For instance, compound **5-3** and **5-4** can be regarded as dimer and trimer, respectively, of laterally extended GNR **4-3**, the structural perfection of which could not be accurately evaluated by the available methods. Investigation of dimer **5-3** and trimer **5-4** will offer indirect, but meaningful additional information regarding the efficiency of the synthesis of GNR **4-3**. Moreover, trimer **5-4** has an unprecedented PAH structure with 186 carbon atoms, which is an interesting target of research for its optoelectronic as well as self-assembling properties.

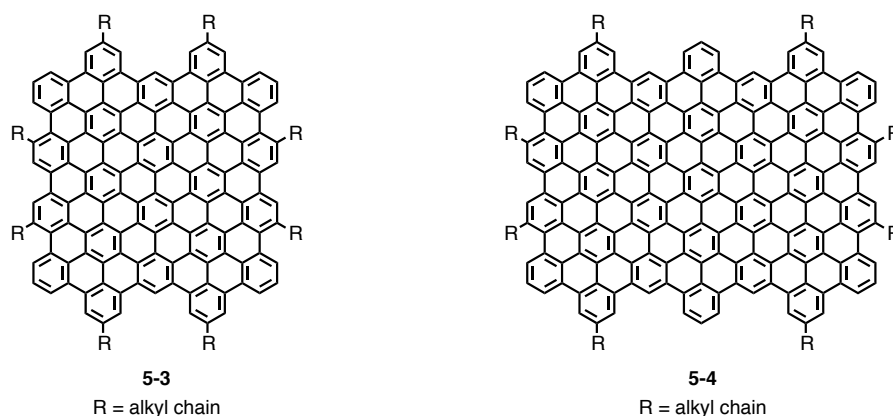


Figure 5-5. Structures of laterally extended dimer **5-3** and trimer **5-4** as model compounds for laterally extended GNR **4-3**.

Furthermore, selective doping of the GNRs is also expected to be possible through the solution-mediated bottom-up synthesis, by using monomers containing heteroatoms such as nitrogen and boron in their core structures. Such doped GNRs possess different electronic properties and band structures from those of their undoped counterparts, which further diversifies the scope of the structurally well-defined GNRs. Particularly, by substituting the benzene rings of the *AB*-type monomer **3-1** with pyridyl or pyrimidyl groups like monomers **5-5** and **5-7**, it might be possible to obtain selectively N-doped GNRs such as **5-6** and **5-8** with high longitudinal extension (>100

nm) and liquid-phase processability (Figure 5-6). Although the preparation of such monomer as well as the polymerization and the cyclodehydrogenation steps are more challenging than the undoped analogues, such long N-doped GNRs show n-type semiconductor properties, and possibly be integrated into single-ribbon FET devices for further investigations and applications. Although an innovative processing method needs to be developed for the processing and device fabrication, these bottom-up synthesized GNRs with various structures and tunable electronic properties may turn out to be advantageous materials for the future nanoelectronics.

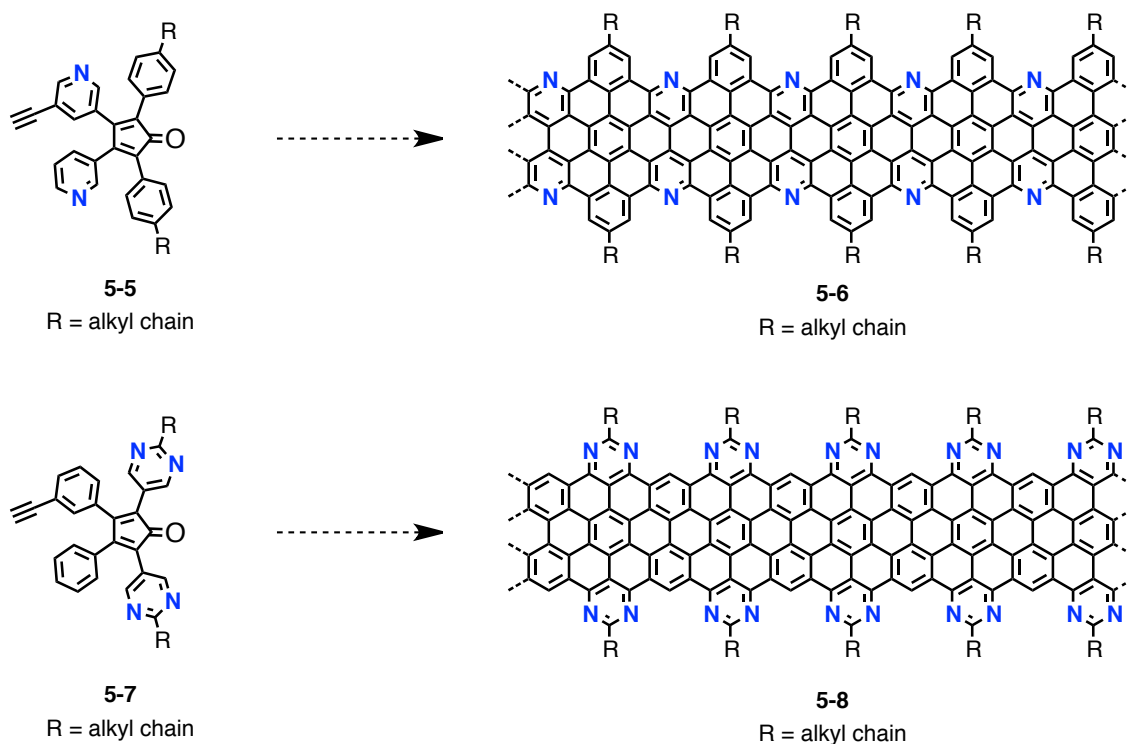


Figure 5-7. Proposed syntheses of selectively N-doped GNRs **5-6** and **5-8** from *AB*-type monomers **5-5** and **5-7**, respectively.

For studying the electronic transport properties within individual GNRs, a use of short oligomers bearing thiol linkers at the termini, such as dimer **5-9** and trimer **5-10** (Figure 5-8), is more promising. Whereas the investigation of GNR **3-43** bearing acetylthio groups through the STM break-junction method did not provide explainable results most probably due to the complex aggregation and relatively broad length distribution of the GNRs, smaller and defined molecules **5-9** and **5-10** are expected to undergo much less aggregation, and allow reliable analyses by the same method to reveal the electronic transport properties of such short nanoribbons. The introduction of four acetylthio groups can enhance the affinity between the molecules and the gold

electrodes as well as avoid the formation of structural isomers during the synthesis. Comparison of the transport properties between dimer **5-9**, trimer **5-10**, and the previously reported HBC with thiol linkers will provide deeper insight into the dependence of the electronic properties of GNRs on their lengths. The synthesis can potentially be extended to longer oligomers bearing the thiol linkers for further investigations.

Moreover, dimer **5-9** and trimer **5-10** can be laterally extended to broader dimer **5-11** and trimer **5-12**, respectively, with the acetylthio groups at the terminals, which can also be studied by the break-junction technique (Figure 5-8). Dimer **5-11** and trimer **5-12** with the larger lateral width are expected to show higher mobilities than those of dimer **5-9** and trimer **5-10**, respectively, based on the theoretical studies on GNRs. Such predictions can be experimentally and precisely examined by comparing the electronic properties of these short molecules with defined widths.

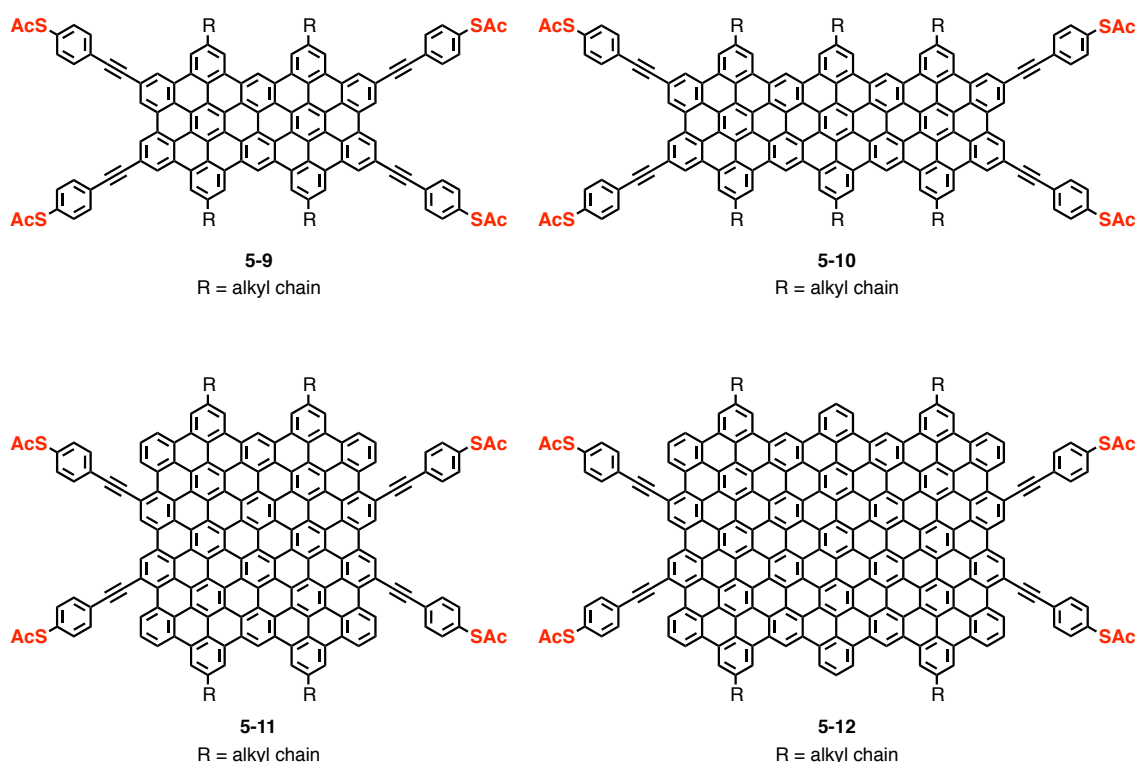


Figure 5-8. Structures of dimer **5-9** and trimer **5-10** as well as laterally extended dimer **5-11** and trimer **5-12**, bearing acetylthio groups, as small and defined model compounds of GNRs with thiol linkers for the investigation of the electronic transport within single molecules by STM break-junction technique.

Chapter 6. Experimental Part

6.1 General

6.1.1 Materials

Materials were purchased from Fluka, Sigma-Aldrich, Acros, ABCR, Merck, TCI, and other commercial suppliers and used as received unless otherwise specified. The following materials were obtained from colleagues in our research group: PAH **2-8** and crude materials of polyphenylene precursor **2-2** from [REDACTED],¹ 1,3-di(biphenyl-3-yl)propan-2-one (**2-14**) and polyphenylene precursor **2-12** from [REDACTED],² and 1-[4-(*S*-acetylthiomethyl)phenyl]acetylene (**3-42**) from [REDACTED]^{3,4} 2,3,4,5-Tetrakis(4-dodecylphenyl)-2,4-clopentadienone (**3-13**),⁵ 1,3-bis(4-bromophenyl)propan-2-one (**3-15**),⁶ 2-decyltetradecyl bromide (**3-27**),⁷ and 4-dodecylphenylboronic acid (**4-11**)^{8,9} were prepared following the reported procedures.

6.1.2 General methods

All reactions dealing with air- or moisture-sensitive compounds were carried out in a dry reaction vessel under argon. Preparative column chromatography was performed on silica gel from Merck with a grain size of 0.063–0.200 mm (silica gel) or 0.04–0.063 mm (flash silica gel, Geduran Si 60). Both analytical and preparative thin layer chromatography (TLC) was performed on silica gel coated substrates “60 F₂₅₄” from Merck. Microwave-assisted reactions were performed using a CEM microwave reactor “Discover-S-Class” with the maximum power of 300 W with activated cooling with manually adjusted air pressure.

6.2 Analytical techniques

6.2.1 Mass spectrometry

Field desorption mass spectra (FD/MS) were obtained with a VG Instruments ZAB 2-SE-FDP using 8 kV accelerating voltage. The high-resolution electrospray ionization mass spectrometry (HR-ESI-MS) was performed at the Institute for Organic Chemistry, Johannes-Gutenberg-Universität of Mainz, on an ESI-Q-TOF system (maXis, BrukerDaltonics, Germany). The instrument was operated in wide pass quadrupole mode for MS experiments with the TOF data being collected between m/z 100–5000. Matrix-assisted laser desorption/ionization time-of-flight (MALDI-TOF) mass spectra were recorded using a Bruker Reflex II utilizing a 337 nm nitrogen laser, calibrated against poly(ethylene glycol) (3000 g/mol). Unless otherwise specified all the PAH, polyphenylene, and GNR samples were measured by solid-state sample preparation with tetracyanoquinodimethane (TCNQ) as matrix.¹⁰ HR-MALDI mass spectra were measured by the MS-service at ETH Zurich on a Bruker Daltonics Solarix ESI/MALDI-FTICR mass spectrometer using trans-2-[3-(4-tert-butylphenyl)-2-methyl-2-propenylidene]malononitrile (DCTB) or 3-Hydroxypicolinic acid (3-HPA) as matrix.

6.2.2 NMR spectroscopy

Solution-state ^1H and ^{13}C NMR spectra were recorded on a Bruker DPX250, AMX300, DRX500, or DRX700 spectrometer and referenced to residual signals of the deuterated solvent. Abbreviations: s = singlet, d = doublet, t = triplet, m = multiplet. All solid-state ^1H NMR experiments were performed by [REDACTED] (MPIP Mainz) on a Bruker AVANCE III 700 operating at a Larmor frequency of 700.21 MHz (16.45 T). The experiments employed a 1.3 mm H-X double-resonance magic-angle spinning (MAS) probe from Bruker, using a MAS frequency of 59524 Hz and a $\pi/2$ -pulse length of 1.8 μs , corresponding to an rf-field strength of 139 kHz. The 2D ^1H - ^1H double quantum-single quantum (DQ-SQ) correlation experiments were recorded using the compensated Back-to-Back (BaBa) dipolar recoupling sequence for both excitation and reconversion of DQ coherences followed by a z-filter, set to one rotor period, prior to a final $\pi/2$ pulse for creating transverse observable magnetization.^{11,12} A phase cycling scheme of 16 steps, a recycle delay of 2 s, and 16 scans per rotor-synchronized t_1

increment were used. Prior to all experiments the magic angle was checked with KBr.¹³ ¹H chemical shifts are reported relative to TMS using solid adamantane as an external reference.¹⁴

6.2.3 *Elemental analysis*

Elemental analysis was carried out on a Foss Heraeus Vario EL as a service of the Institute for Organic Chemistry, Johannes-Gutenberg-Universität of Mainz. Basically, liquid or oily compounds were not analysed, because it is hardly possible to completely remove the residual solvents as well as atmospheric gases such as carbon dioxide.

6.2.4 *UV–vis absorption spectroscopy*

UV–vis absorption spectra were recorded at room temperature on a Perkin-Elmer Lambda 900 spectrophotometer. The baseline was corrected by subtracting a measurement of the cuvette filled with pure solvent used for the measurement. The optical bandgap was calculated based on the onset of p-band for PAHs and from the absorption edge for the GNRs. For the measurements GNR samples were dispersed in organic solvents by sonication (>30 min) in a Branson-1510 ultrasonicator followed by centrifugation (1–5 min at 13.4 krpm).

6.2.5 *Photoluminescence spectroscopy*

Photoluminescence (PL) spectroscopic analysis of GNR **2-3-I** was carried out by [REDACTED] using an Edimburgh Instruments PL (near IR PL) in the group of [REDACTED] (Trinity College Dublin, Ireland). The measurement was performed on a dispersion in *N*-cyclohexyl-2-pyrrolidone (CHP), which showed the identical absorption spectrum as in NMP.

6.2.6 FTIR spectroscopy

Infrared spectra were measured on a Nicolet 730 FT-IR spectrometer equipped with an attenuated total reflection (ATR) setup. The samples were deposited as pristine material on the diamond crystal and pressed on it with a stamp. Measurements with a scan number of 128 were recorded for each sample and the background was subtracted.

6.2.7 Raman spectroscopy

Raman spectra of dimer **3-5**, trimer **3-7**, and GNRs **3-3**, **3-26**, **4-3a**, and **4-3b** were measured by [REDACTED] and [REDACTED] in the groups of [REDACTED] (Freie Universität Berlin, Germany, and University of Manchester, UK) with a Witec Confocal Raman spectrometer, equipped with 633 and 532 nm laser lines. A $\times 100$ objective was used, and the power was kept well below 0.1 mW to avoid damage. Raman spectra of other materials were measured by [REDACTED], [REDACTED], and [REDACTED] in our research group on a Senterra Raman spectrometer with a 488 nm laser line at the power of 0.20 mW and a $\times 100$ or $\times 50$ objective. The measurements have been performed on powder samples placed on glass microscope coverslips.

6.2.8 Photoelectron spectroscopy

Photoelectron spectroscopy measurements were performed by [REDACTED] and [REDACTED] in the group of [REDACTED] (I.S.I.S., Strasbourg, France) under ambient conditions either on powders or on drop casted films (annealed at 200 °C for 15 min inside the glovebox), using a new generation of photoelectron spectroscopies operating at atmospheric conditions (RIKEN AC-2).

6.2.9 Size-exclusion chromatography analysis

Analytical size exclusion chromatography (SEC) was performed on SDV PSS GPC columns using THF as eluent at a temperature of 303 K. Absorbance was determined on a UV S-3702 detector (SOMA) at a fixed wavelength of 270 nm. The

samples were referenced with respect to standard polystyrene (PS) as well as poly(*p*-phenylene) (PPP) calibration curves.

6.2.10 Photon correlation spectroscopy

The photon correlation spectroscopy analysis was carried out by [REDACTED] and [REDACTED] (MPIP Mainz). The sample solutions at concentrations between 0.2–2.0 g/L in THF were filtered through 0.2 μm Millipore filters into (10 mm outer diameter) round glass cells for the measurements. The normalized light scattering intensity ($I(q,t)$) autocorrelation function $G(q,t) \equiv (I(q,t)I(q))/(I(q))^2$ was recorded over broad time range (10^{-7} – 10^3 s) at different scattering wave vectors q with an ALV/LSE-5004 goniometer/correlator setup using a HeNe laser at a wavelength $\lambda = 632$ nm. Both polarized (VV) PCS experiments were performed using vertically polarized (V) incident laser beam and the scattered light polarized vertically (VV-configuration) to the scattered plane (k_i, k_f) was selected. The refractive index contrast dn/dc was measured with a scanning Michelson interferometer in THF at 20 °C.

6.2.11 STM visualization

STM visualizations were performed by the group of [REDACTED] (Katholieke Universiteit Leuven, Belgium) at room temperature using PicoLE (Agilent) operating in constant-current mode. STM tips were prepared by mechanical cutting from Pt/Ir wire (80%/20%, diameter 0.2 mm). A molecular model was constructed using HyperChem 7.0 program (HyperChem(TM) Professional 7.5, Hypercube, Inc., 1115 NW 4th Street, Gainesville, Florida 32601, USA). The images were processed using SPIPTM (Image Metrology A/S, Denmark) software, and calibrated using the graphite lattice as reference for obtaining correct lateral dimensions.

To form films of GNRs for the measurements at the solid-air interface, a small amount of the material was placed into a semi-closed capillary and fixed orthogonally over preheated (~ 130 °C) highly oriented pyrolytic graphite (HOPG, grade ZYB, Advanced Ceramics Inc.) surface. Application of small drops of TCB resulted in gradual etching of the GNR sample accompanied by solvent evaporation and radial deposition of dissolved nanoribbons onto graphite surface in close vicinity to the crystal. The experiments at the solid-liquid interface were performed with the tip immersed in

the supernatant liquid. Prior to imaging, compounds were dissolved in TCB and a drop of this solution was applied onto a surface of a freshly flame-annealed Au(111) (Georg Albert PVD). The unit cell parameters were determined by examining at least 10 images and only the average values are reported.

6.2.12 AFM visualization

AFM measurements were performed by the group of [REDACTED] (Katholieke Universiteit Leuven, Belgium) with a Multimode AFM with a Nanoscope IV controller (Veeco/Digital Instruments, Santa Barbara, USA). For the AFM measurements of GNR **3-26**, GNR powders were dispersed in TCB followed by heat and sonication cycles to ensure dissolution of GNRs. The AFM samples were then prepared by applying a drop of hot TCB dispersion on HOPG followed by evaporation of TCB at higher temperatures ($\sim 100^\circ\text{C}$). For the deposition of GNR **4-3**, the GNR powders were sonicated in TCB for 2 h and then heated at $120\text{--}130^\circ\text{C}$ for 15 min. The hot dispersion was then applied to a hot HOPG surface preheated at 120°C . After the hot deposition, the HOPG sample was heated for another 15 min, and then washed with 2 mL of pure TCB or THF and heated again to completely remove the solvent. Images were recorded at room temperature and processed using SPIPTM (Image Metrology A/S, Denmark) software.

6.2.13 THz spectroscopy

Optical pump-THz probe measurements were performed by [REDACTED] in the group of [REDACTED] (MPIP Mainz), using the output from a titanium sapphire laser generating pulses with a central wavelength of 800 nm, and a duration of ~ 40 fs, with a 1 kHz repetition rate. Pump pulses were frequency doubled to 400 nm in a BBO (Barium Borate) crystal, and impinged on the sample after a mechanically adjustable delay. Single-cycle probe pulses comprising of frequencies in the 0-2 THz range were generated from the 800 nm pulses in a 0.5 mm thick ZnTe crystal by a process called optical rectification.¹⁵ After the sample, the transmitted THz field was detected with a third 800 nm pulse in a second ZnTe crystal using the electro-optic effect.¹⁵ By mechanically delaying the detection pulse, the whole waveform of the THz pulse could be measured, and the frequency resolved conductivity could be obtained.

6.2.14 Determination of the concentration of GNR dispersions

In order to determine the concentration, GNR dispersions were passed through polytetrafluoroethylene (PTFE) filters and dried thoroughly under reduced pressure. The increases in the weight of the filters were measured by using a microbalance (METTLER TOLEDO, MX5) to calculate the concentration of the dispersions.

6.2.15 DFT calculation

Density functional theory (DFT)¹⁶ calculations were performed by [REDACTED] and [REDACTED] (University of Mons, Belgium), applying the screened exchange hybrid density functional according to Heyd-Scuseria-Ernzerhof (HSE).¹⁶⁻¹⁸ All stationary points were optimized and characterized with the 6-31G(d) Gaussian basis set.¹⁹ A k-point sampling of 27 (30) k points that are uniformly positioned along the 1D Brillouin zone is employed for GNRs with armchair (zigzag) shaped edges. Calculations have been carried out using the GAUSSIAN09 program.²⁰

6.2.16 Fabrications and characterizations of FET devices

All the FET devices were fabricated on heavily doped n-type silicon wafers as the gate electrodes and 230 nm thick thermally grown SiO₂ as the dielectric layers. Interdigitated Au source-drain electrodes were prepatterned with different channel lengths of $L = 2.5, 5.0, 10, \text{ and } 20 \mu\text{m}$ and constant channel width of $W = 10 \mu\text{m}$. These substrates were ultrasonically cleaned with acetone and isopropanol prior to device fabrication. FET devices of GNRs **3-3** and **3-26** were fabricated by [REDACTED] in our research group. The SiO₂ dielectric was modified with self-assembled monolayers of hexamethyldisilazane (HMDS) by vapor deposition, resulting in contact angles of $93.2 \pm 1.3^\circ$. In order to prepare bottom-gate bottom-contact transistors, the GNRs were deposited on the top of the SiO₂ dielectric by drop-casting dispersions/suspensions of the GNRs in THF (concentration: ca. 2 mg/mL). All the devices were annealed at 120°C for 30 min, and characterized by using a Keithley SCS 4200 inside a nitrogen filled glovebox (oxygen and humidity < 0.1 ppm, pressure ~1120 Pa) at room temperature (~25°C). The average mobilities were calculated from around 5 devices.

Investigations on the FET devices of GNR **2-13** was performed by [REDACTED] in the group of [REDACTED] (I.S.I.S., Strasbourg, France). In order to fabricate bottom-gate bottom-contact transistors, GNR **2-13** was dispersed/suspended in a 1:1 mixture of ODCB and chloroform by sonication, and then deposited onto the substrates by drop casting inside a glove box. Electrical characterization of the devices was carried out at room temperature in N₂ atmosphere inside a glove-box, using a Cascade Microtech M150 probe station and a Keithley 2636A controlled by associated software. For investigating the photoresponse, the devices were characterized under illumination with a white light (5 mW/cm⁻²) from the top by a Polychrome V (Till Photonics) tunable light source. The light intensity was measured by an analog optical power meter, PM100A (ThorLabs).

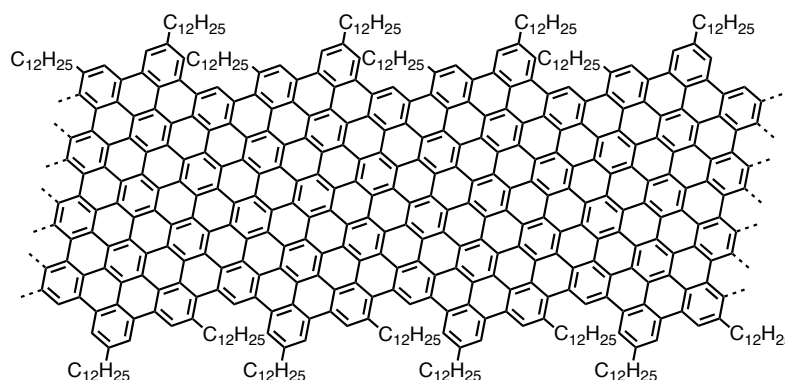
6.2.17 Fabrications and characterizations of photovoltaic devices

For the fabrication of the solar cell devices with GNR **3-26-I** and PCBM as the active materials was carried out together with [REDACTED] in the group of [REDACTED] at University College London, U.K. Glass substrates coated with patterned indium tin oxide (ITO) were cleaned in an ultrasonic bath (acetone and subsequently in isopropanol with ultrasonication for about 10 min each and dried in a stream of nitrogen), and afterwards treated with oxygen plasma for 10 min. The cleaned ITO substrates were then coated with PEDOT:PSS by spin coating (5000 rpm, 2 min), followed by annealing at 140 °C for 10 min under nitrogen atmosphere in a glove box. Dispersions/suspensions of GNR **3-26-I** in chlorobenzene were prepared at the concentration of 0.5 mg/mL, and mixed with solutions of PCBM in chlorobenzene (prepared at 2 mg/ml) to prepare mixtures of GNR **3-26-I** and PCBM at different weight ratios, i.e. 2:1, 1:1, 1:2, and 1:4. These dispersions/suspensions of mixtures of GNR **3-26-I** and PCBM were repeatedly drop-cast on the ITO substrates preheated at 100 °C inside the glove box, followed by annealing at 100 °C for approximately 10 min. Finally, calcium (30 nm) and aluminum (150 nm) were deposited by thermal evaporation in high vacuum conditions ($p \approx 10^{-6}$). The solar cell devices were subsequently mounted on airtight sample holders, and characterized under medium vacuum conditions and under 1 sun AM1.5 illumination. The current-voltage characteristics of the devices were recorded with a Keithley source-measure-unit remotely controlled by a computer and a Sun 3000 Class AAA (Abet Technologies) solar simulator.

6.3 Synthetic procedures

6.3.1 Synthesis of laterally extended GNR 2-3

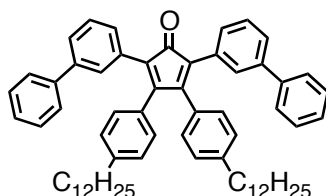
6.3.1.1 Laterally extended GNR 2-3



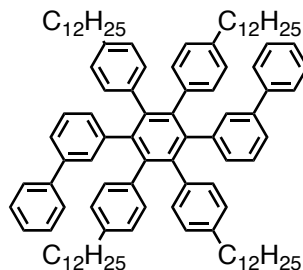
Prior to the synthesis of GNR **2-3**, polyphenylene precursor **2-2** was fractionated, by using recycling preparative SEC, into larger-molecular-weight fraction **2-2-I** (M_w : 30,000–52,000 g/mol, M_n : 27,000–44,000 g/mol, PDI: 1.1–1.2) and smaller-molecular-weight fraction **2-2-II** (M_w : 5,400–7,200 g/mol, M_n : 5,100–6,700 g/mol, PDI: 1.1). A solution of precursor **2-2-I** (20.0 mg) in unstabilized dichloromethane (60 mL) was degassed by argon bubbling for 10 min. To the degassed solution was added a suspension of iron(III) chloride (242 mg, 1.49 mmol, 3 eq. for one hydrogen to be removed) in nitromethane (4.0 mL). After stirring at room temperature for 69 h under continuous bubbling with argon presaturated with dichloromethane, the reaction was quenched by the addition of methanol to form black precipitates. Filtration by suction using a membrane filter and washing intensively with methanol gave GNR **2-3-I** as a black powder (16.9 mg, 87% yield): FTIR (powder) 2,919, 2,850, 1,724, 1,604, 1,582, 1,452, 1,367, 1,337, 1,305, 1,208, 1,150, 1,078, 861, 822, 760, 718, 624 cm^{-1} ; Raman (powder, 488 nm, < 1 mW) 1,316, 1,595, 2,620, 2,910, 3,194 cm^{-1} .

6.3.2 Synthesis of PAHs 2-19 and 2-20

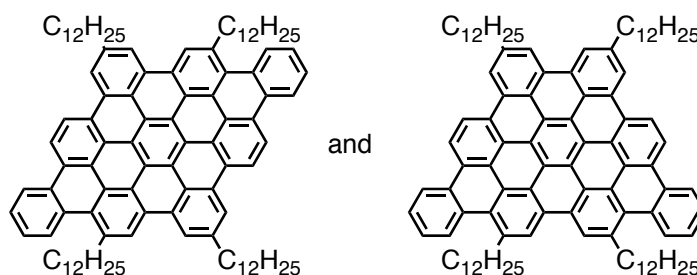
6.3.2.1 2,5-Di([1,1'-biphenyl]-3-yl)-3,4-bis(4-dodecylphenyl)-2,4-cyclopentadienone (2-16)



To a degassed solution of 4,4'-didodecylbenzil (**2-15**)²¹ (400 mg, 0.731 mmol) and 1,3-di(biphenyl-3-yl)propan-2-on (**2-14**)² (265 mg, 0.731 mmol) in *tert*-butanol (10 mL) was added at 80 °C a methanol solution of tetrabutylammonium hydroxide (1.00 M, 1.10 ml, 1.10 mmol). After stirring at 80 °C for 20 min the reaction was quenched with water, and the reaction mixture was extracted three times with dichloromethane. The combined organic layers were washed with brine three times, dried over sodium sulfate, and evaporated to give a purple crude product. Purification by silica gel column chromatography (eluent: 20–25% toluene/hexane) gave the title compound as a purple solid (420 mg, 0.481 mmol, 66% yield): Mp 77–78 °C; ¹H NMR (300 MHz, CD₂Cl₂) δ 0.89 (t, *J* = 6.9 Hz, 6H), 1.40–1.23 (m, 36H), 1.69–1.56 (m, 4H), 2.61 (t, *J* = 7.4 Hz, 4H), 6.94 (d, *J* = 8.1 Hz, 4H), 7.07 (d, *J* = 8.1 Hz, 4H), 7.44–7.26 (m, 16H), 7.48 (dt, *J* = 6.9, 1.9 Hz, 2H); ¹³C NMR (75 MHz, CD₂Cl₂) δ 14.32, 23.14, 29.75, 29.82, 29.95, 30.08, 30.11, 30.13, 30.15, 31.91, 32.38, 36.23, 125.40, 126.39, 127.36, 127.64, 128.51, 128.88, 129.07, 129.39, 129.46, 129.74, 131.02, 132.05, 141.02, 141.25, 144.34, 155.82, 200.69; MS (MALDI-TOF, positive) *m/z* calcd for C₆₅H₇₆O [M]⁺ 872.6, found 873.8; Anal Calcd for C₆₅H₇₆O: C, 89.4; H, 8.8. Found: C, 89.0; H, 9.3.

6.3.2.2 1,4-Bis(biphenyl-3-yl)-2,3,4,5-tetrakis(4-dodecylphenyl)benzene (2-18)

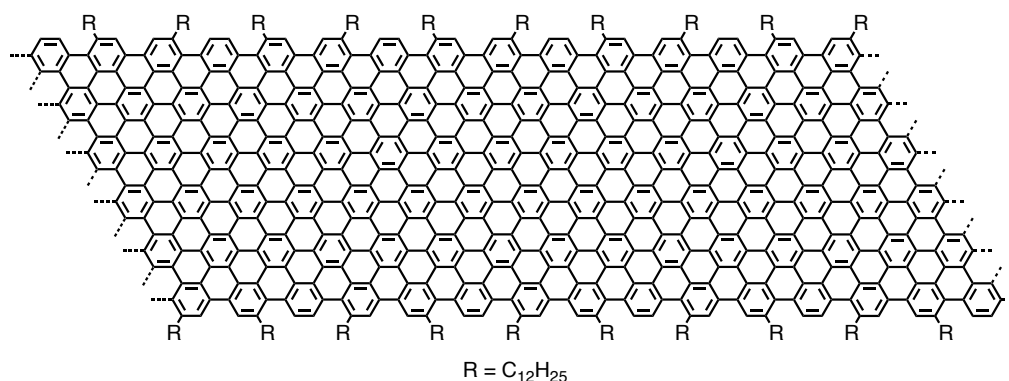
A degassed solution of 2,5-di([1,1'-biphenyl]-3-yl)-3,4-bis(4-dodecylphenyl)-2,4-cyclopentadienone (**2-16**) (300 mg, 0.344 mmol) and bis(4-dodecylphenyl)acetylene (**2-17**)² (178 mg, 0.346 mmol) in diphenyl ether (2.0 mL) was refluxed for 110 h by using a heating mantle. After cooling to room temperature the reaction mixture was diluted with hexane and purified by silica gel column chromatography (eluent: 10% dichloromethane/hexane) to give the title compound as a pale yellow solid (277 mg, 0.204 mmol, 59% yield): Mp 103.6 °C; ¹H NMR (700 MHz, CD₂Cl₂) δ 0.88 (t, *J* = 7.0 Hz, 12H), 1.11–1.04 (m, 8H), 1.33–1.12 (m, 64H), 1.41–1.33 (m, 8H), 2.39–2.31 (m, 8H), 6.68 (t, *J* = 8.4 Hz, 4H), 6.75–6.70 (m, 6H), 6.76 (d, *J* = 7.8 Hz, 2H), 6.80 (d, *J* = 7.9 Hz, 2H), 6.82 (d, *J* = 7.8 Hz, 4H), 6.93 (td, *J* = 7.6, 2.5 Hz, 2H), 7.09–7.05 (m, 4H), 7.16 (t, *J* = 7.2 Hz, 4H), 7.25–7.21 (m, 2H), 7.32–7.27 (m, 4H); ¹³C NMR (75 MHz, CD₂Cl₂) δ 14.33, 23.15, 29.34, 29.84, 29.93, 30.09, 30.13, 30.17, 31.74, 32.40, 35.75, 124.13, 127.08, 127.14, 127.27, 127.35, 128.84, 131.03, 131.24, 131.72, 131.92, 138.67, 139.71, 140.20, 140.77, 140.92, 141.72, 141.83; MS (MALDI-TOF, positive) *m/z* calcd for C₁₀₂H₁₃₄ [M]⁺ 1360.1, found: 1359.2; Anal Calcd for C₁₀₂H₁₃₄: C, 90.1; H, 9.9. Found: C, 90.1; H, 9.3.

6.3.2.3 2,5,13,16-Tetrakis(n-dodecyl)-tribenzo[hi,o,uv]triphenyleno[2,1,12,11-bcdef]ovalene (2-19) and 8,11,19,22-Tetrakis(n-dodecyl)-tribenzo[ef,hi,o]-triphenyleno[2,1,12,11-uvabc]ovalene (2-20) (isomeric mixture)

A solution of 1,4-bis(biphenyl-3-yl)-2,3,4,5-tetrakis(4-dodecylphenyl)benzene (**2-18**) (99.8 mg, 73.4 μmol) in unstabilized dichloromethane (30 mL) was degassed by argon bubbling for 15 min. To the solution was added a suspension of iron (III) chloride (581 mg, 3.58 mmol) in nitromethane (2.0 mL). After stirring at room temperature for 3 h with a continuous argon flow through the reaction mixture, the reaction was quenched by the addition of methanol to form brown precipitates. Filtration and washing intensively with methanol gave the title compounds as brown powder (71.4 mg, 51.1 μmol , 72% yield): Mp >320 $^{\circ}\text{C}$; ^1H NMR (500 MHz, 1,1,2,2-tetrachloroethane- d_2 , 393 K) δ 1.15–0.82 (m, 12H), 1.97–1.18 (m, 72H), 2.37–2.01 (m, 8H), 3.14–3.02 (m, 2H), 3.30–3.14 (m, 2H), 3.77–3.61 (m, 2H), 3.91–3.78 (m, 2H), 8.04–7.78 (m, 4H), 8.49–8.10 (m, 4H), 8.56 (m, 2H), 9.11–8.65 (m, 8H); ^{13}C NMR could not be recorded due to strong aggregation of the compound in the solution even at elevated temperature or diluted conditions^{7,22}; MS (MALDI-TOF, positive) m/z calcd for $\text{C}_{102}\text{H}_{118}$ $[\text{M}]^+$ 1344, found 1344.

6.3.3 Synthesis of $N = 18$ armchair GNR 2-13

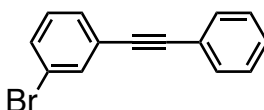
6.3.3.1 $N = 18$ armchair GNR 2-13



A solution of polyphenylene precursor **2-12** (76.6 mg) in unstabilized dichloromethane (80 mL) was degassed by argon bubbling for 15 min. To the solution was added a suspension of iron (III) chloride (1.10 g, 6.76 mmol) in nitromethane (3.5 mL). After stirring at room temperature for 3 days with a continuous argon flow through the reaction mixture, the reaction was quenched by the addition of methanol to form black precipitates, which were collected by centrifugation. The crude product was intensively washed with THF and methanol using Soxhlet extractor for 2 days to give the title compound as a black powder (72.9 mg, 98% yield): FTIR (powder) 2920, 2850, 1595, 1455, 1372, 864, 823, 802, 759, 740, 720 cm^{-1} ; Raman (powder, 488 nm, < 1 mW) 3200, 2922, 2725, 1578, 1325 cm^{-1} .

6.3.4 Synthesis of dimer 3-5

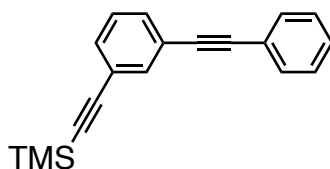
6.3.4.1 3-Bromodiphenylacetylene (**3-10**)²³



To a degassed solution of 1-bromo-3-iodobenzene (**3-8**) (5.03 g, 17.8 mmol) and ethynylbenzene (**3-9**) (2.08 g, 20.4 mmol) in a mixture of tetrahydrofuran (50 mL) and triethylamine (50 mL) were added copper(I) iodide (52.7 mg, 0.277 mmol) and bis(triphenylphosphine)palladium(II) dichloride (376 mg, 0.536 mmol). After stirring at room temperature for 18 h, the reaction mixture was filtered to remove precipitates. The

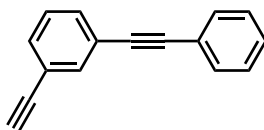
filtrate was diluted with diethyl ether, and washed twice with a saturated aqueous solution of ammonium chloride and three times with brine followed by drying over sodium sulfate and concentration in vacuo. Dark brown crude material was purified by silica gel column chromatography (eluent: hexane) to give the title compound as colorless oil (4.46 g, 98% yield): ^1H NMR (300 MHz, CD_2Cl_2) δ 7.25 (t, $J = 7.9$ Hz, 1H), 7.35–7.41 (m, 3H), 7.46–7.57 (m, 4H), 7.70 (t, $J = 1.7$ Hz, 1H); ^{13}C NMR (75 MHz, CDCl_3) δ 87.77, 90.65, 122.16, 122.73, 125.30, 128.40, 128.61, 129.76, 130.13, 131.36, 131.66, 134.31; Anal Calcd for $\text{C}_{14}\text{H}_9\text{Br}$: C, 65.40; H, 3.53. Found: C, 65.53; H, 3.65. The spectral data were in agreement with the values reported in the literature.²³

6.3.4.2 3-[(Trimethylsilyl)ethynyl]diphenylacetylene (**3-11**)



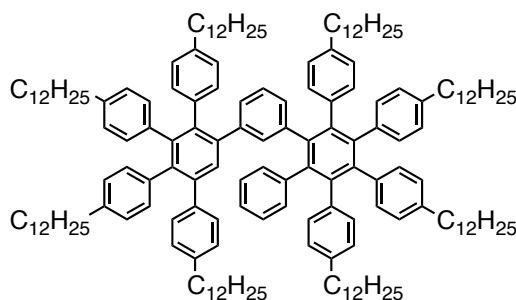
To a degassed suspension of 3-bromodiphenylacetylene (**3-10**) (2.87 g, 11.2 mmol), copper(I) iodide (65.0 mg, 0.341 mmol), and trimethylsilylacetylene (5.00 mL, 35.1 mmol) in a mixture of tetrahydrofuran (30 mL) and triethylamine (30 mL) was added tetrakis(triphenylphosphino)palladium(0) (401 mg, 0.347 mmol). The reaction mixture was stirred at 80 °C for 26 h, and then concentrated in vacuo and diluted with dichloromethane. After washing once with a saturated aqueous solution of ammonium chloride and three times with water, the organic layer was dried over magnesium sulfate and concentrated in vacuo. Purification by silica gel column chromatography (eluent: hexane) yielded the title compound as a yellow oil (3.07 g, 92% yield): ^1H NMR (300 MHz, CD_2Cl_2) δ 0.25 (s, 9H), 7.28–7.44 (m, 5H), 7.47–7.57 (m, 3H), 7.63 (t, $J = 1.5$ Hz, 1H); ^{13}C NMR (75 MHz, CDCl_3) δ 0.053 (3C), 88.67, 90.25, 95.43, 104.30, 123.32, 123.97 (2C), 128.86 (2C), 128.94, 128.96, 131.88, 131.93, 132.00 (2C), 135.17.

6.3.4.3 3-Ehynyldiphenylacetylene (**3-12**)²⁴



To a solution of 3-[(trimethylsilyl)ethynyl]diphenylacetylene (**3-11**) (2.00 g, 7.29 mmol) in a mixture of dichloromethane (100 mL) and methanol (100 mL) was added potassium carbonate (3.02 g, 21.9 mmol). The reaction mixture was stirred at room temperature for 4 h, and then at 40 °C for 18 h, followed by the addition of potassium fluoride (1.34 g, 23.1 mmol). After stirring at room temperature for another 3 h, the solvents were removed in vacuo. Purification by silica gel column chromatography (eluent: hexane) yielded the title compound as a yellow oil (1.04 g, 71% yield): ¹H NMR (300 MHz, CD₂Cl₂) δ 3.18 (s, 1H), 7.31–7.41 (m, 4H), 7.47 (td, *J* = 1.4, 7.8 Hz, 1H), 7.50–7.58 (m, 3H), 7.66 (t, *J* = 1.5 Hz, 1H); ¹³C NMR (75 MHz, CDCl₃) δ 78.13, 82.97, 88.54, 90.38, 122.89, 123.26, 124.07, 128.87 (2C), 129.01 (2C), 132.01 (2C), 132.22, 132.26, 135.35; Anal calcd for C₁₆H₁₀: C, 95.02; H, 4.98. Found: C, 94.95; H, 5.00. The spectral data were in agreement with the values reported in the literature.²⁴

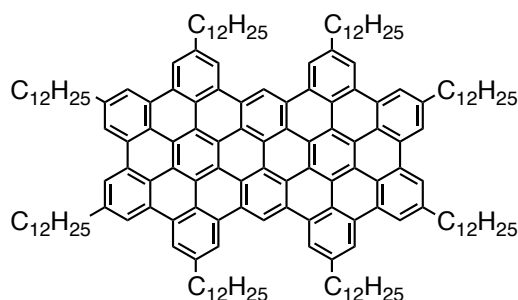
6.3.4.4 4-Dodecyl-4',5',6',3''',4''',5''',6'''-heptakis(4-dodecylphenyl)-1,1':2',1'':3'',1''':2''',1''''-quinquephenyl (**3-4**)



A degassed solution of 3-ehynyldiphenylacetylene (**3-12**) (10.3 mg, 50.9 μmol) and 2,3,4,5-tetrakis(4-dodecylphenyl)-2,4-clopentadienone (**3-13**)⁵ (146 mg, 138 μmol) in diphenyl ether (0.80 mL) was refluxed for 46 h, using a heating mantle. After cooling to room temperature the reaction mixture was diluted with hexane and purified by silica gel column chromatography (eluent: 10% toluene/hexane) to give the title compound as a pale yellow solid (52.5 mg, 46% yield): FTIR (neat) 3,082, 3,051, 3,023, 2,956, 2,920, 2,852, 1,600, 1,516, 1,465, 1,378, 1,184, 1,117, 1,020, 896, 835, 798, 774, 749, 719, 699, 657, 639 cm⁻¹; ¹H NMR (300 MHz, CD₂Cl₂) δ 0.88 (t, *J* = 6.0 Hz, 24H), 1.02–1.64

(m, 160H), 2.27–2.47 (m, 14H), 2.54 (t, $J = 7.4$ Hz, 2H), 6.25 (d, $J = 7.8$ Hz, 1H), 6.45 (t, $J = 7.7$ Hz, 1H), 6.50–6.76 (m, 29H), 6.78 (s, 1H), 6.79–6.90 (m, 5H), 6.94–7.02 (m, 5H); ^{13}C NMR (75 MHz, CDCl_3) δ 12.34 (8C), 23.16 (8C), 29.27, 29.34 (2C), 29.37 (2C), 29.47, 29.57, 29.80, 29.85 (8C), 29.95, 29.99 (5C), 30.05 (2C), 30.16 (16C), 30.20 (8C), 30.23 (8C), 31.66 (2C), 31.73 (2C), 31.78 (3C), 31.93, 32.41 (8C), 35.68, 35.75 (4C), 35.81, 35.87, 35.97, 125.09, 125.52, 125.73, 126.90 (8C), 127.21 (6C), 127.43, 127.47, 127.80 (3C), 129.47, 130.29 (2C), 131.55, 131.73 (8C), 131.87 (2C), 131.91 (2C), 131.95 (2C), 132.14 (2C), 133.65, 137.70, 138.13, 138.41, 138.59, 138.62, 138.67 (2C), 139.25, 139.57, 139.61, 139.92 (2C), 139.96, 140.01, 140.11, 140.37, 140.54, 140.58, 140.66, 140.75, 140.85 (2C), 140.95, 140.99, 141.01, 141.20 (2C), 141.55, 142.09; HRMS (MALDI-TOF, positive) m/z calcd for $\text{C}_{168}\text{H}_{242}$ $[\text{M}]^+$ 2,259.8937, found 2,259.8927.

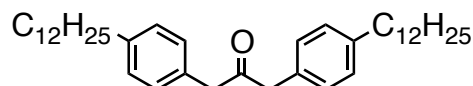
6.3.4.5 2,5,8,11,15,18,21,24-Octakis(*n*-dodecyl)-tetrabenzo[*jk,mn,pq,st*]dibenzo[3,4:9,10]phenanthro[1',10',9',8':5,6,7,8]peryl[2,1,12,11-*bcdef*]ovalene (3-5)²⁵



A solution of 4-dodecyl-4',5',6',3''',4''',5''',6'''-heptakis(4-dodecylphenyl)-1,1':2',1'':3'',1''':2''',1''''-quinquephenyl (**3-4**) (14.9 mg, 6.59 μmol) in unstabilized dichloromethane (40 mL) was degassed by argon bubbling for 10 min. To the degassed solution was added a suspension of iron(III) chloride (185 mg, 1.14 mmol) in nitromethane (1.0 mL). After stirring at room temperature for 4 h under continuous bubbling with argon presaturated with dichloromethane, the reaction was quenched by addition of methanol to form dark yellow precipitates. Filtration by suction using a membrane filter and washing intensively with methanol gave the title compound as a dark yellow powder (14.1 mg, 96% yield): FTIR (powder) 3,061, 2,918, 2,849, 1,694, 1,611, 1,581, 1,464, 1,361, 1,081, 856, 747, 720, 657 cm^{-1} ; ^1H NMR (500 MHz, $\text{C}_2\text{D}_2\text{Cl}_4$, 403 K) δ 0.45–2.80 (m, 200H), 6.25–7.35 (m, 6H), 7.35–9.85 (m, 12H); HRMS (MALDI-TOF, positive) m/z calcd for $\text{C}_{168}\text{H}_{218}$ $[\text{M}]^+$ 2,235.7059, found 2,235.7047.

6.3.5 Synthesis of trimer 3-7

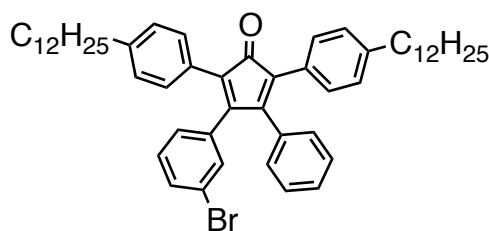
6.3.5.1 1,3-Bis(4-dodecylphenyl)propan-2-one (3-16)²⁶



Dry *N,N*-dimethylacetamide (15 mL) was added to zinc (8.00 g, 122 mmol) and iodine (1.73 g, 6.82 mmol), and stirred at room temperature until the purple color of iodine disappeared. 1-Bromododecane (**3-14**) (20.0 mL, 20.8 g, 83.5 mmol) was then added to the mixture and stirred at 80 °C for 24 h to generate dodecylzinc bromide. To 1,3-bis(4-bromophenyl)propan-2-one (**3-15**)⁶ (5.03 g, 13.7 mmol) and dichloro[1,1'-bis(diphenylphosphino)ferrocene]palladium(II) (0.964 g, 1.37 mmol) was added via a cannula the solution of dodecylzinc bromide. The reaction mixture was stirred at room temperature for 72 h, and then quenched by hydrochloric acid (2 M, 40 mL). The aqueous layer was extracted three times with dichloromethane. The combined organic layers were washed three times with water, dried over sodium sulfate, and evaporated. The crude material passed through a pad of silica gel (eluent: 20–40% dichloromethane/hexane) and recrystallized from hexane to give the title compound as colorless crystals (5.77 g, 77% yield): Mp 75.3–75.5 °C (lit. 72–74 °C)²⁶; ¹H NMR (300 MHz, CD₂Cl₂) δ 0.88 (t, *J* = 6.5 Hz, 6H), 1.18–1.38 (m, 36H), 1.52–1.67 (m, 4H), 2.58 (t, *J* = 7.7 Hz, 4H), 3.69 (s, 4H), 7.03 (d, *J* = 7.9 Hz, 4H), 7.13 (d, *J* = 8.0 Hz, 4H); ¹³C NMR (75 MHz, CD₂Cl₂) δ 14.30 (2C), 23.12 (2C), 29.79 (4C), 29.94 (2C), 30.04 (2C), 30.07 (2C), 30.11 (4C), 31.97 (2C), 32.36 (2C), 35.94 (2C), 49.09 (2C), 129.01 (4C), 129.81 (4C), 131.89 (2C), 142.18 (2C), 206.27; MS (FD, 8 kV) *m/z* calcd for C₃₉H₆₂O [M]⁺ 546.9, found 545.6. The spectral data were in agreement with the values reported in the literature.²⁶

6.3.5.2 3-Bromobenzil (3-17)²⁷

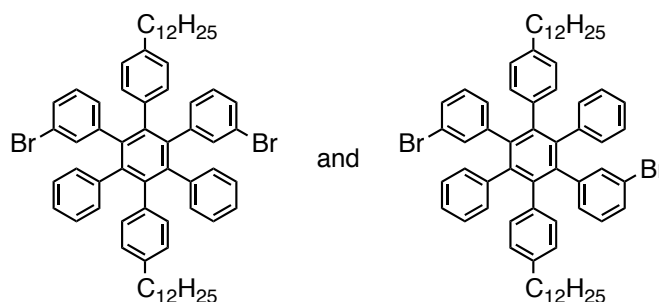
To a solution of 3-bromodiphenylacetylene (**3-10**) (6.38 g, 24.8 mmol) in dimethyl sulfoxide (DMSO) (60 mL) was added iodine (3.15 g, 12.4 mmol). The reaction mixture was degassed and stirred at 155 °C for 20 h. After cooling to room temperature, the reaction was quenched with a saturated aqueous solution of sodium sulfite. Subsequently, the reaction mixture was diluted with dichloromethane, and the aqueous layer was extracted three times with dichloromethane. The combined organic layers were then washed five times with water, dried over sodium sulfate, and concentrated in vacuo. Purification by silica gel column chromatography (eluent: 30–50% dichloromethane/hexane) yielded the title compound as a light yellow solid (4.47 g, 62% yield): Mp 81.6–82.2 °C; ¹H NMR (300 MHz, CD₂Cl₂) δ 7.42 (t, *J* = 7.9 Hz, 1H), 7.51–7.59 (m, 2H), 7.71 (tt, *J* = 7.4, 1.3 Hz, 1H), 7.79–7.84 (m, 1H), 7.89 (dt, *J* = 7.8, 1.2 Hz, 1H), 7.93–7.98 (m, 2H), 8.13 (t, *J* = 1.8 Hz, 1H); ¹³C NMR (75 MHz, CD₂Cl₂) δ 123.61, 128.99, 129.53 (2C), 130.29 (2C), 131.10, 132.79, 133.11, 135.16, 135.59, 138.12, 193.42, 194.08; HRMS (ESI, positive) *m/z* calcd for C₁₄H₉O₂BrNa [M+Na]⁺ 310.9684, found 310.9696; Anal Calcd for C₁₄H₉BrO₂: C, 58.16; H, 3.14. Found: C, 58.21; H, 3.32. The spectral data were in agreement with the values reported in the literature.²⁷

6.3.5.3 3-(3-Bromophenyl)-2,5-bis(4-dodecylphenyl)-4-phenyl-2,4-cyclopentadienone (3-18)

To a solution of 3-bromobenzil (**3-17**) (2.00 g, 6.92 mmol) and 1,3-bis(4-dodecylphenyl)propan-2-one (**3-16**) (3.79 g, 6.93 mmol) in *tert*-butanol (200 mL) was added at 80 °C an aqueous solution of tetraethylammonium hydroxide (20%,

2.05 mL, 2.77 mmol). After stirring at 80 °C for 50 min, the reaction was quenched by the addition of 1 N HCl (40 mL), and the reaction mixture was extracted three times with dichloromethane. The combined organic layers were washed with water three times, dried over sodium sulfate, and evaporated to give a purple crude product. Purification by silica gel column chromatography (eluent: 20% dichloromethane/hexane) gave the title compound as a purple solid (5.05 g, 91% yield): Mp 91.4–92.1 °C; ¹H NMR (300 MHz, CD₂Cl₂) δ 0.86–0.90 (m, 6H), 1.23–1.37 (m, 36H), 1.51–1.66 (m, 4H), 2.52–2.62 (m, 4H), 6.87–6.92 (m, 1H), 6.93–6.98 (m, 2H), 7.04–7.16 (m, 10H), 7.18–7.32 (m, 3H), 7.35–7.41 (m, 1H); ¹³C NMR (75 MHz, CD₂Cl₂) δ 14.30 (2C), 23.12 (2C), 29.75 (2C), 29.79 (2C), 29.92 (2C), 30.02 (2C), 30.07 (2C), 30.09 (2C), 30.11 (2C), 31.74 (2C), 32.36 (2C), 36.13 (2C), 122.25, 125.64, 126.36, 128.12, 128.46 (2C), 128.48 (2C), 128.60 (2C), 128.90, 129.60 (2C), 129.97, 130.25, 130.34 (2C), 130.35 (2C), 131.61, 132.46, 133.63, 136.13, 143.13, 143.38, 152.58, 152.63, 154.27, 200.93; HRMS (ESI, positive) *m/z* calcd for C₅₃H₆₇OBrNa [M+Na]⁺ 821.4273, found 821.4284; Anal Calcd for C₃₉H₆₂O: C, 79.57; H, 8.44. Found: C, 79.59; H, 8.56.

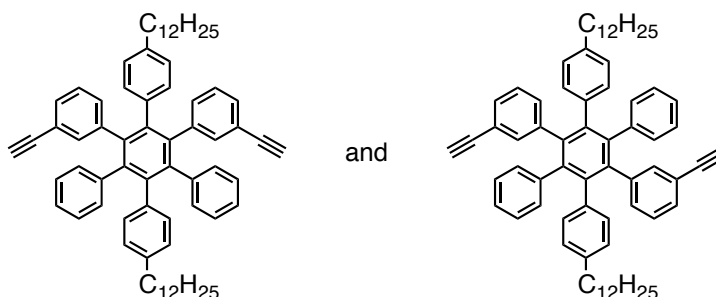
6.3.5.4 3-Bromo-3'-(3-bromophenyl)-4''-dodecyl-5'-(4-dodecylphenyl)-4',6'-diphenyl-1,1':2',1''-terphenyl and 3-bromo-4'-(3-bromophenyl)-4''-dodecyl-5'-(4-dodecylphenyl)-3',6'-diphenyl-1,1':2',1''-terphenyl (3-19) (isomeric mixture)



A degassed solution of 3-bromodiphenylacetylene (**3-10**) (150 mg, 0.583 mmol) and 3-(3-bromophenyl)-2,5-bis(4-dodecylphenyl)-4-phenyl-2,4-cyclopentadienone (**3-18**) (208 mg, 0.260 mmol) in diphenyl ether (3.0 mL) was stirred at 220 °C for 25 h under microwave irradiation with maximum power of 300 W and activated cooling. The solvent was distilled off at 120 °C under reduced pressure, and the resulting crude material was purified by preparative TLC (eluent: 10% dichloromethane/hexane) to give an isomeric mixture of the title compounds as a pale yellow solid (225 mg, 84% yield): ¹H NMR (300 MHz, CD₂Cl₂) δ 0.90 (t, *J* = 6.9 Hz, 6H), 1.03–1.07 (m, 4H),

1.08–1.36 (m, 32H), 1.37–1.51 (m, 4H), 2.33–2.45 (m, 4H), 6.66–7.04 (m, 26H); ^{13}C NMR (75 MHz, CDCl_3) δ 14.33, 23.14, 29.14, 29.17, 29.21, 29.81, 29.91, 30.09, 30.15, 31.49, 31.57, 31.63, 32.38, 35.59, 35.64, 35.69, 119.24, 120.98, 123.65, 125.84, 125.88, 127.07, 127.11, 127.27, 127.42, 128.46, 128.57, 128.62, 130.16, 130.49, 130.53, 131.35, 131.50, 131.53, 131.63, 131.76, 134.73, 137.48, 137.71, 137.92, 139.67, 139.76, 140.33, 140.52, 140.59, 140.75, 140.78, 140.84, 140.97, 141.13, 143.37, 143.41; HRMS (ESI, positive) m/z calcd for $\text{C}_{66}\text{H}_{76}\text{Br}_2\text{Na}$ $[\text{M}+\text{Na}]^+$ 1049.4211, found 1049.4200; Anal Calcd for $\text{C}_{66}\text{H}_{76}\text{Br}_2$: C, 77.03; H, 7.44. Found: C, 76.79; H, 7.33.

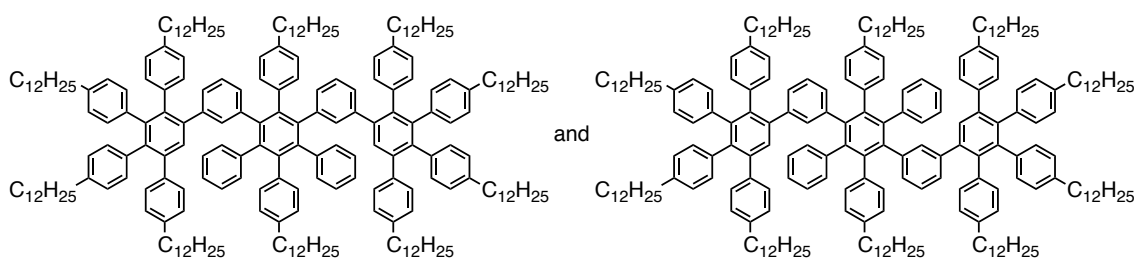
6.3.5.5 4''-Dodecyl-5'-(4-dodecylphenyl)-3-ethynyl-3'-(3-ethynylphenyl)-4',6'-diphenyl-1,1':2',1''-terphenyl and 4''-dodecyl-5'-(4-dodecylphenyl)-3-ethynyl-4'-(3-ethynylphenyl)-3',6'-diphenyl-1,1':2',1''-terphenyl (3-21) (isomeric mixture)



To a degassed suspension of oligophenylene **3-19** (169 mg, 0.164 mmol), copper(I) iodide (5.74 mg, 0.0301 mmol), and trimethylsilylacetylene (0.140 mL, 0.984 mmol) in a mixture of tetrahydrofuran (5.0 mL) and triethylamine (5.0 mL) was added tetrakis(triphenylphosphino)palladium(0) (22.4 mg, 0.0194 mmol). The reaction mixture was stirred at 80 °C for 48 h, and then concentrated in vacuo and diluted with dichloromethane. After washing once with a saturated aqueous solution of ammonium chloride and three times with water, the organic layer was dried over sodium sulfate, concentrated in vacuo, and passed through a pad of silica gel (eluent: dichloromethane). The resulting crude material of oligophenylene **3-20** was subsequently dissolved in a mixture of tetrahydrofuran (5.0 mL) and methanol (5.0 mL) with potassium fluoride (59.9 mg, 1.03 mmol), and stirred at 40 °C for 17 h. Water was then added to quench the reaction, and the aqueous layer was extracted three times with dichloromethane. The combined organic layers were washed three times with water, dried over sodium sulfate, and dried in vacuo. Purification by silica gel column chromatography (eluent: 20% dichloromethane/hexane) yielded an isomeric mixture of the title compounds as a yellow oil (97.0 mg, 64% yield in two steps): ^1H NMR (300 MHz, CD_2Cl_2) δ 0.89 (t, J

= 6.9 Hz, 6H), 1.02–1.16 (m, 4H), 1.17–1.35 (m, 32H), 1.36–1.48 (m, 4H), 2.32–2.43 (m, 4H), 2.94 (s, 2H), 6.65–7.04 (m, 26H); ^{13}C NMR (75 MHz, CDCl_3) δ 14.33, 23.15, 29.15, 29.18, 29.82, 29.92, 30.09, 30.11, 30.16, 31.51, 31.55, 31.59, 32.39, 35.61, 35.64, 35.68, 76.73, 83.97, 119.26, 120.76, 125.78, 127.04, 127.21, 127.32, 129.44, 129.46, 130.18, 131.51, 131.56, 131.71, 131.83, 132.49, 135.31, 135.32, 137.67, 137.87, 138.08, 139.79, 140.06, 140.28, 140.48, 140.63, 140.68, 140.79, 140.91, 140.94, 141.07, 141.59, 141.62; HRMS (ESI, positive) m/z calcd for $\text{C}_{70}\text{H}_{78}\text{Na}$ $[\text{M}+\text{Na}]^+$ 941.6001, found 941.6020.

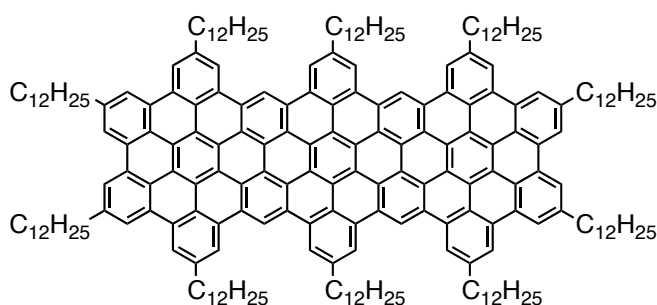
6.3.5.6 4,4''''-Didodecyl-4',5',6',2''',5''',3''''',4''''',5'''''-octakis(4-dodecylphenyl)-4''',6'''-diphenyl-1,1':2',1'':3'',1''':3''',1''''':3''''',1''''':2''''',1''''''-septiphenyl and 4,4''''-Didodecyl-4',5',6',2''',5''',3''''',4''''',5'''''-octakis(4-dodecylphenyl)-3''',6'''-diphenyl-1,1':2',1'':3'',1''':4'',1''':3''',1''''':2''''',1''''''-septiphenyl (3-6) (isomeric mixture)



A degassed solution of oligophenylene **3-21** (37.4 mg, 40.7 μmol) and 2,3,4,5-tetrakis(4-dodecylphenyl)-2,4-clopentadienone (**3-13**) (107 mg, 101 μmol) in diphenyl ether (1.0 mL) was stirred at 200 $^{\circ}\text{C}$ for 22 h under microwave irradiation with maximum power of 300 W. The solvent was distilled off at 130 $^{\circ}\text{C}$ under reduced pressure, and the resulting crude material was purified by preparative TLC (eluent: 20% dichloromethane/hexane), and then by recycling preparative SEC (Japan Analytical Industry JAIGEL-2H+2.5H, eluent: chloroform, 3.0 mL/min) to give an isomeric mixture of the title compounds as a pale yellow solid (51.4 mg, 42% yield): ^1H NMR (300 MHz, CD_2Cl_2) δ 0.89 (t, $J = 6.8$ Hz, 30H), 1.05–1.50 (m, 194H), 1.53–1.64 (m, 4H), 2.27–2.47 (m, 16H), 2.55 (t, $J = 7.8$ Hz, 4H), 6.21–6.28 (m, 2H), 6.42–6.90 (m, 48H), 6.94–7.02 (m, 10H); ^{13}C NMR (75 MHz, CDCl_3) δ 14.34, 23.16, 29.17, 29.34, 29.43, 29.47, 29.51, 29.80, 29.85, 29.89, 29.99, 30.04, 30.09, 30.15, 30.20, 30.21, 30.26, 30.31, 31.51, 31.72, 31.80, 31.92, 31.95, 32.41, 35.60, 35.75, 35.87, 35.97, 125.55, 125.72, 125.73, 126.91, 126.97, 126.99, 127.12, 127.21, 127.49, 127.80, 129.43, 130.30, 131.52, 131.70, 131.87, 131.96, 132.11, 133.64, 137.70, 138.13, 138.40, 138.44, 139.26,

139.61, 140.02, 140.11, 140.37, 140.53, 140.61, 140.68, 140.70, 140.74, 140.78, 140.85, 140.95, 140.99, 141.09, 141.21, 141.43, 142.10; HRMS (MALDI-TOF, positive) m/z calcd for $C_{222}H_{310} [M]^+$ 2,976.4252, found 2,976.4294.

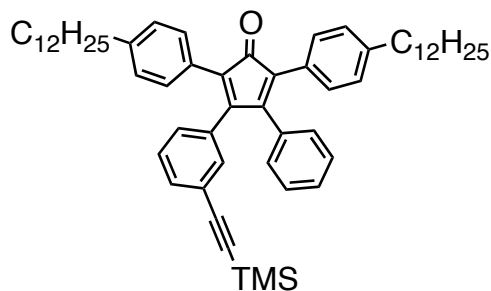
6.3.5.7 Trimer 3-7



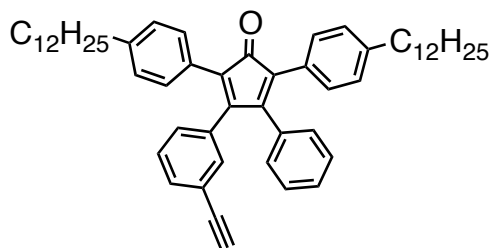
A solution of trimer precursors **3-6** (14.5 mg, 4.87 μmol) in unstabilized dichloromethane (30 mL) was degassed by argon bubbling for 10 min. To the degassed solution was added a suspension of iron (III) chloride (200 mg, 1.23 mmol) in nitromethane (2.0 mL). After stirring at room temperature for 29 h under continuous bubbling with argon presaturated with dichloromethane, the reaction was quenched by the addition of methanol to form dark red precipitates. Filtration by suction using a membrane filter and washing intensively with methanol gave the title compound as a dark red powder (14.2 mg, 99% yield): FTIR (powder) 2,920, 2,850, 1,609, 1,580, 1,464, 1,364, 1,260, 1,213, 1,156, 1,081, 1,014, 856, 800, 747, 719, 611 cm^{-1} ; MS (MALDI-TOF, positive) m/z (%) calcd for $C_{222}H_{274} [M]^+$ 2,940.1 (9), 2,941.1 (22), 2,942.2 (26), 2,943.2 (21), 2,944.2 (13), 2,945.2 (6), 2,946.2 (2), 2,947.2 (1), found 2,940.4 (8), 2,941.4 (18), 2,942.4 (27), 2,943.4 (19), 2,944.4 (14), 2,945.3 (7), 2,946.3 (6); ^1H NMR showed hardly any signal in the aromatic region even at 170 $^\circ\text{C}$ in 1,2-dichlorobenzene- d_4 due to strong self-association typical for large PAHs.^{7,22}

6.3.6 Synthesis of GNR 3-3 with dodecyl chains

6.3.6.1 2,5-Bis(4-dodecylphenyl)-3-phenyl-4-{3-[(trimethylsilyl)ethynyl]phenyl}-2,4-cyclopentadienone (3-22)

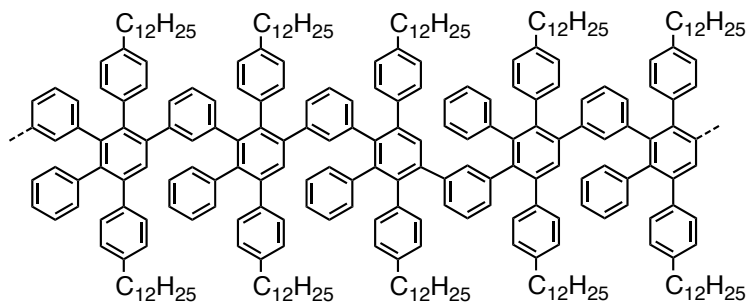


To a degassed suspension of 3-(3-bromophenyl)-2,5-bis(4-dodecylphenyl)-4-phenyl-2,4-cyclopentadienone (**3-18**) (3.00 g, 3.75 mmol) and copper(I) iodide (73.5 mg, 0.386 mmol) in triethylamine (200 mL) were added trimethylsilylacetylene (1.60 mL, 11.3 mmol) and tetrakis-(triphenylphosphino)-palladium(0) (438 mg, 0.379 mmol). After stirring at 80 °C for 19 h, the solvent was removed in vacuo. The resulting purple solid was dissolved in dichloromethane, and then washed once with a saturated aqueous solution of ammonium chloride and twice with brine. Subsequently, the organic layer was dried over sodium sulfate and evaporated. Purification by silica gel column chromatography (eluent: 15% dichloromethane/hexane) yielded the title compound as a purple solid (2.10 g, 69% yield): Mp 96.1–96.8 °C; ^1H NMR (300 MHz, CD_2Cl_2) δ 0.19 (s, 9H), 0.88 (t, $J = 6.7$ Hz, 6H), 1.23–1.36 (m, 36H), 1.55–1.65 (m, 4H), 2.52–2.61 (m, 4H), 6.87–6.92 (m, 1H), 6.92–6.97 (m, 2H), 7.04–7.29 (m, 13H), 7.30–7.35 (m, 1H); ^{13}C NMR (75 MHz, CD_2Cl_2) δ 0.10 (3C), 14.30 (2C), 23.12 (2C), 29.78 (2C), 29.82 (2C), 29.91 (2C), 30.01 (2C), 30.07 (4C), 30.10 (2C), 31.75 (2C), 32.35 (2C), 36.14 (2C), 95.25, 104.61, 123.49, 125.52, 126.01, 128.27, 128.41 (2C), 128.47 (2C), 128.53 (2C), 128.67, 128.81, 129.61 (2C), 129.82, 130.34 (4C), 130.61, 132.07, 132.50, 133.70, 134.47, 143.07, 143.28, 153.43, 154.43, 154.27, 201.13; HRMS (ESI, positive) m/z calcd for $\text{C}_{58}\text{H}_{76}\text{OSiNa}$ $[\text{M}+\text{Na}]^+$ 839.5563, found 839.5552; Anal Calcd for $\text{C}_{58}\text{H}_{76}\text{OSi}$: C, 85.23; H, 9.37. Found: C, 84.84; H, 9.33.

6.3.6.2 2,5-Bis(4-dodecylphenyl)-3-(3-ethynylphenyl)-4-phenyl-2,4-cyclopentadienone (3-1)

Methanol (100 mL) was added to a suspension of 2,5-bis(4-dodecylphenyl)-3-phenyl-4-{3-[(trimethylsilyl)ethynyl]phenyl}-2,4-cyclopentadienone (**3-22**) (1.02 g, 1.25 mmol) and potassium fluoride (361 mg, 6.21 mmol) in tetrahydrofuran (100 mL), and the reaction mixture was stirred at 40 °C for 5 h. After removal of the solvents at 40 °C in vacuo, purification by silica gel column chromatography (eluent: 15% dichloromethane/hexane) yielded the title compound as a purple solid (786 mg, 84% yield): Mp 72.6 °C; ¹H NMR (300 MHz, CD₂Cl₂) δ 0.88 (t, *J* = 6.7 Hz, 6H), 1.23–1.36 (m, 36H), 1.51–1.65 (m, 4H), 2.51–2.61 (m, 4H), 3.04 (s, 1H), 6.91–6.97 (m, 3H), 7.04–7.30 (m, 13H), 7.35–7.39 (m, 1H); ¹³C NMR (75 MHz, CD₂Cl₂) δ 14.33 (2C), 23.14 (2C), 29.80 (4C), 29.93 (2C), 30.03 (2C), 30.09 (4C), 30.12 (2C), 31.75 (2C), 32.37 (2C), 36.14 (2C), 77.93, 83.22, 122.35, 125.61, 126.17, 128.25, 128.44 (2C), 128.48 (2C), 128.52, 128.54, 128.56 (2C), 128.84, 129.63 (2C), 130.19, 130.36 (4C), 132.28, 133.00, 133.69, 134.44, 143.08, 143.27, 153.21, 154.34, 201.06; HRMS (ESI, positive) *m/z* calcd for C₅₅H₆₉O [M+H]⁺ 745.5348, found 745.5334; Anal Calcd for C₅₅H₆₈O: C, 88.65; H, 9.20. Found: C, 88.56; H, 8.75.

6.3.6.3 Polyphenylene precursor 3-2 (isomeric mixture)



Typical procedure for Diels–Alder polymerization in a Ph₂O solution-1

A degassed solution of 2,5-bis(4-dodecylphenyl)-3-(3-ethynylphenyl)-4-phenyl-2,4-cyclopentadienone (**3-1**) (102 mg, 0.137 mmol) in diphenyl ether (0.600 mL, 228 mM) was refluxed for 28 h using a heating mantle. The purple color disappeared and the solution turned pale yellow, indicating the completion of the polymerization. After cooling to room temperature, methanol was added. The precipitates were collected by filtration with a membrane filter to obtain precursor **3-2-II** as a pale yellow solid (94.2 mg, 96% yield, M_w : 73,000–150,000 g/mol, M_n : 19,000–27,000 g/mol, PDI: 3.8–5.6 based on SEC analysis against PPP and PS standards). A part of the crude polymer was fractionated by using recycling preparative SEC system (Waters Ultrastayragel 103 Å, 19 × 300 mm, eluent: chloroform, 3.0 mL/min) to remove low-molecular-weight fractions, leading to precursor **3-2-II'** with M_w of 100,000–220,000 g/mol, M_n of 65,000–120,000 g/mol, and PDI of 1.5–1.8.

Typical procedure for Diels–Alder polymerization in a Ph₂O solution-2

A degassed solution of 2,5-bis(4-dodecylphenyl)-3-(3-ethynylphenyl)-4-phenyl-2,4-cyclopentadienone (**3-1**) (210 mg, 0.281 mmol) in diphenyl ether (0.200 mL, 1410 mM) was refluxed for 20 h using a heating mantle. After cooling to room temperature, methanol was added. The precipitates were collected by filtration with a membrane filter to obtain a crude precursor **3-2-III** as a pale yellow solid (190 mg, 94% yield, M_w of 220,000–530,000 g/mol, M_n of 29,000–41,000 g/mol, and PDI of 7.6–13, based on SEC analysis against PPP and PS standards). A part of the crude polymer was dissolved in tetrahydrofuran, and reprecipitated with methanol (tetrahydrofuran/methanol = 2:1 in volume ratio) followed by centrifugation (13.4 krpm, 1 min). The precipitates were subsequently collected by centrifugation (13.4 krpm, 1 min), and washed with a mixture of tetrahydrofuran and methanol (2:1 volume ratio). This process was repeated for five times to obtain precursor **3-2-III'** with M_w of 270,000–640,000 g/mol, M_n of 160,000–

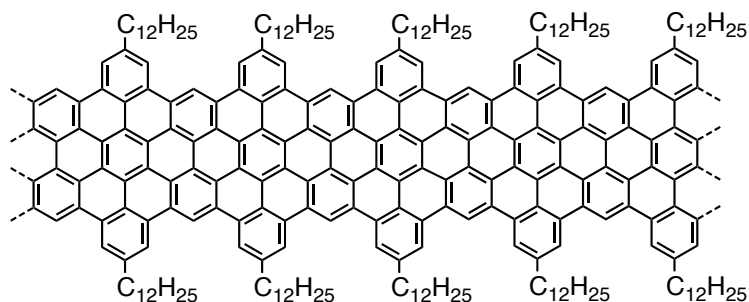
340,000 g/mol, and PDI of 1.7–1.9.

General procedure for *Diels–Alder* polymerization in a melt

A purple powder of 2,5-bis(4-dodecylphenyl)-3-(3-ethynylphenyl)-4-phenyl-2,4-cyclopentadienone (**3-1**) was heated under argon at 260–270 °C using a heating mantle. The powder at first melted and then lost its purple color, turning pale yellow, which indicated the completion of the polymerization. After cooling to room temperature the resulting polymer was dissolved in tetrahydrofuran with a help of sonication, filtered, and dried in vacuo to obtain precursor **3-2** as pale yellow solid.

FTIR (powder) 3,085, 3,057, 3,025, 2,920, 2,852, 1,603, 1,513, 1,467, 1,450, 1,380, 896, 838, 795, 698 cm^{-1} ; ^1H NMR (300 MHz, CD_2Cl_2) δ 0.87, 1.26, 1.45, 1.59, 2.42, 2.54, 6.27, 6.46, 6.55, 6.71, 6.79, 6.85, 6.99.

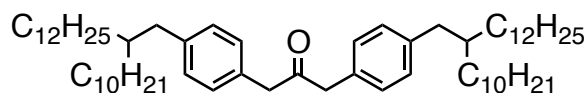
6.3.6.4 GNR 3-3 with dodecyl chains



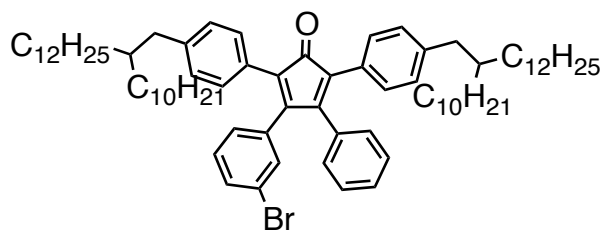
A solution of polyphenylene precursor **3-2** (28.7 mg) in unstabilized dichloromethane (80 mL) was degassed by argon bubbling for 10 min. To the degassed solution was added a suspension of iron(III) chloride (567 mg, 3.50 mmol, 7 eq. for one hydrogen to be removed) in nitromethane (5.0 mL). After stirring at room temperature for 72 h under continuous bubbling with argon presaturated with dichloromethane, the reaction was quenched by addition of methanol to form dark purple precipitates. Filtration by suction using a membrane filter and washing intensively with methanol and THF gave the title compound as a dark purple powder (27.9 mg, 99% yield): FTIR (powder) 2,918, 2,848, 1,613, 1,573, 1,460, 1,350, 1,220, 1,157, 1,077, 863, 751, 720, 670 cm^{-1} ; Raman (powder, 532 nm, < 1 mW) 3188, 2907, 2638, 1597, 1317, 235 cm^{-1} .

6.3.7 Synthesis of GNR 3-26 with 2-decyltetradecyl chains

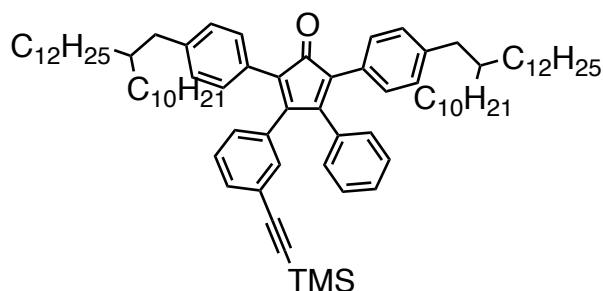
6.3.7.1 1,3-Bis[4-(2-decyltetradecyl)phenyl]propan-2-one (3-28)



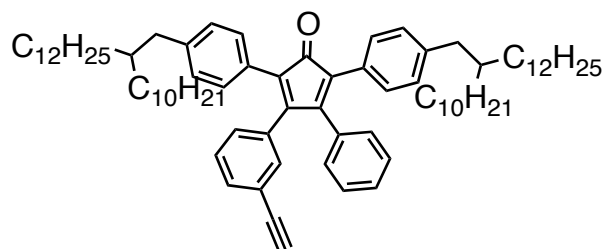
Dry *N,N*-dimethylacetamide (10 mL) was added to zinc (3.21 g, 49.1 mmol) and iodine (0.689 g, 2.71 mmol) in a 100-mL two-necked flask equipped with a condenser, and stirred at room temperature until the purple color of iodine disappeared. 2-Decyltetradecylbromide (**3-27**)⁷ (15.3 g, 36.7 mmol) was then added to the mixture and stirred at 80 °C for 24 h to generate 2-decyltetradecylzinc bromide. To 1,3-bis(4-bromophenyl)propan-2-one (**3-15**)⁶ (2.00 g, 5.43 mmol) and dichloro[1,1'-bis(diphenylphosphino)ferrocene]palladium(II) (0.384 g, 0.544 mmol) in a 100-mL Schlenk flask was added via a cannula the solution of 2-decyltetradecylzinc bromide. The reaction mixture was stirred at room temperature for 18 h, and then quenched by hydrochloric acid (2 M, 40 mL). The aqueous layer was extracted three times with dichloromethane. The combined organic layers were washed three times with water, dried over sodium sulfate, and evaporated. The crude material was then purified by silica gel column chromatography (eluent: 20% dichloromethane/hexane) to give the title compound as pale yellow oil (4.13 g, 86% yield): ¹H NMR (300 MHz, CD₂Cl₂) δ 0.88 (t, *J* = 6.7 Hz, 12H), 1.16–1.37 (m, 80H), 1.55–1.67 (m, 2H), 2.50 (d, *J* = 7.0 Hz, 4H), 3.68 (s, 4H), 7.01 (d, *J* = 8.1 Hz, 4H), 7.09 (d, *J* = 8.1 Hz, 4H); ¹³C NMR (75 MHz, CD₂Cl₂) δ 14.36 (4C), 23.18 (4C), 26.99 (4C), 29.85 (4C), 30.16 (16C), 30.50 (4C), 32.42 (4C), 33.60 (4C), 40.12 (2C), 40.57 (2C), 49.13 (2C), 129.70 (4C), 129.86 (4C), 131.88 (2C), 141.11 (2C), 206.30; MS (FD, 8 kV) *m/z* calcd for C₆₃H₁₁₀O [M]⁺ 883.6, found 883.8; Anal Calcd for C₆₃H₁₁₀O: C, 85.64; H, 12.55. Found: C, 85.71; H, 12.45.

6.3.7.2 3-(3-Bromophenyl)-2,5-bis[4-(2-decyltetradecyl)phenyl]-4-phenyl-2,4-cyclopentadienone (3-29)

To a solution of 3-bromobenzil (**3-17**) (0.808 g, 2.79 mmol) and 1,3-bis[4-(2-decyltetradecyl)phenyl]propan-2-one (**3-28**) (2.55 g, 2.89 mmol) in *tert*-butanol (70 mL) was added at 80 °C an aqueous solution of tetraethylammonium hydroxide (20%, 0.820 mL, 1.12 mmol). After stirring at 80 °C for 40 min, the reaction was quenched by the addition of hydrochloric acid (2 M, 20 mL). The reaction mixture then was concentrated in vacuo, and extracted twice with dichloromethane. The combined organic layers were washed twice with water, dried over sodium sulfate, and evaporated. Purification by silica gel column chromatography (eluent: 10% dichloromethane/hexane) gave the title compound as a purple oil (2.71 g, 85% yield): ^1H NMR (300 MHz, CD_2Cl_2) δ 0.88 (t, $J = 6.7$ Hz, 12H), 1.15–1.35 (m, 80H), 1.55–1.67 (m, 2H), 2.50 (t, $J = 6.4$ Hz, 4H), 6.87 (dt, $J = 7.9, 1.1$ Hz, 1H), 6.92–6.98 (m, 2H), 7.01–7.16 (m, 10H), 7.18–7.32 (m, 3H), 7.35–7.41 (m, 1H); ^{13}C NMR (75 MHz, CD_2Cl_2) δ 14.33 (4C), 23.15 (4C), 26.96 (4C), 29.82 (4C), 30.12 (16C), 30.44 (4C), 32.39 (4C), 33.61 (2C), 33.64 (2C), 40.01 (2C), 40.78 (2C), 122.26, 125.69, 126.42, 128.09, 128.42, 128.47 (2C), 128.49, 128.91, 129.30 (2C), 129.41 (2C), 129.65 (2C), 129.93, 130.20 (4C), 131.62, 132.56, 133.66, 136.13, 142.12, 142.39, 152.55, 154.22, 200.95; HRMS (ESI, positive) m/z calcd for $\text{C}_{77}\text{H}_{116}\text{OBr}$ $[\text{M}+\text{H}]^+$ 1,135.8210, found 1,135.8199.

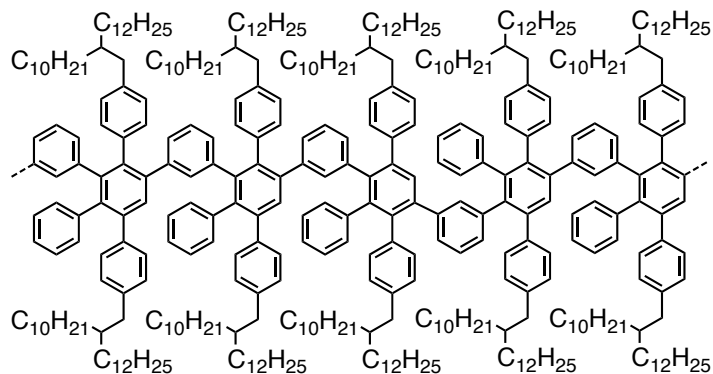
6.3.7.3 2,5-Bis[4-(2-decyltetradecyl)phenyl]-3-phenyl-4-{3-[(trimethylsilyl)ethynyl]phenyl}-2,4-cyclopentadienone (3-30)

To a degassed suspension of 3-(3-bromophenyl)-2,5-bis[4-(2-decyltetradecyl)phenyl]-4-phenyl-2,4-cyclopentadienone (**3-29**) (1.53 g, 1.34 mmol) and copper(I) iodide (30.0 mg, 0.158 mmol) in triethylamine (100 mL) were added trimethylsilylacetylene (0.580 mL, 4.07 mmol) and tetrakis(triphenylphosphino) palladium(0) (158 mg, 0.137 mmol). After stirring at 80 °C for 16 h, the solvent was removed in vacuo. Purification by silica gel column chromatography (eluent: 10% dichloromethane/hexane) yielded the title compound as a purple oil (1.23 g, 79% yield): ^1H NMR (300 MHz, CD_2Cl_2) δ 0.19 (s, 9H), 0.88 (t, $J = 6.8$ Hz, 12H), 1.16–1.36 (m, 80H), 1.53–1.66 (m, 2H), 2.45–2.53 (m, 4H), 6.85–6.97 (m, 3H), 7.00–7.29 (m, 13H), 7.30–7.35 (m, 1H); ^{13}C NMR (75 MHz, CD_2Cl_2) δ 0.05 (3C), 14.35 (4C), 23.16 (4C), 26.93 (2C), 26.97 (2C), 29.83 (4C), 30.13 (16C), 30.44 (4C), 32.40 (4C), 33.60 (2C), 33.66 (2C), 39.95, 40.02, 40.71, 40.80, 95.23, 104.66, 123.55, 125.55, 126.02, 128.25, 128.41 (2C), 128.49, 128.52, 128.83, 129.30 (2C), 129.37 (2C), 129.68 (2C), 129.85, 130.21 (4C), 132.10, 132.55, 133.75, 134.55, 142.07, 142.24, 153.42, 154.43, 201.17; HRMS (ESI, positive) m/z calcd for $\text{C}_{83}\text{H}_{124}\text{ONaSi}$ $[\text{M}+\text{Na}]^+$ 1,175.9319, found 1,175.9371.

6.3.7.4 2,5-Bis[4-(2-decyltetradecyl)phenyl]-3-(3-ethynylphenyl)-4-phenyl-2,4-cyclopentadienone (3-25)

Methanol (15 mL) was added to a suspension of 2,5-bis[4-(2-decyltetradecyl)phenyl]-3-phenyl-4-{3-[(trimethylsilyl)ethynyl]phenyl}-2,4-cyclopentadienone (**3-30**) (110 mg, 0.0953 mmol) and potassium fluoride (54.5 mg, 0.938 mmol) in tetrahydrofuran (15 mL), and the reaction mixture was stirred at 40 °C for 21 h. After removal of the solvents at 40 °C in vacuo, purification by silica gel column chromatography (eluent: 6–10% dichloromethane/hexane) yielded the title compound as a purple oil (93.8 mg, 91% yield): ^1H NMR (300 MHz, CD_2Cl_2) δ 0.88 (t, $J = 6.8$ Hz, 12H), 1.18–1.34 (m, 80H), 1.54–1.67 (m, 2H), 2.46–2.54 (m, 4H), 3.03 (s, 1H), 6.90–6.97 (m, 3H), 7.01–7.30 (m, 13H), 7.34–7.39 (m, 1H); ^{13}C NMR (75 MHz, CD_2Cl_2) δ 14.32 (4C), 23.13 (4C), 26.93 (4C), 29.80 (4C), 30.10 (16C), 30.41 (4C), 32.37 (4C), 33.58 (2C), 33.62 (2C), 39.98 (2C), 40.75 (2C), 77.87, 83.20, 122.34, 125.63, 126.19, 128.19, 128.40 (2C), 128.46, 128.50, 128.83, 129.28 (2C), 129.36 (2C), 129.66 (2C), 130.19 (5C), 132.26, 133.06, 133.69, 134.43, 142.07, 142.25, 153.18, 154.29, 201.09; HRMS (ESI, positive) m/z calcd for $\text{C}_{79}\text{H}_{116}\text{ONa}$ $[\text{M}+\text{Na}]^+$ 1,103.8924, found 1,103.8931.

6.3.7.5 Polyphenylene precursor 3-31 (isomeric mixture)



Typical procedure for *Diels–Alder* polymerization in a Ph₂O solution

A degassed solution of 2,5-bis[4-(2-decyltetradecyl)phenyl]-3-(3-ethynylphenyl)-4-phenyl-2,4-cyclopentadienone (**3-25**) (79.7 mg, 73.7 μ mol) in diphenyl ether (0.490 mL, 151 mM) was refluxed for 88 h, using a heating mantle. The purple color disappeared and the solution turned pale yellow, indicating the completion of the polymerization. After cooling to room temperature methanol was added. The precipitates were collected by centrifugation (13.4 krpm, 1 min) to give precursor **3-31-I** as a pale yellow solid (75.7 mg, 98% yield, M_w : 31,000–54,000 g/mol, M_n : 17,000–21,000 g/mol, PDI: 1.8–2.6 based on SEC analysis against PPP and PS standards). Precursor **3-31-I** was subsequently fractionated by using recycling preparative SEC (Waters Ultrastaygel 103 Å, 19 \times 300 mm, eluent: chloroform, 3.0 mL/min) to remove low-molecular-weight fractions, leading to precursor **3-31-I'** (56.6 mg, 73% yield) with M_w of 36,000–65,000 g/mol, M_n of 27,000–45,000 g/mol, and PDI of 1.3–1.4.

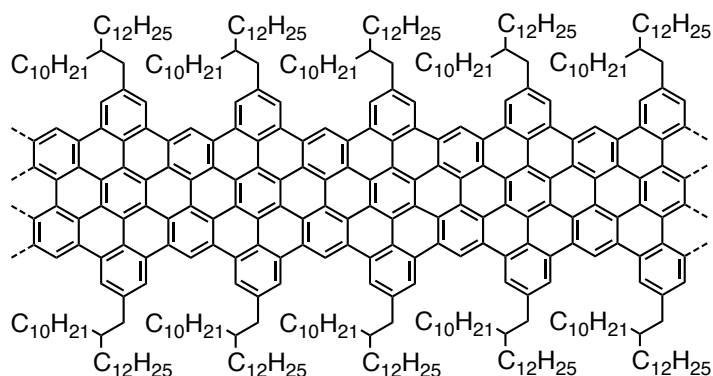
Typical procedure for *Diels–Alder* polymerization in a melt

A purple oil of 2,5-bis[4-(2-decyltetradecyl)phenyl]-3-(3-ethynylphenyl)-4-phenyl-2,4-cyclopentadienone (**3-25**) (48.1 mg, 44.5 μ mol) was heated under argon at 260–270 $^{\circ}$ C for 3 h, using a heating mantle. The purple color disappeared and the oil turned pale yellow, indicating the completion of the polymerization. After cooling to room temperature the resulting polymer was dissolved in tetrahydrofuran with a help of sonication, filtrated, and dried in vacuo to yield precursor **3-31-II** as a pale yellow solid (31.8 mg, 68% yield, M_w : 150,000–350,000 g/mol, M_n : 38,000–58,000 g/mol, PDI: 3.9–6.0 based on the SEC analysis against PPP and PS standards). A part of precursor **3-31-II** was fractionated by preparative gel permeation column chromatography

(Bio-Beads S-X1 support, Bio-Rad Laboratories, eluent: dichloromethane) to obtain precursor **3-31-II'** with M_w of 160,000–370,000 g/mol, M_n of 47,000–75,000 g/mol, and PDI of 3.4–4.9.

FTIR (powder) 3,086, 3,054, 3,022, 2,919, 2,851, 1,603, 1,513, 1,463, 1,403, 1,377, 1,303, 1,260, 1,183, 1,156, 1,106, 1,086, 1,070, 1,023, 897, 840, 793, 711, 698, 620, 611 cm^{-1} ; ^1H NMR (500 MHz, tetrahydrofuran- d_8 , 60 $^\circ\text{C}$) δ 0.88, 1.15, 1.30, 1.49, 1.63, 2.38, 2.50, 6.31, 6.38, 6.45, 6.49, 6.68, 6.78, 6.85, 6.91, 6.97.

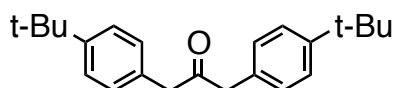
6.3.7.6 GNR 3-26 with 2-decyltetradecyl chains



A solution of polyphenylene precursor **3-31** (28.5 mg) in unstabilized dichloromethane (100 mL) was degassed by argon bubbling for 10 min. To the degassed solution was added a suspension of iron (III) chloride (372 mg, 2.27 mmol, 7 eq. for one hydrogen to be removed) in nitromethane (6.0 mL). After stirring at room temperature for 72 h under continuous bubbling with argon presaturated with dichloromethane, the reaction was quenched by the addition of methanol to form dark purple precipitates. Filtration by suction using a membrane filter and washing intensively with methanol and THF gave the title compound as a dark purple powder (25.2 mg, 89% yield): FTIR (powder) 2,918, 2,848, 1,614, 1,574, 1,463, 1,352, 1,253, 1,154, 1,074, 868, 821, 753, 720, 673, 658 cm^{-1} ; Raman (powder, 488 nm, 0.2 mW) 3211, 2939, 2875, 2653, 1607, 1328 cm^{-1} .

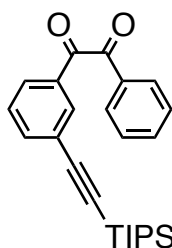
6.3.8 Synthesis of chlorinated GNR 3-33

6.3.8.1 1,3-Bis[4-(*tert*-butyl)phenyl]propan-2-one (3-35)^{28,29}



To a solution of *N,N'*-dicyclohexylcarbodiimide (12.3 g, 59.6 mmol) and 4-dimethylaminopyridine (1.69 g, 13.8 mmol) in dichloromethane (120 mL) was added 4-*tert*-butylphenylacetic acid (**3-34**) (10.2 g, 53.1 mmol) portionwise. After stirring at room temperature for 3 h, the reaction mixture was filtered and the filtrate was evaporate to dryness. Recrystallization from ethanol gave 1.71 g of the title compound as white crystals. Recrystallization from the concentrated mother liquid further yielded 0.56 g of the title compound (27% yield in total): Mp 87.2–88.2 °C; ¹H NMR (300 MHz, CD₂Cl₂) δ 1.32 (s, 18H), 3.71 (s, 4H), 7.08 (dt, *J* = 8.3, 2.1 Hz, 4H), 7.35 (d, *J* = 8.4, 2.0 Hz, 4H); ¹³C NMR (75 MHz, CD₂Cl₂) δ 31.50 (6C), 34.75 (2C), 48.99 (2C), 125.91 (4C), 129.62 (4C), 131.71 (2C), 150.29 (2C), 206.25; HRMS (ESI, positive) *m/z* calcd for C₂₃H₃₀ONa [M+Na]⁺ 345.2194, found 345.2191. The spectral data were in agreement with the values reported in the literature.^{28,29}

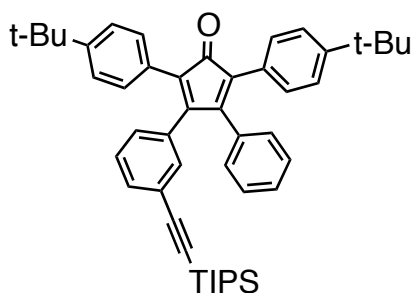
6.3.8.2 3-[(Triisopropylsilyl)ethynyl]benzil (3-36)



To a degassed suspension of 3-bromobenzil (**3-17**) (1.02 g, 3.53 mmol), copper(I) iodide (22.0 mg, 0.116 mmol), and triisopropylsilylacetylene (2.40 mL, 1.95 g, 10.7 mmol) in a mixture of tetrahydrofuran (10 mL) and triethylamine (10 mL) was added tetrakis(triphenylphosphino)palladium(0) (127 mg, 0.110 mmol). The suspension was further degassed by Ar bubbling for 20 min, and then stirring at 80 °C for 14 h. The reaction mixture was then concentrated in vacuo, diluted with dichloromethane, and washed once with a saturated aqueous solution of ammonium chloride and twice with brine. After drying over sodium sulfate and evaporation, the crude product was purified

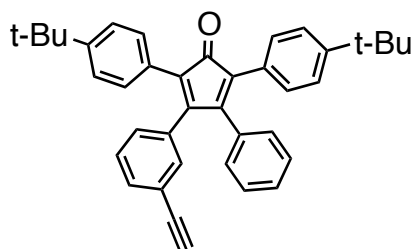
by silica gel column chromatography (eluent: 20% dichloromethane/hexane) to yield the title compound as a yellow oil (1.36 g, 99% yield): ^1H NMR (300 MHz, CD_2Cl_2) δ 1.13 (s, 3H), 1.14 (s, 18H), 7.49 (td, $J = 7.7, 0.48$ Hz, 1H), 7.51–7.58 (m, 2H), 7.70 (tt, $J = 7.4, 1.3$ Hz, 1H), 7.77 (dt, $J = 7.7, 1.4$ Hz, 1H), 7.87–7.91 (m, 1H), 7.93–7.99 (m, 2H), 8.06 (td, $J = 1.7, 0.48$ Hz, 1H); ^{13}C NMR (75 MHz, CD_2Cl_2) δ 11.73 (3C), 18.83 (6C), 93.43, 105.63, 125.17, 129.48, 129.51 (2C), 129.98, 130.29 (2C), 133.11, 133.31, 133.57, 135.47, 138.42, 194.22, 194.44; HRMS (ESI, positive) m/z calcd for $\text{C}_{25}\text{H}_{30}\text{O}_2\text{SiNa}$ $[\text{M}+\text{Na}]^+$ 413.1913, found 413.1922.

6.3.8.3 2,5-Bis[4-(*tert*-butyl)phenyl]-3-phenyl-4-{3-[(triisopropylsilyl)ethynyl]-phenyl}-2,4-cyclopentadienone (3-37)



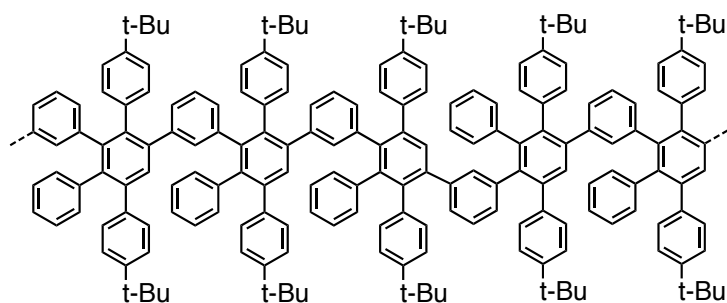
To a solution of 3-[(triisopropylsilyl)ethynyl]benzil (**3-36**) (200 mg, 0.512 mmol) and 1,3-bis[4-(*tert*-butyl)phenyl]propan-2-one (**3-35**) (165 mg, 0.512 mmol) in *tert*-butanol (15 mL) was added at 80 °C a solution of tetrabutylammonium hydroxide in methanol (40%, 0.200 mL, 0.281 mmol). After stirring at 80 °C for 40 min the reaction was quenched by the addition of 2 N HCl (5.0 mL), and the reaction mixture was diluted with dichloromethane. The organic layer was washed three times with water, dried over sodium sulfate, and evaporated to give a purple crude product. Purification by silica gel column chromatography (eluent: 20% dichloromethane/hexane) gave the title compound as purple sticky oil (184 mg, 53% yield): ^1H NMR (300 MHz, CD_2Cl_2) δ 1.07 (s, 21H), 1.296 (s, 9H), 1.301 (s, 9H), 6.91–6.96 (m, 1H), 6.97–7.04 (m, 3H), 7.10–7.35 (m, 13H); ^{13}C NMR (75 MHz, CD_2Cl_2) δ 11.71 (3C), 18.83 (6C), 31.41 (6C), 34.92, 34.93, 91.60, 106.82, 123.69, 125.39 (2C), 125.45 (2C), 125.53, 125.94, 128.18, 128.37, 128.38, 128.48 (2C), 128.86, 129.61 (2C), 129.78, 130.16 (4C), 131.88, 133.36, 133.90, 134.06, 151.07, 151.28, 153.46, 154.59, 201.22; HRMS (ESI, positive) m/z calcd for $\text{C}_{48}\text{H}_{56}\text{OSiNa}$ $[\text{M}+\text{Na}]^+$ 699.3998, found 699.4012; Anal Calcd for $\text{C}_{48}\text{H}_{56}\text{OSi}$: C, 85.15; H, 8.34. Found: C, 84.77; H, 8.73.

6.3.8.4 2,5-Bis[4-(*tert*-butyl)phenyl]-3-phenyl-4-(3-ethynylphenyl)-2,4-cyclopentadienone (3-38)



To a solution of 2,5-bis(4-(*tert*-butyl)phenyl)-3-phenyl-4-{3-[(triisopropylsilyl)ethynyl]phenyl}-2,4-cyclopentadienone (**3-37**) (302 mg, 0.446 mmol) in dry tetrahydrofuran (40 mL) was added a solution of tetra-*n*-butylammonium fluoride in tetrahydrofuran (100 mM, 4.75 mL, 0.475 mmol) dropwise over 5 min. After stirring at room temperature for 10 min, the reaction was quenched by the addition of water. After extraction three times with dichloromethane, the combined organic layers were washed three times with water, dried over sodium sulfate, and evaporated at 40 °C. Purification by silica gel column chromatography (eluent: 25% dichloromethane/hexane) gave the title compound as purple solid (224 mg, 97% yield): ^1H NMR (300 MHz, CD_2Cl_2) δ 1.297 (s, 9H), 1.302 (s, 9H), 3.05 (s, 1H), 6.95–7.01 (m, 3H), 7.08–7.11 (m, 1H), 7.12–7.34 (m, 12H), 7.37 (d, $J = 7.7$ Hz, 1H); ^{13}C NMR (75 MHz, CD_2Cl_2) δ 31.40 (6C), 34.92 (2C), 77.94, 83.24, 122.39, 125.40 (2C), 125.48 (2C), 126.04, 128.08, 128.34, 128.49 (2C), 128.59, 128.84, 129.61 (2C), 130.15 (6C), 132.28, 132.99, 133.77, 134.51, 151.11, 151.29, 153.39, 154.50, 201.18; HRMS (ESI, positive) m/z calcd for $\text{C}_{39}\text{H}_{36}\text{ONa}$ $[\text{M}+\text{Na}]^+$ 543.2664, found 543.2646.

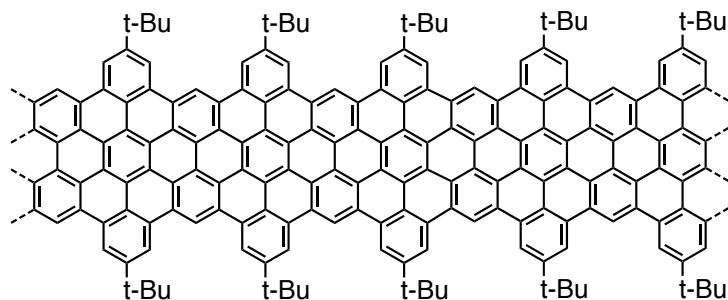
6.3.8.5 Polyphenylene precursor 3-39 (isomeric mixture)



A degassed solution of 2,5-bis(4-(*tert*-butyl)phenyl)-3-phenyl-4-(3-ethynylphenyl)cyclopenta-2,4-dienone (**3-38**) (131 mg, 251 μmol) in diphenyl ether (0.550 mL, 456 mM) was refluxed for 29 h using a heating mantle. The purple color

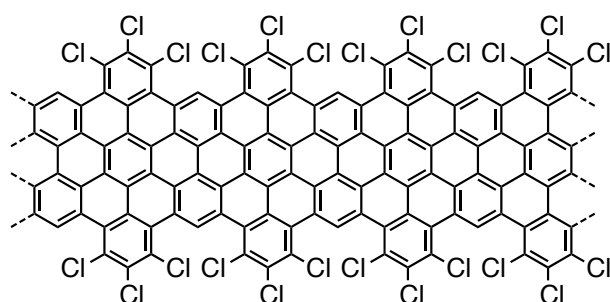
disappeared and the solution turned pale yellow, indicating the completion of the polymerization. After cooling to room temperature a small amount of tetrahydrofuran was added to dissolve all the crude material followed by reprecipitation with methanol and filtration with a membrane filter to provide precursor **3-39** with M_w of 83,000–170,000 g/mol, M_n of 16,000–21,000 g/mol, and PDI of 5.2–8.1 based on the SEC analysis against PPP and PS standards. Precursor **3-39** was dissolved in tetrahydrofuran (15 mL) and reprecipitated with methanol (9.0 mL) followed by centrifugation (13.4 krpm, 1 min) and washing three times with a mixture of tetrahydrofuran and methanol (2:1 volume ratio) to give 13.7 mg (11%) of polymer fraction **3-39-I** with M_w of 120,000–260,000 g/mol, M_n of 87,000–160,000 g/mol, and PDI of 1.4–1.6. All the supernatant solutions and washings were combined and dried in vacuo, dissolved in tetrahydrofuran (10 mL), and reprecipitated with methanol (7.0 mL). The precipitates were collected by centrifugation (13.4 krpm, 1 min) and washed three times with a mixture of tetrahydrofuran and methanol (10:7 volume ratio) to give 56.9 mg (46%) of polymer fraction **3-39-II** with M_w of 120,000–250,000 g/mol, M_n of 81,000–160,000 g/mol, and PDI of 1.5–1.6. All the supernatant solutions and washings were again combined and dried in vacuo, dissolved in tetrahydrofuran (10 mL), and reprecipitated with methanol (8.0 mL). The precipitates were then collected by centrifugation (13.4 krpm, 1 min) and washed three times with a mixture of tetrahydrofuran and methanol (5:4 volume ratio) to give 17.0 mg (14%) of polymer fraction **3-39-III** with M_w of 55,000–100,000 g/mol, M_n of 44,000–77,000 g/mol, and PDI of 1.3–1.4. All the supernatant solutions and washings were again combined and dried in vacuo, dissolved in tetrahydrofuran (5.0 mL), and reprecipitated with methanol (6.0 mL) followed by centrifugation (13.4 krpm, 1 min). The precipitates were washed three times with a mixture of tetrahydrofuran and methanol (5:6 volume ratio) to give 15.2 mg (12%) of polymer fraction **3-39-IV** with M_w of 32,000–58,000 g/mol, M_n of 16,000–24,000 g/mol, and PDI of 2.0–2.4. Polymer fractions **3-39-I** and **3-39-II** were dissolved in tetrahydrofuran and reprecipitated with methanol (1:1 volume ratio) followed by centrifugation (13.4 krpm, 1 min) and washing three times with a mixture of tetrahydrofuran and methanol (1:1 volume ratio) to give 67.9 mg (55%) of precursor **3-39-I+II** with M_w of 120,000–260,000 g/mol, M_n of 87,000–170,000 g/mol, and PDI of 1.4–1.5, which was used for the synthesis of GNR **3-32**: FTIR (powder) 3,081, 3,053, 3,026, 2,957, 2,902, 2,866, 1,599, 1,513, 1,460, 1,394, 1,361, 1,267, 1,118, 1,022, 895, 834, 794, 749, 698 cm^{-1} ; ^1H NMR (300 MHz, CD_2Cl_2) δ 1.17, 1.30, 6.31, 6.41, 6.47, 6.58, 6.73, 6.87, 6.93, 6.98, 7.04, 7.24.

6.3.8.6 GNR 3-32 with *tert*-butyl groups



To a degassed solution of polyphenylene precursor **3-39** (63.0 mg) in unstabilized dichloromethane (190 mL) was added a suspension of iron(III) chloride (1.74 g, 10.7 mmol, 7 eq. for one hydrogen to be removed) in nitromethane (12 mL). The reaction mixture was stirred at room temperature for 72 h under continuous bubbling with argon presaturated with dichloromethane, and then quenched by the addition of methanol (40 mL) to form dark purple precipitates. After removing dichloromethane in vacuo, the precipitates were collected by filtration with a membrane filter and washed intensively with methanol. The resulting crude product was subjected to sonication in tetrahydrofuran (50 mL) for 1 h, collected by filtration with a membrane filter, and washed intensively with tetrahydrofuran to give GNR **3-32** as a dark purple powder (55.6 mg, 90% yield): FTIR (powder) 2,953, 2,904, 2,865, 1,606, 1,573, 1,460, 1,365, 1,253, 866, 752, 640 cm^{-1} ; Raman (powder, 488 nm, 0.2 mW) 3202, 2929, 2866, 2655, 1602, 1326 cm^{-1} .

6.3.8.7 Chlorinated GNR 3-33

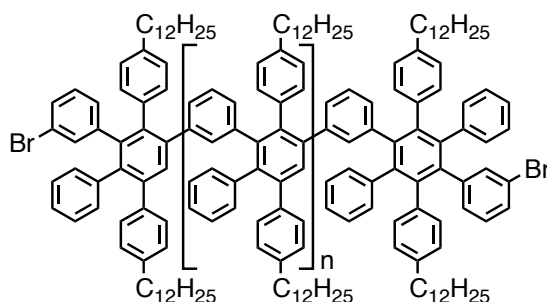


The chlorination of GNR **3-32** was carried out by [REDACTED] in our research group³⁰: A suspension of GNR **3-32** (25 mg), aluminum(III) chloride (26 mg, 0.20 mmol), and an excess amount of iodine monochloride (4.9 g, 30 mmol) in carbon tetrachloride (70 mL) was refluxed at 80 °C for four days. The reaction was then quenched with ethanol (15 mL) and the solvents were removed at 50 °C in vacuo. The

resulting crude material was sonicated in ethanol (30 mL) and filtered, followed by washing with ethanol, hydrochloric acid (1 M), and water to give chlorinated GNR **3-33** as a dark purple powder: FTIR (powder) 2,950, 2,918, 2,847, 1,303, 1,230, 898, 849, 810, 609 cm^{-1} ; Raman (powder, 488 nm, 0.2 mW) 3202, 2929, 2839, 2645, 1603, 1323 cm^{-1} .

6.3.9 Synthesis of GNR **3-43** with acetylthio groups

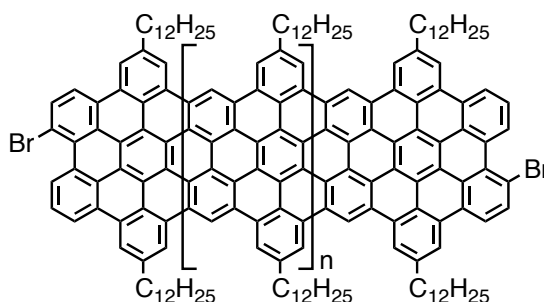
6.3.9.1 Polyphenylene precursor **3-40** with bromo groups



A degassed solution of 2,5-bis(4-dodecylphenyl)-3-(3-ethynylphenyl)-4-phenyl-2,4-cyclopentadienone (**3-1**) (83.5 mg, 0.112 mmol) in diphenyl ether (0.500 mL, 224 mM) was refluxed for 7 h using a heating mantle. The solution still showed the purple color, indicating the presence of the tetraphenylcyclopentadienone moieties at the terminals of the polymers. After cooling to room temperature, 3-(3-bromophenyl)-2,5-bis(4-dodecylphenyl)-4-phenyl-2,4-cyclopentadienone (**3-18**) (30.0 mg, 0.0375 mmol) was added. The reaction mixture was then degassed under reduced pressure and refluxed for another 4 h. After cooling to room temperature, 3-bromodiphenylacetylene (**3-10**) (30.0 mg, 0.117 mmol) was next added. The reaction mixture was subsequently degassed under reduced pressure and further refluxed for 35 h, until when the purple color completely disappeared. After cooling to room temperature, tetrahydrofuran (15 mL) was added to dissolve the crude material, followed by the addition of methanol (30 mL). The resulting precipitates were collected by centrifugation (13.4 krpm, 2 min), and washed with a mixture of tetrahydrofuran and methanol in 1:2 volume ratio. The precipitates were redissolved in tetrahydrofuran (12.0 mL) and reprecipitated with methanol (6.0 mL), followed by centrifugation (13.4 krpm, 2 min) and washing with a mixture of tetrahydrofuran and methanol (2:1 volume ratio). This process was repeated once more to give precursor **3-40-I** (20.4 mg, 25% yield) with M_w of 63,000–130,000 g/mol, M_n of 40,000–70,000 g/mol, and PDI of 1.6–1.9

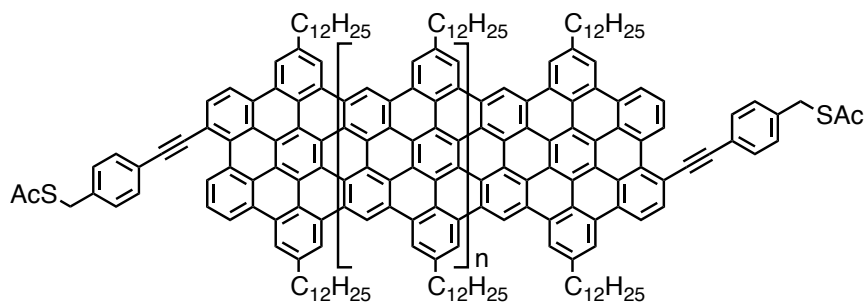
based on the SEC analysis against PPP and PS standards. All the supernatant solutions and washings were combined and dried in vacuo, followed by reprecipitation twice with tetrahydrofuran (2.0 mL) and methanol (4.0 mL), and then twice with tetrahydrofuran (3.0 mL) and methanol (3.0 mL) to provide precursor **3-40-II** (40 mg, 50% yield) with M_w of 20,000–32,000 g/mol, M_n of 12,000–18,000 g/mol, and PDI of 1.7–1.8. The endcapping with the bromo groups could not be confirmed by the available characterization methods due to the extremely small proportion, i.e. <1%, of these functional groups in the polymer structure as well as the formation of cyclic structures for smaller oligomers, which were the only species detected by the reflectron-mode MALDI-TOF MS analysis (see subsection 3.8.2).

6.3.9.2 GNR 3-41 with bromo groups



To a degassed solution of polyphenylene precursor **3-40** (39.1 mg) in unstabilized dichloromethane (140 mL) was added a suspension of iron(III) chloride (759 mg, 4.68 mmol, 7 eq. for one hydrogen to be removed) in nitromethane (9.0 mL). The reaction mixture was stirred at room temperature for 72 h under continuous bubbling with argon presaturated with dichloromethane, and then quenched by the addition of methanol (100 mL) to form dark purple precipitates. After removing dichloromethane in vacuo, the precipitates were collected by filtration with a membrane filter and washed intensively with methanol. The resulting crude product was subjected to sonication in tetrahydrofuran (80 mL) for 15 min, collected by filtration with another membrane filter, and washed intensively with tetrahydrofuran to give GNR **3-41** as a dark purple powder (35.9 mg, 93% yield). The endcapping with the bromo groups could not be confirmed by the available characterization methods due to the extremely small proportion, i.e. <1%, of these functional groups in the polymer structure (see subsection 3.8.2).

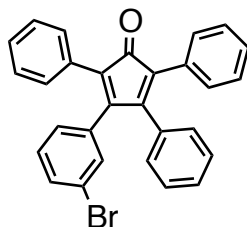
6.3.9.3 GNR 3-42 with acetylthio groups



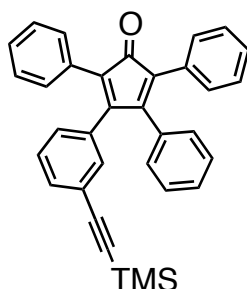
A suspension of GNR **3-41** (9.33 mg), copper(I) iodide (4.71 mg, 0.0247 mmol), and 1-[4-(*S*-acetylthiomethyl)phenyl]acetylene (4.9 mg, 0.0258 mmol) in piperidine (5.0 mL) was sonicated for 15 min, and then degassed by Ar bubbling for 30 min. To the suspension was added tetrakis(triphenylphosphino)palladium(0) (17.6 mg, 0.0152 mmol). The suspension was further degassed by Ar bubbling for 10 min, and then stirring at 90 °C for 43 h. After addition of water (4.0 mL), the reaction mixture was filtered through a membrane filter and washed intensively with water and tetrahydrofuran. The resulting crude product was sonicated in tetrahydrofuran (3.0 mL) and collected by centrifugation (13.4 krpm, 1 min). Further sonication in tetrahydrofuran (3.0 mL) and centrifugation (13.4 krpm, 1 min) provided GNR **3-42** (14.1 mg). Judging from the increase of the weight, copper(I) iodide was encapsulated inside the aggregated GNRs and could not be removed. The endcapping with the 4-(*S*-acetylthiomethyl)phenylethynyl groups could not be confirmed by the available characterization methods due to the extremely small proportion, i.e. <1%, of these functional groups in the polymer structure (see subsection 3.8.2).

6.3.10 Synthesis of AB-type monomer 3-47

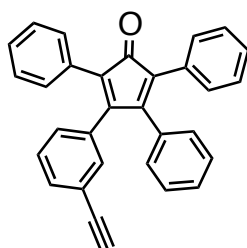
6.3.10.1 3-(3-Bromophenyl)-2,4,5-triphenyl-2,4-cyclopentadienone (3-45)



To a degassed solution of 3-bromobenzil (**3-17**) (300 mg, 1.04 mmol) and 1,3-diphenylpropan-2-one (**3-44**) (226 mg, 1.07 mmol) in *tert*-butanol (40 mL) was added at 80 °C an aqueous solution of tetraethylammonium hydroxide (20%, 0.300 mL, 0.412 mmol). After stirring at 80 °C for 2 h the reaction was quenched by the addition of 1 N HCl (20 mL), and *tert*-butanol was removed in vacuo. After extraction three times with dichloromethane the combined organic layers were washed with water three times, dried over sodium sulfate, and evaporated. Purification by silica gel column chromatography (eluent: 30% dichloromethane/hexane) gave the title compound as purple solid (413 mg, 86% yield): Mp 205.4–205.6 °C; ¹H NMR (300 MHz, CD₂Cl₂) δ 6.89–6.94 (m, 1H), 6.94–7.00 (m, 2H), 7.05–7.12 (m, 2H), 7.19–7.35 (m, 13H), 7.38–7.44 (m, 1H); ¹³C NMR (75 MHz, CD₂Cl₂) δ 122.28, 125.83, 126.54, 127.98, 128.21, 128.41 (2C), 128.45, 128.51 (4C), 129.09, 129.60 (2C), 130.02, 130.52 (4C), 130.84, 131.19, 131.80, 132.43, 133.25, 135.77, 153.18, 154.88, 200.35; HRMS (ESI, positive) *m/z* calcd for C₂₉H₂₀OBr [M+H]⁺ 463.0698, found 463.0710; Anal Calcd for C₂₉H₁₉OBr: C, 75.17; H, 4.13. Found: C, 74.74; H, 3.98.

6.3.10.2 2,3,5-Triphenyl-4-{3-[(trimethylsilyl)ethynyl]phenyl}-2,4-cyclopentadienone (3-46)

To a degassed suspension of 3-(3-bromophenyl)-2,4,5-triphenyl-2,4-cyclopentadienone (**3-45**) (311 mg, 0.671 mmol) and copper(I) iodide (15.0 mg, 0.0788 mmol) in triethylamine (30 mL) were added trimethylsilylacetylene (0.300 mL, 2.11 mmol) and tetrakis(triphenylphosphino)palladium(0) (76.5 mg, 0.0661 mmol). After stirring at 80 °C for 19 h the solvent was removed in vacuo. The resulting purple solid was dissolved in dichloromethane and washed once with a saturated aqueous solution of ammonium chloride and then twice with brine. After drying over sodium sulfate and concentration in vacuo purification by silica gel column chromatography (eluent: 35% dichloromethane/hexane) yielded the title compound as a purple solid (219 mg, 68% yield): Mp 72 °C; ^1H NMR (300 MHz, CD_2Cl_2) δ 0.21 (s, 9H), 6.91 (dt, $J = 7.9, 1.4$ Hz, 1H), 6.94–6.99 (m, 2H), 7.07 (t, $J = 1.4$ Hz, 1H), 7.12–7.32 (m, 14H), 7.35 (dt, $J = 7.8, 1.4$ Hz, 1H); ^{13}C NMR (75 MHz, CD_2Cl_2) δ 0.10 (3C), 95.34, 104.54, 123.56, 125.73, 126.23, 127.94, 128.09, 128.40 (2C), 128.46 (4C), 128.54, 129.01, 129.62 (2C), 129.79, 130.52 (3C), 130.54, 131.01, 131.29, 132.26, 132.48, 133.36, 134.14, 154.08, 155.05, 200.56; HRMS (ESI, positive) m/z calcd for $\text{C}_{34}\text{H}_{28}\text{OSiNa}$ $[\text{M}+\text{Na}]^+$ 503.1807, found 503.1812; Anal Calcd for $\text{C}_{34}\text{H}_{28}\text{OSi}$: C, 84.96; H, 5.87. Found: C, 84.58; H, 6.66.

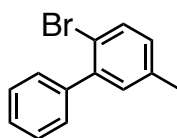
6.3.10.3 3-(3-Ethynylphenyl)-2,4,5-triphenyl-2,4-cyclopentadienone (3-47)

Methanol (15 mL) was added to a suspension of 2,3,5-triphenyl-4-{3-[(trimethylsilyl)ethynyl]phenyl}-2,4-cyclopentadienone (**3-46**) (109 mg, 0.227 mmol)

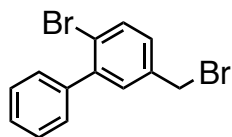
and potassium fluoride (135 mg, 2.32 mmol) in tetrahydrofuran (15 mL), and the reaction mixture was stirred at 40 °C for 3 h. After removal of the solvents at 40 °C in vacuo, purification by silica gel column chromatography (eluent: 25% dichloromethane/hexane) yielded the title compound as a purple solid (81.9 mg, 89% yield): ^1H NMR (300 MHz, CD_2Cl_2) δ 3.05 (s, 1H), 6.92–6.99 (m, 3H), 7.07–7.11 (m, 1H), 7.13–7.32 (m, 14H), 7.36–7.42 (m, 1H); ^{13}C NMR (75 MHz, CD_2Cl_2) δ 77.97, 83.13, 122.37, 125.81, 126.37, 127.94, 128.10, 128.39 (2C), 128.46 (4C), 128.57, 129.02, 129.62 (2C), 130.16, 130.52 (4C), 130.97, 131.26, 132.44, 132.96, 133.32, 134.08, 153.84, 154.94, 200.48; HRMS (ESI, positive) m/z calcd for $\text{C}_{31}\text{H}_{20}\text{ONa}$ $[\text{M}+\text{Na}]^+$ 431.1412, found 431.1432; Anal Calcd for $\text{C}_{31}\text{H}_{20}\text{O}$: C, 91.15; H, 4.93. Found: C, 90.29; H, 5.41.

6.3.11 Synthesis of laterally extended GNR **4-3a** with dodecyl chains

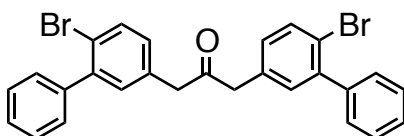
6.3.11.1 2-Bromo-5-methyl-1,1'-biphenyl (**4-8**)



To a degassed suspension of 4-bromo-3-iodotoluene **4-7** (2.01 g, 6.77 mmol), phenylboronic acid (0.842 g, 6.91 mmol), and potassium carbonate (5.60 g, 40.5 mmol) in a mixture of toluene (160 mL), ethanol (40 mL), and water (40 mL) was added tetrakis(triphenylphosphino)palladium(0) (0.237 g, 0.205 mmol). The reaction mixture was further degassed by argon bubbling for 10 min, and then stirred at 60 °C for 22 h. After cooling to room temperature the aqueous layer was extracted with toluene. The combined organic layers were washed three times with water, dried over sodium sulfate, and then evaporated. Purification by silica gel column chromatography (eluent: hexane) gave the title compound as colorless oil (0.919 g, 55% yield): ^1H NMR (300 MHz, CD_2Cl_2) δ 2.34 (s, 3H), 7.02–7.07 (m, 1H), 7.16 (d, $J = 2.1$ Hz, 1H), 7.33–7.47 (m, 5H), 7.54 (d, $J = 8.1$ Hz, 1H); ^{13}C NMR (75 MHz, CD_2Cl_2) δ 20.97, 119.34, 127.90, 128.33 (2C), 129.75 (2C), 130.01, 132.52, 133.13, 137.97, 141.66, 142.57; Anal Calcd for $\text{C}_{13}\text{H}_{11}\text{Br}$: C, 63.18; H, 4.49. Found: C, 63.43; H, 4.54.

6.3.11.2 2-Bromo-5-(bromomethyl)-1,1'-biphenyl (4-9)

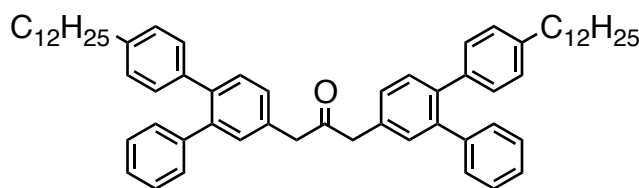
A degassed suspension of 2-bromo-5-methyl-1,1'-biphenyl (**4-8**) (3.06 g, 12.4 mmol), *N*-bromosuccinimide (6.63 g, 37.3 mmol), and benzoyl peroxide (75%, 0.411 g, 1.27 mmol) in carbon tetrachloride (100 mL) was refluxed for 24 h. After cooling to room temperature the reaction mixture was filtered and washed with diethyl ether. The filtrate was washed twice with a saturated aqueous solution of sodium sulfite and twice with brine, dried over sodium sulfate, evaporated, and dried under reduced pressure. The obtained crude mixture of 2-bromo-5-(bromomethyl)-1,1'-biphenyl and 2-bromo-5-(dibromomethyl)-1,1'-biphenyl was dissolved in dry tetrahydrofuran (25 mL) and cooled to 0 °C. To the solution was added diethyl phosphite (19.2 mL, 20.5 g, 149 mmol), and then *N,N*-diisopropylethylamine (26.0 mL, 19.3 g, 149 mmol). The reaction mixture was stirred for 31 h while gradually warmed up to room temperature, and then poured into ice water. After extraction twice with dichloromethane, the combined organic layers were washed with 1 M hydrochloric acid and twice with brine, dried over sodium sulfate, and evaporated. Purification by silica gel column chromatography (eluent: hexane) gave the title compound as a pale yellow solid (2.70 g, 67% yield in two steps): Mp 80.7–81.0 °C; ¹H NMR (300 MHz, CD₂Cl₂) δ 4.50 (s, 2H), 7.27 (dd, *J* = 8.2, 2.3 Hz, 1H), 7.37 (d, *J* = 2.3 Hz, 1H), 7.39–7.49 (m, 5H), 7.66 (d, *J* = 8.2 Hz, 1H); ¹³C NMR (75 MHz, CD₂Cl₂) δ 32.83, 122.81, 128.25, 128.47 (2C), 129.70 (3C), 132.25, 133.91, 137.96, 140.95, 143.37; Anal Calcd for C₁₃H₁₀Br₂: C, 47.89; H, 3.09. Found: C, 48.12; H, 2.96.

6.3.11.3 1,3-Bis(6-bromo-[1,1'-biphenyl]-3-yl)propan-2-one (4-10)

To a solution of 2-bromo-5-(bromomethyl)-1,1'-biphenyl (**4-9**) (1.00 g, 3.07 mmol) and benzyltriethylammonium chloride (21.0 mg, 0.0921 mmol) in dichloromethane (6.75 mL) was added a solution of potassium hydroxide (526 mg, 13.2 mmol) in H₂O (0.560 ml), and the mixture was degassed by Ar bubbling for 30 min and

preheated to 40 °C. Iron pentacarbonyl (0.220 mL, 319 mg, 1.63 mmol) was then added to the mixture dropwise over 5 min. After stirring at 40 °C for 21 h, the reaction was quenched with hydrochloric acid (2M, 7.0 mL), and the aqueous layer was extracted three times with dichloromethane. The combined organic layers were washed three times with brine, dried over sodium sulfate, and evaporated. Purification by silica gel column chromatography (eluent: 3% ethyl acetate/hexane) gave the title compound as a white solid (311 mg, 39% yield): Mp 141.2–141.6 °C; ¹H NMR (300 MHz, CD₂Cl₂) δ 3.78 (s, 4H), 7.04 (dd, *J* = 8.2, 2.3 Hz, 2H), 7.11 (d, *J* = 2.6 Hz, 2H), 7.34–7.47 (m, 10H), 7.62 (d, *J* = 8.2 Hz, 2H); ¹³C NMR (75 MHz, CD₂Cl₂) δ 48.88 (2C), 121.45 (2C), 128.11 (2C), 128.41 (4C), 129.73 (4C), 130.39 (2C), 132.91 (2C), 133.63 (2C), 133.96 (2C), 141.16 (2C), 143.10 (2C), 204.34; HRMS (ESI, positive) *m/z* calcd for C₂₇H₂₀OBr₂Na [M+Na]⁺ 540.9779, found 540.9780; Anal Calcd for C₂₇H₂₀Br₂O: C, 62.33; H, 3.87. Found: C, 61.99; H, 3.61.

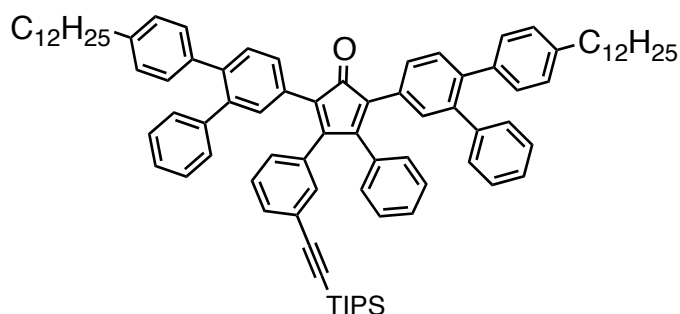
6.3.11.4 1,3-Bis(4-dodecyl-[1,1':2',1''-terphenyl]-4'-yl)propan-2-one (4-12a)



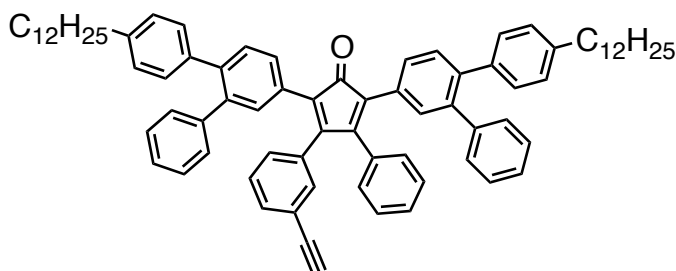
To a degassed suspension of 1,3-bis(6-bromo-[1,1'-biphenyl]-3-yl)propan-2-one (**4-10**) (253 mg, 0.486 mmol), 4-dodecylphenylboronic acid (**4-11**)^{8,9} (394 mg, 1.36 mmol), and potassium carbonate (407 mg, 2.94 mmol) in a mixture of toluene (24 mL), ethanol (6.0 mL), and water (6.0 mL) was added tetrakis(triphenylphosphino)palladium(0) (52.0 mg, 0.0450 mmol). The reaction mixture was further degassed by argon bubbling for 10 min, and then refluxed for 3 h. After cooling to room temperature the aqueous layer was extracted with three times with dichloromethane. The combined organic layers were washed three times with water and once with brine, dried over sodium sulfate, and evaporated. Purification by silica gel column chromatography (eluent: 1% ethyl acetate/hexane) gave the title compound as colorless oil (315 mg, 76% yield): ¹H NMR (300 MHz, CD₂Cl₂) δ 0.89 (t, *J* = 7.0 Hz, 6H), 1.20–1.36 (m, 36H), 1.53–1.64 (m, 4H), 2.56 (t, *J* = 7.9 Hz, 4H), 3.89 (s, 4H), 7.03 (s, 8H), 7.09–7.15 (m, 4H), 7.17–7.26 (m, 10H), 7.37 (d, *J* = 7.7 Hz, 2H); ¹³C NMR (75 MHz, CD₂Cl₂) δ 14.31 (2C), 23.13 (2C), 29.72 (2C), 29.80 (2C), 29.93 (2C), 30.05 (2C), 30.09 (2C), 30.13 (2C), 31.83 (2C), 32.38 (2C), 35.92 (2C), 49.32

(2C), 126.89 (2C), 128.23 (4C), 128.32 (4C), 129.09 (2C), 130.10 (4C), 130.27 (4C), 131.27 (2C), 132.24 (2C), 133.69 (2C), 138.83 (2C), 139.78 (2C), 141.19 (2C), 141.81 (2C), 141.96 (2C), 205.63; HRMS (ESI, positive) m/z calcd for $C_{63}H_{78}ONa$ $[M+Na]^+$ 873.5950, found 873.5966.

6.3.11.5 2,5-Bis(4-dodecyl-[1,1':2',1''-terphenyl]-4'-yl)-3-phenyl-4-{3-[(triisopropylsilyl)ethynyl]phenyl}-2,4-cyclopentadienone (4-13a)

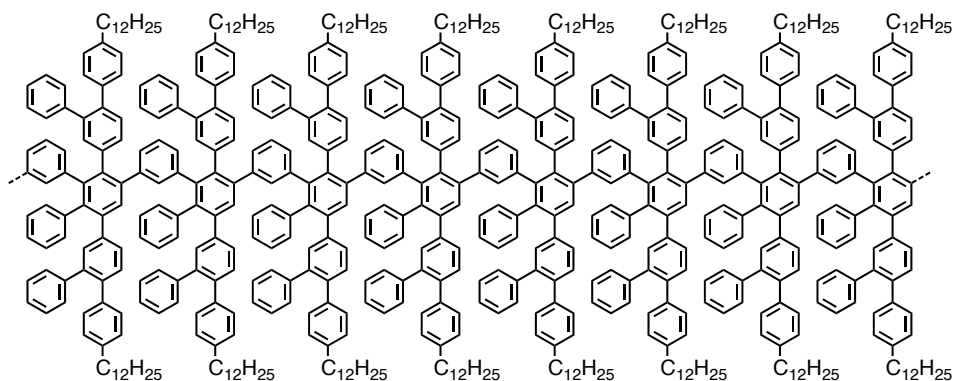


To a degassed solution of 1,3-bis(4-dodecyl-[1,1':2',1''-terphenyl]-4'-yl)propan-2-one (**4-12a**) (301 mg, 0.354 mmol) and 3-[(triisopropylsilyl)ethynyl]benzil (**3-36**) (150 mg, 0.384 mmol) in *tert*-butanol (20 mL) was added at 80 °C a solution of tetrabutylammonium hydroxide in methanol (40%, 0.500 mL, 0.0701 mmol). After stirring at 80 °C for 30 min the reaction was quenched by the addition of hydrochloric acid (1 M, 3.0 mL), diluted with water, and extracted three times with dichloromethane. The combined organic layers were washed three times with brine, dried over sodium sulfate, and evaporated. Purification by silica gel column chromatography (eluent: 25% dichloromethane/hexane) gave the title compound as a purple sticky oil (225 mg, 53% yield): ¹H NMR (300 MHz, CD₂Cl₂) δ 0.90 (t, J = 6.8 Hz, 6H), 1.09 (s, 21H), 1.24–1.36 (m, 36H), 1.54–1.64 (m, 4H), 2.57 (t, J = 8.0 Hz, 4H), 6.92–7.07 (m, 13H), 7.09–7.45 (m, 20H); ¹³C NMR (75 MHz, CD₂Cl₂) δ 11.72 (3C), 14.33 (2C), 18.86 (6C), 23.14 (2C), 29.71 (2C), 29.81 (2C), 29.93 (2C), 30.06 (2C), 30.10 (4C), 30.13 (2C), 31.82 (2C), 32.38 (2C), 35.93 (2C), 91.88, 106.79, 123.90, 125.38, 125.65, 126.79 (2C), 128.14 (4C), 128.28 (2C), 128.33 (2C), 128.60, 128.72 (2C), 129.13, 129.43, 129.50, 129.70 (2C), 129.86, 129.92, 130.02, 130.06 (2C), 130.14 (2C), 130.21 (4C), 130.75, 130.81, 132.15, 132.74, 132.88, 133.48, 133.76, 133.87, 138.75 (2C), 140.15, 140.38, 140.45, 140.64, 141.89 (2C), 141.92, 141.94, 154.08, 155.35, 200.68; HRMS (ESI, positive) m/z calcd for $C_{88}H_{104}OSiNa$ $[M+Na]^+$ 1227.7754, found 1227.7804.

6.3.11.6 2,5-Bis(4-dodecyl-[1,1':2',1''-terphenyl]-4'-yl)-3-(3-ethynylphenyl)-4-phenyl-2,4-cyclopentadienone (4-1a)

To a solution of 2,5-bis(4-dodecyl-[1,1':2',1''-terphenyl]-4'-yl)-3-phenyl-4-{3-[(triisopropylsilyl)ethynyl]phenyl}-2,4-cyclopentadienone (**4-13a**) (131 mg, 0.109 mmol) in dry tetrahydrofuran (10 mL) was added a solution of tetra-*n*-butylammonium fluoride in tetrahydrofuran (14.0 mM, 8.20 mL, 0.115 mmol) dropwise over 3 min. After stirring at room temperature for 10 min, water was added to the reaction mixture and tetrahydrofuran was removed in vacuo at 40 °C. The resulting suspension was extracted three times with dichloromethane, and the combined organic layers were washed five times with water, dried over sodium sulfate, and evaporated at 40 °C. Purification by silica gel column chromatography (eluent: 30% dichloromethane/hexane) gave the title compound as a purple sticky oil (101 mg, 89% yield): ¹H NMR (300 MHz, CD₂Cl₂) δ 0.93 (t, *J* = 6.8 Hz, 6H), 1.24–1.40 (m, 36H), 1.54–1.68 (m, 4H), 2.59 (t, *J* = 8.1 Hz, 4H), 3.11 (s, 1H), 6.96–7.22 (m, 22H), 7.24–7.43 (m, 10H), 7.49 (dt, *J* = 7.7, 1.4 Hz, 1H); ¹³C NMR (75 MHz, CD₂Cl₂) δ 14.37 (2C), 23.17 (2C), 29.74 (2C), 29.84 (2C), 29.96 (2C), 30.08 (2C), 30.12 (4C), 30.16 (2C), 31.83 (2C), 32.40 (2C), 35.96 (2C), 78.22, 83.21, 122.69, 125.29, 125.80, 126.81, 126.85, 128.16 (2C), 128.20 (2C), 128.35 (4C), 128.76 (2C), 128.84, 129.13, 129.46 (2C), 129.72 (2C), 129.84, 130.04 (4C), 130.11, 130.21 (5C), 130.80, 130.86, 132.54, 132.87, 132.90, 133.08, 133.64, 134.36, 138.70, 138.75, 140.20, 140.40, 140.49, 140.62, 141.88 (2C), 141.92, 141.95, 154.07, 155.29, 200.64; HRMS (ESI, positive) *m/z* calcd for C₇₉H₈₄ONa [M+Na]⁺ 1071.6420, found 1071.6425.

6.3.11.7 Polyphenylene precursor 4-2a (isomeric mixture)



Typical procedure for *Diels–Alder* polymerization in a Ph₂O solution

A degassed solution of 2,5-bis(4-dodecyl-[1,1':2,1''-terphenyl]-4'-yl)-3-(3-ethynylphenyl)-4-phenyl-2,4-cyclopentadienone (**4-1a**) (92.6 mg, 0.0882 mmol) in diphenyl ether (0.400 mL, 221 mM) was refluxed for 20 h using a heating mantle. The purple color disappeared and the solution turned pale yellow, indicating the completion of the polymerization. After cooling to room temperature, diphenyl ether was distilled off under reduced pressure to give crude polymer **4-2a** with M_w of 36,000–66,000 g/mol, M_n of 16,000–24,000 g/mol, and PDI of 2.3–2.5 based on the SEC analysis with PPP and PS standards. Subsequent removal of the low-molecular-weight oligomers through fractionation of **4-2a** with recycling preparative SEC (Waters Ultrastaygel 103 Å, 19 × 300 mm, eluent: chloroform, 2.0 mL/min) to yielded 60.8 mg (67% yield) of precursor **4-2a'** as a pale yellow solid with M_w of 42,000–78,000 g/mol, M_n of 31,000–53,000 g/mol, and PDI of 1.4–1.5. The rest of the polymer fractions were separated again by using recycling preparative SEC to yield 7.10 mg (7.9% yield) of precursor **4-2a''** with M_w of 46,000–86,000 g/mol, M_n of 36,000–63,000 g/mol, and PDI of 1.3–1.4 as well as 8.15 mg (9.0% yield) of precursor **4-2a'''** with M_w of 11,000–16,000 g/mol, M_n of 9,000–13,000 g/mol, and PDI of 1.2 as pale yellow solids. Pentamer **4-15** could also be isolated as a pale yellow solid (2.29 mg, 2.6% yield).

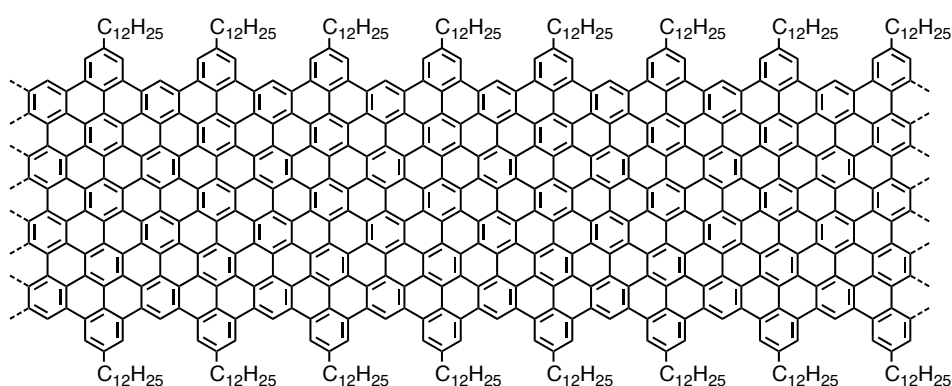
General procedure for *Diels–Alder* polymerization in a melt

A purple sticky oil of 2,5-bis(4-dodecyl-[1,1':2,1''-terphenyl]-4'-yl)-3-(3-ethynylphenyl)-4-phenyl-2,4-cyclopentadienone (**4-1a**) was heated under argon at 260–270 °C using a heating mantle. The disappearance of the purple color, turning pale yellow, indicated the completion of the polymerization. After cooling to room temperature the resulting polymer was dissolved in tetrahydrofuran with a help of

sonication, filtered, and dried in vacuo to obtain precursor **4-2a** as pale yellow solid. The fractionation was performed with recycling preparative SEC (Japan Analytical Industry JAIGEL-2H+2.5H, eluent: chloroform, 2.0 mL/min).

FTIR (powder) 3,082, 3,058, 3,025, 2,923, 2,853, 1,600, 1,573, 1,484, 1454, 1443, 1,373, 1259, 893, 812, 773, 698 cm^{-1} ; ^1H NMR (300 MHz, CD_2Cl_2) δ 0.87, 1.26, 2.49, 6.70, 6.84, 6.96, 7.06.

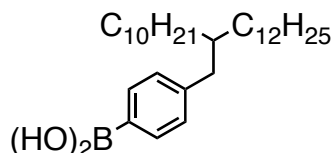
6.3.11.8 Laterally extended GNR 4-3a with dodecyl chains



A solution of polyphenylene precursor **4-2a'** (37.7 mg) in unstabilized dichloromethane (160 mL) was degassed by argon bubbling for 10 min. To the degassed solution was added a suspension of iron(III) chloride (1.30 g, 8.01 mmol, 7 eq. for one hydrogen to be removed) in nitromethane (10 mL). After stirring at room temperature for 97 h under continuous bubbling with argon presaturated with dichloromethane, the reaction was quenched by addition of methanol to form bluish black precipitates. The precipitates were collected by filtration with a membrane filter, washed with methanol and tetrahydrofuran, and then sonicated for 30 min in tetrahydrofuran (50 mL). The precipitates were again collected by filtration with a membrane filter, washed with tetrahydrofuran, and then sonicated for 60 min in *N*-methyl-2-pyrrolidone (25 mL). The precipitates were again collected by filtration with a membrane filter, and washed with tetrahydrofuran and *N*-methyl-2-pyrrolidone to give the title compound as bluish black powder (28.7 mg, 78% yield): FTIR (powder) 2915, 2845, 1675, 1587, 1446, 1287, 1189, 1078, 863, 810, 757, 718 cm^{-1} ; Raman (powder, 488 nm, 0.2 mW) 3211, 2931, 2647, 1608, 1327 cm^{-1} .

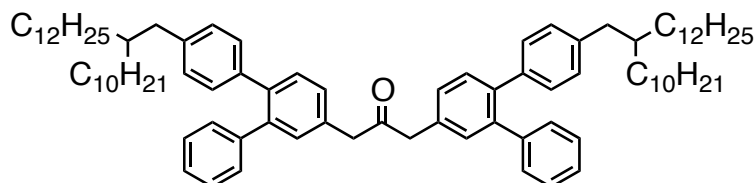
6.3.12 Synthesis of laterally extended GNR **4-3b** with 2-decyltetradecyl chains

6.3.12.1 4-(2-Decyltetradecyl)phenylboronic acid (**4-6**)

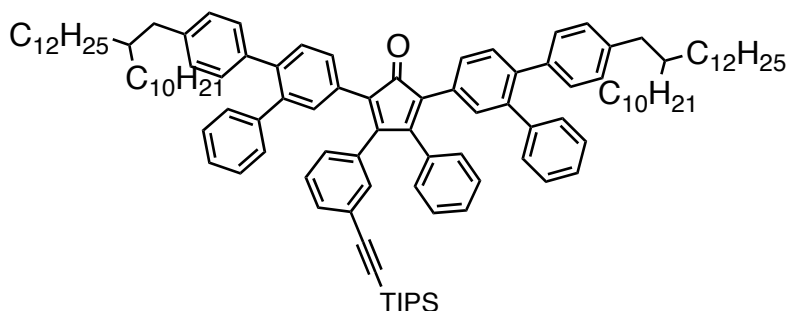


Dry *N,N*-dimethylacetamide (15 mL) was added to zinc (4.30 g, 65.7 mmol) and iodine (1.14 g, 4.49 mmol), and stirred at room temperature until the purple color of iodine disappeared. 2-Decyltetradecylbromide (**3-27**)⁷ (18.4 g, 44.1 mmol) was then added to the mixture and stirred at 80 °C for 19 h to generate 2-decyltetradecylzinc bromide. To 1-bromo-4-(trimethylsilyl)benzene (**4-4**) (4.97 g, 21.7 mmol) and dichloro[1,1'-bis(diphenylphosphino)-ferrocene]palladium(II) (0.916 g, 1.16 mmol) was added via a cannula the solution of 2-decyltetradecylzinc bromide. The reaction mixture was stirred at room temperature for 7.5 h, and then quenched by hydrochloric acid (1 M, 40 mL). The aqueous layer was extracted three times with dichloromethane. The combined organic layers were washed five times with water, dried over sodium sulfate, and evaporated. The crude material was subjected to silica gel column chromatography (eluent: 0–10% dichloromethane/hexane) to give a mixture of 1-(2-decyltetradecyl)-4-(trimethylsilyl)benzene (**4-5**) and **3-27** (14.8 g). To the mixture of **4-5** and **3-27** dissolved in dry dichloromethane (40 mL) was added boron tribromide (3.10 mL, 8.20 g, 32.7 mmol). The reaction mixture was stirred at room temperature for 20 h, and then carefully quenched by slowly adding water. The aqueous layer was extracted three times with dichloromethane. The combined organic layers were washed twice with brine, dried over magnesium sulfate, and evaporated. Purification by silica gel column chromatography (eluent: 30% ethyl acetate/hexane) yielded the title compound as pale yellow oil (7.93 g, 79% yield in two steps): ¹H NMR (300 MHz, CD₂Cl₂) δ 0.84–0.91 (m, 6H), 1.17–1.38 (m, 40H), 1.64–1.76 (m, 1H), 2.62 (d, *J* = 6.9 Hz, 2H), 7.31 (d, *J* = 7.7 Hz, 4H), 8.14 (d, *J* = 7.7 Hz, 2H); ¹³C NMR (75 MHz, CD₂Cl₂) δ 14.25 (2C), 23.07 (2C), 26.88 (2C), 29.74 (2C), 30.04 (8C), 30.35 (2C), 32.31 (2C), 33.59 (2C), 40.02, 41.27, 129.34 (2C), 135.80 (2C), 147.61 (2C); HRMS (ESI, positive) *m/z* calcd for C₃₀H₅₅BO₂Na [M+Na]⁺ 480.4229, found 480.4249.

6.3.12.2 1,3-Bis[4-(2-decyltetradecyl)-[1,1':2',1''-terphenyl]-4'-yl]propan-2-one (4-12b)

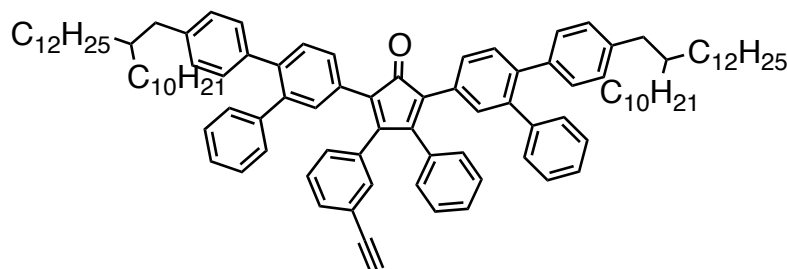


To a degassed suspension of 1,3-bis(6-bromo-[1,1'-biphenyl]-3-yl)propan-2-one (**4-10**) (168 mg, 0.323 mmol), 4-(2-decyltetradecyl)phenylboronic acid (**4-6**) (608 mg, 1.33 mmol), and potassium carbonate (268 mg, 1.94 mmol) in a mixture of toluene (20 mL), ethanol (5.0 mL), and water (5.0 mL) was added tetrakis(triphenylphosphino)palladium(0) (22.7 mg, 0.0196 mmol). The reaction mixture was further degassed by argon bubbling for 10 min, and then refluxed at 100 °C for 15 h. After cooling to room temperature the aqueous layer was extracted with dichloromethane. The combined organic layers were washed three times with water, dried over sodium sulfate, and evaporated. Purification by silica gel column chromatography (eluent: 35% dichloromethane/hexane) gave the title compound as colorless oil (340 mg, 89% yield): ^1H NMR (300 MHz, CD_2Cl_2) δ 0.85–0.91 (m, 12H), 1.15–1.36 (m, 80H), 1.54–1.64 (m, 2H), 2.48 (d, $J = 7.1$ Hz, 4H), 3.89 (s, 4H), 6.96–7.03 (m, 8H), 7.08–7.14 (m, 4H), 7.15–7.26 (m, 10H), 7.39 (d, $J = 7.7$ Hz, 2H); ^{13}C NMR (75 MHz, CD_2Cl_2) δ 14.31 (4C), 23.12 (4C), 26.93 (4C), 29.79 (4C), 30.08 (8C), 30.11 (8C), 30.43 (4C), 32.36 (4C), 33.56 (4C), 40.04 (2C), 40.54 (2C), 49.30 (2C), 126.85 (2C), 128.18 (4C), 129.06 (2C), 120.10 (4C), 129.93 (4C), 130.26 (4C), 131.16 (2C), 132.17 (2C), 133.67 (2C), 138.74 (2C), 139.82 (2C), 140.75 (2C), 141.17 (2C), 141.87 (2C), 205.64; MS (MALDI-TOF, positive) m/z calcd for $\text{C}_{87}\text{H}_{126}\text{O}$ $[\text{M}]^+$ 1187.9, found: 1185.0; Anal Calcd for $\text{C}_{87}\text{H}_{126}\text{O}$: C, 87.96; H, 10.69. Found: C, 87.83; H, 10.77.

6.3.12.3 2,5-Bis[4-(2-decyltetradecyl)-[1,1':2',1''-terphenyl]-4'-yl]-3-phenyl-4-{3-[(triisopropylsilyl)ethynyl]phenyl}-2,4-cyclopentadienone (4-13b)

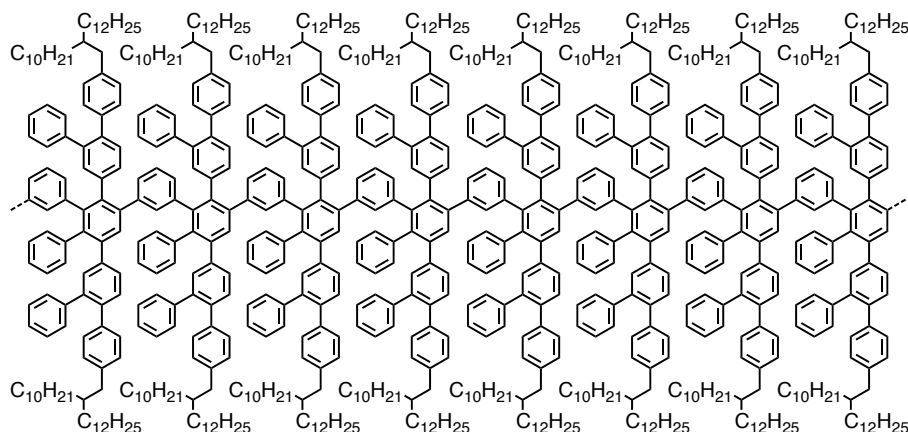
To a degassed solution of 1,3-bis[4-(2-decyltetradecyl)-[1,1':2',1''-terphenyl]-4'-yl]propan-2-one (**4-12b**) (152 mg, 0.128 mmol) and 3-[(triisopropylsilyl)ethynyl]benzil (**3-36**) (56.0 mg, 0.143 mmol) in *tert*-butanol (10 mL) was added at 80 °C a solution of tetrabutylammonium hydroxide in methanol (1.0 M, 0.050 mL, 0.050 mmol). After stirring at 80 °C for 20 min the reaction was quenched by addition of hydrochloric acid (1.0 M, 1.0 mL). The reaction mixture was diluted with dichloromethane, washed twice with water and once with brine, dried over sodium sulfate, and evaporated. Purification by silica gel column chromatography (eluent: 15% dichloromethane/hexane) gave the title compound as a purple sticky oil (141 mg, 71% yield): ^1H NMR (300 MHz, CD_2Cl_2) δ 0.84–0.92 (m, 12H), 1.07 (s, 21H), 1.18–1.35 (m, 80H), 1.54–1.62 (m, 2H), 2.47 (d, $J = 7.0$ Hz, 4H), 6.89–7.04 (m, 13H), 7.08–7.43 (m, 20H); ^{13}C NMR (75 MHz, CD_2Cl_2) δ 11.75 (3C), 14.37 (4C), 18.89 (6C), 23.18 (4C), 26.99 (4C), 29.85 (4C), 30.14 (8C), 30.18 (8C), 30.48 (4C), 32.42 (4C), 33.63 (4C), 40.09 (2C), 40.62 (2C), 91.88, 106.81, 123.92, 125.40, 125.69, 126.79 (2C), 128.13 (4C), 128.61, 128.74 (2C), 129.09 (2C), 129.15 (3C), 129.45, 129.52, 129.73 (2C), 129.90 (3C), 129.94 (3C), 130.16, 130.24 (4C), 130.69, 130.75, 132.16, 132.72, 132.85, 133.53, 133.80, 133.89, 138.69, 138.70, 140.25, 140.48 (2C), 140.67, 141.86, 140.89, 141.85, 141.92, 154.07, 155.32, 200.68; HRMS (ESI, positive) m/z calcd for $\text{C}_{112}\text{H}_{153}\text{OSi}$ $[\text{M}+\text{H}]^+$ 1542.1691, found 1542.1680.

6.3.12.4 2,5-Bis[4-(2-decyltetradecyl)-[1,1':2',1''-terphenyl]-4'-yl]-3-(3-ethynylphenyl)-4-phenyl-2,4-cyclopentadienone (4-1b)



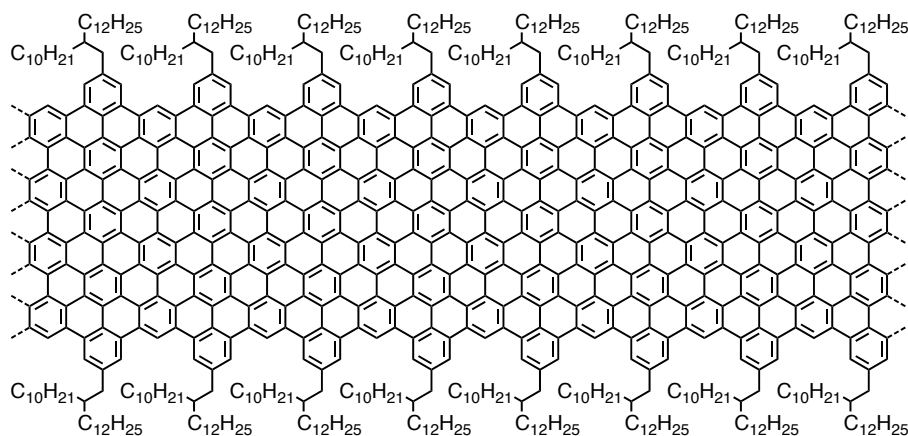
To a solution of 2,5-bis[4-(2-decyltetradecyl)-[1,1':2',1''-terphenyl]-4'-yl]-3-phenyl-4-{3-[(triisopropylsilyl)ethynyl]phenyl}-2,4-cyclopentadienone (**4-13b**) (106 mg, 0.0685 mmol) in dry tetrahydrofuran (10 mL) was added a solution of tetra-*n*-butylammonium fluoride in tetrahydrofuran (14.0 mM, 5.13 mL, 0.0719 mmol) dropwise over 3 min. After stirring at room temperature for 10 min, water was added to the reaction mixture and tetrahydrofuran was removed in vacuo at 40 °C. The resulting suspension was extracted three times with dichloromethane, and the combined organic layers were washed five times with water, dried over sodium sulfate, and evaporated at 40 °C. Purification by silica gel column chromatography (eluent: 15% dichloromethane/hexane) gave the title compound as a purple sticky oil (47.2 mg, 50% yield): ¹H NMR (300 MHz, CD₂Cl₂) δ 0.86–0.92 (m, 12H), 1.16–1.35 (m, 80H), 1.53–1.65 (m, 2H), 2.48 (d, *J* = 6.9 Hz, 4H), 3.10 (s, 1H), 6.90–7.04 (m, 12H), 7.06–7.17 (m, 9H), 7.22–7.40 (m, 11H), 7.46 (dt, *J* = 7.9, 1.4 Hz, 1H); ¹³C NMR (75 MHz, CD₂Cl₂) δ 14.32 (4C), 23.13 (4C), 26.93 (4C), 29.80 (4C), 30.09 (8C), 30.12 (8C), 30.43 (4C), 32.37 (4C), 33.57 (4C), 40.04 (2C), 40.57 (2C), 78.14, 83.18, 122.64, 125.28, 125.79, 126.79, 126.80, 128.09 (2C), 128.12 (2C), 128.72 (2C), 128.80, 129.11 (5C), 129.41 (2C), 129.69 (2C), 129.82, 129.86 (4C), 130.09, 130.20 (6C), 130.67, 130.73, 132.51, 132.76, 132.79, 133.05, 133.62, 134.34, 138.61, 138.65, 140.25, 140.44, 140.47, 140.60, 140.89, 140.91, 141.80, 154.04, 155.26, 200.64; HRMS (ESI, positive) *m/z* calcd for C₁₀₃H₁₃₃O [M+H]⁺ 1386.0356, found 1386.0356.

6.3.12.5 Polyphenylene precursor 4-2b (isomeric mixture)



Typical procedure for *Diels–Alder* polymerization in a Ph₂O solution-1

A degassed solution of 2,5-bis[4-(2-decyltetradecyl)-[1,1':2',1''-terphenyl]-4'-yl]-3-(3-ethynylphenyl)-4-phenyl-2,4-cyclopentadienone (**4-1b**) (27.8 mg, 0.0201 mmol) in diphenyl ether (0.020 mL, 1.0 M) was refluxed for 14 h using a heating mantle. The purple color disappeared and the solution turned pale yellow, indicating the completion of the polymerization. After cooling to room temperature diphenyl ether was distilled off under reduced pressure at 120 °C to give crude polymer **4-2b-II** with M_w of 190,000–460,000 g/mol, M_n of 34,000–51,000 g/mol, and PDI of 5.6–9.0 based on the SEC analysis with PPP and PS standards. Subsequently, low-molecular-weight oligomers were removed by fractionation of **4-2b-II** with recycling preparative SEC (Japan Analytical Industry JAIGEL-2H+2.5H, eluent: chloroform, 2.0 mL/min) to give precursor **4-2b-II-1** (6.3 mg, 23%) with M_w of 250,000–620,000 g/mol, M_n of 110,000–220,000 g/mol, and PDI of 2.3–2.8, precursor **4-2b-II-2** (13.8 mg, 51%) with M_w of 200,000–480,000 g/mol, M_n of 66,000–110,000 g/mol, and PDI of 3.0–4.4, and precursor **4-2b-II-3** (6.3 mg, 23%) with M_w of 120,000–290,000 g/mol, M_n of 14,000–20,000 g/mol, and PDI of 8.6–15 (in total 26.4 mg, 97% yield). Precursor fractions **4-2b-II-2** and **4-2b-II-3** were combined and further fractionated by recycling preparative SEC to yield **4-2b-II-4** (7.0 mg) with M_w of 260,000–630,000 g/mol, M_n of 130,000–240,000 g/mol, and PDI of 2.0–2.6 as well as precursor **4-2b-II''** (5.1 mg) with M_w of 160,000–360,000 g/mol, M_n of 76,000–140,000 g/mol, and PDI of 2.1–2.6. Precursor fractions **4-2b-II-1** and **4-2b-II-4** showed the same molecular weights, considering the margin of error of $\pm 10\%$ for the SEC analysis, and thus were combined to precursor **4-2b-II'**: $^1\text{H NMR}$ (300 MHz, CD_2Cl_2) δ 0.86, 1.25, 2.44, 6.69, 6.79, 6.92, 7.02.

6.3.12.6 Laterally extended GNR 4-3b with 2-decyltetradecyl chains

A solution of polyphenylene precursor **4-2b-II'** (13.3 mg) in unstabilized dichloromethane (40 mL) was degassed by argon bubbling for 20 min. To the degassed solution was added a suspension of iron(III) chloride (334 mg, 2.06 mmol, 7 eq. for one hydrogen to be removed) in nitromethane (3.0 mL). After stirring at room temperature for 72 h under continuous bubbling with argon presaturated with dichloromethane, the reaction was quenched by addition of methanol to form bluish black precipitates. The precipitates were collected by filtration with a membrane filter, washed intensively with methanol and tetrahydrofuran, and then immersed in 2 N hydrochloric acid over night. After washing with water and THF, the precipitates were sonicated in THF (60 mL) for 1 h, diluted with MeOH, filtered through a membrane filter, and washed with MeOH to give GNR **4-3b** as a bluish black powder (11.8 mg, 91% yield).

6.4 References

- (1) Schwab, M. G.; Narita, A.; Hernandez, Y.; Balandina, T.; Mali, K. S.; De Feyter, S.; Feng, X.; Müllen, K. *J. Am. Chem. Soc.* **2012**, *134*, 18169.
- (2) El Gemayel, M.; Narita, A.; Dössel, L.; Sundaram, R.; Kiersnowski, A.; Pisula, W.; Hansen, M. R.; Ferrari, A.; Orgiu, E.; Feng, X.; Müllen, K.; Samori, P. *Nanoscale*, **2014**, Accepted Manuscript, DOI: 10.1039/C4NR00256C.
- (3) Li, Q.; Rukavishnikov, A. V.; Petukhov, P. A.; Zaikova, T. O.; Jin, C.; Keana, J. F. W. *J. Org. Chem.* **2003**, *68*, 4862.
- (4) Angelova, P.; Vieker, H.; Weber, N.-E.; Matei, D.; Reimer, O.; Meier, I.; Kurasch, S.; Biskupek, J.; Lorbach, D.; Wunderlich, K.; Chen, L.; Terfort, A.; Klapper, M.; Müllen, K.; Kaiser, U.; Götzhäuser, A.; Turchanin, A. *ACS Nano* **2013**, *7*, 6489.
- (5) Fogel, Y.; Zhi, L.; Rouhanipour, A.; Andrienko, D.; Räder, H. J.; Müllen, K. *Macromolecules* **2009**, *42*, 6878.
- (6) Sauriat-Dorizon, H.; Maris, T.; Wuest, J. D.; Enright, G. D. *J. Org. Chem.* **2003**, *68*, 240.
- (7) Kastler, M.; Pisula, W.; Wasserfallen, D.; Pakula, T.; Müllen, K. *J. Am. Chem. Soc.* **2005**, *127*, 4286.
- (8) Porada, J. H.; Neudörfl, J.; Blunk, D. *Cryst. Growth Des.* **2011**, *11*, 3648.
- (9) Horiba, K.; Hirose, H.; Imai, A.; Sato, K.; Agata, T. U.S. Pat. Appl. Publ., 20100243995, 30 Sep, 2010.
- (10) Przybilla, L.; Brand, J. D.; Yoshimura, K.; Räder, J.; Müllen, K. *Anal. Chem.* **2000**, *72*, 4591.
- (11) Feike, M.; Demco, D. E.; Graf, R.; Gottwald, J.; Hafner, S.; Spiess, H. W. *J. Magn. Reson. Ser. A* **1996**, *122*, 214.
- (12) Saalwächter, K.; Lange, F.; Matyjaszewski, K.; Huang, C.-F.; Graf, R. *J. Magn. Reson.* **2011**, *212*, 204.
- (13) Frye, J. S.; Maciel, G. E. *J. Magn. Reson.* **1982**, *48*, 125.
- (14) Hayashi, S.; Hayamizu, K. *Bull. Chem. Soc. Jpn.* **1991**, *64*, 685.
- (15) Ulbricht, R.; Hendry, E.; Shan, J.; Heinz, T.; Bonn, M. *Rev. Mod. Phys.* **2011**, *83*, 543.
- (16) Parr, R. G.; Yang, W. *Density Functional Theory of Atoms and Molecules*; Oxford University Press: New York, 1989.

-
- (17) Heyd, J.; Scuseria, G. E.; Ernzerhof, M. *J. Chem. Phys.* **2003**, *118*, 8207.
- (18) Heyd, J.; Scuseria, G. E.; Ernzerhof, M. *J. Chem. Phys.* **2006**, *124*, 219906.
- (19) Rassolov, V. A.; Ratner, M. A.; Pople, J. A.; Redfern, P. C.; Curtiss, L. A. *J. Comp. Chem.* **2001**, *22*, 976.
- (20) Frisch, M. J. *Gaussian 09, Revision A.1*; Gaussian, Inc., Wallingford, 2009.
- (21) Ito, S.; Wehmeier, M.; Brand, J. D.; Kübel, C.; Epsch, R.; Rabe, J. P.; Müllen, K. *Chem.—Eur. J.* **2000**, *6*, 4327.
- (22) Wasserfallen, D.; Kastler, M.; Pisula, W.; Hofer, W. A.; Fogel, Y.; Wang, Z.; Müllen, K. *J. Am. Chem. Soc.* **2006**, *128*, 1334.
- (23) Yan, X.; Cui, X.; Li, B.; Li, L.-s. *Nano Lett.* **2010**, *10*, 1869.
- (24) Li, J.; Huang, P. *Beilstein J. Org. Chem.* **2011**, *7*, 426.
- (25) Iyer, V. S.; Wehmeier, M.; Brand, J. D.; Keegstra, M. A.; Müllen, K. *Angew. Chem. Int. Ed. Engl.* **1997**, *36*, 1604.
- (26) Wehmeier, M.; Wagner, M.; Müllen, K. *Chem.—Eur. J.* **2001**, *7*, 2197.
- (27) Huang, L.; Cheng, K.; Yao, B.; Xie, Y.; Zhang, Y. *J. Org. Chem.* **2011**, *76*, 5732.
- (28) Varughese, S.; Draper, S. M. *Cryst. Growth Des.* **2010**, *10*, 2298.
- (29) Sadhukhan, S. K.; Viala, C.; Gourdon, A. *Synthesis* **2003**, *10*, 1521.
- (30) Tan, Y.-Z.; Tang, B.; Parvez, K.; Narita, A.; Osella, S.; Beljonne, D.; Feng, X.; Müllen, K. *Nat. Commun.* **2013**, *4*, 2646.

List of Publications

Scientific publications

- (1) H. C. Hesse, C. Schaffer, C. Hundschell, A. Narita, X. Feng, K. Müllen, B. Nickel, L. Schmidt-Mende, Large polycyclic aromatic hydrocarbons for application in donor–acceptor photovoltaics. *Phys. Status Solidi A*, **2012**, *209*, 785–789.
- (2) S. Osella, A. Narita, M. Schwab, Y. Hernandez, X. Feng, K. Müllen, D. Beljonne, Graphene nanoribbons as low-band-gap donor materials for organic photovoltaics: Quantum-chemical aided design. *ACS Nano*, **2012**, *6*, 5539–5548.
- (3) M. G. Schwab, A. Narita, Y. Hernandez, T. Balandina, K. Mali, S. De Feyter, X. Feng, K. Müllen, Structurally defined graphene nanoribbons with high lateral extension. *J. Am. Chem. Soc.*, **2012**, *134*, 18169–18172.
- (4) B. Singh, B. R. Mehta, D. Varandani, Govind, A. Narita, X. Feng, K. Müllen, Bipolar resistive switching properties of Ti-CuO/(hexafluoro-hexa-*peri*-hexabenzocoronene)-Cu hybrid interface device: Influence of electronic nature of organic layer. *J. Appl. Phys.*, **2013**, *113*, 203706.
- (5) K. Harano, A. Narita, E. Nakamura, Photocrosslinking of fullerene vesicles that prevents phase transition and decreases water permeation. *Chem. Lett.*, **2013**, *42*, 1176–1178. (Editor’s Choice)
- (6) S. A. Jensen, R. Ulbricht, A. Narita, X. Feng, K. Müllen, T. Hertel, D. Turchinovich, M. Bonn, Ultrafast photoconductivity of graphene nanoribbons and carbon nanotubes. *Nano Lett.*, **2013**, *13*, 5925–5930.
- (7) Y.-Z. Tan, B. Yang, K. Parvez, A. Narita, S. Osella, D. Beljonne, X. Feng, K. Müllen, Atomically precise edge chlorination of graphenes. *Nat. Commun.*, **2013**, *4*, 2646.

- (8) A. Narita, X. Feng, Y. Hernandez, S. A. Jensen, M. Bonn, H. Yang, I. A. Verzhbitskiy, C. Casiraghi, M. R. Hansen, A. H. R. Koch, G. Fytas, O. Ivasenko, B. Li, K. S. Mali, T. Balandina, S. Mahesh, S. De Feyter, K. Müllen, Synthesis of structurally well-defined and liquid-phase-processable graphene nanoribbons. *Nature Chem.*, **2014**, *6*, 126–132.
- (9) M. El Gemayel, A. Narita, L. F. Dössel, R. S. Sundaram, A. Kiersnowski, W. Pisula, A. C. Ferrari, E. Orgiu, X. Feng, K. Müllen, P. Samori, Graphene nanoribbons blends with P3HT: towards enhanced device performance. *Nanoscale*, **2014**, Accepted Manuscript, DOI: 10.1039/C4NR00256C.
- (10) K. Harano, A. Narita, E. Nakamura, Photo-cross-linking of exterior of fullerene bilayer that prevents vesicle aggregation. *Chem. Lett.*, **2014**, Advanced Publication, DOI: 10.1246/cl.140143.
- (11) A. Abbas, G. Liu, A. Narita, M. Orosco, X. Feng, K. Müllen, C. Zhou, Deposition, characterization, and thin-film-based chemical sensing of ultra-long chemically synthesized graphene nanoribbons, *submitted*.
- (12) A. Narita, K. S. Mali, W. Frederickx, I. A. Verzhbitskiy, A. H. R. Koch, M. R. Hansen, G. Fytas, C. Casiraghi, S. De Feyter, X. Feng, K. Müllen, Synthesis of laterally and longitudinally extended graphene nanoribbons. *in preparation*.

Patents

- (1) M. G. Schwab, A. Narita, X. Feng, K. Müllen, Polymeric Precursors for Producing Graphene Nanoribbons and Methods for Preparing Them. WO2013093756 A1, June 27, 2013.
- (2) M. G. Schwab, A. Narita, X. Feng, K. Müllen, Polymeric Precursors for Producing Graphene Nanoribbons and Suitable Oligophenylene Monomers for Preparing Them. *applied*.

Curriculum Vitae

Personal Details

Name: Akimitsu Narita
Place of birth: Yokohama, Japan
Nationality: Japanese
Marital status: Single

University Education

April 2010 – January 2014	PhD studies, Max Planck Institute for Polymer Research Mainz Research adviser: ██████████
April 2008 – March 2010	Master thesis, Department of Chemistry, Graduate School of Science, The University of Tokyo Research adviser: ██████████ Thesis title: <i>Photomodification of the Fullerene Bilayer Vesicles.</i>
April 2008 – March 2010	Master course, Department of Chemistry, Graduate School of Science, The University of Tokyo
April 2007 – March 2008	Bachelor thesis, Department of Chemistry, Faculty of Science, The University of Tokyo Research adviser: ██████████ Thesis title: <i>Construction of Photoresponsive Fullerene Bilayer Vesicles.</i>
April 2004 – March 2008	Bachelor course, Department of Chemistry, Faculty of Science, The University of Tokyo

School Education

April 2001 – March 2004	Kanagawa Prefectural Hakuyo Senior High School, Yokohama, Japan
April 1998 – March 2001	Yokohama City Municipal Noba Junior High School, Yokohama, Japan
April 1992 – March 1998	Yokohama City Municipal Noba Elementary School, Yokohama, Japan

Awards and Fellowships

May 2010 – April 2013	Early-Stage Researcher (ESR), Marie Curie Initial Training Network (ITN) “SUPERIOR” (SUPramolEculaR functional nanoscale archItectures for Organic electronics: a multi-site initial tRaining action)
October 2012	2 nd place Best Poster Award, MPI-P Posterday 2012, awarded by the Association for the Promotion of Polymer Research – Mainz

Acknowledgements

Finally, I would like to thank my family, grandparents, and girlfriend as well as her family and grandparents for their continuous and considerate support and understanding during my PhD studies.

Many thanks also to everybody I might have unintentionally forgotten to mention here.